The chemistry of interstellar Complex Organic Molecules (iCOMs) : modelling and comparison with observations

Arezu Dehghanfar

Université Grenoble Alpes

THÈSE

Pour obtenir le grade de

DOCTEUR DE L'UNIVERSITÉ GRENOBLE ALPES

Spécialité : Astrophysique et Milieux dilues
Arrêté ministériel : 25 mai 2016

Présentée par

Arezu DEHGHANFAR

Thèse dirigée par **Cecilia CECCARELLI,** Astronome, Université Grenoble Alpes

préparée au sein du **Laboratoire Institut de Planétologie et d'Astrophysique de Grenoble**
dans **l'École Doctorale Physique**

La chimie des molécules organiques complexes interstellaires (iCOMs): modélisation et comparaison avec les observations

The chemistry of interstellar Complex Organic Molecules (iCOMs): modelling and comparison with observations

Thèse soutenue publiquement le **28 mars 2022**,
devant le jury composé de :

Monsieur Herve BEUST
ASTRONOME, UNIVERSITE GRENOBLE ALPES, Président
Madame Serena VITI
Professeur, Universiteit Leiden, Rapporteure
Madame Stephanie CAZAUX
Professeur associé, DELFT University of Technology, Rapporteure
Monsieur Claudio CODELLA
Astronome Osservatorio Astrofisico di Arcetri, Examinateur
Madame Ana Lopez Sepulcre
Astronome adjoint, UNIVERSITE GRENOBLE ALPES, Examinatrice
Monsieur François Dulieu
PROFESSEUR LERMA, CY Cergy Paris Université, Membre invité
Monsieur Patrice Theule
PROFESSEUR Aix-Marseille Université, Membre invité

UNIVERSITE GRENOBLE ALPES

DOCTORAL THESIS

The chemistry of interstellar Complex Organic Molecules (iCOMs): modelling and comparison with observations

Author:
Arezu WITZEL-DEHGHANFAR

Supervisor:
Prof. Cecilia CECCARELLI

A thesis submitted in fulfillment of the requirements for the degree of Doctor of Philosophy

in the

Dawn of Organic Chemistry
Institut de Planétologie et d'Astrophysique de Grenoble

March 28th, 2022

Declaration of Authorship

I, Arezu WITZEL-DEHGHANFAR, declare that this thesis titled, "The chemistry of interstellar Complex Organic Molecules (iCOMs): modelling and comparison with observations" and the work presented in it are my own. I confirm that:

- This work was done wholly or mainly while in candidature for a research degree at this University.
- Where any part of this thesis has previously been submitted for a degree or any other qualification at this University or any other institution, this has been clearly stated.
- Where I have consulted the published work of others, this is always clearly attributed.
- Where I have quoted from the work of others, the source is always given. With the exception of such quotations, this thesis is entirely my own work.
- I have acknowledged all main sources of help.
- Where the thesis is based on work done by myself jointly with others, I have made clear exactly what was done by others and what I have contributed myself.

Signed: _____

Date: _____

UNIVERSITE GRENOBLE ALPES

Abstract

Ecole Doctorale de Physique
Institut de Planétologie et d'Astrophysique de Grenoble

Doctor of Philosophy

The chemistry of interstellar Complex Organic Molecules (iCOMs): modelling and comparison with observations

by Arezu WITZEL-DEHGHANFAR

So far, Earth is the only known planet-hosting life, which is based on organic chemistry. The Solar Systems small objects (e.g., comets and asteroids) are enriched with organic compounds, which raises the question of whether the first steps of organic chemistry that led to terrestrial life started during the formation of the Solar System. Stars and planetary systems like our Solar System are formed continuously in the Milky Way. So, in principle, we can study chemistry in those objects to recover the first steps of organic chemistry of the young Solar System. In this thesis, I worked on two main objectives, modeling the chemical evolution in star-forming regions with Grainoble+ and modeling ices formed in an experimental setup with Labice.

The first objective of the thesis focuses on the chemical processes that form and destroy interstellar Complex Organic Molecules (aka iCOMs) in the gas phase and on grain surfaces in Solar-like star-forming regions. For this purpose, I developed an astrochemistry code, Grainoble+. The model is based on an earlier version, Grainoble (Taquet et al., 2012). Grainoble+ is a three-phase gas-grain multi-grain astrochemical code using the latest values for binding energies and diffusion and reaction rates from quantum chemical calculations. I followed two goals with Grainoble+: modeling iCOMs formation in the shocked regions of NGC 1333 IRAS 4A (De Simone et al., 2020) and modeling the ice composition in Taurus MCs (Witzel et al. 2022, submitted.).

The second goal of the thesis is to simulate the layered structure of ices as realized in laboratory experiments and to simulate the thermal desorption of species based on Temperature Programmed Desorption (TPD) techniques. For this purpose, I developed Labice, a model that simulates the TPD experiments with the rate equation approach. Labice is a simpler version of Grainoble+ that uses the three-phase approach to model ice and thermal desorption for a given experimental setup. With this model I can show the impact of the various parameters, such as multi-binding energy or the trapping effect of water ice; parameters that will be used in astrochemical models. In particular I modeled the impact of the multi-binding energy approach on the sublimation of species (Ferrero et al., 2020) and modeling and benchmarking the water and CO composite ices using the CO trapped fraction (Witzel et al. 2022, in prep).

Acknowledgements

I wish to show my gratitude to my adviser and mentor, Cecilia Ceccarelli, for making this thesis possible and guiding me throughout the entire journey.

I would like to thank my husband, Gunther Witzel, for standing by me every second and every day. You are my strength.

Parichehr and Ali, my parents, none of this would have been possible without you. You have made me the person I am today. I wish there were enough words in the world that could help me describe how thankful I am to have you.

I also would like to thank my family, Maria, Arno, Aysan, and Erfan, and my friends, Anna, Aurélien, Mark, Nastaran, and Saba. You have been there for me everyday and helped me carry the weight and the joy of these years.

I would like to show my appreciation to my friends and colleagues, Albert, André, Bertrand, Claudine, Cécile, Eleonora, Fanny, Franciele, Joan, Layal, Lorenzo, Marie, Marta, Mathilde, Nadia, Pedro, Piero, Seyma, Simon, Stefano F., Stefano P., Vianney, Philippe, and Pierre-Olivier, and the members of my thesis committee, Serena, Stephanie, Ana, Claudio, Herve, Francois, and Patrice, for their continuous support.

And last but not least, many thanks to our little Gaia, our 19 months old German Boxer, who brought us immense joy. Thank you for waiting so patiently for me all these months.

Live long and prosper.

Contents

List of Figures

List of Tables

List of Abbreviations

AGB	**A**symptotic **G**iant **B**ranch
ASW	**A**morphous **S**olid **W**ater
BE	**B**inding **E**nergy
C	**C**arbon
CI	**C**rystalline **I**ce
CNM	**C**old **N**eutral **M**edium
CR	**C**osmic **R**ay
CRESU	**C**inéique de **R**éction en **E**coulement **S**upersonique **U**niforme
CTRW	**C**ontinuous-**T**ime **R**andom-**W**alk
DE	**D**iffusion **E**negy
DFT	**D**ensity **F**unctional **T**heory
ER	**E**ley **R**ideal
eV	**e**lectron **V**olt
FA	**F**lowing **A**fterglow
FIR	**F**ar **I**nfra**R**ed
FUV	**F**ar **U**ltra-**V**iolet
GeV	**G**iga **e**lectron **V**olt
GMC	**G**iant **M**olecular **C**loud
H	**H**ydrogen
He	**He**lium
iCOM	**i**nterstellar **C**omplex **O**rganic **M**olecule
ICR	**I**on **C**yclotron **R**esonance
IR	**I**nfra**R**ed
ISM	**I**nter**S**tellar **M**edium
ISRF	**I**nter**S**tellar **R**adiation **F**ield
JWST	**J**ames **W**ebb **S**pace **T**elescope
LH	**L**angmuir-**H**inshelwood
MD	**M**olecular **D**ynamics
MC	**M**olecular **C**louds
MeV	**M**ega **e**lectron **V**olt
ML	**M**ono-**L**ayer
Myrs	**M**ega **y**ea**rs**
N	**N**itrogen
O	**O**xygen
PBC	**P**eriodic **B**oundary **C**ondition
PD	**P**hoto **D**ominated **R**egion
PDR	**P**hoton-**D**issociated **R**egions
PES	**P**otential **E**nergy **S**urface
PSD	**P**hoto**S**timulated **D**esorption
QMS	**Q**uadrupole **M**ass **S**pectroscopy
RAIRS	**R**eflection **A**bsorption **I**nfrared **S**pectra
REMPI	**R**esonance-**E**nhanced **M**ulti**P**hoton **I**onization
S	**S**ulfur

SED	**S**pectral **E**nergy **D**istribution
Si	**S**ilicon
SIFT	**S**elected **I**on **F**low **T**ube
TMC	**T**aurus **M**olecular **C**loud
TPD	**T**emperature **P**rogrammed **D**esorption
TS	**T**ransition **S**tate
UHV	**U**ltra-High Vacuum
UV	**U**ltra-**V**iolet
WCCC	**W**arm **C**arbon **C**hain **C**hemistry
WNM	**W**arm **N**eutral **M**edium
YSO	**Y**oung **S**tellar **O**bject
ZPE	**Z**ero-**P**oint **E**nergy

Part I

Introduction

0.1 Thesis objective

In this dissertation, I have concentrated on modeling (1) the chemical evolution in solar-like star-forming regions and (2) the ice grown in laboratories, specifically in Temperature Programmed Desorption (TPD) experiments.

The first stage in the chemical evolution starts with the chemistry in molecular clouds (MCs). In the cold temperatures in MCs ($\sim 10 - 20$ K), species eventually freeze on the grain ice mantles. The frozen species can be sublimated into the gas phase in the later stages of star formation, enrich the gas phase with molecules and ignite the formation of more complex molecules in the gas phase. It is apparent that understanding *how the ice mantle has been formed is the first question to ask and the first stage to model*. Chap. 6 tries to answer this question using Graionble+ astrochemical model (Chap. 4) that I have re-coded and reimplemented.

The shocked regions along the outflows are perhaps the best place to examine one of the main questions in astrochemistry: *Has organic chemistry originated from surface reactions on grain mantles or through gas-phase reactions?* Thanks to the newest observations, I had the opportunity to model the chemistry in the shocked region of NGC1333 IRAS 4A outflows (Chap. 5).

Astrochemical modeling is interdisciplinary research, the connecting piece of the puzzle between theoretical and experimental chemistry and observations. Laboratory astrochemistry conducts experiments on interstellar ice analogs in interstellar-like conditions (low temperatures and low densities). Modeling experimental ices started as a module to Grainoble+ until it grew into a stand-alone package named Labice. I used the same formalism to be self-consistent with Grainoble+ to derive the physical parameters from the experimental results, such as binding energies, which astrochemical codes will then use (Chap. 7).

Experiments and observations have shown that water ices can trap volatile species even in warm regions ($30 < T < 100$ K). The trapping effect of water strongly impacts the chemical evolution in the protostellar regions. I carried out various simulations to model the trapped fraction in CO and H_2O ice mixtures with the goal of better understanding ices in an experimental setup (Chap. 8).

Interstellar ice in cold regions ($\lesssim 100$ K) has an amorphous nature with an irregular potential surface that creates many different binding sites for solid species. Taking into account the multi-binding energy distribution of solid species in astrochemical models will strongly affect the chemical evolution, which I show in Chap. 9 with the Labice model.

Thesis structure

This thesis starts with three introductory chapters. A short description of star formation is in Chap. 1. This chapter gives a brief overview of the chemical and physical evolution in low mass star forming regions. Chap. 2 focuses on astrochemical models in the literature that have been used to simulate the chemical conditions in star-forming regions. Chap. 3 describes the newest advances in quantum computational and experimental chemistry that were included in Grainoble+.

Chap. 4 describes the model that I have developed in the course of my Ph.D., Grainoble+. I review the algorithm and benchmarking of the model in Apx. C and Apx. A, respectively. The applications of Grainoble+ are presented in Chap. 5 and Chap. 6. The first application of the model is utilized in De Simone et al. (2020) to model the gaseous methanol to acetaldehyde ratio observed in NGC 1333 IRAS 4A outflows. The second application (Witzel et al. 2022 submitted) employs the latest reaction rate and binding energy calculations and physical conditions from observations to simulate the formation of ices in the TMC1 at visual extinction of 20 magnitudes.

Chap. 7 explains the Labice package that I have developed for modeling the results of astrochemical laboratory experiments, specifically, TPD experiments. Its algorithm and applications are laid out in Apx. D and Chap. 8 and 9. Its first application (in chap. 8) is to compare simulations and experiments by simulating the CO trapped fraction in the TPD experiments listed in Kruczkiewicz et al 2022 (in prep). Its second application is used in Ferrero et al. (2020), where we simulated a simple ice analog with water and methanol mixture to examine the impact of multi-binding energy simulations in astrochemical models and compared the results with single-binding energy simulations.

Finally, Chap. 10 concludes the results of this work and discuss the future perspectives.

Chapter 1

Star formation and Chemical evolution

1.1 Cold molecular dark clouds

Cold dark clouds are the dark patches in the sky that obscure the light emanating from within or behind them. Herschel did the first observations in the 1780s, and at the time, he called these black patches holes in the heavens (Herschel, 1785). These dark patches show a filamentary structure in various sizes and masses (André et al., 2014) with irregular edges, for example, Taurus, Ophiuchus, Lupus, and Orion clouds (see, Fig. 1.1).

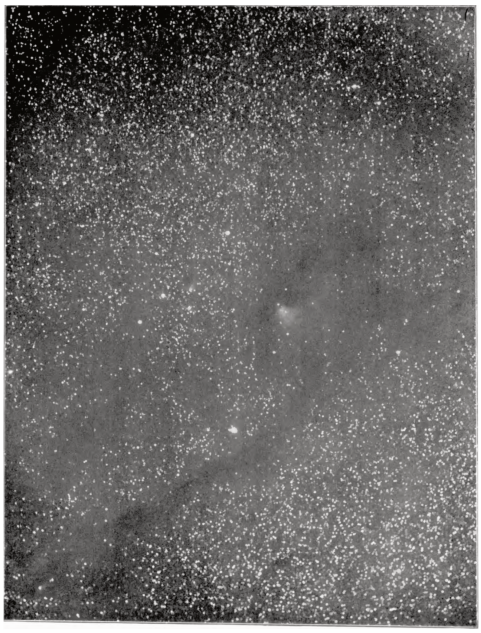

FIGURE 1.1: This figure shows the filamentary structure of Taurus as it was observed by Barnard (1907). He named it the vacant lanes in Taurus. (Image credit: Barnard, 1907)

The discussion over the origin and the constituent of these dark patches proceeded well into the 20th century. The infrared and millimeter observations development allowed us to peek inside the dark filamentary patches. The observations revealed that these dark spots are the birthplace of stars (Bok and Reilly, 1947).

The internal structure of dark clouds is clumpy and fragmented. The perturbed density structure leads to fragmentation and decoupling of the clumps from the rest of the cloud (Bergin and Tafalla, 2007). Clumps (dark dense cores) can also show substructures and can further collapse and create a protostar (Shu, 1976).

Dark clouds are exposed to external influences such as high energy irradiation in the UV from nearby A or B stars. The rate of irradiation decreases towards the deeper parts of the cloud since dust efficiently absorbs Ultra-violet (UV). It effectively only affects the skin of the cloud that is known as Photo Dominated Region (PDR) (Hollenbach and Tielens, 1999; Tielens and Hollenbach, 1985). Cosmic ray (CR) bombardment is another external effect on the cloud. They are highly energetic and can penetrate through the denser regions.

1.1.1 The path towards MCs

Cold neutral atomic regions are believed to be the precursor of MCs. When a neutral cloud reaches enough density and visual extinction, it can shield itself from the external radiation field and form and preserve hydrogen molecules. An H_2 dominated region is called a MC. In a typical Giant Molecular Cloud (GMC) conditions with solar neighborhood metalicity degree, the atomic to molecular hydrogen transition occurs at visual extinction of about 0.1-0.2 magnitude. This corresponds to column density of about $N_H \approx 2 \times 10^{20}$ cm^{-2}. The transition of C^+ to CO takes place at $A_\nu \approx 1$ mag with $N_H \approx 2 \times 10^{21}$ cm^{-2} (see, for example, Gong et al., 2017).

Simulations predict that the temperature range of Cold Neutral Medium (CNM) and MCs is about 100 - 50 K and 20 - 10 K, respectively (Glover and Clark, 2012). Observation of this region is difficult since C^+ that is the main tracer, has only a single fine structure emission line. Therefore, constraining the temperature is challenging. In quiescent regions in MCs, CO is used as a tracer. Therefore, observation and constraining of the temperature are possible. In dense shielded areas, the temperature remains low and constant over several orders of magnitude in density (see e. g., Glover and Clark, 2012; Glover et al., 2015). Fig. 1.2 shows two example gas temperature profiles as a function H-nuclei density.

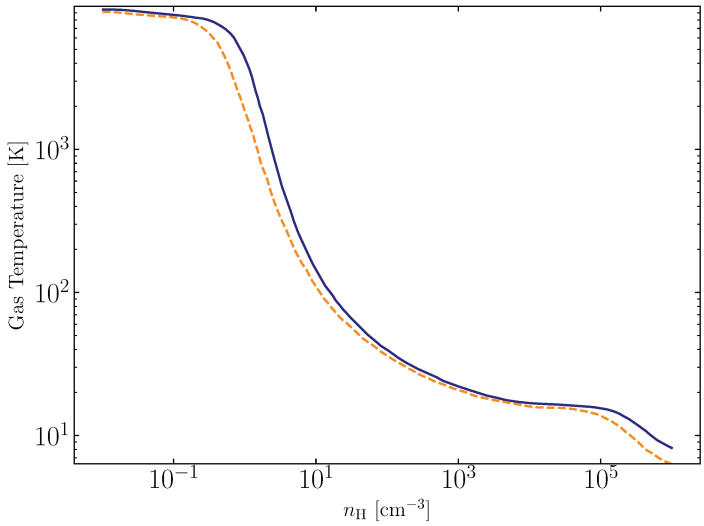

FIGURE 1.2: The figure shows two gas temperature profiles as a function of H-nuclei density. The curves are from the HD simulations of Koyama and Inutsuka (2000, Figure 1). They simulate shock wave propagation inside warm and cold neutral media. The solid curve assumes as its initial parameter an absorbing column of 10^{19} cm^2 and the dashed line assumes a 10^{20} cm^2 absorbing column.

Formation of species such as H_2 or CO have a long characteristic chemical timescales in comparison to the dynamical timescales of a diffuse cloud. This makes their chemical evolution sensitive to dynamical progressions in the cloud, therefore it is important to understand and model the physical transformation of the cloud correctly (Klessen and Glover, 2016).

Two thermal states can co-exist in neutral clouds in an equilibrium state, the Warm Neutral (WNM) and the CNM (Field et al., 1969). The density and the temperature of these two states are $n_H \sim 0.5$ cm^{-3}, and $T \sim 10^4$ K and about $n_H \sim 50$ cm^{-3}, and $T \sim 100$ K, respectively. Gas in any other thermal state eventually reaches one of these two stable states. The system either transforms into a WNM by temperature increase and a density decrease, or it cools down and grows denser and transforms into a CNM. CNM is believed to exist inside WNM in pressure equilibrium in the Interstellar Medium (ISM). The cooling and sound crossing timescales of a CNM are about 10^5 and 10^6 years, respectively. For a WNM, the timescales are 10^7 and 10^6 years, respectively. Supernova explosion rate in the ISM is about 5×10^6 years (Wolfire et al., 2003). It suggests that the WNM is turbulent, but the CNM can reach a state of equilibrium within this period and therefore exist inside WNM.

Several parameters play a crucial role in governing the CNM to MC transformation: self-gravity, chemical composition, magnetic field, and turbulence. (1) Gravity speeds up the agglomeration of material towards the center; (2) Magnetic field, in general, counters the collapse unless the direction of the flow of the material is in alignment with the magnetic field lines. In this case, the magnetic field assists the funneling the material towards the center of the flow. The role of the magnetic field depends on the ionization degree of the cloud. It means the more ionized the cloud is, the more impact it has; (3) Turbulence can counterbalance gravity at large scales or create local collapses on smaller scales; and (4) Chemistry of the cloud governs the cooling and the heating mechanisms in the process (Klessen and Glover, 2016).

Cloud formation scenarios can be categorized into four main classes (a) coagulation of smaller clouds, (b) shock-driven collapse from stellar feedback; (c) converging flows, and (d) collapsing cloud or global hierarchical collapse (see, e. g., Klessen and Glover, 2016; and Vázquez-Semadeni et al., 2019).

The coagulation scenario originally proposed by Oort, 1954 suggests that smaller cold neutral clouds collide, dissipate energy, and merge to form a larger cloud. There have been many studies and numerical simulations based on this assumption (see, e. g., Dobbs, 2008; Dobbs et al., 2015; Tasker and Tan, 2009). However, despite its appealing features, the simulations fail to reproduce the filamentary structure in the MCs. Secondly, the evolution happens over a long timescale of over 10 mega years (Myrs) that is larger than the typical Supernova explosion period (see, Ballesteros-Paredes et al., 2020; Klessen and Glover, 2016).

Stellar feedback such as stellar winds, radiation, protostellar outflows, and supernova explosions can disturb the WNM and CNM stability. They are the main source behind the turbulent and multi-phase structure in the ISM. They work as the resetting clock in the ISM with a dynamical timescale that ticks every 1-10 Myrs (see, e. g., Chevance et al., 2020; Walch et al., 2012). But they can also commence the formation of stars by creating turbulence that ripples in the region and compresses the gas. The perturbed region will collapse and cool down and form MCs. For example, the shock wave from a supernova or a stellar cluster explosion can create a hot superbubble that expands rapidly in the ISM. It then sweeps up gas and the ambient ISM and compresses it at its outer shell (see e. g. Heiles, 1979; Tenorio-Tagle and Bodenheimer, 1988, and references therein). The compressed highly pressured gas cools down first adiabatically then through radiation and collision to form a CNM which is slightly denser than a typical CNM, $n_H \sim 10^{2-3}$ cm^{-3}, (Chevalier, 1977; Cioffi et al., 1988; Woltjer, 1972). The dense CNM can eventually collect enough mass to form a MC. MCs formed at the edges of bubbles have been observed in several sources (see, e. g., Heiles, 1979). However, the total star formation rate in these supernova-driven turbulent ISM is only about 10 % (Joung and Mac Low, 2006). The green curve in Fig. 1.3 shows a shock-driven density evolution from Bergin et al. (2004) as an example.

Another course of MC formation is through the convergence of flows in the neutral medium. It is reasonable to assume that MCs are merely the higher density extend of neutral media

rather than being discrete regions (see, e. g., Bergin et al., 2004; Clark et al., 2012; Franco and Cox, 1986; Hartmann et al., 2001). The main idea is that lower density neutral gas flows and converge into a denser and much cooler medium mostly driven by large-scale gravitational instability and Parker instability (Parker, 1966). This scenario has been successful in explaining many crucial features in clusters and star-forming regions, such as age histories and velocity dispersion (see, Hennebelle et al., 2008, and the references therein).

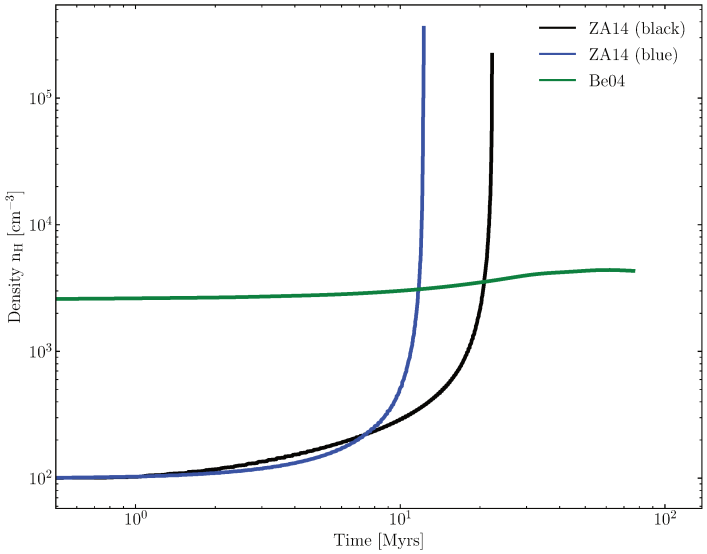

FIGURE 1.3: The cloud density profiles as a function of time are shown based on various simulations. The black and the blue curves show the low mass cloud models with a maximum mass of 10^3 and 10^4 $M_\odot$, respectively from Zamora-Avilés and Vázquez-Semadeni (2014, : ZA14) In ZA14 curves, the collapse of the CNM to form a MC starts once the cloud reaches its Jeans mass. The green curve (Be04) is the formation of a MC under a shock pressure based on Bergin et al. (2004, Figure 1).

In collapsing cloud scenario, the transformation of the atomic cloud is dominated by its self-gravity. This scenario describes a global collapse from the phase transition between WNM and CNM to form a thin sheet of cold atomic gas with supersonic velocity dispersion. The compression continues first slow and then rapidly. The hydrogen phase transformation is gradual and occurs in concurrence. The contraction is in a pressure-less regime that results in filamentary accretion towards denser cores. The timescales of the formation of low-mass stars in this scenario are a few Myrs that are a few folds shorter than the one of high-mass stars. The black and blue curves in Fig. 1.3 show the density evolution under the collapsing clouds scenario from Zamora-Avilés and Vázquez-Semadeni (2014). We summarize the physical parameters of the cloud from a WNM state to a prestellar core in Tab. 1.1.

The transition of hydrogen from an atomic to a molecular form highly impacts the chemical and physical evolution of the cloud. In other words, it changes the course of its evolution. Once hydrogen molecules effectively populate the cloud, they start to shield themselves from external radiation. Therefore, the formation rate of other molecules increases. The cloud's composition becomes primarily molecular. The radiative cooling becomes more effective, leading to a rapid drop in temperature. Additionally, ionization rates decrease which leads to the weakening of the effect of the magnetic field on the cloud and makes it more prone to gravitational collapse. These effects reduce the Jeans mass of the cloud by about one order of magnitude with respect to its previous state and enable turbulence to create regions with higher densities. The combined effect results to an increase in the rate of star formation

TABLE 1.1: The physical characteristic of different phases of ISM.

Phase	time scale [yr]	density n_H [cm^{-3}]	size [pc]	T_{gas} [K]	fractional ionization	column density [cm^{-2}]
WNM	10^7	0.2-0.5	300-400	$6000 - 10^4$	0.1	10^{19}
CNM	10^5	50	100	100*	10^{-4}	10^{20}
MC	10^6	$10^2 - 10^3$	2-20	10-20	$< 10^{-6}$	10^{21-22}
Clumps	10^6	10^{3-4}	0.1-2	10-20	$< 10^{-6}$	$< 10^{23}$
prestellar core	10^5	10^{4-7}	0.03-0.1	7-12	$< 10^{-6}$	$< 10^{24}$

Adapted from Ferrière (2001); Caselli et al. (1998b); Wolfire et al. (2003); Jenkins (2013); and Klessen and Glover (2016). * The dust temperature in CNM is generally less than the gas temperature, 50 Kelvin or lower.

(Federrath and Klessen, 2012; Hennebelle and Chabrier, 2011; Krumholz and McKee, 2005; Padoan and Nordlund, 2011).

1.1.2 Gas and dust in the ISM

The elements in the MCs can be found in the molecular form in the gas phase, the refractory cores of dust grains, and the species frozen in the icy mantle enveloping dust grains (Weinreb et al., 1963). The most abundant gaseous molecules inside the MCs are molecular hydrogen (first observation by Carruthers, 1970, in UV) and CO (first observation by Wilson et al., 1970 at 115 GHz). However, the first molecules detected in the MCs were not the most abundant ones, but those observable in the visible wavelengths: CN and CH[1] (Douglas and Herzberg, 1941; McKellar, 1940; Swings and Rosenfeld, 1937) [2].

Dust grains are mainly made of solid carbonaceous and silicate material (see review papers Draine, 2003; Galliano et al., 2018, and the references therein). The average emission from the dust in the ISM is a continuum black body in mid and far-infrared. AGB (Asymptotic Giant Branch) stars and supernovae are the significant sources of dust in our Galaxy (see Draine et al., 2007).

The total dust mass in the ISM is estimated based on the extinction curve and the elemental depletion studies. It is approximately 0.5-1% of the mass of the ISM. The density of the dust grains is estimated to be 3.3 and 2.2 grcm^{-3} for olivine and carbonaceous grains, respectively (Galliano et al., 2018; Leger et al., 1985).

The extinction curve of the dust suggests that the size of the grains follow a power-law profile ($n(r) \propto r^{(-3.5)}$ in Mathis et al., 1977). It is stronger in the UV band as appose to visible and infrared. It means that smaller dust grains are more abundant than larger ones. The average radius of the grains is about 0.1 μm. The polarization in the emission from the dust suggests that dust grains have an elongated shape (Greenberg and Shalabiea, 1994).

Even though they take up a small fraction of the cloud mass, dust grains play a crucial role in the physical and chemical evolution of the ISM. They efficiently absorb light and govern the opacity and light extinction in the clouds. Dust strongly impacts the chemical evolution in the ISM as well. For example, in densities $n_H > 10^5$ cm^{-3}, it is an efficient coolant of gas temperature through gas-grain collision in environments where dust temperature is lower (Hollenbach et al., 1991; Spaans and Silk, 2006). Hydrogen molecules, water, and methanol are formed efficiently on the dust (Boogert et al., 2015; Gould et al., 1963; Gould and Salpeter,

[1] These observations took place at the Mount Wilson Observatory in Pasadena, California.
[2] first molecules ever detected outside our planet was in the Sun (Russell, 1934).

1963; Hollenbach and Salpeter, 1971; Wakelam et al., 2017). In the coldest regions in prerstellar cores and MCs or in the outer midplane of protoplanetary disks, the icy mantles of dust become the main reservoir of species formed in the gas phase or on the ice surfaces (Fig. 1.4).

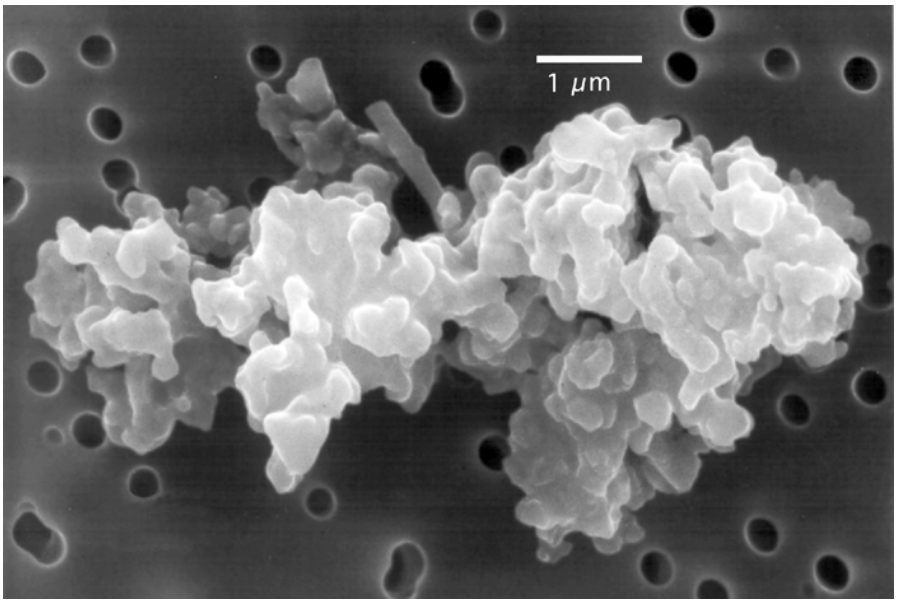

FIGURE 1.4: An imagery of dust refractory cores in the ISM. (image credit: Jessberger et al., 2005).

1.1.3 External influences

Cosmic rays (CRs)

CRs play an essential role in the energy balance and the chemistry of a MC. They are high-energy relativistic particles mostly of nuclei (majority of protons, about 10 % alpha particles, and about 1% are metal nuclei) and only about 1% of electrons (Padovani et al., 2020). Their non-thermal energy distribution ranges from 100 MeV and can go as high as 1 TeV (Grenier et al., 2015; Strong et al., 2007). The total energy density of CRs is about 2 eVcm^{-3}. Most of the galactic CRs originate in shocks in supernova remnants where they become highly energized and accelerated to relativistic velocities carrying away about 5-10 percent of the supernova energy (see, Bell, 1978; Blandford and Ostriker, 1978; Krymskii, 1977; Marcowith et al., 2016).

Only lower energy particles of about a few MeV to GeV can penetrate and interact in diffuse and dense clouds. Therefore, they dominate the heating and ionization of the dense clouds (Padovani et al., 2009). CRs are attenuated with increase of hydrogen column density. The level of decrease depends on the turbulence and ion density in the cloud (Padovani et al., 2020).

The rate of CR ionization per hydrogen molecules ζ_{H_2} [s^{-1}] is indirectly derived in several works (Caselli et al., 1998b; Leger et al., 1985; Neufeld and Wolfire, 2017; Phan et al., 2018; Shen et al., 2004). Fig. 1.5 shows the CR ionization rate per H_2 as a function of the H_2 column density. The scatter points are indirect measurements from various works, and the curves present different CR propagation models. The red, blue, and black curves are best fitting CR propagation models from Padovani et al. (2020), and Padovani and Galli (2013) based on different assumptions. The solid maroon curve shows the predicted ionization rate from Phan et al. (2018) which seems lower by a factor of several tens.

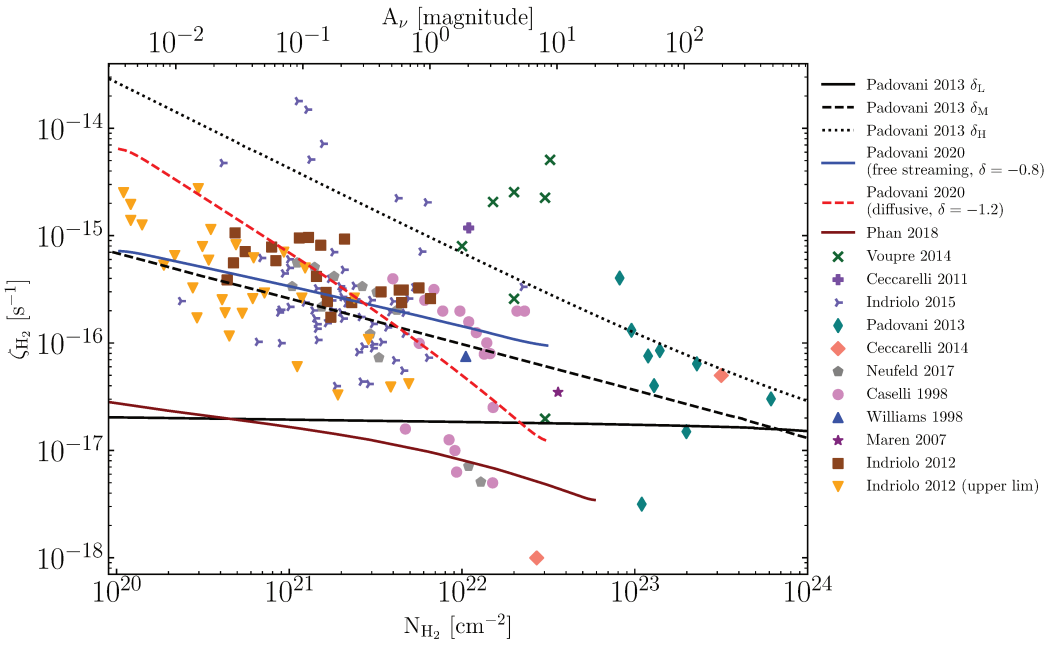

FIGURE 1.5: The CR ionization rate of H_2 as a function of H_2 column density. The datapoint are from Vaupré et al. (2014, green cross); Ceccarelli et al. (2011, purple plus); Caselli et al. (1998a, violet circles); Williams et al. (1998, blue triangle); Maret and Bergin (2007, purple asterisk); Indriolo and McCall (2012, the black squares are data points, while the orange inverted triangles are upper limits); Neufeld and Wolfire (2017, grey pentagons); Indriolo et al. (2015, purple triangle); Padovani and Galli (2013, green diamond); Ceccarelli et al. (2014, pink diamond). The modeled H_2 ionization rates are from Phan et al. (2018, solid maroon line, which is the calculated rate of electrons and protons combined), and the rest are from Padovani and Galli (2013) and Padovani et al. (2020). Solid blue and dashed red curves are best-fit models with different slopes from Figure 6 in Padovani et al. (2020).

UV Radiation field

In general, there are two UV radiation sources in the ISM: the stellar background radiation field (also known as the interstellar radiation field, ISRF, Draine, 1978) and UV photons generated from the interaction of CRs with hydrogen molecules (Prasad and Tarafdar, 1983). The ISRF photoionize atoms and photodissociate molecules and creates electrons that affect the ionization fraction in the outer regions of the cloud where they can penetrate, as for example in the Photon-Dissociated Regions (PDRs). UV irradiation influences the balance between atomic and molecular gas through photodissociation and photoionization reactions.

The UV flux is attenuated as the column density and the visual extinction increase (Tielens and Hollenbach, 1985). Atomic hydrogen absorbs photons with energies larger than 13.6 eV. Therefore, it shields the inner regions in neutral and MCs from external UV radiations. Photons with energies between 6 - 13.6 eV, in far UV (FUV), can penetrate the neutral regions. Habing (1968) estimates that the average FUV interstellar field amounts to 5.29×10^{-14} erg cm^{-3}. Often a unitless parameter known as G_0 is used to measure the FUV field

$$G_0 = \frac{u\,(6 - 13.6)}{5.29 \times 10^{-14}}\,, \tag{1.1}$$

to measure the scale of the radiation field. Draine (1978) and Mathis et al. (1983) have done similar studies to estimate the radiation energy densities in the ISM. They can be expressed relative to the Habing field in the Habing unit $G_0 = 1.69$ and $G_0 = 1.14$, respectively. The availble observations show a better agreement to the Mathis et al. (1983) value (Gondhalekar et al., 1980; Henry et al., 1980).

1.1.4 Chemistry in dark clouds

In the gas phase, the radiative association of hydrogen atoms or H^- and H^+ are the reactions responsible for molecular hydrogen formation. However, the rates are meager and cannot explain the rate of H_2 formation in the MCs. On the contrary, hydrogen molecule easily forms on the dust (Cazaux and Tielens, 2004; Gould et al., 1963; Gould and Salpeter, 1963; Tielens, 2010; Vidali, 2013; Wakelam et al., 2017). High-energy UV photons can quickly destroy molecular hydrogen. The dissociation is line-based which means that H_2 is sensitive to self-shielding (Draine and Bertoldi, 1996). Therefore, it protects and retains itself inside dense clouds.

CRs ignite the chemistry in cold MCs. High energy particles can penetrate through the dark clouds and ionize neutral species such as hydrogen molecules and Helium. Ionized hydrogen reacts with hydrogen molecules and creates H_3^+ that is the most abundant cation in MCs (see reaction chain 1.2)

$$H_2 \xrightarrow{CR} H_2^+ \xrightarrow{H_2} H_3^+\,. \tag{1.2}$$

Ions are highly reactive species. Reactions involving ions often are barrier-less and occur very rapidly even at low ($\sim$ 10 K) temperatures. Therefore, they drive the chemistry in the MCs. Electron recombination reactions are also fast processes that serve as the destruction channels of cations. The first simple molecules synthesized in the dense clouds pave the road towards forming more complex molecules observed in protostellar regions.

The most abundant elements after hydrogen and helium are oxygen and carbon. Almost all the carbon in MCs is locked up in CO. The formation path of CO is also dependent on the rate of ionization of hydrogen by CRs. A simplistic view of the reaction network leading to the formation of CO is shown in fig. 1.6. Similar to H_2, CO can self-shield against external UV radiation. The rate of photodissociation of the molecule decreases inside dense clouds.

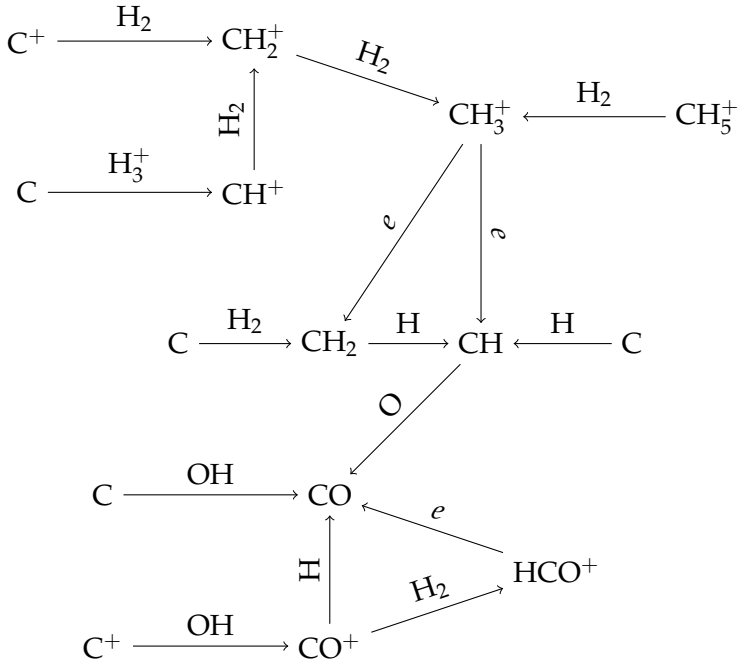

FIGURE 1.6: This network shows a simplistic view of the gaseous CO formation routes.

Dust grains play a vital role in the chemical evolution of MCs. They provide a platform on which molecules can encounter and react (Tielens et al., 1983). Additionally, dust grains deplete the gas phase from heavy elements. A significant fraction of them is locked up in the refractory dust cores and cannot participate in further chemical reactions (Jenkins, 2009). Also, in the coldest regions of the cloud, molecules formed in the gas phase freeze–out onto the grains upon accretion and can no longer react with other molecules in the gas phase. The existence of the dust icy mantles have been known for decades (Gillett and Forrest, 1973; Knacke et al., 1982; Merrill et al., 1976; Smith et al., 1989) at first provided by ground-based telescopes observations.

Amorphous water ice is the primary constituent of ices observed in quiescent clouds with a formation threshold at visual extinction of about 1.6 mags (Whittet et al., 2001). CO_2 ubiquitously accompanies it (see, Fig. 1.7). The formation threshold for CO and methanol is deeper in the cloud at visual extinction of about 3 and 17 mags, respectively. The abundances of other more complex molecules are $\lesssim 1\%$ relative to water abundances in ice. Therefore, they cannot be detected in the infrared band until they sublimate and become observable in the mm and sub-mm wavelengths (Boogert et al., 2015).

Water is synthesized most efficiently on ices. Its abundant presence on ices cannot be explained by gas-phase only reactions (D'Hendecourt et al., 1985; Hasegawa et al., 1992).

Many oxygen- and carbon-bearing molecules in the gas phase cannot be observed with ground-based telescopes, for example, water and atomic oxygen because of the terrestrial atmosphere. CO_2 and CH_4 are not observable in cold gas due to the absence of a permanent dipole moment in both molecules.

In quiescent cold clouds, the elemental oxygen budget is shared among (1) the refractory silicate dust grains ($\sim$ 25%); (2) solid water, CO_2, and more complex molecules such as methanol ($\sim$ 13%); (3) CO in the gas-phase and in ices ($\sim$ 20%); and (4) $\sim$ 40% that are unaccounted for (Jones and Ysard, 2019). The elemental carbon budget is most probably in (1) the refractory dust; and ($\sim$ 50%) and (2) CO, CO_2, and other more complex C-bearing molecules

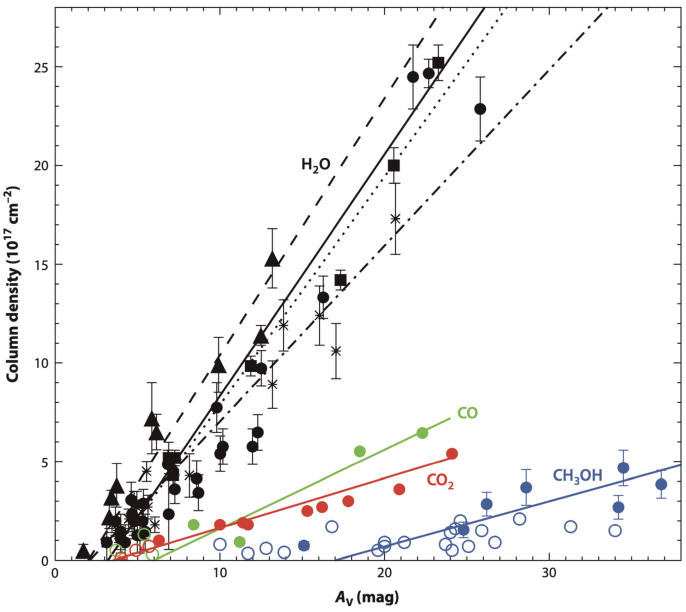

FIGURE 1.7: This plot shows the observed column densities of Water (black), CO (red), CO_2 (blue), and methanol (green) species in quiescent regions as a function of visual extinction. The full and empty circular data points are observations and upper limits towards TMC1. The solid lines are the fitted curves on TMC1 observations for each species. Water in Lupus IV clouds (asterisks points and dash-dotted line), L183 (triangles and dashed line), and IC5146 (squares and dotted line) are also shown in this figure. (Figure from Boogert et al., 2015).

($\sim$ 50%) (Mishra and Li, 2015) The nitrogen budget is divided as such: (1) a substantial portion of N may be in refractory organics and salts (Altwegg et al., 2020; Poch et al., 2020); (2) solid NH_3, NH_4^+ and OCN^- account for ($\sim$ 11%); and (3) the majority of N is unobserved, and is likely present in the form of N_2 (Oberg and Bergin, 2020).

There is an extensive catalog of detcted most abundant oxygen-, carbon-, and nitrogen-bearing molecules in the solid and gaseous forms (see also McGuire, 2021). As an example, Tab. 6.9 lists the detected solid and gaseous abundances in TMC1 which is the closest molecular cloud and is well studied.

1.2 Prestellar cores

Dense cores in MCs are likely the birthplace of low-mass stars (Beichman et al., 1986; Fiorellino et al., 2021; Onishi et al., 1998). Many forces are at work in a dense core inside MCs: the gravitational force, thermal pressure, turbulence, and the magnetic field. Matter can start to move towards the center inside the dense core, but no central object is detected. However, not all the dense cores will end up with a protostar.

A dense core is categorized as (1) a prestellar core; if it show signs of matter movement towards the center; or (2) an unbound core: a dynamically stable, oscillating (Lada et al., 2003) or expanding (Tafalla et al., 2004b) core (Caselli and Ceccarelli, 2012; Keto and Caselli, 2008). The temperature is about 10 K, and the density is about a few 10^4 n_H cm^{-3} at the boundaries and increases to $\gtrsim$ 10^6 cm^{-3} at their center (Benson and Myers, 1989; Myers and Benson, 1983). The prestellar cores density profile often follows the Bonnor–Ebert (BE) isothermal sphere (Bonnor, 1956; Ebert, 1955) which means that the internal thermal energy balances the gravitational force in the presence of an external pressure. If the density in the center goes

TABLE 1.2: Observed abundances of the most abundant solid species and their gaseous counterparts in TMC1.

Species	Solid $\left(X^{a}_{H_2O}\right)^{a}$ [%]	Extinction range [mag]	Gaseous (X_H)	Extinction range [mag]
H_2O	100.	3.2 - 26.0	<1.(-09)[b]	—
CO	0.5 - 28.	6.0 - 24.0	3.2(-05) - 7.0(-5)[c]	3 - 20[c]
CO_2	2.6 - 20.	3.5 - 24.2	—	—
CH_3OH	0.2 - 7.5	17.0 - 26.0	1.4(-09)[d]	—
CH_4	< 3	—	—	—
NH_3	< 7	—	1.2(-08)[e]	—
N_2	$< 0.2 - 60$	—	—	—
HCOOH	< 2		—	—
HOOH	$< 2.0 - 17$			
HCO^+			1.9(-10) - 5.0(-9)[c]	3 - 20
HCN			1.2(-09) - 4.5(-09)[c]	3 - 20
CS			1.6(-09) - 6.5(-09)[c]	3 - 20
SO			4.4(-10) - 1.4(-09)[c]	3 - 20
HCS^+			1.6(-11) - 7.0(-11)[c]	3 - 20
N_2H^+			3.8(-10) - 5.0(-10)[c]	3 - 20
H_2S	$< 0.6 - 1.6$		<2.5(-10)[f]	
OCS	< 0.22		1.1(-9)[g]	
HNC			1.3(-8)[e]	

Most abundant observed species towards Taurus MC in solid form with respect to water ice, X_{H_2O}, and their counter part in the gas phase with respect to hydrogen nuclei, X_H. $a(b) = a \times 10^b$ .The extinction range (column 3) given for solid species are from Fig. 7 of Boogert et al., 2015 based on the fitted line for Taurus. (*a*) The solid species are from Boogert et al. (2015) Table 2 and 3; (*b*) An average value, Hollenbach et al. (2009); (*c*) Fuente et al. (2019) Tab. 6; (*d*) An average value, Spezzano et al. (2022); (*e*) Le Bourlot et al. (1995a); (*f*) Marcelino et al. (2009); (*g*) Gupta et al. (2009).

over critical values, gravity overcomes the thermal equilibrium. The collapse starts, and a protostar could form (see also Bacmann et al., 2000; Caselli and Ceccarelli, 2012).

L1544 in Taurus is an example of a prestellar core. The first identification in sub-millimeter continuum and spectral lines were done by Ward-Thompson et al. (1994) and Caselli et al. (1999) and Tafalla et al. (1998), respectively.

1.2.1 Chemistry at work in the pre–stellar phase

The formation of molecules already starts in the MC. Only two-body reactions are possible in the gas phase in prestellar cores because the H-nuclei densities are below 10^{12} cm^{-3}. The gas-phase reactions consist mainly of barrierless and exothermic reactions in low temperatures. It mainly includes reactions with ions or cations. Cation and electron recombination creates electrically neutral species. Towards the center, the opacity increases, and the formation of simple molecules dominate the landscape. CO, N_2, N_2H^+ and NH_3 are among the observed molecules (see for example Balucani et al., 2015a).

In the cold cores, molecules freeze out onto the dust grains and form an icy mantle around the refractory cores. Once frozen on the surfaces, heavy molecules remain trapped due to low temperatures since they do not have enough thermal energy to escape their bound to the surface (Herbst and Dishoeck, 2009).

At this stage, any sublimation is mainly due to non–thermal processes such as CR hails (Leger et al., 1985) and UV radiation (Gredel et al., 1989; Prasad and Tarafdar, 1983; Shen et al., 2004) and desorption due to occurrence of exothermic reactions (Allen and Robinson, 1975; Garrod et al., 2007). Due to the increase in density towards the center, the rate of UV irradiation decreases and allows the icy mantle to grow and deplete the gas phase from heavy molecules. For example, observations show that about 80 to 90 percent of CO in the phase is depleted onto the icy mantle of dust grains at the center of prestellar cores (Bacmann et al., 2002; Bjerkeli et al., 2011; Caselli et al., 1999; Caselli and Ceccarelli, 2012; Redman et al., 2002).

The ice mantles keep a memory of the chemical evolution of the prestellar cores not only from the gas phase but also from the icy mantles themselves. Heavy molecules are practically frozen on the surfaces in low temperatures and do not move. However, light atoms such as hydrogen and oxygen remain mobile and traverse the surface through thermal hopping or quantum tunneling. They can encounter other species and possibly react and form more molecules. Water, CO_2, and methanol are among these species (see Boogert et al., 2015).

1.3 Protostellar phase

The protostellar phase starts with the collapse of the central zone of the prestellar core until a star and a planetary system are formed. In the following sections, we present a summary of the protostar's evolutionary stages and components.

1.3.1 Evolutionary classes of protostars

Young Stellar Objects (YSOs) have been empirically classified (Class I to III) based on the slope of their infrared spectral energy distribution (SED) (Lada, 1987). Later this classification was expanded by Andre et al. (1993) and Myers and Ladd (1993) who added the Class 0. This classification reflects the evolutionary stages of the protostar. We will describe the classes in the next paragraphs.

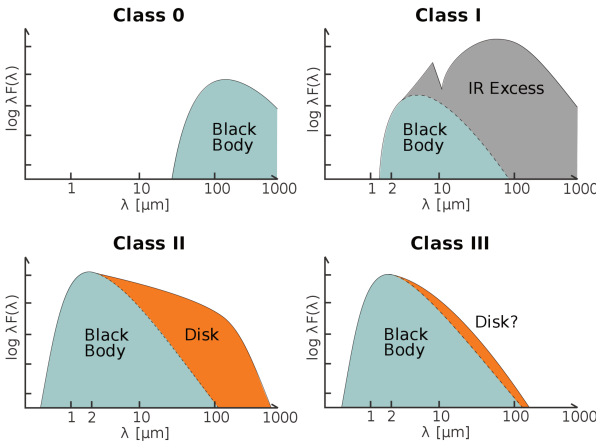

FIGURE 1.8: Lada (1987) classification of the Spectral Energy Distribution (SED) of starforming regions. They reflect the evolutionary classes of the protostellar stage shown in four figures. The top left figure, Class 0, shows a peak in the sub-millimeter and millimeter domain. It is the starting phase in evolution. In this stage, the hot core, the disk, and the outflows start to form. However, the envelope still carries most of the mass and dominates the SED. The peak shifts to the mid and far-infrared domain in the next phase, Class I. The bright central object dominates the luminosity, and the disk is apparent in the Infrared (IR) excess. The material continues to accrete into the core, and the disk and the surrounding envelope start to dissipate. The peak shifts to the visible regime, and the disk appears as an IR excess In Class II and III phases. The envelope is long gone, and planetesimal and planets are forming inside the disk Persson (image credit: 2014)

Class 0

The early stage of a protostar is called Class 0 and it lasts about 10^{4-5} years (Andre et al., 2000; Evans et al., 2003; Maury et al., 2011). At this stage, matter falls towards the central object accreting its mass. However, the envelope still dominates the mass of the protostar. The dust and gas temperatures and the density increase towards the center, the region where the dust temperature exceeds 100 K, which is called hot corino (Ceccarelli et al., 2000b; Ceccarelli et al., 2007). Observations suggest that the outflows and disks also start in this stage. Outflows were detected much earlier (Bontemps et al., 1996; Saraceno et al., 1996) than disks (Maury et al., 2019; Tobin and Vandam Orion Team, 2020). However, most of the continuum emission is from the dust envelope, which is approximately 10 - 30 K black body which peaks in the far-infrared (FIR) to sub-millimeter and millimeter wavelength ranges (see, the top left plot in Fig. 1.8). Therefore, even though other components exist inside, they are difficult to observe since the surrounding envelope is optically thick. IRAS 16293-2422 (Ceccarelli et al., 2000a; Jaber et al., 2014; Jørgensen et al., 2016; Manigand et al., 2020; van Dishoeck et al., 1995) and NGC 1333 IRAS 4A (Blake et al., 1995; Bottinelli et al., 2004; López-Sepulcre et al., 2017) are two examples of Class 0 protostars.

Class I

The surrounding envelope grows thinner due to accretion towards the central object and the evacuation of material by the outflows. However, the envelope still obscures the central parts of the protostar. The light from the core is absorbed and scattered by the surrounding disk and the remaining envelope. The disk is visible in the SED profile in the infrared (IR) excess (see, the top right plot in Fig. 1.8). The timescale of this stage is about 10^5 years. L1555-IRS5

TABLE 1.3: Different regions in low-mass protostars.

component	time scale [yr]	n_H density cm^{-3}	size [AU]	T_{gas} [K]	T_{dust} [K]
hot corino	10^{4-5}	10^{7-9}	0.03-0.2	> 100	> 100
inner mid place	10^6	$> 10^8$	100-300	> 100	> 100
outer mid plane	10^6	10^{6-8}	300-400	$100 - 10$	$100 - 10$
outflow	10^4	10^{4-6}	$10^5 - 4 \times 10^5$	$> 10^3$	10-20
envelope	10^{4-6}	10^{5-7}	10^5	$10 - 30$	$10 - 30$

(Adams et al., 1987; Bianchi et al., 2020; Strom et al., 1976), and SVS13-A (Bianchi et al., 2019; Lefloch et al., 1998; Tobin et al., 2016) are examples of Class I sources.

Class II and III

At this stage, the envelope dissipates, and the coagulation of dust grains in the disk is underway. The luminous young star and the disk are apparent in the SED as a black body emission in visible and IR wavelength and as its extension in longer wavelength, respectively (see, the bottom left plot in Fig. 1.8). The Class II phase lasts about 10^{5-6} years.

Formation of the debris disk and planetesimal brings the region into the Class III phase in which a planetary system formation is well at work. The dust is accreted into the rocky planets and the cores of the Giant planets. On the other hand, gas is swept away from the central star by UV radiation and is accreted in the forming giant planets. Some of the planetesimals may also prevail in the form of comets (see the bottom right plot in Fig. 1.8). HH-30 (Burrows et al., 1996) and HR 8799 (Marois et al., 2008) are two examples of Class II and Class III sources, respectively.

1.3.2 Protostar components

We briefly discuss the physical characteristic of the different regions constituting a protostar in the following sections and Tab. 1.3.

Hot corino

The innermost zone of a protostar envelope is known as the hot corino (Bottinelli et al., 2004; Ceccarelli, 2004). The temperature of the dust rises to above 100 K and the density to 10^{7-9} cm^{-3}. The first detection of the presence of such a warm region was reported in (Ceccarelli et al., 2000a; Ceccarelli et al., 2000b; Ceccarelli et al., 2000c). Subsequent observations then demonstrated the presence of abundant complex organic molecules (Bottinelli et al., 2004; Cazaux et al., 2003; Jørgensen et al., 2016). The observed line spectra, which lie in millimeter-wavelength, are very dense as it is also in the massive hot cores.

Protoplanetary disk

Due to the conservation of angular momentum, the collapse of a dense core is not radially symmetric. The infalling material inside the protostar starts to form a flattened zone surrounding the hot corino. Due to the conservation of angular momentum, a centrifugal barrier is created, which is the crossing zone between the rotationally infalling material into the Keplerian disk (Oya et al., 2016; Sakai et al., 2014) (Fig. 1.9). The outer regions can be exposed to UV irradiation from the central star and the interstellar field. The density decreases from the center of the midplane towards the outer regions while the temperature increases depending

on the protostar's evolutionary stages (§ 1.3.1). The density and temperature increase on the radial axis towards the central object. The temperature gradient creates a separation between the species frozen onto the grain mantles and the gaseous state. The lines of separation are known as snowlines.

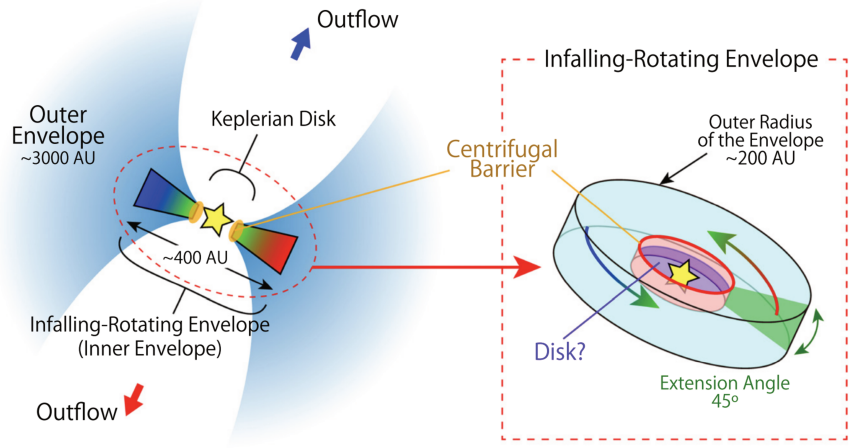

FIGURE 1.9: Depiction of the infalling material during Class 0 source IRAS 16293-2422. The left sketch shows the large-scale structure of the source with its outflow, the outer and the inner envelopes. We see the zoom-in view of the inner envelope pictured as a cylinder to the right. The outer envelope is falling in towards the center, and the inner envelope is rotating. The red cylinder around the central luminous object is the centrifugal barrier of the infalling-rotating envelope. The image is from Oya et al. (2016).

Outflows, jets and shocked regions

Protostars vent off angular momentum by ejecting material back into the cloud in the form of high-velocity and collimated jets and/or lower-velocity outflows. So that shocks are created at the interplaces of jets and molecular outflows with the surrounding quiescent material. In these shocks, the velocity of the ejected material can reach supersonic values. There can be a differential velocity between ions and neutrals due to magnetic fields. The gas temperature can increase to thousands of Kelvin depending on the shock velocity. On the contrary, the temperature of the dust remains below 20 K. The reason is that dust grains are very efficient in dissipating heat and cooling down through black body radiation emission. On the other hand, molecules in the gas phase can only reduce their temperature through line emission. Therefore, their temperature and thermal velocity is high throughout the shocked region.

Besides, the collision between ions and dust grains sputter the icy mantles, ejecting some frozen material into the gas phase. In cases where the outflow is violent ($v_{\rm shock} \gtrsim 25$ kms^{-1}), dust grains can collide and shatter the icy mantle and the refractory core of the grain into the gas phase (see, Draine and McKee, 1993; Gusdorf et al., 2008; Kaufman and Neufeld, 1996; Schilke et al., 1997).

1.3.3 Chemical evolution in the protostellar phase

The chemical composition of protostars is diverse and complex. Starting from the warmest regions, the chemical composition of the gas varies as follows.

Hot corinos at the center of protostars are rich with iCOMs in the gas phase (Cazaux et al., 2003; Ceccarelli et al., 2000b). The high temperature in the center entirely evaporates the ice

mantle of dust grains. It also facilitates reactions with activation energy barriers in the gas phase (Charnley et al., 1992; Skouteris et al., 2019; Vazart et al., 2020).

In the warmer regions relatively close to the central object, the temperature is high enough ($\gtrsim$ 20 K) to allow the radicals to move on the ice surfaces. It can lead to the formation of more complex molecules such as alcohols, hydrocarbons (Álvarez-Barcia et al., 2018; Enrique-Romero et al., 2020; Garrod et al., 2006). Thermal and non-thermal desorption processes release these species into the gas phase.

In regions with temperatures higher than 30 K, iced methane and CO evaporate. Further reaction with C^+ can lead to the formation of carbon-chain molecules giving rise to the Warm Carbon Chain Chemistry (WCCC) phenomenon[3] (Sakai and Yamamoto, 2013).

Farther from the center, the temperature is lower. This region has a chemical characteristic similar to the previous stage, the prestellar core. This zone is also known as the CO-depleted zone (Jørgensen et al., 2005). The dust temperature is below 20-25 K. Therefore, most of the molecules remain frozen in the ice mantles.

In prestellar disks, the outer zones are exposed to external radiation, which destroys the evaporated or newly formed species. Molecules and dust can circulate and fall in on the protoplanetary disk and freeze out onto the dust (Oberg and Bergin, 2020). The frozen molecules on the disk may have been formed before the protostellar phase or inside the hot corino.

In the shocked regions of the protostellar outflows, the chemical compositions are similar to those of hot corinos, simply because the circumstances are very similar: high temperature and sputtering (instead of thermal evaporation) release of the frozen molecules into the gas phase. The high gas temperature ($\gtrsim$ 50 K) triggers reactions with activation energy barriers (Codella et al., 2017; De Simone et al., 2020) which enriches the chemical complexity of the source (see, also, Caselli et al., 1997; Viti et al., 2001a).

1.4 Complex Organic Molecules in the interstellar medium

Over 200 molecules (from H_2 to C_{70}) are detected in star-forming regions[4] and thanks to the ground- and space-based telescopes, the list is ongoing (McGuire, 2021, provides an exhaustive list until June 2021).

iCOMs (interstellar Complex Organic Molecules: C-bearing molecules with 6 or more atoms) could be considered the precursors of pre-biotic molecules (Caselli and Ceccarelli, 2012; Ceccarelli et al., 2017a). These molecules have been observed in various regions: in star forming regions (e. g., Belloche et al., 2017; Cazaux et al., 2003; Kahane et al., 2013; Ligterink et al., 2017; López-Sepulcre et al., 2015; McGuire et al., 2018; Mendoza et al., 2014; Rubin et al., 1971) in the circumstellar envelopes of AGB stars (e. g., Cernicharo et al., 2000), in the shocked regions (Arce et al., 2008; Codella et al., 2017; De Simone et al., 2020; Lefloch et al., 2017), and in external galaxies (Henkel et al., 1987; Qiu et al., 2018; Sewiło et al., 2018).

We need to understand their formation and destruction routes to understanding their presence. Many works have been carried out to answer this question through observation, computational and experimental chemistry, and modeling (e. g. Balucani et al., 2015a; Caselli and Ceccarelli, 2012; Enrique-Romero et al., 2021; Herbst and Dishoeck, 2009; Vasyunin and Herbst, 2013; Vasyunin et al., 2017; Vazart et al., 2020).

The upcoming launch of the James Webb Space Telescope (JWST: Gardner et al., 2006) will present us with the opportunity to (1) observe less abundant species in ices and (2) increase the number of observations towards quiescent MCs due to its improved sensitivity

[3]Sources with high carbon chain molecules to iCOMs ratio are known as Warm Carbon-Chain Chemistry (WCCC) sources. Their composition it thought to depend on the abundance of methane evaporated from the ice mantle into the gas phase.

[4]See the list of the detected molecules in the Cologne Database for Molecular Spectroscopy.

and spatial resolution with respect to its predecessors. The new observations will improve our understanding of ice mantle formation and composition.

Chapter 2

Astrochemical modeling and their goals

As shown in the previous chapter (Chap. 1), stellar evolution and chemical evolution go hand in hand. The goal of my thesis is an in-depth study of the chemistry of the very first phases, i. e. during the molecular cloud formation phase that set up the initial conditions of prestellar cores and protostellar phase. I developed and reimplemented (re-coded) the Grainoble+ gas-grain astrochemical code and introduced new physical and chemical processes for that purpose, which I will discuss in Chap. 4. Using the rate-equation approach, the Grainoble+ model simulates the chemical evolution in star-forming regions.

Astrochemical modeling of star-forming regions has a long history, starting shortly after the discovery of the first molecules in the Interstellar Medium (ISM) (Allamandola et al., 1979; Allen and Robinson, 1977; Tielens and Hagen, 1982a; Watson and Salpeter, 1972). During the past decades, astrochemical modeling has become more sophisticated capturing the complexity of the processes in the gas phase and the ices in various physical conditions. Advances in quantum computational and experimental chemistry, computational modeling, and new telescopes and interferometers facilitate apprehending these details. Astrochemical models aim to utilize and combine the findings from observations, the experimental laboratory results, and theoretical advances to reproduce the abundances observed in the ISM.

The following sections start with a brief review of the gas-phase and gas-grain surface chemical models and their current limitations.

2.1 Gas-phase chemistry models

As mentioned in the previous chapter (Chap. 1), chemical evolution in Molecular Clouds (MCs) starts to take off when molecular hydrogen is formed on grain surfaces. Further chemical reactions leading to more complex molecules occur in the gas phase and on grains surfaces. We discuss the modeling of the chemical evolution in MCs in the gas phase in this section and on grain surfaces in the next section (§ 2.2).

Gas-phase chemical evolution can be modeled using rate equations. Rate equation calculations are rapid and have low computational costs. It allows the models to include more complexities such as large reaction networks, employ time-dependent physical profiles, or couple with hydrodynamic simulations. Therefore, using this approach for star-forming regions is favored by many working groups. A rate equation is a first-order differential equation as a function of time that couples the rate of formation and destruction of a species in the

gas phase

$$\frac{\mathrm{d}\, n_i}{\mathrm{d}\, t} = \underbrace{\sum_{j,k} \kappa_{i,j,k} n_j n_k}_{\text{bi-molecular reactions creating } n_i} - \overbrace{n_i \sum_{l} \kappa_{i,l} n_l}^{\text{bi-molecular reactions destroying } n_i} + \underbrace{\sum_{\delta} \kappa_{i,\delta} n_\delta}_{\text{uni-molecular reactions creating } n_i} - \overbrace{n_i \sum_{\gamma} \kappa_{i,\gamma}}^{\text{uni-molecular reactions destroying } n_i} , \tag{2.1}$$

where n_i is the number density of the species i. The left-hand side denotes its rate of evolution in time with the unit in $\mathrm{cm}^{-3}\mathrm{s}^{-1}$. The first term on the right-hand side is the sum over all the bi-molecular reactions and processes that form n_i with the rate coefficient $\kappa_{i,j,k}$ $[\mathrm{cm}^3\mathrm{s}^{-1}]$. The second term sums over the rates of bimolecular reactions and processes that destroy n_i with the rate coefficient of $\kappa_{i,l}$ $[\mathrm{cm}^3\mathrm{s}^{-1}]$. The third and the fourth terms follow the same pattern for uni-molecular processes, such as adsorption or photodissociation $[\mathrm{s}^{-1}]$.

Astrochemical models use numerical methods that solve stiff ordinary first-order time-dependent rate equations because chemical reaction timescales vary from one another. Some reactions, such Cosmic Ray (CR) ionization, can be quite slow in comparison to ion-neutral reactions (Tielens, 2021). Prasad and Huntress (1980) was one of the first to propose a model with an extended ion-neutral gas-phase network, ∼20% of which was estimated rate coefficients based on experimental studies.

Astrochemical models follow the physical evolution of the model simultaneously. The physical parameters can remain constant over the simulated timescales (also known as pseudo-time-dependent profiles) or evolve following a time-dependent physical profile. For example, modeling a cold MC is often done under the pseudo-time-dependant assumption. In contrast, modeling a core-collapse often consist of two phases, the cold phase with pseudo-time-dependent physical profiles and the collapse (also known as the warm-up phase, Viti and Williams, 1999; Viti et al., 2004) that follows time-dependent profiles (see for example, Aikawa et al., 2020; Bergin et al., 1995; Ceccarelli et al., 1996).

2.2 Grain surface chemistry models

In astrochemical models, the gas and the grains are the two phases in which chemical reactions can occur. These two phases are connected in the models via accretion and desorption processes.

Surface chemistry can be limited in two ways. Accretion limited chemistry and reaction rate limited chemistry. Chemistry in accretion-limit situations has a stochastic nature, and further approximations should be taken into account. We will discuss more on the subject in Sec. 2.2.2. In cases where reaction rates are not limited by the low number of reactants on the surface, the chemical evolution can be evaluated using rate equations similar to rate equation in the gas phase (Eq. 2.1)

$$\frac{\mathrm{d}\, n_i}{\mathrm{d}\, t} = \underbrace{\sum_{j,k} \kappa_{i,j,k} n_j n_k}_{\text{bi-molecular reactions creating } n_i} - \overbrace{n_i \sum_{l} \kappa_{i,l} n_l}^{\text{bi-molecular reactions destroying } n_i} + \underbrace{\kappa_{i,g} n_g}_{\text{accretion}} - \overbrace{n_i \sum_{\gamma} \kappa_{i,\gamma}}^{\text{desorption processes}} , \tag{2.2}$$

where the first two terms on the right-hand side are the sums over the bi-molecular surface reactions that form and destroy species n_i. The latter two are the accretion rate of gaseous species n_g, and the sum over the desorption rates of n_i. The surface reaction rate depends on the diffusion rate of the reactants and the reaction efficiency upon collision.

Two-phase modeling based on the rate equation approach started with Hasegawa et al. (1992). In these models, the ice is treated uniformly. It means the entire ice reservoir is exposed to the gas phase and susceptible to all the processes that are supposed to occur on the grains (desorption, diffusion, surface reactions). A two-phase model can overestimate the sublimation and formation rates in ices. Therefore, some two-phase models included the effect of trapping by allowing a fraction of volatile species, such as CO, to change binding energies to similar values to those trapped within, e. g., CO_2, (see, Viti et al., 2004).

Hasegawa and Herbst (1993a) and Hasegawa and Herbst (1993b) improved their modeling to include the multi-layer nature of the ice mantles. This model added a third phase to the gas and surface phases, the bulk that acts as a reservoir of solid species. In this model, only the surface layer is chemically active. This approach is also known as the three-phase model. However, this approach remained an isolated case in the literature until the work by Taquet et al. (2012), who showed the importance of three-phase modeling with Grainoble.

2.2.1 A brief review on the astrochemical models in the literature

Three-phase modeling is today's widely-used approach. Over the past few decades, motivated to reproduce the observations or to include the latest information from chemical studies or the observations, modelers have introduced many modifications and upgrades. For example, the newest quantum computational studies have provided a more accurate description of the reaction activation energy barriers. Many experimental studies have quantified the probability of desorption due to the exothermicity of surface reactions. In the following paragraphs, we address a non-exhaustive list of the models available in the literature that introduced a new modification[1].

Focused on surface processes Taquet et al. (2012) reemphasized the necessity of employing three-phase models. This paper also examined the effect of porous ice and physical and chemical parameter variation on the abundances. To compute the reaction rate via quantum tunneling, astrochemical models often use the approximation of rectangular energy barriers with a width between 1 and 2 Å (e. g., Garrod and Pauly, 2011; Hasegawa et al., 1992; Tielens and Hagen, 1982a). Taquet et al. (2013) used a more accurate description of the surface reaction energy barrier, following the Eckart formalism (Eckart, 1930). While most models assume diffusion through thermal hopping or quantum tunneling, Reboussin et al. (2014) studied the effect of CR-induced diffusion and compared it in his work with thermal hopping and quantum tunneling to produce radicals.

The rate of surface reactions depends on the diffusion rate of the reactants and the efficiency of the reactions. The diffusion energy in astrochemical models is characterized as a fraction of their binding energy. Penteado et al. (2017) conducted statistical studies on the effect of binding energy on solid species abundances. Iqbal et al. (2018) carried out sensitivity analysis on the effect of diffusion rate uncertainties on solid species abundances. Garrod and Pauly (2011) and Taquet et al. (2014) discussed the evolution of binding energy as a function of layer coverage. All these studies show the importance of accurate calculation of BEs since the gaseous and solid species abundances can be strongly influenced by changes in BEs.

[1]Many of the papers mentioned in this section use the following astrochemical codes: Nautilus (Ruaud et al., 2015), UCLCHEM (Holdship et al., 2017), MagicKAL (Garrod and Widicus Weaver, 2013), and Alchemic (Semenov et al., 2010).

The probability of a reaction on the surface in the earlier models since Hasegawa et al. (1992) was calculated as the probability of transmission through a reaction barrier once the two reactants were in one site (if the reaction required activation energy. Otherwise, the reaction probability of a barrier-less reaction is equal to one). However, in reality, more possible channels can occur when two reactants encounter. Chang et al. (2007) and Garrod and Pauly (2011) proposed a new method to calculate the efficiency of a reaction on the surface by considering the competitive channels, such as diffusion and thermal desorption of the reactants.

Focused on multi-grain models As mentioned in Sec. 1.1.2 the extinction curve from the dust grains indicates that the grains in the ISM are present in various sizes, and smaller size grains are more abundant than the larger ones. Multiple parameters and processes depend on the size of the grain, such as the dust temperature and the CR desorption rate, which in turn affect the gas phase and grain ice abundances. Pauly and Garrod (2016) introduced a multi-grain model in which the dust temperature depends on the size of the grain. They conclude that the abundances in the cold phase are not affected as strongly as they are in the warm-up phase. Iqbal and Wakelam (2018) multi-grain model added the CRs effect on a grain as a function of grain radius. They showed that the abundances strongly depend on the grain size distribution and CR-induced desorption parameter. Sipilä et al. (2020) and Sipilä et al. (2021) conducted a similar study on models with a grain size distribution by attenuating the heating and cooling rates and temperature according to its size. The resulting ice composition varies strongly with the size of the grain.

Focused on desorption processes The presence of some molecules such as CO or methanol in rather large abundances relative to H nuclei ($\sim 5 \times 10^{-5}$: Fuente et al., 2019 and $\sim 1.4 \times 10^{-9}$: Spezzano et al., 2022) in cold regions suggests that non-thermal processes, such as CR induced desorption and chemical desorption, are responsible for the sublimation of these molecules into the gas phase at low temperatures. CRs and Ultra-Violet (UV) photon interaction with the ice mantle do not only lead to desorption; it is also proposed that photolysis or CR-induced reactions can lead to the formation of radicals and interstellar Complex Organic Moleccules (iCOMs) inside the grain mantles.

Shingledecker et al. (2018) introduced a new model for the CR-induced processes in the ices. The energy loss per hit invokes electron and ion production, leading to iCOMs from reactions between electronically excited species that overcome high activation barriers. The paper suggested a list of relevant reactions and evaluated the CR effect on chemical abundances. Wakelam et al. (2021) introduced the effect of CR sputtering of ices. Their model indicated that CR sputtering is more effective at higher densities. However, they also suggested a more substantial desorption method is required to reproduce the observations. Kalvāns (2015b) modeled ices in weakly shielded regions and suggested that ices in this region are subject to intensive photo-processes. Lu et al., 2018 modeled the photon-penetration rate as a function of ice thickness for three-phase models, which is incorporated in Aikawa et al. (2020) core-collapse model.

Chemical desorption was another non-thermal method that is proposed to explain the presence of species like methanol in cold dark clouds. Garrod et al. (2007) and Garrod et al. (2006) introduced a method to estimate the chemical desorption probability based on the energy released by the reaction. They suggested that 1% desorption efficiency can reproduce the observed methanol abundances (see, also, Cazaux et al., 2010; Vasyunin and Herbst, 2013). Cazaux et al. (2016) examined the chemical desorption efficiency effect derived by Minissale et al. (2016b), based on their experimental results, on the abundances. Their model shows a factor of four increase in gaseous methanol and a strong impact on ice abundances, including the Minissale et al. (2016b) results.

Roberts et al. (2007) discussed the effect of desorption processes due to H_2 formation on the surface (where excess energy deposited on the surface results in the evaporation of neighboring species), CR heating, and CR induced photodesorption. They concluded that while H_2 formation-induced desorption yields a higher desorption rate with respect to CR-induced desorption, they still do not reproduce the observed gaseous abundances. They suggest that it is more sensible to use an empirical constraint from observations rather than theoretical calculations due to our poor understanding of the grain surface structure. Hincelin et al. (2015) suggested a new method called encounter desorption to reduce the accumulation of H_2 on ices. In this approach, hydrogen molecules may desorb upon encounter due to a sudden decrease in binding energy to the substrate. They find that gas and grain surface chemistry are strongly affected, especially in high-density environments and core-collapse scenarios. Holdship et al. (2019) proposed that chemical explosion may occur due to excess build of hydrogen atoms in ices. It results in a sudden release of energy up to 1000 K, leading to the desorption of neighboring species. They compared the abundances from their model to TMC1 observations in Taurus Molecular Cloud . However, the inclusion of the method did not show a significant improvement in reproducing the observation. The Takahashi and Williams (2000) Molecular Dynamics (MD) simulations on CO desorption due to the energy released from H_2 formation also conclude that this process is not efficient enough because the heating lifetime is shorter than one required for CO desorption on large grains.

2.2.2 Other approaches

Modified rate approach Rate equation approach models do not treat the stochastic nature of surface chemistry. It means that in regimes in which accretion is limited or, in other words, the number of species on the grain surface is smaller than the number of binding sites on the grains, rate equations lose their accuracy, and stochastic behavior dominates the calculations. This behavior poses a challenge in the rate-equation approach models. Using a semi-empirical approach, Caselli et al. (1998a) proposed adjustments to improve the accuracy of calculations. These modifications were followed by further advancements presented in Garrod (2008). These series of models are also known as modified rate equation models.

Monte Carlo methods Astrochemical models developed Monte Carlo methods to deal with the stochastic nature of surface chemistry. Monte Carlo calculations, unlike rate-equation models, do not provide time-dependent calculations. Tielens and Hagen (1982a) used random number generators to evaluate the accretion history of various species and calculated the probability of possible chemical channels on the surface. The newer method, Continuous-Time Random-Walk (CTRW), considers spatial distribution and the diffusion of particles. It allowed the later works to include grain size and binding energy distribution (Chang et al., 2005), surface structure (Cuppen and Herbst, 2005), and morphology (Cuppen and Herbst, 2007). Monte Carlo methods are exceptionally costly, computationally and time-wise, and challenging to integrate with rate-equation models. While these methods usually consider a limited range of physical conditions and chemical reactions, they can stimulate more surface complexities. Therefore, some works focused on a specific reaction (for example, Cuppen et al., 2009, focused on methanol), or focused on reproducing experimental results to provide benchmarks for astrochemical models (e. g., Fuchs et al., 2009; Lamberts et al., 2014). Garrod, 2008; Vasyunin et al., 2009 carried out a comparison between rate equation, modified rate equation models, and Monte Carlo methods using unified Monte Carlo methods and combining gas and grain surface chemistry over a wide range of densities $2 \times 10^2 - 2 \times 10^5$ cm^{-3} and temperatures 10 -50 K. They showed that the modified rate and Monte Carlo methods agree well ($\sim$ 95 %), while rate equation models are in an acceptable range of $\sim$ 75 % in most conditions (see, also, Chang et al., 2007; Chang and Herbst, 2014, 2016).

Hydrodynamics simulations coupling Another class of astrochemical models is those coupling hydrodynamics simulations to the chemical evolution of the cloud using rate-equation approach. These models simulate the chemical evolution of rapidly changing or widely diverse environments such as disks (Coutens et al., 2020; Henning and Semenov, 2013) or shocked regions (Godard et al., 2019; Louvet et al., 2016). Ordinarily, these models use a reduced chemical network. See for example, the works published using codes: UCLCHEM (Holdship et al., 2017); krome (Grassi et al., 2014); and KIMYA (Castellanos-Ramírez et al., 2018).

2.3 The current limits

Astrochemical models often use approximated reaction or diffusion rates for the reactions on the surface. For example, models mostly approximate the diffusion rate by assuming that the species diffuse via thermal hopping over a diffusion barrier that is approximated as a fraction of its binding energy (see, for example, Aikawa et al., 2020; Garrod, 2013). The newest advances in computational chemistry provide astrochemical models with the reaction and diffusion rates of the most abundant solid species. These efforts are growing in the community, and astrochemical models can implement the latest calculations into their models to understand their impact on chemical evolution. It will become increasingly more critical in the future because James Webb Space Telescope will provide us with more detailed observations of the more complex molecules in ices.

Sublimation processes of solid species into the gas in an interstellar medium are not well understood. As mentioned in the previous section, many astrochemical models have addressed this issue and have proposed solutions. However, we are not close to solving this question. Often in astrochemical models of cold cores, the gaseous abundances are underproduced with respect to the observed abundances.

Additionally, modeling the amorphous nature of the grain surfaces, meaning taking into account the fact that an amorphous surface offers various binding sites, is another issue that should be taken into account in astrochemical models. The diffusion and desorption rate of species on ices is strongly dependent on the binding energies. As we have reviewed in the previous section, statistical studies on the binding energies and diffusion rate of surface species can lead to abundances that are orders of magnitude different. The latest chemical calculations have considered the amorphous nature of the grain surfaces and provided multiple binding energies for solid species. The inclusion of multi-binding energy in astrochemical models will affect the desorption and reaction rate of solid species.

Chapter 3

Theoretical and experimental astrochemistry

The following sections briefly overview the recent advances in grains and gas-phase reaction studies. Each section reviews the quantum computational and experimental approaches. The last section discusses computational and experimental studies in the literature that are relevant to or work in Chap. 6, which focuses on modeling the dense cores in TMC1.

3.1 Grain surface reaction studies

The grain surface chemistry is an essential part of the chemical process in Molecular Clouds (MCs), dense cores, and protostars. First and foremost, dust grains are the platform of hydrogen molecules formation. Second, molecules synthesized in the gas phase freeze onto the grains over time, becoming depleted in the gas phase. Third, saturated molecules, such as water and methanol, can form through the hydrogenation of frozen species on ice surfaces. Fourth, the grain mantles work as a storage place for molecules during the protostellar phase, which is then released back into the gas phase in, for example, hot corinos, where they start a new wave of chemical reactions.

The following section briefly describes the quantification of the kinetics parameter of surface reactions, such as the binding energies (BEs) and reaction rates, using computational and experimental chemistry.

3.1.1 Theoretical studies

The static calculations methods provide the Potential Energy Surface (PES) of the reactants and products, the reaction rate constants, the reactants BEs, and products branching ratios (the relative fraction between the possible products from a reaction). The calculations accuracy levels depend on the methodology used in the simulation. These studies also help us understand the role of the ice in the reaction. It can serve as a catalyst, participate in the reaction, or facilitate the dissipation of excess energy from the reaction (Pantaleone et al., 2020, 2021; Rimola et al., 2018a). Chemists follow two steps: (1) Calculation of the static parameters of the system, such as surface energy barriers and BEs, and (2) Calculation of the system kinetics, such as the reaction rates, branching ratios using the information from the first step.

For the first step, computational chemistry can simulate the surface structure and the electronic potential surface of the system. There are two primary strategies for modeling the surface: the periodic and the cluster approaches. The periodic method applies periodic boundary conditions (PBCs) on the simulated unit cell. On the other hand, in the cluster approach, the system consists of a finite number of species without PBCs. The first quantum chemical calculation applied to ice surface astrochemistry started with only a few water ice molecules (≤ 4) comprising the ice (Woon, 1999, 2001a,b). Later on, the ice slab became more

complicated and included up to 500 water molecules, thanks to the increase of computational power (see, for example, Pantaleone et al., 2021).

For the second step, chemists employ various quantum computational methods, such as the density functional theory (DFT) based on electronic density, and calculate the PES, which is a function of the geometry of the system, to calculate the transition states (TSs) that provide the activation energy barrier of a reaction. Additionally, it is important to know that the results strongly depend on the ice model. The reason is that each ice model has different physical properties that can affect the intermolecular interactions (see, Zamirri et al., 2019, and the references therein).

The static calculations provide the information needed for the kinetic study of reactions to quantify the rate constants. The reaction rate constants can be derived from the classical transition state theory (Eyring, 1935). Transmission through the reaction energy barrier via quantum tunneling may dominate the thermal crossing at low temperatures. Various approaches, such as Eckart potential model or Instanton theory, can be used to estimate the quantum tunneling correction on the transmission rate (see, for example, Álvarez-Barcia et al., 2018; Rimola et al., 2014; Song and Kästner, 2017; Yu et al., 2001) .

3.1.2 Experimental studies

In MCs, the density is about $n_{H_2} \sim 10^{4-5}$ cm^{-3} and the temperature about $\sim 10 - 20$ K. The grain envelopes consist mainly of Amorrphous Solid Water (ASW) with a mix of CO, CO_2, methanol and many more species that have been frozen over the long lifetime of a MC. Recent experimental setups can achieve the low temperatures in the interstellar medium (ISM) ($\sim$ 8 K). On the other hand, the pressure reached by the instruments is about $10^{-7 \div -10}$ mbar[1] These pressures are low enough that keep the setup from contamination through the duration of the experiment. Additionally, experiments simulate a very simple ISM ice analog (typically $\leq$ 3 species) compared to how an ISM ice could be. The reason is to keep the influencing parameters under control (Allodi et al., 2013; Vidali, 2013).

Similar to the computational studies, experiments are designed to study and derive the system static and kinetics properties and the properties and topology of the ice surface. This section discusses the so-called TPD experiments and those designed to study surface and bulk reactions.

Temperature Programmed Desorption (TPD) experiments TPD experiments primarily provide effective BEs and desorption rates. Experiments often focus on mono- or bi-composite ices. The molecules or atoms are beamed on a cryogenically cooled surface known as the substrate. The substrate is usually gold or other noble metals to reduce the chance of any chemical reaction between the substrate and the target material. The ice is warmed-up typically linearly in time, starting from usually about 10 K with a heating rate of about 0.1 to a few 10 Kmin^{-1}. The experiments take place in two regimes: (1) monolayer[2] (ML) and sub-ML and (2) multi-layer. In the sub-ML and ML regimes, quadrupole mass spectroscopy (QMS) (Dawson, 1997) is used to probe the desorbed species. Ices with multiple MLs are studied using the reflection absorption infrared spectra (RAIRS) technique. The reactants and the products are both probed in situ. Often both detection techniques are used to probe an experimental setup since they are complementary (see, Allodi et al., 2013; Burke and Brown, 2010; Congiu et al., 2020; Watanabe and Kouchi, 2008a).

Several TPD-focused experiments have been done in the past decades to obtain BEs, sticking coefficients of relevant species. These experiments help us to understand the ISM ice behavior under the temperature increase. For example, Collings et al. (2004) has surveyed the

[1] A typical pressure in the ISM, $n_{H_2} \sim 10^4$ cm^{-3}, corresponds to $\sim 4 \times 10^{-12}$ mbar (Yamamoto, 2017).

[2] One monolayer (ML) typically corresponds to 10^{15} molecules per square centimeter.

thermal desorption rate of a series of interstellar relevant molecules from a water ice film. Their results show that the ASW can trap volatile species, which effects the gaseous and surface chemistry. Their results have been employed in astrochemical models (Garrod and Herbst, 2006; Viti et al., 2004). Acharyya et al. (2007) conducted a series of TPD experiments on CO and O_2 pure and mixed ices (no water involved) with various ratios to obtain BEs and sticking coefficient. They find that O_2 is less volatile than CO, and that the desorption temperature of O_2 and CO are very close to each other. Therefore, it is unlikely that the freezing of O_2 could explain the missing gaseous oxygen where shows significant CO abundance (see, also, He et al., 2016; Minissale et al., 2016a; Noble et al., 2012b).

Surface reactions The exposure of reactants on a surface can be controlled by regulating the relative flow of the beams and QMS or RAIRs can monitor the products. Obtaining absolute reaction rate is difficult, especially for reactions involving atomic H since they are mobile and H_2 formation is inevitable. It is easier to quantify competing reactions with different species (Tielens, 2021, also, see, Sec. 3.3.2).

Bulk reactions Mono- or multi-component ices exposed to UV photons or high-energy ions are used to study chemical pathways inside the bulk. They can directly induce chemical reactions and are often used to promote energetic reactions. The products are monitored by RAIRS and QMS instruments (if the ice is heated after the experiment). Reactions that may occur during the warm-up can affect the results. Therefore, laser desorption with QMS techniques can be a good alternative in some cases. In laser desorption, the ice is heated locally by a thin laser beam to a high enough temperature to induce desorption (Tielens, 2021; Watanabe and Kouchi, 2008a).

3.2 Gas phase reaction studies

Experimental and computational kinetics study of reactions in the gas phase helps understand and better predict the chemical evolution in dense cold cores and protostars. They can provide the rate constants and branching ratios that characterize a reaction rate in the gas phase and can be used in astrochemical models. Various types of reactions take place in the gas phase in MCs and Young Stellar Objects (YSOs): photodissociation and photoionization, dissociative recombination and electron attachment, radiative association, and neutral-neutral reactions ion-neutral reactions.

Millar et al. (1991) was one of the first to put together a database of gas-phase reactions in the ISM. Today, these efforts are assembled in online databases, such as OSU (Harada et al., 2010), Umist (McElroy et al., 2013), and Kida (Wakelam et al., 2012). The rate constants of a reaction generally depend on the temperature. It can be characterized with three parameters α,β, and γ in a modified form of the Arrhenuis equation

$$\kappa(T) = \alpha \left(\frac{T}{300.}\right)^{\beta} \exp\left(\frac{-\gamma}{T}\right). \tag{3.1}$$

$\kappa(T)$ denotes the rate constants with dependency on temperature T [K]. α has the same units as $\kappa(T)$; β is a only a number, and γ can be thought of as an energy expressed in K. The reaction rate coefficient of each branching product is a product of the rate coefficient, $\kappa(T)$, and the corresponding branching ratio.

Ion-neutral reactions in MCs and cold cores are prominent categories of reactions. Ions are highly reactive, and the reactions are often barrier-less and occur rapidly at cold temperatures. Therefore, most of the observed species are electrically neutral. The most recent

experiments with CRESU (Cinéique de Réction en Ecoulement Supersonique Uniforme, i. e., Reaction Kinetics in Uniform Supersonic Flows) have shown that some neutral-neutral reactions have higher reaction rate coefficients at lower temperatures (see, e. g., Shannon et al., 2013).

3.2.1 Theoretical studies

The gas-phase reactions study employing quantum chemical computations is conceptually similar to those of the surface chemistry simulations. The biggest difference is that a surface model is not required for computing the PES and the kinetics of the gas-phase reactions. This important burden reduction allows quantum computational methods with higher accuracy levels at lower costs. This also allows the study of reactions between larger species than those considered in surface reaction simulations (typically with ≤ 4 atoms) (see, for example, Barone et al., 2015; Holtom et al., 2005; Redondo et al., 2014; Skouteris et al., 2017; Skouteris et al., 2015, 2018, 2019; Vazart et al., 2016; Vazart et al., 2020; Wakelam et al., 2017).

3.2.2 Experimental studies

The conditions in the ISM are extreme, which poses a challenge to the performance of these experiments. Reactions in MC conditions occur at about $\sim 10 - 20$ K and at $\gtrsim 100$ K, in hot corinos. It means that various instruments are required to quantify the reaction rate parameters to cover the temperature range. There are two possible difficulties on the way. Some reactions are difficult to study at low temperatures, in which case chemists propose an extrapolation from higher temperatures. Or if a reaction cannot be studied with current instruments, the reaction rate coefficient needs to be estimated (Smith, 2011; Wakelam et al., 2010a). The study of branching ratios in experimental laboratories is another matter that poses a significant challenge. In some cases, it can be inferred from the thermodynamical property of the products, assuming hat the reaction outcome is determined by thermodynamic control. However, in cases where both are energetically accessible, branching ratio estimations become difficult (Seakins, 2007; Smith, 2011).

Each apparatus used to study chemical reactions is optimized for a specific temperature range. The breakthrough instrument in studying astrochemically relevant reactions was CRESU that made studying the ion-neutral reactions down to $\sim$ 8 K possible (Rowe and Marquette, 1987; Sims et al., 1994). Electron attachment and neutral-neutral reactions are the other applications of this instrument (Canosa et al., 2008). CRESU technique is used to study neutral-neutrals reactions below 80 K. Although it was initially designed for studying ion-neutral reactions, it was adapted to study reactions involving radicals such as C, O, Si, B, and OH. Recent studies have shown that the rate of some neutral-neutral reactions increases with lowering the temperature, especially those between radicals and unsaturated species and radical-radicals.

Other instruments are used to study the reactions at a higher temperature. For example, the ion cyclotron resonance (ICR) method can be used to examine ion-neutral reactions at room temperature. This method uses an electric and magnetic field to trap the ions. Or the flowing afterglow (FA) method with the selected ion flow tube (SIFT) is employed to quantify ion-radical reactions. It uses a Helium stream as its buffer gas and injects the ions and the neutral co-reactant into the tube. Experiments quantifying neutral-neutral reaction rates are similar to those for ion-neutral reactions. For a temperature range of $\sim$200 - 400 K, techniques similar to FA and SIFT can be used (see Kaufman 1984), and the pulsed photolysis techniques are used for temperatures down to $\sim$80 K.

3.3 A brief review on relevant work

In the following sections, we provide a brief overview of the recent experimental and computational chemistry studies on binding and diffusion energies, diffusion and reaction rates, and chemical desorption rates that are relevant to the work presented in Chap. 6. This chapter focuses on modeling the ice composition in the dense cold cores in TMC1, where I present the impact of some of the discussed parameters on the chemical composition in the models. The concerning matters in the formation of ices in cold MCs are species diffusion on the surface and the formation rate of other species in ices. At MC temperatures, practically only hydrogen and oxygen atoms are mobile.

Therefore, the following paragraphs focus on binding and diffusion energy and diffusion rate of hydrogen and other atoms, hydrogenation of CO and formaldehyde, and the formation rates in water and CO_2 formation network. The last part reviews modeling of chemical desorption probability based on quantum computational and experimental studies.

3.3.1 Binding and diffusion energies

The species landing on a surface can bind to the surface by van der Waals interaction (physisorbed) or via chemical bond to the surface (chemisorbed). Chemisorption consists of a chemical bond of the adsorbate species. On the other hand, physisorbed species experience minimal interaction with the surface. The physisorption generally happens at a larger distance to the surface and with lower BE than chemisorption (Tielens, 2021). A species BE depends on the nature of the molecule, the substrate and its composition, and its relative orientation to the surface. The surface of the icy mantle of dust grains in the ISM is mainly composed of dense amorphous water (Jenniskens et al., 1995). In the cold MC, water ice is in an amorphous state. The amorphous surface creates a somewhat irregular electrostatic potential. On the other hand, the crystalline water ice surface displays an orderly and regular variation in the electric potential that limits the ways molecules can bond to the surface. It means that the ASW surface binding sites have a greater variety than a crystalline surface.

BE calculation of atomic oxygen, carbon, and nitrogen is challenging. However, recent experimental and computational works have provided us with their BEs on ASW surface. He et al. (2015) experimental results on porous ASW estimate atomic oxygen BE of 1660±60 K, while Minissale et al. (2016a) suggested BE is 1320 K on compact ASW, and Shimonishi et al. (2018) quantum computation derives 1440±160 K. Quantum chemical computations from various authors have shown that carbon is chemisorbed on water ice surfaces. It forms a chemical bond with the atomic oxygen of the water molecule (**duflot_2021**; Shimonishi et al., 2018). While studies, such as Molpeceres et al., 2021, suggest that atomic carbon can react with water to form formaldehyde, other studies, such as Ortman et al. (1990) and Schreiner and Reisenauer (2006) report non-reactions. Minissale et al. (2016a) BE for atomic nitrogen on compact ASW estimates 720 K BE. Shimonishi et al. (2018) quantum chemical calculations suggest 400 K, which is an underestimation due to insufficient descriptions of the van der Waals interaction.

Cooke et al. (2018), Cuppen et al. (2017), Garrod (2013), Hama and Watanabe (2013), Öberg et al. (2009e), Penteado et al. (2017), Taquet et al. (2014), and Wakelam et al. (2017) provided extensive list of measured or calculated BEs on various substrates from experimmental and computational chemistry studies. Additional to those above, the latest quantum computational studies have concentrated their work on providing a distribution of BE for astrochemically relevant species given the nature of the ice in the ISM (Bovolenta et al., 2020; Ferrero et al., 2020; Grassi et al., 2020, see also Sec. 3.3.1 for more detail). For example, Ferrero et al. (2020) calculated the BE of 21 species on crystalline and amorphous surfaces using DFT methods. Simulated crystalline and amorphous water slabs are enforced with PBCs, and 8 binding

sites are chosen on the amorphous slab to calculate the BE. They show that BE on crystalline ice have a smaller variation and are generally higher than on the amorphous slab.

Diffusion energy The diffusion energy is poorly constrained as it is inherently difficult to measure (see Cuppen et al., 2017; Hama and Watanabe, 2013, reviews). Although challenging, many groups have researched to measure its value for astrochemically relevant species. The diffusion energy of a species is commonly expressed as a fraction of its BE in astrochemical models. Accordingly, in models, the diffusion to BE ratio, ƒ, is often adopted as an input parameter. The range of adopted ratios in the literature is between 0.3-0.85 (see e. g. Cooke et al., 2018; Cuppen et al., 2009; Hama et al., 2012; Karssemeijer and Cuppen, 2014; Katz et al., 1999; Lauck et al., 2015; Livingston et al., 2002; Maté et al., 2020; Mispelaer et al., 2013; Perets et al., 2005; Ruffle and Herbst, 2000; Tielens and Hagen, 1982a; Watanabe et al., 2010). The latest experimental studies in the past few years agree more on a ratio within 0.3 - 0.5. For example, the experimental work of He et al. (2018) on light species on ASW finds a range between 0.3 - 0.6 (see their Table 3). On the other hand, the theoretical work of Karssemeijer and Cuppen (2014) on CO and CO_2 suggest a smaller range of 0.3 - 0.4 for those molecules. Minissale et al. (2016a) experiments on atomic oxygen and nitrogen suggest 0.55 for the ratio.

Binding energy of atomic hydrogen The most abundant gaseous and solid species in MCs and cold cores are hydrogen molecules and water (formed through hydrogenation of O, or OH). Methanol is another species that is efficiently formed on ices through successive hydrogenation of CO.

Pierre et al. (1985) have measured the BE of atomic H on a quantum crystal of H_2 as 45 K. The Molecular Dynamics (MD) simulations of Buch and Zhang (1991) estimated the atomic H BE on ASW to be in the range of 650±195 K. MD simulations of Al-Halabi and van Dishoeck (2007) estimated the BE to be 650±10 K on ASW and 400±5 K on crystalline ice. Garrod (2013) lists 450 K and Wakelam et al. (2017) 580 K, based on experimental data. Senevirathne et al. (2017) estimates the hydrogen BE distributions by considering the zero-point energy correction within the range of 255 - 730 K (see, their Table 2).

Diffusion energy of atomic hydrogen The diffusion energy of atomic hydrogen is not well constrained because of its volatility and high reactivity. The measured energy depends on the substrate structure. These differences are the source of discrepancies and a wide range of diffusion energies from different working groups. Experimental works measured the diffusion energy of hydrogen atoms through their recombination after diffusion on the surface. Manicò et al. (2001) estimates the diffusion energy by conducting TPD experiments in which they co-deposit atomic H and D and measure their diffusion rate through their recombination rate, which estimates the diffusion energy of hydrogen to be between 475 and 640 K. Hama et al. (2012) conducted direct detection experiments of atomic H on ASW. They used photo-stimulated desorption (PSD) and resonance-enhanced multiphoton ionization (REMPI). They categorize the binding sites on the ice surface according to their depth to shallow, middle, and deep sites. They estimate the diffusion energy of atomic H to 209 ± 23, 255 ± 12, and $\geqslant\sim$ 348 K for these categories respectively. Senevirathne et al. (2017) estimated the diffusion to BE ratio for atomic H to be 0.37, corresponding to a range of 94 - 270 K based on their BE distribution obtained with quantum chemical methods.

3.3.2 Diffusion and reaction rates

Species on the surface can diffuse using thermal hopping or, if light enough, by quantum tunneling through the potential barriers on the surface. The following paragraphs discuss

the most recent studies on hydrogen, oxygen, carbon, and nitrogen diffusion rates and the reaction rates in the methanol, water, and CO_2 networks.

Hydrogen atom diffusion rate Studying the diffusion rates of atomic and molecular hydrogen is essential since they affect the hydrogenation rate of species in ices and the composition of the ice. In 1999, Katz et al. (1999) carried out a series of experiments and concluded that the rate of diffusion of atomic H via quantum tunneling is negligible in comparison to the thermal hopping rate. Later, Hama et al. (2012) confirmed that thermal hopping is likely dominating the H-diffusion in ASW. However, Kuwahata et al. (2015a) carried out experiments of H diffusion on polycrystalline ice surfaces at 10 K and found that tunneling dominates over thermal hopping, even though they caution that "Whether diffusion is by tunneling or thermal hopping also depends on the diffusion length of the atoms and the morphology of the surface". The recent theoretical study by Senevirathne et al. (2017) suggests that the diffusion rate of atomic H via quantum tunneling on both crystalline and ASW surfaces dominate over the thermal hopping rate by orders of magnitude (see, Figure 7a and 7c in their paper) at about 10 K. The diffusion rate on ASW is larger than the rates on crystalline ice in all temperatures.

Oxygen, carbon, and nitrogen atoms diffusion rate Congiu et al., 2014 investigates the diffusion rate of oxygen in the 6.5 - 25 K temperature range on porous and non-porous ices. Their results show that the oxygen diffusion rate via quantum tunneling is non-negligible (see, their Figure 3). They derive an empirical formula to fit the measured rate in Table 1.
Quantum chemical computations from various authors have shown that carbon is chemisorbed on water ice surfaces. It forms a chemical bond with the oxygen of the ice water molecule (**duflot_2021**; Shimonishi et al., 2018). Zaverkin et al. (2021) computed the diffusion rate of nitrogen using machine-learning and kinetic Monte Carlo simulations. They conclude that diffusion of nitrogen is practically impossible on ASW at 10 K, and the effect of quantum tunneling is negligible.

Reaction rates in the methanol formation network The successive addition of H-atoms to frozen CO leads to formaldehyde and methanol (Tielens and Hagen, 1982a):

$$\mathrm{CO} \xrightarrow{\mathrm{H}} \mathrm{HCO} \underset{\mathrm{H}}{\overset{\mathrm{H}}{\rightleftarrows}} \mathrm{H_2CO} \xrightarrow{\mathrm{H}} \mathrm{CH_3O} \xrightarrow{\mathrm{H}} \mathrm{CH_3OH}\,. \tag{3.2}$$

This reaction chain has been revisited by many experimental works, such as, Fuchs et al., 2009; Hiraoka et al., 2002; Minissale et al., 2016b; Watanabe and Kouchi, 2002. While (HCO + H) and (CH_3O + H) are barrier-less, (CO + H) and (H_2CO + H) involve activation energy barriers, which several groups have theoretically characterized. For example, Rimola et al. (2014) and Song and Kästner (2017) have studied the reactions on water substrates using quantum chemical calculations, and Goumans et al., 2007 investigated the methanol formation network on silica grains and provided activation energies for CO and formaldehyde hydrogenation.

Rimola et al. (2014) computed the Eckart model parameters to characterize the reaction energy barriers in the methanol reaction network using DFT methods and a 32-water molecule slab to model the surface. Song and Kästner (2017) have characterized the kinetic parameters of the formaldehyde hydrogenation reaction, including the tunneling correction. They find three possible reactive channels: CH_3O, H_2 + HCO, and CH_2OH. These authors found that the H-abstraction leading to HCO and H_2 is less efficient than the methoxy formation (with 0.2 and 0.8 branching ratio fractions, respectively), while the formation of CH_2OH is negligible. They provide rate constant parameters for a modified form of the Arrhenius equation

(their Equation 2)

$$\kappa(T) = \alpha \left(\frac{T}{300\mathrm{K}}\right)^{\beta} \exp\left(-\frac{\gamma(T+T_0)}{T^2+T_0^2}\right) , \tag{3.3}$$

to calculate the rate coefficient $\kappa(T)$ as a function of the temperature. Their best-fit parameters for an LH reaction are reported in their Table 3.

Reaction rates in water formation network Hydrogenation of frozen O, O_2 and O_3 via barrierless reactions, plus other reactions involving H_2 and OH, lead to water formation on ice surfaces (Tab. 4.7 and 4.8). Two of the reactions (OH + H_2) and (HOOH + H) require activation energies. Nguyen et al. (2011) conducted semiclassical transition-state theory calculation and computed the Eckart model potential parameters for (OH + H_2) reaction. Ellingson et al., 2007 calculated the reaction potential energy barrier parameters of hydrogen peroxide hydrogenation using high-level quantum chemical calculations and including the Zero-Point Energy (ZPE) corrections (see also, Lamberts et al., 2016; Meisner et al., 2017).

Reaction rates in CO_2 formation network CO_2 formation network starts with oxygenation of HCO and CO (Ruffle and Herbst, 2001). HCO oxygenation is barrierless (Baulch et al., 2005), while the CO one has an activation energy. Experiments show that oxygenation of CO in cold temperatures is possible but with a very low efficiency (Raut and Baragiola, 2011). The quantum calculations of Goumans and Andersson, 2010; Goumans et al., 2008; Talbi et al., 2006 also show that the transmission probability is rather low $\sim 5 \times 10^{-23}$. Another route to CO_2 formation is via OH radical reaction with CO that goes through intermediate steps forming *trans*- and *cis*-HOCO (Oba et al., 2010).

HOCO radicals can also react with abundant atomic H and form CO_2 + H, H_2O + CO, and HCOOH (Goumans et al., 2008). HCOOH and HOCO radical has not been observed in the Oba et al. (2010) experiment, suggesting that CO_2 is formed from excited HOCO radicals before reaching their steady-state. The experiments by Ioppolo et al., 2011; Noble et al., 2011; Oba et al., 2010 at 10 - 20 K indicate that (CO + OH) has a small energy barrier. Yu et al. (2001) calculated the potential energy surface parameters for the (CO + OH) reaction using ab initio quantum chemical computations and provided the Eckart model potential parameters. Goumans and Andersson, 2010 gas-phase study suggest that CO and atomic oxygen can form a van der Waals complex of O...CO. They also suggest that hydrogenation of the complex can lead to excited *trans*-HOCO which then forms CO_2 + H, CO + OH, and stabilized t-HOCO (see, also, Taquet et al., 2013, for a detailed review on the reaction network).

3.3.3 Chemical desorption

The energy released from exothermic reactions on the ices can potentially eject the reaction product into the gas phase. This process is commonly known as chemical or exothermic desorption. This mechanism has been put forward in astrochemical modeling because of observed complex molecules in the gas phase below their desorption temperature in cold MCs and dense cores (see, for example, Bacmann et al., 2012; Vastel et al., 2014). The most notable one is methanol, whose main formation route is believed to be through successive hydrogenation of CO on ice surfaces (Garrod et al., 2006; Hidaka et al., 2004; Williams, 1968).

The probability of desorption depends on the nature of the reactants, the product, and the surface composition. It decreases with the increase of surface coverage (see Dulieu et al., 2010; Minissale and Dulieu, 2014). There are many experimental, MD simulations and theoretical works on chemical desorption (e. g., Cazaux et al., 2010; Dulieu et al., 2010; Dulieu et al., 2013; Garrod et al., 2007; Minissale and Dulieu, 2014; Minissale et al., 2016b; Oba et al., 2018; Pantaleone et al., 2020; Vasyunin and Herbst, 2013).

Garrod et al. (2006) put forward a formalism based on the competitive processes the rate of exothermic desorption and the rate of energy dissipation. The probability of desorption is

$$f = \frac{k}{1+k}\,, \tag{3.4}$$

where

$$k = a\left[1 - \frac{E_{\rm des}}{E_{\rm react}}\right]^{3N-6}\,. \tag{3.5}$$

N is the number of atoms in the product, $E_{\rm react}$ is the exothermicity of the reaction, and a is an efficiency parameter that that can take a value between 0.01 and 0.1. This paper suggests that the 1% probability is adequate to reproduce methanol observation in MCs.

Experiments and models show that the probability highly depends on the reaction pathway and its product(s). For example, Dulieu et al. (2013) conducted an experiment on the formation of water molecules in sub-ML regime and found that the desorption of the products is significant perhaps in parts due to the lack of binding opportunity. The desorption rate decreases in the multilayer regime (Minissale and Dulieu, 2014). Oba et al. (2018) shows H_2S, the product of sulfur hydrogenation has 60% probability of desorption. Experiments and computations on CO hydrogenation give upper limits of 1% (Chuang et al., 2018; Pantaleone et al., 2021). Minissale et al. (2016b) conduct a series of experiments to measure the chemical desorption probability for astrochemically relevant species. The desorption probability and upper limits of the products from the water, CO_2, and methanol networks range from 0.5 to 80% (see, Table 1 in their paper). They proposed a new methodology to calculate the probability

$$\rho_{\rm CD} = \exp\left(\frac{-E_{\rm b}}{\epsilon \Delta H_{\rm R}/N}\right) \tag{3.6}$$

based on the kinetic energy available for ejection of the molecules perpendicular to the surface $\epsilon\Delta H_{\rm R}/N$, and the BE of the product $E_{\rm b}$ (see their equation 2). The proposed estimate is in agreement with their experimental results.

Part II

Grainoble+ and its applications

Chapter 4

Astrochemical model, Grainoble+

Grainoble+ is an astrochemical model simulating the chemical evolution in the gas and the formation and destruction of the ices on the dust in starforming regions. The code Grainoble+ is a re-coded and upgraded version of the code Grainoble (Taquet et al., 2012, 2013).

Briefly, Grainoble+ is 3-phase, gas-grain, and multi-grain chemical model, which follows the formalism of Hasegawa and Herbst (1993b) to describe the chemistry in the gas and layered structure of the ice. The phases are (1) the gas phase, (2) the active layer in which the grain-surface chemistry takes place, the part of the mantle that is exposed to the gas phase, and (3) the bulk of the ice underneath the surface, which is considered chemically inactive. The mantle has a layered structure, where the composition of each monolayer is stored. Two important processes link the gas phase and the mantle: absorption from the gas into the mantle and thermal and non-thermal desorption from the mantle to the gas. Three processes are considered for non-thermal desorption: cosmic-ray (CR) desorption, chemical desorption, and photo-desorption. The latter two and thermal desorption only take place in the active layer, while CR desorption involves the entire mantle (e. g., Hasegawa and Herbst, 1993b; Leger et al., 1985). Species adsorbed on the active layer can diffuse, and upon encounter, they may react.

The major differences of Grainoble+ relative to Grainoble are described in the following.

a) Grain assisted charge exchange treatment: we introduced a more comprehensive treatment of this process, based on the work by Draine and Sutin (1987) (§ 4.4.2).

b) The reaction rate coefficient of CO and formaldehyde hydrogenation on ices are included directly from Witzel et al. 2022 (submitted) and Song and Kästner (2017), respectively (§ 3.3.2 and 4.4.4).

c) The rate of diffusion of hydrogen and oxygen atoms are included directly from Senevirathne et al. (2017). and Congiu et al. (2014), respectively (§ 3.3.2 and 4.4.4).

d) The thermal desorption rate of hydrogen atom and CO are included directly from quantum chemical calculations presented in Witzel et al. 2022 (submitted).

e) The surface reaction efficiency now follows the Enrique-Romero et al. (2021) formalism (§ 4.4.4).

f) The code is now capable of including the multi-grain phase. The grain size distribution can be modeled based on a selected model, for example, the MRN model. Processes, such as CR desorption, vary as a function of grain radius, which affects the general chemical composition in gaseous and solid forms (§ 4.2.1).

g) Grainoble+ has implemented a modular structure that facilitates any process's addition, modification, or removal. It also provides an easy user interface in Python for the Fortran core code. The algorithm and the newest technical additional of the model is in Appx. C.

In the following sections, we describe the essence of our model. Sec. 4.1 reviews the physical conditions, or in other words, the macro-physical parameters. Sec. 4.2 describes the modeling of grain cores, the icy mantle, and the grain size distribution model. Sec. 4.3 focuses on the initial elemental abundances, the sticking coefficient parameter, and the binding and diffusion energies. Finally, Sec. 4.4 describes the chemical processes included in the models, such as gas-phase reactions, grain surface reactions, adsorption, and thermal and non-thermal desorption processes. Chap. 5 and Chap. 6 are the two applications of Grainoble+

4.1 Physical structure of the cloud

As discussed in Sec. 1.1.1, a molecular cloud (MC) is formed through the collapse of a Cold Neutral Medium (CNM). Once enough material is collected together to shield itself from the external irradiation effectively, it can produce and sustain its molecular hydrogen population and consequently CO and other complex molecules. In MCs and dense cores, the temperature is $\leq$ 20 K, which leads to the freeze-out of synthesized gaseous molecules on the dust grains and an ice envelope starts to grow on the grains.

In MCs and dense cores, the density is about $10^{4-6} n_{\rm H}$ cm^{-3} and the gas and dust temperature are $\leq$ 20 K. The Cosmic Ray (CR) ionization rate of hydrogen is $\sim 10^{-17 \div -18}$ s^{-1} (Phan et al., 2018) and the external Ultra-Violet (UV) irradiation at the edges of the cloud is about 10^{8-10} cm^{-2}s^{-1} which is attenuated with the increase of visual extinction, $e^{-\gamma A_v}$, as it propagates inside the cloud ($\gamma = 1.8$, Shen et al., 2004; Tielens and Hollenbach, 1985). The UV flux due to CR reaction with hydrogen is $\sim 10^4$ cm^{-2}s^{-1} inside dense cores (Gredel et al., 1987). For example, see Fig. 4.1 that shows the density and the gas and dust temperature as a function of visual extinction derived from observations in three different parts in TMC1 in Taurus Molecular Cloud.

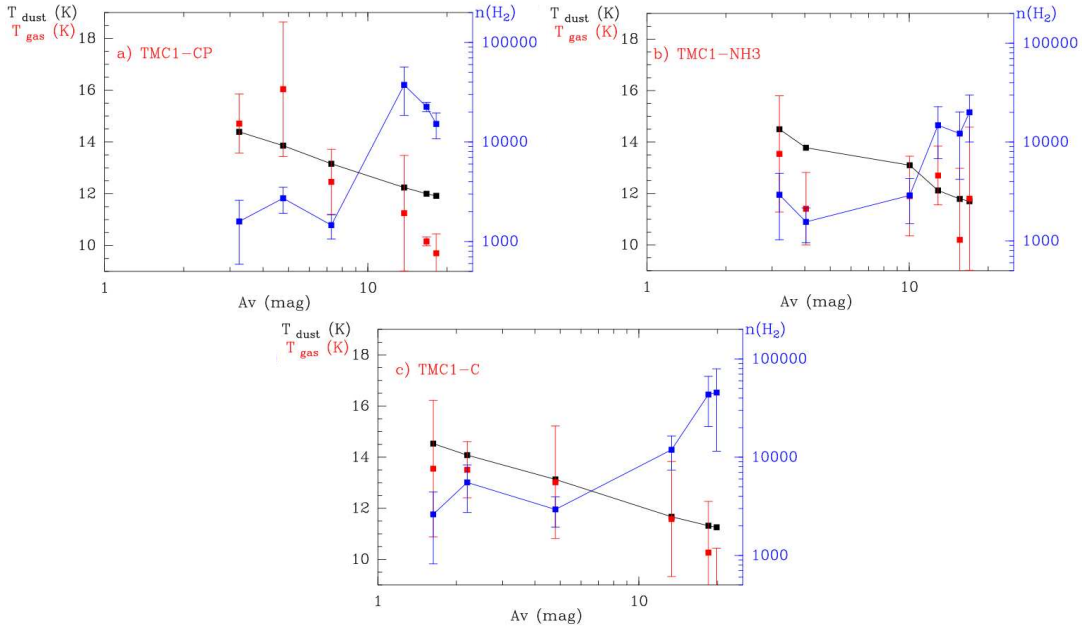

FIGURE 4.1: The figure (from Fuente et al., 2019) shows the density, gas and dust temperature as a function of visual extinction for TMC1-CP (a), TMC1-NH3 (b), and TMC1-C (c).

4.2 The dust grains and their ice envelopes

Dust in the Interstellar Medium (ISM) absorbs light over a wide range of frequencies. The observed extinction curve displays broad distinct features, unlike line-like features from molecules. Additionally, local observations show substantial depletion of heavy elements such as silicon and iron when compared with abundances in the Sun (§ 4.3.1). Another indication of dust presence in the ISM is the continuum black body emission in mid and far-infrared.

The extinction curve correspond to the dust grain size distribution (see, § 4.2.1). It is stronger in UV band than visible and infrared, which means smaller dust grains are more abundant than larger ones. The bumps in the curve tell us about the composition of the dust. For example, the 217.5 nm bump is associated with graphite (Mathis et al., 1977) and the 9.7 and 18 μm feature to amorphous silicates (e. g., Draine and Lee, 1984; Draine et al., 2007). Due to low temperatures and high visual extinction in dense cores, molecules formed in the gas phase freeze out on the grain cores and form an ice envelope.

As mentioned in the introduction of this chapter, Grainoble+, is a three-phase and multi-grain model. The surface layer(s) are chemically active, while the bulk (the lower layers in the ice mantle) remain inert. The bulk is susceptible only to CR-induced desorption process. The model parameters defining the dust grains and the ice mantle are as follows:

- The total mass of the dust: it is typically about 1% of the total mass of the gas.
- The density of the refractory core: it is 3 [gr cm^{-3}] (Leger et al., 1985), which is roughly the average density for a silicate graphite core.
- The grain radius: Grainoble+ has implemented the grain size distribution feature into the model, which will be explored in future work. In models with homogeneous size grains, the radius is typically 0.1 μm.
- Ice layer model: Grainoble+ models the layered structure of the ice and keeps a memory of the individual layers.
- The surface layer(s): Usually the number of mononlayers in the surface is 1. However, one can increase the number of monolayers in the surface (that are chemically active) with an input parameter in Grainoble+.
- The species concentration on a layer: Grainoble+ assumes each species binding site occupies a square with a width of 3 - 4 Å. The model usually takes an average width, 3.5 Å (Jenniskens et al., 1995). Each square is called a lattice site in the model.
- Grain radius growth: the model can consider the grain radius development as the ice envelope builds up. The thickness of each layer equals the width of a lattice binding site. The change in radius affects the cross-section of the grain and the surface area in each layer, especially in small grains.

4.2.1 Grain size distribution

Mathis et al. (1977) fitted a power-law grain size disrtibution on the observed interstellar extinction in the wavelength range of 0.11 - 1.0 μm. The grain size distribution is proportional to $n(r) \propto r^{-3.5}$. The graphite size distribution is between 0.005 - 1.0 μm, and for grains with other compositions, this distribution is in a narrower range, 0.025 to 0.25 μm. Based on this distribution, smaller grains total larger surface area, whereas larger grains constitute most of the mass of the total distribution. As mentioned before, many processes depend on the grain size, such as non-thermal desorptions, affecting the abundances in the gas phase and

the ice composition. We will employ this feature of Grainoble+ and examine the grain size distribution effect in future works.

Grainoble+ has implemented the ability to run models using grain size distribution. To do so, the model derives the number density distribution of the grains as a function of the grain radius

$$\frac{1}{n_{\rm H}}\frac{{\rm d}\, n_{\rm gr}}{{\rm d}\, r} = C r^{-3.5}\,, \tag{4.1}$$

where $n_{\rm H}$ and $n_{\rm gr}$ are the H-nuclei and grain number density and C is known as the grain constant, which is equal to $10^{-25.11}$ cm$^{2.5}$ for silicate grains and $10^{-25.13}$ cm$^{2.5}$ for graphite grains, where $0.005 < r < 0.25$ μm (Weingartner and Draine, 2001b). In our model we discretizes the distribution into a finite number of bins which can vary with an input parameter (see, e. g., Acharyya et al., 2011; Iqbal and Wakelam, 2018).

4.3 Species

4.3.1 Initial elemental abundances

Hydrogen, deuterium, and helium are created in the first few minutes of our universe, the primordial nucleosynthesis phase. Heavier elements, such as carbon, nitrogen, oxygen, and sulfur are synthesized inside small and large stars through fusion reactions, and the heavier elements[1] in the ISM are formed inside giant stars and supernovae. The death of a star refreshes the flow of elements in the ISM. After a star's life is ended, the elements are ejected into the ISM in dust or gas. The ejected material is extremely hot and can ionize the surrounding gas rapidly, initially. The material can eventually cool down and grow denser and form the CNM, which constitutes the progenitor of a MC (e. g., Ballesteros-Paredes et al., 2020, and Chap. 1).

The elemental abundances can vary in different galaxies or local regions depending on the number of stars in a region. For example, the total elemental abundance increases towards the Galactic Center due to the increase in the number of stars. It is also observed that the local variation also increases (e. g., Esteban et al., 2015). The total sum of the elements relative to hydrogen nuclei in the refractory dust, in the volatile mantles (if present), and in the gas phase is called the cosmic elemental abundances. The chemical composition in the Sun's photosphere is used as a quantitative reference for the cosmic abundances in the solar neighborhood. There has been many studies on this matter since Russell (1929) (for example, Asplund et al., 2009, listed in Tab. 4.1, column 2, and shown in Fig. 4.2).

Depletion of elements, namely their disappearance from the gas phase in the refractory grain cores and volatile mantles, varies in different regions of the ISM. In general, depletion is higher in regions with higher densities and lower temperatures (Jenkins et al., 1986; Shull and van Steenberg, 1985; van Steenberg and Shull, 1988a,b, 1989) and slightly less in warm ionized media in comparison to CNM (Howk et al., 1999).

In CNM to MC, the temperature is low enough that the refractory dust is thought to remain intact. It means that any element that is initially locked up in the refractory dust cores in that region will remain there and does not further take part in the chemical processes. Therefore, it is crucial to quantify the depletion fraction from the cosmic abundances to determine the available elements in the gas phase for the chemical composition in CNM and MCs.

Jenkins (2009) carried out an extended study on the depletion of elements in diffuse and dense clouds with column density between 10^{19} and 10^{22} cm^{-2} (majority of which are around 10^{21} cm^{-2}). He provided values for minimum and maximum depletion of each element from

[1] Note that, generally, in astronomy, metals refer to elements with atomic numbers six and larger.

TABLE 4.1: Elemental abundances.

element	solar abundances $\left(\frac{n_X}{n_H}\right)$	gas phase abundances $\left(\frac{n_X}{n_H}\right)$	depleted percentage
H	1.00	1.00	0.00
He	8.51(-2)	8.50(-2)	0.00
C	2.69(-4)	1.66(-4)	38.0
N	6.76(-5)	5.25(-5)	22.0
O	4.90(-4)	2.84(-4)	42.0
Mg	3.98(-5)	2.14(-6)	95.0
Si	3.23(-5)	1.41(-6)	96.0
S	1.32(-5)	2.55(-6)	80.0
Fe	3.16(-5)	2.00(-7)	99.0

Column 2 lists the solar elemental abundances normalized to the abundance of Hydrogen (Asplund et al., 2009). The third column is the gas phase elemental abundances calculated from Jenkins (2009, Table 4 column seven, F_1^*), which correspond to the highest depletion and lowest temperature in Cold Neutral Medium. As for Sulfur, we take the recommended value from Jenkins (2009).

the gas phase (see, their Table 4, columns 6 (F_0^*) and 7 (F_1^*), respectively). On average, hydrogen and helium are not depleted from the gas phase. The depletion percentage of carbon, oxygen, and nitrogen is about 20 - 40%, whereas heavier elements such as magnesium, silicon, and iron are depleted above 75 - 99 % of their cosmic abundances (see Tab. 4.1, 3^{rd} column). Altogether, the depleted elements in the refractory dust constitute a mass of about 0.5 to 1 percent of the total mass of the region in molecular clouds (Ferrière, 2001).

In Tab. 4.1, we list the gas phase abundance with respect to hydrogen nuclei of the solar abundances (Asplund et al., 2009), and those assuming the maximum depletion estimated by Jenkins (2009), which refer to the denser regions of the ISM in that study. In practice, we use the value (F_1^*) in the third column of his Table 4. The sulfur line features are saturated. Therefore, it is challenging to study, and it is handled separately in his paper. We used their recommended value for F_1^* in Section 9 (see, Fig. 4.2). In our models, we employ the elemental abundances in the gas suggested by Jenkins (2009) (Tab. 4.1, column 3).

The depleted fraction of oxygen from diffuse phase to dense cloud is highly debated in the community and is addressed in many works (see, for example, Caux et al., 1999a; Hincelin et al., 2011; Jenkins, 2009; Jones and Ysard, 2019; Poteet et al., 2015; Whittet, 2010). In summary, studies have found that about 30-50 % of oxygen abundances from a diffuse to dense cloud phase is not accounted for and cannot be explained by CO in the gas phase and silicate and oxides in the refractory core of the dust. For example, Jones and Ysard (2019) suggests that the missing oxygen abundances can only be locked up in carbon chains with high oxygen ratios since carbon is the most abundant in the ISM after oxygen. Consequently, the abundance of carbon in the onset of the dense cloud phase is perhaps also affected. These studies emphasize the importance of the ongoing effort and discussion in the community on the choice of elemental abundances, especially for modeling purposes. To compare with Jenkins (2009) suggested values, we also consider Jones and Ysard (2019) values for oxygen $n_O^{gas} = 3.73 \times 10^{-4}$ and carbon $n_C^{gas} = 1.27 \times 10^{-4}$ which are slightly higher and lower, respectively, relative to Jenkins (2009) suggested values.

In CNM and MCs, gas can be ionized prevalently by UV photons and cosmic rays emitted from A, B, and O. The ionization of an element depends on its ionization energy and the energy of the radiation field by definition. Inside the CNM, only photons with energies smaller

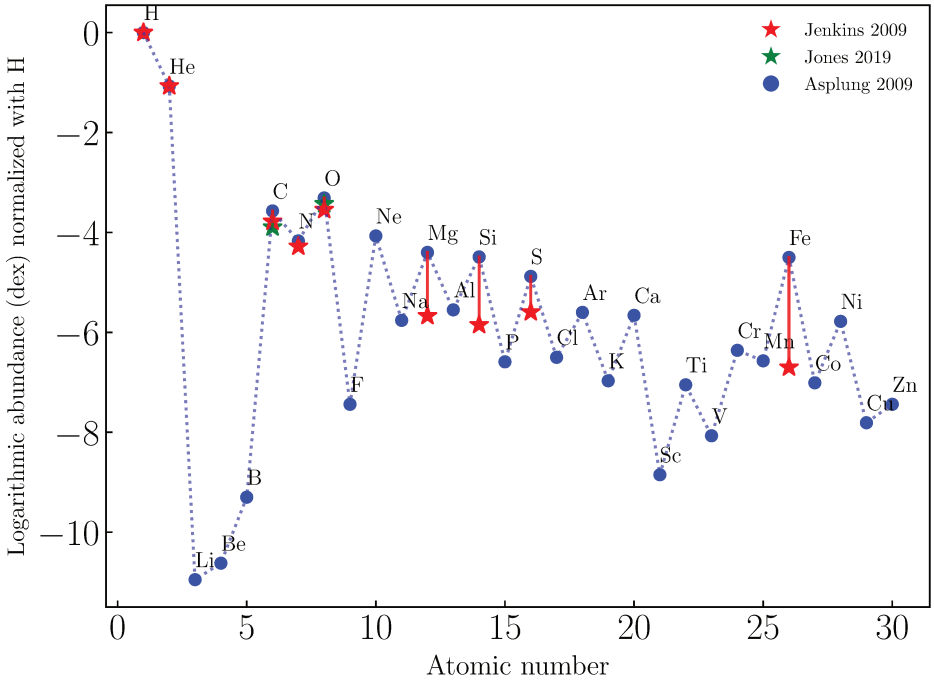

FIGURE 4.2: The blue points represent the Solar photospheric elemental abundances as a function of atomic number normalized to abundances of hydrogen, which is defined as $\log(\epsilon_{\mathrm{H}}) = 12$ in Asplund et al. (2009). The red points are the initial elemental abundances in the gas phase used in our modeling based on Jenkins (2009). The green points those with depletion percentage from Jones and Ysard (2019) for oxygen and carbon.

than 13.6 eV can penetrate the cloud. Photons with higher energies are absorbed in the ionized outer layers of the cloud. Therefore, inside the CNM and MCs, hydrogen, helium, and oxygen remain neutral. At the same time, carbon and the other elements with an ionization potetial smaller than 13.6 eV are ionized in the CNM. Dust is the major absorbent of UV photons. It means that UV photons can only penetrate and ionize low-density clouds with visual extinctions ≤ 1 mag.

4.3.2 Sticking coefficient of neutral species

Grains are the ideal surface for molecules to release excess energy. An incoming species from the gas phase can deposit its kinetic energy to the grain, in other words, thermalize and stick in a physisorbed binding site. Afterward, until the kinetic energy of the species is spent, some species can migrate to a chemisorbed binding site (carbon atom, for example, Shimonishi et al., 2018), desorb (for example, helium that has a shallow binding energy), or remain mobile on the surface (for example, atomic hydrogen). The sticking probability of a particle on a grain depends on their translational energy (the faster the molecules, the smaller the sticking coefficient), energy transfer efficiency, binding energy to the surface, incoming angle (the closer to a normal angle, the higher the sticking probability), and the substrate's state (for example, the probability of atomic hydrogen sticking to Amorphous Solid Water (ASW) is higher than crystalline ice, Al-Halabi et al., 2002) (Tielens, 2021).

The experimental study of the molecular H sticking coefficient involves directing a molecular beam on the surface and using a Quadrupole Mass Spectroscopy (QMS) to detect the desorbed molecules. Studying atomic H sticking in an experimental setup is difficult since

atomic H is highly reactive. Molecular Dynamics (MD) simulations can address this question better.

Molpeceres and Kästner (2020) studied the sticking coefficient of H_2 on amorphous water on a wide range of temperatures through quantum chemical simulations. They find that the coefficient strongly depends on the H_2 kinetics energy and the dust temperature. Their results agree closely with Buch and Zhang (1991). However, they are higher than the sticking coefficients from Matar et al. (2010). Al-Halabi et al. (2004) computed the sticking coefficient of CO to be $\sim$ 1 using classical trajectory calculation at T=90 K. He et al. (2016) conducts experiments and measures the sticking probability of light molecules such as CO and H_2 and provides a formula as a function of the dust temperature and the species binding energy.

Dupuy et al. (2016) uses classical MD to calculate the sticking coefficient of atomic H in a temperature range. They conclude that the sticking depends highly on the kinetic energy of the incident atom. Their results is in relatively good agreement with Al-Halabi and van Dishoeck (2007), Al-Halabi et al. (2002), and Veeraghattam et al. (2014). On the other hand, Buch and Zhang (1991) report a lower sticking coefficient for similar kinetic energy. One should note that Al-Halabi et al. (2002) simulate a crystalline ice surface.

Chaabouni et al. (2012) conducted experimental and theoretical studies on the sticking coefficient of H and D atoms and molecules on amorphous silicate and water. They confirm that measuring the sticking of atomic H in an experimental setup is extremely difficult.

Following the experimental study by He et al. (2016), we assumed that the sticking coefficient on amorphous water ice is equal to unity for all species (at low temperatures, $\sim$ 10 K) except atomic hydrogen, for which we followed the formalism in Hollenbach and McKee (1979):

$$\xi = \left(1 + 0.04\sqrt{T_g + T_d} + 2 \times 10^{-3} T_g + 8 \times 10^{-6} T_g^2\right)^{-1}, \tag{4.2}$$

which models the sticking coefficient of atomic H as a function of gas, T_g, and dust, T_d, temperatures (Hollenbach and McKee, 1979). Fig. 4.3 shows the contour plot of the atomic H sticking coefficient as a function of gas and dust temperatures.

4.3.3 Binding and diffusion energies

As discussed in Sec. 3.3.1, the binding energy (BE) is the energy required for a molecule to break off its bound from a surface. The energy depends on the absorbate molecules and the surface composition and structure.

The binding energies with respect to different substrates used in Grainoble+ are listed in Tab. 4.2. To have a visual comparison, the binding energies listed in Tab. 4.2 and those discussed in Sec. 3.3.1 are plotted in Fig. 4.4 in K. The species are arranged in ascending order relative to their binding energy on an ASW substrate (dark blue circles in the plot). Eb_{ASW} denotes binding energy on an ASW substrate, Eb_{H_2} on a H_2 substrate, Eb_x on a substrate same as the absorbate, Eb_b on a silicate or graphite substrate, and Eb_{CI} on crystalline water. The two light green and pink boxes for H_2 are the BE ranges calculated by Bovino et al. (2017) and Molpeceres and Kästner (2020), respectively. The light blue patch for atomic hydrogen is the range calculated in Senevirathne et al. (2017). The various star markers are the atomic H bindings from different works (§ 3.3.1). In almost all the cases where we have Eb_{cr}, it is larger than its Eb_{ASW}.

The diffusion energy is the energy required for a species to overcome the energy barriers on the surface to hop from one binding site to another on a substrate. In astrochemical

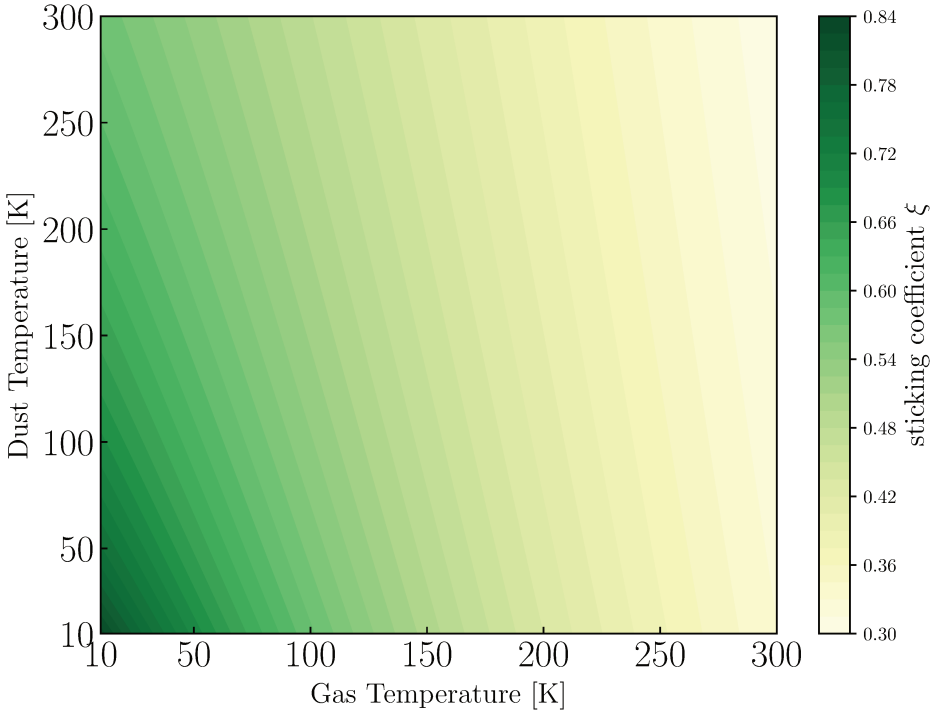

FIGURE 4.3: H-atom sticking coefficient as a function of gas and dust temperature (see Eq. 4.2) from Hollenbach and McKee (1979).

models, diffusion energy is characterized as a fraction of its binding energy,

$$\mathfrak{f} = \frac{E_{\rm diff}}{E_{\rm b}} \,. \tag{4.3}$$

Given the uncertainties in the measurements, in our models, we include $\mathfrak{f}$ as an input parameter for each species and vary the ratio in different models to examine its effect on the abundance of frozen species (see § 3.3.1 for more discussion).

Binding energy dependence of surface coverage

The surface of an icy mantle (substrate) is not purely made of amorphous water. It is composed of many different molecules accreted or synthesized on ices. It is commonly referred to as dirty ices. The icy composition changes the electric potential of the substrate and consequently the BE of the molecule (see, for example, Cuppen and Herbst, 2007). We follow the formalism suggested in Garrod and Pauly (2011) to compute the effective BE of a species x,

$$E_b^x = \sum_i P_i E b_i^x + \left(1 - \sum_i P_i\right) E b_{\rm aws}^x \,, \tag{4.4}$$

where P_i denotes the fraction of a surface that is covered by species i, Eb_i^x is the BE of the species x, on a substrate of species i (see respective BEs on different substrates in Tab. 4.2). We assume the rest of the substrate is ASW.

4.4 Processes

In the introductory chapters, we have emphasized that:

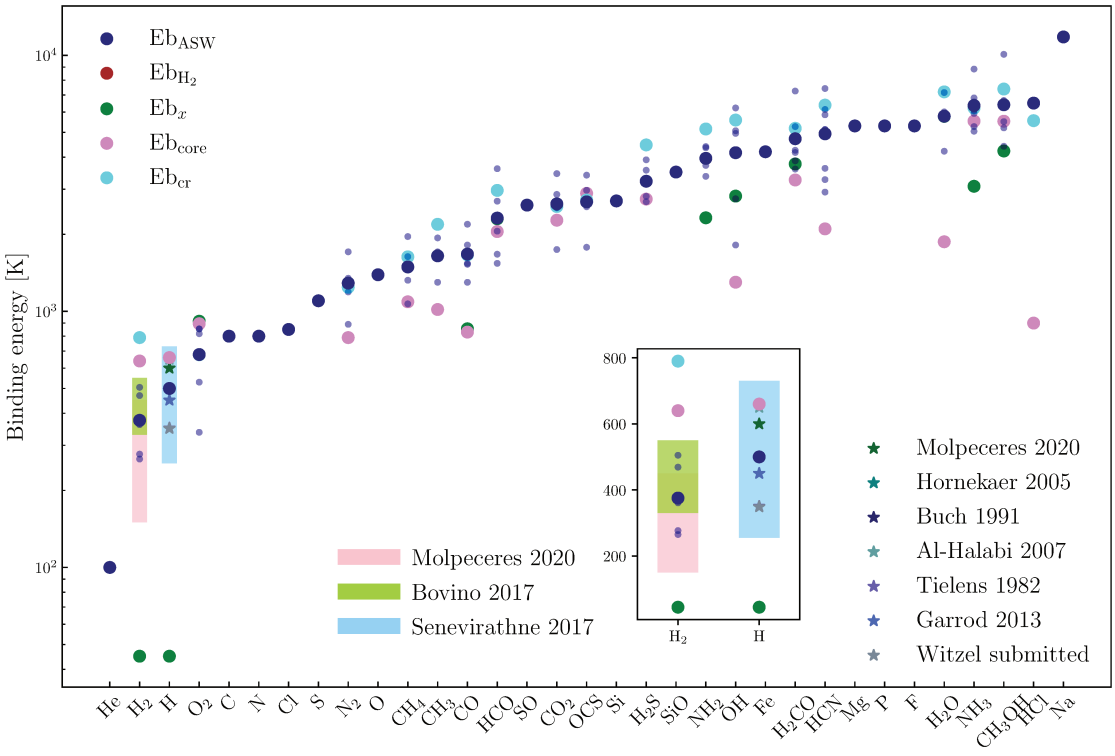

FIGURE 4.4: The figure shows the binding energies of species listed in Tab. 4.2 in K in ascending order with respect to their BE to ASW. If multi-binding energies are listed, we show them in the smaller dark blue circles, and the larger dark blue circle is the average BE. Eb_{ASW} denotes binding energy on ASW substrate, Eb_{H_2} is on H_2 substrate, Eb_x on a substrate same as the absorbate, Eb_{core} on a silicate or carbonaceous substrate, and Eb_{cr} on a crystalline water. The two light green and pink boxes for H_2 are the BE ranges calculated by Bovino et al. (2017) and Molpeceres and Kästner (2020). The light blue patch for atomic hydrogen is the range calculated in Senevirathne et al. (2017). The various star markers are the atomic H bindings from different works. BE of atomic and molecular H are plotted separately in the smaller subplot.

TABLE 4.2: Binding energies

molecules	Eb_{H_2}	Eb_x	Eb_b	Eb_{ASW}	Eb_{CI}	reference
H	45	45	660	349		(7, 3, 20)
He		100	100	100		(10)
C		800	800	800		(23)
N		720	720	720		(24)
O		1320	1390	1320		(24,14)
Si		2700	2700	2700		(6)
S		1100	1100	1100		(4)
Fe		4200	4200	4200		(6)
Mg		5300	5300	5300		(6)
H_2	45	45	640	(375.4) 265 277 361 469 505	790	(3, 7, 19)
O_2		915	895	(678.4) 337 529 818 854 854	677	(19, 16, 13)
N_2		790	790	(1289.4) 890 1191 1311 1347 1708	1242	(19, 11)
CH_4		1090	1090	(1491.2) 1070 1323 1467 1636 1960	1633	(19, 15)
CO		855	830	1792.0	1663	(19, 16, 18)
CO_2		2270	2270	(2629.4) 1744 2538 2550 2863 3452	2568	(19, 16, 5)
OCS		2890	2890	(2677.4) 1780 2562 2670 2971 3404	2722	(19, 9)
HCl		900	900	6507	5557	(19, 1)
HCN		2100	2100	(4937.25) 2923 3271 3620 5124 5136 5857 6146 7421	6392	(19, 21)
H_2O		5775	1870	(5785.2) 4222 5689 5845 6014 7156	7200	(19, 2)
H_2S		2745	2745	(3223.2) 2682 2814 3151 3560 3909	4468	(19, 9)
NH_3		3080	5535	(6369.57) 5052 5268 5930 6098 6579 6820 8840	6235	(19, 9, 22)
CH_3OH		4230	5530	(6412.125) 4414 5208 5509 6362 6519 6531 6663 10091	7385	(19, 9, 22)
H_2CO		3765	3260	(4723.875) 3596 3873 4174 4258 4594 4775 5268 7253	5187	(19, 17)
OH		2820	1300	(4166.2) 1816 2754 4955 5076 6230	5588	(19, 12, 8)
HCO		2300	2050	(2314.2) 2057 1540 1672 2694 3608	2968	(19, 21)
CH_3		1017	1017	(1647.67) 1299 1708 1936	2188	(19, 21)
NH_2		2320	3960	(3960.0) 3368 3716 4354 4402	5156	(19, 21)
SiO		3500	3500	3500		(10)
SO		2600	2600	2600		(10)

The binding energy (BE) of selected species on different substrates in K. EbH_2 denotes the BE on an H_2 substrate, Eb_x on the same substrate, Eb_b on a bare grain, Eb_{ASW} on an ASW surface, and Eb_{CI} on a crystalline water surface. If BEs in paranthesis are the average BE from a multi-BE distribution. (1) McElroy et al., 2013 (2) Avgul et al., 1971, (3) Pierre et al., 1985, (4) Tielens and Allamandola, 1987, (5) Sandford and Allamandola, 1990, (6) Hasegawa and Herbst, 1993b , (7) Katz et al., 1999 , (8) Fraser et al., 2002, (9) Collings et al., 2004, (10) Garrod and Herbst, 2006, (11) Bisschop et al., 2006, (12) Cuppen and Herbst, 2007, (13) Acharyya et al., 2007, (14) Bergeron et al., 2008, (15) Herrero et al., 2010, (16) Noble et al., 2012b, (17) Noble et al., 2012a, (18) Acharyya et al., 2020, (19) Ferrero et al., 2020, (20) Witzel et al. 2022 (submitted), and (21) Taquet et al. (2014), (22) Sandford and Allamandola (1993), Tielens and Hagen (1982a), and (24) Minissale et al. (2016a).

a) Complex molecules have been observed in various environments from MCs to different regions in protostars, such as the hot corinos and the shocked regions.

b) Dust plays a crucial role in MCs and protostar physical and chemical evolution. It absorbs UV irradiation and regulates the thermal balance inside the deep regions in MCs, which is the birthplace of stars. It provides a platform on which H_2 molecules and other saturated molecules, such as water and methanol, can form.

c) The formation pathways to organic and pre-biotic molecules go through gas-phase and grain surface chemical reactions (Álvarez-Barcia et al., 2018; Balucani et al., 2015a; Garrod, 2013; Holdship et al., 2019).

d) Several processes connect the gas and the solid forms: adsorption, which depletes the gas phase from species, and thermal and non-thermal desorption, which infuse the gas phase with frozen species.

These processes and reactions affect the distribution of abundances in the gas phase and on ices. The following sections describe the types of reactions in the gas phase and on ice surfaces and the connecting processes such as adsorption and desorption used in our models.

4.4.1 Gas phase chemistry

Reactions in the gas phase occur for a variety of reasons. Some reactions form more complex species and other reactions destroy or ionize the molecules. The rate of each reaction is calculated, measured, or estimated based on the latest experimental and quantum computational research when available (Chap. 3). The reactions can be categorized into 3 classes: CR induced ionization ($H_2 + \zeta \longrightarrow H_2^+ + e$), photodissociation via external UV or secondary UV irradiation ($CO + h\nu \longrightarrow C + O$), and bimolecular reactions. The latter can be subdivided into neutral–neutral ($A + B \rightarrow C + D$), ion–neutral ($A^{\pm} + B \rightarrow C^{\pm} + D$), ion–cation recombination ($A^- + B^+ \rightarrow C + D$), dissociative neutral attachment ($A + B \rightarrow AB^+ + e$), charge exchange ($A + B^+ \rightarrow A^+ + B$) and ($A^- + B^+ \rightarrow A^+ + B^-$), radiative association ($A + B \rightarrow AB + h\nu$) and $\left(A + B^+ \rightarrow AB^+ + h\nu\right)$, associative detachment ($A^- + B \rightarrow AB + e$), dissociative electronic recombination ($AB^+ + e \rightarrow A + B$), and electronic attachement , and $\left(AB^+ + e \rightarrow AB + h\nu\right)$ and radiative recombination $\left(A + e \rightarrow A^- + h\nu\right)$.

The UMIST Database for Astrochemistry (UDfA, McElroy et al., 2013) and the KInetic Database for Astrochemistry (KIDA, Wakelam et al., 2012) are the most widely used networks publicly available for the community. In Grainoble+ modeling, we use the gas-phase network GRETOBAPE-GAS that our group has updated and used in several previous works. It is based on the KIDA2014 network (Wakelam et al., 2015). Several reactions have been modified, removed, or added following measured or computed reaction pathways and rate coefficients in the literature or derived in our group (see e. g., Ascenzi et al., 2019; Ayouz et al., 2019; Balucani, 2020; Balucani et al., 2015a; Balucani et al., 2018; Codella et al., 2017, 2020; Fontani et al., 2017; Hamberg et al., 2010; Loison et al., 2014, 2016; Neufeld et al., 2015; Rosi et al., 2018; Skouteris et al., 2017; Skouteris et al., 2018, 2019; Tinacci et al., 2021; Urso et al., 2016, 2019; Vazart et al., 2016; Vazart et al., 2020; Vigren et al., 2013).

CR induced ionization

Most CRs are protons and alpha particles with energies above 1 MeV. These particles are energetic enough to penetrate through dense clouds. The high-energy particles ionize molecules and atoms in the gas phase (see, Sec. 1.1.4).

The rate of CR ionization of hydrogen molecules ζ_{H_2} [s^{-1}] has been estimated in several works (see, for example, Caselli et al., 1998b; Leger et al., 1985; Phan et al., 2018 and Sec. 1.1.3 and Fig. 1.5). The CR ionization rate coefficient of other species

$$\kappa_{CR} = \alpha \zeta_{H_2} \, , \tag{4.5}$$

are calculated relative to one of hydrogen with a prefactor, α, calculated in Wakelam et al. (2010a).

CR produced UV induced photo-dissociation

The CR reactions with H_2 inside the dense cores create high-energy UV photons that can ionize or photo-dissociate other species. This process is known as the Prasad-Tarafdar mechanism (Prasad and Tarafdar, 1983). The rate coefficient of this process is defined as follows

$$\kappa_{CRP} = \frac{\alpha}{1-\omega} \left(\frac{n_{H_2}}{n_{H_2} + n_H} \right) \zeta_{H_2} \, . \tag{4.6}$$

ω is the albedo of the grain in the far UV light, which we assume is 0.5, n_{H_2} and n_H are the number density of molecular and atomic hydrogen, and ζ_{H_2} is the cosmic ionization rate of the hydrogen molecule (Gredel et al., 1989; Wakelam et al., 2012). The KIDA database provides the prefactor to ζ_{H_2}.

External field UV photo-dissociation

The photo-dissociation rate coefficient due to the UV field radiation in a cloud depends on its penetration depth inside the cloud, namely it depends on the visual extinction of the cloud,

$$\kappa_{phdis} = \alpha \, e^{-\gamma A_v} \, . \tag{4.7}$$

α is the unattenuated photodissociation rate in the reference radiation field, $e^{-\gamma A_v}$ is the continuum attenuation from the dust, γ is a constant relative to each species, and A_v denotes the visual extinction (e. g., Draine, 1978; Mathis et al., 1983).

Self shielding The external UV field photons photodissociating H_2 and CO are absorbed in the outer regions of the cloud by H_2 and CO in the gas phase. These molecules are highly abundant in the gas phase and practically shield the CO and hydrogen molecules inside the dense regions from photo-dissociation. To take this effect into account and attenuate the photo-dissociation rate in the dense regions, we follow the work by Lee et al. (1996) and Le Petit et al. (2006), similar to Grainoble (the former version). These works have provided the rates of photodissociation of H_2 and CO as a function of column density and extinction A_v (see, also, Draine and Bertoldi, 1996; Visser et al., 2009).

Bimolecular reactions in the gas phase

As mentioned in Chap. 3, experimental and quantum computational chemistry provide us with the gas-phase reaction kinetic parameters: the rate coefficient and the branching ratios.

The rate coefficient of a bimolecular reaction is calculated using the Arrhenius–Kooij formula,

$$\kappa_{Bi}(T) = \alpha \left(\frac{T_g}{300.} \right)^{\beta} \exp\left(\frac{-\gamma}{T_g} \right) , \tag{4.8}$$

as a function of temperature. The reaction rate constants α, β, and γ are derived from the kinetics studies.

In some cases, where an ion-neutral reaction rate measurement or quantum computation is not possible in the temperature range in consideration, it is estimated using the Su-Chesnavich capture approach (Chesnavich et al., 1980; Su and Chesnavich, 1982). The rate coefficient, κ_{SuCh} is estimated using the Langevin model,

$$\kappa_{\mathrm{L}} = 2\pi e \sqrt{\frac{\alpha}{\mu}}, \tag{4.9}$$

where e is the electron charge, α is the (orientation-averaged) polarizability of the neutral species, and μ is the reactants' reduced mass.

For low temperatures, such that

$$\frac{\mu_{\mathrm{D}}}{\sqrt{2\alpha k_{\mathrm{B}} T}} \gtrsim 2\,, \tag{4.10}$$

where μ_{D} is the dipole moment and α is the dipole polarizability, the rate coefficient is estimated as follows:

$$\kappa_{\mathrm{SuCh}} = (0.4767x + 0.6200)\,\kappa_{\mathrm{L}} \tag{4.11}$$

and for higher temperatures

$$\kappa_{\mathrm{SuCh}} = \left[\frac{(x + 0.5090)^2}{10.526} + 0.9754\right]\kappa_{\mathrm{L}}\,. \tag{4.12}$$

4.4.2 Grain assisted charge exchange

Secondary UV photons from CR collisions with atomic and molecular hydrogen are energetic enough to extract an electron from a neutral or negatively charged grain ($\mathrm{G}^- \longrightarrow \mathrm{e} + \mathrm{G}$) and ($\mathrm{G} \longrightarrow \mathrm{e} + \mathrm{G}^+$). In this case, the rate of extraction reads as follows:

$$\kappa_{\mathrm{xch}} = \alpha\zeta\,, \tag{4.13}$$

where $\alpha = 6.3 \times 10^7$ for electron extraction from a neutral grain and $\alpha = 4.1 \times 10^8$ from negatively charged grains (Walmsley et al., 2004).

The free cations in the gas phase can collide with negatively charged grains and neutralize the grain by taking the electron. See Tab. 4.3 for the list of charge exchange reactions between the negatively charged grains and the most abundant cations (Flower and Pineau des Forêts, 2003; Wakelam et al., 2012). Cations and electrons dissociative recombination mainly occur in the gas phase in dense clouds. However, a small fraction of highly abundant cations in the gas phase can exchange charge on the surface of negatively charged grains (Aikawa et al., 1999).

To calculate the rate of charge exchange, we follow the work of Draine and Sutin (1987). They show that the grain polarization due to the electric field of the electron on the grain affects the cross-section of the grain (in the presence of an electric charge, it is known as the capture cross-section). Their work calculates the correction term, the reduced cross-section, for various situations. Three cases can occur: (1) The attractive case, when the grain and the incoming charged species carry opposite charges ($\mathrm{X}^{\pm} + \mathrm{G}^{\mp} \rightarrow \mathrm{X} + \mathrm{G}$), (2) The neutral case, when the incoming species is charged and the grain is neutral ($\mathrm{X}^{\pm} + \mathrm{G} \rightarrow \mathrm{X} + \mathrm{G}^{\pm}$), and (3) The repulsive case, when both grain and the incoming species carry the same charge

$(X^{\pm} + G^{\pm} \rightarrow X^{\pm} + G^{\pm})$. This section does not discuss the third case because the species and the grain remain unaffected after an encounter.

The capture cross-section, $\tilde{\sigma} = \sigma\tilde{J}(\tau, \nu)$, can be calculated as a product of the geometrical cross-section, σ, and the reduced cross-section, $\tilde{J}(\tau, \nu)$, which is a function of the reduced temperature,

$$\tau = \frac{K_b T_g}{K_c q^2 / a} , \tag{4.14}$$

and the kinetic to potential energy ratio,

$$\nu = \frac{Ze}{q} . \tag{4.15}$$

k_b and k_c are the Boltzmann and the Coulmb constants, T_g is the temperature in the gas, q the electron charge, a is the radius of the grain, and Ze is the number of electrons on the grain.

The reduced cross-section term is approximated differently for the three cases mentioned above. The following paragraphs present the attractive and the neutral cases.

The attractive case For the case of attractive force between a charged species and an oppositely charged grain $(X^{\pm} + G^{\mp} \rightarrow X + G)$, the reduced cross section $\tilde{J}$ can be approximated to

$$\tilde{J} = \left(1 - \frac{\nu}{\tau}\right)\left[1 + \sqrt{\frac{2}{\tau - 2\nu}}\right] . \tag{4.16}$$

The second term on the right-hand side of the Eq. 4.16 is the short range correction on $\tilde{J}$.

The neutral case In the case of interaction of a charged species with a neutral grain $(X^{\pm} + G \rightarrow X + G^{\pm})$ the effective cross section $\tilde{J}$ is approximated to

$$\tilde{J} = 1 + \sqrt{\frac{\pi}{2\tau}} . \tag{4.17}$$

Fig. 4.5 shows the reduced cross-section as a function of reduced temperature for the three cases: neutral (green), attractive (red), and repulsive (blue).

The effective rate coefficient due to the presence of electric potential reads as follows (Draine and Sutin, 1987):

$$\kappa_{xch} = \xi v_{th} \sigma \tilde{J}(\tau, \nu)\, n_d . \tag{4.18}$$

ξ is the sticking coefficient of ions on the grain taken as 0.5 (Weingartner and Draine, 2001a). v_{th} denotes the thermal velocity

$$v_{th} = \sqrt{\frac{8 k_b T_g}{\pi m}} , \tag{4.19}$$

of the species in the gas phase with k_b the Boltzman constant, T_g the temperature in the gas and m the mass of the species and n_d is the number density of the dust. Note that the cation's sticking coefficient is lower than its neutral counterpart, likely because the charged species accelerate because of the Coulomb potential. After electron recombination, the velocity of the neutral species is still high. Therefore, sticking will not be probable (Tielens, 2021).

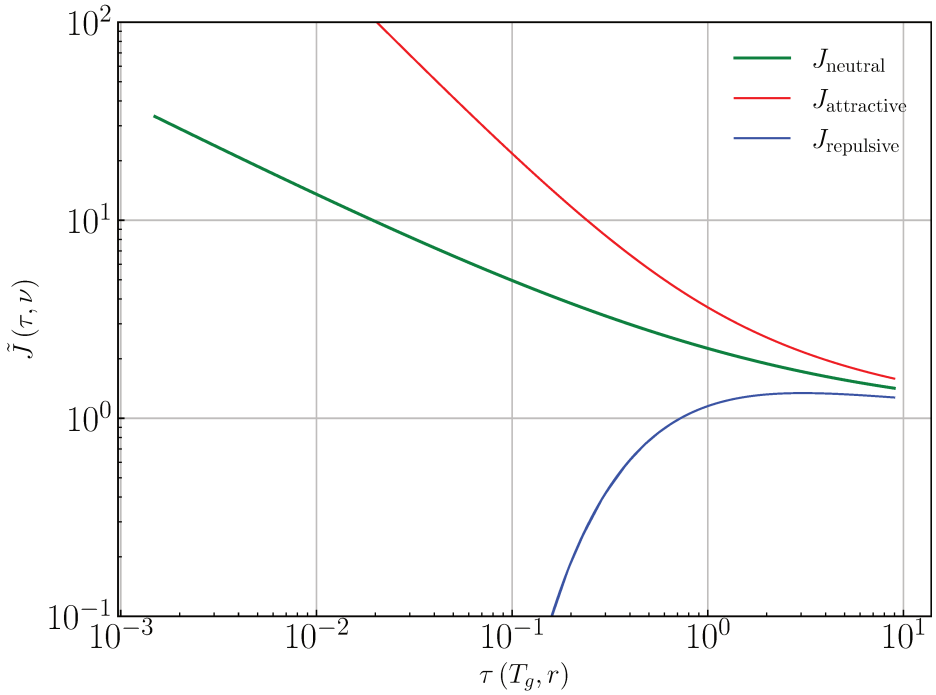

FIGURE 4.5: This figure shows the reduced cross section of the grain in the presence of an electric potential for the three cases: (1) The attractive case, $(X^{\pm} + G^{\mp} \rightarrow X + G)$, (2) The neutral case, $(X^{\pm} + G \rightarrow X + G^{\pm})$, and (3) The repulsive case, $(X^{\pm} + G^{\pm} \rightarrow X^{\pm} + G^{\pm})$. This figure is adapted from Draine and Sutin (1987).

To have a better comparison of the rates, Fig. 4.6 shows the rate coefficient of $(C^+ + G^- \rightarrow C + G)$ reaction as a function of temperature for grain with 0.1 μm radius in three cases: (1) the rate calculated using the reduced cross-section correction term discussed above (Draine and Sutin, 1987) in solid line (2) the rate without the $\tilde{J}$ correction term in dashed, and (3) the rate of C^+ accretion on the grain ignoring coulomb forces and assuming a sticking coefficient 1 in dotted line (which is practically the rate of adsorption, see, Sec. 4.4.3). While the effect of the reduced crossed section might not be so significant at room temperature, it is about a factor of 1.5 larger at 10 K.

4.4.3 Adsorption

Neutral species move in the gas phase with a thermal velocity that scales with the square root of temperature over its mass (Eq. 4.19). The species can accrete on the grains upon encounter. As discussed in Sec. 4.3.2, species heavier than hydrogen and helium practically remain stuck on the grains. The rate of accretion of neutral species is given by

$$\kappa_{\text{acc}} = \xi \sigma_{\text{d}} v_{\text{th}} n_{\text{d}} \,, \tag{4.20}$$

where ξ is the sticking coefficient (see Sec. 4.3.2), σ_{d} is the geometrical grain cross-section, v_{th} the thermal velocity (Eq. 4.19) of the incoming species, and n_{d} is the number density of the grains. The rate is proportional to the inverse square root of the species mass. It indicates that the depletion timescales for heavier species are much longer than species such as hydrogen. We should note that whether or not they remain frozen on the grains depends on many variables, not only their adsorption timescales—parameters such as sticking coefficient, binding energy, the rate of desorption processes. In our model, charged species only exchange charge

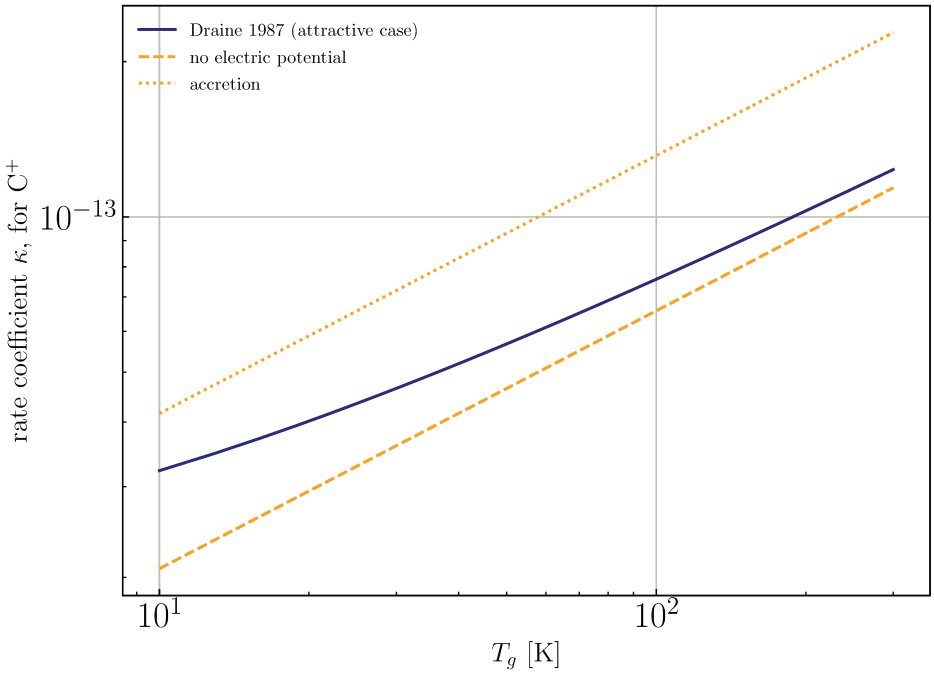

FIGURE 4.6: The figure shows the charge exchange rate coefficient for $(C^+ + G^- \rightarrow C + G)$ as a function of the gas temperature for three cases. (1) With the reduced cross-section correction term in solid line, (2) without the correction term in dashed line, and (3) the rate of accretion of C^+ on a grain ignoring the electric potentials and setting the sticking coefficient to 1. The latter case is plotted for comparison.

TABLE 4.3: Grain assisted charge exchange reactions.

Reactions		
$e + G$	$\longrightarrow$	G^-
$C^+ + G^-$	$\longrightarrow$	$C + G$
$Fe^+ + G^-$	$\longrightarrow$	$Fe + G$
$H^+ + G^-$	$\longrightarrow$	$H + G$
$He^+ + G^-$	$\longrightarrow$	$He + G$
$Mg^+ + G^-$	$\longrightarrow$	$Mg + G$
$N^+ + G^-$	$\longrightarrow$	$N + G$
$Na^+ + G^-$	$\longrightarrow$	$Na + G$
$O^+ + G^-$	$\longrightarrow$	$O + G$
$S^+ + G^-$	$\longrightarrow$	$S + G$
$Si^+ + G^-$	$\longrightarrow$	$Si + G$
$H_3^+ + G^-$	$\longrightarrow$	$H_2 + H + G$
$HCO^+ + G^-$	$\longrightarrow$	$H + CO + G$

Grain is denoted with G.

with the grain; they do not remain frozen (see, Sec. 4.4.2). Only neutral species can accrete and stay on the grains

4.4.4 Grain surface reactions

In the previous chapters, we have emphasized the importance of grain surface processes in the chemical and physical evolution of dense cores and protostars. This section reviews the rate of reactions in our grain surface network. In our network, two mechanisms describe a reaction mechanism on surfaces: Langmuir-Hinshelwood[2] (LH) and the Eley Rideal (ER) mechanisms. The former assumes that two reactants encounter after one or both have scanned the surface. Therefore, the reaction rate depends on the diffusion rates and the reaction efficiency. The latter describes a reaction occurrence once an incoming species hits a frozen species on the surface[3]. The following sections will explain the mechanisms in more detail.

Langmuir Hinshelwood reactions

LH mechanism describes a two-body reaction on the surface that occurs after one or both have diffused and finally encountered. In our models, we follow the rate coefficient formalism introduced by Hasegawa et al. (1992). The rate coefficient of the reaction reads

$$\kappa_{\rm LH} = \varepsilon_{ij} \frac{\kappa^{i}_{\rm diff} + \kappa^{j}_{\rm diff}}{n_{\rm d}} \tag{4.21}$$

where ε_{ij} is the reaction probability or efficiency of the two reactants i and j upon encounter. $\left(\kappa^{i}_{\rm diff} + \kappa^{j}_{\rm diff}\right)$ is the sum of the diffusion rate of the two reactants, and $n_{\rm d}$ is the number density of the dust grains.

Diffusion Species can diffuse on ice surfaces through thermal hopping or quantum tunneling through the energy barriers on the surface. Astrochemical models assume that a species scan the entire surface at each time. Therefore, the diffusion rate can be quantified as

$$\kappa_{\rm diff} = \frac{\kappa_{\rm hop}}{n_{\rm sites}} , \tag{4.22}$$

namely as the rate of one step diffusion, $\kappa_{\rm hop}$, over the total number of sites on a surface, $n_{\rm sites}$ ($\approx 10^6$ for a grain with a radius of 0.1 μm), (Hasegawa et al., 1992). In the low temperatures of MCs, most molecules are practically stuck where they fall. However, the lighter species, such as hydrogen and oxygen, can still be mobile and react with frozen species. The most notable products are water, methano,l and CO_2. The increase of temperature in various regions in protostars ($10 \lesssim T \lesssim 100$) increases the rate of mobility and encounter, which gives rise to radical-radical reactions. The rate of thermal hopping for a species from one binding site to another is calculated in the following way

$$\kappa_{\rm hop_{th}} = \nu_0 \exp\left(\frac{-E_{\rm diff}}{T_{\rm d}}\right) , \tag{4.23}$$

[2]Irving Langmuir was granted Nobel Prize in chemistry in 1932 for his researches in surface chemistry. Cyril Hinshelwood was also granted Nobel Prize in the same field in 1956 for his research in reaction mechanisms.

[3]Hot atom (Harris-Kasemo) is another mechanism that can take place on the surface. An incoming species can migrate on the surface while thermalizing, and during this process, it might encounter another species and react. The process can also start with a chemical reaction producing a highly excited and mobile species.

where T_d is the dust temperature, and E_{diff} is the energy required to hop over the diffusion energy barrier that is often approximated as a fraction of the species binding energy (§ 3.3.1). ν_0 is the diffusion pre-factor, often approximated as the vibrational frequency of a particle in a square box (Landau and Lifshitz, 1975; Tielens and Allamandola, 1987),

$$\nu_0 = \sqrt{\frac{2k_b E_b}{\pi^2 a_{site}^2 m}}, \tag{4.24}$$

where k_b is the Boltzmann constant, m is the mass of the species, a_{site}^2 is the occupying area (site) of a molecules on a surface.

For lighter species such as hydrogen, quantum tunneling from one binding site to another can become the dominant mean of diffusion in low temperatures. As mentioned in Sec. 3.3.2, quantum chemical calculations and solid phase experimental studies can provide us with the rate coefficients. For example, Senevirathne et al. (2017) and Congiu et al. (2014) have calculated the rate of hydrogen and oxygen diffusion on ASW (Tab.6.13) which we employ in our models (see, Sec. 3.3.2 for detailed discussion).

TABLE 4.4: The rate constant fitting parameters for atomic hydrogen and oxygen.

atom	t [K]	α [s^{-1}]	β	γ	K_0
hydrogen[a]	1–16.5	9.2×10^2	0.19	-1.7×10^{-2}	—
hydrogen[a]	16.5–21	4.7×10^{112}	1.1×10^2	-1.12×10^3	—
Oxygen[b]	6.5 - 25	1.	3.	1.21	

(a) The best fit parameters for the function $\kappa(T) = \alpha\,(T/300.)^{\beta} \exp(-\gamma/T)$ within the given temperature ranges; (b) The empirical fit parameters of Oxygen diffusion rate constant for the function $\kappa(T) = K_0/10^{-15} + \alpha(T/10.)^{\beta}$ from Congiu et al. (2014, Table 1, Figure 3) for no-ASW ices.

In cases where calculations are not feasible, astrochemical models calculate the diffusion rates by assuming a rectangular diffusion energy barrier. The height of the barrier is the E_{diff} and the width is an arbitrary number that is poorly constrained and is typically assumed $1-2$ Å (Garrod and Pauly, 2011; Hasegawa et al., 1992; Tielens and Hagen, 1982a),

$$\kappa_{tun_{SQ}} = \nu_0 \exp\left(\frac{-2w_b}{\hbar}\sqrt{2k_b m E_{diff}}\right). \tag{4.25}$$

$\hbar = h/2\pi$ is the reduced Planck constant. w_b is the barrier width of the energy barrier.

Figure 4.7 shows, as an example, the atomic H diffusion rates via quantum tunneling (Senevirathne et al., 2017) and through thermal hopping as a function of temperature. For comparison, we also plot the H diffusion rate with the H binding energy of 450 K, used by Garrod (2013) and other groups. The figure shows that the choice of the method, binding energy, and ƒ can lead to differences in the diffusion rate by several orders of magnitude.

Reaction efficiency Hasegawa et al. (1992) assumed the reaction efficiency equals the probability of transmission through a reaction barrier upon one encounter once the two reactants are in one site (if the reaction requires activation energy; otherwise, the reaction probability of a barrier-less reaction is equal to one). However, more possible channels can probably occur once the two reactants are in one site. Chang et al. (2007) and Garrod and Pauly (2011) proposed for reactions that require activation energy to consider the competitive channels in

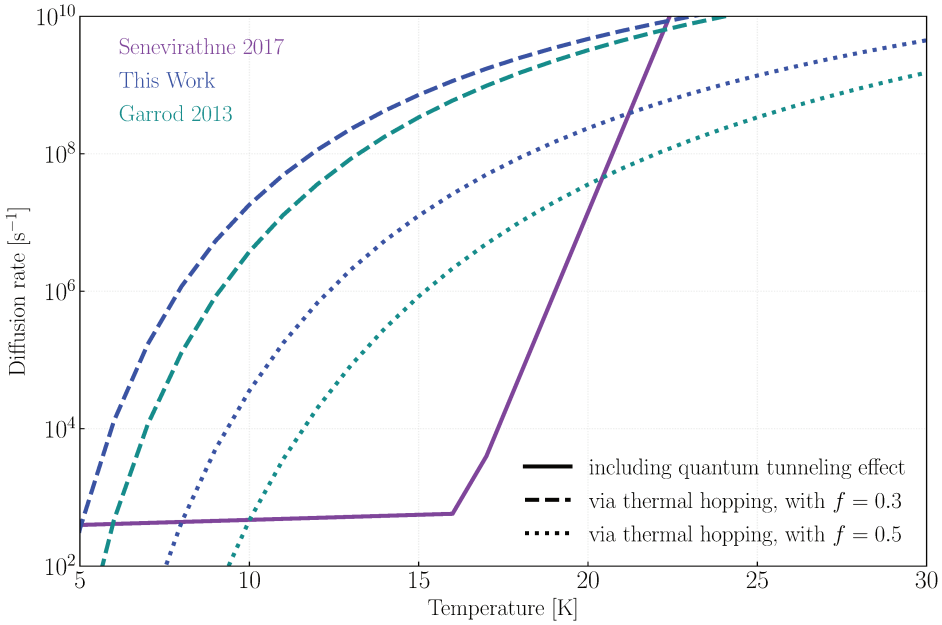

FIGURE 4.7: The figure shows the diffusion rate of hydrogen [s^{-1}] as a function of temperature. The purple line shows the rate of hydrogen diffusion adopted from Senevirathne et al. (2017, figure 7c). The dashed and dotted lines are the diffusion rates via thermal hopping with diffusion to binding ratios of ϱ = 0.3 and 0.5, respectively. The blue lines are the diffusion rate via thermal hopping based on the binding energy in Witzel et al. submitted, and the green lines are diffusion rates via thermal hopping as a function of BE = 450 K, provided by (Garrod, 2013, table 3).

calculating the efficiency of a reaction on the surface. In the new method, the efficiency is

$$\varepsilon_{ij} = \frac{\kappa_{\rm re}}{\kappa_{\rm re} + \sum_i \text{competitive channels}} \,, \tag{4.26}$$

the ratio between the rate of reaction over the sum over all the possible channels. $\kappa_{\rm re}$ is the reaction rate coefficient. Chang et al. (2007) takes the diffusion and the desorption rates coefficients of the most mobile species into account, while Garrod and Pauly (2011) assumed a sum over the diffusion rate coefficients of the two reactants. Enrique-Romero et al. (2021) generalized the definition to account for diffusion and desorption rate of both reactants

$$\varepsilon_{ij} = \frac{\kappa_{\rm re}}{\kappa_{\rm re} + \kappa_{\rm diff_i} + \kappa_{\rm diff_j} + \kappa_{\rm des_i} + \kappa_{\rm des_j}} \,, \tag{4.27}$$

where $\kappa_{\rm des_*}$ and $\kappa_{\rm diff_*}$ are the desorption and diffusion (only from one binding site to another site) rate of the reactants i and j. We follow the Enrique-Romero et al. (2021) approach in our models.

Surface reaction rate coefficient As discussed in Sec. 3.3.2, for some reactions, quantum chemical calculations have provided the static and kinetics parameters which we employ in Grainoble+. For example, we directly include the rate of (CO + H → HCO) reaction recommended in our work, Witzel et al. 2022 (submitted), which provides updated calculations upon Rimola et al. (2014) using the same ice model. The rate constant parameters of hydrogenation and hydrogen abstraction of formaldehyde are from the work of Song and Kästner

(2017). The rate constants and the modified Arrhenius formulas are listed in Tab. 6.12 (see, also, Sec. 3.3.2).

TABLE 4.5: The rate constant fitting parameters for methanol formation network using modified Arrhenius formula.

Reaction	t [K]	α [s^{-1}]	β	γ [K]	T_0 [K]	branching ratio
CO + H $\rightarrow$ HCO^a	5–15	1.27×10^{6}	1.62	-4.35	—	—
CO + H $\rightarrow$ HCO^a	15–30	1.15×10^{7}	2.72	-20.9	—	—
H_2CO + H $\rightarrow$ CH_3O^b	—	3.14×10^{10}	1.0	830.0	119.6	0.8
H_2CO + H $\rightarrow$ HCO + H_2^b	—	4.13×10^{10}	1.0	1222.0	147.7	0.2

(a) The modified Arrhenius formula used here is $k = \alpha(T/300.)^{\beta} \exp -\gamma/T$, with T the temperature in Kelvin within the temperature range in the second columnn and α, β, and γ three fitting parameters. (b) The modified Arrhenius formula used here is $\kappa(T) = \alpha\,(T/300)^{\beta} \exp\left(-\gamma(T+T_0)/\left(T^2+T_0^2\right)\right)$, with T the temperature in K and α, β, and γ the rate constants from SK17, table 3.

In cases where we do not have the kinetics parameters from chemical studies, we need to approximate the rate coefficient assuming a potential shape to calculate the transmission probability and a pre-factor, $\kappa_{re} = \nu_{enc.}\rho_{re}$. The pre-factor, $\nu_{enc.}$, can be approximated as the frequency of encounter matched by the largest of the vibrational frequencies (Eq. 4.24) of the two reactants (Garrod and Pauly, 2011). The idea is that two reactants may encounter many times before they react or before the other competitive channels occur. As for the transmission probability, ρ_{re}, we are left with two alternatives: (1) if the Eckart model potential parameters are available from the literature, we calculate the probability using Taquet et al. (2013) provided formalism. (2) Otherwise, we need to approximate the probability assuming a rectangular barrier with a given activation energy and width (see, for example, Garrod, 2013; Ruffle and Herbst, 2000). The transmission probability through a rectangular barrier reads

$$\rho_{sqr} = \exp\left(\frac{-2w_b}{\hbar}\sqrt{2\mu E_a}\right), \tag{4.28}$$

where ω_b is the barrier width, $\hbar$ and k_b are the reduced Planck and Boltzmann constants, respectively. μ is the reduced mass of the reactants, and E_a is the activation energy.

Fig. 6.3 shows the rate constants of the (CO + H $\rightarrow$ HCO) and (H + H_2CO $\rightarrow$ CH_3O, HCO + H_2) reactions as a function of the temperature. In the figure, we also show the rate constants obtained with the treatment used by Garrod, 2013 and several other groups (e.g. Aikawa et al., 2020). The rate coefficients based on the two treatments differ with over three orders of magnitudes.

Eckart model energy barrier A better alternative to a rectangular barrier is to parametrize the energy barrier with Eckart model parameters: the forward and backward potentials (V_f and V_r), and the imaginary mode's frequency of the transition state Ω_s (see Joohnston and Heicklen, 1962; Taquet et al., 2013, for detailed calculation). The Eckart model fits the potential energy profile better than an square potential. The width in square potentials is poorly constrained and is often taken as an arbitrary number between 1 and 2 Å (Garrod and Pauly, 2011; Tielens and Hagen, 1982a). Taquet et al. (2013) has shown that the square energy barrier can underestimate the reaction probability up to seven orders of magnitudes. The Eckart model provides a more realistic transmission probability than a rectangular barrier approximation. In Fig. 4.9, we show a schematic view of an asymmetric barrier according to the Eckart model potential. Also, see Tab 4.6 for the list of Eckart model parameters for the reactions we included in our network.

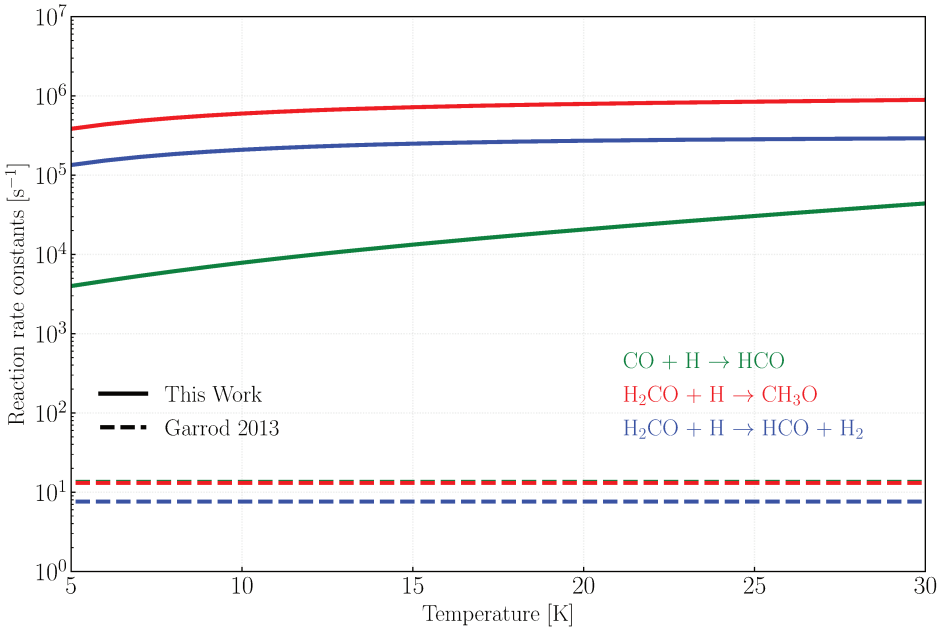

FIGURE 4.8: The figure shows the reaction rate constants of CO (green) and formaldehyde (red and blue) hydrogenation as a function of temperature. The products of H + H_2CO are CH_3O (red) and H_2 + HCO (blue) with 0.8 and 0.2 branching ratios, respectively. The solid lines are the calculated rates in Witzel et al. submitted that are based on quantum computational calculations, and the dashed lines are the reaction rates calculated assuming a rectangular barrier with the activation energies and barrier widths provided in Garrod (2013, table 3).

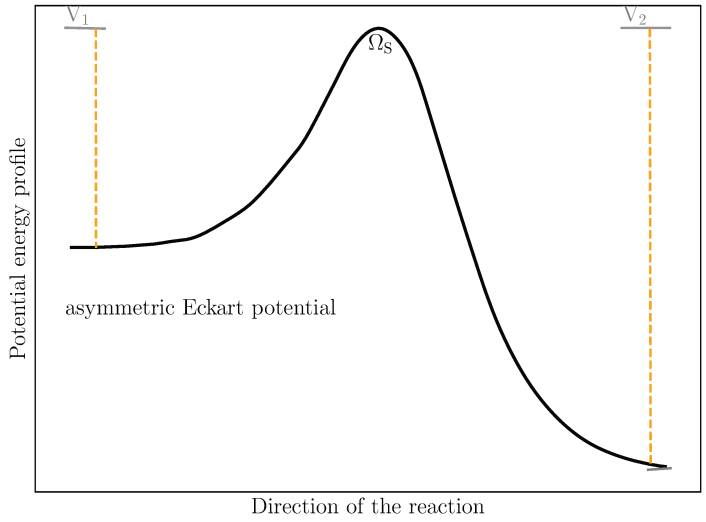

FIGURE 4.9: The figure shows a schematic representation of an asymmetric Eckart potential on ice surfaces. x is the position in the potential, and the y axis is the potential relative to its zero-point energy. V_1 and V_2 are the potential energy levels of the reactants and products, respectively and Ω_s is the frequency of the imaginary mode of the transition state (Adopted from Joohnston and Heicklen, 1962).

TABLE 4.6: The list of reactions with the calculated Eckart model potential parameters.

network	reactions		V_f [K]	V_r [K]	Ω [cm^{-1}]	reference
Methaol	CO + H $\longrightarrow$	HCO	1.624(3)	1.264(4)	6.057(2)	(6)
	H_2CO + H $\longrightarrow$	CH_3O	1.299(3)	1.588(4)	7.013(2)	(1)
Water	OH + H_2 $\longrightarrow$	H_2O + H	2.935(3)	1.021(4)	1.293(3)	(2)
	HOOH + H $\longrightarrow$	H_2O + OH	2.508(3)	3.636(4)	1.054(3)	(5,3)
Carbon dioxide	CO + OH $\longrightarrow$	CO_2 + H	2.850(2)	1.305(4)	2.610(2)	(4)
	CO + OH $\longrightarrow$	tHOCO	2.850(2)	1.305(4)	2.610(2)	(4)
	CO + OH $\longrightarrow$	cHOCO	2.128(3)	1.405(4)	3.790(2)	(4)
	O...CO + H $\longrightarrow$	tHOCO	7.754(2)	1.305(4)	2.610(2)	(4)
	O...CO + H $\longrightarrow$	cHOCO	2.618(3)	1.405(4)	3.790(2)	(4)
	tHOCO $\longrightarrow$	CO + OH	1.305(4)	2.850(2)	2.610(2)	(4)
	tHOCO $\longrightarrow$	cHOCO	4.114(3)	3.272(3)	5.840(2)	(4)
	cHOCO $\longrightarrow$	tHOCO	3.272(3)	4.114(3)	5.840(2)	(4)
	cHOCO $\longrightarrow$	CO_2 + H	1.244(4)	1.290(4)	2.053(3)	(4)

$a(b) = a \times 10^b$; O...CO is a CO and O van der Waals complex (Goumans and Andersson, 2010); the V_f and V_b are the forward and backward potentials in K and ω is the frequency of the transition state in cm^{-1}. The references: (1) Rimola et al. (2014); (2) Nguyen et al. (2011); (3) Ellingson et al. (2007); (4) Yu et al. (2001); (5) Koussa et al. (2006); and (6) Witzel et al. 2022 (submitted).

Eley Rideal reactions

The ER mechanism describes a reaction that occurs upon the accretion of a species on the surface. These reactions are often exothermic and barrierless and mainly involve radicals. The ER reactions are most important in high surface coverage or low mobility cases (Ruffle and Herbst, 2001). For example, during the catastrophic freeze-out of CO in prestellar cores when CO surface coverage is high, and the rate of CO_2 or methanol formation through the ER mechanism might become significant (Cuppen et al., 2017; Pontoppidan, 2006).

The rate of reaction depends on the adsoption rate of the molecules from the gas phase. It reads

$$\kappa_{ER} = \xi \sigma v_{th} \frac{n_d}{n_{site}} , \tag{4.29}$$

where ξ is the sticking coefficient (Sec. 4.3.2), σ is the cross section of the dust grain, v_{th} is the thermal velocity of the incoming species (Eq. 4.19), n_d is the number density of the dust grains, and n_{site} the number density of sites on the surface.

We include only one reaction under the ER mechanism in our models in the CO_2 formation network: (O + CO $\rightarrow$ O...CO). The landing oxygen atom forms a van der Waals complex with the frozen CO (Goumans and Andersson, 2010).

The surface reaction networks

The Grainoble+ models consider the formation networks of the most abundant molecules observed in ices towards prestellar cores and protostellar envelopes: water, carbon dioxide,

methanol, and ammonia and lesser found species such as trioxygen, methane, silyl, and silicon dioxide. Tab. 4.7 and 4.8 list the reactions with the branching ratio and the activation energies.

4.4.5 Desorption

In the following sections we discuss the implementation of thermal and non-thermal desorption processes in the Grainoble+ model.

Thermal desorption

Thermal energy of frozen species can lead to their evaporation from the surface. The rate of evaporation is calculated according to the Boltzmann law and can be characterized by the binding energy of the species, E_b, its pre-factor, ν_0 (Eq. 4.24), and the dust temperatures, T_d (Watson and Salpeter, 1972)

$$\kappa_{\text{thdes}} = \nu_0 \exp\left(\frac{-E_b}{k_b T_d}\right), \tag{4.30}$$

where ν_0 is the vibrational frequency (Eq. 4.24).

Cosmic ray desorption

High energy CRs interact with the icy mantle of the grain. CRs are energetic enough that they can penetrate through the grain and exit from the other side (Hasegawa and Herbst, 1993b). While penetrating the grain, they can heat the grain to about 70 Kelvin (Leger et al., 1985). The temperature increase leads to the thermal evaporation of the species in the surrounding with the rate of

$$\kappa_{\text{CRdes}} = 3.16 \times 10^{-19} \left(\frac{r}{10^{-5}[\text{cm}]}\right)^2 \left(\frac{\zeta_{H_2}}{3.0 \times 10^{-17}[\text{s}^{-1}]}\right) \nu_0 \exp\left(-E_b/70.[K]\right), \tag{4.31}$$

where r is the grain radius, 3.16×10^{-19} is the "duty cycle" of the grain at the elevated temperature, nnamely the ratio between cooling timescale of the grain due to desorption of CO ($\approx 10^{-5}$ s), and heating timescale of the grain due to CR collision to 70 K (for $\zeta_{H_2} = 3 \times 10^{-17}$ [s^{-1}] for a grain of 0.1 μm radius). The heating rate depends on the CR flux, the grain inverse cross-section, and the energy loss of CRs as it passes through the grain that scales with the square of the atomic number of CR, Z^2. Leger et al. (1985) estimates this timescale for Fe CR flux with energies of 20-70 MeV to 3.16×10^{13} s (Hasegawa and Herbst, 1993b). ν_0 is the prefactor (Eq. 4.24), the exponential part is the rate of thermal desorption of the species as if it was heated to 70 K.

Photodesorption

High-energy FUV photon irradiation in MCs can originate from two sources: (1) InterStellar Radiation Field (ISRF), which is more dominant in the envelope of starforming regions (Hollenbach and Tielens, 1997; van Dishoeck and Blake, 1998), and (2) CR induced UV irradiation from the interaction with atomic and molecular hydrogen (Prasad and Tarafdar, 1983). Far Ulttra-Violet (FUV) photons can dissociate or ionize the molecules in the gas phase (see §1.1.3 and 4.4.1). Or they can be absorbed by molecules in ice. The absorbed energy by solid species in ices can lead to dissociation (photodissociation) or sublimation (photodesorption) (see, e. g., Hagen et al., 1979; Öberg et al., 2009a). In the surrounding envelope of the starforming region, photodesorption can dominate the sublimation of icy species into the gas phase

TABLE 4.7: List of surface reactions considered in our model.

network	reactions	branching ratio	activation energy [K]	reference
Hydrogen	$H + H \longrightarrow H_2$			(1)
Methanol (CH_3OH)	$CO + H \longrightarrow HCO$		2000.0	(11, 1, 2)
	$HCO + H \longrightarrow H_2CO$			(1, 2)
	$H_2CO + H \longrightarrow CH_3O$		2000.0	(11, 1, 2)
	$CH_3O + H \longrightarrow CH_3OH$			(11, 1, 2)
Trioxygen	$O + O \longrightarrow O_2$			(1)
	$O_2 + O \longrightarrow O_3$			(1)
	$O_3 + H \longrightarrow O_2 + OH$			(17, 24, 25, 26)
Water (H_2O)	$O + H \longrightarrow OH$			(11, 19, 21)
	$OH + H \longrightarrow H_2O$			(11, 19, 21)
	$OH + OH \longrightarrow HOOH$	0.8		(6)
	$OH + OH \longrightarrow H_2O + O$	0.2		(6)
	$OH + H_2 \longrightarrow H_2O + H$		2100.0	(6, 9)
	$O_2 + H \longrightarrow O_2H$			(18, 22, 20, 25, 26)
	$O_2H + H \longrightarrow HOOH$			(18, 22, 20, 25, 26)
	$HOOH + H \longrightarrow H_2O + OH$		2100.0	(18, 22, 20, 25, 26)
Ammonia	$N + H \longrightarrow NH$			(1, 3)
	$NH + H \longrightarrow NH_2$			(1, 3)
	$NH_2 + H \longrightarrow NH_3$			(1, 3)
Methane	$C + H \longrightarrow CH$			(1)
	$CH + H \longrightarrow CH_2$			(1)
	$CH_2 + H \longrightarrow CH_3$			(1)
	$CH_3 + H \longrightarrow CH_4$			(1)
Silyl	$Si + H \longrightarrow SiH$			(4)
	$SiH + H \longrightarrow SiH_2$			(4)
	$SiH_2 + H \longrightarrow SiH_3$			(4)
	$SiH_3 + H \longrightarrow SiH_4$			(4)
Silicon dioxide	$Si + O \longrightarrow SiO$			(4, 5)
	$SiO + O \longrightarrow SiO_2$		1000.0	(4, 5)
	$SiO + OH \longrightarrow SiO_2 + H$		80.0	(4, 5)

The references are listed in Tab. 4.8.

TABLE 4.8: List of surface reactions considered in our model (continued).

network	reactions		branching ratio	activation energy [K]	reference reference
Carbon dioxide	HCO + O ⟶	CO_2 + H			(14, 2)
	CO + O ⟶	CO_2		1000.0	(2, 15)
		CO_2 + H	0.98	80.0	(6,2,8,22,
	CO + OH ⟶	tHOCO	0.01	80.0	23,8,10,18,
		cHOCO	0.01	80.0	27,28,19)
		CO_2 + H_2	0.333		
	tHOCO + H ⟶	H_2O + CO	0.333		(1)
		HCOOH	0.333		
		CO_2 + H_2	0.333		
	cHOCO + H ⟶	H_2O + CO	0.333		(1)
		HCOOH	0.333		
	O* + CO ⟶	O...CO			(1, 7, 6)
		CO_2 + H	0.49		
	O...CO + H ⟶	tHOCO	0.495		(1, 7, 6)
		cHOCO	0.01	1000.0	
		CO + OH	0.495		

Surface reactions of species already residing on the surface. The product stays on the surface as well, only a fraction of them can chemically desorb. The chemical desorption fraction of the products is an input parameter in the model. We discuss our approach in Sec. 4.4.5. (1) Taquet et al. (2013), (2) Ruffle and Herbst (2000) , (3) Jonusas et al. (2020), (4) Ceccarelli et al. (2018), (5) Martín et al. (2009), (6) Oba et al. (2010), (7) Goumans and Andersson (2010). (8) Roser et al. (2001) (9) Atkinson et al. (2004), (10) Madzunkov et al. (2006) (11) Hiraoka et al. (1998), (14) Baulch et al. (2005) , (15) Talbi et al. (2006), (17) Cuppen and Herbst (2007), (18) Miyauchi et al. (2008), (19) Dulieu et al. (2010) (20) Cuppen et al. (2010), (22) Ioppolo et al. (2011); (23) Noble et al. (2011), (24) Taquet et al. (2012). (25) Hiraoka et al. (2002), (26) Watanabe and Kouchi (2002),(27) Ioppolo et al. (2008), (28) Mokrane et al. (2009), (∗) This reaction is based on the Eley Rideal mechanism (see Sec. 4.4.4). In this reaction Oxygen reacts with CO that is already on the surface upon arrival and forms a van det Waals complex O...CO.

(van Dishoeck and Blake, 1998) or along the outflow cavity walls (Öberg et al., 2010), or in diffuse clouds (Guzmán et al., 2013). It may be that photodesorption can explain the presence of molecules in the gas phase in regions with $T \leq 100$ K where they would be frozen (see, Oberg, 2016; Tielens, 2021, and the references therein).

What happens is that the FUV photon adsorbed by the ices may lead to a species electronic or vibrational excitation. The excitation can translate to translational motion due to collision with the neighboring species. It can also break the species. The high kinetic energy gains by the UV collision can lead to the desorption of surface species. However, the excited species well within the ice may not have a chance to escape. They may excite the neighboring species and lead to their desorption. It means that even species that do not absorb FUV light (6 - 13.6 eV) may have a chance of induced desorption (Tielens, 2021).

Recent experimental chemistry research and MD simulations have aimed to quantify the yield of photo-induced processes in ices. The following paragraphs review a few from the non-exhaustive list of works hoping to paint a general picture.

Öberg et al. (2009c, 2007, 2009f) have conducted experiments on pure H_2O, CO, N_2, CO_2 10-MLs (mono-layers) ices in $T \leq 20$ K and UHV conditions and measured the desorption and dissociation yield per photon for each species. They determined that photodesorption and photodissociation occur parallel and are only effective in the first 1 or 2 MLs. Additionally, the water and CO_2 product yield increased with temperature due to increased mobility. The UV yield for each species depends on the temperature and the wavelength of the UV photon. For example, Muñoz Caro et al. (2010) and Chen et al. (2014) have found CO desorption yield to be one and two orders of magnitude higher than Öberg et al. (2009c) results due to the difference in the lamp spectrum.

Andersson et al. (2006) MD study calculated the desorption yield of water to 0.5-1 %. Andersson and van Dishoeck, 2008 extended the simulations to study photodissociation of water. Their results are in agreement with Arasa et al. (2010) MD simulations and the experiments outcomes. Photodesorption is highly efficient in the top few MLs, and the trapping probability of photodissociation products is higher deeper in the ice (see also, Andersson et al., 2005, 2006).

In summary, the number of experiments and MD simulations conducted to quantify the yield of photo-processes in ices has increased significantly in the past two decades. The desorption and dissociation yields for water, CO_2, CO, methanol, and a few more species have been examined by several groups. While for each species, the results may vary due to differences in temperature or the wavelength band of the irradiation lamp, some conclusions remained in agreement: Photodesorption is efficient in the few top MLs, and trapping is more probable in the deeper MLs in the ice. Smaller molecules, such as CO and N_2, do not fragment, but they can desorb. On the other hand, larger species, such as methanol or water, are prone to dissociation. If a hydrogen atom is among the fragments, it will carry most of the excess energy. The desorption probability scales approximately with the inverse of binding energy. For example, methane desorbed with more likelihood in comparison to methanol. UV irradiation of mixed ices with an initial interstellar-like composition can produce complex molecules like acetaldehyde, dimethyl ether, and glycolaldehyde (Cuppen et al., 2017; Gerakines et al., 1996; Öberg et al., 2009a; Oberg, 2016; Tielens, 2021).

Grainoble+ includes the photodesorption process in the surface layer(s) because it is unlikely that species can sublimate from deeper layers. The models we focused on mainly use MC and dense core conditions where the UV flux is strongly diminished due to high visual extinction. Additionally, the trace of radicals or molecules more complex than methanol in ices is minimal ($\leq$ 1% relative to water ice) in these conditions (Boogert et al., 2015). Therefore, in our models, we did not consider the photodissociation process (see, also Cuppen et al., 2009; Taquet et al., 2012). Nevertheless, we emphasize that it is crucial to investigate their

role in forming radicals and more complex molecules in relevant physical conditions, and it can be a topic of future work.

In the current models, the rate coefficient of photodesorption reads

$$\kappa_{\mathrm{UVdes}} = F_{\mathrm{UV}} y_{\mathrm{UV}} \frac{\sigma}{n_{\mathrm{site}}} \,. \tag{4.32}$$

F_{UV} is the flux of UV and y_{UV} is the yield per photon. σ is the grain's cross-section, and n_{site} is the number of sites on the surface. The rate coefficient calculates the yield per site on the surface. Grainoble+ takes the yields provided in the literature: CO, N_2, O_2 from Bertin et al. (2013) and Fayolle et al. (2013), CO_2 from Fillion et al. (2014), and water from Westley et al. (1995). For the rest of the species, the yield is scaled from the water's yield using their binding energy ratio

$$y^x_{\mathrm{UV}} = y^{\mathrm{H_2O}}_{\mathrm{UV}} \frac{E_b^{\mathrm{H_2O}}}{E_b^x} \,. \tag{4.33}$$

.

Chemical desorption

The energy released from exothermic reactions on the ices can eject the product(s) into the gas phase. This process is commonly known as chemical desorption (see § 3.3.3 for further discussions). The latest astrochemical modeling and experimental data suggest that the chemical desorption rate is uncertain and poorly constrained. It is in parts because the desorption rate depends on the substrate structure, the reactants, and the products. Therefore, in our modelings, we examine various assumptions. For example, we assumed three sets of assumptions for chemical desorption probability in Witzel et al. 2022 (submitted): (1) 1% probability for all the surface reactions which is widely used in astrochemical models; (2) calculated values listed in Minissale et al. (2016b, Table 1) and 1% for the rest of the reactions in our network that are not listed in their table; and (3) 10.% for all the species. The latter choice is to examine the effect of chemical desorption level on gaseous abundances, specifically for the case of methanol (see, Chap. 6).

4.5 Rate equations

Grainoble+ is a three-phase, multi-grain model, which considers uni- and bi-species processes. Uni-molecular, such as adsorption and desorption and bi-molecular, such as bimolecular reactions in the gas phase or on ices.

In summary, the chemical processes concerning a species in each phase are as follows.

(a) Gas-phase species: A species in the gas phase can undergo adsorption and accrete on the grains, it can interact with other gaseouos species and form new ones, or can be formed through bi-molecular or dissociative (uni-molecular) reactions, it can be destroyed by external influences such as the CRs or UV photons, or it can be sublimated from the ices through thermal and non-thermal desorption processes. The rate equation of gaseous species is shown in Eq. 2.1.

(b) Grain-surface species: Species on the surface can evaporate into the gas phase through thermal and non-thermal processes, can be accreted onto the surface from the gas-phase and undergo LH or ER reaction and form other species or be formed through the same mechanisms, or it can emerge from the bulk to the surface layer where or vise versa Eq. 2.2 is the rate equation of surface species in its general form.

(c) Bulk reaction: species enter the bulk phase because another surface layers was made on the top. These species can sublimate through CR interaction with the grain following the rate equation

$$\frac{\mathrm{d}\, n_i}{\mathrm{d}\, t} = - \kappa_{\mathrm{CRdes}} n_i \,. \tag{4.34}$$

Chapter 5

Application I: Interstellar complex organic molecules in the NGC 1333 IRAS 4A outflows

In this chapter, we present the work published in De Simone et al. (2020) in collaboration with M. De Simone, C. Codella, C. Ceccarelli, A. López-Sepulcre, R. Neri, N. Balucani, P. Caselli, C. Favre, F. Fontani, B. Lefloch, J. Ospina-Zamudio, J. E. Pineda, and V. Taquet. The following paragraphs present a summary of the work. I have contributed in the astrochemical modelling part of the paper (§ 5.7), the discussions (§ 5.8), and conclusions (§ 5.9). This chapter starts with a summary of the published work and follows the paper.

Context There are two proposed formation routes of the interstellar Complex Organic Molecules (iCOMs): formation on the ice mantle and direct sublimation, or formation through gas-phase reactions after the parental species have sublimated from ices. The shocked regions along the low-mass protostar outflows provide a unique environment to study and examine this hypothesis because the kinetical age of a shocked region can provide an additional constraint, time dependency, on the model predictions. This type of study on the observed iCOMs in the shocked regions has been done only for the L1157-B1 outflows (Codella et al., 2017). To understand whether the case of L1157-B1 is unique, we imaged and studied the IRAS 4A outflows in the NGC 1333 star forming region.

The IRAS 4A source IRAS 4A is part of the IRAS 4 multiple systems located at 299 $\pm$ 15 pc distance in the NGC 1333 region of the Perseus complex (Tab. 2). It is a binary system with two Class 0 hot corinos, 4A1 and 4A2, separated by 1.”8. Three outflow lobes emanate from the binary system. The southeast (SE) outflow is driven by the IRAS 4A1, while the North (N) and the SouthWest (SW) ones are from 4A2 (Fig. 1 and 2).

The methodology and results from observations To image the large-scale bipolar outflows driven by the IRAS 4A binary system, we used the NOrthern Extended Millimeter Array (NOEMA) interferometer in the 3 mm band (Tab. 1). We report for the first time the detection of several iCOMs in the outflows of IRAS 4A1 and IRAS 4A2: six lines of methanol (CH_3OH), eight of acetaldehyde (CH_3CHO), one of formamide (NH_2CHO), and four of dimethyl ether (CH_3OCH_3). Their calculated column densities are reported in Tab. 4. We found a significant chemical difference between the outflows. The methanol to acetaldehyde ratio, CH_3OH/CH_3CHO, in the SE and the N lobes are relatively low (8 -20), whereas the SW lobe shows a ratio of $\sim$ 44.

Astrochemical modeling To reproduce of the observations and understand the difference in the observed CH_3OH/CH_3CHO ratio, we ran a series of models with Grainoble+. Our

model assumed that methanol is formed in the ice mantles and is sublimated directly from the grains in the shocked regions. We discussed two possible formation routes for acetaldehyde, formation on ice surfaces through the CH_3 + HCO radical-radical reaction and direct sublimation into the gas-phase and formation via gas-phase reaction CH_3CH_2 + O, where ethyl radical, CH_3CH_2, is injected from ices.

To simulate the passage of a shock in IRAS 4A, we employed the gas-phase mode of GRAINOBLE+. Since the micro-physical parameters governing the formation of solid species are poorly understood and we only aimed to reproduce the observed gaseous abundances, to keep the influential parameters under control, we chose to employ the gas-phase mode of GRAINOBLE+. The simulations follow two steps: (1) the pre-shock stage: a cold molecular gas-phase with H-nuclei density of 2×10^4 cm^{-3} and at 10 K; and (2) the shocked stage: a post-shock gas phase where density and temperature jump to 2×10^6 cm^{-3} and 70 K derived from observations. The CR ionization rate of H_2 in both steps is $\zeta_{H_2} = 3 \times 10^{-16}$ s^{-1} in analogy with L1157-B1 shocked region. The second stage inherits the gas-phase chemical composition from the previous stage. Our model assumes that the ice mantle is formed in the first stage and grain sputtering at the beginning of stage two, which infuses the gas phase with ice mantle composition (Tab. 5).

Firstly, we ran a grid of 169 models varying the infused abundances of methanol and CH_3CH_2 within $4 \times 10^{-8} - 4 \times 10^{-6}$ and $4 \times 10^{-9} - 4 \times 10^{-7}$, respectively (all abundances in our models are relative to hydrogen nuclei). Fig. 5 shows the contour plot of methanol to acetaldehyde ratio as a function of methanol and ethyl radical infused abundances at 1000 years after the passage of shock.

Secondly, we studied the influence of density and CR ionization rate of the ratio as a function of time. We chose a model from the previous modeling step that reproduced the CH_3OH/CH_3CHO ratio at 1000 years in all three lobes, SW, N, and SE. In this model, methanol and ethyl radical abundances are 3×10^{-6} and 3×10^{-7}, respectively. We ran two additional models varying the density and ζ_{H_2} to 2×10^5 cm^{-3} and 3×10^{-17} s^{-1}, respectively with respect to the chosen model in this step. Fig. 6 shows the abundances and the ratios of the three models as a function of time after the passage of shock. Methanol abundance was unaffected by the changes in the density and ζ_{H_2} and remains constant until $\sim 2 \times 10^3$ years. The formation of acetaldehyde after the passage of shock decreases by lowering the density due to the increase in reactions with ions. ζ_{H_2} does not affect acetaldehyde in the early years.

Finally, we ran one model assuming that acetaldehyde is synthesized on ices and ejected directly into the gas phase by the passage of shock. The abundance of acetaldehyde in the early years does not change, similar to methanol which shows that the difference between grain- or gas- synthesized assumptions in our models is only in the first 200 years after the shock passage.

Conclusions After L1157-B1, the IRAS 4A outflow is now the second to show an evident chemical complexity. Four iCOMs have been observed along the IRAS 4A outflows in this study. Dimethyl ether and formamide seem concentrated in an apparent interface spot between the 4A1 and 4A2 outflows. On the other hand, methanol is widespread, while acetaldehyde is the brightest in the southern lobes. The methanol to acetaldehyde ratio in SE (associated with the 4A1 outflow) is $\sim$ 2 times larger than SW and N (associated with 4A2). We ran various cases with Grainoble+ and reproduced the observed methanol to acetaldehyde ratio by assuming methanol is synthesized on ices and directly sublimated at the shock passage, and acetaldehyde is produced via the gas phase reaction CH_3CH_2 + O. Furthermore, the chemical differentiation between the two outflows suggests that the IRAS 4A1 outflow is likely younger than the IRAS 4A2. Further investigation is needed to constrain the age of the outflow. In addition, observations of even younger shocks is necessary to confirm and substantiate our conclusion. It would also be interesting to observe CH_3CH_2 to constrain the

acetaldehyde formation mechanism, but given that its frequencies are unknown, future spectroscopic studies on this species are needed. The observed L1157 B1 outflows (130– 250) ratio is larger than IRAS 4A outflows, which could be due to the difference in the chemical composition or the kinetic age of the outflow. A similar ratio difference can be seen when comparing class 0 and class I sources, which could indicate a chemical composition difference between those sources and IRAS 4A outflows (Fig. 7).

5.1 Abstract

The interstellar Complex Organic Molecules (iCOMs) are C-bearing molecules containing at least six atoms; two main approaches of their formation are invoked: a direct formation in the icy mantle of the dust grains, or through the reaction in gas phase of released grain mantle species. The shocked gas along outflows driven by low-mass protostars is a unique environment to study how the iCOMs can be formed, as the composition of the dust mantles is sputtered into the gas phase. The chemical richness in shocked material associated with low–mass protostellar outflows has been so far studied in the prototypical L1157 blue shifted outflow to investigate the iCOMs formation routes. To understand whether the case of L1157-B1 is unique, we imaged and studied the IRAS 4A outflows in the NGC 1333 star forming region. We used the NOEMA (NOrthern Extended Millimeter Array) interferometer as part of the IRAM SOLIS (Seeds Of Life in Space) Large Program to image the large scale bipolar outflows driven by the IRAS 4A system in the 3 mm band, and we compared the observation with the GRAINOBLE+ astrochemical model. We report the first detection, in the IRAS 4A outflows, of several iCOMs: six lines of methanol (CH_3OH), eight of acetaldehyde (CH_3CHO), one of formamide (NH_2CHO) and four of dimethyl ether (CH_3OCH_3), all sampling upper excitation energy up to $\sim$30 K. We found a significant chemical differentiation between the south east outflow driven by the IRAS 4A1 protostar, showing a richer molecular content, and the north–south west one driven by the IRAS 4A2 hot corino. The CH_3OH/CH_3CHO abundance ratio is lower by a factor $\sim$4 in the former; furthermore the ratio in the IRAS 4A outflows is lower by a factor $\sim$10 with respect to the values found in different hot corinos. After L1157-B1, IRAS 4A outflow is now the second outflow to show an evident chemical complexity. Given that CH_3OH is a grain surface species, the astrochemical gas phase model run with GRAINOBLE+ reproduced our observation assuming that acetaldehyde is formed mainly through the gas phase reaction of ethyl radical (CH_3CH_2) and atomic oxygen. Furthermore, the chemical differentiation between the two outflows suggests that the IRAS 4A1 outflow is likely younger than the IRAS 4A2 one. Further investigation is needed to constrain the age of the outflow. In addition, observation of even younger shocks are necessary. In order to provide strong constraints on the CH_3CHO formation mechanisms it would be interesting to observe CH_3CH_2, but given that its frequencies are not known, future spectroscopic studies on this species are needed.

5.2 Introduction

Since the discovery of interstellar Complex Organic Molecules (iCOMs[1], molecules containing carbon and at least six atoms: Ceccarelli et al., 2017b; Herbst and Dishoeck, 2009) in Solar-type protostars (Cazaux et al., 2003), the question whether they had a role in the appearance of life on Earth (and elsewhere in the Universe) has been raised. Although they are extremely small molecules when compared to the biotic ones, iCOMs may have provided the bricks to build them. The presence of amino acids in meteorites and comets has certainly revived this possibility (e.g. Altwegg et al., 2016; Elsila et al., 2009; Pizzarello et al., 2006).

In addition to their possible role in the emergence of life, iCOMs have represented a challenge for astrochemistry, as their synthesis is all but obvious. Nowadays, two main paradigms are invoked (see e.g. Herbst, 2017), that argue that iCOMs are either synthesized on the grain surfaces (e.g. Garrod, 2008; Garrod and Herbst, 2006) or in the gas phase (e.g.

[1] Please note that we added "i" to the commonly used COMs acronym in order to be clear that these molecules are only complex in the interstellar context, contrary to what chemists would consider complex in the terrestrial context.

Balucani et al., 2015b; Millar et al., 1991; Skouteris et al., 2018a). As a starting point, both pathways have the formation of simple hydrogenated molecules on dust grain mantles during the prestellar phase. Constraining which of the two ways to synthesize iCOMs is efficient and where the iCOMs formation happen, is not a simple task. Many methods have been used, from the comparison of the iCOMs measured abundances in hot cores/corinos with model predictions to their measured deuterium fractionation (Ceccarelli et al., 1998; Coutens et al., 2016; Jørgensen et al., 2018; Skouteris et al., 2017; Turner, 1990).

One method that turned out to be very efficient is to compare observations towards low-mass outflow shocks with model predictions (Codella et al., 2017). The advantage of this method is that the outflow shocks provide the time dependence as additional constraint. In fact, once localized the iCOMs emission in a precise region (thanks to high spatial resolution observations), it is possible to identify in that region a shock event that corresponds naturally to a precise kinematical age (e.g. Gueth et al., 1996; Podio et al., 2016). After the passage of the shock, the chemistry in the shocked region evolves with time. Therefore, the comparison of observed iCOMs abundances with model predictions provides strong constraints on the formation routes because it is possible to do the comparison at the precise kinematical shock age. This method was successfully applied in the L1157–B1 outflow shock to constrain the formation route of formamide. In fact, thanks to interferometric high spatial resolution observations, Codella et al. (2017) found a difference in the spatial distribution between acetaldehyde and formamide emission, and consequently, they could constrain the formamide formation as due to gas-phase reactions. Of course, those conclusions apply to L1157-B1 only. Given its power, it is important to apply the same method to other iCOMs and other protostellar shocks.

Unfortunately, observations of iCOMs in low-mass protostellar shocks are very few. To our knowledge, iCOMs other than methanol have been detected only towards a handful of objects: several iCOMs towards L1157-B1 (Arce et al., 2008; Lefloch et al., 2017), formamide towards L1157-B2 (Mendoza et al., 2014), acetaldehyde towards IRAS 2A and IRAS 4A (Holdship et al., 2019) and acetaldehyde and dimethyl ether towards SMM4-W (Öberg et al., 2011). However, it is worth noticing that all these works refer to (relatively low spatial angular resolution) single-dish observations and are, by definition, unable to disentangle the different spatial distribution of iCOMs caused by the age of the shocks, so that the method described above cannot be used.

In this work, we present new high spatial observations towards the two outflows from IRAS 4A. This source is one of the target of the Large Program SOLIS (Seeds Of Life In Space: Ceccarelli et al., 2017b), at the IRAM/NOEMA (NOrthern Extended Millimeter Array) interferometer, whose goal is to investigate the iCOM chemistry during the earliest formation phases of Solar–type stellar systems. The observations targeted three iCOMs in addition to methanol (CH_3OH): acetaldehyde (CH_3CHO), dimethyl ether (CH_3OCH_3) and formamide (NH_2CHO). All these iCOMs were detected in our data set. The detection of different iCOMs in the outflowing gas of IRAS 4A with high spatial resolution observations allows us to apply the method of model-observations comparison described above.

The article is organized as follows: we first give the IRAS 4A source background in Section 5.3, then present the observations in Section 5.4 and the results in Section 5.5; we derive the abundance ratios of the detected iCOMs in different positions of the IRAS 4A outflows (Section 5.6), and the model predictions to interpret them (Section 5.7); in Section 5.8 we discuss what our new observations imply and finally, Section 5.9 summarizes our work.

5.3 IRAS 4A: Source Background

IRAS 4A is part of the multiple system IRAS 4, located at a distance of 299±15 pc in the NGC 1333 region of the Perseus complex (Zucker et al., 2018). The system IRAS 4A is constituted by four objects: 4A, 4B, 4B′ and 4C (Choi, 2001; Di Francesco et al., 2001; Lay et al., 1995; Looney et al., 2000; Smith et al., 2000). IRAS 4A is itself a binary system with two Class 0 objects, 4A1 and 4A2, separated by 1″8 (∼ 540 au; Looney et al., 2000; López-Sepulcre et al., 2017; Maury et al., 2019; Santangelo et al., 2015). In the millimeter wavelengths, 4A1 is three times brighter than 4A2. However, their respective luminosity is unknown since they are not resolved in the sub-millimeter to IR wavelengths where the luminosity peak lies. The bolometric luminosity of the whole IRAS 4A system is 9.1 $L_\odot$ (Karska et al., 2013; Kristensen et al., 2012).

IRAS 4A is the second ever discovered hot corino (Bottinelli et al., 2004), after IRAS 16293-2422 (Cazaux et al., 2003). Interferometric IRAM/PdBI (Plateau de Bure Interferometer, now evolved into NOEMA) observations have later suggested that iCOMs emission originates rather from 4A2 than 4A1 (De Simone et al., 2017; Taquet et al., 2015). More recently, López-Sepulcre et al. (2017) obtained high resolution (∼0″.5) ALMA images of IRAS 4A and confirmed the huge contrast between 4A1 and 4A2: while 4A2 shows a hot corino activity with enriched iCOMs emission, no sign of iCOMs is detected in 4A1. López-Sepulcre et al. (2017) suggest that either 4A1 does not host any hot corino or, alternatively, the hot corino size is less than ∼15 au (after scaling to 299 pc the distance adopted by López-Sepulcre et al., 2017), namely six times smaller than the 4A2 one.

As for many Class 0 protostars, IRAS 4A is associated with a spectacular large–scale (few arcminutes) bipolar outflow observed with several tracers, such as CO, SiO, SO, HCN (Blake et al., 1995; Choi, 2005; Choi et al., 2011; Lefloch et al., 1998). Choi (2005) well traced the high velocity component with SiO emission using VLA observations at 2″ spatial resolution. From their map, it is possible to distinguish two different blue–shifted lobes towards south and only one northern red–shifted lobe with a peculiar bending toward north–east at 20″ from the protostars. Using IRAM/PdBI high spatial resolution observations ($< 1''$), Santangelo et al. (2015) mapped the outflows at lower scale (∼30″) with respect to the SiO map from Choi (2005). They traced different velocity component (from ∼10 km s^{-1} to ∼ 60 km s^{-1}) using CO, SiO and SO as tracers. With their study, Santangelo et al. (2015) were able to clearly disentangle the two southern lobes revealing a fast collimated jet associated with bright H_2 emission and driven by 4A1 (south–east lobe) and a slower and precessing jet driven by 4A2 (south–west lobe). Furthermore, the jets present different morphologies: the 4A2 jet shows a large spatial extent and a S–shape pattern on small scales, probably due to jet precession; the 4A1 jet is faster than the 4A2 one, covers a smaller extent (∼ 15″) and presents a C-shape tilted towards east of 4A1.

Thanks to a detailed study on sulfur species using interferometric observations, for the first time, Taquet et al. (2019) were able to distinguish the outflow driven by 4A1 from the one driven by 4A2 also in the northern lobe.

The left panel of figure 5.1 summarizes the situation: it shows the distribution of the dust cores at large scale, trace by the continuum at 1.3 mm using the IRAM 30m (Lefloch et al., 1998), together with large scale high velocity outflow traced by the SiO (1-0) line using the VLA interferometer (Choi, 2005).

5.4 Observations

IRAS 4A was observed with the IRAM/NOEMA interferometer during several tracks in June and September 2016. Two frequency setups were used, called 1 and 3 in Ceccarelli et al.

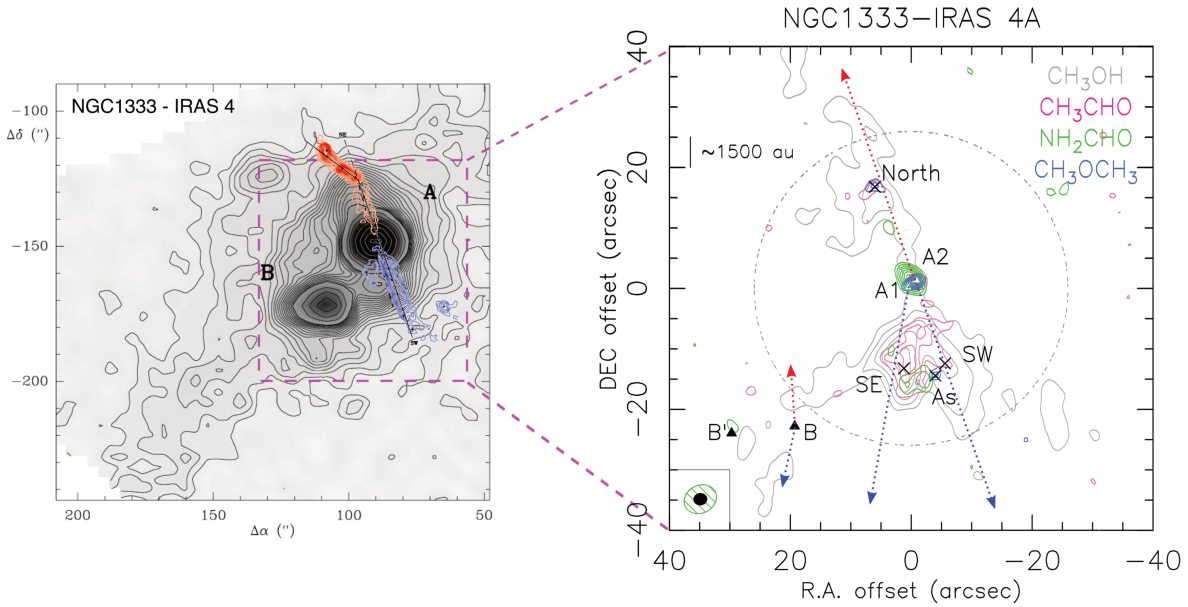

FIGURE 5.1: *Left:* Overlap of the contour map of the 1.25 mm continuum emission from NGC 1333 IRAS 4 region in Perseus, observed with the IRAM 30m antenna (Lefloch et al., 1998), with the map of SiO line (VLA observations; Choi, 2005). Axes offsets are in arcseconds from SVS 13 (ff(2000) = $03^h29^m3^s9$ and $\delta(2000) = 31°16'8''$). *Right:* Zoom in in the IRAS 4A system with NOEMA-SOLIS observations. Axes offsets are in arcseconds from IRAS 4A. A spatial separation of $5''$ correspond to $\sim$ 1500 au at a distance of 299 pc (Zucker et al., 2018). The white triangles mark the position of the sources 4A1 and 4A2, while the black triangles mark the position of the sources 4B and 4B′ (coordinates in Table 5.2). The black crosses mark the analyzed positions in the outflows (SE, SW, North and As; coordinates in Table 5.2). The dashed blue and red arrows indicate the direction of the blue– and red–shifted 4B outflow (from the HCN observations of Choi, 2001) and of the 4A ones. The contour map represents the iCOMs emission at 3 mm in the IRAS 4A outflows (this work). For all the iCOMs the contours start at 3σ with steps of 1σ, except for methanol whose contours have steps of 20σ. The emission distribution is the following: 1) methanol (CH_3OH in grey), integrated over the transitions $2_{0,2} - 1_{0,1}$ A, $2_{0,2} - 1_{0,1}$ E and $2_{-1,2} - 1_{-1,1}$ E with $\sigma = 75$ mJy/beam km/s; 2) acetaldehyde (CH_3CHO, in magenta), here in the $5_{0,5} - 4_{0,4}$ A emission with $\sigma = 11$mJy/beam km/s; 3) formamide (NH_2CHO, in green), $4_{1,4} - 3_{1,3}$ emission with $\sigma = 10$ mJy/beam km/s; dimethyl ether (CH_3OCH_3, in blue), $4_{1,4} - 3_{0,3}$ emission with $\sigma = 9$ mJy/beam km/s. The synthesized beams for the formamide line (green, $\sim 4''$) and for the other species (black, $\sim 2''$) are indicated in the lower left corner. The primary beam ($\sim 52''$) is shown with a dashed grey circle.

TABLE 5.1: List of the characteristics of the SOLIS WideX backend setups.

Setup	Frequency Range (GHZ)	Spectral resolution		Spatial resolution		Synthesized Beam	Primary Beam	
	[GHz]	[km s^{-1}]	[MHz]	[″]	[au]^a	[″×″ (°)]	[″]	[au]^a
1	80.8-84.4	7	2	4	∼1200	4.5×3.5 (27)	61.″4	∼2×10^4
3	95.5-99.5	6	2	4	∼1200	2.2×1.9 (96)	59.″2	∼2×10^4

a computed at the distance of the NGC 1333 region (∼299 pc; Zucker et al., 2018).

(2017b, Table 4), centered at ∼82 and ∼97 GHz, respectively. The array was used in configurations D and C with baselines from 15 m to 304 m for Setup 3 and from 16 m to 240 m for Setup 1. Here, we present the data obtained using the WideX backend, whose characteristics are summarized in Table 5.1

The phase center is on the IRAS 4A1 source, whose coordinates are listed in Table 5.2. The bandpass was calibrated on 3C454.3 and 3C84, while the flux was calibrated using MWC349 and LKHA101. The calibration of phase and amplitude was done observing 0333+321. The system temperatures ranged typically between 50 and 200 K. The calibration error associated to the absolute flux is $\leq$ 15%. The data were reduced using the packages CLIC and MAPPING of the GILDAS[2] software collection. The data were self-calibrated in phase only; the self-calibration solutions were applied to the data spectral cube, which was then cleaned. A continuum map (see Figure 5.2) was obtained by averaging line-free channels from the self–calibrated data. The resulting synthesized beam is $2''.2 \times 1''.9$ (P.A.=96°), for Setup 3, and $4''.5 \times 3''.5$ (P.A.=27°) for Setup 1. The half power primary beam is $59''.2$ and $61''.4$ for Setup 3 and Setup 1 respectively.

5.5 Results

5.5.1 Dust continuum emission

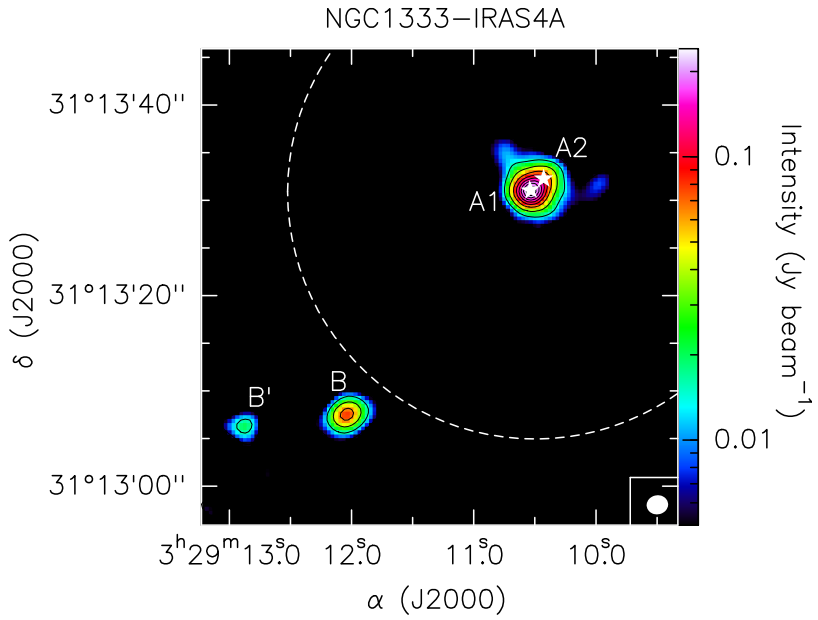

FIGURE 5.2: Dust continuum emission maps of IRAS 4A at 95.85-99.45 GHz (Setup 3, see Table 5.1). Contours start at 3σ and increase by steps of 20σ, with σ = 1.5mJy/beam. The synthesized beam ($\sim 2''$) is represented in white in the lower right corner of the panel, the primary beam ($\sim 52''$) is shown with a dashed white circle. The millimeter continuum sources in the field are labeled following the nomenclature used by Choi (2001) for 4A1 and 4A2 and Di Francesco et al. (2001) for B and B′.

Figure 5.2 shows the map of the dust continuum emission at 3 mm, whose emission peaks at the position of 4A1 and 4A2. As expected, the two sources are not disentangled as the angular resolution of $\sim 2''$ is too close to their angular separation ($\sim 1''$; Section 5.4). In addition, the two protostars IRAS 4B and IRAS 4B′ (e.g. Choi, 2001; Di Francesco et al., 2001;

[2]http://www.iram.fr/IRAMFR/GILDAS

TABLE 5.2: Coordinates of the protostars, (see also: Choi, 2001; Di Francesco et al., 2001; López-Sepulcre et al., 2017; Maury et al., 2019), and the analyzed emission peaks (chosen from methanol and dimethyl ether emission, see text) in the outflows.

Position	α(2000)	δ(2000)
4A1	$03^h29^m10^s536$	$31°13'31''07$
4A2	$03^h29^m10^s428$	$31°13'32''27$
4B	$03^h29^m12^s000$	$31°13'08''10$
4B′	$03^h29^m12^s813$	$31°13'06''97$
SE peak	$03^h29^m10^s591$	$31°13'17''53$
SW peak	$03^h29^m10^s061$	$31°13'18''61$
North peak	$03^h29^m10^s966$	$31°13'47''87$
As region	$03^h29^m10^s184$	$31°13'16''62$

Looney et al., 2000; Maury et al., 2019) were detected, even if they were located outside the primary beam of our observations ($\sim$ 52″). The coordinates of all the four protostars are reported in Table 5.2.

The root mean square (RMS) noise level is 1.5 mJy/beam and the peak flux towards IRAS 4A1+4A2 is 240±40 mJy/beam. Taking the error on the measured flux into account and considering the slightly different wavelength (2.7 mm) and angular resolution ($\sim$ 1″) of the observations, this flux value is consistent with the one found by López-Sepulcre et al. (2017). The uncertainties in the flux measurements include the amplitude calibration error ($\sim$ 15%) that dominates the RMS.

5.5.2 Line emission: maps

The present observations allow us to image both 4A1 and 4A2 and their molecular outflows. The study of the molecular content around 4A1 and 4A2 protostars is out of the scope of the present paper. Instead, we focus here on the molecular composition of the outflows.

Several lines from methanol (CH_3OH), acetaldehyde (CH_3CHO), dimethyl ether (CH_3OCH_3) and formamide (NH_2CHO) were detected along the outflows with a signal to noise ratio (S/N) larger than 3. Table 5.3 lists the detected lines with their spectroscopic properties. In Setup 3, we detected six lines of methanol which cover a range of upper level energy (E_{up}) from 7 to 28 K, eight lines of acetaldehyde with E_{up} between 13 and 23 K, and four lines of dimethyl ether, blended together and all with E_{up}=10 K. In Setup 1, we detected one line of formamide with E_{up} of 28 K.

Figure 5.1 shows the distribution of the line emission of the four detected iCOMs. To obtain the methanol map we integrated from -36 km s^{-1} to 36 km s^{-1} with respect to the systematic velocity of the source ($\sim$ 6.5 km s^{-1}), for acetaldehyde between -15 km s^{-1} to 15 km s^{-1}, while for formamide and dimethyl ether we integrated from -9 km s^{-1} to 9 km s^{-1}. First, the methanol emission is extended ($\sim$ 1′) and covers the lobes of the two outflows from the two protostars: north (North) and south-west (SW) lobes of the outflow from 4A2, and the south-east (SE) lobe from 4A1. Second, acetaldehyde emission is less extended than the methanol one($\sim$ 15″) and it is bright towards the southern lobes, especially towards the SE one. The dimethyl ether emission is not resolved being less than the beam size (2″) in two positions, in the North lobe and in the region As (named by Ceccarelli et al., 2017b) where SE and SW lobes seem to cross. Finally, formamide emission is also compact ($\sim$ 6″) and is located around the As position (see also Ceccarelli et al., 2017b). The same iCOMs are also detected in the central protostars (4A1+4A2): please note that the methanol and acetaldehyde emission is not visible in Figure 5.1 because hidden by the dimethyl ether and formamide contours.

Figure 5.1 clearly shows a first important result: the evidence of a spatial segregation between the different iCOMs due to the fact that their emission covers different outflow regions.

5.5.3 Line emission: spectra and intensities

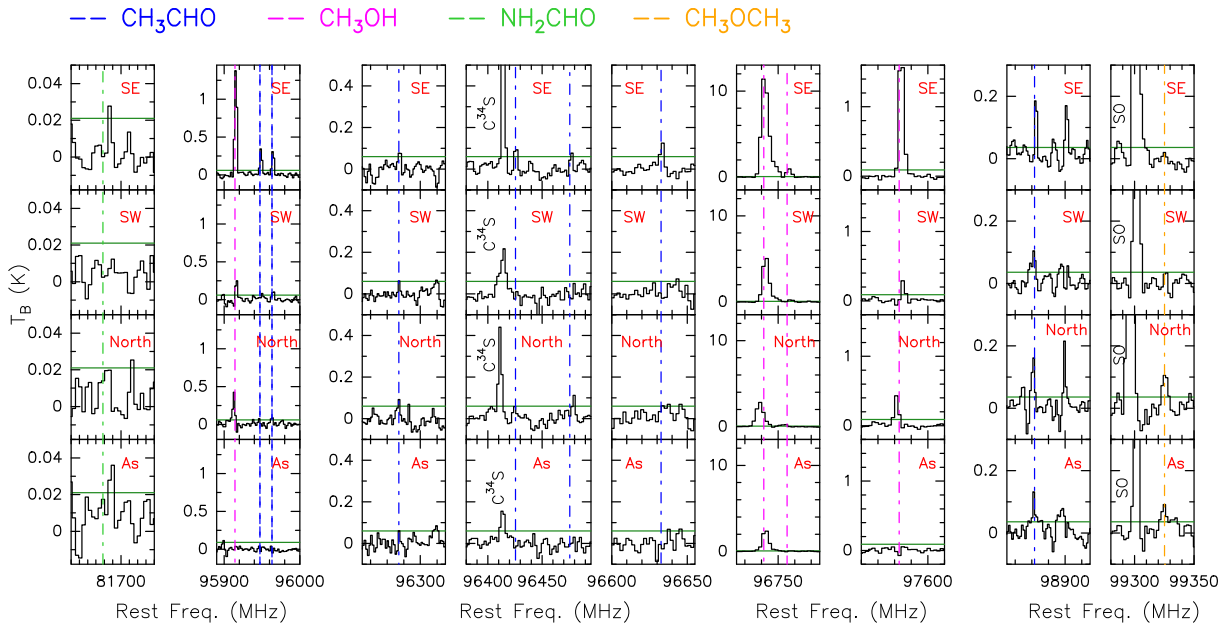

FIGURE 5.3: Spectra towards the four positions along the outflows of IRAS 4A, listed in Table 5.2. The horizontal green lines represent the 3σ levels (reported in Table 5.3); the vertical dashed lines in blue and magenta represent the rest frequency of acetaldehyde and methanol lines, respectively. The rest frequency corresponds to the protostar LSR velocity (6.5 km s^{-1}).

In order to do a quantitative analysis, we extracted the spectra from different positions of the three lobes, where both methanol and acetaldehyde emit. The first two selected positions correspond to the emission peaks of methanol in the two southern lobes, named SE and SW, while the last selected position corresponds to the emission peak of dimethyl ether in the north lobe, named North (Figure 5.1). A fourth position is the one where formamide and dimethyl ether emit, named As. The spectra extracted at the pixels corresponding to the four positions are shown in Fig. 5.3. It is immediately evident that the SE position is richer and brighter in iCOMs when compared to the other ones (SW, North and As).

We then derived the velocity-integrated line intensities of each detected transition using a Gaussian fit, obtained with the CLASS package of the GILDAS software. All the lines used for the analysis are not contaminated by other species and are well isolated. For instance, three of the six detected methanol lines, namely $2_{-1,2}$–$1_{-1,1}$ E (E_{up}=13 K), $2_{0,2}$–$1_{0,1}$ A (E_{up}=7 K), $2_{0,2}$–$1_{0,1}$ E (E_{up}=21 K), are blended together at the WideX resolution (∼2 MHz): therefore they were not used in the analysis described in the next section. Table 5.3 reports the fit results; in case of non-detection, is reported the 3σ limit.

5.6 Derivation of the column densities and abundance ratios

5.6.1 Methanol and acetaldehyde

We used the detected lines of methanol and acetaldehyde to estimate their column densities in the four positions of Table 5.2. We used the standard rotational diagram method (Goldsmith

TABLE 5.3: Spectral parameters and fit results of the detected iCOMs emission lines observed using the NOEMA WideX backend towards the IRAS 4A outflow peaks (see text and Table 5.2).

Transition	Spectral Parameters			Outflow SE			Outflow SW			Outflow North			Region As [a]		
	Frequency[b] [GHz]	E_{up}[b] [K]	$logA_{ij}$[b]	Area[c] [K km s^{-1}]	T_{peak} [K]	RMS[d] [mK]	Area[c] [K km s^{-1}]	T_{peak} [K]	RMS[d] [mK]	Area[c] [K km s^{-1}]	T_{peak} [K]	RMS[d] [mK]	Area[c] [K km s^{-1}]	T_{peak} [K]	RMS[d] [mK]
CH_3OH															
$2_{1,2}$–$1_{1,1}$ A	95.91431	21.4	-5.6	17.1(0.9)	1.4	20	2.7(0.3)	0.4	20	5.1(0.5)	0.4	20	$\leq$ 0.5	$\leq$ 0.05	30
$2_{-1,2}$–$1_{-1,1}$ E [e]	96.73936	12.5	-4.6												
$2_{0,2}$–$1_{0,1}$ A [e]	96.74138	6.9	-5.6	199 (4)	12	20	69(4)	5	30	48(4)	3	20	37(1)	2.5	30
$2_{0,2}$–$1_{0,1}$ E [e]	96.74454	20.1	-5.5												
$2_{1,1}$–$1_{1,0}$ E	96.75550	28.0	-5.5	11.2(0.3)	0.9	20	2.0(0.2)	0.3	30	3.2(0.3)	0.2	20			
$2_{1,1}$–$1_{1,0}$ A	97.58280	21.6	-5.6	21.5(0.2)	1.9	20	2.5(0.3)	0.3	30	4.4(0.3)	0.4	30	$\leq$ 0.5	$\leq$ 0.05	30
CH_3CHO															
$5_{0,5}$–$4_{0,4}$ E	95.94744	13.9	-4.5	3.9(0.2)	0.4	20	$\leq$ 0.6	$\leq$ 0.06	20	0.8(0.4)	0.1	20	$\leq$0.5	$\leq$0.05	30
$5_{0,5}$ - $4_{0,4}$ A	95.96346	13.8	-4.5	3.7(0.3)	0.4	20	1.7(0.4)	0.1	20	1.3(0.5)	0.1	20	$\leq$0.5	$\leq$0.05	30
$5_{2,4}$ - $4_{2,3}$ A	96.27425	22.9	-4.6	1.1(0.4)	0.1	30	0.7(0.3)	0.07	20	1.0(0.2)	0.1	30	0.5(0.3)	0.1	20
$5_{2,4}$ - $4_{2,3}$ E	96.42561	22.9	-4.6	1.1(0.2)	0.2	30	$\leq$ 0.7	$\leq$ 0.07	20	0.8(0.3)	0.06	30	$\leq$0.3	$\leq$0.03	20
$5_{2,3}$ - $4_{2,2}$ E	96.47552	23.0	-4.6	0.8(0.2)	0.1	20	$\leq$ 0.7	$\leq$ 0.07	20	$\leq$ 0.8	$\leq$ 0.08	30	$\leq$0.3	$\leq$0.03	20
$5_{2,3}$ - $4_{2,2}$ A	96.63266	23.0	-4.6	1.5(0.3)	0.1	20	$\leq$ 0.7	$\leq$ 0.07	20	$\leq$ 0.8	$\leq$ 0.08	30	$\leq$0.3	$\leq$0.03	20
$5_{1,4}$ - $4_{1,3}$ E	98.86331	16.7	-4.5	2.3(0.4)	0.2	20	1.6(0.8)	0.1	20	2.1(0.5)	0.2	30	2.8(0.6)	0.1	20
$5_{1,4}$ - $4_{1,3}$ A	98.90094	16.5	-4.5	2.5(0.5)	0.2	20	$\leq$ 0.6	$\leq$ 0.06	20	1.9(0.3)	0.2	30	2.0 (0.3)	0.1	20
CH_3OCH_3															
$4_{1,4}$ - $3_{0,3}$ EA [e]	99.32443	10.2	-5.3												
$4_{1,4}$ - $3_{0,3}$ AE [e]	99.32443	10.2	-5.3	$\leq$ 0.2	$\leq$ 0.02	15	$\leq$ 0.3	$\leq$ 0.03	15	2.1(0.3)	0.12	15	1.8(0.5)	0.09	15
$4_{1,4}$ - $3_{0,3}$ EE [e]	99.32521	10.2	-5.3												
$4_{1,4}$ - $3_{0,3}$ AA [e]	99.32607	10.2	-5.3												
NH_2CHO[f]															
$4_{1,4}$ - $3_{1,3}$	81.69354	12.8	-4.5	$\leq$ 0.2	$\leq$ 0.02	7	$\leq$ 0.1	$\leq$ 0.01	7	$\leq$ 0.06	$\leq$ 0.006	7	0.4(0.1)	0.04	10

[a] Region where formamide and dimethyl ether emits (Ceccarelli et al., 2017b);
[b] Frequencies and spectroscopic parameters are retrieved from the JPL (Jet Propulsion Laboratory; Pickett et al., 1998) molecular database and from the CDMS (Cologne Database for Molecular Spectroscopy; Müller et al., 2005): for CH_3OH by Xu et al. (2008), for CH_3CHO by Kleiner et al. (1996), for CH_3CHO_3 by Neustock et al. (1990), for NH_2CHO by Kirchhoff et al. (1973). Upper level energies refer to the ground state of each symmetry.
[c] Mean velocity–integrated line flux over the whole velocity emission range from the spectra extracted at the CH_3CHO and CH_3OH transitions at each outflow peaks (see Table 5.2). In case of non–detection we report the 3σ limit. The lines are centered at $\sim$ 3 km s^{-1}, $\sim$ 1 km s^{-1}, $\sim$ 11 km s^{-1} for outflow SE, SW and North respectively, in agreement with the expected outflow velocity (Santangelo et al., 2015) given the WideX channel resolution ($\sim$ 6 km s^{-1}).
[d] The rms is computed over a 200 km s^{-1} band around each line.
[e] These lines are blended together at the WideX resolution ($\sim$2 MHz), therefore they are not used for the non-LTE analysis.
[f] From Setup 1.

and Langer, 1999), which assumes local thermodynamic equilibrium (LTE) and optically thin line emission. Note that we checked a posteriori that the latter assumption is valid. Also, because the map shown in Figure 5.1 shows that the emission is more extended with respect to the observation beam, we did not apply any dilution factor. The used error bar of each data point includes the spectral RMS and the calibration error ($\sim$15%).

Figure 5.4 shows the rotational diagrams of methanol and acetaldehyde in SE, SW and North positions (Table 5.2) and Table 5.4 lists the fitted values. In the As position, we could not build a rotational diagram for either of the two species, as not enough lines were detected. In this case, we obtained an estimate of their column density, by assuming a rotational temperature ranging from 10 to 30 K (range that includes the temperatures found in the other positions, SE, SW and North). If no line was detected we used the 3σ limit.

To compute the methanol over acetaldehyde abundance ratios, quoted in Table 5.4, we adopted the assumptions that the lines emitted by the two species come from the same region and, therefore, possess the same rotational temperature T_{rot}. Under these two assumptions, the column density ratio R between the two species is obtained by taking the column density N_x of each species at the same rotational temperature T_{rot}, namely R=$N_1(T_{rot})/N_2(T_{rot})$. The error bar δR is then obtained by computing R at the smallest and largest T_{rot} of the two species. For example, in the Outflow SE the derived T_{rot} is equal to (11$\pm$3) K and (9$\pm$2) K in methanol and acetaldehyde, respectively; therefore, to estimate the error δR we computed $R(T_{rot})$ at 7 and 14 K. Note that the method described above allows to reduce the error bar in the abundance ratio because the calibration uncertainty, which enters in the column density estimate of each species, cancels out when considering the column density of two species derived with the same observation data set.

For methanol, we obtain a column density $N_{CH_3OH} \simeq 9 - 50 \times 10^{14}$ cm^{-2} and a rotational temperature T_{CH_3OH} between 11 K and 23 K. For acetaldehyde, we obtain $N_{CH_3CHO} \simeq 0.6 - 1.3 \times 10^{14}$ cm^{-2} and T_{CH_3CHO} between 9 K and 23 K. Their abundance ratio varies

from 10–20 to ∼44 in the three lobes; more precisely, the SE lobe is the one with the largest CH_3OH/CH_3CHO abundance ratio. In As, we only derive a lower limit to the CH_3OH/CH_3CHO abundance ratio, ≥20. Note that our observations provide different values of the CH_3OH/CH_3CHO abundance ratio compared to those previously derived by Holdship et al. (2019, ∼300) towards the south and north lobes of the IRAS 4A outflows via single-dish observations. We attribute this difference to the fact that the single-dish observations of IRAS 4A by Holdship et al. (2019) include emission from a much larger region (including also some from the central protostars) with respect to that probed by the present SOLIS observations. Moreover Holdship et al. (2019) do not explicitly derive the emitting size, even though they minimize with respect to this parameter: since the maximization is done independently for each species, their column density ratio has a relatively large intrinsic uncertainty. Therefore the interferometric images allow us to minimize the risk of mixing different gas components (indeed typical of shocked regions).

The abundance ratio analysis confirms what we could see from the emission maps (Figure 5.1), namely that the methanol and acetaldehyde emission (and their relative abundance) is quite different in the SE lobe with respect to the SW and Northern lobes. We emphasize that the difference cannot be attributed to excitation effects, having the methanol and acetaldehyde lines with similar upper level energies (E_{up} from 7 K to 28 K), similar Einstein coefficients ($A_{ij} \sim 10^{-5}$ s^{-1}) and comparable derived temperature, within the measurement errors.

To summarize, the southern–west and northern lobes have a relatively low CH_3OH/CH_3CHO abundance ratio (8–20), whereas the southern–east lobe presents a ratio at least twice larger ($\sim$ 44). Since the SW and North lobes belong to the same outflow emanating from 4A2 and the SE lobe traces the outflow emanating from 4A1, it seems reasonable to attribute the observed difference to an intrinsic difference in the two outflows. We will explore this hypothesis in the next section with the help of an astrochemical model.

5.6.2 Dimethyl ether and formamide

Regarding formamide and dimethyl ether, we detected only one line at most of the latter and four lines (blended at the WideX resolution, ∼2 MHz) of the former in any position (see Table 5.3. For this reason, we did not carry out the rotational diagram analysis as we did for the other iCOMs. Furthermore, while formamide is marginally resolved at the As position, dimethyl ether is not resolved in any outflow peaks (see Figure 5.1). In presence of detection, we derived the column densities using the integrated area of the $4_{1,4} - 3_{1,3}$ line for formamide and the blended ones for dimethyl ether, assuming fixed rotational temperatures. As for methanol and acetaldehyde, we used 11, 16 and 19 K for SE, SW and North, respectively and 10–30 for As. In case of non detection, an upper limit on the column density is derived considering the 3σ limit of the spectra and using the above rotational temperatures. The derived values are reported in Table 5.4.

5.7 Astrochemical modelling

We ran our model GRAINOBLE+ in order to reproduce the observations and understand what could be the cause of the observed difference in the CH_3OH/CH_3CHO abundance ratio in the different lobes of the IRAS 4A outflows.

There is solid (observational, theoretical and from laboratory experiments) evidence that methanol is synthesized on the grain surfaces via the hydrogenation of iced CO by successive addition of H atoms (Boogert et al., 2015a; Tielens and Hagen, 1982b; Watanabe and Kouchi,

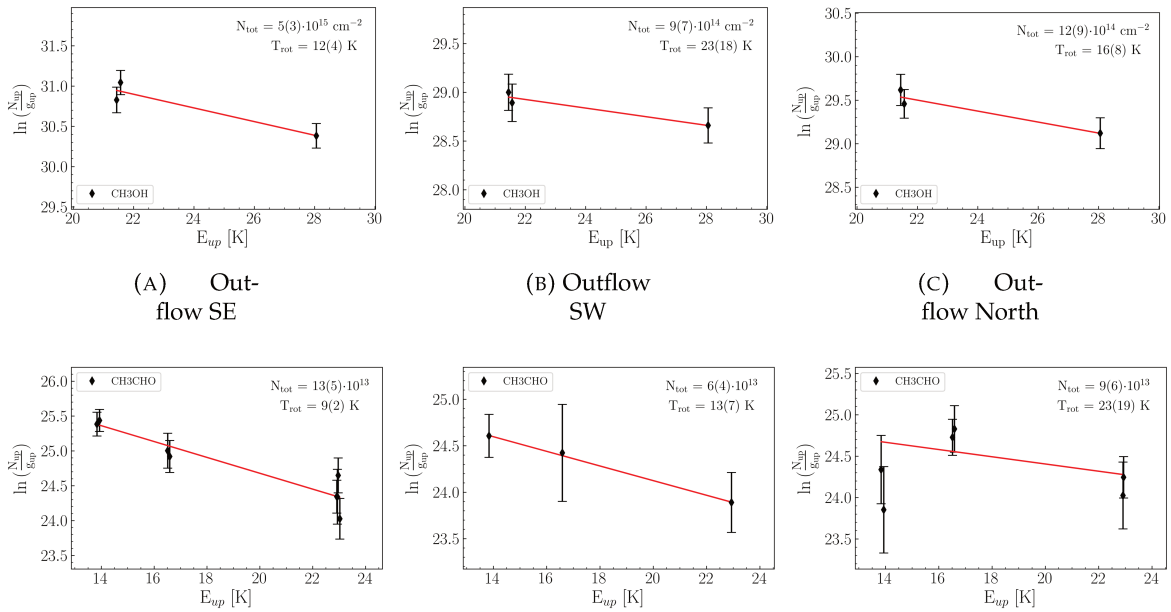

(A) Outflow SE (B) Outflow SW (C) Outflow North

FIGURE 5.4: *Upper panels:* Rotational Diagrams of methanol (CH_3OH) in outflow SE, SW and North from left to right; *Lower panels:* Rotational Diagrams of acetaldehyde (CH_3CHO) in outflow SE, SW and North. The parameters N_{up}, g_{up}, and E_{up} are the column density, the degeneracy, and the energy of the upper level. The error bars on $\ln(N_{up}/g_{up})$ are computed by taking the calibration error on the integrated flux (15%) into account. The red lines represent the best fits.

TABLE 5.4: Results of the LTE analysis with the Rotational diagrams, for each outflow peaks, using the observation with the NOEMA WideX backend. In the last row are shown the values of the abundance ratio between methanol and acetaldehyde for each outflow peak.

Molecule			Outflow SE	Outflow SW	Outflow North	Region As[a]	L1157-B1[b]
CH_3OH	N_{tot}	[10^{14} cm^{-2}]	50(30)	9(7)	12(9)	5-15	130(30)
	T_{rot}	[K]	11(3)	23(18)	18(8)	10-30[c]	10.0(1.1)
CH_3CHO	N_{tot}	[10^{14} cm^{-2}]	1.3(0.5)	0.6(0.4)	0.9(0.6)	$\leq$ (0.25-0.5)	0.7(0.3)
	T_{rot}	[K]	9(2)	13(7)	23(19)	10-30[c]	8(1)
CH_3OCH_3	N_{tot}	[10^{14} cm^{-2}]	$\leq$ 0.5	$\leq$ 0.7	1.6(0.7)	1.0(0.4)	3
	T_{rot}	[K]	11	16	19	10-30[c]	9
NH_2CHO	N_{tot}	[10^{14} cm^{-2}]	$\leq$ 0.02	$\leq$ 0.02	$\leq$ 0.02	0.03(0.02)	–
	T_{rot}	[K]	11	16	19	10-30[c]	–
$\frac{CH_3OH}{CH_3CHO}$ [d]			44(5)	11(3)	17(3)	$\geq$ 20	190(60)

[a] Region where formamide and dimethyl ether emits (Ceccarelli et al., 2017b);
[b] From Codella et al. (2019) based on interferometric observations;
[c] Fixed rotational temperature used to derive a range of possible N_{tot};
[d] Abundance Ratio computed dividing the best fit column densities derived assuming that the two species are tracing the same gas with the same properties (see text).

TABLE 5.5: The injected abundances (with respect to H-nuclei) into the gas phase at the second step of the model. These values are based on previous observations towards L1157-B1 (Codella et al., 2017).

molecules	injected abundances (/H)
CO_2	3×10^{-5}
H_2O	2×10^{-4}
OCS	2×10^{-6}
H_2CO	1×10^{-6}
NH_3	2×10^{-5}

2002b). On the contrary, the acetaldehyde formation route is less clear, and the two paths, formation in the gas phase or on the grain surfaces, are still debated. Specifically, grain surface models predict that CH_3CHO could be formed through the combination of the two radicals CH_3 and HCO (previously formed by photodissociation of methanol and formaldehyde, respectively) on the surface of the grains (Garrod and Herbst, 2006). However, recent quantum chemistry computation by Enrique-Romero et al. (2016a) and Enrique-Romero et al. (2019a) show that alternative channels leading back to the two simple species CH_4 and CO are competitive. Conversely, gas phase models claims that acetaldehyde formation could occur by the oxidation of hydrocarbons (formed previously on the grain mantles as hydrogenation of carbon chains; Charnley, 2004; Charnley et al., 1992). In particular, the injection from grain mantles of ethane (C_2H_6) is expected to drive CH_3CH_2 that will then react in the gas phase with atomic oxygen, giving CH_3CHO (Charnley, 2004). The crucial reaction is, therefore:

$$CH_3CH_2 + O \rightarrow CH_3CHO + H \tag{5.1}$$

Following these two possibilities, we ran a grid of astrochemical models in order to reproduce our observations and to understand the possible cause of the difference in the observed CH_3OH/CH_3CHO values in the two IRAS 4A outflows.

5.7.1 Model description

GRAINOBLE+ is a gas–grain model simulating the chemical evolution of gas and ices. It is the upgraded version of GRAINOBLE, initially developed by Taquet et al. (2012a); in particular it is re-coded and improved in terms of computational efficiency and treatment of processes. The GRAINOBLE+ version[3] allows an easy incorporation of many complicated processes that occur in the gas and on the grain surfaces. The code can carry out an easy implementation of evolution of physical conditions of a cloud with a given time dependent physical profile. Additionally, the new code allows a distribution of size for the grains, multilayer formation of the grain ice mantle, growth and depletion of the ice, and desorption.

In this work, we used a chemical network of 522 species and 7785 reactions based on the KIDA database[4] which has been updated from various recent works (e.g. Balucani et al., 2015b; Loison et al., 2014; Skouteris et al., 2017; Skouteris et al., 2018a).

In order to simulate the passage of a shock in IRAS 4A, we employed the gas–phase mode of GRAINOBLE+. The simulation follows two steps: (1) a cold molecular gas phase at 10 K and $2 \times 10^4 cm^{-3}$ H–nuclei density (n_H); (2) a post–shock gas phase where density and temperature suddenly jump to $2 \times 10^6 cm^{-3}$ and 70 K.

[3] A detailed description of the GRAINOBLE+ model will be reported in a forthcoming dedicated article.
[4] http://kida.obs.u-bordeaux1.fr

In other words, the second phase inherits the evolved chemical composition of the cloud from the cold phase[5]. Additionally, the gas is infused by species that were formerly synthesized in ice mantles due to the grain sputtering caused by the shock passage.

It is possible that, before reaching the temperature of 70 K, the shocked gas passes through a short initial phase with high temperature. However, this phase unlikely affects the results reported in Fig. 5.6 because there are not known gas–phase reactions with activation barrier forming acetaldehyde. This is confirmed by models taking into account the temperature evolution in the shocked gas (e.g. Burkhardt et al., 2019; Nesterenok, 2018).

We do not have precise estimates of the density and temperature in the positions where we derived the CH_3OH/CH_3CHO abundance ratio. However, the values derived at positions close to the ones selected here, via a non-LTE analysis of observed SO_2 lines, (Taquet et al., 2019) are similar to those adopted in our modelling. We assumed that the cosmic ray ionization rate is the same than towards L1157-B1 ($\iota = 3 \times 10^{-16}$ s^{-1}, Podio et al., 2014) and that the abundance of the injected species are also similar to the ones adopted for L1157–B1 (see Table B1 of Codella et al., 2017), listed in Table 5.5.

We ran series of models to compare the observed CH_3OH/CH_3CHO abundance ratio with the predicted one and to understand what the ratio depends on. We start exploring the gas phase formation route of acetaldehyde assuming that its formation is dominated by reaction 5.1 in the passage of shock. Oxygen is much more abundant than the injected ethyl radical in the post–shock phase; therefore, CH_3CH_2 is the bottleneck of the rate of the reaction 5.1.

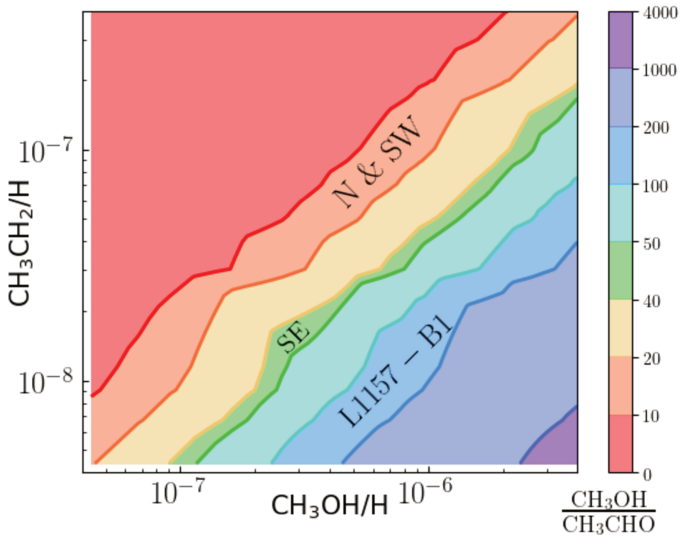

FIGURE 5.5: Contour map of the CH_3OH/CH_3CHO abundance ratio at 1000 year after the start of the shock passage. The x and y axis are the injected abundances of methanol $[4 \times 10^{-8}, 4 \times 10^{-6}]$ and the parent molecule of acetaldehyde, ethyl radical CH_3CH_2 $[4 \times 10^{-9}, 4 \times 10^{-7}]$, respectively. The measured methanol to acetaldehyde abundance ratio of North and SW outflows $(8 - 20)$ fall in the orange band and the SE one $(38 - 50)$ in the green band; L1157-B1 value $(130 - 250)$ is covered by the blue band (Codella et al., 2019).

First, we ran a grid of 169 models with different injected abundances in the beginning of the shocked phase for ethyl radical (CH_3CH_2), and methanol from $[4 \times 10^{-9}, 4 \times 10^{-7}]$ and $[4 \times 10^{-8}, 4 \times 10^{-6}]$ ranges respectively. The methanol abundance range is chosen in order

[5]Note that we do not compute the grain mantle composition as this is treated as a parameter in the following analysis.

to include the observed values in the hot corinos and in the protostellar shocks (the L1157-B1 outflow in particular); the ethyl radical one is chosen in order to match our observed CH_3OH/CH_3CHO abundance ratio. The results are shown in Figure 5.5 and described in the next section.

Second, we studied the influence of the density and cosmic ray ionization rate ζ, on the chemical evolution and how the CH_3OH and CH_3CHO abundances and their relative ratio depend on the time, after the shock passage. Note in fact that protostellar shocks could be local accelerators of cosmic ray protons (Padovani et al., 2016) and therefore, in this work ζ is an unknown parameter. We ran then two additional models. In the first one, we lower down the chosen n_H density value up to 2×10^5 cm^{-3}; in the second one, we lower down the chosen cosmic ray ionization rate value up to $\zeta = 3 \times 10^{-17}$ s^{-1} for the post–shock phase. The injected abundances of methanol is 3×10^{-6} and for ethyl radical it is 3×10^{-7} in both cases. These values are chosen such that the models reproduce the observed CH_3OH/CH_3CHO abundance ratios for the SW and North lobes (8-20) at 1000 yr (orange band of Figure 5.5) and for the SE one as well. The results are shown in Figure 5.6 and described in the next section.

Finally, we ran a model with the assumption that acetaldehyde is synthesized on the ice mantles and injected directly into the gas phase at the passage of the shock.

5.7.2 Model results

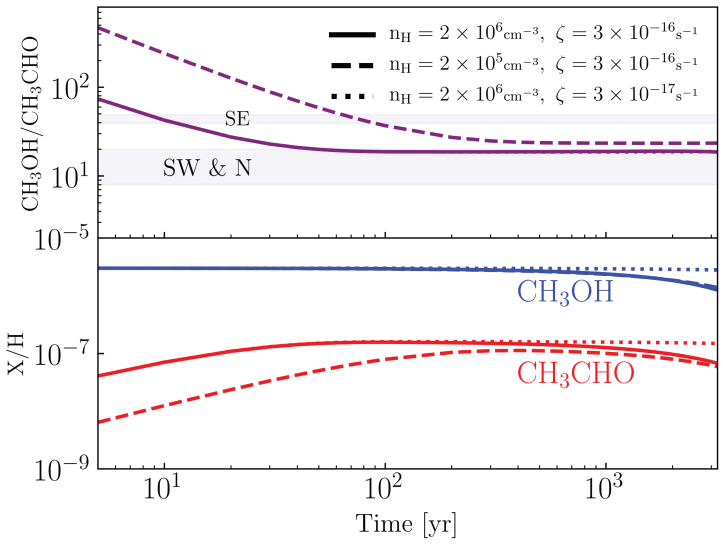

FIGURE 5.6: Time evolution of abundances of methanol in blue and acetaldehyde in red (bottom) and their ratios in purple (top) for the same injected methanol abundance, 3×10^{-6}, and ethyl radical one, 3×10^{-7}. The different line styles correspond to models run with different conditions, as reported in the upper panel legend. Please note that the CH_3OH/CH_3CHO abundance ratio is constant if both species are directly injected from the grain mantles (see text).

Figure 5.5 shows the contour map of the CH_3OH/CH_3CHO abundance ratio at 1000 years after the shock passage, as a function of the injected methanol and ethyl radical, assuming that acetaldehyde is entirely synthesized in the gas phase. Note that the chosen age (1000 yr) is in the order of magnitude of the kinematical age of L1157-B1 (Codella et al., 2017; Podio et al., 2016) and, likely, IRAS 4A outflows.First, the figure shows that there is a linear dependence of the CH_3OH/CH_3CHO abundance ratio both on the injected methanol and

ethyl radical abundance, in the range explored in our simulations. Second, reasonable values of methanol and ethyl radical abundance can reproduce the observed values in the four IRAS 4A outflow positions that we studied (Table 5.2).

In Figure 5.6, we show the evolution of methanol and acetaldehyde abundance as a function of the time after the shock passage, for different densities n_H and cosmic ray ionization rates ζ. Given that methanol is a grain surface product, even by varying n_H or ζ, the injected abundance remains constant in the early stages of the shock up to $\sim 2 \times 10^3$ years. The time evolution of acetaldehyde in the early stages is different from the one of methanol; while the latter remains constant, acetaldehyde abundance increases soon after the shock passage. This is expected, since we assumed that acetaldehyde is a gas phase product and its evolution is dominated by the formation through ethyl radical reaction (5.1). Furthermore, the time evolution of acetaldehyde in the post–shock phase is influenced by variation of n_H or ζ. Lower density slows down the formation rate of acetaldehyde in the early stages; this is due the fact that in lower density gas the ion abundance is higher. Therefore, the contribution of destruction rates is higher in the evolution. Similar to methanol, a lower cosmic ray ionization rate does not affect the early stages.

Finally, we ran a model in which acetaldehyde is synthesized on the icy dust surfaces and injected directly into the gas phase. Therefore, in the model, the species injected into the gas phase right after the shock, is not anymore the ethyl radical but the acetaldehyde, whose abundance is chosen to be equal to the observed one. Therefore, the gas–phase production of acetaldehyde is, in this case, negligible. As for methanol, the abundance of acetaldehyde, now injected from grains, remains constant up to $\sim 2{\times}10^3$ yr when the destruction by ions (H_3O^+ in this specific case) becomes dominant. Therefore, the difference in the abundance of acetaldehyde between the gas– and grain– synthesized is only within the first 200 years of the shocked phase, when acetaldehyde takes time to be formed by the reactions between ethyl radical with atomic oxygen.

5.8 Discussion

5.8.1 The two IRAS 4A outflows

Our new SOLIS observations show that the two outflows emanating from 4A1 and 4A2, previously identified by Choi (2005) and Santangelo et al. (2015) via simple molecules (SiO, CO and SO), are enriched with methanol all across the three (visible) lobes. Conversely, acetaldehyde is spread only over the southern lobes and is concentrated in a compact spot in the northern one. Therefore, a first conclusion of this work is that, in the protostellar post–shock regions there is the release in gas phase of methanol, previously formed on the grain surfaces, and the production of acetaldehyde. The statistic is very poor for the moment, with the two IRAS 4A outflows and the L1157–B1 one in which acetaldehyde is detected with interferometric observations (Codella et al., 2015, 2017, 2019).

Regarding the IRAS 4A outflows, the SE lobe is richer in both methanol and acetaldehyde, namely the outflow emanating from 4A1. We notice that this is an opposite behavior with respect to the SiO emission, which is instead brighter along the 4A2 outflow (Choi, 2005). This anti-correlation with SiO is also seen in other (simple) molecules, such as NH_3, H_2CO and HCN by Choi et al. (2011). As Choi et al. suggested, it could be due to a different strength of the shock (the sputtering of Si could require different shock velocities with respect to the other molecules) or because the SiO traces different physical conditions with respect to the other molecules. For example, SiO could trace the jet while the other molecules could be originated in the gas entrained by the jet (e.g. Bachiller et al., 1998; Ospina-Zamudio et al., 2018; Ospina-Zamudio et al., 2019). Linked with this, the different spatial distribution between SiO and other species, could be due to time-evolution effects, namely different ages of the shocks, as

previously observed in other outflows (e.g. Castets et al., 2001). We will discuss more this point in the next section.

Finally, it is not clear what is the origin of the iCOMs emission in the As position. It does not seem to be clearly associated with any of the two southern lobes but rather with a point where they intersect. That would imply that additional shocks can occur at the interface of the swept-up cavities opened up by the jets. Higher spatial resolution observations are needed to confirm or reject this hypothesis.

5.8.2 The CH_3OH/CH_3CHO abundance in IRAS 4A1 and 4A2 outflows

In Section 5.6, we measured the methanol over acetaldehyde abundance ratio towards the three positions of the two IRAS 4A outflows, in the North, SW and SE lobes, respectively (Table 5.4). While the North and SW lobes have a similar values, between 8 and 20 (considering the error bars), the SE lobe has larger CH_3OH/CH_3CHO, 38–50. In other words, the methanol over acetaldehyde abundance ratio is about twice larger in the outflow emanating from 4A1 with respect to the one from 4A2. In this section, we try to understand the origin of this difference, having in mind that, while methanol is a past grain-surface product, acetaldehyde can either be itself a past grain-surface or a gas-phase product.

One easy possible explanation, then, of the CH_3OH/CH_3CHO difference is that the grain mantle composition is different in the two outflows. However, this seems unlikely, because, on one hand, no gradient in the ratio is seen between the North and SW lobes of the 4A2 outflow; moreover, the SW and SE lobes are very close in space, closer than the two 4A2 outflow positions where we estimated the CH_3OH/CH_3CHO abundance ratio. Therefore, although we cannot totally exclude it, it seems to us that the different grain composition is an improbable explanation.

If acetaldehyde is synthesized by the gas-phase reaction (5.1), there are more possibilities other than a different grain mantle composition. As shown by the modelling of section 5.7, a smaller density or a younger age of the 4A1 outflow with respect to the 4A2 one would explain the observed CH_3OH/CH_3CHO difference. Specifically, if the two outflows are very young and 4A1 is younger than about 200 yr, then this would explain why its ratio is larger than the 4A2 one (see Figure 5.6).

Unfortunately, our observations did not have enough methanol lines to allow a meaningful non-LTE analysis to derive the volume density, so we do not know if the density in the 4A1 outflow is lower than in the 4A2 outflow. With a non-LTE analysis on SO_2, Taquet et al. (2019) suggest that there is no significant difference in density between the outflow driven by 4A1 and the one from 4A2. On the other hand, assuming a typical shock velocity of 100 km/s, we estimate a kinematical age of $\sim$200 yr for the 4A1 outflow which has a very short extent; this seems to support the younger age of 4A1 hypothesis. Furthermore, Santangelo et al. (2015), using high spatial resolution observations of CO, SiO and SO, showed that the 4A1 jet is faster than the 4A2 one; this, combined with the smaller spatial extension again support the hypothesis that 4A1 outflow is younger than the 4A2 one. In favor of a different age of the two outflows there is also the observed chemical differentiation between the two driving sources, 4A1 and 4A2: the former is bright in the continuum but lacks iCOMs line emission, exactly the opposite of 4A2 (e.g. López-Sepulcre et al., 2017). One of the possible explanation for this situation is the smaller hot corino size, which could also imply a younger age of 4A1, and this agrees with the younger age of its outflow too.

In summary,the different CH_3OH/CH_3CHO abundance ratio measured in the 4A1 and 4A2 outflows is unlikely caused by a different grain mantle composition of the two outflows, because the more extended 4A2 outflow shows no significant variation of this ratio over a scale of about 6000 au. On the contrary, the observed CH_3OH/CH_3CHO abundance ratio is consistent with the scenario in which (i) the 4A1 outflow is younger (and, consequently,

faster) than the 4A2 one and (ii) in both outflows acetaldehyde is synthesized in the gas phase. The major reaction is that between atomic oxygen and ethyl radical. The gas-phase synthesis hypothesis also agrees with theoretical quantum chemistry studies (Enrique-Romero et al., 2016a; Enrique-Romero et al., 2019a). Thus, although terrestrial laboratory experiments show that acetaldehyde can be formed on the surfaces of dust grains (e.g Bennett et al., 2005a,b; Öberg et al., 2009b), our results provide evidence that the gas phase formation route cannot be neglected and actually appears to be the dominant one in the IRAS 4A outflows. We emphasize that these conclusions are robust, as they very little depend on the details of the modeling being based on known reactions in the gas-phase.

5.8.3 Comparison with other Solar-type objects

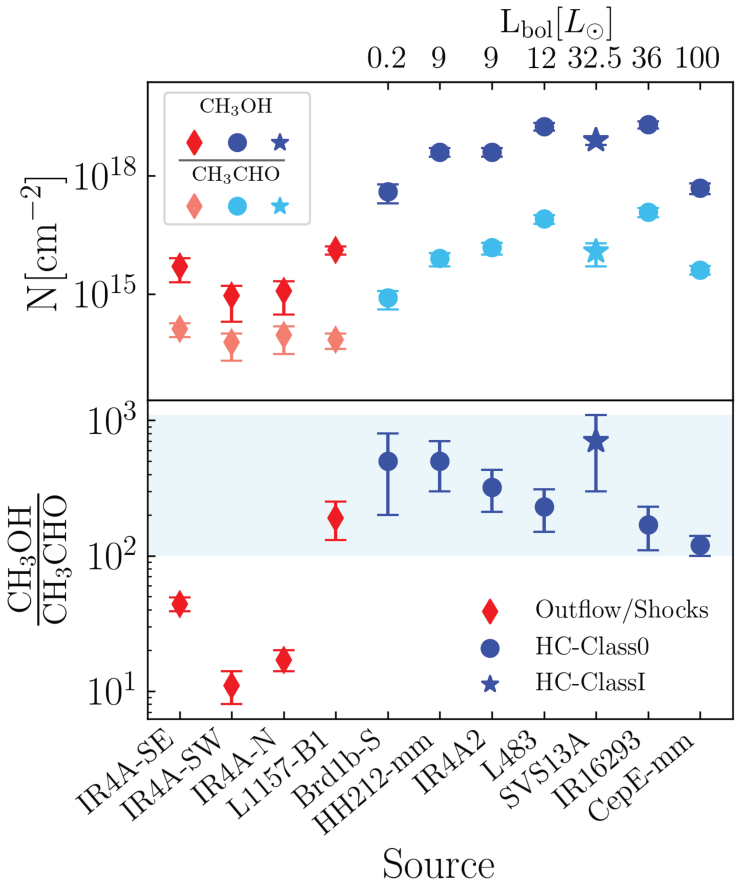

FIGURE 5.7: Abundance ratios between CH_3OH and CH_3CHO (*Bottom panel*), CH_3OH and CH_3CHO column density (*Upper panel*) compared to different sources for which the emitting size has been estimated via interferometric observations: the values in the outflows of IRAS 4A (this paper), in the outflow of L1157-B1 (Codella et al., 2019), the Class I source SVS 13A (Bianchi et al., 2019), and the Class 0 sources, in decreasing order of bolometric luminosity, Barnard1b-S (Marcelino et al., 2018), HH212-mm (Bianchi et al., 2017; Codella et al., 2019), IRAS 4A2 (López-Sepulcre et al., 2017; Taquet et al., 2015), L483 (Jacobsen et al., 2018), IRAS 16293-2422B (Jørgensen et al., 2016), CepE-mm (Ospina-Zamudio et al., 2018). The outflow values are shown with red (pink for CH_3CHO) markers, the hot corinos in blue (cyan for CH_3CHO), using diamonds for the outflows, dots for Class 0 and star for the Class I source. The cyan band represents the area in which the the hot corinos values fall.

Figure 5.7 shows the methanol over acetaldehyde abundance ratio in the IRAS 4A outflows, compared with the values measured in other low/intermediate star forming regions for which the emitting size as been estimated via interferometric observations: the L1157-B1 molecular shock and seven hot corinos.

First, the IRAS 4A outflows have a definitively lower CH_3OH/CH_3CHO with respect to the L1157–B1 value (130-250), reliably measured by Codella et al. (2019). Following the discussion of the previous section, this could be due to a difference in the composition of the grain mantles, to a lower density or to a younger age of the 4A outflows with respect to the L1157-B1 one. At present, the information in our hands is not enough to be able to support or rule out any of these three possibilities; a more accurate analysis of the IRAS 4A outflows is needed. Obviously, having more information of one key actor, the abundance of ethyl radical in these outflows, could shed more light on why the two outflow systems are different.

Finally, the same difference observed between the IRAS 4A and L1157 outflows, if not larger, is observed with respect to the values measured in Class 0 and I hot corinos (Bianchi et al., 2017, 2019; Codella et al., 2019; Jacobsen et al., 2018; Jørgensen et al., 2016; López-Sepulcre et al., 2017; Marcelino et al., 2018; Ospina-Zamudio et al., 2018; Taquet et al., 2015).

In Figure 5.7, we ordered the hot corinos according their (increasing) bolometric luminosity L_{bol}, keeping in mind that the measure of L_{bol} is relatively uncertain. It is possible to notice an interesting trend: in the Class 0 hot corinos,the CH_3OH/CH_3CHO abundance ratio decreases with increasing L_{bol}. Our modeling, (Section 5.7), is not directly applicable to the hot corino case for two main reasons: 1) the hot corinos density ($n_H \sim 10^7 cm^{-3}$) is larger than those used in our model (Figure 5.6, and 2) there is continuous injection of the infalling material towards the center. Having said that, it seems improbable that the behavior shown in Figure5.7 has something to do with a time effect. In the hot corino conditions (higher density and low cosmic ionization rate) the synthesis in the gas phase is fast during the first decades while the destruction by molecular ions is slow in the latest stages($\geq 10^5$ yr), leading to a CH_3OH/CH_3CHO abundance ratio almost constant.

On the contrary, a possible interpretation is that larger luminosity correspond to larger hot corino sizes (namely larger regions with a dust temperature $\geq$100 K; Ceccarelli et al., 2007) and, assuming a central peaked density distribution, regions with lower densities. Since methanol is produced during the prestellar phase by hydrogenation of frozen CO (Taquet et al., 2012b; Vasyunin et al., 2017), a larger density will bring a larger methanol abundance; acetaldehyde, on the other hand, could be either a past grain-surface or a present-day gas-phase product (see Section 5.7). Therefore, the decreasing CH_3OH/CH_3CHO abundance ratio could indicate that, while methanol abundance decreases with density, acetaldehyde or its gas-phase precursors do not. We emphasize that these conclusions have to be taken with caution as the errors on the hot corinos bolometric luminosity are relatively large, but they are worth a deeper study.

5.9 Conclusions

In this work we reported new observations using the IRAM/NOEMA interferometer in the context of the SOLIS large program, and the detection of several iCOMs in the two outflows emanating from IRAS 4A1 and 4A2, respectively: methanol, acetaldehyde, dimethyl ether and formamide. This is the second ever outflow system, after the Solar-type protostellar L1157 outflow, where multiple iCOMs have been detected using interferometers. Our main conclusions are the following:

- As in the case of L1157-B1 (Codella et al., 2017), iCOMs are not homogeneously distributed across the IRAS 4A outflows: methanol is more widespread over the two outflows, while acetaldehyde emission is only bright in the southern lobes, and dimethyl

ether and formamide are concentrated in a spot at the (apparent) interface between the south lobes of the 4A1 and 4A2 outflows. We, therefore, forewarn that derivation of iCOMs abundance ratios from single-dish observations could be hazardous.

- The measured methanol over acetaldehyde abundance ratio is twice larger in the 4A1 outflow with respect to that in the 4A2 one; the comparison between these results with model predictions suggests that: 1) the 4A1 outflow is younger than the 4A2 one and 2) acetaldehyde is synthesized in the gas phase by the reaction of atomic oxygen with ethyl radical. Alternatively, the grain mantle distribution should vary widely on small scale, which seems unlikely since the larger scale 4A2 outflow shows a similar CH_3OH/CH_3CHO in two distant points of the southern and northern lobes.

- Considering the CH_3OH/CH_3CHO abundance ratio, the two IRAS 4A outflows show a sharp difference with respect to the L1157-B1 one. This may indicate that either the grain mantles or the gas volume densities are very different in the two regions. Additional observations are necessary to better constrain the reason of the observed difference.

- The methanol over acetaldehyde abundance ratio in the Solar-type hot corinos is at least ten times larger than in the IRAS 4A outflows, again pointing to different grain mantles composition or densities. Interestingly, we noticed that CH_3OH/CH_3CHO tentatively decreases with increasing bolometric luminosity of the Class 0 hot corino; a possible reason could be the larger sizes of the hot corinos.

Chapter 6

Application II: Interstellar icy mantle formation in molecular clouds

In this chapter, I present my first author paper we are about to submit in collaboration with C. Ceccarelli, J. Enrique-Romero, and A. López-Sepulcre.

6.1 Introduction

How molecular clouds (MC) form from the more diffuse neutral ones, and in particular from the Cold Neutral Media (CNM), and how long MCs live are questions that have been discussed for decades. Observations of molecular lines and theoretical hydrodynamical/magneto-hydrodynamical models show that MCs can form in various ways which end in different masses, densities, and sizes. MC formation scenarios can be categorized into four main classes: (a) coagulation of smaller clouds (e. g., Ballesteros-Paredes et al., 2020; Dobbs et al., 2015, and the references therein); (b) shock-driven collapse from stellar feedback such as supernova explosion (e. g., Joung and Mac Low, 2006); (c) converging flows and formation of filamentary structure (e. g., Bergin et al., 2004; Clark et al., 2012; Franco and Cox, 1986; Hartmann et al., 2001; Hennebelle et al., 2008, and the references therein); and (d) collapsing cloud or global hierarchical collapse (e. g., Klessen and Glover, 2016; Vázquez-Semadeni et al., 2019).

In this work, informed by observation of the icy mantle encapsulating silicate and carbonaceous refractory dust grains, we aim to constrain MC formation processes. The existence of the dust icy mantles has been known for decades, first observed with ground-based telescopes (Gillett and Forrest, 1973; Smith et al., 1989). Information provided by observations with space-based telescopes, such as the Infrared Space Observatory (ISO: Gry et al., 2003; Kessler et al., 2003; Laureijs et al., 2003; Leech et al., 2003; *The ISO Handbook Volume II: CAM - The ISO Camera (v 2.0)* 2003), Spitzer (Werner, 2009, 2012), and AKARI (Onaka and Salama, 2009), has revolutionised and further enriched our knowledge on the major constituents of the dust mantles in different environments. In MCs, the most abundant components of the dust mantles are (amorphous) H_2O, CO_2, CO, and CH_3OH. The abundance of other iced species, if any, is less than about 0.1 percent with respect to water ice abundance (see, e. g., Boogert et al., 2015, for a review).

The James Webb Space Telescope (JWST: Gardner et al., 2006) will present us with the opportunity to (1) observe less abundant species in ices and (2) increase the number of observations towards quiescent MCs, due to its improved sensitivity and spatial resolution with respect to its predecessors. The new observations will improve our understanding of ice mantle formation and composition in MCs under different physical conditions.

Since the first observations of the icy dust mantles, several astrochemical models have been developed to reproduce the observations, starting with the pioneering work by Tielens and Hagen (1982a). At present, while there is still a debate on the formation of "trace" frozen species, there is an ample consensus on the processes leading to the formation of the main icy mantle constituents. Specifically, water is believed to be the results of the hydrogenation of frozen atomic and molecular oxygen on the grain surfaces (e. g., Dulieu et al., 2010; He and Vidali, 2014; Lamberts and Kästner, 2017). After much debate, CO_2 is at present thought to be the result of the oxidation of HCO (e. g., Baulch et al., 2005; Ruffle and Herbst, 2000). Iced CO is due to the freeze-out of gaseous CO, and CH_3OH is the result of sequential hydrogenation of CO on the grain surfaces (e. g., Rimola et al., 2014; Watanabe and Kouchi, 2002).

Three major parameters entering the mantle formation process are the binding and diffusion energy of the reactants and the reaction rate constants of surface reactions. Although there is still much uncertainty, recent progress has also been achieved in these aspects. On the binding energy (BE) of the species, several studies have recently been carried out, particularly theoretical ones, such as Bovolenta et al., 2020; Das et al., 2018; Ferrero et al., 2020; Grassi et al., 2020; Penteado et al., 2017; Wakelam et al., 2017. The diffusion energy (DE) is often assumed to be a fraction of the BE. The diffusion to desorption energy ratio, ϱ, depends highly on the structure and composition of the surface. Recent studies have constrained this ratio to be from 0.3 to 0.5 (e. g., Hama and Watanabe, 2013; He et al., 2018; Karssemeijer

and Cuppen, 2014; Manicò et al., 2001). Calculations of the rate constants for crucial reactions on ice surfaces have been published in the last few years (e.g. Enrique-Romero et al., 2020; Enrique-Romero et al., 2019b; Lamberts and Kästner, 2017; Rimola et al., 2014; Song and Kästner, 2017).

In this work, we take advantage of the progress described above, on both the observations of the icy mantle composition and the comprehension of how the main constituents are formed, to add new constraints to the MC formation process. To this end, we used the astrochemical code GRAINOBLE+, which is the re-implemented and upgraded version of GRAINOBLE (Taquet et al., 2012), to build a set of models and compare their predictions with the observations toward a well studied MC, the Taurus Molecular Cloud 1 (TMC-1). We also upgraded the ab initio calculations of the HCO formation on the grain-surfaces from the hydrogenation of frozen CO carried out by Rimola et al., 2014.

The article is organised as follows. In Sec. 6.2, we review the observations of the major volatile reservoirs of oxygen, carbon and nitrogen with a focus on the TMC-1 observations; Sec. 6.3 focuses on the micro-physical processes and crucial parameters on the surface; Sec. 6.4 describes new quantum chemistry calculations of the hydrogenation of CO; in Sec. 6.5, we describe the astrochemical model, Gainoble+ and the adoped parameters; in Sec. 6.6 we report the results of our simulations and we discuss them in Sec. 6.7. Finally, Sec. 6.8 summarises the main results of this work.

6.2 Oxygen and carbon budget in TMC

As mentioned in the Introduction, the goal of the present work is to compare astrochemical model simulations with observations of the major volatile reservoirs in cold molecular clouds, namely the gas-phase and solid-phase major components, with a specific focus on the O- and C- bearing species. In this section, we review the observations used for the comparison.

We will use the observations towards the region of the Taurus Molecular Cloud (TMC) called TMC1, a very well studied dark cloud (e.g. Fuente et al., 2019). Specifically, we will focus on the region shown in Fig. 6.1, where the visual extinction is about 20–25 mag, and described below in § 6.2.1. Table 6.1 summarises the observed abundance of the major oxygen and carbon reservoirs towards TMC1, in the solid- (§ 6.2.2) and gas- (§ 6.2.3) phases, respectively (see the complete table is in the appendix, Tab. 6.9).

6.2.1 Overview of TMC1

TMC1 has been the target of several observational studies. Already the first spectral surveys in the radio to millimeter wavelengths towards TMC1 showed that it is a relatively chemically rich and differentiated region. For example, it possess a region particularly enriched with cyanopolyynes and carbon rich molecules, called TMC1-CP, as well as region enriched with N-bearing molecules, called TMC1-NH_3. More recently, TMC1 has been the focus of an in-depth spectral survey, GEMS (Fuente et al., 2019), whose goal is to measure the elemental abundances in this dark cloud. Finally, the latest sensitive spectral surveys in the radio domain ($\sim$40 GHz), QUIJOTE (e.g. Agúndez et al., 2022; Cernicharo et al., 2021, 2022) and GOTHAM (e.g. Lee et al., 2021; McGuire et al., 2020; Siebert et al., 2022), have discovered severral very large molecules, detected for the first time in the ISM. Therefore, TMC1 actually hosts an unexpected very rich chemistry, despite it is a cold and dense cloud.

Models of the chemical composition of TMC1 tend to suggest that it is a relatively young MC, with the age of TMC1-CP estimated to be around 10^5 yrs (Agúndez and Wakelam, 2013; Howe et al., 1996; Ruaud et al., 2016).

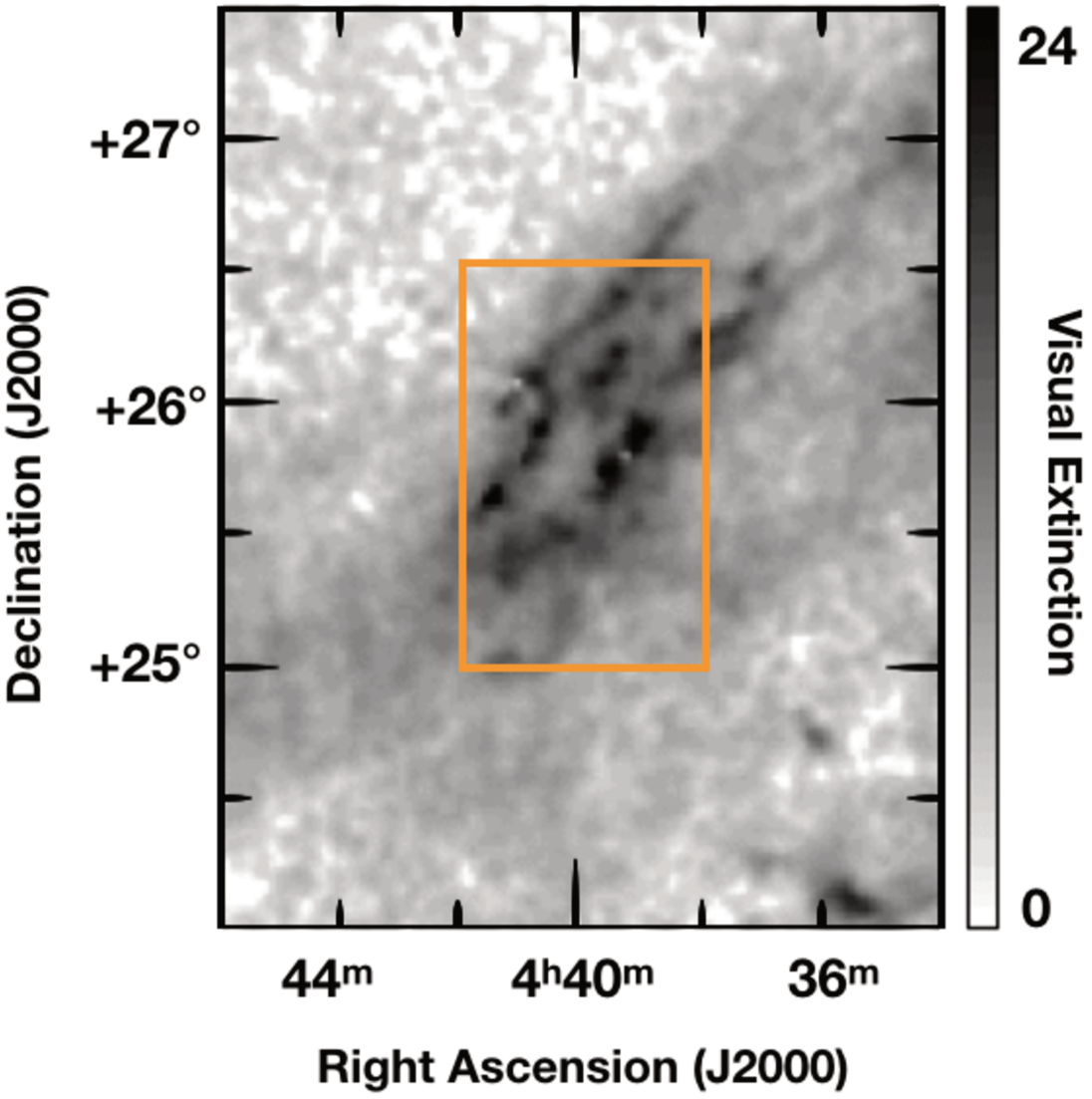

FIGURE 6.1: Visual extinction map of TMC1 (adapted from Pineda et al., 2010). The TMC1 region which is used in the present work for comparing the model predictions of the major C and O bearing species is marked by the orange box.

Since TMC1, like any other MC, is far to be a homogeneous cloud, in order to have a reliable observational dataset to compare with, we considered four lines of sight, relatively close to each other (Fig. 6.1), towards TMC1-CP, TMC1-NH_3, Tamura-8 and Elias 3-16. As already mentioned above, the first two are clumps well studied in the gas-phase content. The latter two lines of sight have IR sources behind the cloud, and, therefore, provide information on the solid-phase content.

Finally, the recent study by Fuente et al. (2019) shows that, in the regions of TMC1 with a visual extinction around 20 mag, the H_2 density varies between 1 and 8 $\times 10^4$ cm^{-3} while the temperature varies between 8 and 14 K.

6.2.2 Solid-phase O- and C- major reservoirs in TMC1

Based on several observational and theoretical works, it is expected that the major reservoirs of oxygen and carbon in the solid phase are water, CO, CO_2, methanol, methane and possibly O_2.

Overview of the observations in TMC The most abundant solid-phase O- and C- bearing species observed towards TMC are H_2O, CO, CO_2, and CH_3OH (Boogert et al., 2015). Boogert et al., 2015 also report a compilation of the column densities of solid H_2O, CO, CO_2, and CH_3OH as a function of A_v towards TMC. In general, they all increase monotonically with A_v, each species appearing from a specific A_v threshold. The threshold of solid H_2O and CO_2 is $A_v \sim 1.6$ mag, while solid CO appears at ~ 3 mag. The solid CH_3OH threshold is the largest one, with $A_v = 9 \pm 3$ mag, probably reflecting the late CO freeze-out (Boogert et al., 2015). The N_X versus A_v plot, shown in their Fig. 7, also shows a relatively large scatter around the best-fit lines. Note that the larger the A_v the lower is the number of observations, so that at $A_v \sim 20$ mag, just a couple of observations are available for H_2, CO and CO_2, respectively, and only upper limits for CH_3OH. At $A_v \sim 20$ mag, using N(H_2O)=2 $\times$ 10^{18} cm^{-2} (which corresponds to solid $H_2O/H_2 \sim 1.1 \times 10^{-4}$), the Boogert et al. fit gives $CO/H_2O \sim$ 0.3, $CO_2/H_2O \sim$ 0.2 and $CH_3OH/H_2O \leq$ 0.05.

Solid methane is also a possible major reservoir of carbon. However, Boogert et al. report only an upper limit of 3% with respect to solid water. Finally, solid O_2 unfortunately lacks sensitive IR signatures so that only upper limits toward two YSOs have been so far reported, suggesting that it is not more than 75% of the CO_2 (Vandenbussche et al., 1999).

Observations towards Tamura-8 and Elias 3-16 Old and recent observations of the solid H_2O, CO and CO_2 towards Tamura-8 and Elias 3-16 have been reported by Whittet et al. (2007). These authors quote N(H_2O)$\sim$ 2.5 $\times$ 10^{18} cm^{-2}, and CO/H_2O and CO_2/H_2O both $\sim$ 0.25 towards both lines of sight. On the contrary, only upper limits to the CH_3OH column densities have been reported (Chiar et al., 1996).

6.2.3 Gas-phase O and C major reservoirs

The most abundant gaseous O- and C- species are expected to be CO, atomic oxygen and, at a less extent, O_2 and possibly CO_2. Although gaseous methanol is not a major O- and C- reservoir, we also consider its abundance in our comparison with the model predictions because it allows to provide some interesting constraints.

Observations of CO As known, the measure of the gaseous CO abundance in MCs is not completely straightforward and, in fact, there is a mismatch between the values derived from millimeter emission and IR absorption CO observations. This also applies to the TMC1 case.

Millimeter observations from the GEMS project provide a CO abundance (with respect to H_2) at $A_v \sim 20$ mag of $\sim 1 \times 10^{-4}$ (Fuente et al., 2019). Note, however, that new estimates by Spezzano et al. (2022) indicate a slightly lower value, $\sim 8 \times 10^{-5}$.

At odds with these estimates, IR simultaneous observations of gaseous H_2 and CO towards Tamura-8 and Elias 3-16 rather indicate a value CO/H_2=1.4–1.8$\times 10^{-4}$ (Lacy et al., 2017).

Observations of other O- and C- bearing molecules For the other abundances of the expected major gaseous O- and C- bearing species the situation is more complicated because many of them are not observable with ground-based telescopes. For example, there are no specific studies on the abundance of atomic oxygen and water towards TMC1. Therefore, we assumed the average H_2O/H_2 measured in cold molecular clouds, $\leq 10^{-8}$ (Hollenbach et al., 2009; Snell et al., 2000; van Dishoeck et al., 2021).

There are a few observations of atomic O towards cold MCs in the literature with puzzling results (e. g., Caux et al., 1999b; Goldsmith et al., 2021; Lis et al., 2001; Vastel et al., 2000, 2002). These works have found that there is a substantial fraction of gaseous atomic oxygen in clouds with column densities possibly comparable to or even larger than CO column density, which is in contrast with astrochemical model predictions. However, much of the atomic oxygen could be associated with gas exposed to UV and not directly the inner part of the dense cloud (see, e. g., Goldsmith et al., 2021). Therefore, we assumed that atomic O is not a significant oxygen reservoir in TMC1.

Regarding O_2, a possible major gaseous O-bearing species, again, no specific observations towards TMC1 have been published. However, numerous studies show that O_2 abundance in cold clouds is not a prominent actor (e. g., Goldsmith et al., 2000; Wirström et al., 2016).

Finally, neither CO_2 nor CH_4 are observable in cold gas because of the absence of a permanent dipole moment in both molecules, but they are not expected to be major gaseous species.

Methanol Gaseous methanol is a trace gaseous species in TMC1. Its average abundance at $A_v \sim$20 mag is $\sim 8.6 \times 10^{-10}$ relative to H_2 (Spezzano et al., 2022).

6.3 Processes on the grain surfaces and crucial parameters

Some of the crucial micro-physics processes entering in the grain-surface chemistry and parameters that regulate them are relatively well known, whereas others are still uncertain and debated. In the following, we describe and discuss the latter, emphasizing what has been adopted in the present work. For the other processes and parameters, we refer the reader to the GRAINOBLE description in Taquet et al. (2012), Taquet et al. (2014), and Taquet et al. (2016) and Ceccarelli et al. (2018).

6.3.1 Binding and diffusion energies

The binding energy (BE) and diffusion energy (DE) of species on the grain surfaces are crucial parameters in any astrochemical model. They regulate the freezing of the species and their diffusion rate over the grain surfaces, respectively. In the following, we summarise the literature on the value of these two parameters for the atomic H and the other species separately.

TABLE 6.1: Observed abundances in gaseous and solid O and C major reservoirs in TMC1.

Species	Abundances
CO	8.8(-05)$^{(a)}$
s-CO	3.0(-05)$^{(b)}$
s-CO_2	2.2(-05)$^{(b)}$
s-H_2O	1.1(-04)$^{(b)}$
s-CH_3OH	4.0(-06)$^{(b)}$
s-CH_4	$\leq$3.3(-06)$^{(c)}$
H_2O	$\leq 1.0(-08)^{(d)}$

All abundance are with respect to H_2 molecules at visual extinction of 20 magnitudes assuming N(H_2)=$A_v \times 10^{21}$ (Fuente et al., 2019). The number format is $a(b) = a \times 10^b$ and the solid species are denoted with "s-" prefix.
$^{(a)}$ An average over the three cores TMC 1-C, TMC 1-CP, and TMC 1-NH3 at $A_v \sim$ 20 mags from Fuente et al. (2019, Figure 8) and Spezzano et al. (2022, Table B.1) (average range in the three cores: 5.245(-5) - 1.135(-4)), where the abundances are calculated with $\sim$ 10 % uncertainty on N(H_2);
$^{(b)}$ From Boogert et al. (2015, Figure 7) fitted curve for Taurus at 20 mags visual extinction;
$^{(c)}$ The upper limit for s-CH_4 is 3% of the s-H_2O abundance at 20 magnitudes (Boogert et al., 2015, Table 2, BG stars column) assuming N(H_2)=$A_v \times 10^{21}$;
$^{(d)}$ An average abundance (Hollenbach et al., 2009; Snell et al., 2000; van Dishoeck et al., 2021).

Binding energy of atomic hydrogen

The BE of atomic hydrogen is particularly important because, with the DE, it is at the basis of the hydrogenation of the species frozen on the grain surfaces, such as O and CO, which form water and methanol, respectively. For this reason, many experimental and theoretical groups have carried out studies to evaluate these two parameters. Successively, Buch and Zhang, 1991 carried out classical molecular dynamic (MD) simulations and estimated the BE on amorphous solid water (ASW) to be in the range of 650±195 K. Similarly, Al-Halabi and van Dishoeck, 2007 MD simulations estimated the BE to be 650±10 K on ASW and 400±5 K on crystalline ice. In a more recent work, Senevirathne et al., 2017 carried out quantum mechanical (QM) ab initio calculations of the H BE over both a crystalline and an amorphous ice surface. In both cases, they found that the BE is not a single value but rather a distribution of values. Specifically, in the crystalline ice, the H BE has a bimodal distribution with the two peaks around 230 and 280 K, respectively. In the ASW, BE covers a larger range, between 255 and 730 K. More recently, Duflot et al. (2021) carried out a study of the H BE over ASW and found a distribution whose average is 116 K. Finally, in the present work, we report new ab initio computations, described in § 6.4, which provide a value of 350 K, in the range of the values by Senevirathne et al. (2017).

In this work, we adopt our computed value, 350 K, and explore the effect of changing it to the higher values used in other astrochemical models, 450 K (Garrod, 2013) and 580 K (Wakelam et al., 2017).

Diffusion energy of atomic hydrogen

The diffusion energy of atomic hydrogen is not well constrained as it is difficult to measure. As for the BE, the measured and computed DE depends on the surface structure, either crystalline or amorphous, and it results into a distribution of values. Generally, the experimental works measure the DE of atomic hydrogen via their combination into H_2 following the diffusion of H on the surface. For example, Manicò et al., 2001 estimated the H DE via Temperature Programmed Desorption (TPD) experiments in which they co-deposited atomic H and D and measured their diffusion rate through their H_2 and HD formation rate, which depends on their DE. They estimated a H DE between 475 and 640 K. Later, Hama et al., 2012 conducted direct detection experiments of atomic H on ASW using Photo-Stimulated Desorption (PSD) and Resonance-Enhanced Multi-Photon Oonization (REMPI) techniques. They found that the H binding sites can be classified into shallow, middle, and deep sites (see also Senevirathne et al., 2017) and estimated the corresponding DE to be 209 $\pm$ 23, 255 $\pm$ 12, and $\geqslant$ 350 K, respectively. Finally, Senevirathne et al., 2017 estimated the diffusion to binding energy ratio for atomic H to be about 0.37, corresponding to a range of 90–260 K based on their BE distribution, described above.

The value and formalism used in the present work is described when discussing the diffusion process, at § 6.3.2.

Binding energy of heavy atoms and molecules

Here we discuss the BE values of the three most abundant heavy elements, oxygen, carbon and nitrogen, as well as CO and the various species entering in the astrochemical modeling.
Atomic oxygen: He et al. (2015) experimental measures on porous ASW estimated an atomic oxygen BE of 1660±60 K, while Minissale et al. (2016a) suggested BE is 1320 K on compact ASW. In agreement with the experimental values, the theoretical QM computations by Shimonishi et al. (2018) provided 1440±160 K.

In the present work, we adopt the value 1320 K, which is consistent with the most recent estimates.

Atomic carbon: Quantum chemical computations from various authors have shown that carbon is actually chemisorbed on water ice surfaces, namely it forms a chemical bond with the atomic oxygen of the water molecule resulting in a very high BE, of about 14100 K (Duflot et al., 2021; Shimonishi et al., 2018). While studies, such as Molpeceres et al., 2021 and Perrero et al., 2022, suggest that atomic carbon can react with water to form formaldehyde and ethanol, some experimental studies, such as Ortman et al. (1990) and Schreiner and Reisenauer (2006), found non-reaction occurring by the adsorption of C on water ice.

In the present work, we assume that the atomic carbon BE is 14100 K, as estimated by Shimonishi et al., 2018.

Atomic nitrogen: Minissale et al. (2016a) measured the BE on compact ASW and estimated a value of about 720 K. On the other hand, Shimonishi et al. (2018) QM calculations provided an estimate of about 400 K, which the authors themselves suspect being an underestimation of the real value caused by the insufficient descriptions of the used van der Waals interaction.

Therefore, in the present work we use the suggested value by Minissale et al. (2016a), namely 720 K.

CO: The BE of CO has been studied for a long time. Here we summarise the most recent works. From the experimental point of view, He et al., 2016 obtained values on ASW both compact and porous. They found a range of BE values from 870 to 1600 K in the former, and from 980 to 1940 K in the latter. On the theoretical side, ab initio calculations of the CO BE interacting with one and six water molecules gave a value of 1290 and 1300 K, respectively (Das et al., 2018; Wakelam et al., 2017). More recent calculations on a cluster of 60 water molecules provided a range of 1110–1879 K for the BE (Ferrero et al., 2020), computed over five different adsorbing sites. From those computations as well as the He et al., 2016 measurements, therefore, it is difficult to extract a distribution of the CO BEs.

In the present work, we use the value from the ab initio calculations presented in § 6.4, namely 1792 K, and we will discuss the case with the lowest value too, namely 1100 K, which is closer to the median of the He et al., 2016 values.

Other species: The BE of the other species not listed above and that are relevant in the astrochemical context on different substrates have been measured or computed in several different works. Briefly, five recent works have provided either new estimates or compilations of BEs. Wakelam et al., 2017 provided estimates based on ab initio calculations that considered one water molecule, Das et al. (2018) used up to six water molecules, and Ferrero et al., 2020 used a cluster of 60 water molecules. From the experimental point of view, the most recent work is from He et al., 2016 and a compilation of the measured BEs is reported in Penteado et al. (2017).

In the Appendix Table 6.14, we list the BEs adopted in the present work with the relevant references.

Diffusion energy of heavy atoms and molecules

As mentioned before, DE is poorly constrained as it is inherently difficult to measure (see, Cuppen et al., 2017; Hama and Watanabe, 2013, reviews). Although difficult, many groups have attempted to measure its value for astrochemically relevant species. The DE of a species is commonly expressed as a fraction of its BE. Accordingly, in models, the DE to BE ratio, ϝ, is often adopted as an input parameter. The range of adopted ratios in the literature is between 0.3 - 0.85 (see, e. g., Cooke et al., 2018; Cuppen et al., 2009; Hama et al., 2012; Karssemeijer and Cuppen, 2014; Katz et al., 1999; Lauck et al., 2015; Livingston et al., 2002; Maté et al., 2020; Mispelaer et al., 2013; Perets et al., 2005; Ruffle and Herbst, 2000; Tielens and Hagen, 1982a; Watanabe et al., 2010). The most recent studies agree more on a ratio within 0.3 - 0.5. For example, the experimental work by He et al., 2018 on light species on ASW finds a range between 0.3 - 0.6. Minissale et al., 2016a experiments on atomic oxygen and nitrogen suggest

a ƒ ratio of about 0.55. On the other hand, the theoretical work by Karssemeijer and Cuppen, 2014 on CO and CO_2 suggest a smaller range of 0.3 - 0.4.

Given the uncertainty in the ƒ value, in the present work, we adopt 0.3 as a bona fide value, and we explore the variation of the model predictions taking 0.4 and 0.5 too.

6.3.2 Diffusion: via thermal hopping and quantum tunneling

Diffusion over the grain surfaces can occur either because of the thermal hopping over the potential barriers of the species from one site to the next one or via quantum tunneling trough them. The latter process is only possible for the light species, mainly the atomic and molecular hydrogen. We, therefore, treat this case a part with respect to the other species.

Hydrogen atoms and molecules

How atomic hydrogen and, to a lesser extent, molecular hydrogen diffuse is particularly critical, as this strongly affects the hydrogenation rate of frozen species, namely the formation of water, formaldehyde, methanol and ammonia.

The first models that introduced the ice formation on the grain surfaces argued that the diffusion of atomic hydrogen through thermal hopping dominates over its diffusion via quantum tunneling (Tielens and Hagen, 1982a). In 1999, Katz et al., 1999 carried out a series of experiments and concluded that indeed the rate of diffusion of atomic H via quantum tunneling is negligible in comparison to the rate of thermal hopping. Later, Hama et al., 2012 confirmed that thermal hopping likely dominates the H-diffusion in ASW. However, Kuwahata et al., 2015a carried out experiments of H diffusion on polycrystalline ice surfaces at 10 K and found that quantum tunneling dominates over thermal hopping. Finally, and somewhat in contrast with the above experiments, the recent ab initio QM study by Senevirathne et al., 2017 concluded that the diffusion rate of atomic H via quantum tunneling on both crystalline and ASW surfaces dominate over the rate of thermal hopping by orders of magnitude at 10 K, whereas the situation is inverted above ∼16 K.

Considering that both processes may be at work, even though in different situations, we considered thermal hopping and quantum tunneling for the atomic H diffusion in the present work. To this end and to quantify the impact of the different treatment of the two processes, we used two methods:

1) Senevirathne et al. (2017) results: We use the diffusion rate computed by Senevirathne et al. (2017, see their Fig. 7c), shown in our Fig. 6.2. Note that the Senevirathne et al. (2017) curves take into account thermal hopping and quantum tunneling in a self-consistent way, computed by considering the many sites of their ASW model. We derived the parameters of the equation, commonly used in astrochemical models, of the constant rate κ as a function of the temperature T:

$$\kappa(T) = \alpha \left(\frac{T}{300K}\right)^{\beta} \exp(-\gamma/T). \tag{6.1}$$

We derived the parameters α and β by fitting the curve in two temperature intervals and imposing γ equal to zero. The resulting α and β are reported in the Appendix Tab. 6.13.

2) Thermal hopping on the diffusion energy (DE) barrier: We also computed the rate of thermal hopping considering the DE is a fraction of the species BE (see § 6.3.2).

In the present work, we consider the atomic H BE computed in Sec. 6.4 and a diffusion over binding energy ratio ƒ of 0.3, but we also explored values of 0.4 and 0.5.

Figure 6.2 shows the H diffusion rates obtained with the two methods as a function of the temperature. For comparison, we also plot the H diffusion rate with the H binding energy of 450 K, used by Garrod, 2013 and other groups. The figure shows that the choice of the method, binding energy and ƒ can lead to differences in the diffusion rate by several orders of magnitude.

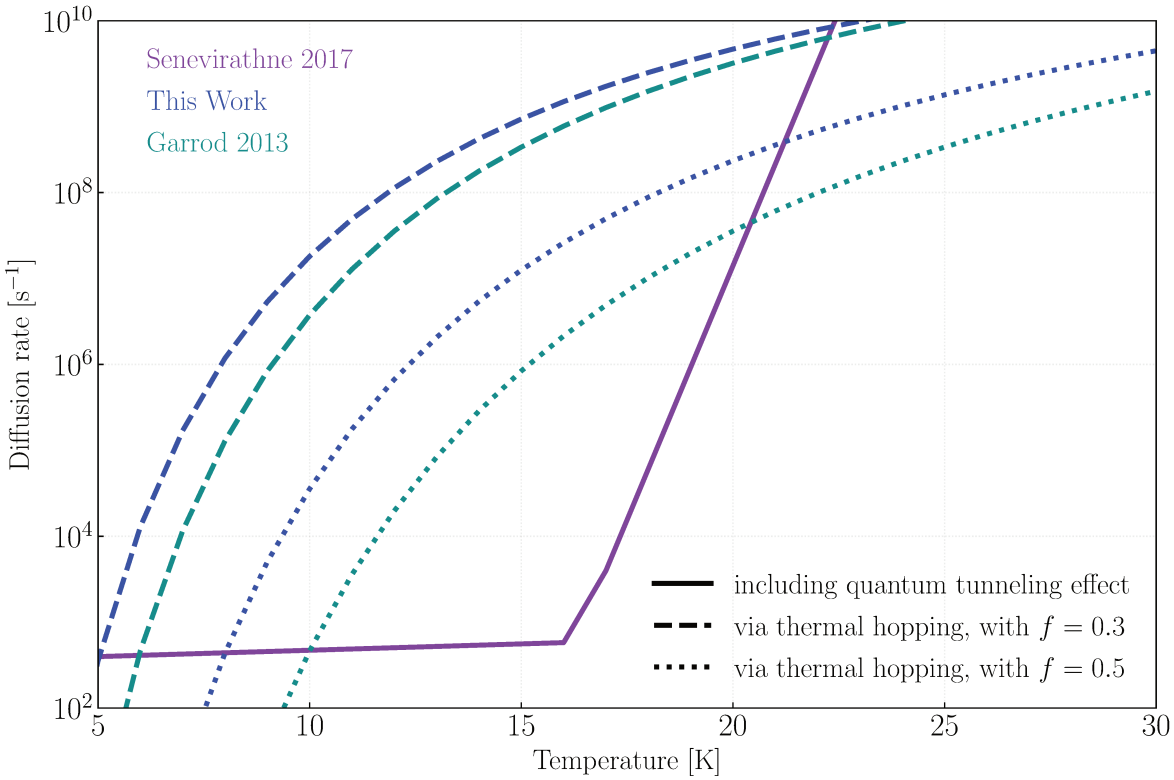

FIGURE 6.2: The diffusion rate of atomic hydrogen as a function of temperature. The purple line shows the rate of H diffusion computed by Senevirathne et al. (2017, Figure 7c). The dashed and dotted blue lines are the H diffusion rate via thermal hopping using the H BE computed in this work, namely 350 K (§6.4), with ƒ = 0.3 and 0.5 ratios, respectively. The dashed and dotted green lines show the H diffusion rates via thermal hopping assuming H BE quoted by Garrod (2013, see their Table 3), equal to 450 K, and ƒ = 0.3 and 0.5 ratios, respectively.

Molecules and heavy atoms

Molecules can not tunnel and, if they diffuse on the grain surfaces, they do it via thermal hopping. As already discussed in § 6.3.1, this happens considering diffusion energies a fraction of the species BE.

In this work, we assume ƒ = 0.3.

Atomic oxygen: Congiu et al., 2014 investigates the diffusion rate of oxygen in the 6.5 - 25 K temperature range on porous and non-porous ices. Their results show that the oxygen diffusion rate via quantum tunneling is non-negligible and derive an empirical formula to fit the measured rate.

In the present work, we adopt their recipe, reported in Appendix Tab. 6.13.

Atomic carbon: As said in the previous section, carbon atoms form a chemical bond with the water molecules of the ice, so that C does not diffuse on the grain surfaces.

Atomic nitrogen: Zaverkin et al. (2021) computed the diffusion rate of nitrogen using machine-learning and kinetic Monte Carlo simulations. They concluded that diffusion of nitrogen is practically impossible on ASW at 10 K, and the effect of quantum tunneling is negligible.

6.3.3 Reaction activation barriers

Reactions on the grain surfaces require an activation barrier in several cases, even when two radicals are involved (e.g., Enrique-Romero et al., 2016b; Enrique-Romero et al., 2020; Enrique-Romero et al., 2019b; Enrique-Romero et al., 2021, 2022). Since the barriers are often too high to be surmounted at the temperatures of the molecular clouds, the reactions can occur through quantum tunneling only. To compute the reaction rate via quantum tunneling, astrochemical models often approximate a rectangular energy barrier with a width between 1 and 2 Å (e. g., Garrod and Pauly, 2011; Hasegawa et al., 1992; Tielens and Hagen, 1982a). In GRAINOBLE, Taquet et al., 2013 used a more accurate description of the barrier, following the Eckart formalism Eckart, 1930 (see also Joohnston and Heicklen, 1962; Senevirathne et al., 2017). In the following, we review the hydrogenation of CO and the formation of methane on the grain surfaces. The formation of water and CO_2 are described in Taquet et al., 2013.

CO hydrogenation network

The CO hydrogenation on the grain ice mantle surfaces leading to formaldehyde and methanol is an essential surface process. It governs the distribution of the carbon budget frozen and stored in ices. For example, given the vastly different BEs of methanol and CO, depending on the CO hydrogenation efficiency, much of the carbon may be trapped in the mantles as methanol in lukewarm ($\sim$ 30 K) regions rather than in the gas. Thus, here we discuss this process in detail.

The successive addition of atomic hydrogen to frozen CO leads to formaldehyde and methanol as follows:

$$\mathrm{CO} \xrightarrow{+\mathrm{H}} \mathrm{HCO} \underset{+\mathrm{H}}{\overset{+\mathrm{H}}{\rightleftarrows}} \mathrm{H_2CO} \xrightarrow{+\mathrm{H}} \mathrm{CH_3O} \xrightarrow{+\mathrm{H}} \mathrm{CH_3OH} \tag{6.2}$$

While Steps 2 (HCO + H) and 4 (CH_3O + H) are barrierless, Steps 1 (CO + H) and 3 (H_2CO + H) involve activation energy barriers, which have been theoretically characterised (e. g., Rimola et al., 2014; Song and Kästner, 2017).

CO + H : Rimola et al., 2014 computed the barrier for this reaction (and the other hydrogenation steps) using a model of 32 water molecules for the ASW model. In this work, we have improved the calculations of the CO + H reaction to obtain the rate constant to be used in the present work. The calculations and the rate constants as a function of the temperature are described in Sec. 6.4.

H_2CO + H : Song and Kästner, 2017 have characterized the kinetic parameters of the formaldehyde hydrogenation reaction. These authors found that the H-abstraction leading to HCO and H_2 is less efficient than the methoxy formation (with 0.2 and 0.8 branching ratio fractions, respectively), while the formation of CH_2OH is negligible. They provide formulae for the rate constants κ as a function of the temperature T, following the equation:

$$\kappa(T) = \alpha \left(\frac{T}{300\mathrm{K}}\right)^{\beta} \exp\left(-\frac{\gamma(T+T_0)}{T^2+T_0^2}\right) . \tag{6.3}$$

In the present work, we adopted their results specifically their α, β, γ and T_0, reported in our Appendix Tab. 6.12.

Fig. 6.3 shows the rate constants of the Steps 1 and 3 reactions as a function of the temperature. In the figure, we also show the rate constants obtained with the treatment used by Garrod, 2013 (see their Table 3) and several other groups (e. g., Aikawa et al., 2020), namely considering the tunneling trough a rectangular barrier of height 2320 K for H + CO → HCO and H + H_2CO → CH_3O, and 2960 K for H + H_2CO → HCO + H_2[1]. The width of the barriers are assumed to be 1.35 Å except for the H + H_2CO → HCO + H_2 reaction which has a barrier width of 1.22 Å. It can be seen that the two treatments, ours and the one by Garrod, 2013, lead to rate constants different by more than two orders of magnitude.

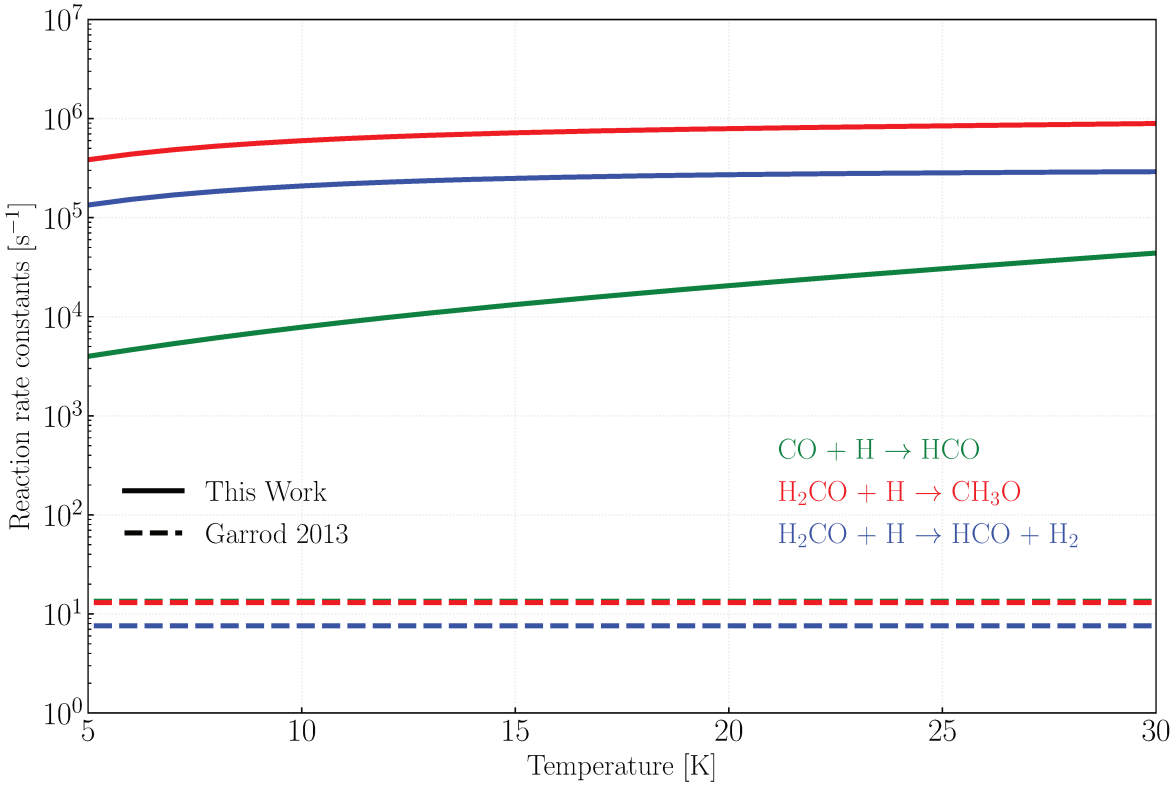

FIGURE 6.3: The reaction rate constants of CO (green) and formaldehyde (red and blue) hydrogenation as a function of temperature. The products of H + H_2CO are CH_3O (red) and H_2 + HCO (blue) with 0.8 and 0.2 branching ratios, respectively. The solid lines are the calculated rates in this work (Sec. 6.4) and the dashed lines are the reaction rates calculated with the activation energies and barrier widths provided in Garrod, 2013 (see text).

C hydrogenation and methane formation network

Until recently, it has been assumed that methane is formed through successive hydrogenation of carbon atoms, as suggested in the experiment by Qasim et al., 2020. However, since all theoretical calculations indicate that carbon forms a chemical bond with the water molecules of the ice (Duflot et al., 2021; Molpeceres et al., 2021; Perrero et al., 2022; Shimonishi et al., 2018, see § 6.3.1), in this work we assume that atomic carbon is not hydrogenated and that methane is formed by additions of H atoms to frozen CH, CH_2, and CH_3. However, to evaluate the impact of this assumption, we also run a model in which also C can be hydrogenated on the

[1]Please note that Garrod, 2013 also assume a barrier of 4500 K for the reaction H + H_2CO → CH_2OH. The three reactions H + H_2CO are also assumed to have a branching ratio equal to 0.33 each.

grain surface. We assume that the hydrogen addition reactions are barrierless, and there are no H-abstraction competing channels in the network.

6.3.4 Reaction efficiency

The study of the efficiency of surface reactions between two species that require activation energy is of high importance since it strongly affects the rate of surface reactions. In the early work of Hasegawa et al., 1992, the efficiency was estimated by the probability of quantum tunneling of the reactants through the rectangular activation energy barrier after one single collision. However, the occurrence of a reaction does not depend only on a single collision. In fact, the two reactants have the opportunity to collide multiple times or hop away to an adjacent binding site or even evaporate before a reaction occurs. The latter two are competing channels against the formation route. This means that the efficiency of a reaction depends not only on the quantum tunneling but also on the frequency of the collision of the two reactants and their rate of diffusion and desorption. Later studies, such as Chang et al., 2007, Garrod and Pauly, 2011 and Enrique-Romero et al., 2021, consider these possibilities in estimating the efficiency of reaction.

In this work, if the reaction between species is barrierless, we assume the efficiency to be unity. Otherwise, we calculate the efficiency ε by following the work of Enrique-Romero et al., 2021, as follows:

$$\varepsilon = \frac{\kappa}{\kappa + \kappa^i_{\rm diff} + \kappa^i_{\rm des} + \kappa^j_{\rm diff} + \kappa^j_{\rm des}}. \tag{6.4}$$

where κ is the reaction rate constant and $\kappa_{\rm diff}$ and $\kappa_{\rm des}$ are the rate constants of diffusion and desorption of the species i and j, respectively.

6.3.5 Chemical desorption

The energy released from exothermic reactions on the ices can eject a fraction of the reaction product into the gas phase (e.g. Duley and Williams, 1993; Garrod et al., 2007; Minissale and Dulieu, 2014; Minissale et al., 2016b). This process is commonly known as chemical desorption.

The probability of desorption depends on the reactants, the products and the surface. There are many experimental and theoretical works on the chemical desorption(e. g., Dulieu et al., 2013; Fredon and Cuppen, 2018; Fredon et al., 2021; Minissale and Dulieu, 2014; Minissale et al., 2016b; Oba et al., 2018; Pantaleone et al., 2020, 2021). All these works have relatively discordant results and predictions. For example, the experimental work by Oba et al., 2018 shows that the hydrogenation of HS into H_2S provokes 60% of desorbed H_2S. On the contrary, experiments by Minissale et al., 2016b on the CO hydrogenation process gives an upper limit of 1% to the desorption of the species formed, a result confirmed by the theoretical study of Pantaleone et al., 2020.

Minissale et al. (2016b) carried out a systematic study on several species and surfaces and proposed to calculate the probability of chemical desorption based on the reaction energy and the binding energy of the product. Given these uncertainties, in the present work, we treat the chemical desorption as an input parameter and allow three possibilities: (1) assume 1% probability for all products from surface reactions, which is the assumption widely used in astrochemical models; (2) use the values listed in Table 1 of Minissale et al. (2016b) and 1% for the reactions not present in Minissale et al.; (3) assume 10% for all the species. The latter choice is to examine the effect of the chemical desorption on the gaseous abundances, particularly for the case of methanol.

6.4 CO + H reaction: quantum chemical calculations

In this section, we provide a new estimate of the efficiency ε of the formation of HCO from the H + CO reaction on a ASW model. To this scope, we follow the formalism of Eq. 6.4, which needs the calculation of the constant rates of the reaction, κ, as well as of the diffusion, κ_{diff}, and desorption, κ_{des}, of the reactants. The last two rates depend on the BE and DE of H and CO, which we also re-compute here.

6.4.1 Reaction constant rates

In a recent paper, Enrique-Romero et al. (2021) used density functional theory (DFT) to calculate the potential energy surface (PES) of the H + CO → HCO hydrogenation surface reaction based on the work of Rimola et al. (2014). This was done in order to qualitatively compare the effect of strong quantum tunneling on this reaction to the one of the CH_3 + HCO → CH_3CHO/CH_4 + CO surface radical–radical reactions, which is either non-existent (acetaldehyde formation) or small (CO + CH_4 formation) (Enrique-Romero et al., 2022).

In this work, we improve the calculations on the H + CO → HCO reaction by Enrique-Romero et al., 2021, using the M08HX (Zhao and Truhlar, 2008a) functional combined with the D3 dispersion correction by Grimme et al. (2010), and the double-ζ basis set 6-31+G(d,p) for optimisations and frequency calculations. The choice of this functional is motivated by a benchmark study in which M08HX-D3 has the best performance, with average unsigned errors <5% (see Appendix 6.10). The final energy values are further refined by running single-point energy calculations at the M08HX-D3/6-311++G(2df,2pd) level. All calculations were run in the unrestricted formalism.

The stationary points of the reaction can be seen in Fig. 6.4, and the rate constant associated to the activation energy barrier in Appendix Fig. 6.9. The energy barrier including the zero-point energy (ZPE) was found to be 15.7 kJ mol^{-1}, and the rate constant, calculated employing the Rice–Ramsperger–Kassel–Marcus (RRKM) theory, was found to have a strong tunneling effect taking values around 10^4 s^{-1}, at temperatures between 5 and 20 K (see Appendix Fig. 6.9). Fittings following the modified Arrhenius equation are available in Table 6.2.

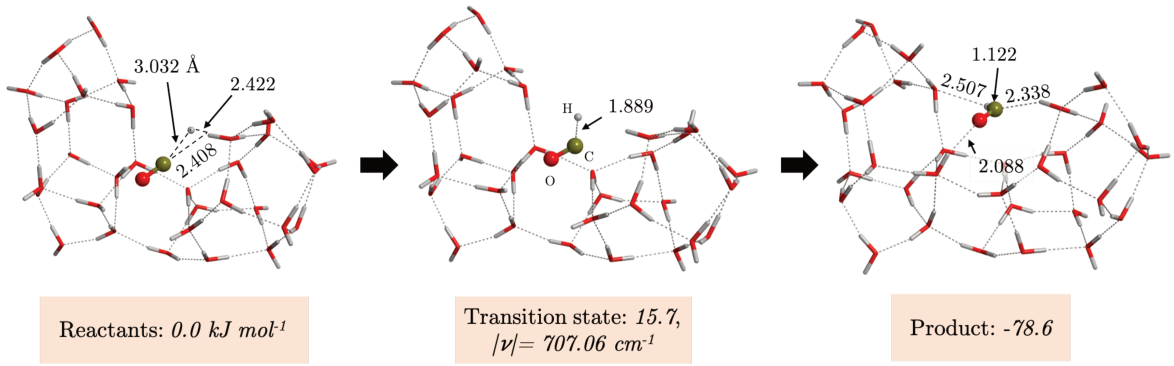

FIGURE 6.4: Stationary points of the potential energy surface of the H + CO → HCO reaction. All geometries were fully optimised and characterized as minima or transition state (TS) by frequency calculations at the M08HX-D3/6-31+G(d,p) level. Energy values were refined at M08HX-D3/6-311++G(2df,2pd) level. Energy and distance units are kJ mol^{-1} and Å, respectively.

6.4.2 H and CO binding energies

We calculated the binding energies (Tab. 6.14) of both CO and H on cavity of the 33 water molecules cluster, employing the BHLYP (Becke, 1993; Lee et al., 1988a) functional combined with the D3(BJ) dispersion correction by Grimme et al. (2011a). This functional was chosen according to a benchmark study in which this method showed the best performance with deviations on binding energies ~ 0.6 kJ mol^{-1} (see Appendix 6.10). The binding energies are 1792 and 349 K for CO and H, respectively.

These values agree well with other works in the literature (see § 6.3). Duflot et al., 2021 carried out an accurate binding energy study employing crystalline and amorphous water ice models for a number of species including atomic hydrogen. These authors found a distribution of binding energies reaching up to 673 K, with average value of 116 K, for H atoms on ASW ice models. Regarding CO adsorptions, Ferrero et al., 2020 found a distribution of binding energy values going from 1109 to 1869 K on an ASW model.

Diffusion energy barriers are estimated by employing the same methodology as in Enrique-Romero et al., 2021, i.e. setting the diffusion barrier as a fraction of its binding energy, with all thermal and entropic corrections. This parameter, ƒ, is set to 0.3 for our main model. Setting a higher value for ƒ would result in diminished diffusion rates. Please note that this methodology is different from the one employed by Senevirathne et al. (2017) as we do not have precise information about the diffusion barrier nor we have studied a distribution of binding sites. Our approach is closer to astrochemical models, as explained in Enrique-Romero et al., 2021.

In Appendix Fig. 6.9, we have plotted the desorption and diffusion rates of CO and H with different ƒ ratios and the rate constants of the CO + H $\rightarrow$ HCO reaction. Notice that the effect of quantum tunneling is clearly noticeable in the rate constant of HCO formation as it deviates from linearity.

TABLE 6.2: The rate constant fitting parameters for CO + H reaction using the modified Arrhenius formula.

T [K]	α [s^{-1}]	β	γ [K]
5–15	1.27×10^{6}	1.62	-4.35
15–30	1.15×10^{7}	2.72	-20.9

The modified Arrhenius formula used here is $k = \alpha(T/300.)^{\beta}\exp -\gamma/T$, with T the temperature in Kelvin and α, β and γ three fitting parameters. The raw data is available in Appendix 6.10.

6.5 The astrochemical model

In this section, we describe our code, GRAINOBLE+ (§ 6.5.1), the adopted gas-phase and grain-surface reaction networks (§ 6.5.2), the physical model of the cloud (§ 6.5.3) and the adopted initial elemental abundances (§ 6.5.4). A last section (§ 6.5.5), will provide a summary of the run models and the strategy.

6.5.1 The GRAINOBLE+ code

The code GRAINOBLE+ is a re-implemented and upgraded version of the code GRAINOBLE (Taquet et al., 2012, 2013). Briefly, GRAINOBLE+ is a 3-phase (Hasegawa and Herbst, 1993b) gas-grain chemical model. The phases are (1) the gas phase, (2) the active layer in which the grain-surface chemistry takes place, i.e. the part of the mantle that is exposed to the gas-phase, and (3) the bulk of the mantle underneath the surface, which is considered chemically inactive. The mantle has a layered structure, where the composition of each monolayer is stored (see Taquet et al., 2012, Figure 3).

Two major processes link the gas phase and the mantle: absorption from the gas into the mantle, and thermal and non-thermal desorption from the mantle to the gas. Three process are taken into account for the non-thermal desorption: cosmic-ray (CR) desorption, chemical desorption and photo-desorption. The latter two and thermal desorption only take place in the active layer, while CR desorption involves the entire mantle (e. g., Hasegawa and Herbst, 1993b; Leger et al., 1985).

Species adsorbed on the active layer can diffuse and upon encounter, they may react. Note that, in this work, we do not include photolysis processes in the ices, as we are interested in the major components of the mantles such as water, CO, CO_2 and methanol which are minimally affected by photolytic processes (Cuppen et al., 2009; Taquet et al., 2012).

The major differences of GRAINOBLE+ with respect to GRAINOBLE are:

1. Inclusion of the grain assisted charge exchange treatment based on the work by Draine and Sutin, 1987.

2. Treatment of thermal hopping and tunneling of H atoms according to the Senevirathne et al., 2017 work, as described in § 6.3.2 and reported in Appendix Tab. 6.13.

3. Inclusion of the tunneling of O atoms following the Congiu et al., 2014 recipe, reported in Appendix Tab. 6.13 and discussed in § 6.3.2.

4. New treatment of the CO hydrogenation network, which takes into account our new ab initio computations, presented in § 6.4, and those by Song and Kästner, 2017, as discussed in § 6.3.3 (see, also Fig. 6.3).

5. New treatment of the hydrogenation network leading to methane, which takes into account the chemisorption of atomic C, as described in § 6.3.3.

6. The surface reaction efficiency follows the Enrique-Romero et al., 2021 formalism, described in § 6.3.4.

7. Introduction of the possibility to chose the chemical desorption percentage, including the Minissale and Dulieu, 2014 values, as described in § 6.3.5.

In addition, GRAINOBLE+ has implemented a modular structure that facilitates the addition, modification, or removal of any process. It also provides an easy user interface in Python for the Fortran core code.

6.5.2 Chemical reaction networks

The chemical networks involving the formation and destruction of the O and C major reservoirs in the gas phase and on the grain surfaces are a crucial element of the modeling. In the following, we describe separately the adopted gas-phase and grain-surface networks.

Gas-phase reaction network We used the gas-phase network GRETOBAPE-GAS that our group has updated and used in several previous works. It is based on the KIDA2014 network (Wakelam et al., 2015)[2]. Several reactions have been modified, removed, or added following measured or computed reaction pathways and rate coefficients in the literature, or derived by our group (see, e. g., Ascenzi et al., 2019; Ayouz et al., 2019; Balucani, 2020; Balucani et al., 2015a; Balucani et al., 2018; Codella et al., 2020; Fontani et al., 2017; Skouteris et al., 2019; Tinacci et al., 2021; Urso et al., 2016, 2019; Vazart et al., 2020).

Grain-surface reaction network We include the formation network involving the most abundant species observed in ices: water, carbon dioxide, carbon monoxide, methanol, ammonia and methane (see also § 6.3.3). Reactions on the surface follow the Langmuir-Hinshelwood (LH) and Eley-Rideal (ER) mechanisms.

The full list of reactions along with their activation energy, barrier width, and branching ratios, when relevant, are given in Appendix 6.12.

6.5.3 Pseudo-time dependant physical model

As previous works by several authors, we assume that MC form from a translucent cloud with constant density and temperature, where only hydrogen is in the molecular form and the other elements are ionised or neutral atoms, depending on their ionization potential with respect to 13.6 eV. The model then follows the chemical evolution up to 10 Myr.

Aiming at simulating the dense part of TMC1, as described in the Introduction, we adopted A_v=20 mag and the standard external UV radiation flux with $\chi = 10$ in Draine units (Draine, 1978) and the UV flux from the ionization of hydrogen by CR equal to 10^4 cm^{-2} s^{-1}.

As described in § 6.2.1, the density and temperature in TMC1 vary between 1 and 8 $\times 10^4$ cm^{-3}, and 8 and 14 K. We, therefore, ran a grid of models as follows: four values for density, with n_{H_2} = 1, 2, 4, and 8 $\times 10^4$ cm^{-3}; five values for temperature, with T = 8, 9 , 10, 12, and 14 K. We ran twice the grid of models, with the CR ionization rate of H_2 ζ_{H_2} equal to 3×10^{-18} and 1×10^{-17} s^{-1}, respectively. Therefore, we ran in total 40 models, whose parameters are summarised in Tab. 6.3.

TABLE 6.3: The physical parameters used in the pseudo-time dependant model grid.

Parameter	Value
duration [Myrs]	10
n_{H_2} [cm^{-3}]	1(4), 2(4), 4(4), and 8(4)
A_v [mag]	20.
ζ_{H_2} [s^{-1}]	3(-18), and 1(-17)
T_{gas} = T_{dust} [K]	8, 9, 10., 12, and 14
χ [Draine unit]	10.

6.5.4 Initial gaseous elemental abundances

The adopted initial elemental abundances are obviously a crucial factor in the astrochemical modeling and, at the same time, a source of uncertainty, as they cannot be directly measured and are only indirectly estimated (see, for example, the discussion in § 6.2). In this work, in order to evaluate the impact of this factor, we will use four sets of elemental initial abundances, described in the following and listed in Tab. 6.4.

[2]kida's website

EA1: Following the extensive work by Jenkins, 2009, the EA1 set of initial elemental abundances adopts the maximum depletion factor for each element estimated by Jenkins for all elements (see his Table 4, column 7) except for sulfur, for which we adopt his recommended value of 2.6×10^{-6} (with respect to H nuclei).

EA2: The depleted fraction of oxygen, carbon, nitrogen and sulfur from the diffuse phase to the dark cloud phases are highly debated in the community and is addressed in many works (see, for example, Boogert et al., 2015; Hincelin et al., 2011; Jones and Ysard, 2019; Poteet et al., 2015; Whittet, 2010). Briefly, about the 30–50 % of oxygen and 10–20 % of carbon content from a diffuse to dense cloud phase are not accounted for and cannot be explained by CO in the gas phase and silicate and oxides in the refractory core of the dust. It is possible that the missing elements are hidden in the refractory cores of the interstellar grains, as O-rich carbonates that are difficult to observe (e.g. Jones and Ysard, 2019). Solid O_2 and HCOOH could also contribute to about 10 % (Whittet, 2010) and less than 10 % (Vandenbussche et al., 1999), respectively. Nitrogen and sulfur are the two elements for which the major reservoirs in MC are "missing", about 70% and 95%, respectively. Nitrogen could be locked in gaseous atoms, gaseous and solid N_2 and refractory organics or salts (Altwegg et al., 2020; Poch et al., 2020). To take into account these uncertainties and to compare with the EA1 values, EA2 uses the volatile elemental oxygen and carbon abundances estimated by Jones and Ysard, 2019.

EA3: To examine the influence of a larger depletion of the elements heavier than oxygen on the chemical evolution, we assume a factor 100 lower abundance for them with respect to the values of EA1.

EA-TMC1: Finally, we assumed that the total carbon and oxygen elemental abundances equal the sum of the largest measured abundances towards TMC1, described in § 6.2. The other elements are as EA1.

TABLE 6.4: Gaseous elemental abundances used in this work.

Element	EA1	EA2	EA3	EA-TMC1
H_2	0.5	0.5	0.5	0.5
He	8.5(-2)	8.5(-2)	8.5(-2)	8.5(-2)
O	2.8(-4)	3.7(-4)	2.8(-4)	1.44(-4)
C^+	1.7(-4)	1.3(-4)	1.7(-4)	7.8(-5)
N	5.3(-5)	5.3(-5)	5.3(-5)	5.3(-5)
S^+	2.6(-6)	2.6(-6)	2.6(-8)	2.6(-6)
Mg^+	2.1(-6)	2.1(-6)	2.1(-8)	2.1(-6)
Si^+	1.4(-6)	1.4(-6)	1.4(-8)	1.4(-6)
Fe^+	2.0(-7)	2.0(-7)	2.0(-9)	2.0(-7)

NOTES The elemental abundances are reported with respect to H nuclei ($x(y) = x \times 10^y$). The description of the four data sets is reported in § 6.5.4.

6.5.5 Summary of the run models and strategy

We run several grids of models with the aim of evaluating the influence on the model predictions of the various parameters entering into the modeling. The latter can be separated in two broad classes: the macro-physics parameters, which describe the cloud to model, and the micro-physics parameters, which enter into the physics of the chemical processes occurring in the gas phase and on the grain surfaces. We adopted a multi-step strategy to evaluate the effects separately due to the two classes of parameters.

Step 0: We first defined a "reference" model, which contains the parameters that, a priori, best describe both the TMC1 cloud and the micro-physics processes, following the discussions in § 6.2 and § 6.3. The parameters of the reference model are summarised in Tab. 6.5.

Step 1: We ran a grid of models varying the gas density and temperature, within the range of the values observed in TMC1, for two likely values of the CR ionization rates, as summarised in Tab. 6.3. For this step, we used all the other parameters of the reference model.

Step 2: We ran the same grid of Step 1, but with the EA-TMC1, EA2 and EA3 initial elemental abundances set (Tab. 6.4).

Step 3: We ran the same grid of Step 1, with the lowest CO BE, namely 1100 K, following the discussion in § 6.3.1.

Step 4: From the previous runs, we selected the parameters of Step 1 to Step 3 grids whose model predictions better fit the observations. Then we ran a grid of models where we varied the micro-physics processes and parameters that are uncertain (§ 6.3). Their list is summarised in Tab. 6.6.

Step 5: We select the model that best-fit the observations considering all the variations of the previous steps.

TABLE 6.5: List of the processes and parameters adopted in the reference model.

Parameter	Value
Macro-physics parameters	
n_{H_2}	2×10^4 cm^{-3}
T	10 K
ζ_{H_2}	3×10^{-18} s^{-1}
Elemental abundances	EA1
Micro-physics parameters	
H BE	350 K
O, C and N BE	1320, 14100, 720 K
CO BE	1792 K
H diffusion	Se17[1]
O diffusion	Co14[2]
ƒ=DE/BE	0.3
CO hydrogenation	CO + O : this work (§ 6.4), H_2CO + H : SK17[3]
C hydrogenation	no
Chemical desorption	1%

[1] Senevirathne et al., 2017;
[2] Congiu et al., 2014;
[3] Song and Kästner, 2017.

TABLE 6.6: List of Step 4 model grid with the varied micro-physics parameters (see § 6.5.5).

Model ID	Diffusion H	Diffusion O	C hydrogenation	CD [%]
1	Se17	Co14	no	1
2	TH ($\mathfrak{f} = 0.3$)	TH ($\mathfrak{f} = 0.3$)	no	1
3	TH ($\mathfrak{f} = 0.4$)	TH ($\mathfrak{f} = 0.4$)	no	1
4	TH ($\mathfrak{f} = 0.5$)	TH ($\mathfrak{f} = 0.5$)	no	1
5	Se17	TH ($\mathfrak{f} = 0.3$)	no	1
6	Se17	TH ($\mathfrak{f} = 0.4$)	no	1
7	Se17	TH ($\mathfrak{f} = 0.5$)	no	1
8	Se17	Co14	yes	1
9	Se17	Co14	no	10
10	Se17	Co14	no	Mi16

NOTES The first column lists the model identification. The second and the third columns list the adopted diffusion mechanism of H and O atoms (§ 6.3): (i) via quantum tunneling following the Senevirathne et al., 2017 results (Se17), (ii) via thermal hopping (TH) with different $\mathfrak{f}$, (iii) using the Congiu et al., 2014 results for the O atoms (Co14). The fourth column shows the choice of including the C atom hydrogenation in the CH_4 formation reaction network (§ 6.3.3). The last column lists the adopted chemical desorption (CD) percentage: (i) 1%, (ii) 10%, (iii) the values reported in Minissale et al., 2016b

6.6 Results

6.6.1 The reference model

Figure 6.5 shows the evolution with time of the major O and C reservoirs in the reference model. At 10 Myr, water is the most abundant solid species followed by CO_2, CO and CH_3OH, with methane about 100 times lower than water. This order is valid most of time, except before 0.1 Myr, where solid CO is less abundant of methanol and methane. This is because the formation of CO in the gas-phase is not complete until about 0.1 Myr and soon after, at 0.2–0.3 Myr, CO freezes out increasing the methanol formation. Methane formation is not very efficient because it follows the formation in the gas-phase of CH and CH_2, which are then hydrogenated into CH_4, and the freezing of CH_4 formed in the gas-phase. On the other hand, CO is the most abundant gas-phase O- and C- bearing species during the whole evolution. It is worth to notice, though, that after about 1 Myr, CO abundance crashes to very low values. We will discuss this point later on (§ 6.6.3).

Figure 6.6 shows the number of layers and the mantle composition as a function of the time. At the end of the evolution, the mantle is constituted by ∼240 layers, while at ∼1 Myr the layers are less than half this value. At about 0.1 Myr, only ∼40 layers are formed.

At the beginning of the evolution, solid water represents more than 50% of the mantle species, but, after ∼ 1 Myr, its relative abundance decreases to 0.33%. Also, atomic carbon is abundant in the first ∼40 layers, when the gaseous C that freezes out is chemisorbed and, therefore, remains inert on the surface. This represents about 90% of the overall solid C-bearing species at the end of the evolution.

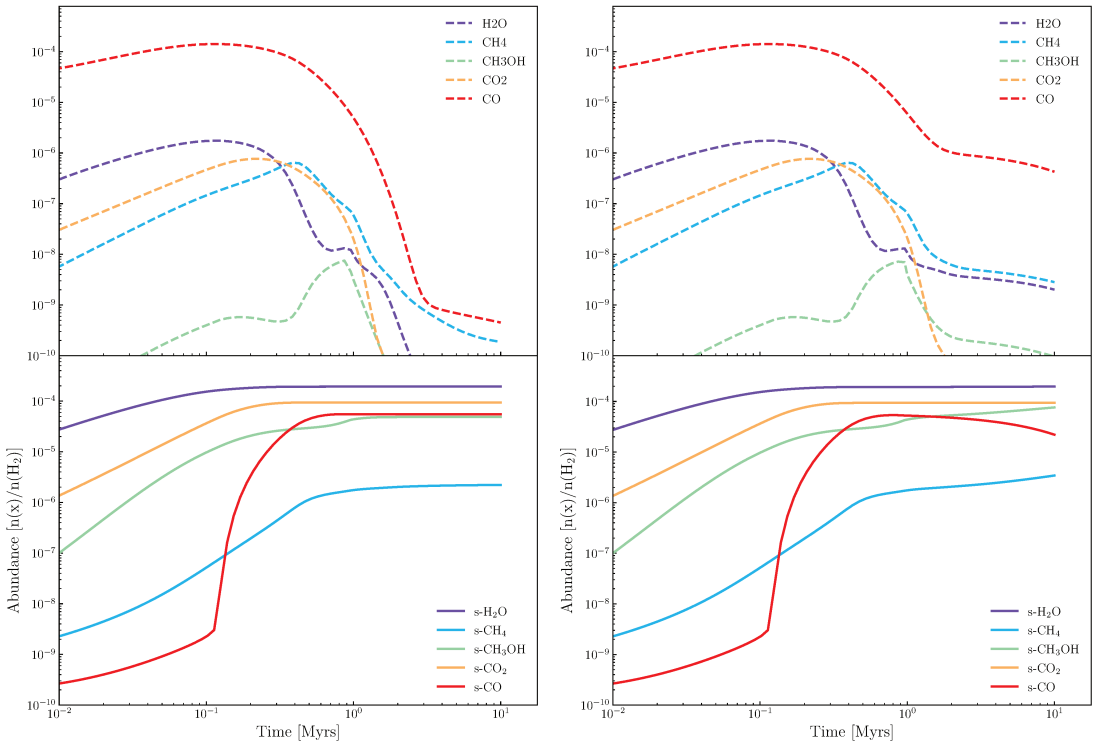

FIGURE 6.5: Abundances of the major O and C reservoirs as a function of time in the reference model (left panels) and the same but with the CO BE equal to 1100 K (right panels): H_2O (purple), CO (red), CO_2 (orange), CH_3OH (green) and CH_4 (blue). Top panels show the abundances in the gas-phase while the bottom panels those in the solid-phase. All abundances are with respect to H_2.

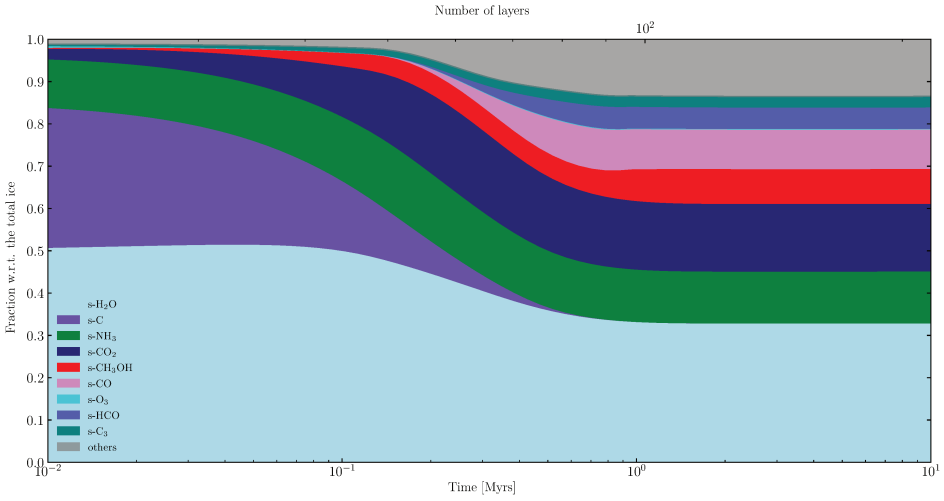

FIGURE 6.6: The abundance of solid species relative to the total composition of the grain mantle as a function of time, reported in bottom x-axis. The number of layers is reported in the top x-axis.

6.6.2 Grid with varied physical parameters

Figure 6.9 shows the results of the predicted abundances with respect to those measured in TMC1, for the 40 models of the Step 1 grid. Since the age of TMC1 is an important parameter, given the evolution of the species as a function of time (§ 6.6.1), we computed the predicted over observed abundances at the time in which, for each model, the observed solid and gaseous CO abundances are best reproduced by the model. We chose to minimize the predictions using only the latter species since they are the two crucial species that vary the most with time.

In practice, the best fit is obtained at 0.6–0.8 Myr in the lowest density models ($n_{H_2} = 1 \times 10^4$ cm^{-3}) whereas, and at 0.06–0.09 Myr in the highest density models ($n_{H_2} = 8 \times 10^4$ cm^{-3}),

In general, solid water is reproduced by all 40 models, within a factor of 2. Gaseous CO is also reproduced by all models, whereas solid CO is best reproduced with the lowest ζ_{H_2} and the two lowest densities, or with the largest densities if ζ_{H_2} is larger. Models with the lowest temperature, T=8–10 K, better reproduce solid CO. Solid CO_2 is overproduced by almost all models, by about a factor 4. Finally, solid methanol is overproduced in almost all models by more than a factor 5 except with the lower ζ_{H_2}, highest T and largest n_{H_2}.

In summary, our models have difficulties in simultaneously reproducing solid CO and methanol and gaseous CO.

6.6.3 Low CO binding energy

Figure 6.5 shows the evolution with time of the major O and C reservoirs when the CO BE is low, 1100 K (see the discussion in § 6.3.1).

The most evident (and expected) difference with respect to the reference model is the evolution of the gaseous abundance of CO. This leads to a slightly decrease of the abundance of solid CO and increase of solid methanol at 10 Myr, whereas the abundance of all other species does not change sensibly.

However, if we consider the predicted over observed abundances for the 40 models with different physical properties, we expect that the situation will change with respect to the results obtained with the larger CO BE (§ 6.6.2), providing better results. We postpone this part to the next version of this work.

6.7 Discussion

Several authors have discussed the dependence of the astrochemical model predictions on the adopted macro-physics, such as density, temperature, initial elemental abundances, CR ionization rate (the literature is rich in these studies and we just reference a very few as representative examples, being aware that the list is far to be exhaustive: Aikawa et al., 2020; Holdship and Viti, 2022; Kalvāns, 2021; Viti et al., 2001b; Wakelam et al., 2006a, 2010b). Similarly, there have been several studies devoted to evaluate the impact on the model predictions of the gas-phase reaction networks (again, we reference only a few works as representative examples Wakelam et al., 2006a,b) and some parameters of the grain-surface chemistry (Cazaux et al., 2010, 2016; Penteado et al., 2017; Quénard et al., 2018).

In the present work, we focus particularly on the several parameters that influence the grain-surface chemistry and the impact that they have on the predicted abundances in a dark cloud, taking as a reference the well studied TMC1. We only focus on the solid and gaseous major O and C reservoirs, because if they are not reproduced correctly by the model there is no utility in trying to reproduce trace species, whose abundance heavily depend on how much carbon or oxygen is left free for them to form. Since the major reservoir in dark clouds

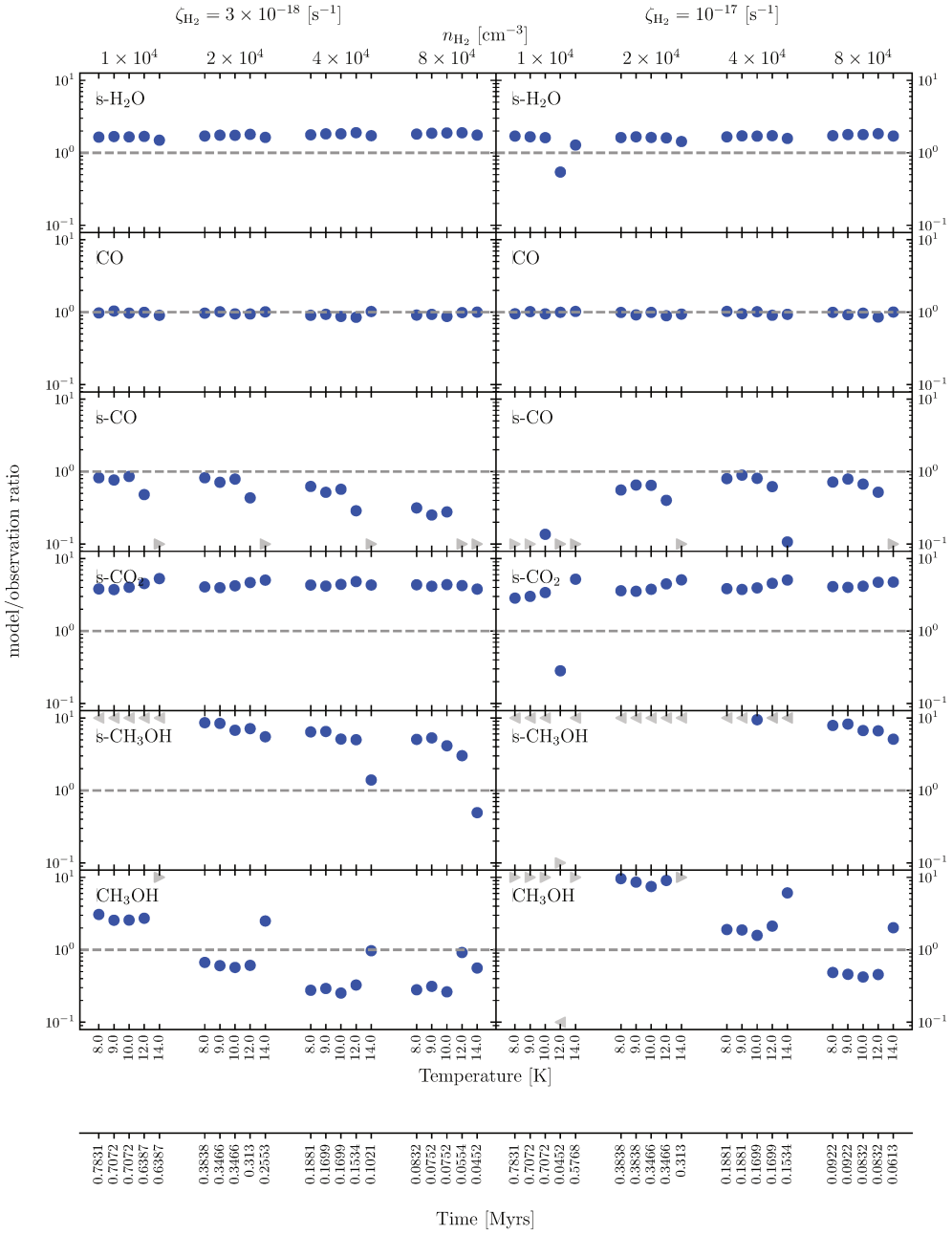

FIGURE 6.7: Comparison between the predicted and observed abundances of the major O and C reservoirs for models with different densities and temperatures (Tab. 6.3). The observed abundances are listed in Tab. 6.9. The predicted abundances are those at the evolution time which best reproduces the gaseous and solid CO (see text). These times are annotated at the bottom of the figure for each model. The left and right panels refer to ζ_{H_2} equal to 3×10^{-18} and 1×10^{-17} s^{-1}, respectively. For each density, marked at the top of the upper panels, there is a group of model with different temperatures, marked at the bottom panels. From the top to the bottom, the rows show the solid water, gaseous CO, solid CO, solid CO_2, solid and gaseous methanol, respectively. The grey points indicate the models with ratios less than 0.1 or larger than 10.

are in the solid form, with the exception of gaseous CO, it is extremely important to well characterise the surface chemistry, which plays the major role in this respect. With respect to the above mentioned works, we used the most recent results of experimental and theoretical

studies on the grain-surface chemistry and carefully highlighted the uncertainties associated with it (§ 6.3). We then ran various models to quantify the impact on the model predictions given by these uncertainties.

As first comment, not much surprising, the poorly known micro-physics processes and parameters discussed in § 6.3 have a huge influence on the resulting model predictions. The most affected species are the solid and gaseous CO along with the solid methanol. There is a very straightforward link between these three species, as they all depend on each other.

A second comment regards the impact of the age of the cloud on the grain mantle composition and observability. In fact, the small number of layers in young clouds may impact the detection of the solid-state species. For example, if the cloud is very young, as it seems the case of TMC1, a relatively small number of layers are present in the mantle: 40 at 0.1 Myr against 240 at 10 Myr. In practice, a very young cloud mantle has about a factor 6 less column density of solid material with respect to an older cloud. Also, the composition depends on the age of the cloud. A 0.1 Myr young cloud would have a smaller column density of solid CO with respect to an older one and even the absence of methanol. The observed scatter in the measurements of the solid column densities of these two species could (§6.2), therefore, be due to a different evolutionary status of the different regions of the cloud.

As remarked by several other authors, water is the first to form and, therefore, it is expected to be less deuterated with respect to later species, such as methanol (e.g. Taquet et al., 2013; Taquet et al., 2014). It is also possible that since young cloud have less solid water, protostars born in those clouds would have a smaller abundance of gaseous water in the water sublimation regions, notably the hot corinos (e.g. Ceccarelli et al., 2000a; van Dishoeck et al., 2021).

Finally, the recent results on the chemisorption of C atoms on the icy grain surfaces leads to the prediction that an important fraction of the initial carbon is actually in frozen C, which is completely impossible to detect. In the reference model, we found that about half of the initial elemental carbon could reside in this form. Whether this is the missing carbon mentioned in § 6.5.4 remains an interesting possibility to investigate further. Interesting to investigate farther, even though much more speculative, is also the possibility that this carbon accounts for the formation of new dust in dark clouds invoked by some authors to explain the extinction curves at high red-shifts (e.g. Asano et al., 2013; Ginolfi et al., 2018) even though the problem seems to have been mitigated by the most recent models (e.g. De Looze et al., 2020; Nanni et al., 2020).

6.8 Conclusions

We carried out a systematic theoretical study of the O- and C- major reservoirs in dark clouds. To this end, we used the code GRAINOBLE+ and ran a large number of models where we varied the most important macro-physics and micro-physics parameters. We payed a particular attention to the processes and parameters that govern the grain-surface chemistry, as the major O and C major reservoirs are in the solid form, with the exception of gaseous CO. We took the well studied dark cloud TMC1 as a reference to compare the model predictions with observations. The comparison helps to constrain some of the micro-physics processes and parameters and provide a constrain on the age of TMC1, around 0.1 Myr. Our models, which incorporate the new theoretical results on the C chemisoprtion on the icy grain surfaces, suggest that the diffuse-to-MC "missing" carbon claimed by several authors could be in the form of frozen atomic carbon.

6.9 Appendix 1) The physical parameters shared among all the models in this work

In this section, we list the model parameters we have employed that are commonly used in the literature.

Dust grain properties We assume the dust to gas mass ratio is 1.0%. The density of the grain refractory core is 3 g cm^{-3} (Leger et al., 1985) with an average radius of 0.1 μm. Each molecule on a layer occupies a square with an average width of 3.5 Å (see, Jenniskens et al., 1995 for more information).

Sticking coefficients Many computational and experimental works have measured the sticking probability of light species on various substrates (See, for example, Al-Halabi and van Dishoeck, 2007; Al-Halabi et al., 2004; Chaabouni et al., 2012; Dupuy et al., 2016; He et al., 2016; Hollenbach and Salpeter, 1971; Matar et al., 2010; Molpeceres and Kästner, 2020; Pierre et al., 1985; Veeraghattam et al., 2014). Following the experimental study by He et al., 2016, we assumed that the sticking coefficient on amorphous water ice is equal to unity for all species except for atomic hydrogen, for which we followed the formalism in Hollenbach and McKee, 1979. In contrast, charged species in the gas phase do not attach to the grain, they only exchange their charge. The sticking coefficient for charged species is 0.5 (Weingartner and Draine, 2001a).

The effect of self-shielding We also incorporate self-shielding of H_2 and CO molecules based on the work of Lee et al., 1996 and Le Petit et al., 2006 which provide the shielding factor of these two species as a function of column density.

6.10 Appendix 2) Computational quantum chemistry benchmarks

We have employed a surface toy model made of 3 water molecules (see, Fig. 6.8) in order to mimic the effect of a water-ice surface on (i) the hydrogenation of CO into HCO, and (ii) the binding energies of H and CO to the surface.

In this benchmark we checked the performance of six hybrid DFT methods, all of whom are corrected for dispersion (in some cases using the bare D3 correction, and some others using the D3(BJ) one).

The initial structures employed in this benchmark study were obtained from all-atom optimisations at BHLYP-D3(BJ)/6-31+g(d,p) level. Energy minima (e. g., ice + admolecule complexes, reactants and products) and maxima (the H + CO $\rightarrow$ HCO transition state) in the PES were characterized as such by running frequency calculations at the same level of theory. Furthermore, the connection between the minima and the TS in the reaction was checked by intrinsic reaction coordinate calculations. Following the PES exploration, single-point energy calculations at DFT-D/6-311++g(2df,2pd) level were performed.

In order to find the most accurate method, we compared the relative DFT-D/triple-ζ energies to the ones obtained at the highly accurate CCSD(T)/aug-cc-pVTZ level.

Tab. 6.7 contains the relative energies of the reaction and their unsigned errors, and Tab. 6.8 those of the interaction energies (that is, $E_{int} = E_{complex} - E_X - E_{surface}$) together with their unsigned deviations. In both cases we have used six DFT-D methods. The one with the highest accuracy for the HCO formation reaction is M08HX-D3 with an average unsigned error of about 4%, followed by M062X-D3 (average unsigned error $\sim$8%). The rest of the methods result in rather poorly accurate values with average unsigned errors above 16%.

Regarding the interaction energies, the best method is BHLYP-D3(BJ), closely followed by PW6B95-D3(BJ) and MPWB1K-D3(BJ) (average deviation of 0.6, 0.7 and 1.3 kJ mol^{-1}, respectively). The worst ones, especially for the binding energy of atomic hydrogen, are M08HX-D3, M062X-D3, and wB97X-D3 (average unsigned deviations of 2.2, 2.6, and 3.3 kJ mol^{-1}, respectively. Additionally, for the latter two the interaction energy at the BHLYP-D3-optimised geometry is repulsive (positive interaction energies).

Therefore, the best method for the reaction energy is one of the not so good for the binding energies, and *vice-versa*. Notice that even if the binding energies are computed on the M08HX-D3/triple-ζ fully optimised geometries, the results are almost identical (binding energies of 5.7 and 8.8 kJ mol^{-1}) as in the M08HX-D3/triple-ζ//BHLYP-D3(BJ)/double-ζ ones.

From these results, we decided to use M08HX-D3 for the reaction and activation energy calculations, and BHLYP-D3(BJ) for the binding energies.

TABLE 6.7: Benchmark of reaction and activation energies for the hydrogenation of CO into HCO on a cluster of three water molecules.

	Relative energies (kJ mol^{-1})		Unsigned errors (%)	
Method	$\Delta E^{\ddagger}$	ΔE^{RX}	$\Delta E^{\ddagger}$	ΔE^{RX}
CCSDt	15.5	-89.4	–	–
BHLYP-D3(BJ)	8.8	-110.6	43	24
MPWB1K-D3(BJ)	12.0	-106.7	22	19
M062X-D3	14.7	-99.5	5	11
PW6B95-D3(BJ)	9.4	-107.5	39	20
wB97X-D3	15.8	-117.2	2	31
M08HX-D3	16.1	-93.7	4	5

TABLE 6.8: Interaction energy benchmark of CO and H on a cluster of 3 water molecules.

	Interaction energies (kJ mol^{-1})		Unsigned deviations (kJ mol^{-1})	
Method	H	CO	H	CO
CCSDt	-1.5	-9.9	–	–
BHLYP-D3(BJ)	-2.0	-9.3	0.6	0.6
MPWB1K-D3(BJ)	-0.9	-7.9	0.5	2.0
M062X-D3	1.1	-7.3	2.6	2.6
PW6B95-D3(BJ)	-1.4	-8.5	0.0	1.4
wB97X-D3	3.3	-11.8	4.7	1.9
M08HX-D3	-5.0	-9.0	3.5	0.9

6.11 Appendix 3) Observations towards TMC1

6.12 Appendix 4) Surface reactions and diffusion rate parameters

In this section, we list the surface reactions used in our model in Tab. 6.10; the Eckart model parameters in Tab. 6.11; the rate constant fitting parameters in the methanol formation network in Tab. 6.12; and the diffusion rate best fit parameters of atomic oxygen and hydrogen in Tab. 6.13.

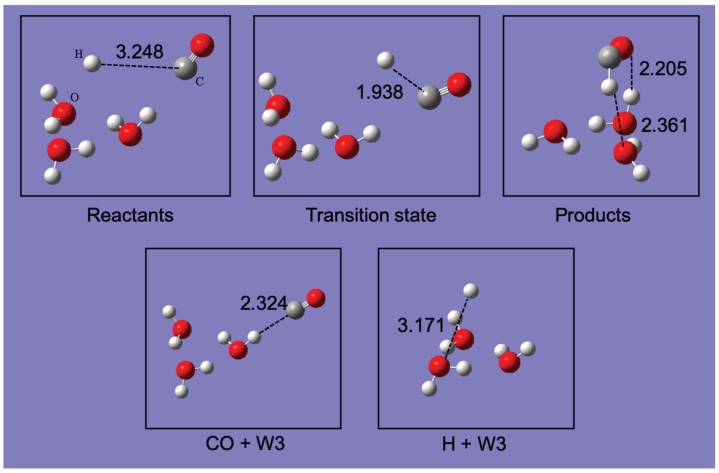

FIGURE 6.8: Geometries employed for the benchmark study, optimised at BHLYP-D3(BJ)/6-31+G(d,p) level. Notice that we have referred to the ice cluster as W3.

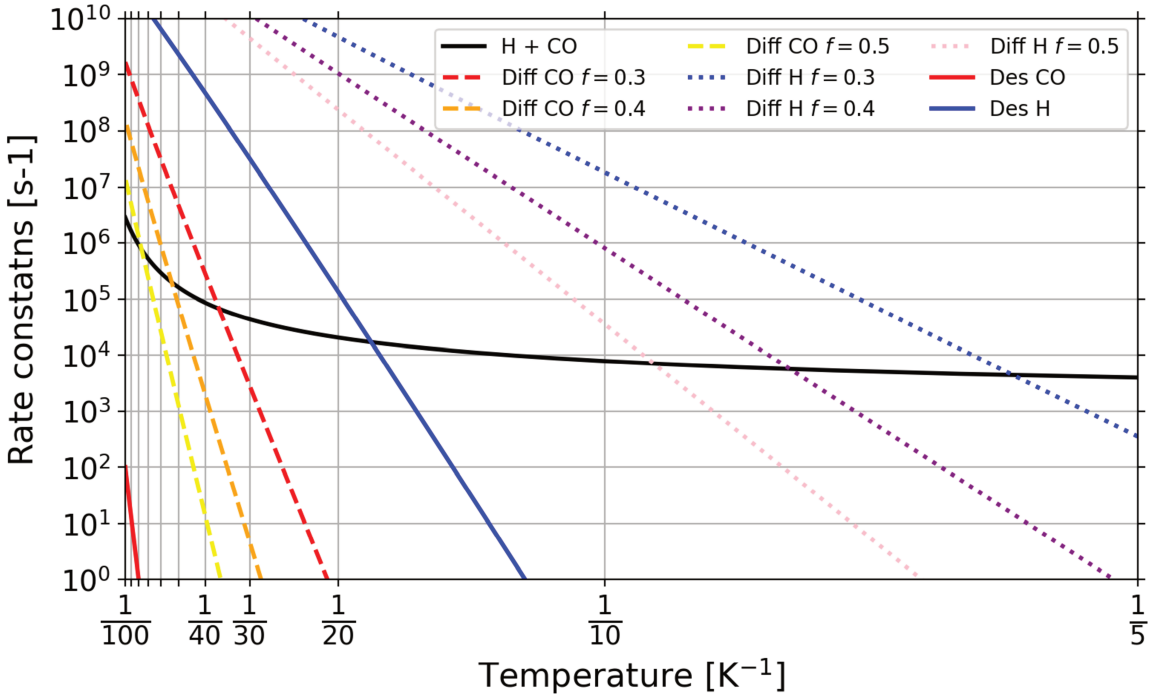

FIGURE 6.9: The rate constant of the H + CO reaction in the solid black curve. The desorption rate of CO and H in solid red and blue curves. and the diffusion rates of H and CO in dotted and dashed lines with various different diffusion to desorption energy ratios.

TABLE 6.9: Observed abundances in gaseous and solid O and C major reservoirs in TMC1.

		TMC-1[m]	Tamura 8[n]	Elias 3-16[o]	range	average
	$N(H_2)$ [cm^{-2}]	2.0(22)[p]	1.7(22)[g]	1.5(22)[g]	1.5(22) - 2.0(22)	1.74(22)
	A_v [mag]	20.	24.2[g]	24.3[g]	20.0 - 24.3	22.84
Abundances [N(x)/N(H_2)]	CO	8.8(-05)[a]	1.47(-04)[g]	1.7(-04)[g]	8.8(-05) - 1.7(-04)	1.34(-04)
	s-CO	3.0(-05)[b]	3.53(-05)[j]	4.34(-05)[k]	3.0(-05) - 4.34(-05)	3.62(-05)
	s-CO_2	2.2(-05)[b]	—[l]	3.6(-05)[k]	2.2(-05) - 3.6(-05)	2.9(-04)
	s-H_2O	1.1(-04)[b]	1.45(-04)[j]	1.71(-04)[k]	1.1(-04) - 1.71(-04)	1.42(-04)
	s-CH_3OH	4.0(-06)[b]	$\leq 1.113(-05)$[h]	$\leq 4.8(-06)$[i]	4.0(-06) - 1.113(-05)	$\leq$6.64(-06)
	s-CH_4	$\leq$3.3(-06)[d]	$\leq$4.35(-06)[d]	$\leq$4.8(-06)[d]	3.3(-06) - 4.8(-06)	4.15(-06)
	CH_3OH	8.6(-10)[e]	—	—	—	8.6(-10)
	H_2O	$\leq 1.(-08)$[c]	$\leq 1.(-08)$[c]	$\leq 1.(-08)$[c]	—	$\leq 1.(-08)$
	H_2CO	5.(-08)[f]	—	—	—	5.(-08)

All abundance are with respect to H_2 molecules. The number format is $a(b) = a \times 10^b$ and the solid species are denoted with "s-" prefix.
[a] An average over the three cores TMC 1-C, TMC 1-CP, and TMC 1-NH3 at $A_v \sim 20$ mags from Fuente et al. (2019, Figure 8) and Spezzano et al. (2022, Table B.1) (average range in the three cores: 5.245(-5) - 1.135(-4)), where the abundances are calculated with $\sim$ 10 % uncertainty on $N(H_2)$;
[b] From Boogert et al. (2015, Figure 7) fitted curve for Taurus at 20 mags visual extinction;
[c] An average abundance (Hollenbach et al., 2009; Snell et al., 2000; van Dishoeck et al., 2021);
[d] The upper limit for s-CH_4 is 3% of the s-H_2O abundance at 20 magnitudes (Boogert et al., 2015, Table 2, BG stars column) assuming $N(H_2)=A_v \times 10^{21}$;
[e] An average value over the three cores at $\sim$ 20 mags from Spezzano et al. (2022, Table B.1);
[f] Ohishi and Kaifu (1998) observation towards the cyanopolyyne peak in TMC-1;
[g] Lacy et al. (2017, Table 2) columns N_{H_2} and N_{COcog} for gaseous H_2 and CO, respectively. The uncertainties on N_{H_2} and N_{COcog} are about 25% and 20%, respectively;
[h] N(s-CH_3OH)<1.92(17) (Chiar et al., 1996);
[i] N(s-CH_3OH)<7.2(16) (Chiar et al., 1996);
[j] N(s-CO)=6.0(17) cm^{-2}, N(s-H_2O)=24.7(17) cm^{-2} (Whittet et al., 2007, Table 2);
[k] N(s-CO)=6.5(17) cm^{-2}, N(s-H_2O)=25.7(17) cm^{-2}, N(s-CO_2)=5.4(17) cm^{-2} (average value) (Whittet et al., 2007, Table 2);
[l] No s-CO_2 coverage (Whittet et al., 2007);
[m] source IDs: TMC 1-CP (044141.90+254127.1), TMC 1-NH3 (044121.30+254807.0), and TMC 1-C 044138.80+255942.0);
[n] source ID 044057.5+255413;
[o] source ID 043938.9+261125;
[p] Derived from visual extinction assuming $N(H_2)=A_v \times 10^{21}$ (Fuente et al., 2019);
[*] The gaseous CO_2 and CH_4 are not observable in cold gas because of the absence of a permanent dipole moment in both molecules.

TABLE 6.10: Barrier-less surface reactions and reactions with rectangular activation potential barrier.

network	reactions	branching ratio	E_a [K]	barrier width [Å]	reference
hydrogen	$H + H \longrightarrow H_2$				(1)
(CH_3OH)	$HCO + H \longrightarrow H_2CO$				(1,2)
	$CH_3O + H \longrightarrow CH_3OH$				(11,1,2)
Trioxygen	$O + O \longrightarrow O_2$				(1)
	$O_2 + O \longrightarrow O_3$				(1)
	$O_3 + H \longrightarrow O_2 + OH$				(17,24,25,26)
Water (H_2O)	$O + H \longrightarrow OH$				(11,19,21)
	$OH + H \longrightarrow H_2O$				(11,19,21)
	$OH + OH \longrightarrow \begin{cases} HOOH \\ H_2O + O \end{cases}$	0.8 0.2			(6)
	$O_2 + H \longrightarrow O_2H$				(18,22,20,25,26)
	$O_2H + H \longrightarrow HOOH$				(18,22,20,25,26)
Ammonia	$N + H \longrightarrow NH$				(1,3)
	$NH + H \longrightarrow NH_2$				(1,3)
	$NH_2 + H \longrightarrow NH_3$				(1,3)
Methane	$CH + H \longrightarrow CH_2$				(1)
	$CH_2 + H \longrightarrow CH_3$				(1)
	$CH_3 + H \longrightarrow CH_4$				(1)
Silyl	$Si + H \longrightarrow SiH$				(4)
	$SiH + H \longrightarrow SiH_2$				(4)
	$SiH_2 + H \longrightarrow SiH_3$				(4)
	$SiH_3 + H \longrightarrow SiH_4$				(4)
Silicon dioxide	$Si + O \longrightarrow SiO$				(4,5)
	$SiO + O \longrightarrow SiO_2$		1000.0	1.0	(4,5)
	$SiO + OH \longrightarrow SiO_2 + H$		80.0	1.0	(4,5)
Carbon dioxide	$HCO + O \longrightarrow CO_2 + H$				(14,2)
	$CO + O \longrightarrow CO_2$		1000.0	1.0	(2,15)
	$O^* + CO \longrightarrow O\ldots CO$				(1,7,6)
	$O\ldots CO + H \longrightarrow \begin{cases} CO_2 + H \\ tHOCO \\ cHOCO \\ CO + OH \end{cases}$	0.49 4.95(-3) 0.01 0.495	1000.0	1.0	(1,7,6)
	$O + CO \longrightarrow O\ldots CO$			(1,7)	

Notes Surface reactions of species already residing on the surface. (1) Taquet et al., 2013; (2) Ruffle and Herbst, 2000; (3) Jonusas et al., 2020; (4) Ceccarelli et al., 2018; (5) Martín et al., 2009; (6) Oba et al., 2010; (7) Goumans and Andersson, 2010; (8) Roser et al., 2001; (9) Atkinson et al., 2004; (10) Madzunkov et al., 2006; (11) Hiraoka et al., 1998; (14) Baulch et al., 2005; (15) Talbi et al., 2006; (17) Cuppen and Herbst, 2007; (18) Miyauchi et al., 2008; (19) Dulieu et al., 2010; (20) Cuppen et al., 2010; (22) Ioppolo et al., 2011; (23) Noble et al., 2011; (24) Taquet et al., 2012; (25) Hiraoka et al., 2002; (26) Watanabe and Kouchi, 2002; (27) Ioppolo et al., 2008; (28) Mokrane et al., 2009; (*) This reaction is based on the ER mechanism. In this reaction oxygen reacts with CO that is already on the surface upon arrival and forms a Van der Waals complex O...CO.

TABLE 6.11: Surface reaction with calculated Eckart model parameters.

network	reactions		V_f [K]	V_r [K]	ω [cm^{-1}]	reference
methanol	CO + H $\longrightarrow$	HCO	1.624(3)	1.264(4)	6.057(2)	(1)
	H_2CO + H $\longrightarrow$	CH_3O	1.299(3)	1.588(4)	7.013(2)	(2)
Water	OH + H_2 $\longrightarrow$	H_2O + H	2.935(3)	1.021(4)	1.293(3)	(3)
	HOOH + H $\longrightarrow$	H_2O + OH	2.508(3)	3.636(4)	1.054(3)	(4, 5)
Carbon dioxide	CO + OH $\longrightarrow$	CO_2 + H	2.850(2)	1.305(4)	2.610(2)	(6)
	CO + OH $\longrightarrow$	tHOCO	2.850(2)	1.305(4)	2.610(2)	(6)
	CO + OH $\longrightarrow$	cHOCO	2.128(3)	1.405(4)	3.790(2)	(6)
	O...CO + H $\longrightarrow$	tHOCO	7.754(2)	1.305(4)	2.610(2)	(6)
	O...CO + H $\longrightarrow$	cHOCO	2.618(3)	1.405(4)	3.790(2)	(6)
	tHOCO $\longrightarrow$	CO + OH	1.305(4)	2.850(2)	2.610(2)	(6)
	tHOCO $\longrightarrow$	cHOCO	4.114(3)	3.272(3)	5.840(2)	(6)
	cHOCO $\longrightarrow$	tHOCO	3.272(3)	4.114(3)	5.840(2)	(6)
	cHOCO $\longrightarrow$	CO_2 + H	1.244(4)	1.290(4)	2.053(3)	(6)

NOTES V_f and V_b are the forward and back potentials in K and ω is the frequency of transition state in cm^{-1}. O...CO is the CO and O van der Waals complex.
(1) Enrique-Romero et al., 2021; (2) Rimola et al., 2014; (3) Nguyen et al., 2011; (4) Ellingson et al., 2007; (5) Koussa et al., 2006; (6) Yu et al., 2001.

TABLE 6.12: The rate constant fitting parameters for methanol formation network using modified Arrhenius formula.

Reaction	t [K]	α [s^{-1}]	β	γ [K]	T_0 [K]	branching ratio
CO + H $\rightarrow$ HCO^a	5–15	1.27×10^6	1.62	-4.35	—	—
CO + H $\rightarrow$ HCO^a	15–30	1.15×10^7	2.72	-20.9	—	—
H_2CO + H $\rightarrow$ CH_3O^b	—	3.14×10^{10}	1.0	830.0	119.6	0.8
H_2CO + H $\rightarrow$ HCO + H_2^b	—	4.13×10^{10}	1.0	1222.0	147.7	0.2

[(a)] The modified Arrhenius formula used here is $k = \alpha(T/300.)^\beta \exp -\gamma/T$, with T the temperature in Kelvin within the temperature range in the second column and α, β, and γ three fitting parameters.
[(b)] The modified Arrhenius formula used here is $\kappa(T) = \alpha\,(T/300)^\beta \exp\left(-\gamma(T+T_0)/\left(T^2+T_0^2\right)\right)$, with T the temperature in K and α, β, and γ the rate constants from SK17, Table 3.

TABLE 6.13: The rate constant fitting parameters for atomic hydrogen and oxygen.

atom	t [K]	α [s^{-1}]	β	γ	K_0
hydrogen^a	1–16.5	9.2×10^2	0.19	-1.7×10^{-2}	—
hydrogen^a	16.5–21	4.7×10^{112}	1.1×10^2	-1.12×10^3	—
Oxygen^b	6.5 - 25	1.	3.	—	1.21

[(a)] The best fit parameters for the function $\kappa(T) = \alpha\,(T/300.)^\beta \exp\,(-\gamma/T)$ within the given temperature ranges;
[(b)] The empirical fit parameters of Oxygen diffusion rate constant for the function $\kappa(T) = K_0/10^{-15} + \alpha(T/10.)^\beta$ from Congiu et al. (2014, Table 1, Figure 3) for no-ASW ices.

6.13 Appendix 5) Binding energies

A selected list of binding energies used in our work are listed in Tab. 6.14.

TABLE 6.14: List of binding energies.

Species	E_{b_x}	E_{b_b}	$E_{b_{ASW}}$	Species	E_{b_x}	E_{b_b}	$E_{b_{ASW}}$
H	$45^{(a)}$	$660^{(b)}$	$349^{(c)}$	HCO			$2198.0^{(g)}$
C			$14100^{(d)}$	H_2CO		$3728^{(k)}$	$4632.5^{(g)}$
N			$720^{(e)}$	CH_3OH	$4235^{(l)}$		$6194.0^{(g)}$
O		$1850^{(f)}$	$1320^{(e)}$	CH_3			$1381.5^{(g)}$
H_2	$45^{(a)}$	$542^{(b)}$	$328.5^{(g)}$	CH_4			$1294.0^{(g)}$
O_2	$912^{(h)}$	$895^{(i)}$	$508.0^{(g)}$	N_2	$800^{(m)}$		$1109.0^{(g)}$
O_3			$2100^{(n)}$	NH_2			$3667.5^{(g)}$
OH			$3436.0^{(g)}$	NH_3	$3075^{(l)}$		$5931.5^{(g)}$
H_2O	$4858.0^{(g)}$		$4858.0^{(g)}$	H_2S			$2814.5^{(g)}$
HOOH			$6000^{(n)}$	OCS			$2213.5^{(g)}$
CO	$856^{(h)}$	$830^{(i)}$	$1792.0^{(c)}$	HCN			$4416.5^{(g)}$
CO_2	$2690^{(j)}$	$2270^{(i)}$	$2218.5^{(g)}$				

NOTES The binding energy (BE) of selected species on different substrates in K. Eb_x on the same substrate, Eb_b on a bare grain, and Eb_{ASW} on an ASW surface.
(a) Pierre et al. (1985); (b) Katz et al. (1999); (c) This work (§ 6.4); (d) Shimonishi et al. (2018); (e) Minissale et al. (2016a); (f) He et al. (2015); (g) Ferrero et al. (2020, Table 3, the median value from the ASW column); (h) Acharyya et al. (2007); (i) Noble et al. (2012b); (j) Sandford and Allamandola (1990); (k) Noble et al. (2012a); (l) Sandford and Allamandola (1993); (m) Bisschop et al. (2006); (n) Dulieu et al. (2013); $(*)$ and the rest of the BEs are from Penteado et al. (2017).

Part III

Labice and its applications

Chapter 7

Modeling ices formed in experimental setups with Labice

Labice is a model aiming to simulating the layered structure formed in an experimental setup and Interstellar ice mantle using rate-equation approach to stay self-consistent with astrochemical codes, such as Grainoble+. Labice aims at extracting the major parameters that characterize the ice, such as the binding energy of the species that constitute the ice, the porosity, and the homogeneity of the ice, the information which can ultimately be used by astrochemical models. Briefly, Labice is a three-phase, multilayer, multi-binding energy, multi-substrate, and multi-phase model. Labice can generate multilayer ices with a random species distribution in the layers. The species composition in each layer is distributed homogeneously. The three phases are the surface consisting of the layer or the layer part(s) that are exposed in the chamber, the bulk consisting of the layer(s) and layer part(s) below the surface, and the gas phase that is the chamber of the apparatus. The model can consider the binding energy distribution of species on a single substrate. It also takes into account the different binding energies relative to various substrates. The model simulates empty fractions homogeneously distributed in a layer to model the porosity.

This code was initially designed as one of the modules of the astrochemical model, Grainoble+, but it grew into a stand-alone model. It uses the same formalism so that it stays self-consistent with astrochemical codes. Like Grainoble+, Labice is also a modular package and provides easy handles to add or remove processes (see, Apx. D for a description of the model's algorithm).

To simulate a laboratory-grown ice with our model, we first need to understand what parameters control its shape and morphology. The following section (§ 7.1) briefly reviews the Temperature Programmed Desorption (TPD) experiments and the ice structure and its morphology evolution under heating. Sec. 7.2 describes the Labice model in detail and Sec. 7.3 shows the impact of the variation of the model parameter on the desorption rates. Chapters 8 and 9 are the two applications of the model.

7.1 TPD experiments

As we have discussed in Sec. 3.1.2, a TPD experiment is designed as follows. The ice is formed by beaming the species onto a cryogenically cooled substrate inside a chamber under Ultra-High Vacuum (UHV) conditions. The deposition flux regulates the ratio between the co-deposited species inside the ice film. After the ice is formed, the temperature increases with a fixed heating rate. The evaporated species can be probed by a quadrupole mass spectroscopy (QMS) apparatus, while the ice constitute can be monitored with a reflection absorption infrared spectra (RAIRS) instrument. The collected data provide information on the morphology and the phase transition kinetics of the ice and the kinetics parameters of the involved species from the desorption rate.

The following sections review the structure of the ice formed in the laboratory, the morphology evolution of ices under heating, crystallization of water ice, and the trapping of volatile species. A summary concludes this section.

7.1.1 The ice structure and porosity

In the laboratories, water ice formed at low temperatures (< 100 K) has a highly interconnected porous structure. Porosity is due to the low mobility of the water molecules. The deposition parameters, such as the deposition angle, surface temperature, and deposition rate, regulate the level of porosity in the ices (Cazaux et al., 2015; Clements et al., 2018; He et al., 2019; Kimmel et al., 2001a). Many experiments and simulations have been conducted to quantify the porosity dependency on the deposition parameters. The following paragraphs review the findings from the works mentioned here.

Kimmel et al. (2001a) conducted a series of TPD experiments to study the morphology of the amorphous solid water (ASW) and crystalline ice (CI). They grew ice films from various deposition angles and ices formed by vapor (background) deposition. To trace the ice slab porosity and structure, they deposited N_2 on top of the ice film and measured its adsorption through the surface. The N_2 molecules diffuse on the surface and fill out the pores. Their study indicated that ices formed at any angle show porous structure to some degree and are highly interconnected. Ices deposited with a normal or close to a normal incident angle ($\lesssim 30^\circ$) are compact and relatively smooth. In contrast, ices formed by wide deposition angles or vapor deposition are less compact and more porous. For example, the N_2 adsorption on a film of ice formed from a 60° incident angle is one order of magnitude larger than the N_2 adsorption on ice grown from a normal angle deposition. They observed similar porosity features in their 3D ballistic simulations (Kimmel et al., 2001b). Kimmel et al. (2001b) Figure 7 (also shown here in Fig. 7.1) shows the density of the ice film as a function of height for simulated 50 ML (monolayers) of ASW ice films grown at different angles. They showed that the larger the incident angle is, the faster the drop in density, indicating an increase in porosity structure. For zero angle deposited ASW, the density remains above 75% up to 50 ML height and then drops rapidly to 70 ML. This simulation suggests that for all deposition angles, ice shows porosity and that the lowest layers are much denser than the top layers. Furthermore, Kimmel et al. (2001a) indicated that at any incident angle, the ice porosity structure does not vary strongly with ice thickness for ices with ML $\gtrsim 25$ and thinner ices have not fully developed the porosity observed in ices $\gtrsim 25$ MLs.

Clements et al. (2018) simulated the morphology evolution of the ice using an off-lattice Monte Carlo kinetics model to investigate the impact of various deposition parameters on the morphology of the ice: deposition angle and rate, and the surface temperature. Their simulations show that ices formed from zero-angle deposition still show porous structure, which increases with an increase in incident angle, similar to Kimmel et al. (2001a). Furthermore, they found that ices created on surfaces with higher temperatures or lower deposition rates are more compact (see, their Figure 4). At higher temperatures, loosely-bound water molecules can diffuse into nearby potential minima more efficiently and create smoother ices. As for the deposition rate, if the deposition rate is higher than the diffusion rate of molecules, they cannot move to a lower energy site before another molecule lands and sticks resulting in a more porous structure. For example, for ices formed with normal angle deposition, the ice formed at 120 K surface temperature is more than a factor of two denser than the one formed at 10 K. Fig. 7.2 shows the simulated ices created under various deposition parameters from Clements et al., 2018. The column and porosity structure of the ice increases by an increase in deposition angle and deposition rate and by a decrease in the surface temperature.

He et al. (2019) created vapor-deposited ices and used CO to probe the porosity. Similar to the previous experiments, their results also show the presence of interconnected porosity in

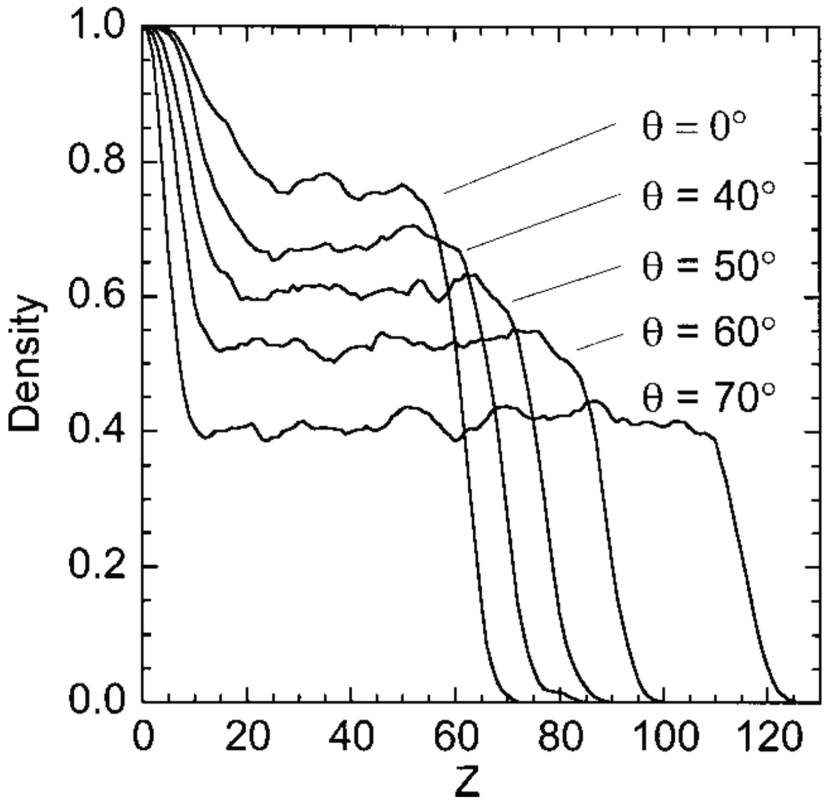

FIGURE 7.1: Figure from Kimmel et al. (2001b). The layer density as a function of height for variety of growth angle. The density decreases with height until it reaches the bulk density and deceases further on the surface layers. The drop in density increases with the growth angle. The surface roughness is measured as the width of the transition from the bulk density to zero.

the ices. Additionally, they used kinetic Monte Carlo simulations to calculate the percentage of surface molecules to the total number of molecules as a function of MLs at 10 K (see, their figure 15, also shown here in Fig. 7.3). The first ∼10 MLs shows a large surface percentage ($\gtrsim$ 25%). The surface percentage decreases smoothly with layer thickness above the 10 MLs. They concluded that the ices above the threshold thickness of $>$ 10 ML seem homogeneous. Therefore, their 200 ML ice films study can be extrapolated to thinner ices down to $\sim$ 10 ML thickness. Their conclusion is in accord with Kimmel et al. (2001a) study, only it differs in the thickness threshold (25 MLs in Kimmel et al., 2001a).

7.1.2 Ice morphology under heating

Heating an ice film changes the morphology of the ice. The ice becomes more compact, less porous and the surface area reduces. Bossa et al. (2012) and Isokoski et al. (2014) showed that a background deposited ice is compacted by $\sim$ 12% while heated from 20 to 120 K. The compaction is less in ices with less porosity and is negligible for crystalline solid water. Isokoski et al. (2014) and Mitterdorfer et al. (2014) showed that while ice becomes more compact, it still retains its porosity. The same effect has also been shown in Cazaux et al. (2015) simulations. They performed a Kinetic Monte Carlo simulation on amorphous ice to simulate the pore evolution in ices as a function of temperature. Their simulation reproduces a background deposited experiment. They showed that the total volume of the pores decreases only slightly,

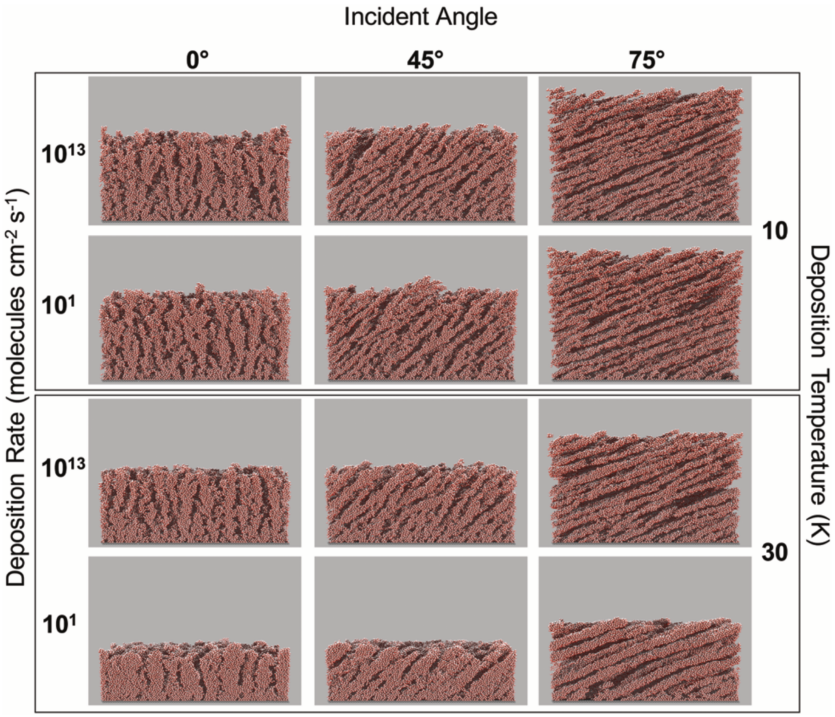

FIGURE 7.2: Figure from Clements et al. (2018). A side-view of simulated ices at different deposition angles, 0°, 45°, and 75°, at two deposition temperatures, 10 and 30 K, and two deposition rates, 10^1 and 10^{13} molecules $cm^{-2}s^{-1}$. Columns of ices are formed in the direction of the deposition angle. The ice porosity increases with an increase in deposition angle, an increase in deposition rate, and a decrease in deposition temperature.

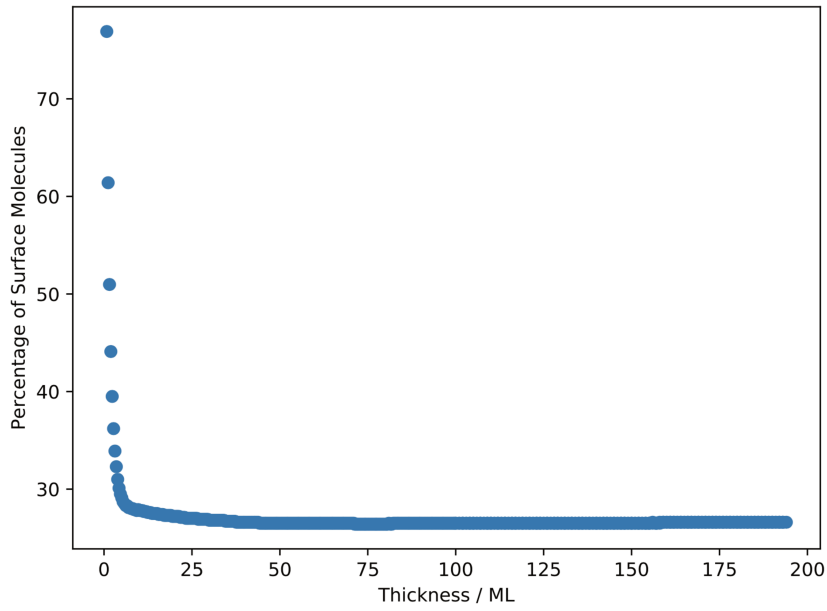

FIGURE 7.3: Figure from He et al. (2019). The percentage of surface molecules as a function of thickness.

which is due to the merger of smaller pores. In contrast, the total surface area decreases significantly (see, their Figure 6), a mechanism that they call pore coalescence. He et al. (2019) shows similar results (see, their Figure 14). They also indicate that the ice porosity does not

completely disappear after being heated, which is in agreement with Kimmel et al. (2001a) conclusions.

7.1.3 Water ice phase transition (Crystalization)

ASW is formed from the coalescence of water molecules on a cooled surface at temperatures lower than $\sim$ 130 K. ASW is in a kinetically metastable state. It means that when heated or left in an isothermal state for an extended period, ASW transforms to a thermodynamically stable state, crystalline ice (Alan May et al., 2013; May et al., 2013). Crystallization nucleates at random positions in the ice and grows isotropically in all directions. Therefore, it induces cracks that propagate through the ice slab. The crystallization growth can be parametrized using an integrated form of the Avrami equation

$$x(t) = 1. - \exp\left(-\langle \kappa^n(t) \rangle\right), \tag{7.1}$$

where $x(t)$ is the crystallized fraction in the ice as a function of time, n is a crystallization parameter equal to 4 for spatially random nucleation and isotropic 3-dimentional growth mechanism of crystalline ice, and $\kappa(t)$ is the Arrhenius rate constant given by

$$\langle \kappa(t) \rangle = \int_0^t \kappa(\tau) \mathrm{d}\tau, \tag{7.2}$$

for a linearly heated experiment with a heating rate $\beta = \mathrm{d}T/\mathrm{d}t$ (Smith et al., 2011). Crystallization manifests itself in the desorption rate of water as a function of time as a small bump before the desorption peak (see, for example, Figure 1 in Smith et al., 2011).

7.1.4 Trapping of volatile species

The experiments carried out by Collings and collaborators showed that the desorption behavior of mixed ices is, in fact, not straightforward (Collings et al., 2003; Collings et al., 2004). They argue that volatile species, such as CO, O_2 or N_2, become physically entrapped due to the change in water ice morphology and closing of pores in ices (see, also, Ayotte et al., 2001; Horimoto et al., 2002). The trapped volatile species can evaporate at two possible 'events'. First, when water crystallizes, some of the trapped molecules can escape due to the crystallization-induced crack formation. Second, when the crystalized water-ice evaporates, the remaining trapped volatile species can evaporate alongside them. The first phenomenon is known as volcano desorption (Smith et al., 1997). The volcano desorption peak aligns with the crystallization bump of water. The second phenomenon is known as the co-desorption effect (Collings et al., 2004). The co-desorption peak is aligned with the desorption peak of water. The trapped fraction (the intensity of the co-desorption peak) increases with water film thickness. May et al. (2013) experiments on water mixes with Ar, Kr, Xe, CH_4, N_2, O_2, and CO show that while the fraction increases with water thickness, it starts to eventually plateau, showing a sigmoidal behavior. The same behavior is seen in Kruczkiewicz et al. 2022 (in prep.) experiments with water and CO mix ices. I discuss more on those experiments and the simulations I have done in the next chapter (Chap. 8).

7.1.5 In summary

Many working groups have conducted experiments and simulations to quantify the ice structure formation as a function of the deposition parameters and quantify the kinetics of the ice morphology evolution and phase transition under heating. Here, we briefly summarize the

key concluding points from the experiments and simulations on the ice morphology discussed in the previous sections.

ASW ice grown under any condition shows some degree of porosity. The porosity increases with an increase in the incident angle and the surface temperature and a decrease in the deposition rate. The porosity structure in thick ices ($\gtrsim 10-25$ MLs, depending on the study) decreases slightly with an increase in the ice thickness. In contrast, thinner ices show an exceptionally high surface area, indicating that the ice structure is somewhat irregular and the porous structure observed in thicker ices is not fully developed. Furthermore, The ASW ice under heating becomes denser but retains its porosity. The change in morphology under heating physically entraps volatile species in mixed ices, which are released during the water transition phase (ASW to CI) due to the formation of crystallization-induced cracks and when the water starts to evaporate itself. The fraction of the trapped volatile species increases with water thickness.

7.2 The Labice ice model

Labice simulates a TPD experiment using the rate equation approach with a few input parameters: the distribution of species and porosity over the layers, the starting temperature, and the heating rate. The model can assume a distribution of binding energies relative to a given substrate for a species (see, Chap. 9, as investigating the impact of this parameter is one of the Labice applications).

Labice simulates a multi-layer ice analogue, where each layer corresponds to one ML in the TPD experiments[1]. It assumes that the species are homogeneously distributed in each layer. The ice layers can be modeled in two ways: (1) Each layer composition is specified in the input parameters, or (2) only the total deposition of the species is specified in the input parameter.

The first case is simple. The model simulates an ice layer structure based on the input layer fractions without further assumptions.

In the second case, the model assumes that the species are randomly distributed over the layers, while the bulk ratio between the co-deposited species is fixed. The ratio in each layer is the given bulk ratio with a deviation drawn from a uniform distribution equal to a scaling factor. The scaling factor in our model is an input parameter called the stochasticity parameter. It is defined as a percentage of 1 ML in the model, the stochastic mixing of the molecules in each layer. Stochasticity is a deviation from the deposition ratio in each layer. It tells us how to distribute the species in dual-composite ices in multi-layer models. Physically, it tells us how the two components are mixed in each MLs, how homogeneously the species are distributed in each MLs. The second case is designed to simulate the stochastic distribution of molecules over the layers in an laboratory-grown ice. Fig. 7.4 shows three ice model examples of H_2O:CO composition with a 3:1 ratio. The layer distribution from left to right uses 2%, 10%, and 20% stochasticity factors.

Our models mostly simulate a TPD experiments in which the species are deposited from zero-angle incident beaming (Chap. 8) or an interstellar grain mantle analog (Chap. 9). These ices are compact and show a small porosity structure. Nevertheless, the model can assume, as an input parameter, empty fractions in the layers that are homogeneously distributed. The empty fractions in our model simulate the pores inside the ice.

In the present version of the model the ice morphology does not change, during the TPD modeling. It means that the model does not simulate compaction and diffusion. Only the surface is exposed in the chamber and available for thermal desorption at each iteration. The evaporation of the surface composition exposes the lower layer parts.

[1] One ML of ice typically consists of 10^{15} molecules per square centimeter.

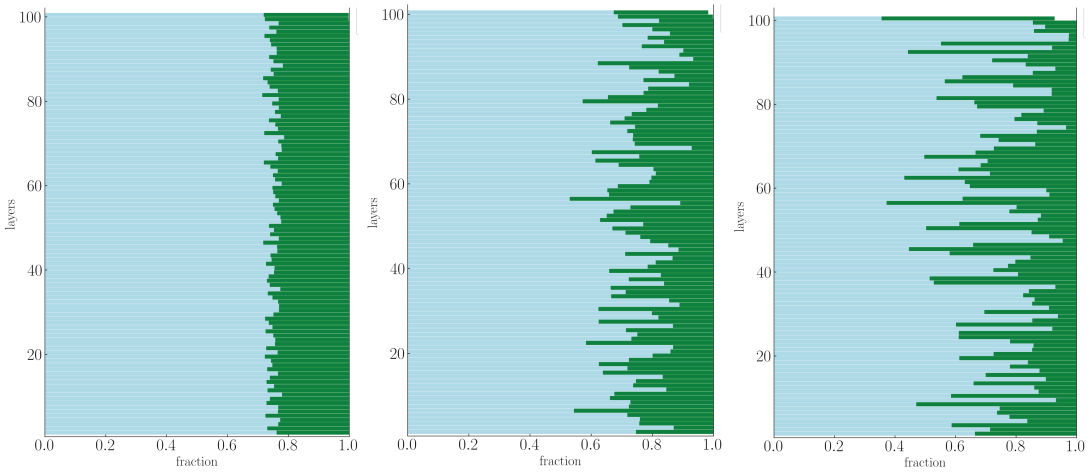

FIGURE 7.4: A depiction of the layers with H_2O:CO composition in blue and green in the Labice model. The water to CO overall ratio is 3:1, and the stochasticity levels from left to right are 2%, 10%, and 20%.

TABLE 7.1: The CO and H_2O binding energies on different substrates.

species	ν_0 [s^{-1}]	Eb [kj/mol]	substrate	reference
CO		9.8 ± 0.2	H_2O	(1)
CO		7.1 ± 0.1	CO	(3)
H_2O	$1.1 \times 10^{+18}$	54.54	H_2O	(2)
H_2O	$1.3 \times 10^{+18}$	55.89	H_2O (CI)	(2)

CI: crystalline ice; (1) Burke and Brown (2010), Table 1, 2, and 3; (2) Smith et al. (2011), table 2; (3) Acharyya et al. (2007), Table 2.

The model solves the rate equation as a function of time for the species in the gas phase and on the surface. The rate equations in a general case are as follows.

$$\begin{aligned} \frac{\mathrm{d}\, n_{\mathrm{gas}}}{\mathrm{d}\, t} &= \kappa_{\mathrm{thdes}} n_{\mathrm{x}}^{\mathrm{s}} \,, \\ \frac{\mathrm{d}\, n_{\mathrm{x}}^{\mathrm{s}}}{\mathrm{d}\, t} &= -\kappa_{\mathrm{thdes}} n_{\mathrm{x}}^{\mathrm{s}} \,, \end{aligned} \tag{7.3}$$

where n_{gas} and n_{x} denote the gaseous and solid species fractional abundances, s superscript denote that the species is on the surface, and

$$\kappa_{\mathrm{thdes}} = \nu_0 \exp\left(\frac{-E_{\mathrm{b}}}{k_{\mathrm{b}} T}\right) . \tag{7.4}$$

is the thermal desorption rate coefficient with a pre-factor ν_0 and surface temperature T.

7.3 The impact of parameter variation

This section discusses the impact of the parameter variation on the desorption rates of water and CO using Labice. In these simulations we used the binding energies listed in Tab. 7.1.

ML regime, varying the number of MLs

We simulate ASW at 10 K on a water substrates that is heated at the rate of $\beta = 0.2$ K/s. We varied the thickness from 1 to 7 MLs. Fig. 7.5 shows the desorption rate [ML/s] of water ices with various number of MLs. The increase in water thickness shifts the desorption peak to higher temperature, while the onset of desorption starts at $\sim$ 140 K for all the models.

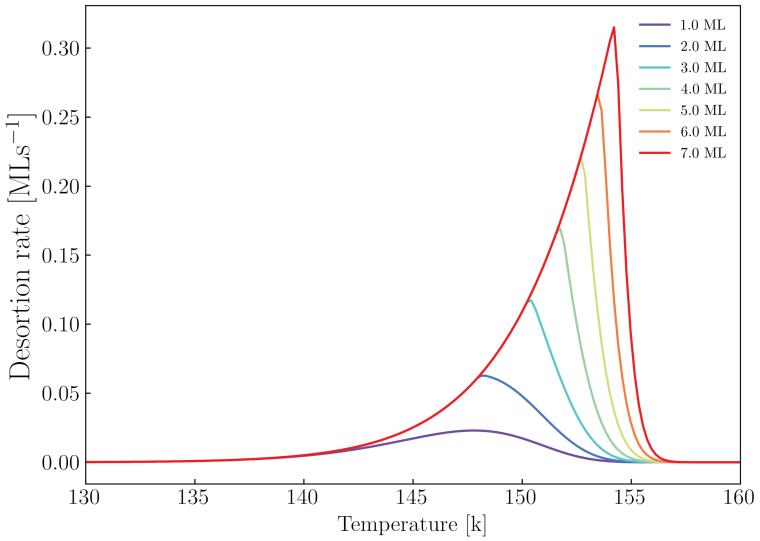

FIGURE 7.5: The desorption rate of water ice deposited at 10 K and heated at a rate of 0.2 K/s for ices with different number of MLs, from 1 (purple) to 7 (red) MLs.

ML regime, varying the heating rate

In the second case, we varied the heating rate from 0.001 to 3.0 K/s for 10 ML ASW ices. Fig. 7.6 shows the desorption rate [ML/K] of these models. The peak of desorption shifts to higher temperatures as the heating rate increases.

CO desorption in the Sub-ML regime

We simulated the desorption of CO from a ASW substrate in the subML regime. CO was deposited at 10 K and heated with a rate of 0.2 K/s. The CO thickness varies from 0.2 to 1.4 MLs (Fig. 7.7 provides a simple depiction of the 1.4 MLs ice structure). The left panel in Fig. 7.8 shows the desorption rate of CO in the various experiments conducted by Kruzckiwiecz and collaborators. The right panel shows the Labice simulations. The double peaks appearing for 1.15 and 1.4 MLs in the simulation and in the curve associated with 1.4 MLs in the experiments are due to the change of CO binding energies from a CO substrate to a ASW substrate.

The first CO desorption peak in the simulations is slightly shifted comparing with the first peak of CO desorption in the experiments. The reason is that the model uses the CO BE on a CO substrate from Acharyya et al. (2007) results instead of deriving them from the experimental data themselves (this will be the focus of a forthcoming work). The broadening in the peaks in the experiments is due the distribution of BEs of CO on the amorphous substrate. In the simulations we have used single BE on each substrate. However, the models did not reproduce the merging of the peaks in the 1.4 MLs simulation, or the shift of the second peaks from 0.2 to 1.4 MLs. It can be due to the fact that thin ices in experiments have a high surface

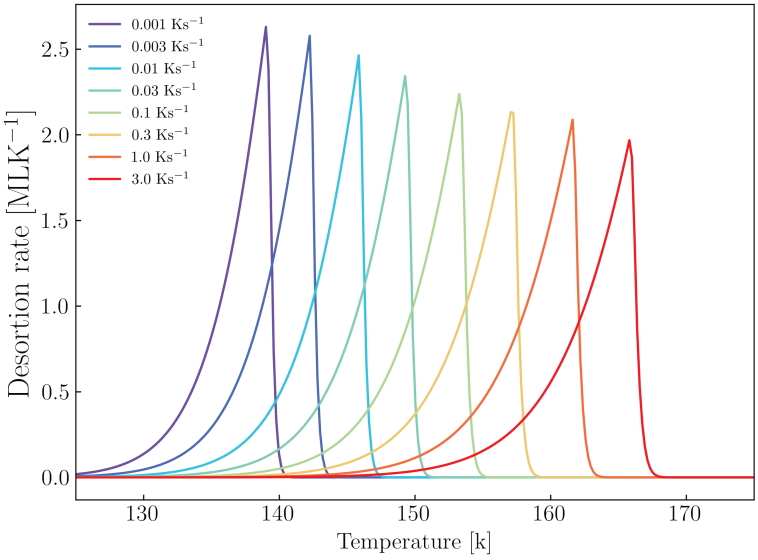

FIGURE 7.6: The desorption rate [ML/K] of water ice with 10 ML deposited at 10 K by varying the heating rate from 0.001 to 3.0 K/s.

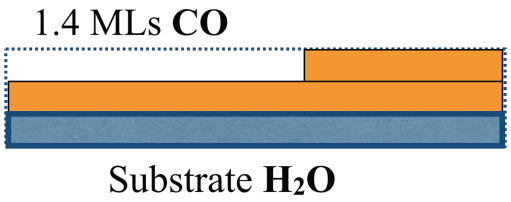

FIGURE 7.7: A depiction of 1.4 MLs of CO on a water substrate.

area which indicates that the shape of the ice is not regular and does not have the porous structure seen in thicker ice models (see, e. g., He et al., 2019; Kimmel et al., 2001b), while our models assumes a simple layer structure (see, Fig. 7.7 and Sec. 7.1). The comparison between experiments and simulations are described in detail in Chap. 8.

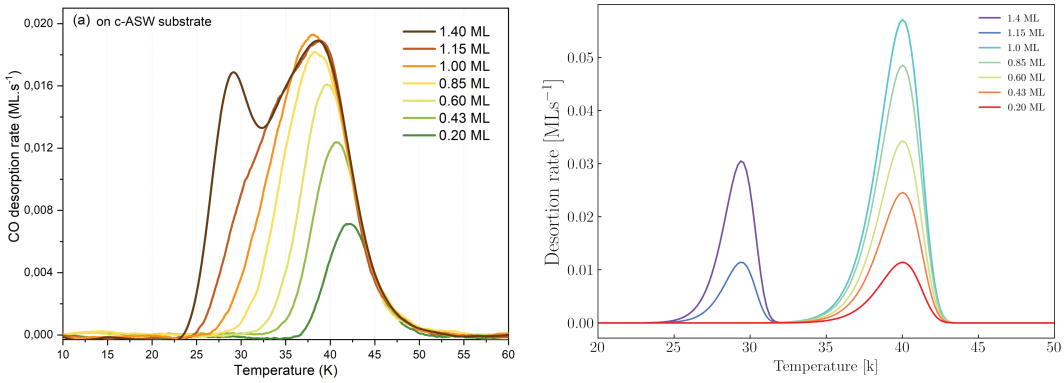

FIGURE 7.8: The desorption rate of CO from a water ice experiments (left) and Labice (right) simulations on sub ML regime. The experiments were done by F. Kruczkiewicz and collaborators.

Chapter 8

Application I: The fraction of CO trapped in ices: experimental versus Labice simulations

As mentioned in Chap. 7, Labice is designed to simulate ice analogues formed in experiments. It uses the rate-equation approach similar to astrochemical models, such as Grainoble+, to stay self-consistent with astrochemical models.

This chapter describes the modeling of the CO trapped fraction in water and CO mixed ices. We focus on simulating the CO trapped fraction from the TPD experiments carried out by Kruczkiewicz and collaborators (Kruczkiewicz et al. 2022, in prep., hereafter Kr2022) with Labice model described in Chap. 7.

The following sections describe the experiments carried out by Kr2022, the simulations of the ice with the Labice model, the results, and the discussion and conclusion.

8.1 Kruczkiewicz and collaborators TPD Experiments

Kr2022 conducted a series of TPD experiments in UHV conditions using TPD techniques and a RAIRS apparatus monitoring the ice composition. The series of experiments were designed with increasing complexity in a controlled way to allow the astrochemical models to use them for benchmarking purposes. Thirteen experiments were conducted with H_2O:CO composition mix with various total thicknesses, from 3 to 83 MLs, summarized in Tab. 8.1. They used a zero-angle incident beaming to co-deposit the H_2O and CO onto a gold substrate at 10 K. The co-deposition ratio of H_2O:CO in 6 experiments is 3:1, and 2:1 in the rest. In all the experiments, the ice is warmed up with a heating rate of 0.2 K/s until the ice was fully evaporated. Their TPD results show that a fraction of the CO remains trapped inside the ice until it evaporates during the crystallization and evaporation of the water molecules. Fig. 8.1 shows the desorption rates of H_2O:CO as a function of temperature for four of the experiments corresponding to experiments 1, 6, 7, and 13 in Tab. 8.1.

We define the trapped fraction of CO with respect to the total CO, $f_{CO} = CO_{trp.}/CO_{total}$, that desorbs with water ice (ASW or CI). In other words, the trapped fraction is the amount of CO that is desorbed integrated over the volcano and co-desorption peaks. The red and the blue points in Fig. 8.2 show the measured trapped fraction as a function of water thickness for ices with 3:1 (red) and 2:1 (blue) composition ratio listed in Tab. 8.1. In the Kr2022 experiments, the trapped fraction of CO increases with an increase in ASW thickness and starts to plateau in ices with water thickness above $\sim$40 ML, showing a sigmoidal behavior. This behavior has been seen in both (3:1) and (2:1) ratio ice experiments, which indicates that the trapping efficiency of ASW increases with thickness and eventually plateaus in thicker ices. To reproduce the trapped CO fraction f_{CO} measured in the experiments described above

TABLE 8.1: Summary of the Kr2022 experiments on H_2O + CO ice composites.

Number	Ratio	H_2O [ML]	CO [ML]	Total thickness [ML]
1	3 : 1	3.36	1.04	4.40
2		6.00	2.00	8.00
3		9.45	3.20	12.65
4		19.70	6.95	26.65
5		36.55	12.25	48.80
6		61.70	21.15	82.85
7	2 : 1	1.82	0.93	2.75
8		3.55	1.70	5.25
9		6.55	3.70	10.25
10		9.20	4.55	13.75
11		15.44	6.96	22.40
12		20.95	11.65	32.60
13		40.50	19.10	59.60

The 2nd column shows the co-deposition ratio between water and CO. The 3rd, the 4th, and the 5th columns shows the total deposited water, CO, and the sum of the two in unit of ML.

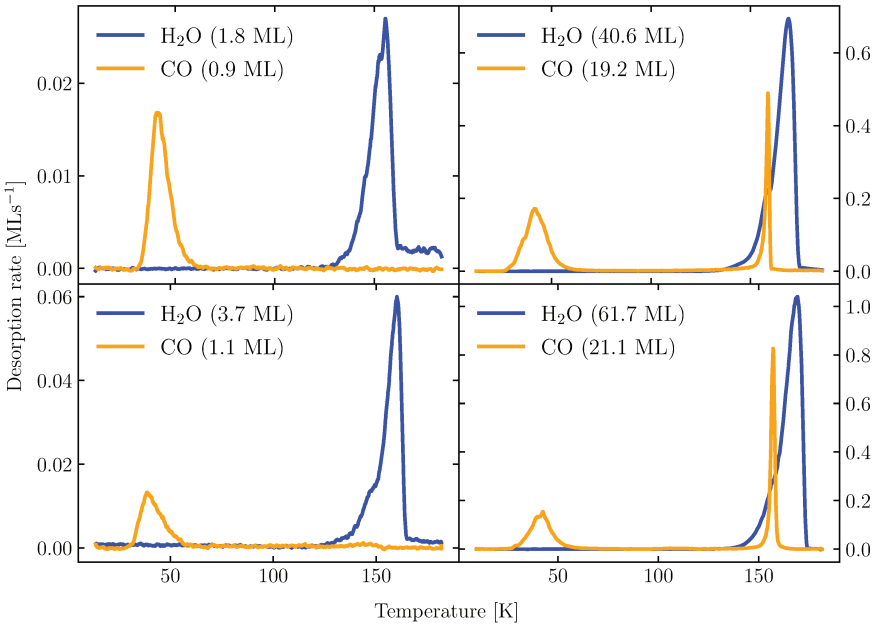

FIGURE 8.1: The desorption rate of a mix of H_2O:CO (in blue and orange, respectively) as a function of temperature with different thicknesses as measured by Kr2022. The corresponding number of the experiments in Tab. 8.1 from left to right and top to bottom are 1, 6, 7, and 13. The composition ratio in the top two panels is 3:1 and 2:1 in the bottom two. Note that the y-axis scale in the four panels is not the same.

(§ 8.1), we fitted the experimental results with a sigmoidal-like curve

$$y = \alpha\,(1. - \exp(-\beta a))\ , \tag{8.1}$$

where y is the trapped fraction, a is the H_2O thickness in ML and α and β are the fitting

parameters (see, also, May et al., 2013). The best fit of the curves for ices with 3:1 ratio gives, $\alpha = 0.55$ and $\beta = 0.06$ (shown in red in the Fig. 8.2), and for ices with 2:1 ratio, $\alpha = 0.38$ and $\beta = 0.08$ (in blue in the Fig. 8.2).

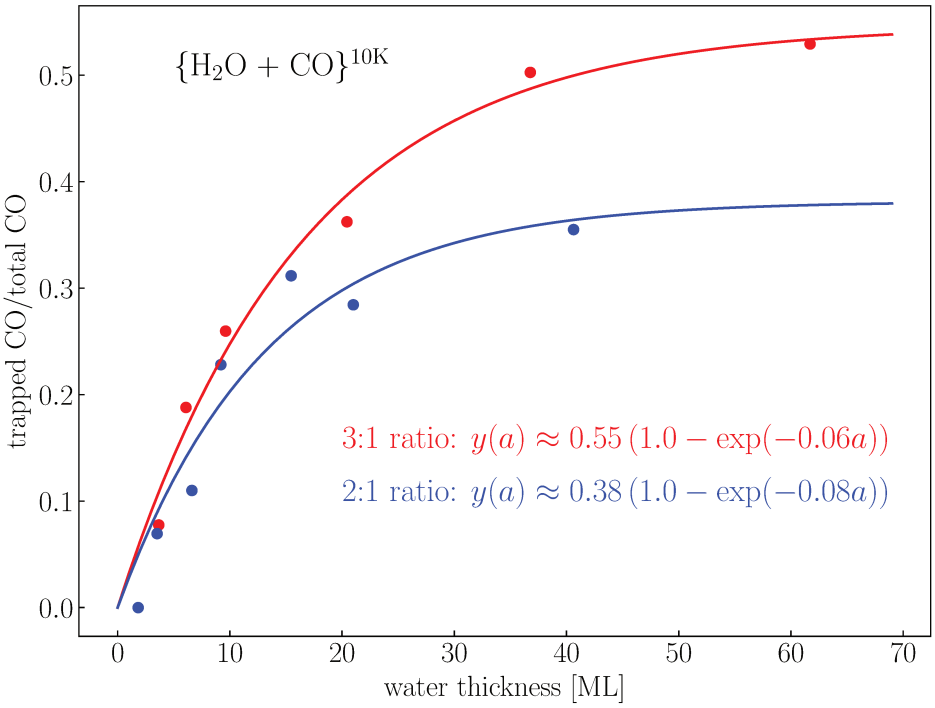

FIGURE 8.2: The CO trapped fraction in H_2O:CO ices with 3:1 (red) and 2:1 (blue) ratios as a function of water thickness in MLs. The solid curves are the fitted functions (Eq. 8.1) for the two sets.

8.2 Simulations of the CO trapped fraction

We ran a series of models simulating conditions similar to Kr2022 experiments (Sec. 8.1): Ices with H_2O:CO composition formed on a substrate with 10 K and warmed up on a linear heating ramp with $\beta = 0.2$ K/s. We did not include water phase transition in these models because it does not change the fraction that becomes trapped inside the water ice.

We ran two sets of models with 3:1 and 2:1 ratios without any porosity parameter. For each set, we varied the total number of MLs from 1 to 100 MLs and the stochasticity levels from 1 to 25 %. We ran in total $>$ 50000 models to show the spread and increase our statistics. The distribution over the layers in each ice was created as a function of stochasticity parameter following the random uniform distribution model described in Sec. 7.2.

Fig. 8.3 and Fig. 8.4 shows the CO trapped fraction as a function of the H_2O thickness for ices with 3:1 and 2:1 ratio, respectively. The panels from left to right and top to bottom show the models with 2, 5, 10, and 20% stochasticity levels, in each figure. The figure shows that: (1) one single stochasticity parameter for all the models cannot reproduce the CO trapped fraction fitted curve; (2) in ices with $\gtrsim$ 8 MLs water thickness, it seems that models with lower stochasticity parameters better reproduce the experimental fitted function; and (3) in ices with $\lesssim$ 8 MLs water thickness in our models, there seems to be no dependency on the stochasticity parameter.

To better understand this behavior, we find the minimum χ^2 among the models with the same water thickness and composition ratio and different stochasticity percentage. Fig. 8.5

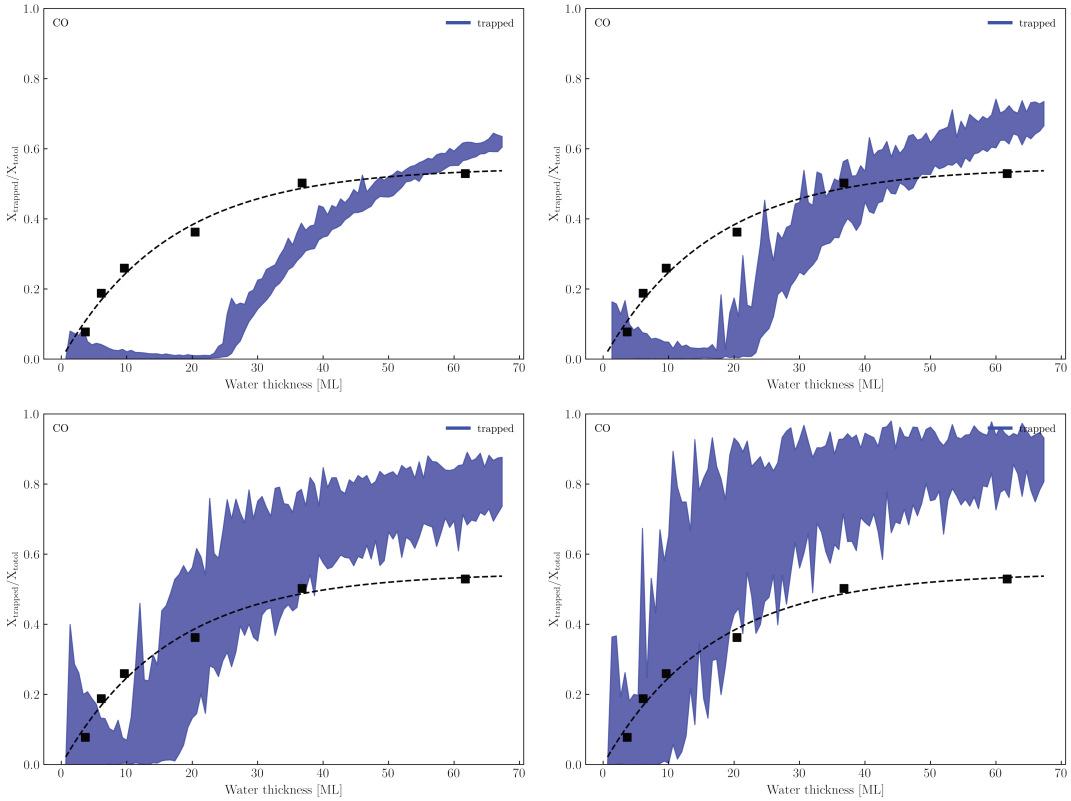

FIGURE 8.3: CO trapped fraction as a function of water thickness (in MLs) for H_2O:CO 3:1 ratio ices with different stochasticty levels: 2% (top left), 5% (top right), 10% (bottom left), and 25% (bottom right). The black points are the measured CO trapped fractions of kr022 experiments. The dashed black curve is the fit of the experimental data. The blue colored areas are the trapped fraction from the Labice simulations. .

shows the model stochasticity percentage that show the minimum χ^2 as a function of water thickness for both sets of experiments (3:1 ratio ices on the left and 2:1 ratio ices on the right). In ices with water thickness $\gtrsim$ 8 MLs, the stochasticity percentage decreases from 25% to 1 % with water thickness. For ices with water thickness below $\sim$8 MLs the situation is more complex. We will discuss the the implications of the results in the next section (Sec. 8.3).

8.3 Discussion and conclusions

We have simulated the TPD experiments carried out by Kr2022 with H_2O:CO composition with 3:1 and 2:1 ratios with Labice. The goal of the simulations is to reproduce the CO trapped fraction. We calculated the CO trapped fraction for each model (Fig. 8.3 and 8.4). Fig. 8.5 shows the stochasticity percentage of the models that best reproduced the CO trapped fraction as a function of water thickness.

We discuss the implications of our simulations in two regimes, above 8 MLs water thickness and below it.

As for thinner ices, while Fig. 8.5 shows that below $\sim$ 8 MLs water thickness, the stochasticity decreases with a decrease in water thickness, Fig. 8.3 and 8.4 show that higher stochastic percentages could also reproduce the trapped fraction. It shows that our models, under the assumption of no porosity, cannot conclusively reproduce the trapped fraction for ices with water thickness below $\sim$ 8 MLs. It may suggest that these ices do not have a regular porous

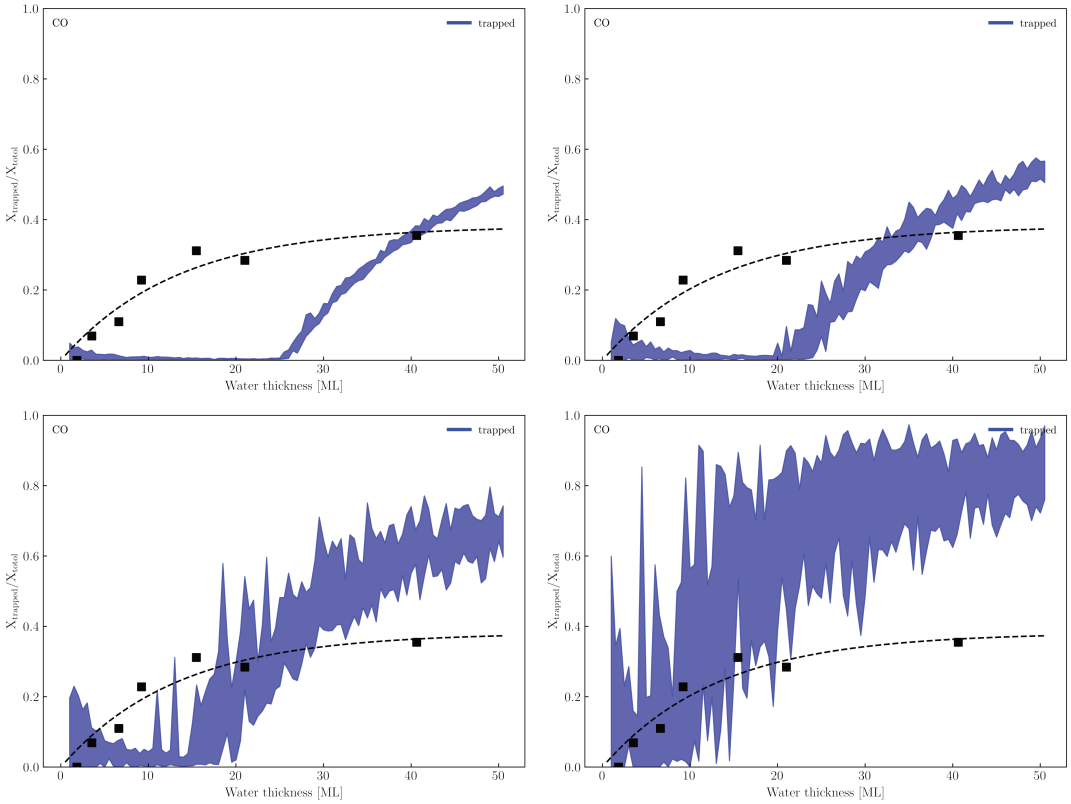

FIGURE 8.4: Similar to Fig. 8.3, but for ices with 2:1 water and CO ratio.

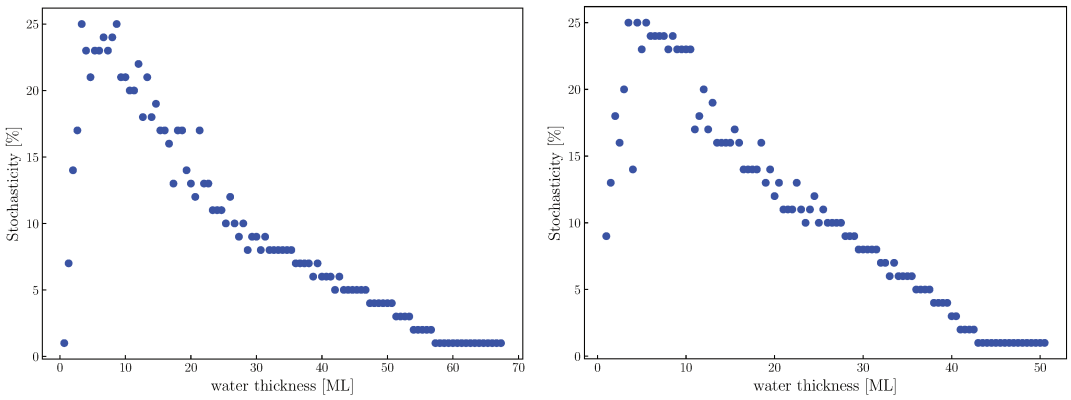

FIGURE 8.5: The best fit stochasticty percentage as a function of water thickness (in MLs) for ices with H_2O:CO composition and 3:1 (left) and 2:1 (right) ratios, respectively.

structure (as seen in thicker ices) and show a high surface area, similar to the conclusions of He et al. (2019) and Kimmel et al. (2001a)

Out simulations indicate that the stochasticity percentages decrease with water thickness above $\sim$ 8 MLs from $\sim$ 25% to $\sim$ 1%. This result may indicate that the stochasticity may be dependent to the water thickness. It could mean that the ratio between water and CO in each layer does not deviate largely from the co-deposition ratio and this deviation decreases with water thickness. It may indicate that the homogeneity in water and CO mixing over the layers increases with water thickness.

Previous experiments and simulations have shown that ices grown at zero incident angle are rather compact. He et al. (2019) simulations have shown that water ices above $\sim$ 10 MLs

have small surface area percentage that decreases slowly with water thickness. These experiments and simulations were done on water ices without mixing. Our results may suggest that water ice mixtures (in this case, with CO) above a threshold of $\sim$ 8 MLs water thickness (corresponding to $\sim 10-12$ MLs total thickness) may also have a compact and low porous structure in which the water and CO mixture are increasingly more homogeneously distributed over the layers, similar to He et al. (2019) results, which shows that the effective surface area decreases with an increase in the number of MLs.

The results show that porosity and diffusion of the molecules and the mergers of the pores can be highly influential factors in the model even in compact ices formed with zero-angle beams and should be taken into account in the models. It is also important to not only compare the results with experiments but also with Monte Carlo simulations to create a more reliable model that can be used to extract static and kinetic parameters from experiments, which then can be used in astrochemical models. Inclusion of porosity is the next step in our models to understand their impact on the results.

Chapter 9

Application II: Binding Energies of Interstellar Molecules on Crystalline and Amorphous Models of Water Ice by Ab Initio Calculations

In this chapter, we present the work published in Ferrero et al. (2020) in collaboration with Stefano Ferrero, Lorenzo Zamirri, Cecilia Ceccarelli, Albert Rimola, and Piero Ugliengo. The following paragraphs present a summary of the work.

I have contributed in the astrochemical modeling and implications (Sec. 9.5.2) and the relevant discussions and conclusions part of the paper (Sec. 9.6) . This chapter starts with a summary of the published work and follows the paper.

Context The near-infrared observations of dense cold cores in the ISM show the presence of sub-micron dust grains enveloped with icy mantles. The ice is comprised mainly of water that is mixed with other volatile species in smaller quantities. A precise evaluation of a species binding energy (BE) is crucial for astrochemical models to reproduce the observations since BEs govern sublimation and diffusion rates of species on ice surfaces. BEs can be inferred from experiments or by theoretical computations.

The BE computations We calculate the BE of 21 astrochemically relevant species (including 4 radicals) using quantum computational methods (Fig. 4). To mimic the nature of an interstellar grain ice surface, we consider both crystalline (Fig. 1) and amorphous surface (Fig. 2 and 3) models using a periodic approach. We also fully consider the hydrogen bond cooperativity in small ice clusters. We used Density Functional Theory (DFT) methods to predict the system (the surface and the species) structure and BEs,.

We simulated the structure and the adsorption energetic features of the 21 molecules. The simulations show that ASW surfaces show a wide variety of adsorption binding sites, while crystalline surfaces show a limited range in comparison (Fig. 9 and Tab. 1 and 2). The spread in the distribution depends on the ice surface structure and the absorbate position, which results in a distribution of BEs on an ASW surface. A crystalline surface is denser than an ASW surface; therefore, the interaction network is tighter. It results in a smaller geometry relaxation cost upon adsorption than an ASW system. Due to this behavior, the computed BEs on a crystalline slab are generally higher than those on an ASW one.

Comparison with the values in the literature The obtained BEs mostly agree with the values derived from experiments, except for O_2 and to a lesser extend H_2 (Tab. 3 and Fig. 11). Our O_2 BE is lower from experiments values. We also compared our results with the work of Wakelam et al. (2017) and Das et al. (2018) that simulated surfaces with 1 and 6 water

molecules, respectively. The periodic approach in our ice model allows us to consider the hydrogen bond cooperativity. It enhances the interaction strength of the adsorbate and the terminal dH atoms exposed on the surface. The two mentioned theoretical works did not account for this effect, which could explain the discrepancy in the results. For example, in our results, the CH_3CN and HCOOH BE are larger, whereas the H_2 and O_2 BE are comparatively lower. We arrive at similar conclusions comparing our results to the KIDA and UMIST databases, as both are collections of experimental and previous theoretical works.

Astrochemical implications We developed a toy model to show the potential impact of assuming multi-BEs in astrochemical models. The goal of the simulations is not to compare with the TPD experiments or observations but to show the impact of the different BE on the sublimated species. This toy model simulated a 10 layered ice of water and methanol composite. The bottom five layers consist only of water, while the top five layers contain 20% methanol and 80% water. The layered structure of the ice means that at any given time, only the species that are exposed and available for sublimation. The layers below remain trapped until the one(s) above sublimate. We run two simulations. The first assumes a normal distribution of BEs calculated in our work for each species, CH_3OH and H_2O, and the second uses a single BE from the KIDA database for each one. In these simulations, we increase the temperature from 10 K to 400 K over 10^5 years to mimic the heating rate of a collapsing solar-like protostar. Fig. 12 shows the desorption rate of the two simulations in solid and dashed lines (normalized to 1 in the lower subplot). The simulation with single BEs show one desorption peak at $\sim$ 110 K for water and two for methanol at $\sim$ 95 K and $\sim$ 110 K. The methanol peaks correspond to sublimation of non-trapped molecules and those co-desorbed with water ice, respectively. The multi-BE simulation shows multiple peaks for both species extending from $\sim$ 75 to $\sim$ 190 K, resulting from the multi-BE assumption.

As mentioned before, this model aims to demonstrate the impact of assuming multi-BEs in astrochemical models. We considered a normal distribution of BEs, but in reality, this distribution depends on the structure and composition of the surface. Compared to single BE simulations, we can conclude that the distribution of BEs may be the reason species can be present in the gas phase at temperatures lower than what is expected from astrochemical models assuming single BEs.

Discussion and conclusions In this work, we computed the BE of 21 astrochemically relevant molecules on ASW and crystalline ice slabs using quantum computational DFT methods. The results show that due to the spread of binding sites on ASW ice, the BEs for each species show a distribution. The new CO and N_2 BEs might explain why N_2H^+ depletion is later than CO in prestellar cores. Our results show that HCl dissociates on the water ice surface. It could explain the low abundances observed in protostellar sources. Our new model does not allow us to estimate the distribution function of BEs for each species. A statistical study is necessary for such estimation. The present study shows the importance of theoretical binding energy calculations on ice surfaces simulated as realistically as possible since they significantly impact astrochemical model predictions. More such studies need to be done to include more molecules used in the astrochemical models to understand the chemical evolution of the ISM better.

9.1 Abstract

In the denser and colder ($\leq$20 K) regions of the interstellar medium (ISM), near-infrared observations have revealed the presence of sub-micron sized dust grains covered by several layers of H_2O-dominated ices and "dirtied" by the presence of other volatile species. Whether a molecule is in the gas or solid-phase depends on its binding energy (*BE*) on ice surfaces. Thus, *BEs* are crucial parameters for the astrochemical models that aim to reproduce the observed evolution of the ISM chemistry. In general, *BEs* can be inferred either from experimental techniques or by theoretical computations. In this work, we present a reliable computational methodology to evaluate the *BEs* of a large set (21) of astrochemical relevant species. We considered different periodic surface models of both crystalline and amorphous nature to mimic the interstellar water ice mantles. Both models ensure that hydrogen bond cooperativity is fully taken into account at variance with the small ice cluster models. Density functional theory adopting both B3LYP-D3 and M06-2X functionals was used to predict the species/ice structure and their *BEs*. As expected from the complexity of the ice surfaces, we found that each molecule can experience multiple *BE* values, which depend on its structure and position at the ice surface. A comparison of our computed data with literature data shows agreement in some cases and (large) differences in others. We discuss some astrophysical implications that show the importance of calculating *BEs* using more realistic interstellar ice surfaces to have reliable values for inclusion in the astrochemical models.

9.2 Introduction

The presence of molecules in the extreme physical conditions of the interstellar medium (ISM) was considered impossible by astronomers, until the first diatomic species (CN, CH and CH^+) were detected in the ISM from optical and ultraviolet transitions (Douglas and Herzberg, 1942; McKellar, 1940; Swings and Rosenfeld, 1937). Nowadays more than 200 gaseous molecular species (including radicals and ions) have been identified in the diffuse and dense regions of the ISM, thanks to their rotational and vibrational lines in the radio to Far-Infrared (FIR) wavelengths (e.g. see the review by McGuire, 2018). In the coldest ($\leq$20–90 K) and densest ($\geq 10^3$ cm^{-3}) ISM, some of these molecules are also detected in the solid state via Near-Infrared (NIR) observations (e.g. see the review by Boogert et al., 2015b).

We now know that the solid-state molecules are frozen species that envelop the sub-micron dust grains that permeate the ISM and whose refractory core is made of silicates and carbonaceous materials (e.g. Jones, 2013; Jones et al., 2017). The grain iced mantles composition is governed by the adsorption of species from the gas phase and by chemical reactions occurring on the grain surfaces. For example, the most abundant component of the grain mantles is H_2O, which is formed by the hydrogenation of O, O_2 and O_3 on the grain surfaces (e.g. Dulieu et al., 2010; Hiraoka et al., 1998; Oba et al., 2012).

The water-rich ice is recognized from two specific NIR bands at about 3 and 6 μm which are associated with its O-H stretching and H-O-H bending modes, respectively (e.g. see the review by Boogert et al., 2015b). In addition, species like CO, CO_2, NH_3, CH_4, CH_3OH and H_2CO have also been identified as minor constituents of the ice mantles, which, for this reason, are sometimes referred to as "dirty ices" (Boogert et al., 2015b). Furthermore, the comparison between the astronomical spectroscopic observations and the laboratory spectra of interstellar ice sample analogous, principally based on the O-H stretching feature, has shown that the mantle ices very likely possess an amorphous-like structure resembling that of amorphous solid water (ASW) (e.g. Boogert et al., 2015b; Oba et al., 2009; Watanabe and Kouchi, 2008b).

Ice surfaces are known to have an important role in the interstellar chemistry because they can serve as catalysts for chemical reactions which cannot proceed in the gas phase, such as the formation of H_2, the most abundant molecule in ISM (Hollenbach and Salpeter, 1971). Ice surfaces can catalyze reactions either by behaving as: i) passive third body, this way absorbing part of the excess of energy released in the surface processes (adsorption and/or chemical reaction) (e.g. Pantaleone et al., 2020); ii) chemical catalyst, this way directly participating in the reaction reducing the activation energies (e.g. (Enrique-Romero et al., 2020; Enrique-Romero et al., 2019c; Rimola et al., 2018b)); and iii) reactant concentrator, this way retaining the reactants and keeping them in close proximity for subsequent reaction (e.g., CO adsorption and retention for subsequent hydrogenation to form H_2CO and CH_3OH (e.g. Rimola et al., 2014; Watanabe and Kouchi, 2002a; Zamirri et al., 2019). All three processes depend on the binding energies (*BEs*) of the molecules either directly (e.g. the adsorption of the species) or indirectly (e.g. because the diffusion of a particle on the grain surfaces is a fraction of its *BE*) (see Cuppen et al., 2017). In addition, molecules formed on the grain surfaces can be later transferred to the gas phase by various desorption processes, most of which depend, again, by the *BE* of the species. In practice, *BEs* are crucial properties of the interstellar molecules and play a huge role in the resulting ISM chemical composition. This key role of *BEs* is very obvious in the astrochemical models that aim at reproducing the chemical evolution of interstellar objects, as clearly shown by two recent works by Wakelam et al., 2017 and Penteado et al., 2017, respectively.

Experimentally, the *BEs* of astrochemical species are measured by temperature programmed desorption (TPD) experiments. These experiments measure the energy required to desorb a particular species from the substrate, namely a desorption enthalpy, which is equal to the *BE* only if there are no activated processes (He et al., 2016) and if thermal effects are neglected. A typical TPD experiment consists of two phases. In the first one, the substrate, maintained at a constant temperature, is exposed to the species that have to be adsorbed coming from the gas phase. In the second phase, the temperature is increased until desorption of the adsorbed species–collected and analyzed by a mass spectrometer–occurs. The *BE* is then usually extracted by applying the direct inversion method on the Polanyi-Wigner equation (e.g. Dohnalek et al., 2001; Noble et al., 2012). The *BE* values obtained in this way strongly depend on the chemical composition and morphology of the substrate and also on whether the experiment is conducted in the monolayer or multilayer regime (e.g. Chaabouni et al., 2018; He et al., 2016; Noble et al., 2012). Another issue related to the TPD technique is that it cannot provide accurate B*BEs* for radical species as they are very reactive. In literature, there are many works that have investigated the desorption processes by means of the TPD technique (e.g. Collings et al., 2004; Dulieu et al., 2013; Fayolle et al., 2016; He et al., 2016; Noble et al., 2012; Smith et al., 2016) but they have been conducted for just a handful of important astrochemical species, whereas a typical network of an astrochemical model can contain up to five hundred species and very different substrates. In a recent work, Penteado et al. (2017) collected the results of these experimental works, trying to be as homogeneous as possible in terms of different substrates, estimating the missing *BE* values from the available data and performing a systematic analysis on the effect that the *BE* uncertainties can have on astrochemical model simulations.

BE values can also be obtained by means of computational approaches which, in some situations, can overcome the experimental limitations. Many computational works have so far focused on a few important astrochemical species like H, H_2, N, O, CO, CO_2, in which *BEs* are calculated on periodic/cluster models of crystalline/amorphous structural states using different computational techniques (e.g. Al-Halabi and Van Dishoeck, 2007; Ásgeirsson et al., 2017; Karssemeijer and Cuppen, 2014; Karssemeijer et al., 2014; Senevirathne et al., 2017; Shimonishi et al., 2018; Zamirri et al., 2019). In addition, other works have computed *BE* in a larger number of species but with a very approximate model of the substrate. For example,

in a recent work by Wakelam et al. (2017) *BE* values of more than 100 species are calculated by approximating the ASW surface with a single water molecule. The authors then fitted the most reliable *BE* measurements (16 cases) against the corresponding computed ones, obtaining a good correlation between the two data sets. In this way, all the errors in the computational methods and limitations due to the adoption of a single water molecule are compensated by the fitting with the experimental values, in the view of the authors. The resulting parameters are then used to scale all the remaining computed *BE* to improve their accuracy. This clever procedure does, however, consider the proposed scaling universal, leaving aside the complexity of the real ice surface and the specific features of the various adsorbates. In a similar work, Das et al. (2018) have calculated the *BEs* of 100 species by increasing the size of a water cluster from one to six molecules, noticing that the calculated *BE* approaches the experimental value when the cluster size is increased. As we will show in the present work, these approaches, relying on an arbitrary and very limited number of water molecules, cannot, however, mimic a surface of icy grain. Furthermore, the strength of interaction between icy water molecules as well as with respect to the adsorbates depends on the hydrogen bond cooperativity, which is underestimated in small water clusters.

In this work, we followed a different approach, focusing on extended periodic ice models, either crystalline or amorphous, adopting a robust computational methodology based on a quantum mechanical approach. We simulate the adsorption of a set of 21 interstellar molecules, whose 4 are radical species, on several specific exposed sites of the water surfaces of both extended models. *BE* values have been calculated for more than one binding site (if present) to provide the spread of the *BE* values that a same molecule can have depending on the position in the ice. Different approaches, with different computational cost, have been tested and compared, and the final computed *BEs* have been compared with data from the computational approaches of Wakelam et al., 2017 and Das et al., 2018 and data from UMIST and KIDA databases as well as available experimental data (e.g. McElroy et al., 2013; Wakelam et al., 2015). One added value of this work is the definition of both a reliable, computationally cost-effective ab-initio procedure designed to arrive to accurate *BE* values and an ice grain atomistic model, that can be applied to predict the *BEs* of any species of astrochemical interest.

9.3 Computational details

9.3.1 Structure of the ice: periodic simulations

Water ice surfaces have been modelled enforcing periodic boundary conditions to define icy slabs of finite thickness either entirely crystalline or of amorphous nature. Adsorption is then carried out from the void region above the defined slabs. Periodic calculations have been performed with the ab initio CRYSTAL17 code (Dovesi et al., 2018). This software implements both the Hartree-Fock (HF) and Kohn-Sham self-consistent fields methods for the solution of the electronic Schrödinger equation, fully exploiting, if present, the crystalline or molecular symmetry of the system under investigation. CRYSTAL17 adopts localized Gaussian functions as basis sets, similar to the approach followed by molecular codes. This allows CRYSTAL17 to perform geometry optimizations and vibrational properties of both periodic (polymer, surfaces and crystals) and non-periodic (molecules) systems with the same level of accuracy. Furthermore, the definition of the surfaces through the slab model allows to avoid the 3D fake replica of the slab as forced when adopting plane waves basis set.

Computational parameters are set to values ensuring good accuracy in the results. The threshold parameters for the evaluation of the Coulomb and exchange bi-electronic integrals (TOLINTEG keyword in the CRYSTAL17 code; Dovesi et al., 2018) have been set equal to 7, 7, 7, 7, 14. The needed density functional integration are carried out numerically over

a grid of points, which is based on an atomic partition method developed by Becke, 1988. The standard pruned grid (XLGRID keyword in the CRYSTAL17 code; Dovesi et al., 2018), composed by 75 radial points and a maximum of 974 angular points, was used. The sampling of the reciprocal space was conducted with a Pack-Monkhorst mesh (Pack and Monkhorst, 1977), with a shrinking factor (SHRINK in the code CRYSTAL17; Dovesi et al., 2018) of 2, which generates 4 k points in the first Brillouin zone. The choice of the numerical values we assigned to these three computational parameters is fully justified in the Appendix 9.7.

Geometry optimizations have been carried out using the Broyden-Fletcher-Goldfarb-Shanno (BFGS) algorithm (Broyden, 1970; Fletcher, 1970; Goldfarb, 1970; Shanno, 1970), relaxing both the atomic positions and the cell parameters. We adopted the default values for the parameters controlling the convergence, i.e., difference in energy between two subsequent steps, 1×10^{-7} Hartree; and maximum components and root-mean-square of the components of the gradients and atomic displacements vectors, 4.5×10^{-4} Hartree Bohr^{-1} and 3×10^{-4} Hartree Bohr^{-1}, and 1.8×10^{-3} Bohr and 1.2×10^{-3} Bohr, respectively. All periodic calculations were grounded on either the density functional theory (DFT) or the HF-3c method (Hohenberg and Kohn, 1964; Sure and Grimme, 2013). Within the DFT framework, different functionals were used to describe closed- and open-shell systems. For the former, we used the hybrid B3LYP method (Becke, 1993; Lee et al., 1988b), which has been shown to provide a good level of accuracy for the interaction energies of non-covalent bound dimers (Kraus and Frank, 2018), added with the D3-BJ correction for the description of dispersive interactions (Grimme et al., 2010, 2011b). For open-shell systems, treated with a spin-unrestricted formalism (Pople et al., 1995), we used the hybrid M06-2X functional (Zhao and Truhlar, 2008b), which has been proved to give accurate results in estimating the interaction energy of non-covalent binary complexes involving a radical species and a polar molecule (Tentscher and Arey, 2013). The choice of these two different functionals is justified by two previous works describing the accuracy on the energetic properties of molecular adducts (Kraus and Frank, 2018; Tentscher and Arey, 2013). For all periodic DFT calculations we used the Ahlrichs' triple-zeta quality VTZ basis set, supplemented with a double set of polarization functions (Schäfer et al., 1992). In the following, we will refer to this basis set as "A-VTZ*" (see Appendix 9.10 for details of the adopted basis set).

The HF-3c method is a new method combining the Hartree-Fock Hamiltonian with the minimal basis set MINI-1 (Tatewaki and Huzinaga, 1980) and with three a posteriori corrections for: i) the basis set superposition error (BSSE), arising when localized Gaussian functions are used to expand the the basis set (Jansen and Ros, 1969; Liu and McLean, 1973); ii) the dispersive interactions; iii) short-ranged deficiencies due to the adopted minimal basis set (Sure and Grimme, 2013).

Harmonic frequency calculations were carried out on the optimized geometries of both crystalline and amorphous ices to characterize the stationary points of each structure. Vibrational frequencies have been calculated at the Γ point by diagonalizing the mass-weighted Hessian matrix of second order energy derivatives with respect to atomic displacements (Pascale et al., 2004; Zicovich-Wilson et al., 2004). The Hessian matrix elements have been evaluated numerically by a six-points formula (NUMDERIV=2 in the CRYSTAL17 code; Dovesi et al., 2018), based on two displacements of ± 0.003 Å for each nuclear cartesian coordinates from the minimum structure.

To avoid computational burden, only a portion of the systems has been considered in the construction of the Hessian matrix, including the adsorbed species and the spatially closest interacting water molecules of the ice surface. This "fragment" strategy for the frequency calculation has already been tested by some of us in previous works and is fully justified by the non-covalent nature of the interacting systems where the coupling between the vibrational modes of bulk ice and adsorbate moieties is negligible (Rimola et al., 2008; Tosoni et al., 2005; Zamirri et al., 2017).

From the set of frequencies resulting from the "fragment" calculations we worked out the zero point energy (ZPE) for the free crystalline ice surface, the free adsorbate, the ice-surface/adsorbate complex to arrive to the corresponding correction ΔZPE, as reported in Appendix 9.7.1. From the ΔZPE we corrected the electronic BE for each adsorbates as: $BE(0) = BE - \Delta ZPE$ and found a good linear correlation *BE(0)=0.854 BE*, as shown in Figure 9.13 of the Appendix 9.7.1. While the "fragment frequency" strategy is fine for computing the ΔZPE of the crystalline ice model due to the structural rigidity enforced by the system symmetry, the same does not hold for the amorphous ice. In that case, the large unit cell (60 water molecules) and their random organization renders the ice structure rather sensitive to the adsorbate interaction which causes large structural water molecules rearrangement. This, in turn, alter significantly the whole set of normal modes and the numerical value of the ΔZPE becomes ill-defined. Nevertheless, considering that the kind of interactions operative for the crystal ice are of the same nature of those for the amorphous one, we adopted the same scaling factor 0.854 computed for the crystalline ice to correct the electronic BE for the amorphous one. In the following, we compared the experimental BE usually measured for amorphous ices with the *BE(0)* values. To discuss the internal comparison between adsorption features of different adsorbates on the crystalline ice, we still focused on the uncorrected *BEs*.

9.3.2 Binding energies calculation and Counterpoise correction

When Gaussian basis sets are used, a spurious contribution arises in the calculation of the molecule/surface interactions, called BSSE (basis set superposition error) (e. g., Boys and Bernardi, 1970). In this work, the BSSE for DFT calculations has been corrected making use of the a posteriori Counterpoise correction (CP) by Boys and Bernardi (Davidson and Feller, 1986).

The CP-corrected interaction ΔE^{CP} energy has been calculated as

$$\Delta E^{CP} = \Delta E^{*} + \delta E + \Delta E_L - BSSE \tag{9.1}$$

where ΔE^{*} is the deformation free interaction energy, δE is the total contribution to the deformation energy, and ΔE_L is the lateral interaction (adsorbate-adsorbate interaction) energy contribution. Details on the calculation of each energetic term of Eq. (9.1) can be found in the Appendix 9.7. By definition, BE is the opposite of the CP-corrected interaction energy:

$$\Delta E^{CP} = -BE \tag{9.2}$$

9.3.3 BE refinement with the embedded cluster method

With the aim of refining the periodic DFT BE values for the crystalline ice model, single point energy calculations have been carried out on small clusters, cut out from the crystalline ice model, using a higher level of theory than the DFT methods with the Gaussian09 program (Frisch et al., 2009). The adopted cluster models were derived from the periodic systems and are described in § 9.4.2. These refinements have been performed through the ONIOM2 approach (Dapprich et al., 1999), dividing the systems in two parts that are described by two different levels of theory. The *Model system* (i.e., a small moiety of the whole system including the adsorbate and the closest water molecules) was described by the *High* level of theory represented by the single- and double-electronic excitations coupled-cluster method added with a perturbative description of triple excitations (CCSD(T)). The *Real system* (i.e., the whole system) was described by the DFT level of theory adopted in the periodic calculations with the two different functionals for open- and closed-shell species. In the ONIOM2 methodology, the BE can be written as:

$$BE(ONIOM2) = -BE(Low, Real) + \Delta BE \tag{9.3}$$
$$\Delta BE = BE(High, Model) - BE(Low, Model) \tag{9.4}$$

The final BE(ONIOM2) is also corrected by the BSSE following the same scheme described above. Our choices about the *Model* and *Real system* will be extensively justified in § 9.4.2.

9.4 Results

9.4.1 Ice surface models

Crystalline ice model

Despite the amorphous and perhaps porous nature of the interstellar ice, we adopted, as a paradigmatic case, a proton-ordered crystalline bulk ice model usually known as *P-ice* ($Pna2_1$ space group) (Casassa et al., 1997). From P-ice bulk, we cut out a slab model i.e. a 2D-periodic model representing a surface. Consequently, periodic boundary conditions are maintained only along the two directions defining the slab plane, while the third direction (z-axis) is non-periodic and defines the slab thickness. The slab model adopted in this work represents the P-ice (010) surface, in accordance with previous work (Zamirri et al., 2018). This slab consists of twelve atomic layers, is stoichiometric and has a null electric dipole moment across the z-axis. This ensure an electronic stability of the model with the increase of the slab thickness (Tasker, 1979). The slab structure has been fully optimized (unit cell and atomic fractional coordinates) at both B3LYP-D3/A-VTZ* and M06-2X/A-VTZ* DFT levels. As it can be seen from Figure 9.1 (panel A) the (010) P-ice unit cell is rather small, showing only one dangling hydrogen (dH) and oxygen (dO) as binding sites. For large molecules, to increase the number of adsorption sites and minimize the lateral interactions among replicas of the adsorbate we also considered a 2x1 supercell. The electrostatic potential maps (EPMs, see Fig. 9.1, panels B and C), clearly reveal positive (blue EPM regions) and negative (red EPM regions) potentials around the dH and dO sites, respectively.

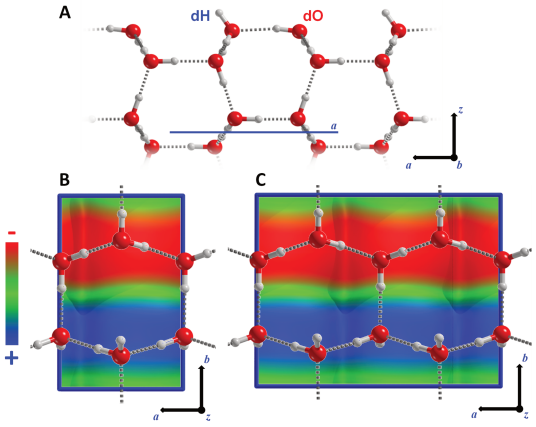

FIGURE 9.1: (010) slab model of P-ice. A) Side view along the $\boldsymbol{b}$ lattice vector. B) Top view of the 1x1 unit cell ($|\boldsymbol{a}|$ = 4.500 Å and $|\boldsymbol{b}|$ = 7.078 Å) superimposed to the electrostatic potential map, EPM. C) Top view of the 2x1 supercell ($|\boldsymbol{a}|$ = 8.980 Å, $|\boldsymbol{b}|$ = 7.081 Å) superimposed to the EPM. The iso-surface value for the electron density where the electrostatic potential is mapped is set equal to 10^{-6} au. Colour code: +0.02 au (blue, positive), 0.00 au (green, neutral) and -0.02 au (red, negative).

Amorphous solid water (ASW)

As anticipated, the (010) P-ice surface might not be a physically sound model to represent actual interstellar ice surfaces, due to the evidence, from the spectroscopic feature of the interstellar ice, of its amorphous nature (Boogert et al., 2015b). The building up of amorphous surface models is a non-trivial and not unique procedure, because of the lack of a consistent and universally-accepted strategy. One common approach is to start from a crystalline model and heat it up to relatively high temperature by running molecular dynamics simulations (MDs) for few picoseconds. This step is followed by thermal annealing to freeze the ice in a glassy amorphous state. In this work, we adopted a different strategy. We refer to a recent work by Shimonishi et al., 2018 in which the *BEs* of a set of atomic species were computed on several water clusters, previously annealed with MD simulations. We re-optimized (at B3LYP-D3/A-VTZ* level only) the whole set of ice clusters and the three most stable clusters, composed by 20 water molecules each, were merged together to define a unit cell of an amorphous periodic ice. This procedure mimics somehow the collision of nanometric scale icy grains occurring in the molecular clouds. The merge of the three clusters was carried out by matching the dHs regions of one cluster with the dOs ones of the other. As a result, we ended up with a large 3D-periodic unit cell (with lattice parameters $|\boldsymbol{a}|$ = 21.11 Å, $|\boldsymbol{b}|$ = 11.8 Å and $|\boldsymbol{c}|$ = 11.6 Å) envisaging 60 water molecules. This initial bulk model was optimized at HF-3c level in order to fully relax the structure from the internal tensions of the initial guess. After this step, we cut out a 2D-periodic slab from the bulk structure. The amorphous slab is composed by 60 water molecules in the unit cell, and was further fully optimized (unit cell size and atomic coordinates) at the HF-3c level, B3LYP-D3/A-VTZ* and M06-2X/A-VTZ* levels of theory. The three final structures show little differences in the positions of specific water molecules and, on the whole, the structures are very similar (Fig. 9.2). The computed electric dipole moment across the non-periodic direction (1.2, 0.7 and 0.1 Debyes for the HF-3c, B3LYP-D3 and M06-2X structures, respectively) showed a very good agreement between different models, also considering the dependence of the dipole value on the adopted quantum mechanical method. These amorphous slab models show different structural features for the upper and lower surfaces which imparts the residual dipole moment across the slab, and, consequently, exhibit a variety of different binding sites for adsorbates. To characterize the electrostatic features of these sites, which in turn dictate the adsorption process, we resorted to the EPMs for the top/bottom surfaces of each optimized slab (Fig. 9.3). The general characteristics are very similar for the three models: B3LYP-D3 and M06-2X giving the closest maps. HF-3c tends to enhance the differences between positive/negative regions due to overpolarization of the electron density caused by the minimal basis set. "Top" surfaces show a hydrophobic cavity (the central greenish region, Fig. 9.3, absent in the P-ice slab, surrounded by dHs positive spots. "Bottom" surfaces shows several prominent negative regions (from five dOs) mixed with less prominent positive potentials (due to four buried dHs).

9.4.2 BEs on crystalline ice

BE computed with DFT//DFT method

In this work, we simulated the adsorption of 17 closed-shell species and 4 radicals, shown in Fig. 9.4. For each molecule/surface complex, geometry optimizations (unit cell plus all atomic coordinates without constraints) were performed. Initial structures were guessed by manually setting the maximum number of H-bonds between the two partners. The pure role of dispersion is estimated by extracting the D3 contribution from the total energy at B3LYP-D3 level of theory. The energetics of the adsorption processes were then computed according to Eq. (9.1).

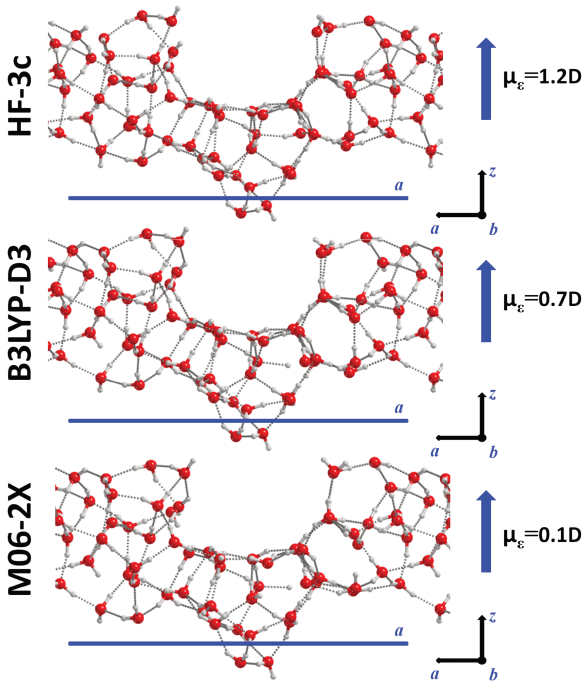

FIGURE 9.2: Side view of the amorphous slab models. The cell parameter ***a*** is highlighted as a blue line. Electric dipole moments μ_ϵ along the **z** direction are shown on the right side.

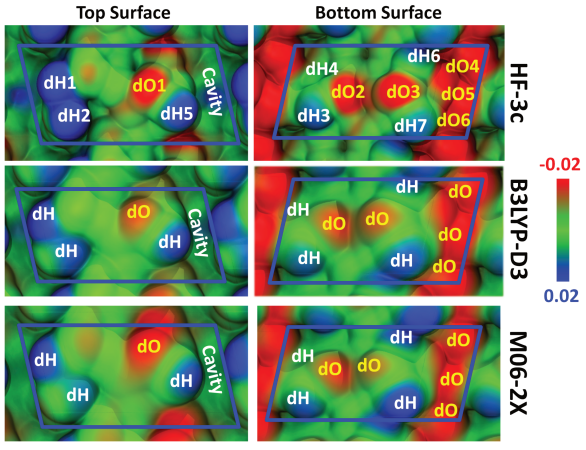

FIGURE 9.3: Colour-coded electrostatic potential energy maps (EPMs) mapped to the electron density for the "top" and "bottom" surfaces of the amorphous slab (HF-3c, B3LYP-D3 and M06-2X optimized geometries). dO and dH sites are also labelled. The iso-surface value for the electron density is set equal to 10^{-6} au to which the electrostatic potential is mapped out. EPM color code: +0.02 au (blue, positive), 0.00 au (green, neutral) and -0.02 au (red, negative)..

As it can be seen from the results of Table 9.1, a range of interactions of different strength is established between the adsorbed species and the crystalline P-ice surface. Some molecules do not possess a net electric dipole moment, while exhibiting relevant electric quadrupole moments (i.e., H_2, N_2 and O_2) or multipoles moments of higher order (i.e., CH_4, see their EPMs in **??**). For these cases, only weak interactions are established so that *BEs* are lower than 1800 K (see *BE* disp values in Table 9.1). Interestingly, for the N_2, O_2 and CH_4 cases, interactions are almost repulsive if dispersive contributions are not accounted for in the total *BE* (compare *BE disp* with *BE no disp* values of Table 9.1). Therefore, the adsorption is dictated by dispersive forces, which counterbalance the repulsive electrostatic interactions. For the H_2 case, electrostatic interactions are attractive mainly because of the synergic effect of both the surface dH and the dO on the negative and positive parts of the H_2 quadrupole, respectively (see Fig. **??**).

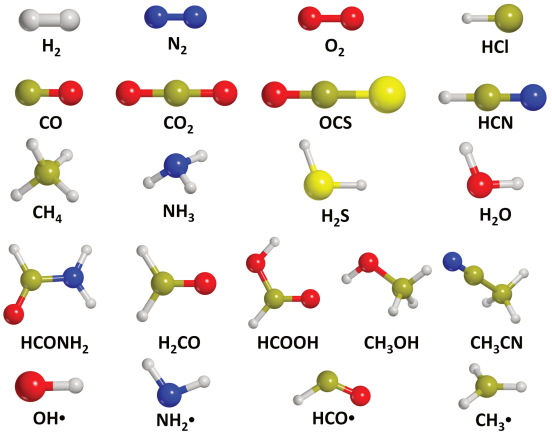

FIGURE 9.4: Set of molecular and radical species adopted within this work for the calculation of binding energy on different ice models. O_2 is an open-shell (spin-triplet) species (Borden et al., 2017).

CO, OCS and CO_2 also exhibit a quadrupole moment, but due to the presence of heteroatoms in the structure, they can also establish H-bonds with the dH site. Consequently, *BEs* are larger than the previous set of molecules (i.e., $>$ 2400 K, see Table 9.1). For these three cases, pure electrostatic interactions are attractive, but the dispersion contribution is the most dominant one over the total *BE* values (compare *BE disp* with *BE no disp* values of Table 9.1). CO, in addition to a net quadrupole, also possesses a weak electric dipole, with the negative end at the carbon atom (see its EPM in **??**) (Zamirri et al., 2017). Thus, although the two negative poles (C and O atoms) of the quadrupole, both can interact with the positive dH site, the interaction involving the C atom is energetically slightly favoured over the O atom (Zamirri et al., 2017, 2019). Accordingly, we only considered the C-down case, the computed *BE* being in good agreement with previous works (Zamirri et al., 2017, 2018). OCS also possesses a dipole and can interact with the surface through either its S- or O-ends, through dO or dH sites. However, due to the softer basic character of S compared to O, the interaction through oxygen is preferred and only considered here.

NH_3, H_2O, HCl, HCN and H_2S are all amphiprotic molecules that can both serve as acceptors and donors of H-bonds from/to the dH and dO sites. The relative strong H-bonds with the surface result in total *BE* values that are almost twice higher than the values of the previous set of molecules (i.e., CO, OCS and COS). Although also in these cases dispersive forces play an important contribution to the BE, the dominant role is dictated by the H-bonding contribution.

For the adsorption of CH_3OH, CH_3CN and the three carbonyl-containing compounds, i.e., H_2CO, $HCONH_2$ and HCOOH, all characterized by large molecular sizes, we adopted

the 2x1 supercell (shown in Fig. 9.1) to minimize the lateral interactions between adsorbates. Consequently, two dHs and two dOs are available for adsorption. Therefore, for some of these species (i.e., the carbonyl-containing ones), we started from more than one initial geometry to improve a better sampling of the adsorption features on the (010) P-ice surface (the different cases on the supercell are labeled as SC1 and SC2 in Table 9.1 and the geometries are reported in **??**). The *BE* values of these species are among the highest ones, due to the formation of multiple H-bonds with the slab (and therefore increasing the electrostatic contribution to the interactions), and a large dispersion contribution due to the larger sizes of these molecules with respect to the other species.

The adsorption study has also been extended to four radicals (i.e., OH• NH_2• CH_3• HCO•), since they are of high interest due to their role in the formation of interstellar compounds (Bennett and Kaiser, 2007; Sorrell, 2001). OH• and NH_2• form strong H-bonds with the dH and dO sites of the slab, at variance with CH_3• and HCO• cases, as shown by the higher *BE* values. Because of the nature of the M06-2X functional, we cannot separate the dispersion contributions to the total *BEs*. Interestingly, in all cases, we did not detect transfer of the electron spin density from the radicals to the ice surface, i.e., the unpaired electron remains localized on the radical species upon adsorption.

The ONIOM2 correction and the accuracy of the DFT//DFT *BE* values

As described in the Computational Details section, the ONIOM2 methodology has been employed to check the accuracy of the B3LYP-D3/A-VTZ* and M06-2X/A-VTZ* theory levels, both representing the *Low* level of calculation. For this specific case, to reduce the computational burden, we only considered 15 species, leaving aside N_2, O_2, H_2O, CH_4, CH_3CN and CH_3• radical. Here, the *Real system* is the periodic P-ice slab model without adsorbed species. Therefore, the BE(*Low*,*Real*) term in Eq. (9.3) corresponds to the *BEs* at the DFT theory levels, hereafter referred to as BE(*DFT*, *Ice*). The *Model system* is carved from the optimized geometry of the periodic system: it is composed by the adsorbed molecule plus n ($n = 2, 6$; the latter only for the H_2 case) closest water molecules of the ice surface to the adsorbates. For the *Model systems*, two single point energy calculations have been carried out: one at the *High* level of theory, i.e., CCSD(T), calculated with Gaussian09, and the other at the *Low* level of theory, employing the same DFT methods as in the periodic calculations, calculated with CRYSTAL17. For the sake of clarity, we renamed the two terms BE(*High*,*Model*) and BE(*Low*,*Model*) in Eq. (9.3) for any molecular species μ, as BE(CCSD(T), μ-$n$$H_2O$) and BE(DFT, μ-$n$$H_2O$), respectively.

As CCSD(T) is a wavefunction-based method, the associated energy strongly depend on the quality of the adopted basis set (Cramer, 2002). Consequently, accurate results are achieved only when complete basis set extrapolation is carried out (Cramer, 2002); accordingly, we adopted correlation consistent basis sets (Dunning Jr, 1989), here named as cc-pV*N*Z, where "cc" stands for correlation consistent and *N* stands for double (D), triple (T), quadruple (Q), etc... Therefore, we performed different calculations improving the quality of the basis set from **Jun**-cc-pVDZ to **Jun**-cc-pVQZ (and even **Jun**-cc-pV5Z when feasible) (Bartlett and Musiał, 2007; Papajak et al., 2011), extrapolating the BE(CCSD(T), μ-$n$$H_2O$) values for $N \to \infty$. Figure 9.5 shows, using NH_3 as illustrative example, the plot of the BE(CCSD(T), μ-$n$$H_2O$) values as a function of $1/L^3$ where L is the cardinal number corresponding to the N value for each correlation-consistent basis set. For all other species, we observed similar trends. This procedure was used in the past to extrapolate the *BE* value of CO adsorbed at the Mg(001) surface (Ugliengo and Damin, 2002).

The procedure gives for the extrapolated BE(CCSD(T), μ-$n$$H_2O$) a value of 4089 K in excellent agreement with the value computed by the plain B3LYP-D3/A-VTZ* at periodic level of 4390 K (see Fig. 9.5). Very similar agreement was computed for all considered species as

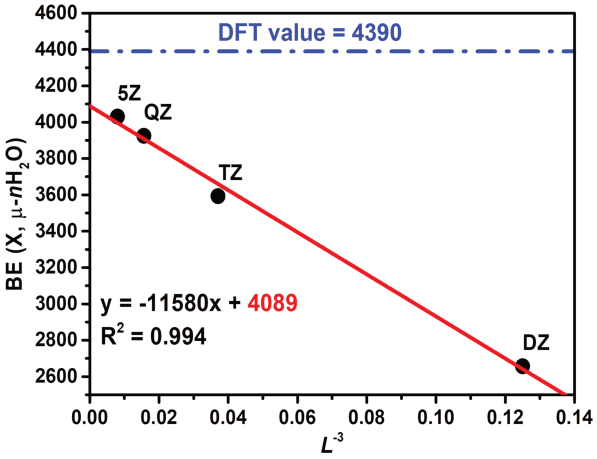

FIGURE 9.5: BE(X, μ-$n$$H_2O$) extrapolated value at infinite basis set for the case of NH_3. The dashed-dot blue line represents the *BE* computed for the *BE*(DFT, μ-$n$$H_2O$) at DFT//A-VTZ* level (4390 K). Solid red line represents the linear fit of the BE(CCSD(T), μ-$n$$H_2O$) values (red squares) calculated with DZ, TZ, QZ and 5Z basis sets. The extrapolated BE(X, μ-$n$$H_2O$) at infinite basis set is highlighted in red in the fitting equation (4089 K).

shown in Fig. 9.6, in which a very good linear correlation is seen between BE(ONIOM2) and BE(DFT). Therefore, we can confidently assume the periodic B3LYP-D3/A-VTZ* (closed shell molecules) or the M06-2X/A-VTZ* (radical species) plain *BE* values as reliable and accurate enough and are those actually used in this work.

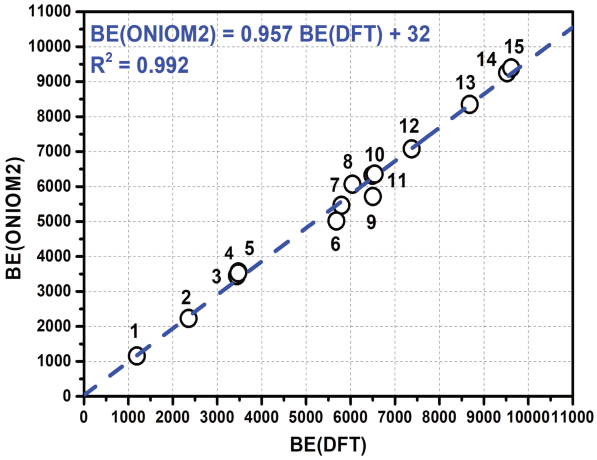

FIGURE 9.6: Linear fit between periodic DFT/A-VTZ* *BE* values (*BE(DFT)*) and the basis set extrapolated ONIOM2 *BE* values (*BE(ONIOM2)*). All values are in K. Fit parameters are also reported. Legend: 1:H_2; 2:CO; 3:CO_2; 4:HCO•; 5:OCS; 6:H_2S; 7:HCN; 8:NH_2•; 9:H_2CO; 10:HCl; 11:OH•; 12:NH_3; 13:CH_3OH; 14:HCOOH; 15:$HCONH_2$.

BE computed with composite DFT/HF-3c method

In the previous Section we proved the DFT/A-VTZ* as a reliable and accurate method to compute the *BEs* of molecules and radicals on the crystalline (010) P-ice ice slab. However, this approach can become very computational costly when moving from crystalline to amorphous model of the interstellar ice, as larger unit cells are needed to enforce the needed randomness

in the water structure. Therefore, we tested the efficiency and accuracy of the cost-effective computational HF-3c method (see § 9.3).

To this end, we adopted a composite procedure which has been recently assessed and extensively tested in the previous work by some of us on the structural and energetic features of molecular crystals, zeolites and biomolecules (Cutini et al., 2016, 2017, 2019). We started from the DFT/A-VTZ* optimized structure just discussed for the crystalline ice. We re-optimize each structure at HF-3c level to check the changes in the structures resulting from the more approximated method. Then we run a single point energy calculations at the DFT/A-VTZ* (B3LYP-D3 and M06-2X) levels to evaluate the final *BE* values. The results obtained are summarized in Fig. 9.7, showing a very good linear correlation between the *BE* values computed as described.

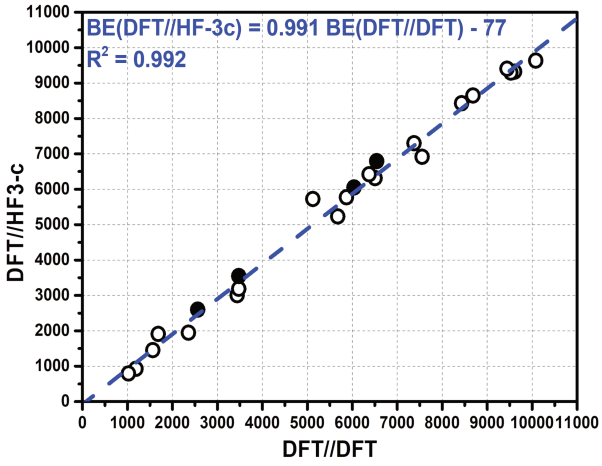

FIGURE 9.7: Linear fit between the *BE* values calculated with the full DFT computational scheme and the *BE* values calculated with the composite DFT//HF-3c computational scheme for the crystalline ice model (all values in K). Black-filled and empty triangles stand for open-shell and closed-shell species, respectively.

The largest percentage differences are found for the smallest BEs, that is, those dominated by dispersion interactions or very weak quadrupolar interactions (i.e., N_2, O_2, H_2 and CH_4) in which the deficiencies of the minimal basis set encoded in the HF-3c cannot be entirely recovered by the internal corrections. For higher *BE* values, the match significantly improves, in some cases being almost perfect. Even for radicals, the composite approach gives good results. It is worth mentioning that HF-3c optimized geometries are very similar to the DFT-optimized ones (only slight geometry alterations occurred), indicating that the adducts are well-defined minima in both potential energy surfaces. This successful procedure calibrated on crystalline ice is therefore adopted to model the adsorption of all 21 species on the proposed amorphous slab model, a task which would have been very expensive at the full DFT/A-VTZ* level.

9.4.3 BEs on amorphous solid water (ASW)

On the ASW model, due to the presence of different binding sites, a single *BE* value is not representative of the whole adsorption processes as it is the case for almost all adsorbates on the crystalline surface. Therefore, we computed the *BE* with the composite DFT//HF-3c procedure (see § 9.4.2) by sampling different adsorption sites at both the "top" and "bottom" surfaces of the amorphous slab. The starting initial structures of each adsorbate were setup by hand, following the maximum electrostatic complementarity between the EPMs (see Fig. 9.3) of the ice surface and that of a given adsorbate. For each molecule, at least four *BE* values

TABLE 9.1: Summary of the *BE* values (in Kelvin) obtained for the crystalline P-ice (010) slab with DFT//DFT and DFT//HF-3c methods. Legend: "*BE disp*" = *BE* value including the D3 contribution, "*BE no disp*" = *BE* values not including D3 contribution; "-disp(%)" = absolute (percentage) contribution of dispersive forces to the total *BE disp*.

Species	**(010) P-ice crystalline slab DFT//DFT**			**(010) P-ice crystalline slab DFT//HF-3c**		
	BE disp	*BE no disp*	-disp(%)	*BE disp*	*BE no disp*	-disp(%)
H_2	1191	565	625(53)	926	241	686(74)
O_2	1022	-373	1034(137)	794	-84	878(110)
N_2	1564	-72	1636(104)	1455	-180	1636(160)
CH_4	1684	-229	1912(113)	1912	-349	2261(118)
CO	2357	698	1660(71)	1948	60	1888 (97)
CO_2	3440	1540	1900(55)	3007	938	2069(69)
OCS	3476	120	3356(97)	3187	265	2923(92)
HCl	6507	4402	2093(32)	6314	3488	2237(39)
HCN	5124	3067	2057(29)	5725	3271	3043(48)
H_2O	8431	6844	1588(19)	8431	6808	1612(19)
H_2S	5677	3380	2297(40)	5232	3199	2105(40)
NH_3	7373	5533	1852(25)	7301	5484	1816(25)
CH_3CN	7553	4450	3103(41)	6916	3259	2598(44)
CH_3OH	8684	6014	2670(31)	8648	6026	2237(27)
H_2CO-SC1	5869	3885	1985(34)	5773	4053	2369(37)
H_2CO-SC2	6375	3692	2682(42)	6423	3716	2057(36)
$HCONH_2$-SC1	9610	6459	3151(33)	9321	6158	3163(34)
$HCONH_2$-SC2	10079	6483	3608(36)	9634	6074	3560(37)
HCOOH	9526	7325	2189(23)	9297	7168	2117(23)
HCOOH-SC	9442	7301	2021(21)	9405	7541	1864(20)
OH•	6543*			6795*		
HCO•	3476*			3548*		
CH_3•	2562*			2598*		
NH_2•	6038*			6050*		

*Notes: For radical species (energy at M06-2X level) we cannot discern between *disp* and *no disp* data.

have been computed on different surface sites. Figure 9.8 reports the examples of methanol and formamide: for each molecule, we show the geometry on the crystalline ice and in two different sites of ASW, as well as the *BE* associated with each geometry. For methanol, the *BE* is 8648 K in the crystalline ice, whereas it is 4414 and 10091 K in the two shown ASW sites. Similarly, for formamide, *BE* is 9285 K on the crystalline ice and 6639 and 8515 K on the ASW. These two examples show that *BEs* on ASW can differ more than a twice depending on the site and that the value on the crystalline ice can also be substantially different to that on the ASW.

Figure 9.9 shows the computed BEs, on crystalline ice and ASW, for the studied species. The list of all computed *BE* values on ASW is reported in Table 9.2, while Table 9.3 reports the computed minimum and maximum *BE* values on ASW and the *BEs* on the crystalline ice for all the studied species. As already mentioned when presenting the methanol and formamide examples, the amorphous nature of the ice can yield large differences in the calculated *BEs* with respect to the crystalline values. Figure 9.9 shows that while the *BEs* for crystalline *versus* amorphous ices are very close to each other for H_2, O_2, N_2, CH_4, CO, CO_2, OCS, the ones computed for the remaining molecules for the crystalline ice fall in the highest range of the distribution of the amorphous *BE* values. This behavior can be explained considering the smaller distortion energy cost upon adsorption for the crystalline ice compared to the amorphous one. The different local environment provided by crystalline *versus* amorphous

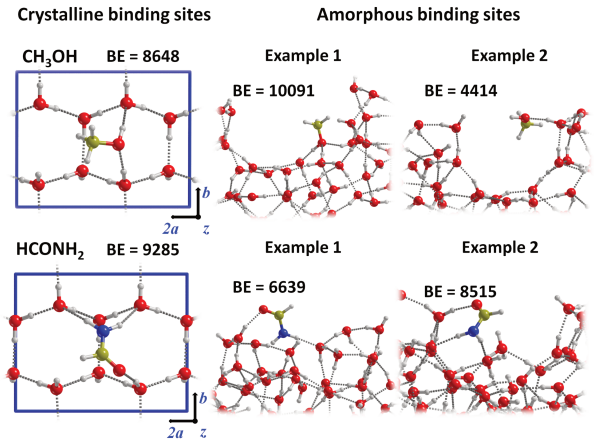

FIGURE 9.8: Comparison of the final optimized geometries for CH_3OH and $HCONH_2$ (as illustrative examples) on the crystalline ice (§ 9.4.1) and on the ASW (§ 9.4.1). The *BE* values (in Kelvin) are reported in each plot.

ices is also the reason for HCl being molecularly adsorbed at the crystalline ice while becomes dissociated at the amorphous one. Further details about the case of HCl are reported in section 9.7.2 of the Appendix. Probably this will not occur for HF, not considered here, which is expected to be molecularly adsorbed on both ices due to its higher bond strength compared to HCl. Nevertheless, as we did not explore exhaustively all possible configurations of the adsorbates at the amorphous surfaces, we cannot exclude that some even more/less energetic binding cases remain to be discovered.

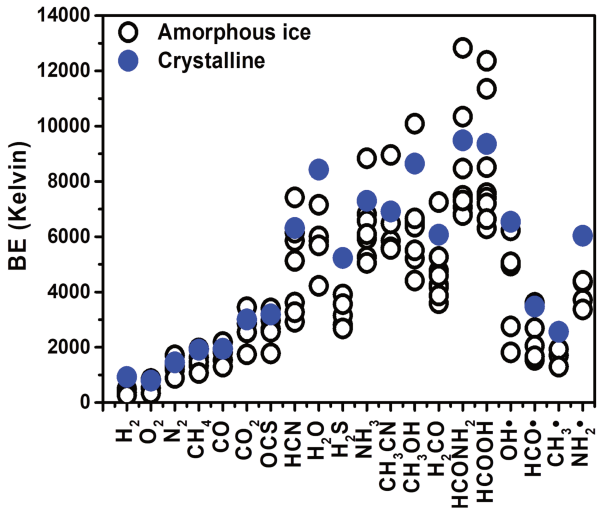

FIGURE 9.9: Comparison between the DFT//HF-3c *BEs* (in Kelvin) computed on the crystalline ice (filled blue circles) and ASW (open circles), respectively, for 20 species studied here: HCl is missing as it dissociates on the ASW (see text).

Some adsorbates show similar trends in the BEs, despite their different chemical nature. This is shown in Fig. 9.10, in which we plot the *BE* values on ASW for four molecules that have been adsorbed at the same adsorption sites: formaldehyde, formic acid, formamide and methanol. The *BE* distributions for the H_2CO and HCOOH are very similar (in their relative values), and those for CH_3OH and $HCONH_2$ show some similarities, despite the large difference in the chemical functionality.

TABLE 9.2: *BE* values (K) calculated with DFT//HF-3c method for every case on the amorphous slab model, **where the ZPE correction has not been added.**

	Amorphous ice *BE* values							
Species	**Case 1**	**Case 2**	**Case 3**	**Case 4**	**Case 5**	**Case 6**	**Case 7**	**Case 8**
H_2	469	505	277	361	265			
O_2	818	854	854	529	337			
N_2	1347	1708	1311	1191	890			
CH_4	1323	1960	1636	1467	1070			
CO	1816	2189	1540	1527	1299			
CO_2	2863	3452	2538	2550	1744			
OCS	3404	2971	2670	2562	1780			
HCN	2923	5124	3620	5136	3271	5857	6146	7421
H_2O	7156	5845	6014	5689	4222			
H_2S	2814	3909	3151	3560	2682			
NH_3	8840	5268	6820	5930	6579	6098	5052	
CH_3CN	8960	5857	5617	5557	6483			
CH_3OH	6531	4414	6519	6362	5208	6663	5509	10091
H_2CO	3596	4258	4174	4775	5268	4594	3873	7253
$HCONH_2$	12833	7481	10344	6820	8467	7072	6783	7313
HCOOH	7577	7409	8515	12364	6302	7204	6639	11354
OH•	6230	1816	4955	2754	5076			
HCO•	2694	2057	1540	3608	1672			
CH_3•	1708	1936	1299					
NH_2•	4354	3716	4402	3368				

9.5 Discussion

A first rather expected result of our computations is that the *BE* of a species on the ASW is not a single value: depending on the species and the site where it lands, the *BE* can largely differ, even by more than a factor two (Table 9.3). This has already discussed in the literature, for instance for H adsorption on both crystalline and amorphous ice models (Ásgeirsson et al., 2017). This has important consequences both when comparing the newly computed *BEs(0)* with those in the literature § 9.5.1 and for the astrophysical implications § 9.5.2. We will discuss these two aspects separately in the next two sections.

9.5.1 Comparison *BE* values in literature

Being such a critical parameter, *BEs* have been studied from an experimental and theoretical point of view. In this section, we will compare our newly computed values with those in the literature, separating the discussion for the experimental and theoretical values, respectively. We will then also comment on the values available in the databases that are used in many astrochemical models.

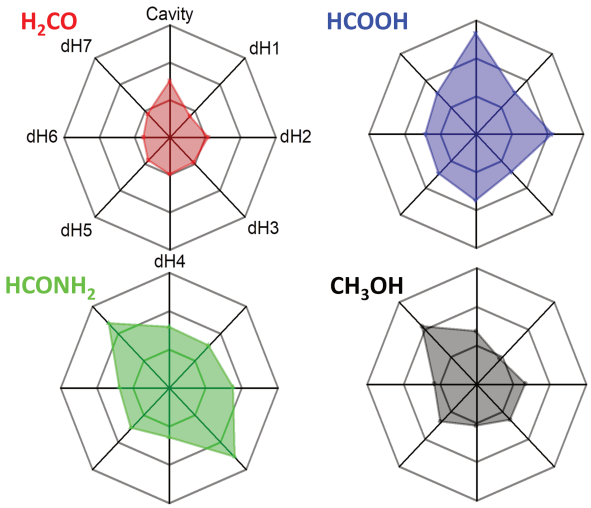

FIGURE 9.10: Spider graphs of the DFT//HF-3c *BE* values (in Kelvin) calculated on the same adsorption eight sites of the ASW for the H_2CO (red), CH_3OH (black), $HCONH_2$ (green) and HCOOH (blue) molecules. The *BE* values scale goes from 0 Kelvin (center of the graph) to 14433 Kelvin (vertices of the polygon) in steps of 4811 Kelvin. Labeling of dH and dO sites is referring to Fig. 9.3

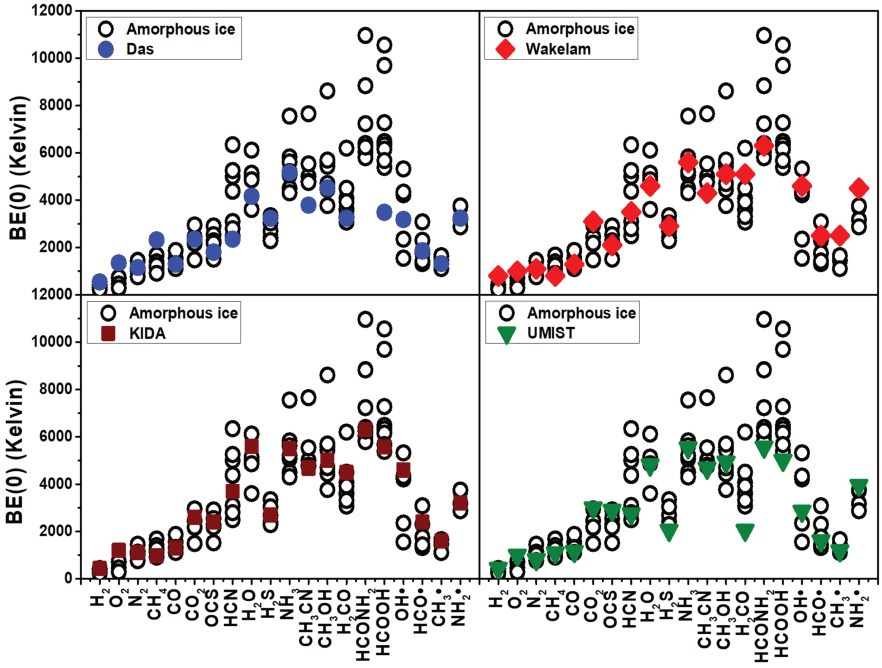

FIGURE 9.11: Comparison of the computed zero point energy corrected *BE(0)s* for the amorphous ice model with respect to those by Das et al., Wakelam et al. and reported in the KIDA and UMIST databases (Das et al., 2018; McElroy et al., 2013; Wakelam et al., 2015, 2017).

TABLE 9.3: Summary of our computed *BEs* and comparison with data from the literature. The first column reports the species, the columns 2 to 4 the *BEs* computed in the present work and corrected for the ZPE, columns 5 and 6 the values obtained via calculations from other authors, column 7 and 8 the values in the two astrochemical databases KIDA and UMIST (see text), and the last columns the values measured in different experiments. Units are in K and the references are listed in the notes below.

	BEs from this work			**BEs from literature**					
	Crystalline ice	**ASW**		**Computed**		**Databases**		**Experiments**	
Species	BE(**0**) *disp*	Min	Max	Das[a]	Wakelam[b]	UMIST[c]	KIDA[d]	Penteado[e]	Others
H_2	790	226	431	545	800	430	440	480 ± 10	322-505[f]
O_2	677	287	729	1352	1000	1000	1200	914-1161	920-1520[f]
N_2	1242	760	1458	1161	1100	790	1100	1200	790-1320[f1]
									900-1800[f1]
CH_4	1633	914	1674	2321	800	1090	960	1370	960-1947[f,g,h]
CO	1663	1109	1869	1292	1300	1150	1300	863-1420	870-1600[f]
									980-1940[f1]
CO_2	2568	1489	2948	2352	3100	2990	2600	2236-2346	
OCS	2722	1520	2907	1808	2100	2888	2400	2325**	2430[i]
HCl	5557	(l)	(l)	4104	4800		5172		5172[m]
HCN	6392	2496	6337	2352	3500	2050	3700		
H_2O	7200	3605	6111	4166	4600	4800	5600	4815-5930	
H_2S	4468	2291	3338	3232	2500-2900	2743	2700	2296**	
NH_3	6235	4314	7549	5163	5600	5534	5500	2715**	
CH_3CN	5906	4745	7652	3786	4300	4680	4680	3790**	
CH_3OH	7385	3770	8618	4511	4500-5100	4930	5000	3820**	3700-5410[n,o,p]
H_2CO	5187	3071	6194	3242	5100	2050	4500	3260±60	
$HCONH_2$	8104	5793	10960		6300	5556			7460-9380[q]
HCOOH	7991	5382	10559	3483		5000	5570	4532**	
OH•	5588	1551	5321	3183	3300-5300	2850	4600	1656-4760	
HCO•	2968	1315	3081	1857	2300-2700	1600	2400		
CH_3•	2188	1109	1654	1322	2500	1175	1600		
NH_2•	5156	2876	4459	3240	2800-4500	3956	3200		

*Notes: [a](Das et al., 2018); [b]Wakelam et al., 2017; [c]McElroy et al., 2013; [d]Wakelam et al., 2015; [e]Penteado et al., 2017; [f]He et al., 2016, note that [f1] refers to porous ice; [g]Raut et al., 2007; [h]Smith et al., 2016; [i]Ward et al., 2012; [l]HCl molecule dissociate; [m]Olanrewaju et al., 2011b [n]Minissale et al., 2016 [o]Martín-Doménech et al., 2014 [p]Bahr et al., 2008 [q]Chaabouni et al., 2018 note that the *BE* refers to the silicate substrate because it is larger than that of water ice; ** Results estimated from the work of Collings et al., 2004, reported in Table 2 of Penteado et al., 2017

Comparison with experimental values

In the present computer simulation we have computed the binding energy (*BE*) released when a species is adsorbed on the surfaces of the ice models (either crystalline or amorphous) at very low adsorbate coverage θ ($\theta \longrightarrow 0$). The correct comparison with experiments would therefore be with microcalorimetric measurements at the zero-limit adsorbate coverage. In astrochemical laboratories, Temperature Programmed Desorption (TPD) is, instead, the method of choice and is related to the desorption activation energy (*DAE*). *DAE* derives indirectly from the TPD peaks through the Readhead's method (Redhead, 1962), or more sophisticated techniques. TPD usually start from an ice surface hosting a whole monolayer of the adsorbate and therefore depends also on θ (He et al., 2016), rendering the comparison with the theoretical *BE* not straightforward (King, 1975). Ice restructuring processes may also affect the final *DAE*. Sometimes, TPD experiments only provide desorption temperature peaks T_{des}, without working out the *DAE*. This is the case of the fundamental work by Collings et al (Collings et al., 2004). Therefore, *BE* reported in the review by Penteado et al (Penteado et al.,

2017) relative to the Collings et al data (see Table 9.3) were computed through the approximate formula: $BE(X) = [T_{des}(X)/T_{des}(H_2O)]BE(H_2O)$, in which $T_{des}(X)$ is the desorption temperature of the X species contrasted with that of water $T_{des}(H_2O)$ to arrive to the corresponding *BE(X)* by assuming that of water to be 4800 K. For the above reasons, a one-by-one comparison between experiment and modeling is outside the scope of the present paper.

Following the above warnings we can now analyze Table 9.3 reporting the recent compilation by Penteado et al. (2017) (*vide supra*) *plus* the values appeared in the literature after that compilation. We start with the cases of two measurements carried out by He et al. (2016) on porous amorphous ice surfaces, for N_2 and CO. Table 9.3 shows two values, reported by He et al. for the two extreme cases of when the ice is completely covered by the species (the smaller value) and when, on the contrary, it is less than a monolayer (the largest value), which is the one to compare with our computed values. Our *BE* on amorphous ice models are in reasonable agreement with that measured by He et al. for CO (1109-1869 K versus 1940 K), and on the lower side for N_2 (760-1455 K versus 1800 K). It is worth-noting that the comparison is much better when referring to the non-porous amorphous ice measurements by the same authors: for CO and N_2 the measured *BE* values are 1600 K and 1320 K, indeed well bracketed by our *BE(0)*.

Data from Penteado et al (Penteado et al., 2017) extracted from the TPD of Collings et al (Collings et al., 2004) for NH_3 adsorbed on ice layer gave a *BE* of 2715 K. This value is, however, identical to that from the TPD of NH_3 adsorbed on gold surface (no water ice), proving that that *BE* is relative to the NH_3/NH_3 lateral interaction within the adsorbed NH_3 multilayer and not due to the interaction with the ice surface. For reasons explained in Collings et al (Collings et al., 2004) the *BE* of NH_3 on ice is assumed of the same order of that of water, i.e. around 4800 K, in better agreement with the UMIST value of 5500 K (McElroy et al., 2013). Indeed, our data (see Table 9.3, ZPE corrected) of 4300-7500 K brackets the experimental ones. The computed highest values emphasize the H-bond acceptor capability of NH_3 occurring on few specific sites characterized by very high electrostatic potential, only important for very low NH_3 coverage, not easily accessible in the TPD experiments. For the H_2O case, the computed *BE(0)s* (Table 9.3) for the amorphous ice are in the 3605-6111 K range, reasonably bracketing the experimental one of 4815-5930 K.

In general, the comparison of our *BE* values computed on the ASW with those measured by the various experiments reported in Table 9.3 shows an excellent agreement, when considering the ranges in our values and the ranges in the values of the experiments. Only one species seems to have a relatively different computed and measured BEs: O_2. For O_2, experiments tend to provide larger values with respect to what we computed (our largest value is 729 K while the lowest measured value is 914 K). For many other species, except H_2, our computed lowest *BEs(0)* are within the range of the measured ones, but we predict sites where *BEs(0)* are larger, which may have important astrophysical implications (§ 9.5.2). Finally, for H_2 we predict sites where the *BE(0)* is (slightly) lower than the measured ones.

Comparison with computed values

In the literature, there are two works that reported computations of *BEs* for a large set of molecules, those by Wakelam et al., 2017 and by Das et al., 2018. The former carried out computations considering only one water molecule whereas the latter considered a cluster of up to six water molecules.

The first aspect to notice is, therefore, that none of these two studies can, by definition, reproduce the strong adsorption sites that we have in our ASW model. Indeed, only the adoption of more realistic and periodically extended ice models allows to fully considering the hydrogen bond cooperativity, which will enhance the strength of the interaction with adsorbates at the terminal dangling hydrogen atoms exposed at the surface. This important

effect is entirely missed by the two above mentioned works. It is not surprising, then, that our crystalline and ASW *BEs* differ, sometimes substantially, from the Wakelam et al. and Das et al. values (as, by the way, they differ between themselves as well). This is clearly shown in Fig. 9.11 where we report the comparison of our computed values with those by Wakelam et al. and Das et al., respectively. In general, both work values tend to lay in the low end of our computed *BEs*. As extreme examples, our ASW *BEs* are larger for CH_3CN and HCOOH. The inverse effect is observed for the smallest studied species: our *BEs* are smaller than those computed by Wakelam et al. and Das et al. for H_2 and O_2.

Comparison with values in astrochemical databases

Two databases list the *BE* of the species used by the astrochemical models: the KIDA (Kinetic Database for Astrochemistry, `http://kida.astrophy.u-bordeaux.fr/`; Wakelam et al. (2015)) and UMIST (`http://udfa.ajmarkwick.net/index.php`; McElroy et al. (2013)). The comparison between our newly computed values and those reported in the two databases is shown in Fig. 9.11. The general remarks that we wrote for the comparison with the literature experimental and theoretical values (§ 9.5.1 and 9.5.1) roughly apply here: the databases quote *BE* values in the low end of ours. This is not surprising, as the databases are compiled based on the experimental and theoretical values in the literature. We just want to emphasize here, once again, that the sites with large binding energies are lacking and this may have important consequences in the astrochemical model predictions.

9.5.2 Astrophysical implications

BEs enter in two hugely important ways in the chemical composition of interstellar objects/clouds: (i) they determine at what dust temperature the frozen species sublimate, and (ii) at what rate the species can diffuse in the ice, as the diffusion energy is a fraction of the *BE* species. Both processes are mathematically expressed by an exponential containing the *BE*. Therefore, even relatively small variations of the *BE* can cause huge differences in the species abundances in the gas phase and on the grain surfaces, where they can react with other species.

In this context, probably the most important astrophysical implication of the present study is that in our ASW model (which is likely the best description to represent the interstellar amorphous ice so far available in the context of the *BE* estimates) a species does not have a single value, but a range of values that depend on the species itself and the site where it is bound. The range can spread by more than a factor two: this obviously can have a huge impact on the modeling and, consequently, our understanding of the interstellar chemical evolution.

Impact of multiple *BEs* in astrochemical modeling

To give a practical example of the impact on the gaseous abundance, we built a toy model for the interstellar ice and simulated the desorption rate of the ice as a function of the temperature. Our scope here is not to compare the toy model predictions with astronomical observations or laboratory experiments: we only mean to show how multiple *BEs* (we used the electronic *BEs*) would lead, in principle, to a different behavior of the ice sublimation process. Therefore, we developed a toy model that does not contain diffusion or reaction processes on the ice surface or rearrangement of the ice during the ice heating, but only a layered structure with two species, specifically water and methanol, where molecules have the range of *BEs* calculated in section 9.4. We then show how the multiple *BEs* affect the temperature at which peaks of desorption appear, considering that only species at the surface of the ice, namely exposed to the void, can sublimate (and not the entire bulk). In this toy model, we

considered ten layers for an icy grain mantle, where the bottom five are made entirely of water and each of the top five layers contains 80% of water and 20% of methanol. The methanol molecules with different *BEs* are distributed randomly on each layer, with a same proportion of *BE* sites. Looking at the *BE* values computed with the DFT//HF-3c method on the ASW model, methanol has eight *BE* values (4414, 5208, 5509, 6362, 6519, 6531,6663 and 10091 K) and, at each layer, there will be 12.5% of methanol molecules with each of the eight *BEs*. The same applies for water molecules, for which we have computed five possible *BEs* (4222, 5689, 5845, 6014 and 7156 K), with 20% molecule with each *BE*. In this model, only molecules of the layers in contact with the void can evaporate: for example, methanol molecules can be trapped if they have water molecules with larger *BEs* on top of them.

We start with an ice temperature of 10 K and at the end it reaches 400 K in 10^5 yr, to simulate the heating of a collapsing Solar-like protostar. The plot of the desorption rates is shown in Fig. 9.12, where we also show them assuming the *BE* values from the KIDA database for methanol and water, respectively. First, when only the KIDA values for *BE* are assumed, water molecules desorb at about 110 K; methanol has two peaks of desorption rates, the first at about 95 K, corresponding to the desorption of the methanol molecules not trapped by the water molecules, and the second peak at about 110 K, when all water molecules desorb so that no methanol molecules are trapped. Note that the desorption of the water molecules of the bottom layers arrives at a slightly larger temperature.

Not surprising, the introduction of multiple *BEs* produces multiple peaks of desorption, both for water and methanol. Figure 9.12 shows that the water desorption rate has a small peak at ∼75 K, a larger one at ∼120 K, then another at ∼140 K and, finally, a last peak at ∼190 K. Methanol starts to desorb at 80 K, the bulk is desorbed between 120 and 140 K, and a last peak is seen around 190 K. We emphasize again that this is a toy model meant to show the potential impact of the new *BEs* on the astrochemical modeling. The details will depend on the real structure of the water ice and how molecules are distributed on the icy mantles. They will determine how many sites have a certain *BE* value and how molecules are trapped in the ice. As a very general remark, we can conclude that species can be in the gas phase at lower and higher dust temperatures than if one only considers a single *BE*.

Looking forward: implementation of multiple *BEs* in astrochemical models

Our toy model introduced in the previous subsection shows the importance of considering multiple *BEs* for each species in the astrochemical models to have more realistic predictions. In this work, we provide the possible *BEs* for 21 species (Table 9.3). Very likely, they cover most of the possibilities, as they span a large range of H-bonds within the water molecules of the ASW. However, from a computational standpoint, such an adsorption variability has to be fully explored, in which plotting the different calculated *BEs* in histograms is useful to provide insights on the shape of the *BE* distribution (Song and Kästner, 2017). Moreover, in order to build a reliable astrochemical model one would also need to know the relative probability for each *BE* and our present study is unable to provide sensible numbers. For that, a statistical study on an ASW model that is much larger than the one used here is necessary. This is a step that we indeed plan to take in future studies. Meanwhile, we adopted a distribution in which we assign an equal fraction of molecules to each *BE*. If one looks carefully at the distribution of the *BEs* for each molecule, they are not uniformly distributed but peak around some values: for example, methanol has a peak around 6000 K and an extreme value of 10091 K only, so that, very likely, this site will be less populated than the sites around 6000 K, as shown by Figure 9.10. Yet, considering even a smaller fraction of these extreme values may have important consequences, for example in the so-called snow lines of protoplanetary disks, or even on the observed abundances towards hot cores and hot corinos, or, finally, towards prestellar cores.

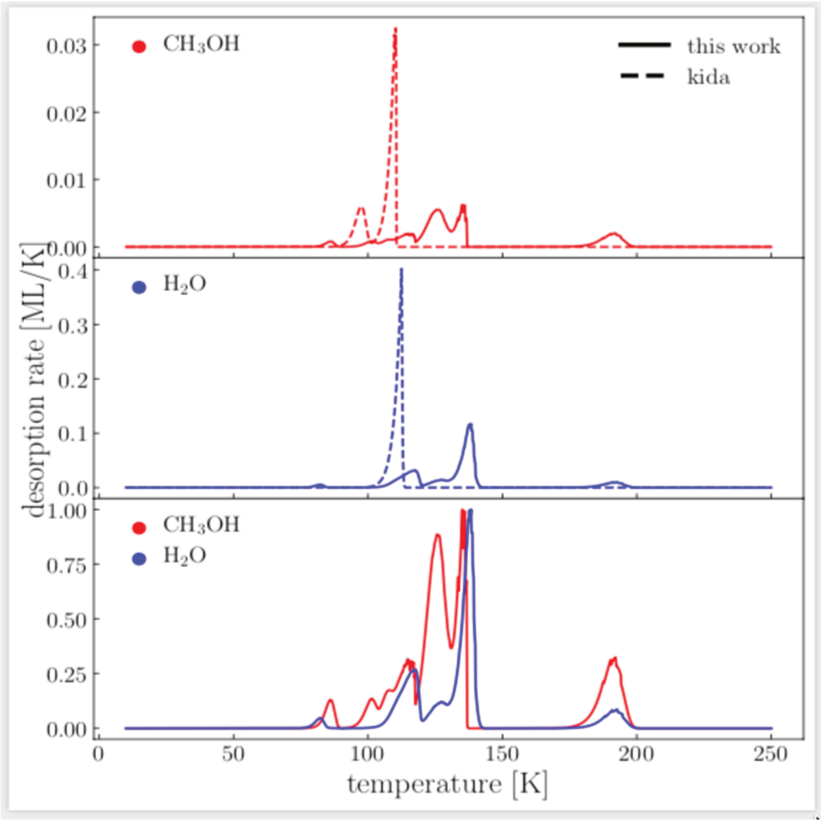

FIGURE 9.12: Desorption rate of methanol (red curves) and water (blue curves) as a function of the temperature. In these computations, the ice is assumed to be composed by ten layers: the bottom five layers contain water while the top fives contain 80% of water and 20% of methanol. The ice is assumed to be at 10 K at the beginning of the simulation and it reaches 400 K in 10^5 yr. The curves refer to the case when a single *BE* (from the KIDA database) is considered for water and methanol, respectively (dashed line), and when the multiple *BEs* of this work are considered (solid line). The bottom panel shows the methanol and water desorption rates normalised to one.

Comments on N_2, CO and HCl

Finally, we would like to comment on three species of the studied list, N_2, CO and the hydrogen chloride (HCl).

N_2 and CO: Our computations show that the *BE* of CO is definitively larger than that of N_2, against the values that are in the astrochemical databases (see Table 9.3): on average, our computed *BEs* differ by about 400 K whereas in the data bases the difference is 200 and 360 K in KIDA and UMIST, respectively. This difference very likely can explain why observations detect N_2H^+, which is formed in the gas phase from N_2, where CO is already frozen on the grain mantles (e.g. Bergin et al., 2002; Redaelli et al., 2019; Tafalla et al., 2004a), a debate which has been going on for almost two decades (e.g. Öberg et al., 2009d; Pagani et al., 2012).

In order to quantify the effect a specifically focused modeling will be necessary, which is out of the scope of the present work. Here we want just to alert that the new *BEs* might explain some long-standing mysteries. Another comment regards the difference in the *BEs* on crystalline surfaces and ASW. Again the CO binding energy is about 500 K larger than that of N_2, and both are larger by about 300 K than those on the ASW, a difference that also has an impact on the snow lines of these two species in protoplanetary disks, where crystalline water ices have been detected (Terada and Tokunaga, 2012).

HCl: Astrochemical models predict that HCl is the reservoir of Cl in molecular gas (e.g. Acharyya and Herbst, 2017; Neufeld and Wolfire, 2009; Schilke et al., 1995). However, all the observations so far carried out have found that only a tiny fraction of Cl is in the gaseous HCl, even in sources where all the grain mantles are supposed to be completely sublimated (Codella et al., 2011; Kama et al., 2015; Peng et al., 2010). One possible explanation is that HCl, once formed in the gas phase, is adsorbed on the grain icy mantles and dissociates, as shown by our calculations on the ASW model and also by previous calculations on the crystalline P-ice model (Casassa, 2000) and for more sophisticated proton-disordered crystalline ice models (Svanberg et al., 2000). It is a matter to be studied whether the sublimation of the water, when the dust reaches about 100-120 K, would also provide a reactive channel transforming the Cl anion in the neutral atom, this latter obviously unobservable. This would help solving the mystery of HCl not being observed in gas-phase. Furthermore, if that would be the case, the population of the chemically reactive atomic Cl will be increased, with important role in the gas-phase chemistry (see e.g. Balucani et al., 2015c; Skouteris et al., 2018b).

9.6 Conclusions

In this work, we present both a new computational approach and realistic models for crystalline and amorphous water ice to be used to address an important topic in Astrochemistry: the binding energies (*BEs*) of molecules on interstellar ice surfaces. We simulated such surfaces by means of two (antipodal) models, in both cases adopting a periodic approach: a crystalline and an amorphous 2D slab models. We relied on density functional theory (DFT) calculations, using the B3LYP-D3 and M06-2X widely used functionals. This approach was further validated by an ONIOM-like correction at CCSD(T) level. Results from this combined procedure confirm the validity of the *BEs* computed with the adopted DFT functionals. The reliability of a cost-effective HF-3c method adopted to optimize the structures at the amorphous ice surface sites was proved by comparing the binding energies computed at the crystalline ice surface at DFT//DFT and DFT//HF-3c level, which were found in very good agreement.

On both ice surface models, we simulated the structure and adsorption energetic features of 21 molecules, including 4 radicals, representative of the most abundant species of the dense ISM. A main conclusion is that the crystalline surfaces only show very limited variability in the adsorption sites, whereas the amorphous surfaces provide a wide variety of adsorption

binding sites, resulting in a distribution of the computed *BE*. Furthermore, *BE* values at crystalline ice surface are in general higher than those computed at the amorphous ice surfaces. This is largely due to the smaller geometry relaxation cost upon adsorption compared to the amorphous cases, imposed by the tighter network of interactions of the denser crystalline ice over the amorphous ice.

Finally, the *BEs* obtained by the present computations were compared with literature data, both from experimental and computational works, as well as those on the public astrochemical databases KIDA and UMIST. In general, our *BEs* agree relatively well with those measured in laboratory, with the exception of O_2 and, at less extent, H_2. On the contrary, previous computations of *BEs*, which considered a very small ($\leq$ 6) water molecules, provide generally lower values with respect to our new computations and, with no surprise, miss the fact that *BEs* have a spread of values which depend on the position of the molecule on the ice. Since the two astrochemical databases mentioned above are based on the literature data, our *BEs* differ, sometimes substantially, from those quoted and do not report multiple *BEs* values.

We discussed some astrophysical implications, showing that the multiple computed *BEs* give rise to a complex process of interstellar iced mantles desorption, with multiple peaks as a function of the temperature that depends (also) on the ice structure. Our new computations do not allow to estimate how the *BEs* are distributed for each molecule as only a statistical study is necessary for that. The new (multiple) *BEs* of N_2 and CO might explain why N_2H^+ deplete later than CO in prestellar cores, while the relatively low abundance of HCl, observed in protostellar sources, could be due to the fact that it dissociates into the water ice, as shown by our calculations.

Finally, the present study shows the importance of theoretical calculations of *BEs* on as realistic as possible ice surfaces. This first study of 21 molecules needs to be extended to the hundreds molecules that are included in the astrochemical models to have a better understanding of the astrochemical evolution of the ISM.

9.7 Appendix A: Computational details

In CRYSTAL17, the multielectron wavefunction is built as a Slater determinant of crystalline/molecular orbitals which are linear combinations of localized functions on the different atoms of the structure which are called Atomic Orbitals (AOs). In a similar manner, the AOs are constructed by linear combinations of localized Gaussian functions which form a basis set. The basis set employed for this work is an Ahlrichts-TVZ (Schäfer et al., 1992), added with polarization functions.

9.7.1 Binding energies, Counterpoise and zero point energy corrections

In a periodic treatment of surface adsorption phenomena one of the most relevant energy value, useful to describe the interacting system, is the binding energy *BEs* which is related to the interaction energy ΔE, so that:

$$BE = -\Delta E \tag{9.5}$$

The binding energy per unit cell per adsorbate molecule *BE* is a positive quantity (for a bounded adsorbate) defined as:

$$BE = [E_m(M//M) + E(S//S)] - E(SM//SM) \tag{9.6}$$

where $E(SM//SM)$ is the energy of a fully relaxed unitary cell containing the surface slab S in interaction with the adsorbate molecules M, $E(S//S)$ is the energy of a fully relaxed

unitary cell containing the slab alone and $E_{\mathrm{m}}(M//M)$ is the molecular energy of the free fully optimized adsorbate molecule (the symbol following the double slash identifies the geometry at which the energy h

$$BE = BE^* - \delta E_S - \delta E_M \tag{9.7}$$
$$\delta E_S = E(S//SM) - E(S//S) \tag{9.8}$$
$$\delta E_M = E(M//SM) - E_{\mathrm{m}}(M//M) \tag{9.9}$$
$$BE^* = [E(S//SM) + E(M//SM)] - E(SM//SM) \tag{9.10}$$

in which δE_S is the deformation energy of the surface ($\delta E_S > 0$) whereas δE_M (=$\Delta E_M + \Delta E_L$) counts both the deformation energy of the molecule (ΔE_M) and the lateral intermolecular interactions (ΔE_L) between the infinite molecule images in the same spatial configuration occurring in the SM periodic system. The purely molecule's deformation energy can be computed as:

$$\Delta E_M = E_m(M//SM) - E_m(M//M) \tag{9.11}$$

in which $E_m(M//SM)$ is the molecular energy of the molecule frozen at the geometry occurring on the surface and $E_m(M//M)$ is the molecular energy of a fully optimized free molecule, so that $\Delta E_M > 0$. The lateral intermolecular interactions, ΔE_L are defined as:

$$\Delta E_L = E(M//SM) - E_m(M//SM) \tag{9.12}$$

and can be either positive (repulsion) or negative (attraction). With those positions, the BE^* interaction energy is then deformation and lateral interactions free, being the result of energy differences between periodic calculations carried out at the geometry of the SM system. For instance, $E(M//SM)$ is the energy of the unit cell of a crystal containing only a molecule in the same geometry assumed in the SM system. The above BE definition can be easily recast to include the basis set superposition error ($BSSE$) correction, using the same counterpoise method adopted for intermolecular complexes (Boys and Bernardi, 1970; Davidson and Feller, 1986). The definition of the $BSSE$ corrected interaction energy BE^C is then:

$$BE^C = BE^{*C} - \delta E_S - \Delta E_M - \Delta E_L^C \tag{9.13}$$
$$BE^{*C} = [E(S[M]//SM) + E([S]M//SM)] - E(SM//SM) \tag{9.14}$$
$$BSSE = BE - BE^C \tag{9.15}$$

in which $E(S[M]//SM)$ and $E([S]M//SM)$ are the energy of the slab plus the ghost functions of the molecules and the energy of the infinite replica of molecules with the ghost functions of the underneath slab, respectively. Because the variational theorem ensures that $BE^{*C} < BE^*$ it immediately results that $BSSE > 0$.

Each of the terms of equation 9.6 can be corrected by the zero point vibrational contribution (in the harmonic approximation), ZPE, therefore arriving to the definition of the zero point correct binding energy $BE(0)$ as:

$$BE(0) = [E_m(M//M) + E(S//S)] - E(SM//SM) + [ZPE(M) + ZPE(S) - ZPE(SM)] \tag{9.16}$$
$$BE(0) = BE - \Delta ZPE \tag{9.17}$$

$$\Delta ZPE = ZPE(SM) - ZPE(M) - ZPE(S) \tag{9.18}$$

In this work the ΔZPE has been evaluated for the crystalline ice cases only and the same correction was adopted also to correct the BE for the the amorphous ice model for the reason described in the Computational Details section.

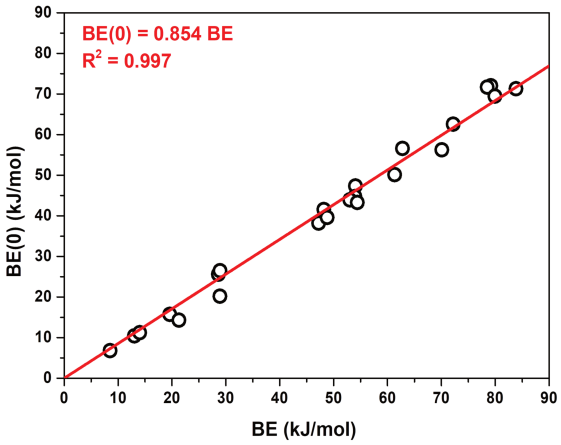

FIGURE 9.13: Linear regression between BE and $BE(0)$ (zero point corrected) values computed for the considered adsorbates on the crystalline ice

9.7.2 Details on HCl adsorbed on crystalline and amorphous ices

Our calculations showed that HCl remains molecularly adsorbed at the crystalline ice surface. At the amorphous one it spontaneously deprotonates making a locally stable ion-pair (Cl^-/H_3O^+) (see the figure below). The reason is that for the surface selected to represent the crystalline ice, the ion pair cannot be stabilized by a large enough network of H-bonds due to the rigidity of the structure. On the contrary, at amorphous surface, Cl^- is engaged in three H-bonds while the hydronium ion remains embedded in the H-bonds provided by the ice surface. A good solvation of the ion-pair is the key determining the final fate of HCl at the ice surfaces (molecular or ion pair) as already pointed out many years ago by Novoa and Sosa for a small water cluster hosting HCl (Novoa and Sosa, 1995). While deprotonation of HCl cannot be excluded for specific crystalline ice surface sites as simulated by Svanberg *et al* (Svanberg et al., 2000) when enough dangling hydrogen can stabilize the anion, deprotonation would be much more common at amorphous ice surface or locally distorted crystalline ones, due to the presence of favorable local environment (see Figure 9.14). Dissociative adsorption was early found by Horn *et al* (Horn et al., 1992) through RAIRS spectroscopy of DCl adsorption on thin D_2O film, and by Olanrewaju *et al* (Olanrewaju et al., 2011a) through thermal and electron-stimulated desorption experiments.

9.7.3 CRYSTAL17 computational parameters

In order to optimize the values of the shrinking factor, the tolerances on integrals of the integration grid (SHRINK, TOLINTEG and GRID parameters (Dovesi et al., 2018) in the code) as described in §9.3 of the article, NH_3 has been adopted as a test case. Geometry optimizations for the adsorption process on the crystalline slab model have been run with the previously described computational scheme, varying one-by-one the aforementioned parameters, with convergence on the pure ΔE as define by Equation (9.5) being the threshold. For this benchmark calculations, $BSSE$, distortion and lateral interaction contributions have not been computed. Results are resumed in what follows.

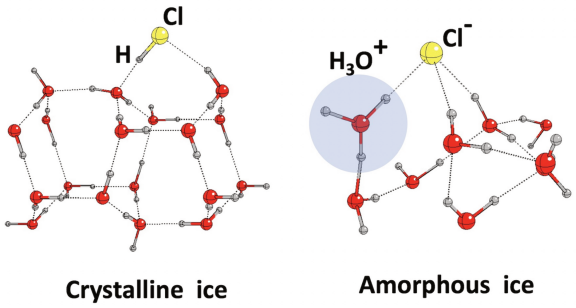

FIGURE 9.14: Enlarged views of HCl adsorbed on a crystalline and amorphous ice models

TABLE 9.4: Optimization of the SHRINK parameter. Tolerances of integrals (TOLINTEG) and integration grid (XLGRID) are fixed to default values.

SHRINK	k points in BZ	ΔE (K)
2 2	4	7873
3 3	5	7889
4 4	10	7889
5 5	13	7890
6 6	20	7890
7 7	25	7890
8 8	34	7890

From Table 9.4 it is clear that ΔE is practically unaffected by the SHRINK value, thus SHRINK = (2 2) has been used for all calculations, allowing the saving of computational time.

TABLE 9.5: Optimization of the TOLINTEG parameter (SHRINK = 2 2 and XLGRID).

TOLINTEG	ΔE (K)
6 6 6 6 12	7889
7 7 7 7 14	7906
8 8 8 8 16	8063
9 9 9 9 18	7981
10 10 10 10 20	7890

As for the SHRINK parameter, the variations of TOLINTEG values does not practically affect the final ΔE value. Consequently, its values have been set equal to 7, 7, 7, 7, and 14.

TABLE 9.6: Optimization of the integration grid parameter (SHRINK = 2 2 and TOLINTEG = 7 7 7 7 14).

GRID	ΔE (K)
XLGRID	7951
XXLGRID	7951

Again, the ΔE is practically unaffected by the changing the adopted grid, therefore XLGRID was selected for all the remaining calculations. Resuming, every other calculation has

been carried out with SHRINK = (2 2), TOLINTEG = (7 7 7 7 14) and XLGRID as computational parameters.

9.7.4 Description of dispersive forces

We optimized the geometry of two parallel benzene rings which interact with each other just because of dispersive forces given the apolar nature of the molecule. The results of Figure 9.15 clearly show that the B3LYP functional needs some a posteriori correction (like the Grimme's D3) for dispersive forces in order to describe correctly the interaction (Grimme et al., 2010), whereas the M06-2X functional is able to describe it correctly without any a posteriori correction (Zhao and Truhlar, 2008b).

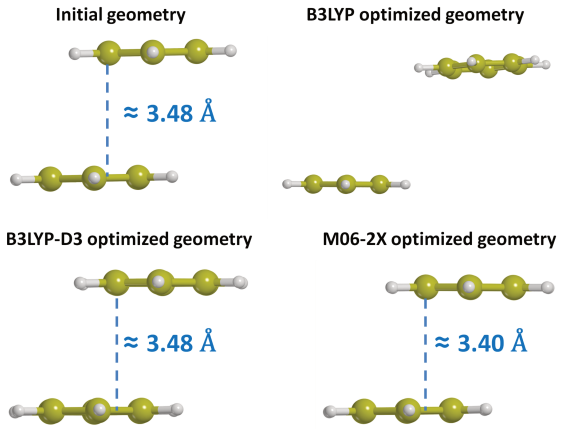

FIGURE 9.15: Initial and optimized geometry of two parallel benzene rings obtained with B3LYP (without dispersion corrections), B3LYP-D3 and M06-2X functionals. Distances between the planes of the two rings are reported in Angstrom.

9.7.5 ONIOM2 correction

Hereafter we summarize the single components (namely *BE*(CCSD(T), μ-2H_2O) extrapolated, *BE*(DFT, μ-2H_2O), *BE*(DFT, ice) and finally the corrected *BE*(ONIOM2)) of the ONIOM2 correction done with the extrapolation procedure already described in § 9.3.

9.8 Appendix B: Crystalline adsorption geometries

The final optimized structures, together with *BEs* and structural properties for every molecule in our set are presented in this section. For some notable cases, more than one initial structure has been modeled. All energetic quantities are in Kelvin (K), while distances are in Å. For every molecule, the gas phase optimized geometry together with its ESP map are also present. In the latter, the isovalue for the electron density is set equal to 1×10^{-6} au, while the values for the ESP (again in au) vary case by case and thus are reported close to the RGB scale legend. "The complete figure set (24 images) is available in the online journal".

TABLE 9.7: Summary of the components used for the calculation of the ONIOM2 correction to the *BEs*. The last column shows the absolute value of the difference between the *BE*(DFT, μ-2H_2O) value and the corrected *BE*(ONIOM2).

Species	***BE*(CCSD(T), μ-nH_2O) extrapolated**	***BE*(DFT, μ-nH_2O)**	***BE*(DFT, ice)**	***BE*(ONIOM2)**	**|Diff|**
H_2	843	796	1192	1240	47
CO	1127	1165	2356	2318	38
CO_2	1939	1817	3442	3564	121
OCS	1354	1138	3478	3695	216
H_2S	2443	2875	5679	5248	432
HCN	3300	3453	5795	5642	153
H_2CO	3199	3114	6490	6575	85
HCl	3993	4475	6501	6019	482
NH_3	4246	4389	7376	7233	143
CH_3OH	5196	5275	8681	8602	79
HCOOH	6263	6223	9522	9562	40
$HCONH_2$	5080	5056	9614	9638	24
OH•	4492	4502	6542	6532	10
NH_2•	3021	2788	6043	6276	233
HCO•	2339	2088	3474	3725	251

9.9 Appendix C: Surface distortion energy on ASW

Hereafter we present the distortion energy contributions calculated on the amorphous slab will be compared with the same contributions calculated on the (010) P-ice model for some notable cases.

TABLE 9.8: Comparison of the distortion energy contributions (in Kelvin) calculated on the (010) P-ice slab and the mean value of these contributions calculated on the different adsorption cases on the amorphous ice model

Species	δE_s crystalline ice	$\langle \delta\ E_s \rangle$ amorphous ice
CH_3OH	662	2790
H_2O	565	3211
HCN	589	1299
HCOOH	878	1660
NH_3	734	1082

9.10 Appendix D: Basis set A-VTZ*

TABLE 9.9: Basis set for the H atom in CRYSTAL17 format used in this work

H	0		
S	3	1	
		34.06134	6.03E-03
		5.123575	4.50E-02
		1.164663	0.201897
S	1		
		0.32723	1
S	1		
		0.103072	1
P	1		
		0.8	1

TABLE 9.10: Basis set for the C atom in CRYSTAL17 format used in this work

C	0		
S	5	1	
		8506.038	5.34E-04
		1275.733	4.13E-03
		290.3119	2.12E-02
		82.0562	8.24E-02
		26.47964	0.240129
S	1		
		9.241459	1
S	1		
		3.364353	1
S	1		
		0.871742	1
S	1		
		0.363524	1
S	1		
		0.128731	1
P	4		
		34.7095	5.33E-03
		7.959088	3.59E-02
		2.378697	0.142003
		0.815401	0.342031
P	1		
		0.289538	1
P	1		
		0.100848	1
D	1		
		1.6	1
D	1		
		0.4	1

TABLE 9.11: Basis set for the N atom in CRYSTAL17 format used in this work

N	0		
S	5	1	
		11913.42	-5.23E-04
		1786.721	-4.04E-03
		406.5901	-2.08E-02
		114.9253	-8.12E-02
		37.10588	-0.23871
S	1		
		12.97168	1
S	1		
		4.730229	1
S	1		
		1.252518	1
S	1		
		0.512601	1
S	1		
		0.179397	1
P	4		
		49.21876	5.55E-03
		11.34894	3.81E-02
		3.428509	0.149414
		1.179951	0.348982
P	1		
		0.417261	1
P	1		
		0.142951	1
D	1		
		2	1
D	1		
		0.5	1

TABLE 9.12: Basis set for the O atom in CRYSTAL17 format used in this work

O	0		
S	5	1	
		15902.65	5.15E-04
		2384.954	3.98E-03
		542.7196	2.05E-02
		153.4041	8.03E-02
		49.54572	0.237668
S	1		
		17.33965	1
S	1		
		6.330336	1
S	1		
		1.699588	1
S	1		
		0.689545	1
S	1		
		0.23936	1
P	4		
		63.27052	6.07E-03
		14.62331	4.19E-02
		4.448952	0.161569
		1.528151	0.356828
P	1		
		0.529973	1
P	1		
		0.175094	1
D	1		
		2.4	1
D	1		
		0.6	1

TABLE 9.13: Basis set for the S atom in CRYSTAL17 format used in this work

S	0		
S	5		
		103954	2.47E-04
		15583.79	1.92E-03
		3546.129	9.96E-03
		1002.681	4.04E-02
		324.9029	0.130675
S	1		
		115.5123	1
S	2		
		44.52821	0.504036
		18.39789	0.230681
S	1		
		5.510068	1
S	1		
		2.125987	1
S	1		
		0.436919	1
S	1		
		0.157309	1
P	5		
		606.6937	2.32E-03
		143.507	1.86E-02
		45.74616	8.60E-02
		16.87291	0.252484
		6.63992	0.446327
P	1		
		2.672714	1
P	1		
		1.000009	1
P	1		
		0.354389	1
P	1		
		0.116713	1
D	1		
		1.1	1
D	1		
		0.275	1

TABLE 9.14: Basis set for the Cl atom in CRYSTAL17 format used in this work

Cl	0		
S	5		
		117805.8	2.42E-04
		17660.27	1.87E-03
		4018.597	9.74E-03
		1136.223	3.95E-02
		368.1206	0.127972
S	1		
		130.8615	1
S	2		
		50.47901	0.428741
		20.91681	0.196685
S	1		
		6.353139	1
S	1		
		2.494801	1
S	1		
		0.543359	1
S	1		
		0.194344	1
P	5		
		681.0688	2.37E-03
		161.1136	1.89E-02
		51.38664	8.78E-02
		18.95851	0.257074
		3.003516	0.371524
P	1		
		7.456529	1
P	1		
		1.060936	1
P	1		
		0.39452	1
P	1		
		0.133233	1
D	1		
		1.3	1
D	1		
		0.325	1

Part IV

Conclusions and perspectives

Chapter 10

Conclusions and perspectives

10.1 Conclusions

In the course of my Ph.D., I focused on modeling the early steps in the chemical evolution in low mass star forming regions. I have explored two objectives, modeling the chemical evolution in star-forming regions with Grainoble+ and modeling experimental ice with Labice.

10.1.1 Astrochemical modeling with Graionble+

The first objective of the thesis was to understand the chemical processes that form and destroy interstellar Complex Organic Molecules (aka iCOMs) in Solar-like star-forming regions. For this purpose, I developed an astrochemistry code, Grarinoble+. I followed two goals with Grainoble+, modeling iCOMs formation in the shocked regions of NGC 1333 IRAS 4A and modeling the ice composition in Taurus MCs.

Goal I, iCOMs formation in the shocked regions of NGC 1333 IRAS 4A: The shocked regions along the low-mass protostar outflows provide a unique environment to study and examine the iCOMs formation paradigms (through gas-phase chemistry or on grain surfaces) because the kinetical age of a shocked region can provide an additional constraint, time dependency, on the model predictions (see, Codella et al., 2017, for the modeling on L1157-B1 outflows). I ran different models varying the initial chemical composition and physical conditions with the Grainoble+ gas-phase mode to predict the abundances in the shocked regions along the outflows of IRAS 4A1 and IRAS 4A2.

I reproduced the observed methanol to acetaldehyde ratio in the shocked regions of the IRAS 4A source by assuming methanol is synthesized on ices and directly sublimated at the shock passage, and acetaldehyde is produced via the gas phase reaction CH_3CH_2 + O where CH_3CH_2 is sublimated from the grain mantles. Furthermore, the methanol/acetaldehyde ratio between the shocked regions of the two outflows ($CH_3OH/CH_3CHO \sim 44$ in IRAS 4A1 and 8-20 in the IRAS 4A2 outflows) and the results from the astrochemical models I conducted suggest that the IRAS 4A1 outflow is likely younger than the one of IRAS 4A2. The ratios are much smaller than the ratios observed in L1157 B1 outflows (130– 250), which suggests that the chemical composition and the kinetic age of the outflows in these two sources are different.

Goal II, Ice mantle composition in Taurus MCs: Chemical complexity starts in Molecular Clouds (MCs).

I used Grainoble+ to model the CNM to MC transition, specifically in Taurus MC at visual extinction 20 mags, and predict the gaseous and icy chemical composition in MCs, which consists mostly of water, CO, CO_2, and methanol. The predictions depend on macroscopic quantities that describe the physical condition of the cloud in the model and microscopic parameters that describe the kinetics of chemical processes in the gas phase and on grain

surfaces. The latter set of parameters is poorly known. The current astrochemical models adopt reactions that use estimated kinetics parameters in the gas phase and on grain surfaces. However, the newest quantum chemical computations have provided us with the binding energies and reaction and diffusion rates on grain surfaces in MCs, such as the water and methanol formation network (see, e. g., Enrique-Romero et al., 2021; Ferrero et al., 2020; He et al., 2018; Senevirathne et al., 2017; Vazart et al., 2020), which I have included in our model.

I ran several models varying the physical conditions within the observed range in the TMC1 to find the physical parameter set that best reproduces the observed ice mantle composition. In he second step, I ran a grid of models varying the chemical parameters and the initial elemental abundance in the model.

Our results show that the model with $n_{H_2} = 2 \times 10^4$ cm^{-3}, T=10 K, and $\zeta_{H_2} = 3 \times 10^{-18}$ best reproduce the ice composition in the TMC1 cloud. The main results from the second step are as follows. Our models have constrained some of the micro-physics processes and parameters and provide a constrain on the age of TMC1, around 0.1 Myr. Our models, which incorporate the new theoretical results on the C chemisoprtion on the icy grain surfaces, suggest that the diffuse-to-MC "missing" carbon claimed by several authors could be in the form of frozen atomic carbon.

10.1.2 Simulation of ices grown in experimental setups with Labice

I developed the Labice model that simulates the TPD experiments, which uses the rate equation approach similar to Grainoble+. I pursued two goals with the Labice model, modeling the water and CO composite ices using the CO trapped fraction and modeling the impact of the multi-binding energy approach on the sublimation of species.

Goal I, Modeling the water and CO composite ices using the CO trapped fraction: Here, I aimed to simulate a TPD experiment and compare the CO trapped fraction and the ice model with the results from previous experiments. I modeled various compact ices in which the total ice composition is fixed while their ratio in each layer deviates from the total bulk ratio drawn from a uniform distribution to simulate the stochastic distribution of species over the layers. I varied the total number of layers and the stochasticity parameter of the ice to reproduce the CO trapped fraction as a function of water thickness in H_2O:CO ices with 3:1 and 2:1 ratios.

The simulations in thinner ices ($<$ 8 MLs) cannot conclusively reproduce the trapped fraction for ices with water thickness below $\sim$ 8 MLs, assuming no porosity. This suggests that these ices do not have a regular porous structure (as seen in thicker ices) and show a high surface area, similar to the conclusions of He et al. (2019) and Kimmel et al. (2001a)

Our simulations indicate that the stochasticity percentages decrease with water thickness above $\sim$ 8 MLs from $\sim$ 25% to $\sim$ 1% which may indicate that the stochasticity may be dependent on the water thickness. It means that the homogeneity in water and CO mixing over the layers possibly increases with water thickness. Previous experiments and simulations on pure water ices have shown that ices grown at zero incident angle are rather compact, and those above $\sim$ 10 MLs thickness have a small surface area percentage that decreases slowly with water thickness (He et al., 2019). Our results seem to suggest that water ice mixtures (in this case, with CO) above a threshold of $\sim$ 8 MLs water thickness (corresponding to $\sim 10-12$ MLs total thickness) can also have a compact and low porous structure in which the water and CO are increasingly more homogeneously distributed over the layers.

Goal II, The impact of multiple binding energies in the desorption of volatile species: The interstellar grain icy mantle is comprised mainly of water that is mixed with other volatile species in smaller quantities. A precise evaluation of a species binding energy (BE) is crucial for astrochemical models to reproduce the observations since BEs govern sublimation and

diffusion rates of species on ice surfaces. BEs can be inferred from experiments or theoretical computations. This work computed the BE of 21 astrochemically relevant molecules on ASW and crystalline ice slabs using quantum computational methods. The results show that due to the spread of binding sites on ASW ice, the BE for each species show a distribution.

I used the Labice model to show the potential impact of assuming multi-BEs in astrochemical models and sublimated species in this work. Labice simulated a 10 layered ice of water and methanol composite where the top 5 layers contain 20% methanol. I simulated an increase in temperature from 10 K to 400 over ten thousand years to mimic the warm-up phase of a collapsing solar-like protostar. I ran two simulations. The first assumes a normal distribution of BEs calculated in this work for each species, and the second uses a single BE from the KIDA database for each one.

While single BE simulation shows one desorption peak at $\sim$ 110 K for water and two for methanol at $\sim$ 95 K and $\sim$ 110 K corresponding to thermal desoption and co-desorption peaks, respectively, the multi-BE simulation shows multiple peaks for both species extending from $\sim$ 75 to $\sim$ 190 K, resulting from the multi-BE assumption. This could be reason why some species are present in the gas phase at lower temperatures than single-binding energy models predict.

10.2 Perspectives

10.2.1 Grainoble+ perspective

I developed Grainoble+ in a modular way such that it can easily be modified or upgraded. Additionally, I designed a python interface so that other users can easily employ Grainoble+ for their modelings. Therefore, a wide variety of projects can follow up my thesis work. The following list is the few example projects that can be done with Grainoble+ with minimal to no further modifications in the code with respect to its current status.

Core collapse modeling I can model a core collapse using time-dependent physical profiles as the next step. The model will consist of two stages: static and collapse. This step can use Witzel et al. 2022 (submitted) physical and chemical assumptions and the ice mantle composition to calculate the iCOMs abundances that can be formed during the collapse phase. I focused on modeling the TMC1 in our paper, and I can follow up with modeling L1544 prestellar core and HL tau Class I sources, both of which are studied extensively (e. g., Scibelli and Shirley, 2020).

Multi-grain modelling Grainoble+ has implemented the basis of multi-grain modeling. Two projects can follow up (1) showing the impact of multi-grain modeling on the ice mantle composition in the TMC1 cloud. I can use the same parameters in Witzel et al. submitted (2022) with the multi-grain option. (2) Simulating a core-collapse model using multi-grain and examining its impact on the formation of iCOMs.

CR desorption processes I am also interested in modeling the CR-induced processes proposed by Shingledecker et al. (2018) as a variation on the three projects mentioned above and to examine its effect on the iCOMs abundances.

H_2 formation induced desorption Roberts et al. (2007) have shown the formation of H_2 on ices can have a substantial effect on the desorption of solid species in cold cores modeling but it is possibly not enough to reproduce the gaseous abundances. Pantaleone et al. (2021) work has confirmed that, given the rate of H_2 formation and accretion of CO on ice surfaces,

it is possible that the H_2 formation-induced desorption can have a significant impact on the desorption rate of CO in cold MCs. I have implemented the basis of this process in Grainoble+, while waiting for follow-up work by Pantaleone and collaborators on Pantaleone et al. (2021). After, I can finalize the modification in Grainoble+ and start modeling the formation of a MC and examining this impact.

Modeling the chemical evolution in the shocked regions along the outflows I have modeled the shocked regions of NGC 1333 IRAS 4A (IRAS 4A hereafter) in De Simone et al. (2020) to reproduce the methanol to acetaldehyde ratio and to examine the formation route of acetaldehyde (if it is originated in the gas phase or if it is synthesized on grain mantles). IRAS 4A and the L1157-B1 are the two shocked regions that have been observed and studied extensively, so far. The preliminary results by Bouvier and collaborators have detected methanol and acetaldehyde along the extended outflow of fir6c-a in the OMC-2/3. This outflow can be the third region to model and examine the iCOMs formation paradigm.

Multi-binding energy modeling As we have shown in Ferrero et al. (2020), modeling with multi-binding energy assumption may have a substantial effect on the abundance of sublimated species (see, for example, Grassi et al., 2020). It will be interesting to see its impact on the surface reaction rates and the abundance of sublimated species. This paper can be a follow-up paper on the Witzel et al.2022 (submitted) and the core-collapse project.

10.2.2 Labice perspective

The Labice model is also implemented in a modular fashion with an easy-to-use interface. Therefore, one can include more processes if needed, such as crystalization and surface reactions.

Porosity Experiments and simulations have shown that water ice grown under any deposition conditions has a porous structure. Additionally, porosity increases the effective surface area in ices, which affects the desorption and the trapping of volatile species in mixed ices. To accurately model ices formed in experimental setups, it is imperative to compare the simulations with experimental results. As the next step to our current results, Labice can model the porosity of water ice mixtures, simulate the desorption of the ice composition, and compare the results with the existing experiments and simulations, such the experiments conducted by Kruczkiewicz and collaborators.

Multi-binding energy As we have shown in Ferrero et al. (2020), multi-binding energy modeling has a significant impact on the abundance of sublimated species. In Ferrero et al. (2020), I assumed a uniform distribution on the BEs due to the lack of statistical information on the distribution of BEs. As the next step, I can consider other distributions, for example, a Gaussian distribution or distributions from theoretical works (e. g., Bovolenta et al., 2020). The idea is to discretize the distribution into a finite number of bins. The questions are: How many bins are sufficient to see the impact on the desorption rates?, Where is the limit where the results starts to lose sensitivity to the number of bins in the distribution?, Where is the limit after which the model does not produce sensible results due to perhaps numerical inaccuracies that may rise?

Labice can simulate multi-binding energy assumptions and derive the limiting parameters before its implementation in astrochemical codes, which are generally more complex.

Water crystallization Amorphous water is in a metastable state. It means that over time, whether in an isothermal state or under heating, it transforms into crystalline ice. The crystalization of water ice leads to the release of trapped volatile species through the crystalization-induced cracks (volcano desorption). Labice can model the crystalization using the rates derived from experiments (Smith et al., 2011) to simulate the volcano desorption peak of volatile species.

Water formation The Labice model uses the three-phase rate-equation approach. In principle, it can include and model surface or bulk reactions. The model can consist of simple reaction networks, such as methanol or water formation, and compare the results with the existing experiments and Monte Carlo simulations (Cuppen et al., 2009, 2010).

Bibliography

Acharyya, K. et al. (May 2007). "Desorption of CO and O_2 interstellar ice analogs". In: 466.3, pp. 1005–1012. DOI: 10.1051/0004-6361:20066272. arXiv: astro-ph/0702322 [astro-ph].

Acharyya, Kinsuk and Eric Herbst (2017). "Gas-grain fluorine and chlorine chemistry in the interstellar medium". In: 850.1, p. 105.

Acharyya, Kinsuk, George E. Hassel, and Eric Herbst (May 2011). "The Effects of Grain Size and Grain Growth on the Chemical Evolution of Cold Dense Clouds". In: 732.2, 73, p. 73. DOI: 10.1088/0004-637X/732/2/73.

Acharyya, Kinsuk, Sean W. Schulte, and Eric Herbst (Mar. 2020). "The Effect of Chemisorption on the Chemical Evolution of Star-forming Regions". In: 247.1, 4, p. 4. DOI: 10.3847/1538-4365/ab6599.

Adams, Fred C., Charles J. Lada, and Frank H. Shu (Jan. 1987). "Spectral Evolution of Young Stellar Objects". In: 312, p. 788. DOI: 10.1086/164924.

Agúndez, M. et al. (Jan. 2022). "Detection of the propargyl radical at λ 3 mm". In: 657, A96, A96. DOI: 10.1051/0004-6361/202142678. arXiv: 2112.05370 [astro-ph.GA].

Agúndez, Marcelino and Valentine Wakelam (Dec. 2013). "Chemistry of Dark Clouds: Databases, Networks, and Models". In: *Chemical Reviews* 113.12, pp. 8710–8737. DOI: 10.1021/cr4001176. arXiv: 1310.3651 [astro-ph.GA].

Aikawa, Yuri, Eric Herbst, and Fedor N. Dzegilenko (Dec. 1999). "Grain Surface Recombination of HCO^+". In: 527.1, pp. 262–265. DOI: 10.1086/308079.

Aikawa, Yuri et al. (July 2020). "Chemical Variation among Protostellar Cores: Dependence on Prestellar Core Conditions". In: 897.2, 110, p. 110. DOI: 10.3847/1538-4357/ab994a. arXiv: 2006.11696 [astro-ph.SR].

Al-Halabi, A. and E. F. van Dishoeck (Dec. 2007). "Hydrogen adsorption and diffusion on amorphous solid water ice". In: 382.4, pp. 1648–1656. DOI: 10.1111/j.1365-2966.2007.12415.x.

Al-Halabi, A and EF Van Dishoeck (2007). "Hydrogen adsorption and diffusion on amorphous solid water ice". In: *MNRAS* 382.4, pp. 1648–1656.

Al-Halabi, A. et al. (2002). "Sticking of Hydrogen Atoms to Crystalline Ice Surfaces: Dependence on Incidence Energy and Surface Temperature". In: *The Journal of Physical Chemistry B* 106.25, pp. 6515–6522. DOI: 10.1021/jp020007y. eprint: https://doi.org/10.1021/jp020007y. URL: https://doi.org/10.1021/jp02000.

Al-Halabi, A. et al. (Aug. 2004). "Adsorption of CO on amorphous water-ice surfaces". In: 422, pp. 777–791. DOI: 10.1051/0004-6361:20035939.

Alan May, R., R. Scott Smith, and Bruce D. Kay (2013). "The release of trapped gases from amorphous solid water films. II. "Bottom-up" induced desorption pathways". In: *The Journal of Chemical Physics* 138.10, p. 104502. DOI: 10.1063/1.4793312. eprint: https://doi.org/10.1063/1.4793312. URL: https://doi.org/10.1063/1.4793312.

Allamandola, L. J., J. M. Greenberg, and C. A. Norman (Aug. 1979). "On the middle infrared fluorescence and absorption of molecules in grain mantles." In: 77.1-2, pp. 66–74.

Allen, M. and G. W. Robinson (Jan. 1975). "Formation of molecules on small interstellar grains." In: 195, pp. 81–90. DOI: 10.1086/153306.

— (Mar. 1977). "The molecular composition of dense interstellar clouds." In: 212, pp. 396–415. DOI: 10.1086/155059.

Allodi, M. A. et al. (Dec. 2013). "Complementary and Emerging Techniques for Astrophysical Ices Processed in the Laboratory". In: 180.1-4, pp. 101–175. DOI: 10.1007/s11214-013-0020-8.

Altwegg, K. et al. (May 2016). "Prebiotic chemicals–amino acid and phosphorus–in the coma of comet 67P/Churyumov-Gerasimenko". en. In: *Science Advances* 2.5, e1600285. DOI: 10.1126/sciadv.1600285. URL: https://ui.adsabs.harvard.edu/abs/2016SciA...2E0285A/abstract (visited on 09/29/2019).

Altwegg, Kathrin et al. (Jan. 2020). "Evidence of ammonium salts in comet 67P as explanation for the nitrogen depletion in cometary comae". In: *Nature Astronomy* 4, pp. 533–540. DOI: 10.1038/s41550-019-0991-9. arXiv: 1911.13005 [astro-ph.EP].

Álvarez-Barcia, S. et al. (Sept. 2018). "Hydrogen transfer reactions of interstellar complex organic molecules". In: 479.2, pp. 2007–2015. DOI: 10.1093/mnras/sty1478. arXiv: 1806.02062 [astro-ph.GA].

Amiaud, L. et al. (Oct. 2007). "Interaction of atomic and molecular deuterium with a nonporous amorphous water ice surface between 8 and 30 K". In: 127.14, pp. 144709–144709. DOI: 10.1063/1.2746323.

Andersson, S. and E. F. van Dishoeck (Dec. 2008). "Photodesorption of water ice. A molecular dynamics study". In: 491.3, pp. 907–916. DOI: 10.1051/0004-6361:200810374. arXiv: 0810.1916 [astro-ph].

Andersson, Stefan, Geert-Jan Kroes, and Ewine F. van Dishoeck (June 2005). "Photodissociation of water in crystalline ice: A molecular dynamics study". In: *Chemical Physics Letters* 408.4-6, pp. 415–421. DOI: 10.1016/j.cplett.2005.04.073. arXiv: astro-ph/0505621 [astro-ph].

Andersson, Stefan et al. (Feb. 2006). "Molecular-dynamics study of photodissociation of water in crystalline and amorphous ices". In: 124.6, pp. 064715–064715. DOI: 10.1063/1.2162901. arXiv: astro-ph/0512596 [astro-ph].

Andre, P., D. Ward-Thompson, and M. Barsony (May 2000). "From Prestellar Cores to Protostars: the Initial Conditions of Star Formation". In: *Protostars and Planets IV*. Ed. by V. Mannings, A. P. Boss, and S. S. Russell, p. 59. arXiv: astro-ph/9903284 [astro-ph].

André, P. et al. (Jan. 2014). "From Filamentary Networks to Dense Cores in Molecular Clouds: Toward a New Paradigm for Star Formation". In: *Protostars and Planets VI*. Ed. by Henrik Beuther et al., p. 27. DOI: 10.2458/azu_uapress_9780816531240-ch002. arXiv: 1312.6232 [astro-ph.GA].

Andre, Philippe, Derek Ward-Thompson, and Mary Barsony (Mar. 1993). "Submillimeter Continuum Observations of rho Ophiuchi A: The Candidate Protostar VLA 1623 and Prestellar Clumps". In: 406, p. 122. DOI: 10.1086/172425.

Arasa, C. et al. (May 2010). "Molecular dynamics simulations of the ice temperature dependence of water ice photodesorption". In: 132.18, pp. 184510–184510. DOI: 10.1063/1.3422213. arXiv: 1005.3617 [physics.chem-ph].

Arce, Héctor G. et al. (July 2008). "Complex Molecules in the L1157 Molecular Outflow". In: 681.1, p. L21. DOI: 10.1086/590110. arXiv: 0805.2550 [astro-ph].

Arce, Héctor G. et al. (July 2008). "Complex Molecules in the L1157 Molecular Outflow". In: *The Astrophysical Journal Letters* 681, p. L21. ISSN: 0004-637X. DOI: 10.1086/590110. URL: http://adsabs.harvard.edu/abs/2008ApJ...681L..21A (visited on 04/09/2019).

Asano, Ryosuke S. et al. (Mar. 2013). "Dust formation history of galaxies: A critical role of metallicity for the dust mass growth by accreting materials in the interstellar medium". In: *Earth, Planets and Space* 65.3, pp. 213–222. DOI: 10.5047/eps.2012.04.014. arXiv: 1206.0817 [astro-ph.GA].

Ascenzi, Daniela et al. (May 2019). "Destruction of dimethyl ether and methyl formate by collisions with He^+". In: 625, A72, A72. DOI: 10.1051/0004-6361/201834585. arXiv: 1903.07204 [astro-ph.SR].

Ásgeirsson, V, H Jónsson, and KT Wikfeldt (2017). "Long-Time Scale Simulations of Tunneling-Assisted Diffusion of Hydrogen on Ice Surfaces at Low Temperature". In: *The Journal of Physical Chemistry C* 121.3, pp. 1648–1657.

Asplund, Martin et al. (Sept. 2009). "The Chemical Composition of the Sun". In: 47.1, pp. 481–522. DOI: 10.1146/annurev.astro.46.060407.145222. arXiv: 0909.0948 [astro-ph.SR].

Atkinson, R. et al. (Sept. 2004). "Evaluated kinetic and photochemical data for atmospheric chemistry: Volume I - gas phase reactions of O_x, HO_x, NO_x and SO_x species". In: *Atmospheric Chemistry & Physics* 4.6, pp. 1461–1738. DOI: 10.5194/acp-4-1461-2004.

Avgul, Nn et al. (1971). "CALCULATION OF ADSORPTION OF CARBON DIOXIDE ON NON-POROUS AND MICROPOROUS CRYSTALLINE ADSORBENTS FROM VIRIAL EQUATIONS". In: *RUSSIAN JOURNAL OF PHYSICAL CHEMISTRY,USSR* 45.2, 243–. ISSN: 0036-0244.

Ayotte, Patrick et al. (Dec. 2001). "Effect of porosity on the adsorption, desorption, trapping, and release of volatile gases by amorphous solid water". In: 106.E12, pp. 33387–33392. DOI: 10.1029/2000JE001362.

Ayouz, M. A. et al. (Nov. 2019). "Dissociative electron recombination of NH_2CHOH^+ and implications for interstellar formamide abundance". In: 490.1, pp. 1325–1331. DOI: 10.1093/mnras/stz2658.

Bachiller, R. et al. (Nov. 1998). "A molecular jet from SVS 13B near HH 7-11". en. In: *Astronomy and Astrophysics* 339, p. L49. URL: https://ui.adsabs.harvard.edu/1998A&A...339L..49B/abstract (visited on 10/01/2019).

Bacmann, A. et al. (Sept. 2000). "An ISOCAM absorption survey of the structure of pre-stellar cloud cores". In: 361, pp. 555–580. arXiv: astro-ph/0006385 [astro-ph].

Bacmann, A. et al. (July 2002). "The degree of CO depletion in pre-stellar cores". In: 389, pp. L6–L10. DOI: 10.1051/0004-6361:20020652. arXiv: astro-ph/0205154 [astro-ph].

Bacmann, A. et al. (May 2012). "Detection of complex organic molecules in a prestellar core: a new challenge for astrochemical models". In: 541, L12, p. L12. DOI: 10.1051/0004-6361/201219207.

Bahr, S, C Toubin, and V Kempter (2008). "Interaction of methanol with amorphous solid water". In: *The Journal of chemical physics* 128.13, p. 134712.

Ballesteros-Paredes, Javier et al. (June 2020). "From Diffuse Gas to Dense Molecular Cloud Cores". In: 216.5, 76, p. 76. DOI: 10.1007/s11214-020-00698-3. arXiv: 2006.01326 [astro-ph.GA].

Balucani, Nadia (Dec. 2020). "An atomistic approach to prebiotic chemistry: A tool to overcome the limits of laboratory simulations. Comment on "Prebiotic chemistry and origins of life research with atomistic computer simulations"". In: *Physics of Life Reviews* 34, pp. 136–138. DOI: 10.1016/j.plrev.2019.03.006.

Balucani, Nadia, Cecilia Ceccarelli, and Vianney Taquet (Apr. 2015a). "Formation of complex organic molecules in cold objects: the role of gas-phase reactions". In: *Monthly Notices of the Royal Astronomical Society* 449, pp. L16–L20. ISSN: 0035-8711. DOI: 10.1093/mnrasl/slv009. URL: http://adsabs.harvard.edu/abs/2015MNRAS.449L..16B (visited on 03/31/2019).

Balucani, Nadia, Cecilia Ceccarelli, and Vianney Taquet (Apr. 2015b). "Formation of complex organic molecules in cold objects: the role of gas-phase reactions". In: *Monthly Notices of the Royal Astronomical Society* 449, pp. L16–L20. ISSN: 0035-8711. DOI: 10.1093/mnrasl/slv009. URL: http://adsabs.harvard.edu/abs/2015MNRAS.449L..16B (visited on 03/31/2019).

— (Feb. 2015c). "Formation of complex organic molecules in cold objects: the role of gas-phase reactions". In: *MNRAS: Letters* 449.1, pp. L16–L20. ISSN: 1745-3925. DOI: 10.1093/mnrasl/slv009. eprint: https://academic.oup.com/mnrasl/article-pdf/449/1/L16/9419858/slv009.pdf.

Balucani, Nadia et al. (Nov. 2018). "A theoretical investigation of the reaction between the amidogen, NH, and the ethyl, C_2H_5, radicals: a possible gas-phase formation route of interstellar and planetary ethanimine". In: *Molecular Astrophysics* 13, pp. 30–37. DOI: 10.1016/j.molap.2018.10.001. arXiv: 1810.10416 [astro-ph.EP].

Barnard, E. E. (Apr. 1907). "On a nebulous groundwork in the constellation Taurus." In: 25, pp. 218–225. DOI: 10.1086/141434.

Barone, V. et al. (Oct. 2015). "Gas-phase formation of the prebiotic molecule formamide: insights from new quantum computations." In: 453, pp. L31–L35. DOI: 10.1093/mnrasl/slv094. arXiv: 1507.03741 [astro-ph.GA].

Bartlett, Rodney J and Monika Musiał (2007). "Coupled-cluster theory in quantum chemistry". In: *Rev Mod Phys* 79.1, p. 291.

Baulch, D. L. et al. (2005). "Evaluated Kinetic Data for Combustion Modeling: Supplement II". In: *Journal of Physical and Chemical Reference Data* 34.3, p. 757. DOI: 10.1063/1.1748524. URL: https://doi.org/10.1063/1.1748524.

Becke, Axel D (1988). "A multicenter numerical integration scheme for polyatomic molecules". In: *J Chem Phys* 88.4, pp. 2547–2553.

Becke, Axel D. (Jan. 1993). "A new mixing of Hartree-Fock and local density-functional theories". In: 98.2, pp. 1372–1377. DOI: 10.1063/1.464304.

Becke, Axel D. (1993). "A new mixing of Hartree–Fock and local density-functional theories". In: *The Journal of Chemical Physics* 98.2, pp. 1372–1377. DOI: 10.1063/1.464304.

Beichman, C. A. et al. (Aug. 1986). "Candidate Solar-Type Protostars in Nearby Molecular Cloud Cores". In: 307, p. 337. DOI: 10.1086/164421.

Bell, A. R. (Jan. 1978). "The acceleration of cosmic rays in shock fronts - I." In: 182, pp. 147–156. DOI: 10.1093/mnras/182.2.147.

Belloche, A. et al. (May 2017). "Rotational spectroscopy, tentative interstellar detection, and chemical modeling of N-methylformamide". In: 601, A49, A49. DOI: 10.1051/0004-6361/201629724. arXiv: 1701.04640 [astro-ph.GA].

Bennett, Chris J and Ralf I Kaiser (2007). "On the formation of glycolaldehyde (HCOCH2OH) and methyl formate (HCOOCH3) in interstellar ice analogs". In: 661.2, p. 899.

Bennett, Chris J. et al. (2005a). "A Combined Experimental and Computational Investigation on the Synthesis of Acetaldehyde [$CH_3CHO(X\ ^1A')$] in Interstellar Ices". In: 624.2, pp. 1097–1115. DOI: 10.1086/429119.

Bennett, Chris J. et al. (2005b). "Laboratory Studies on the Formation of Three C_2H_4O Isomers-Acetaldehyde (CH_3CHO), Ethylene Oxide (c-C_2H_4O), and Vinyl Alcohol (CH_2CHOH)-in Interstellar and Cometary Ices". In: 634.1, pp. 698–711. DOI: 10.1086/452618.

Benson, P. J. and P. C. Myers (Sept. 1989). "A Survey for Dense Cores in Dark Clouds". In: 71, p. 89. DOI: 10.1086/191365.

Bergeron, H. et al. (Oct. 2008). "OH Formation from O and H Atoms Physisorbed on a Graphitic Surface through the Langmuir-Hinshelwood Mechanism: A Quasi-Classical Approach". In: *Journal of Physical Chemistry A* 112, pp. 11921–11930. DOI: 10.1021/jp8050966.

Bergin, E. A., W. D. Langer, and P. F. Goldsmith (Mar. 1995). "Gas-Phase Chemistry in Dense Interstellar Clouds Including Grain Surface Molecular Depletion and Desorption". In: 441, p. 222. DOI: 10.1086/175351.

Bergin, Edwin A. and Mario Tafalla (Sept. 2007). "Cold Dark Clouds: The Initial Conditions for Star Formation". In: 45.1, pp. 339–396. DOI: 10.1146/annurev.astro.45.071206.100404. arXiv: 0705.3765 [astro-ph].

Bergin, Edwin A. et al. (2002). "N[TINF]2[/TINF]H[TSUP][/TSUP] and C[TSUP]18[/TSUP]O Depletion in a Cold Dark Cloud". In: 570.2, pp. L101–L104. DOI: 10.1086/340950.

Bergin, Edwin A. et al. (Sept. 2004). "Molecular Cloud Formation behind Shock Waves". In: 612.2, pp. 921–939. DOI: 10.1086/422578. arXiv: astro-ph/0405329 [astro-ph].

Bertin, Mathieu et al. (Dec. 2013). "Indirect Ultraviolet Photodesorption from CO:N_2 Binary Ices — an Efficient Grain-gas Process". In: 779.2, 120, p. 120. DOI: 10.1088/0004-637X/779/2/120. arXiv: 1312.4571 [astro-ph.GA].

Bianchi, E. et al. (Oct. 2017). "Deuterated methanol on a solar system scale around the HH212 protostar". en. In: *Astronomy and Astrophysics* 606, p. L7. DOI: 10.1051/0004-6361/201731404. (Visited on 07/17/2019).

Bianchi, E. et al. (Feb. 2019). "The census of interstellar complex organic molecules in the Class I hot corino of SVS13-A". en. In: *Monthly Notices of the Royal Astronomical Society* 483.2, p. 1850. DOI: 10.1093/mnras/sty2915. URL: https://ui.adsabs.harvard.edu/abs/2019MNRAS.483.1850B/abstract (visited on 07/17/2019).

Bianchi, E. et al. (Nov. 2020). "FAUST I. The hot corino at the heart of the prototypical Class I protostar L1551 IRS5". In: 498.1, pp. L87–L92. DOI: 10.1093/mnrasl/slaa130. arXiv: 2007.10275 [astro-ph.SR].

Bisschop, S. E. et al. (Apr. 2006). "Desorption rates and sticking coefficients for CO and N_2 interstellar ices". In: 449.3, pp. 1297–1309. DOI: 10.1051/0004-6361:20054051. arXiv: astro-ph/0601082 [astro-ph].

Bjerkeli, P. et al. (Sept. 2011). "Herschel observations of the Herbig-Haro objects HH 52-54". In: 533, A80, A80. DOI: 10.1051/0004-6361/201116846. arXiv: 1106.5440 [astro-ph.GA].

Blake, Geoffrey A. et al. (Mar. 1995). "A Molecular Line Study of NGC 1333/IRAS 4". In: 441, p. 689. DOI: 10.1086/175392.

Blake, Geoffrey A. et al. (Mar. 1995). "A Molecular Line Study of NGC 1333/IRAS 4". en. In: *The Astrophysical Journal* 441, p. 689. ISSN: 0004-637X. DOI: 10.1086/175392. URL: https://ui.adsabs.harvard.edu/abs/1995ApJ...441..689B/abstract (visited on 09/29/2019).

Blandford, R. D. and J. P. Ostriker (Apr. 1978). "Particle acceleration by astrophysical shocks." In: 221, pp. L29–L32. DOI: 10.1086/182658.

Bok, Bart J. and Edith F. Reilly (Mar. 1947). "Small Dark Nebulae." In: 105, p. 255. DOI: 10.1086/144901.

Bonnor, W. B. (Jan. 1956). "Boyle's Law and gravitational instability". In: 116, p. 351. DOI: 10.1093/mnras/116.3.351.

Bontemps, S. et al. (July 1996). "Evolution of outflow activity around low-mass embedded young stellar objects". In: 311, pp. 858–872.

Boogert, A. C. Adwin, Perry A. Gerakines, and Douglas C. B. Whittet (Aug. 2015). "Observations of the icy universe." In: 53, pp. 541–581. DOI: 10.1146/annurev-astro-082214-122348. arXiv: 1501.05317 [astro-ph.GA].

Boogert, A. C. Adwin, Perry A. Gerakines, and Douglas C. B. Whittet (Aug. 2015a). "Observations of the icy universe." In: *Annual Review of Astronomy and Astrophysics* 53, pp. 541–581. ISSN: 0066-4146. DOI: 10.1146/annurev-astro-082214-122348. URL: http://adsabs.harvard.edu/abs/2015ARA%26A..53..541B (visited on 04/05/2019).

Boogert, AC Adwin, Perry A Gerakines, and Douglas CB Whittet (2015b). "Observations of the icy universe". In: *Annu Rev Astron Astrophys* 53, pp. 541–581.

Borden, Weston Thatcher et al. (2017). "Dioxygen: what makes this triplet diradical kinetically persistent?" In: *JACS* 139.26, pp. 9010–9018.

Bossa, J. B. et al. (Sept. 2012). "Thermal collapse of porous interstellar ice". In: 545, A82, A82. DOI: 10.1051/0004-6361/201219340.

Bottinelli, S. et al. (Nov. 2004). "Complex Molecules in the Hot Core of the Low-Mass Protostar NGC 1333 IRAS 4A". In: 615.1, pp. 354–358. DOI: 10.1086/423952. arXiv: astro-ph/0407154 [astro-ph].

Bottinelli, S. et al. (Nov. 2004). "Complex Molecules in the Hot Core of the Low-Mass Protostar NGC 1333 IRAS 4A". en. In: *The Astrophysical Journal* 615.1, p. 354. DOI: 10.1086/423952. URL: https://ui.adsabs.harvard.edu/abs/2004ApJ...615..354B/abstract (visited on 09/29/2019).

Bovino, S. et al. (Nov. 2017). "H_2 Ortho-to-para Conversion on Grains: A Route to Fast Deuterium Fractionation in Dense Cloud Cores?" In: 849.2, L25, p. L25. DOI: 10.3847/2041-8213/aa95b7. arXiv: 1708.02046 [astro-ph.GA].

Bovolenta, Giulia et al. (Dec. 2020). "High level ab initio binding energy distribution of molecules on interstellar ices: Hydrogen fluoride". In: *Molecular Astrophysics* 21, 100095, p. 100095. DOI: 10.1016/j.molap.2020.100095. arXiv: 2010.09138 [astro-ph.GA].

Boys, S F_ and FJMP Bernardi (1970). "The calculation of small molecular interactions by the differences of separate total energies. Some procedures with reduced errors". In: *Mol Phys* 19.4, pp. 553–566.

Broyden, C. G. (Mar. 1970). "The Convergence of a Class of Double-rank Minimization Algorithms 1. General Considerations". In: *IMA J Appl Math* 6.1, pp. 76–90. ISSN: 0272-4960. DOI: 10.1093/imamat/6.1.76. eprint: https://academic.oup.com/imamat/article-pdf/6/1/76/2233756/6-1-76.pdf.

Buch, V. and Q. Zhang (Oct. 1991). "Sticking Probability of H and D Atoms on Amorphous Ice: A Computational Study". In: 379, p. 647. DOI: 10.1086/170537.

Burke, Daren J. and Wendy A. Brown (Jan. 2010). "Ice in space: surface science investigations of the thermal desorption of model interstellar ices on dust grain analogue surfaces". In: *Physical Chemistry Chemical Physics (Incorporating Faraday Transactions)* 12.23, p. 5947. DOI: 10.1039/b917005g.

Burkhardt, Andrew M. et al. (Aug. 2019). "Modeling C-shock Chemistry in Isolated Molecular Outflows". In: *The Astrophysical Journal* 881, p. 32. ISSN: 0004-637X. DOI: 10.3847/1538-4357/ab2be8. URL: http://adsabs.harvard.edu/abs/2019ApJ...881...32B (visited on 04/23/2020).

Burrows, Christopher J. et al. (Dec. 1996). "Hubble Space Telescope Observations of the Disk and Jet of HH 30". In: 473, p. 437. DOI: 10.1086/178156.

Canosa, André et al. (2008). *Gas Phase Reactive Collisions at Very Low Temperature: Recent Experimental Advances and Perspectives*. DOI: 10.1142/9781848162105_0002.

Carruthers, George R. (Feb. 1970). "Atomic and Molecular Hydrogen in Interstellar Space". In: 10.4, pp. 459–482. DOI: 10.1007/BF00172535.

Casassa, Silvia (2000). "Ab initio study of periodic ice surfaces containing HCl". In: *Chem Phys Lett* 321.1-2, pp. 1–7.

Casassa, Silvia, Piero Ugliengo, and Cesare Pisani (1997). "Proton-ordered models of ordinary ice for quantum-mechanical studies". In: *J Chem Phys* 106.19, pp. 8030–8040.

Caselli, P., T. W. Hartquist, and O. Havnes (June 1997). "Grain-grain collisions and sputtering in oblique C-type shocks." In: *Astronomy and Astrophysics* 322, pp. 296–301. ISSN: 0004-6361. (Visited on 04/21/2019).

Caselli, P., T. I. Hasegawa, and Eric Herbst (Mar. 1998a). "A Proposed Modification of the Rate Equations for Reactions on Grain Surfaces". In: 495.1, pp. 309–316. DOI: 10.1086/305253.

Caselli, P. et al. (May 1998b). "The Ionization Fraction in Dense Cloud Cores". In: 499.1, pp. 234–249. DOI: 10.1086/305624.

Caselli, P. et al. (Oct. 1999). "CO Depletion in the Starless Cloud Core L1544". In: 523.2, pp. L165–L169. DOI: 10.1086/312280.

Caselli, Paola and Cecilia Ceccarelli (Oct. 2012). "Our astrochemical heritage". In: *Astronomy and Astrophysics Review* 20, p. 56. ISSN: 0935-4956. DOI: 10.1007/s00159-012-0056-x. (Visited on 03/15/2019).

Castellanos-Ramírez, A. et al. (Oct. 2018). "KIMYA, a Code for Solving Chemical Reaction Networks in Astrophysics". In: 54, pp. 409–422.

Castets, A. et al. (Aug. 2001). "Multiple shocks around the low-luminosity protostar IRAS 16293-2422". en. In: *Astronomy and Astrophysics* 375, p. 40. DOI: 10.1051/0004-6361:20010662. URL: https://ui.adsabs.harvard.edu/2001A&A...375...40C/abstract (visited on 10/01/2019).

Caux, E. et al. (July 1999a). "Large atomic oxygen abundance towards the molecular cloud L1689N". In: 347, pp. L1–L4.
— (July 1999b). "Large atomic oxygen abundance towards the molecular cloud L1689N". In: 347, pp. L1–L4.
Cazaux, S. and A. G. G. M. Tielens (Mar. 2004). "H_2 Formation on Grain Surfaces". In: 604.1, pp. 222–237. DOI: 10.1086/381775.
Cazaux, S. et al. (Aug. 2003). "The Hot Core around the Low-mass Protostar IRAS 16293-2422: Scoundrels Rule!" In: 593.1, pp. L51–L55. DOI: 10.1086/378038.
Cazaux, S. et al. (Aug. 2003). "The Hot Core around the Low-mass Protostar IRAS 16293-2422: Scoundrels Rule!" en. In: *The Astrophysical Journal* 593.1, p. L51. DOI: 10.1086/378038. URL: https://ui.adsabs.harvard.edu/abs/2003ApJ...593L..51C/abstract (visited on 09/29/2019).
Cazaux, S. et al. (Nov. 2010). "Water formation on bare grains: When the chemistry on dust impacts interstellar gas". In: 522, A74, A74. DOI: 10.1051/0004-6361/201014026. arXiv: 1007.1061 [astro-ph.SR].
Cazaux, S. et al. (Jan. 2015). "Pore evolution in interstellar ice analogues. Simulating the effects of temperature increase". In: 573, A16, A16. DOI: 10.1051/0004-6361/201424466. arXiv: 1410.6343 [astro-ph.SR].
Cazaux, S. et al. (Jan. 2016). "Dust as interstellar catalyst. II. How chemical desorption impacts the gas". In: 585, A55, A55. DOI: 10.1051/0004-6361/201527187. arXiv: 1511.02461 [astro-ph.SR].
Ceccarelli, C. (Dec. 2004). "The Hot Corinos of Solar Type Protostars". In: *Star Formation in the Interstellar Medium: In Honor of David Hollenbach*. Ed. by D. Johnstone et al. Vol. 323. Astronomical Society of the Pacific Conference Series, p. 195.
Ceccarelli, C. et al. (Oct. 1998). "Detection of doubly deuterated formaldehyde towards the low-luminosity protostar IRAS 16293-2422". en. In: *Astronomy and Astrophysics* 338, p. L43. URL: https://ui.adsabs.harvard.edu/abs/1998A%26A...338L..43C/abstract (visited on 10/04/2019).
Ceccarelli, C. et al. (Oct. 2000a). "Search for glycine in the solar type protostar IRAS 16293-2422". In: 362, pp. 1122–1126.
Ceccarelli, C. et al. (May 2000b). "The hot core of the solar-type protostar IRAS 16293-2422: H_2CO emission". In: 357, pp. L9–L12.
Ceccarelli, C. et al. (Mar. 2000c). "The structure of the collapsing envelope around the low-mass protostar IRAS 16293-2422". In: 355, pp. 1129–1137.
Ceccarelli, C. et al. (2007). "Extreme Deuteration and Hot Corinos: The Earliest Chemical Signatures of Low-Mass Star Formation". In: *Protostars and Planets V*, pp. 47–62. URL: http://adsabs.harvard.edu/abs/2007prpl.conf...47C (visited on 04/19/2019).
Ceccarelli, C. et al. (Oct. 2011). "Supernova-enhanced Cosmic-Ray Ionization and Induced Chemistry in a Molecular Cloud of W51C". In: 740.1, L4, p. L4. DOI: 10.1088/2041-8205/740/1/L4. arXiv: 1108.3600 [astro-ph.GA].
Ceccarelli, C. et al. (July 2014). "Herschel Finds Evidence for Stellar Wind Particles in a Protostellar Envelope: Is This What Happened to the Young Sun?" In: 790.1, L1, p. L1. DOI: 10.1088/2041-8205/790/1/L1.
Ceccarelli, C. et al. (Dec. 2017a). "Seeds Of Life In Space (SOLIS): The Organic Composition Diversity at 300-1000 au Scale in Solar-type Star-forming Regions". In: *The Astrophysical Journal* 850, p. 176. ISSN: 0004-637X. DOI: 10.3847/1538-4357/aa961d. URL: http://adsabs.harvard.edu/abs/2017ApJ...850..176C (visited on 02/13/2019).
— (Dec. 2017b). "Seeds Of Life In Space (SOLIS): The Organic Composition Diversity at 300-1000 au Scale in Solar-type Star-forming Regions". In: *The Astrophysical Journal* 850, p. 176. ISSN: 0004-637X. DOI: 10.3847/1538-4357/aa961d. URL: http://adsabs.harvard.edu/abs/2017ApJ...850..176C (visited on 02/13/2019).

Ceccarelli, Cecilia, David J. Hollenbach, and Alexand er G. G. M. Tielens (Nov. 1996). "Far-Infrared Line Emission from Collapsing Protostellar Envelopes". In: 471, p. 400. DOI: 10.1086/177978.

Ceccarelli, Cecilia et al. (May 2018). "The evolution of grain mantles and silicate dust growth at high redshift". In: 476.1, pp. 1371–1383. DOI: 10.1093/mnras/sty313. arXiv: 1802.01142 [astro-ph.GA].

Cernicharo, J., M. Guélin, and C. Kahane (Mar. 2000). "A lambda 2 mm molecular line survey of the C-star envelope IRC+10216". In: 142, pp. 181–215. DOI: 10.1051/aas:2000147.

Cernicharo, J. et al. (Dec. 2021). "Discovery of HCCCO and C_5O in TMC-1 with the QUIJOTE line survey". In: 656, L21, p. L21. DOI: 10.1051/0004-6361/202142634. arXiv: 2112.01130 [astro-ph.GA].

Cernicharo, J. et al. (Jan. 2022). "Discovery of C_5H^+ and detection of C_3H^+ in TMC-1 with the QUIJOTE line survey". In: 657, L16, p. L16. DOI: 10.1051/0004-6361/202142992. arXiv: 2201.02434 [astro-ph.GA].

Chaabouni, H. et al. (Feb. 2012). "Sticking coefficient of hydrogen and deuterium on silicates under interstellar conditions". In: 538, A128, A128. DOI: 10.1051/0004-6361/201117409. arXiv: 1202.2473 [astro-ph.IM].

Chaabouni, Henda et al. (2018). "Thermal desorption of formamide and methylamine from graphite and amorphous water ice surfaces". In: 612, A47.

Chang, Q., H. M. Cuppen, and E. Herbst (May 2005). "Continuous-time random-walk simulation of H_2 formation on interstellar grains". In: 434.2, pp. 599–611. DOI: 10.1051/0004-6361:20041842.

— (July 2007). "Gas-grain chemistry in cold interstellar cloud cores with a microscopic Monte Carlo approach to surface chemistry". In: 469.3, pp. 973–983. DOI: 10.1051/0004-6361:20077423. arXiv: 0704.2704 [astro-ph].

Chang, Qiang and Eric Herbst (June 2014). "Interstellar Simulations Using a Unified Microscopic-Macroscopic Monte Carlo Model with a Full Gas-Grain Network Including Bulk Diffusion in Ice Mantles". In: 787.2, 135, p. 135. DOI: 10.1088/0004-637X/787/2/135. arXiv: 1405.0840 [astro-ph.EP].

— (Mar. 2016). "Unified Microscopic-Macroscopic Monte Carlo Simulations of Complex Organic Molecule Chemistry in Cold Cores". In: 819.2, 145, p. 145. DOI: 10.3847/0004-637X/819/2/145. arXiv: 1603.04011 [astro-ph.SR].

Charnley, S. B. (2004). *Acetaldehyde in star-forming regions - NASA/ADS*. en. URL: https://ui.adsabs.harvard.edu/abs/2004AdSpR..33...23C/abstract (visited on 07/22/2019).

Charnley, S. B., A. G. G. M. Tielens, and T. J. Millar (Nov. 1992). "On the Molecular Complexity of the Hot Cores in Orion A: Grain Surface Chemistry as "The Last Refuge of the Scoundrel"". en. In: *The Astrophysical Journal* 399, p. L71. ISSN: 0004-637X. DOI: 10.1086/186609. URL: https://ui.adsabs.harvard.edu/abs/1992ApJ...399L..71C/abstract (visited on 07/22/2019).

Chen, Y. J. et al. (Jan. 2014). "Vacuum Ultraviolet Emission Spectrum Measurement of a Microwave-discharge Hydrogen-flow Lamp in Several Configurations: Application to Photodesorption of CO Ice". In: 781.1, 15, p. 15. DOI: 10.1088/0004-637X/781/1/15.

Chesnavich, Walter J., Timothy Su, and Michael T. Bowers (1980). "Collisions in a noncentral field: A variational and trajectory investigation of ion–dipole capture". In: *The Journal of Chemical Physics* 72.4, pp. 2641–2655. DOI: 10.1063/1.439409. eprint: https://doi.org/10.1063/1.439409. URL: https://doi.org/10.1063/1.439409.

Chevalier, R. A. (Jan. 1977). "The interaction of supernovae with the interstellar medium." In: 15, pp. 175–196. DOI: 10.1146/annurev.aa.15.090177.001135.

Chevance, Mélanie et al. (Apr. 2020). "The lifecycle of molecular clouds in nearby star-forming disc galaxies". In: 493.2, pp. 2872–2909. DOI: 10.1093/mnras/stz3525. arXiv: 1911.03479 [astro-ph.GA].

Chiar, J. E., A. J. Adamson, and D. C. B. Whittet (Dec. 1996). "Three Micron Hydrocarbon and Methanol Absorption in Taurus". In: 472, p. 665. DOI: 10.1086/178097.

Choi, Minho (May 2001). "High-Resolution Observations of the Molecular Clouds in the NGC 1333 IRAS 4 Region". In: *The Astrophysical Journal* 553, pp. 219–226. ISSN: 0004-637X. DOI: 10.1086/320657. URL: http://adsabs.harvard.edu/abs/2001ApJ...553..219C (visited on 03/15/2019).

— (Sept. 2005). "Variability of the NGC 1333 IRAS 4A Outflow: Silicon Monoxide Observations". In: *The Astrophysical Journal* 630, pp. 976–986. ISSN: 0004-637X. DOI: 10.1086/432113. URL: http://adsabs.harvard.edu/abs/2005ApJ...630..976C (visited on 03/15/2019).

Choi, Minho et al. (Dec. 2011). "Radio Imaging of the NGC 1333 IRAS 4A Region: Envelope, Disks, and Outflows of a Protostellar Binary System". en. In: *Publications of the Astronomical Society of Japan* 63, p. 1281. DOI: 10.1093/pasj/63.6.1281. URL: https://ui.adsabs.harvard.edu/abs/2011PASJ...63.1281C/abstract (visited on 07/02/2019).

Chuang, K. J. et al. (Sept. 2018). "H_2 chemistry in interstellar ices: the case of CO ice hydrogenation in UV irradiated CO:H_2 ice mixtures". In: 617, A87, A87. DOI: 10.1051/0004-6361/201833439. arXiv: 1809.10507 [astro-ph.SR].

Cioffi, Denis F., Christopher F. McKee, and Edmund Bertschinger (Nov. 1988). "Dynamics of Radiative Supernova Remnants". In: 334, p. 252. DOI: 10.1086/166834.

Clark, Paul C. et al. (Aug. 2012). "How long does it take to form a molecular cloud?" In: 424.4, pp. 2599–2613. DOI: 10.1111/j.1365-2966.2012.21259.x. arXiv: 1204.5570 [astro-ph.GA].

Clements, Aspen R. et al. (Feb. 2018). "Kinetic Monte Carlo simulations of water ice porosity: extrapolations of deposition parameters from the laboratory to interstellar space". In: *Physical Chemistry Chemical Physics (Incorporating Faraday Transactions)* 20, pp. 5553–5568. DOI: 10.1039/C7CP05966C.

Codella, C et al. (2011). "First detection of hydrogen chloride toward protostellar shocks". In: 744.2, p. 164.

Codella, C. et al. (Apr. 2015). "Astrochemistry at work in the L1157-B1 shock: acetaldehyde formation." en. In: *Monthly Notices of the Royal Astronomical Society* 449, p. L11. DOI: 10.1093/mnrasl/slu204. URL: https://ui.adsabs.harvard.edu/abs/2015MNRAS.449L..11C/abstract (visited on 07/23/2019).

Codella, C. et al. (Sept. 2017). "Seeds of Life in Space (SOLIS). II. Formamide in protostellar shocks: Evidence for gas-phase formation". In: 605, L3, p. L3. DOI: 10.1051/0004-6361/201731249. arXiv: 1708.04663 [astro-ph.EP].

Codella, C. et al. (Sept. 2017). "Seeds of Life in Space (SOLIS). II. Formamide in protostellar shocks: Evidence for gas-phase formation". In: *Astronomy and Astrophysics* 605, p. L3. ISSN: 0004-6361. DOI: 10.1051/0004-6361/201731249. URL: http://adsabs.harvard.edu/abs/2017A%26A...605L...3C (visited on 02/13/2019).

Codella, C. et al. (Sept. 2019). "Seeds of Life in Space (SOLIS) V. Methanol, acetaldehyde, and complex organics in the protostellar shocks L1157-B0 and B1". In: *Astronomy & Astrophysics* submitted.

Codella, C. et al. (Mar. 2020). "Seeds of Life in Space (SOLIS). V. Methanol and acetaldehyde in the protostellar jet-driven shocks L1157-B0 and B1". In: 635, A17, A17. DOI: 10.1051/0004-6361/201936725. arXiv: 2001.00217 [astro-ph.SR].

Collings, M. P. et al. (Feb. 2003). "Carbon Monoxide Entrapment in Interstellar Ice Analogs". In: 583.2, pp. 1058–1062. DOI: 10.1086/345389.

Collings, Mark P. et al. (Nov. 2004). "A laboratory survey of the thermal desorption of astrophysically relevant molecules". In: 354.4, pp. 1133–1140. DOI: 10.1111/j.1365-2966.2004.08272.x.

Collings, Mark P et al. (2004). "A laboratory survey of the thermal desorption of astrophysically relevant molecules". In: *MNRAS* 354.4, pp. 1133–1140.

Congiu, E. et al. (Dec. 2020). "A new multi-beam apparatus for the study of surface chemistry routes to formation of complex organic molecules in space". In: *Review of Scientific Instruments* 91.12, 124504, p. 124504. DOI: 10.1063/5.0018926. arXiv: 2004.10668 [astro-ph.IM].

Congiu, Emanuele et al. (Jan. 2014). "Efficient diffusive mechanisms of O atoms at very low temperatures on surfaces of astrophysical interest". In: *Faraday Discussions* 168, p. 151. DOI: 10.1039/C4FD00002A. arXiv: 1402.5855 [astro-ph.GA].

Cooke, Ilsa R. et al. (Jan. 2018). "CO Diffusion and Desorption Kinetics in CO_2 Ices". In: 852.2, 75, p. 75. DOI: 10.3847/1538-4357/aa9ce9. arXiv: 1711.09967 [astro-ph.GA].

Coutens, A. et al. (May 2016). "The ALMA-PILS survey: First detections of deuterated formamide and deuterated isocyanic acid in the interstellar medium". en. In: *Astronomy and Astrophysics* 590, p. L6. DOI: 10.1051/0004-6361/201628612. URL: https://ui.adsabs.harvard.edu/abs/2016A%26A...590L...6C/abstract (visited on 10/04/2019).

Coutens, A., B. Commerçon, and V. Wakelam (Nov. 2020). "Chemical evolution during the formation of a protoplanetary disk". In: 643, A108, A108. DOI: 10.1051/0004-6361/202038437. arXiv: 2010.05108 [astro-ph.SR].

Cramer, CJ (2002). *Essentials of computational chemistry (England*.

Cuppen, H. M. and Eric Herbst (Aug. 2005). "Monte Carlo simulations of H_2 formation on grains of varying surface roughness". In: 361.2, pp. 565–576. DOI: 10.1111/j.1365-2966.2005.09189.x.

— (Oct. 2007). "Simulation of the Formation and Morphology of Ice Mantles on Interstellar Grains". In: 668.1, pp. 294–309. DOI: 10.1086/521014. arXiv: 0707.2744 [astro-ph].

Cuppen, H. M. et al. (Dec. 2009). "Microscopic simulation of methanol and formaldehyde ice formation in cold dense cores". In: 508.1, pp. 275–287. DOI: 10.1051/0004-6361/200913119. arXiv: 0911.0283 [astro-ph.GA].

Cuppen, H. M. et al. (Jan. 2010). "Water formation at low temperatures by surface O2 hydrogenation II: the reaction network". In: *Physical Chemistry Chemical Physics (Incorporating Faraday Transactions)* 12.38, p. 12077. DOI: 10.1039/C0CP00251H. arXiv: 1009.5273 [astro-ph.SR].

Cuppen, H. M. et al. (Oct. 2017). "Grain Surface Models and Data for Astrochemistry". In: 212.1-2, pp. 1–58. DOI: 10.1007/s11214-016-0319-3.

Cuppen, HM et al. (2017). "Grain surface models and data for astrochemistry". In: *SSRev* 212.1-2, pp. 1–58.

Cutini, Michele et al. (2016). "Assessment of different quantum mechanical methods for the prediction of structure and cohesive energy of molecular crystals". In: *JCTC* 12.7, pp. 3340–3352.

Cutini, Michele, Marta Corno, and Piero Ugliengo (2017). "Method Dependence of Proline Ring Flexibility in the Poly-L-Proline Type II Polymer". In: *JCTC* 13.1, pp. 370–379.

Cutini, Michele, Bartolomeo Civalleri, and Piero Ugliengo (2019). "Cost-effective quantum mechanical approach for predicting thermodynamic and mechanical stability of pure-silica zeolites". In: *ACS omega* 4.1, pp. 1838–1846.

Dapprich, Stefan et al. (1999). "A new ONIOM implementation in Gaussian98. Part I. The calculation of energies, gradients, vibrational frequencies and electric field derivatives". In: *J Mol Struc:THEOCHEM* 461, pp. 1–21.

Das, Ankan et al. (July 2018). "An Approach to Estimate the Binding Energy of Interstellar Species". In: 237.1, 9, p. 9. DOI: 10.3847/1538-4365/aac886. arXiv: 1805.08075 [astro-ph.GA].

Das, Ankan et al. (2018). "An Approach to Estimate the Binding Energy of Interstellar Species". In: 237.1, p. 9.

Davidson, Ernest R and David Feller (1986). "Basis set selection for molecular calculations". In: *Chem Rev* 86.4, pp. 681–696.

Dawson, P. H. (Jan. 1997). "Quadrupole Mass Spectrometry and Its Applications". In: *Elsevier 1976* 1, p. 372. DOI: https://doi.org/10.1016/B978-0-444-41345-1.50005-8.

De Looze, I. et al. (Aug. 2020). "JINGLE - IV. Dust, H I gas, and metal scaling laws in the local Universe". In: 496.3, pp. 3668–3687. DOI: 10.1093/mnras/staa1496. arXiv: 2006.01856 [astro-ph.GA].

De Simone, M. et al. (Mar. 2017). "Glycolaldehyde in Perseus young solar analogs". In: *Astronomy and Astrophysics* 599, A121. ISSN: 0004-6361. DOI: 10.1051/0004-6361/201630049. (Visited on 03/15/2019).

De Simone, M. et al. (Aug. 2020). "Seeds of Life in Space (SOLIS). X. Interstellar complex organic molecules in the NGC 1333 IRAS 4A outflows". In: 640, A75, A75. DOI: 10.1051/0004-6361/201937004. arXiv: 2006.09925 [astro-ph.SR].

D'Hendecourt, L. B., L. J. Allamandola, and J. M. Greenberg (Nov. 1985). "Time dependent chemistry in dense molecular clouds. I. Grain surface reactions, gas/grain interactions and infrared spectroscopy." In: 152, pp. 130–150.

Di Francesco, James et al. (Dec. 2001). "Infall, Outflow, Rotation, and Turbulent Motions of Dense Gas within NGC 1333 IRAS 4". In: *The Astrophysical Journal* 562, pp. 770–789. ISSN: 0004-637X. DOI: 10.1086/323854. URL: http://adsabs.harvard.edu/abs/2001ApJ...562..770D (visited on 03/26/2019).

Dobbs, C. L. (Dec. 2008). "GMC formation by agglomeration and self gravity". In: 391.2, pp. 844–858. DOI: 10.1111/j.1365-2966.2008.13939.x. arXiv: 0809.1942 [astro-ph].

Dobbs, C. L., J. E. Pringle, and A. Duarte-Cabral (Feb. 2015). "The frequency and nature of 'cloud-cloud collisions' in galaxies". In: 446.4, pp. 3608–3620. DOI: 10.1093/mnras/stu2319. arXiv: 1411.0840 [astro-ph.GA].

Dohnalek, Zdenek et al. (2001). "Physisorption of CO on the MgO (100) Surface". In: *J Phys Chem B* 105.18, pp. 3747–3751.

Douglas, A. E. and G. Herzberg (Sept. 1941). "Note on CH{+} in Interstellar Space and in the Laboratory." In: 94, p. 381. DOI: 10.1086/144342.

Douglas, AE and G Herzberg (1942). "Band spectrum and structure of the CH+ molecule; identification of three interstellar lines". In: *Canadian Journal of Research* 20.6, pp. 71–82.

Dovesi, Roberto et al. (2018). "Quantum-mechanical condensed matter simulations with CRYSTAL". In: *Wiley Interdiscip Rev Comput Mol Sci* 8.4, e1360.

Draine, B. T. (Apr. 1978). "Photoelectric heating of interstellar gas." In: 36, pp. 595–619. DOI: 10.1086/190513.

— (Jan. 2003). "Interstellar Dust Grains". In: 41, pp. 241–289. DOI: 10.1146/annurev.astro.41.011802.094840. arXiv: astro-ph/0304489 [astro-ph].

Draine, B. T. and Frank Bertoldi (Sept. 1996). "Structure of Stationary Photodissociation Fronts". In: 468, p. 269. DOI: 10.1086/177689. arXiv: astro-ph/9603032 [astro-ph].

Draine, B. T. and H. M. Lee (Oct. 1984). "Optical Properties of Interstellar Graphite and Silicate Grains". In: 285, p. 89. DOI: 10.1086/162480.

Draine, B. T. and Brian Sutin (Sept. 1987). "Collisional Charging of Interstellar Grains". In: 320, p. 803. DOI: 10.1086/165596.

Draine, B. T. et al. (July 2007). "Dust Masses, PAH Abundances, and Starlight Intensities in the SINGS Galaxy Sample". In: 663.2, pp. 866–894. DOI: 10.1086/518306. arXiv: astro-ph/0703213 [astro-ph].

Draine, Bruce T. and Christopher F. McKee (Jan. 1993). "Theory of interstellar shocks." In: 31, pp. 373–432. DOI: 10.1146/annurev.aa.31.090193.002105.

Duflot, Denis, Céline Toubin, and Maurice Monnerville (Mar. 2021). "Theoretical determination of binding energies of small molecules on interstellar ice surfaces". In: *Frontiers in Astronomy and Space Sciences* 8, 24, p. 24. DOI: 10.3389/fspas.2021.645243.

Duley, W. W. and D. A. Williams (Jan. 1993). "The formation of H2 on interstellar dust". In: 260.1, pp. 37–42. DOI: 10.1093/mnras/260.1.37.

Dulieu, F. et al. (Mar. 2010). "Experimental evidence for water formation on interstellar dust grains by hydrogen and oxygen atoms". In: 512, A30, A30. DOI: 10.1051/0004-6361/200912079. arXiv: 0903.3120 [astro-ph.IM].

Dulieu, F et al. (2010). "Experimental evidence for water formation on interstellar dust grains by hydrogen and oxygen atoms". In: 512, A30.

Dulieu, François et al. (Feb. 2013). "How micron-sized dust particles determine the chemistry of our Universe". In: *Scientific Reports* 3, 1338, p. 1338. DOI: 10.1038/srep01338.

Dulieu, François et al. (2013). "How micron-sized dust particles determine the chemistry of our Universe". In: *Sci Rep* 3, p. 1338.

Dunning Jr, Thom H (1989). "Gaussian basis sets for use in correlated molecular calculations. I. The atoms boron through neon and hydrogen". In: *J Chem Phys* 90.2, pp. 1007–1023.

Dupuy, John L., Steven P. Lewis, and P. C. Stancil (Nov. 2016). "A Comprehensive Study of Hydrogen Adsorbing to Amorphous Water ice: Defining Adsorption in Classical Molecular Dynamics". In: 831.1, 54, p. 54. DOI: 10.3847/0004-637X/831/1/54. arXiv: 1608.05158 [astro-ph.GA].

Ebert, R. (Jan. 1955). "The Influence of Dust on the Equation of State of a contracting Cloud and the Formation of Stars". In: *Liege International Astrophysical Colloquia*. Vol. 6. Liege International Astrophysical Colloquia, pp. 666–672.

Eckart, Carl (1930). "The Penetration of a Potential Barrier by Electrons". In: *Phys. Rev.* 35 (11), pp. 1303–1309. DOI: 10.1103/PhysRev.35.1303. URL: https://link.aps.org/doi/10.1103/PhysRev.35.1303.

Ellingson, Benjamin A. et al. (2007). "Reactions of hydrogen atom with hydrogen peroxide". In: *JOURNAL OF PHYSICAL CHEMISTRY A* 111.51, 13554–13566. ISSN: 1089-5639. DOI: {10.1021/jp077379x}.

Elsila, J. E., D. P. Glavin, and J. P. Dworkin (Oct. 2009). "Cometary glycine detected in samples returned by Stardust". en. In: *Meteoritics and Planetary Science* 44.9, p. 1323. DOI: 10.1111/j.1945-5100.2009.tb01224.x. URL: https://ui.adsabs.harvard.edu/abs/2009M%26PS...44.1323E/abstract (visited on 09/29/2019).

Enrique-Romero, J. et al. (June 2016a). "The (impossible?) formation of acetaldehyde on the grain surfaces: insights from quantum chemical calculations". In: *Monthly Notices of the Royal Astronomical Society* 459, pp. L6–L10. ISSN: 0035-8711. DOI: 10.1093/mnrasl/slw031. URL: http://adsabs.harvard.edu/abs/2016MNRAS.459L...6E (visited on 04/05/2019).

— (June 2016b). "The (impossible?) formation of acetaldehyde on the grain surfaces: insights from quantum chemical calculations". In: *Monthly Notices of the Royal Astronomical Society* 459, pp. L6–L10. ISSN: 0035-8711. DOI: 10.1093/mnrasl/slw031. URL: http://adsabs.harvard.edu/abs/2016MNRAS.459L...6E (visited on 04/05/2019).

Enrique-Romero, J. et al. (Apr. 2020). "Revisiting the reactivity between HCO and CH_3 on interstellar grain surfaces". In: 493.2, pp. 2523–2527. DOI: 10.1093/mnras/staa484. arXiv: 2002.06101 [astro-ph.GA].

Enrique-Romero, J et al. (2020). "Revisiting the reactivity between HCO and CH3 on interstellar grain surfaces". In: *MNRAS* 493.2, pp. 2523–2527.

Enrique-Romero, Joan et al. (Oct. 2019b). "Reactivity of HCO with CH3 and NH2 on Water Ice Surfaces. A Comprehensive Accurate Quantum Chemistry Study". In: *ACS Earth and Space Chemistry*. eprint: Arxiv:1909.12686v1. URL: http://arxiv.org/abs/1909.12686.

— (Oct. 2019a). "Reactivity of HCO with CH3 and NH2 on Water Ice Surfaces. A Comprehensive Accurate Quantum Chemistry Study". In: *ACS Earth and Space Chemistry* 3.10, pp. 2158–2170. DOI: 10.1021/acsearthspacechem.9b00156. URL: https://doi.org/10.1021/acsearthspacechem.9b00156.

— (2019c). "Reactivity of HCO with CH3 and NH2 on Water Ice Surfaces. A Comprehensive Accurate Quantum Chemistry Study". In: *ACS Earth Space Chem* 3.10, pp. 2158–2170.

Enrique-Romero, Joan et al. (July 2021). "Theoretical computations on the efficiency of acetaldehyde formation on interstellar icy grains". In: *In press: Astronomy & Astrophysics* –, pp. –,–.

Enrique-Romero, Joan et al. (Jan. 2022). "Quantum mechanical simulations of the radical-radical chemistry on icy surfaces". In: *arXiv e-prints*, arXiv:2201.10864, arXiv:2201.10864. arXiv: 2201.10864 [astro-ph.GA].

Esteban, C., J. García-Rojas, and V. Pérez-Mesa (Sept. 2015). "The radial abundance gradient of chlorine in the Milky Way". In: 452.2, pp. 1553–1560. DOI: 10.1093/mnras/stv1367. arXiv: 1506.05621 [astro-ph.GA].

Evans Neal J., II et al. (Aug. 2003). "From Molecular Cores to Planet-forming Disks: An SIRTF Legacy Program". In: 115.810, pp. 965–980. DOI: 10.1086/376697. arXiv: astro-ph/0305127 [astro-ph].

Eyring, Henry (1935). "The Activated Complex in Chemical Reactions". In: *The Journal of Chemical Physics* 3.2, pp. 107–115. DOI: 10.1063/1.1749604. eprint: https://doi.org/10.1063/1.1749604. URL: https://doi.org/10.1063/1.1749604.

Fayolle, E. C. et al. (Aug. 2013). "Wavelength-dependent UV photodesorption of pure N_2 and O_2 ices". In: 556, A122, A122. DOI: 10.1051/0004-6361/201321533. arXiv: 1309.4773 [astro-ph.GA].

Fayolle, Edith C et al. (2016). "N2 and CO Desorption Energies from Water Ice". In: 816.2, p. L28.

Federrath, Christoph and Ralf S. Klessen (Dec. 2012). "The Star Formation Rate of Turbulent Magnetized Clouds: Comparing Theory, Simulations, and Observations". In: 761.2, 156, p. 156. DOI: 10.1088/0004-637X/761/2/156. arXiv: 1209.2856 [astro-ph.SR].

Ferrero, Stefano et al. (Nov. 2020). "Binding Energies of Interstellar Molecules on Crystalline and Amorphous Models of Water Ice by Ab Initio Calculations". In: 904.1, 11, p. 11. DOI: 10.3847/1538-4357/abb953. arXiv: 2009.09763 [astro-ph.GA].

Ferrière, Katia M. (Oct. 2001). "The interstellar environment of our galaxy". In: *Reviews of Modern Physics* 73.4, pp. 1031–1066. DOI: 10.1103/RevModPhys.73.1031. arXiv: astro-ph/0106359 [astro-ph].

Field, G. B., D. W. Goldsmith, and H. J. Habing (Mar. 1969). "Cosmic-Ray Heating of the Interstellar Gas". In: 155, p. L149. DOI: 10.1086/180324.

Fillion, Jean-Hugues et al. (Jan. 2014). "Wavelength resolved UV photodesorption and photochemistry of CO2 ice". In: *Faraday Discussions* 168, pp. 533–552. DOI: 10.1039/C3FD00129F.

Fiorellino, E. et al. (Feb. 2021). "The census of dense cores in the Serpens region from the Herschel Gould Belt Survey". In: 500.4, pp. 4257–4276. DOI: 10.1093/mnras/staa3420. arXiv: 2010.15241 [astro-ph.GA].

Fletcher, Roger (1970). "A new approach to variable metric algorithms". In: *Comput J* 13.3, pp. 317–322.

Flower, D. R. and G. Pineau des Forêts (Aug. 2003). "The influence of grains on the propagation and structure of C-type shock waves in interstellar molecular clouds". In: 343.2, pp. 390–400. DOI: 10.1046/j.1365-8711.2003.06716.x.

Fontani, F. et al. (Sept. 2017). "Seeds of Life in Space (SOLIS). I. Carbon-chain growth in the Solar-type protocluster OMC2-FIR4". In: 605, A57, A57. DOI: 10.1051/0004-6361/201730527. arXiv: 1707.01384 [astro-ph.GA].

Franco, Jose and Donald P. Cox (Oct. 1986). "Molecular clouds in galaxies with different Z: fragmentation of diffuse clouds driven by opacity." In: 98, pp. 1076–1079. DOI: 10.1086/131876.

Fraser, HJ, MP Collings, and MRS McCoustra (2002). "Laboratory surface astrophysics experiment". In: *REVIEW OF SCIENTIFIC INSTRUMENTS* 73.5, 2161–2170. ISSN: 0034-6748. DOI: {10.1063/1.1470232}.

Fredon, A. and H. M. Cuppen (Feb. 2018). "Molecular dynamics simulations of energy dissipation and non-thermal diffusion on amorphous solid water". In: *Physical Chemistry Chemical Physics (Incorporating Faraday Transactions)* 20, pp. 5569–5577. DOI: 10.1039/C7CP06136F.

Fredon, Adrien, Gerrit C. Groenenboom, and Herma M. Cuppen (Aug. 2021). "Molecular Dynamics Simulations of Energy Dissipation on Amorphous Solid Water: Testing the Validity of Equipartition". In: *ACS Earth and Space Chemistry* 5.8, pp. 2032–2041. DOI: 10.1021/acsearthspacechem.1c00116.

Frisch, MJTGW et al. (2009). "Gaussian 09, Revision, A. 1". In: *Inc., Wallingford CT* 121, pp. 150–166.

Fuchs, G. W. et al. (Oct. 2009). "Hydrogenation reactions in interstellar CO ice analogues. A combined experimental/theoretical approach". In: 505.2, pp. 629–639. DOI: 10.1051/0004-6361/200810784.

Fuente, A. et al. (Apr. 2019). "Gas phase Elemental abundances in Molecular cloudS (GEMS). I. The prototypical dark cloud TMC 1". In: 624, A105, A105. DOI: 10.1051/0004-6361/201834654. arXiv: 1809.04978 [astro-ph.GA].

Galliano, Frédéric, Maud Galametz, and Anthony P. Jones (Sept. 2018). "The Interstellar Dust Properties of Nearby Galaxies". In: 56, pp. 673–713. DOI: 10.1146/annurev-astro-081817-051900. arXiv: 1711.07434 [astro-ph.GA].

Gardner, Jonathan P. et al. (Apr. 2006). "The James Webb Space Telescope". In: 123.4, pp. 485–606. DOI: 10.1007/s11214-006-8315-7. arXiv: astro-ph/0606175 [astro-ph].

Garrod, R. T. (Nov. 2008). "A new modified-rate approach for gas-grain chemical simulations". In: 491.1, pp. 239–251. DOI: 10.1051/0004-6361:200810518. arXiv: 0809.2934 [astro-ph].

Garrod, R. T. (Nov. 2008). "A new modified-rate approach for gas-grain chemical simulations". In: *Astronomy and Astrophysics* 491, pp. 239–251. ISSN: 0004-6361. DOI: 10.1051/0004-6361:200810518. URL: http://adsabs.harvard.edu/abs/2008A%26A...491..239G (visited on 04/01/2019).

Garrod, R. T. and E. Herbst (Oct. 2006). "Formation of methyl formate and other organic species in the warm-up phase of hot molecular cores". In: 457.3, pp. 927–936. DOI: 10.1051/0004-6361:20065560. arXiv: astro-ph/0607560 [astro-ph].

Garrod, R. T. and E. Herbst (Oct. 2006). "Formation of methyl formate and other organic species in the warm-up phase of hot molecular cores". In: *Astronomy and Astrophysics* 457, pp. 927–936. ISSN: 0004-6361. DOI: 10.1051/0004-6361:20065560. URL: http://adsabs.harvard.edu/abs/2006A%26A...457..927G (visited on 04/01/2019).

Garrod, R. T. and T. Pauly (July 2011). "On the Formation of CO_2 and Other Interstellar Ices". In: 735.1, 15, p. 15. DOI: 10.1088/0004-637X/735/1/15. arXiv: 1106.0540 [astro-ph.GA].

Garrod, R. T., V. Wakelam, and E. Herbst (June 2007). "Non-thermal desorption from interstellar dust grains via exothermic surface reactions". In: 467.3, pp. 1103–1115. DOI: 10.1051/0004-6361:20066704. arXiv: astro-ph/0703188 [astro-ph].

Garrod, Robin et al. (Jan. 2006). "Are gas-phase models of interstellar chemistry tenable? The case of methanol". In: *Faraday Discussions* 133, p. 51. DOI: 10.1039/b516202e.

Garrod, Robin T. (Mar. 2013). "A Three-phase Chemical Model of Hot Cores: The Formation of Glycine". In: 765.1, 60, p. 60. DOI: 10.1088/0004-637X/765/1/60. arXiv: 1302.0688 [astro-ph.GA].

Garrod, Robin T. and Susanna L. Widicus Weaver (Dec. 2013). "Simulations of Hot-Core Chemistry". In: *Chemical Reviews* 113.12, pp. 8939–8960. DOI: 10.1021/cr400147g.

Gerakines, P. A., W. A. Schutte, and P. Ehrenfreund (Aug. 1996). "Ultraviolet processing of interstellar ice analogs. I. Pure ices." In: 312, pp. 289–305.

Gillett, F. C. and W. J. Forrest (Jan. 1973). "Spectra of the Becklin-Neugebauer point source and the Kleinmann-Low nebula from 2.8 to 13.5 microns." In: 179, p. 483. DOI: 10.1086/151888.

Ginolfi, M. et al. (Feb. 2018). "Where does galactic dust come from?" In: 473.4, pp. 4538–4543. DOI: 10.1093/mnras/stx2572. arXiv: 1707.05328 [astro-ph.GA].

Glover, Simon C. O. and Paul C. Clark (Mar. 2012). "Is molecular gas necessary for star formation?" In: 421.1, pp. 9–19. DOI: 10.1111/j.1365-2966.2011.19648.x. arXiv: 1105.3073 [astro-ph.GA].

Glover, Simon C. O. et al. (Apr. 2015). "Modelling [C I] emission from turbulent molecular clouds". In: 448.2, pp. 1607–1627. DOI: 10.1093/mnras/stu2699. arXiv: 1403.3530 [astro-ph.GA].

Godard, B. et al. (Feb. 2019). "Models of irradiated molecular shocks". In: 622, A100, A100. DOI: 10.1051/0004-6361/201834248. arXiv: 1901.04273 [astro-ph.GA].

Goldfarb, Donald (1970). "A family of variable-metric methods derived by variational means". In: *Math Comput* 24.109, pp. 23–26.

Goldsmith, P. F. et al. (Aug. 2000). "O_2 in Interstellar Molecular Clouds". In: 539.2, pp. L123–L127. DOI: 10.1086/312854.

Goldsmith, Paul F. and William D. Langer (May 1999). "Population Diagram Analysis of Molecular Line Emission". en. In: *The Astrophysical Journal* 517.1, p. 209. DOI: 10.1086/307195. URL: https://ui.adsabs.harvard.edu/abs/1999ApJ...517..209G/abstract (visited on 05/21/2019).

Goldsmith, Paul. F. et al. (July 2021). "Interstellar Cloud Conditions Based on 63 μm [O I] Emission and Absorption in W3". In: 916.1, 6, p. 6. DOI: 10.3847/1538-4357/abfb69.

Gondhalekar, P. M., A. P. Phillips, and R. Wilson (May 1980). "Observations of the interstellar ultraviolet radiation field from the S2/68 sky-survey telescope". In: 85.3, pp. 272–280.

Gong, Munan, Eve C. Ostriker, and Mark G. Wolfire (July 2017). "A Simple and Accurate Network for Hydrogen and Carbon Chemistry in the Interstellar Medium". In: 843.1, 38, p. 38. DOI: 10.3847/1538-4357/aa7561. arXiv: 1610.09023 [astro-ph.GA].

Gould, R. J., T. Gold, and E. E. Salpeter (Aug. 1963). "The Interstellar Abundance of the Hydrogen Molecule. II. Galactic Abundance and Distribution." In: 138, p. 408. DOI: 10.1086/147655.

Gould, Robert J. and Edwin E. Salpeter (Aug. 1963). "The Interstellar Abundance of the Hydrogen Molecule. I. Basic Processes." In: 138, p. 393. DOI: 10.1086/147654.

Goumans, T. P. M. and Stefan Andersson (Aug. 2010). "Tunnelling in the O + CO reaction". In: 406.4, pp. 2213–2217. DOI: 10.1111/j.1365-2966.2010.16836.x.

Goumans, T. P. M. et al. (Dec. 2007). "Silica grain catalysis of methanol formation". In: 382.4, pp. 1829–1832. DOI: 10.1111/j.1365-2966.2007.12491.x.

Goumans, T. P. M., Madeeha A. Uppal, and Wendy A. Brown (Mar. 2008). "Formation of CO_2 on a carbonaceous surface: a quantum chemical study". In: 384.3, pp. 1158–1164. DOI: 10.1111/j.1365-2966.2007.12788.x.

Grassi, T. et al. (Apr. 2014). "KROME - a package to embed chemistry in astrophysical simulations". In: 439.3, pp. 2386–2419. DOI: 10.1093/mnras/stu114. arXiv: 1311.1070 [astro-ph.GA].

Grassi, T. et al. (Nov. 2020). "A novel framework for studying the impact of binding energy distributions on the chemistry of dust grains". In: 643, A155, A155. DOI: 10.1051/0004-6361/202039087. arXiv: 2009.03900 [astro-ph.GA].

Gredel, R., S. Lepp, and A. Dalgarno (Dec. 1987). "The C/CO Ratio in Dense Interstellar Clouds". In: 323, p. L137. DOI: 10.1086/185073.

Gredel, R. et al. (Dec. 1989). "Cosmic-Ray–induced Photodissociation and Photoionization Rates of Interstellar Molecules". In: 347, p. 289. DOI: 10.1086/168117.

Greenberg, J. M. and O. M. Shalabiea (Jan. 1994). "Comets as Reflection of Interstellar Medium Chemistry". In: *Asteroids, Comets, Meteors 1993*. Ed. by Andrea Milani, Michel di Martino, and A. Cellino. Vol. 160. IAU Symposium, p. 327.

Grenier, Isabelle A., John H. Black, and Andrew W. Strong (Aug. 2015). "The Nine Lives of Cosmic Rays in Galaxies". In: 53, pp. 199–246. DOI: 10.1146/annurev-astro-082214-122457.

Grimme, Stefan et al. (Apr. 2010). "A consistent and accurate ab initio parametrization of density functional dispersion correction (DFT-D) for the 94 elements H-Pu". In: 132.15, pp. 154104–154104. DOI: 10.1063/1.3382344.

Grimme, Stefan et al. (2010). "A consistent and accurate ab initio parametrization of density functional dispersion correction (DFT-D) for the 94 elements H-Pu". In: *J Chem Phys* 132.15, p. 154104.

Grimme, Stefan, Stephan Ehrlich, and Lars Goerigk (2011a). "Effect of the damping function in dispersion corrected density functional theory". In: *Journal of computational chemistry* 32.7, pp. 1456–1465.

— (2011b). "Effect of the damping function in dispersion corrected density functional theory". In: *J Comput Chem* 32.7, pp. 1456–1465.

Gry, C. et al. (2003). *The ISO Handbook, Volume III - LWS - The Long Wavelength Spectrometer*.

Gueth, F., S. Guilloteau, and R. Bachiller (Mar. 1996). "A precessing jet in the L1157 molecular outflow." In: *Astronomy and Astrophysics* 307, pp. 891–897. ISSN: 0004-6361. (Visited on 04/30/2019).

Gupta, H. et al. (Feb. 2009). "A Survey of C_4H, C_6H, and C_6H^- With the Green Bank Telescope". In: 691.2, pp. 1494–1500. DOI: 10.1088/0004-637X/691/2/1494.

Gusdorf, A. et al. (May 2008). "SiO line emission from C-type shock waves: interstellar jets and outflows". In: 482.3, pp. 809–829. DOI: 10.1051/0004-6361:20078900. arXiv: 0803.2791 [astro-ph].

Guzmán, V. V. et al. (Dec. 2013). "The IRAM-30 m line survey of the Horsehead PDR. IV. Comparative chemistry of H_2CO and CH_3OH". In: 560, A73, A73. DOI: 10.1051/0004-6361/201322460. arXiv: 1310.6231 [astro-ph.GA].

Habing, H. J. (Jan. 1968). "The interstellar radiation density between 912 A and 2400 A". In: 19, p. 421.

Hagen, W., L. J. Allamandola, and J. M. Greenberg (Sept. 1979). "Interstellar Molecule Formation in Grain Mantles: The Laboratory Analog Experiments, Results and Implications". In: 65.1, pp. 215–240. DOI: 10.1007/BF00643502.

Hama, Tetsuya and Naoki Watanabe (Dec. 2013). "Surface Processes on Interstellar Amorphous Solid Water: Adsorption, Diffusion, Tunneling Reactions, and Nuclear-Spin Conversion". In: *Chemical Reviews* 113.12, pp. 8783–8839. DOI: 10.1021/cr4000978.

Hama, Tetsuya et al. (Oct. 2012). "The Mechanism of Surface Diffusion of H and D Atoms on Amorphous Solid Water: Existence of Various Potential Sites". In: 757.2, 185, p. 185. DOI: 10.1088/0004-637X/757/2/185.

Hamberg, M. et al. (May 2010). "Experimental studies of the dissociative recombination processes for the dimethyl ether ions $CD_3OCD_2^+$ and $(CD_3)_2OD^+$". In: 514, A83, A83. DOI: 10.1051/0004-6361/200913891.

Hänggi, Peter, Peter Talkner, and Michal Borkovec (Apr. 1990). "Reaction-rate theory: fifty years after Kramers". In: *Reviews of Modern Physics* 62.2, pp. 251–342. DOI: 10.1103/RevModPhys.62.251.

Harada, Nanase, Eric Herbst, and Valentine Wakelam (Oct. 2010). "A New Network for Higher-temperature Gas-phase Chemistry. I. A Preliminary Study of Accretion Disks in Active Galactic Nuclei". In: 721.2, pp. 1570–1578. DOI: 10.1088/0004-637X/721/2/1570.

Hartmann, Lee, Javier Ballesteros-Paredes, and Edwin A. Bergin (Dec. 2001). "Rapid Formation of Molecular Clouds and Stars in the Solar Neighborhood". In: 562.2, pp. 852–868. DOI: 10.1086/323863. arXiv: astro-ph/0108023 [astro-ph].

Hasegawa, T. I. and E. Herbst (Aug. 1993a). "Three-Phase Chemical Models of Dense Interstellar Clouds - Gas Dust Particle Mantles and Dust Particle Surfaces". In: 263, p. 589. DOI: 10.1093/mnras/263.3.589.

Hasegawa, Tatsuhiko I. and Eric Herbst (Mar. 1993b). "New gas-grain chemical models of quiscent dense interstellar clouds :the effects of H2 tunnelling reactions and cosmic ray induced desorption." In: 261, pp. 83–102. DOI: 10.1093/mnras/261.1.83.

Hasegawa, Tatsuhiko I., Eric Herbst, and Chun M. Leung (Sept. 1992). "Models of Gas-Grain Chemistry in Dense Interstellar Clouds with Complex Organic Molecules". In: 82, p. 167. DOI: 10.1086/191713.

He, Jiao and Gianfranco Vidali (June 2014). "Experiments of Water Formation on Warm Silicates". In: 788.1, 50, p. 50. DOI: 10.1088/0004-637X/788/1/50.

He, Jiao et al. (Mar. 2015). "A New Determination of the Binding Energy of Atomic Oxygen On Dust Grain Surfaces: Experimental Results and Simulations". In: 801.2, 120, p. 120. DOI: 10.1088/0004-637X/801/2/120. arXiv: 1501.03836 [astro-ph.GA].

He, Jiao, Kinsuk Acharyya, and Gianfranco Vidali (July 2016). "Binding Energy of Molecules on Water Ice: Laboratory Measurements and Modeling". In: 825.2, 89, p. 89. DOI: 10.3847/0004-637X/825/2/89. arXiv: 1603.02191 [astro-ph.IM].

He, Jiao, Kinsuk Acharyya, and Gianfranco Vidali (2016). "Binding Energy of Molecules on Water Ice: Laboratory Measurements and Modeling". In: 825.2, p. 89.

He, Jiao, Kinsuk Acharyya, and Gianfranco Vidali (May 2016). "Sticking of Molecules on Nonporous Amorphous Water Ice". In: 823.1, 56, p. 56. DOI: 10.3847/0004-637X/823/1/56. arXiv: 1602.06341 [astro-ph.IM].

He, Jiao, SM Emtiaz, and Gianfranco Vidali (Aug. 2018). "Measurements of Diffusion of Volatiles in Amorphous Solid Water: Application to Interstellar Medium Environments". In: 863.2, 156, p. 156. DOI: 10.3847/1538-4357/aad227. arXiv: 1806.06980 [astro-ph.IM].

He, Jiao et al. (June 2019). "The Effective Surface Area of Amorphous Solid Water Measured by the Infrared Absorption of Carbon Monoxide". In: 878.2, 94, p. 94. DOI: 10.3847/1538-4357/ab1f6a. arXiv: 1905.00969 [astro-ph.IM].

Heiles, C. (Dec. 1979). "High-velocity clouds and H I supershells." In: 91, p. 611.

Henkel, C. et al. (Dec. 1987). "The detection of extragalactic methanol." In: 188, pp. L1–L4.

Hennebelle, P. et al. (Aug. 2008). "From the warm magnetized atomic medium to molecular clouds". In: 486.3, pp. L43–L46. DOI: 10.1051/0004-6361:200810165. arXiv: 0805.1366 [astro-ph].

Hennebelle, Patrick and Gilles Chabrier (Dec. 2011). "Analytical Star Formation Rate from Gravoturbulent Fragmentation". In: 743.2, L29, p. L29. DOI: 10.1088/2041-8205/743/2/L29. arXiv: 1110.0033 [astro-ph.GA].

Henning, Thomas and Dmitry Semenov (Dec. 2013). "Chemistry in Protoplanetary Disks". In: *Chemical Reviews* 113.12, pp. 9016–9042. DOI: 10.1021/cr400128p. arXiv: 1310.3151 [astro-ph.GA].

Henry, R. C., R. C. Anderson, and W. G. Fastie (Aug. 1980). "Far-ultraviolet studies. VII - The spectrum and latitude dependence of the local interstellar radiation field". In: 239, pp. 859–866. DOI: 10.1086/158170.

Herbst, Eric (Apr. 2017). "The synthesis of large interstellar molecules". In: *International Reviews in Physical Chemistry* 36.2, pp. 287–331. ISSN: 0144-235X. DOI: 10.1080/0144235X.2017.1293974. URL: https://doi.org/10.1080/0144235X.2017.1293974 (visited on 04/01/2019).

Herbst, Eric and Ewine F. van Dishoeck (Sept. 2009). "Complex Organic Interstellar Molecules". In: *Annual Review of Astronomy and Astrophysics* 47, pp. 427–480. ISSN: 0066-4146. DOI: 10.1146/annurev-astro-082708-101654. (Visited on 03/15/2019).

Herrero, Víctor J. et al. (Jan. 2010). "Interaction of CH4 and H2O in ice mixtures". In: *Physical Chemistry Chemical Physics (Incorporating Faraday Transactions)* 12.13, p. 3164. DOI: 10.1039/b922598f.

Herschel, William (Jan. 1785). "On the Construction of the Heavens." In: *Philosophical Transactions of the Royal Society of London Series I* 75, pp. 213–266.

Hidaka, H. et al. (Oct. 2004). "Conversion of H_2CO to CH_3OH by Reactions of Cold Atomic Hydrogen on Ice Surfaces below 20 K". In: 614.2, pp. 1124–1131. DOI: 10.1086/423889.

Hincelin, U. et al. (June 2011). "Oxygen depletion in dense molecular clouds: a clue to a low O_2 abundance?" In: 530, A61, A61. DOI: 10.1051/0004-6361/201016328. arXiv: 1104.1530 [astro-ph.SR].

Hincelin, U., Q. Chang, and E. Herbst (Feb. 2015). "A new and simple approach to determine the abundance of hydrogen molecules on interstellar ice mantles". In: 574, A24, A24. DOI: 10.1051/0004-6361/201424807. arXiv: 1410.7375 [astro-ph.SR].

Hindmarsh, A. C. (1983). "ODEPACK, A Systematized Collection of ODE Solvers". In: *Scientific Computing*, pp. 55–64.

Hiraoka, Kenzo et al. (May 1998). "Gas-Grain Processes for the Formation of CH_4 and H_2O: Reactions of H Atoms with C, O, and CO in the Solid Phase at 12 K". In: 498.2, pp. 710–715. DOI: 10.1086/305572.

Hiraoka, Kenzo et al. (1998). "Gas-grain processes for the formation of CH4 and H2O: Reactions of H atoms with C, O, and CO in the solid phase at 12 K". In: 498.2, p. 710.

Hiraoka, Kenzo et al. (Sept. 2002). "Formation of Formaldehyde by the Tunneling Reaction of H with Solid CO at 10 K Revisited". In: 577.1, pp. 265–270. DOI: 10.1086/342132.

Hohenberg, Pierre and Walter Kohn (1964). "Inhomogeneous electron gas". In: *Phys Rev* 136.3B, B864.

Holdship, J. and S. Viti (Feb. 2022). "History-independent tracers. Forgetful molecular probes of the physical conditions of the dense interstellar medium". In: 658, A103, A103. DOI: 10.1051/0004-6361/202142398. arXiv: 2201.01312 [astro-ph.GA].

Holdship, J. et al. (July 2017). "UCLCHEM: A Gas-grain Chemical Code for Clouds, Cores, and C-Shocks". In: 154.1, 38, p. 38. DOI: 10.3847/1538-3881/aa773f. arXiv: 1705.10677 [astro-ph.GA].

Holdship, Jonathan et al. (June 2019). "Investigating the Efficiency of Explosion Chemistry as a Source of Complex Organic Molecules in TMC-1". In: 878.1, 65, p. 65. DOI: 10.3847/1538-4357/ab1f7b. arXiv: 1905.01901 [astro-ph.GA].

Holdship, Jonathan et al. (Aug. 2019). "Observations of CH₃OH and CH₃CH
in a Sample of Protostellar Outflow Sources". en. In: *The Astrophysical Journal* 880.2, p. 138. DOI: 10.3847/1538-4357/ab1f8f. URL: https://ui.adsabs.harvard.edu/abs/2019ApJ...880..138H/abstract (visited on 09/29/2019).

Hollenbach, D. and C. F. McKee (Nov. 1979). "Molecule formation and infrared emission in fast interstellar shocks. I. Physical processes." In: 41, pp. 555–592. DOI: 10.1086/190631.

Hollenbach, D. J. and A. G. G. M. Tielens (Jan. 1997). "Dense Photodissociation Regions (PDRs)". In: 35, pp. 179–216. DOI: 10.1146/annurev.astro.35.1.179.

— (Jan. 1999). "Photodissociation regions in the interstellar medium of galaxies". In: *Reviews of Modern Physics* 71.1, pp. 173–230. DOI: 10.1103/RevModPhys.71.173.

Hollenbach, David and E. E. Salpeter (Jan. 1971). "Surface Recombination of Hydrogen Molecules". In: 163, p. 155. DOI: 10.1086/150754.

Hollenbach, David and EE Salpeter (1971). "Surface recombination of hydrogen molecules". In: 163, p. 155.

Hollenbach, David et al. (Jan. 2009). "Water, O_2, and Ice in Molecular Clouds". In: 690.2, pp. 1497–1521. DOI: 10.1088/0004-637X/690/2/1497. arXiv: 0809.1642 [astro-ph].

Hollenbach, David J., Takamasa Takahashi, and A. G. G. M. Tielens (Aug. 1991). "Low-Density Photodissociation Regions". In: 377, p. 192. DOI: 10.1086/170347.

Holtom, Philip D. et al. (June 2005). "A Combined Experimental and Theoretical Study on the Formation of the Amino Acid Glycine (NH_2CH_2COOH) and Its Isomer ($CH_3NHCOOH$) in Extraterrestrial Ices". In: 626.2, pp. 940–952. DOI: 10.1086/430106.

Horimoto, Noriko, Hiroyuki S. Kato, and Maki Kawai (2002). "Stepwise morphological change of porous amorphous ice films observed through adsorption of methane". In: *The Journal of Chemical Physics* 116.11, pp. 4375–4378. DOI: 10.1063/1.1458937. eprint: https://doi.org/10.1063/1.1458937. URL: https://doi.org/10.1063/1.1458937.

Horn, A B et al. (1992). "missing". In: *Journal of Chemical Society Faraday Transaction* 88, p. 1077.

Howe, D. A., S. D. Taylor, and D. A. Williams (Mar. 1996). "The chemistry of core collapse in TMC1". In: 279.1, pp. 143–151. DOI: 10.1093/mnras/279.1.143.

Howk, J. Christopher, Blair D. Savage, and Dirk Fabian (Nov. 1999). "Abundances and Physical Conditions in the Warm Neutral Medium toward μ Columbae". In: 525.1, pp. 253–293. DOI: 10.1086/307888. arXiv: astro-ph/9905187 [astro-ph].

Indriolo, Nick and Benjamin J. McCall (Jan. 2012). "Investigating the Cosmic-Ray Ionization Rate in the Galactic Diffuse Interstellar Medium through Observations of $H^+{}_3$". In: 745.1, 91, p. 91. DOI: 10.1088/0004-637X/745/1/91. arXiv: 1111.6936 [astro-ph.GA].

Indriolo, Nick et al. (Feb. 2015). "Herschel Survey of Galactic OH^+, H_2O^+, and H_3O^+: Probing the Molecular Hydrogen Fraction and Cosmic-Ray Ionization Rate". In: 800.1, 40, p. 40. DOI: 10.1088/0004-637X/800/1/40. arXiv: 1412.1106 [astro-ph.GA].

Ioppolo, S. et al. (Oct. 2008). "Laboratory Evidence for Efficient Water Formation in Interstellar Ices". In: 686.2, pp. 1474–1479. DOI: 10.1086/591506. arXiv: 0807.0129 [astro-ph].

Ioppolo, S. et al. (May 2011). "Surface formation of CO_2 ice at low temperatures". In: 413.3, pp. 2281–2287. DOI: 10.1111/j.1365-2966.2011.18306.x.

Iqbal, Wasim and Valentine Wakelam (July 2018). "Nautilus multi-grain model: Importance of cosmic-ray-induced desorption in determining the chemical abundances in the ISM". In: 615, A20, A20. DOI: 10.1051/0004-6361/201732486. arXiv: 1802.07979 [astro-ph.GA].

Iqbal, Wasim, Valentine Wakelam, and Pierre Gratier (Dec. 2018). "Statistical study of uncertainties in the diffusion rate of species on interstellar ice and its impact on chemical model predictions". In: 620, A109, A109. DOI: 10.1051/0004-6361/201833804. arXiv: 1811.03488 [astro-ph.GA].

Isokoski, K. et al. (2014). "Porosity and thermal collapse measurements of H2O, CH3OH, CO2, and H2O:CO2 ices". In: *Phys. Chem. Chem. Phys.* 16 (8), pp. 3456–3465. DOI: 10.1039/C3CP54481H. URL: http://dx.doi.org/10.1039/C3CP54481H.

Jaber, Ali A. et al. (Aug. 2014). "The Census of Complex Organic Molecules in the Solar-type Protostar IRAS16293-2422". In: 791.1, 29, p. 29. DOI: 10.1088/0004-637X/791/1/29. arXiv: 1406.7195 [astro-ph.SR].

Jacobsen, Steffen K. et al. (Sept. 2018). "The organic chemistry in the innermost, infalling envelope of the Class 0 protostar L483". en. In: *arXiv e-prints*, arXiv:1809.00390. URL: https://ui.adsabs.harvard.edu/abs/2018arXiv180900390J/abstract (visited on 07/17/2019).

Jansen, HB and P Ros (1969). "Non-empirical molecular orbital calculations on the protonation of carbon monoxide". In: *Chem Phys Lett* 3.3, pp. 140–143.

Jenkins, E. B., B. D. Savage, and Jr. Spitzer L. (Feb. 1986). "Abundances of Interstellar Atoms from Ultraviolet Absorption Lines". In: 301, p. 355. DOI: 10.1086/163906.

Jenkins, Edward B. (Aug. 2009). "A Unified Representation of Gas-Phase Element Depletions in the Interstellar Medium". In: 700.2, pp. 1299–1348. DOI: 10.1088/0004-637X/700/2/1299. arXiv: 0905.3173 [astro-ph.GA].

— (Feb. 2013). "The Fractional Ionization of the Warm Neutral Interstellar Medium". In: 764.1, 25, p. 25. DOI: 10.1088/0004-637X/764/1/25. arXiv: 1301.3144 [astro-ph.GA].

Jenniskens, P. et al. (Jan. 1995). "High-Density Amorphous Ice, the Frost on Interstellar Grains". In: 455, p. 389. DOI: 10.1086/176585.

Jessberger, E. K. et al. (Sept. 2005). *Properties of Interplanetary Dust: Information from Collected Samples*. DOI: transferredfrom|en.wikipedia|CommonGood|CommonsHelper.

Jones, A. P. and N. Ysard (July 2019). "The essential elements of dust evolution. A viable solution to the interstellar oxygen depletion problem?" In: 627, A38, A38. DOI: 10.1051/0004-6361/201935532. arXiv: 1906.01382 [astro-ph.GA].

Jones, AP (2013). "Heteroatom-doped hydrogenated amorphous carbons, aC: H: X-"Volatile" silicon, sulphur and nitrogen depletion, blue photoluminescence, diffuse interstellar bands and ferro-magnetic carbon grain connections". In: 555, A39.

Jones, AP et al. (2017). "The global dust modelling framework THEMIS". In: 602, A46.

Jonusas, Mindaugas, Killian Leroux, and Lahouari Krim (Nov. 2020). "N + H surface reaction under interstellar conditions: Does the $NH/NH_2/NH_3$ distribution depend on N/H ratio?" In: *Journal of Molecular Structure* 1220, 128736, p. 128736. DOI: 10.1016/j.molstruc.2020.128736.

Joohnston, HS and J Heicklen (1962). "TUNNELLING CORRECTIONS FOR UNSYMMETRICAL ECKART POTENTIAL ENERGY BARRIERS". In: *JOURNAL OF PHYSICAL CHEMISTRY* 66.3, 532–&. ISSN: 0022-3654. DOI: {10.1021/j100809a040}.

Jørgensen, J. K., F. L. Schöier, and E. F. van Dishoeck (May 2005). "Molecular freeze-out as a tracer of the thermal and dynamical evolution of pre- and protostellar cores". In: 435.1, pp. 177–182. DOI: 10.1051/0004-6361:20042092. arXiv: astro-ph/0501623 [astro-ph].

Joung, M. K. Ryan and Mordecai-Mark Mac Low (Dec. 2006). "Turbulent Structure of a Stratified Supernova-driven Interstellar Medium". In: 653.2, pp. 1266–1279. DOI: 10.1086/508795. arXiv: astro-ph/0601005 [astro-ph].

Jørgensen, J. K. et al. (Nov. 2016). "The ALMA Protostellar Interferometric Line Survey (PILS). First results from an unbiased submillimeter wavelength line survey of the Class 0 protostellar binary IRAS 16293-2422 with ALMA". en. In: *Astronomy and Astrophysics* 595, A117. DOI: 10.1051/0004-6361/201628648. (Visited on 07/17/2019).

Jørgensen, J. K. et al. (Dec. 2018). "The ALMA-PILS survey: isotopic composition of oxygen-containing complex organic molecules toward IRAS 16293-2422B". en. In: *Astronomy and Astrophysics* 620, A170. DOI: 10.1051/0004-6361/201731667. URL: https://ui.adsabs.harvard.edu/abs/2018A%26A...620A.170J/abstract (visited on 10/04/2019).

Kahane, C. et al. (Feb. 2013). "Detection of Formamide, the Simplest but Crucial Amide, in a Solar-type Protostar". In: 763.2, L38, p. L38. DOI: 10.1088/2041-8205/763/2/L38.

Kalvāns, J. (June 2015a). "Ice Chemistry in Starless Molecular Cores". In: 806.2, 196, p. 196. DOI: 10.1088/0004-637X/806/2/196. arXiv: 1504.06065 [astro-ph.GA].

— (Apr. 2015b). "The effect of selective desorption mechanisms during interstellar ice formation". In: 803.2, 52, p. 52. DOI: 10.1088/0004-637X/803/2/52. arXiv: 1502.00504 [astro-ph.GA].

Kalvāns, Juris (Mar. 2021). "The Connection between Warm Carbon-chain Chemistry and Interstellar Irradiation of Star-forming Cores". In: 910.1, 54, p. 54. DOI: 10.3847/1538-4357/abe30d. arXiv: 2102.02681 [astro-ph.GA].

Kama, M et al. (2015). "Depletion of chlorine into HCl ice in a protostellar core-The CHESS spectral survey of OMC-2 FIR 4". In: 574, A107.

Karska, A. et al. (Apr. 2013). "Water in star-forming regions with Herschel (WISH). III. Far-infrared cooling lines in low-mass young stellar objects". In: *Astronomy and Astrophysics* 552, A141. ISSN: 0004-6361. DOI: 10.1051/0004-6361/201220028. (Visited on 03/26/2019).

Karssemeijer, L. J. and H. M. Cuppen (Sept. 2014). "Diffusion-desorption ratio of adsorbed CO and CO_2 on water ice". In: 569, A107, A107. DOI: 10.1051/0004-6361/201424792. arXiv: 1409.3038 [astro-ph.GA].

Karssemeijer, LJ and HM Cuppen (2014). "Diffusion-desorption ratio of adsorbed CO and CO2 on water ice". In: 569, A107.

Karssemeijer, LJ, GA de Wijs, and HM Cuppen (2014). "Interactions of adsorbed CO 2 on water ice at low temperatures". In: *PCCP* 16.29, pp. 15630–15639.

Katz, N et al. (1999). "Molecular hydrogen formation on astrophysically relevant surfaces". In: *ASTROPHYSICAL JOURNAL* 522.1, 1, 305–312. ISSN: 0004-637X. DOI: {10.1086/307642}.

Kaufman, Michael J. and David A. Neufeld (Jan. 1996). "Far-Infrared Water Emission from Magnetohydrodynamic Shock Waves". In: 456, p. 611. DOI: 10.1086/176683.

Kessler, M. F. et al. (2003). *The ISO Handbook, Volume I - Mission & Satellite Overview*.

Keto, Eric and Paola Caselli (Aug. 2008). "The Different Structures of the Two Classes of Starless Cores". In: 683.1, pp. 238–247. DOI: 10.1086/589147. arXiv: 0804.0822 [astro-ph].

Kimmel, Greg A. et al. (Mar. 2001a). "Control of amorphous solid water morphology using molecular beams. I. Experimental results". In: 114.12, pp. 5284–5294. DOI: 10.1063/1.1350580.

Kimmel, Greg A. et al. (Mar. 2001b). "Control of amorphous solid water morphology using molecular beams. II. Ballistic deposition simulations". In: 114.12, pp. 5295–5303. DOI: 10.1063/1.1350581.

King, D A (1975). "Thermal desorption from metal surfaces: A review". In: *Surface Science* 47, pp. 384–402.

Kirchhoff, W. H., D. R. Johnson, and F. J. Lovas (1973). "Microwave spectra of molecules of astrophysical interest. 2. Methylenimine." In: *Journal of Physical and Chemical Reference Data* 2.1, pp. 1–10. DOI: 10.1063/1.3253110.

Kleiner, I., F. J. Lovas, and M. Godefroid (1996). "Microwave Spectra of Molecules of Astrophysical Interest. XXIII. Acetaldehyde". In: *Journal of Physical and Chemical Reference Data* 25.4, pp. 1113–1210. DOI: 10.1063/1.555983.

Klessen, Ralf S. and Simon C. O. Glover (Jan. 2016). "Physical Processes in the Interstellar Medium". In: *Saas-Fee Advanced Course* 43, p. 85. DOI: 10.1007/978-3-662-47890-5_2. arXiv: 1412.5182 [astro-ph.GA].

Knacke, R. F. et al. (Sept. 1982). "Observation of interstellar ammonia ice". In: 260, pp. 141–146. DOI: 10.1086/160241.

Koussa, H. et al. (2006). "Kinetic study of the reaction H2O2+H -> H2O+OH by ab initio and density functional theory calculations". In: *JOURNAL OF MOLECULAR STRUCTURE-THEOCHEM* 770.1-3, 149–156. ISSN: 0166-1280. DOI: {10.1016/j.theochem.2006.05.050}.

Koyama, Hiroshi and Shu-Ichiro Inutsuka (Apr. 2000). "Molecular Cloud Formation in Shock-compressed Layers". In: 532.2, pp. 980–993. DOI: 10.1086/308594. arXiv: astro-ph/9912509 [astro-ph].

Kraus, Peter and Irmgard Frank (2018). "Density functional theory for microwave spectroscopy of noncovalent complexes: A benchmark study". In: *J Phys Chem A* 122.21, pp. 4894–4901.

Kristensen, L. E. et al. (June 2012). "Water in star-forming regions with Herschel (WISH). II. Evolution of 557 GHz 110-101 emission in low-mass protostars". In: *Astronomy and Astrophysics* 542, A8. ISSN: 0004-6361. DOI: 10.1051/0004-6361/201118146. (Visited on 03/26/2019).

Krumholz, Mark R. and Christopher F. McKee (Sept. 2005). "A General Theory of Turbulence-regulated Star Formation, from Spirals to Ultraluminous Infrared Galaxies". In: 630.1, pp. 250–268. DOI: 10.1086/431734. arXiv: astro-ph/0505177 [astro-ph].

Krymskii, G. F. (June 1977). "A regular mechanism for the acceleration of charged particles on the front of a shock wave". In: *Akademiia Nauk SSSR Doklady* 234, pp. 1306–1308.

Kuwahata, K. et al. (Sept. 2015a). "Signatures of Quantum-Tunneling Diffusion of Hydrogen Atoms on Water Ice at 10 K". In: 115.13, 133201, p. 133201. DOI: 10.1103/PhysRevLett.115.133201.

— (Sept. 2015b). "Signatures of Quantum-Tunneling Diffusion of Hydrogen Atoms on Water Ice at 10 K". In: 115.13, 133201, p. 133201. DOI: 10.1103/PhysRevLett.115.133201.

Lacy, John H. et al. (Mar. 2017). "H_2, CO, and Dust Absorption through Cold Molecular Clouds". In: 838.1, 66, p. 66. DOI: 10.3847/1538-4357/aa6247. arXiv: 1703.09826 [astro-ph.GA].

Lada, Charles J. (Jan. 1987). "Star formation: from OB associations to protostars." In: *Star Forming Regions*. Ed. by Manuel Peimbert and Jun Jugaku. Vol. 115, p. 1.

Lada, Charles J. et al. (Mar. 2003). "The Dynamical State of Barnard 68: A Thermally Supported, Pulsating Dark Cloud". In: 586.1, pp. 286–295. DOI: 10.1086/367610. arXiv: astro-ph/0211507 [astro-ph].

Lamberts, T. et al. (Oct. 2014). "Relevance of the H_2 + O reaction pathway for the surface formation of interstellar water. Combined experimental and modeling study". In: 570, A57. DOI: 10.1051/0004-6361/201424252. arXiv: 1409.3055.

Lamberts, Thanja and Johannes Kästner (Sept. 2017). "Influence of Surface and Bulk Water Ice on the Reactivity of a Water-forming Reaction". In: 846.1, 43, p. 43. DOI: 10.3847/1538-4357/aa8311. arXiv: 1708.05555 [astro-ph.GA].

Lamberts, Thanja et al. (2016). "Quantum tunneling during interstellar surface-catalyzed formation of water: the reaction H + H2O2 H2O + OH". In: *Phys. Chem. Chem. Phys.* 18 (48), pp. 33021–33030. DOI: 10.1039/C6CP06457D. URL: http://dx.doi.org/10.1039/C6CP06457D.

Landau, Lev Davidovich and E. M. Lifshitz (1975). *The classical theory of fields*.

Lauck, Trish et al. (Mar. 2015). "CO Diffusion into Amorphous H_2O Ices". In: 801.2, 118, p. 118. DOI: 10.1088/0004-637X/801/2/118. arXiv: 1502.07772 [astro-ph.GA].

Laureijs, R. J. et al. (2003). *The ISO Handbook, Volume IV - PHT - The Imaging Photo-Polarimeter*.

Lay, O. P., J. E. Carlstrom, and R. E. Hills (Oct. 1995). "NGC 1333 IRAS 4: Further Multiplicity Revealed with the CSO-JCMT Interferometer". en. In: *The Astrophysical Journal* 452, p. L73. DOI: 10.1086/309713. URL: https://ui.adsabs.harvard.edu/abs/1995ApJ...452L..73L/abstract (visited on 10/01/2019).

Le Bourlot, J. et al. (Aug. 1995a). "Infrared Diagnostics of the Formation of H 2 on Interstellar Dust". In: 449, p. 178. DOI: 10.1086/176043.

Le Bourlot, J. et al. (Oct. 1995b). "On the uniqueness of the solutions to the chemical rate equations in interstellar clouds: the gas-dust interface." In: 302, p. 870.

Le Petit, Franck et al. (June 2006). "A Model for Atomic and Molecular Interstellar Gas: The Meudon PDR Code". In: 164.2, pp. 506–529. DOI: 10.1086/503252. arXiv: astro-ph/0602150 [astro-ph].

Lee, Chengteh, Weitao Yang, and Robert G Parr (1988a). "Development of the Colle-Salvetti correlation-energy formula into a functional of the electron density". In: *Physical review B* 37.2, p. 785.

— (1988b). "Development of the Colle-Salvetti correlation-energy formula into a functional of the electron density". In: *Phys Rev B* 37.2, p. 785.

Lee, H. H. et al. (July 1996). "Photodissociation of H_2_ and CO and time dependent chemistry in inhomogeneous interstellar clouds." In: 311, pp. 690–707.

Lee, Kin Long Kelvin et al. (Mar. 2021). "Interstellar Detection of 2-cyanocyclopentadiene, C_5H_5CN, a Second Five-membered Ring toward TMC-1". In: 910.1, L2, p. L2. DOI: 10.3847/2041-8213/abe764. arXiv: 2102.09595 [astro-ph.GA].

Leech, K. et al. (2003). *The ISO Handbook, Volume V - SWS - The Short Wavelength Spectrometer*.

Lefloch, B. et al. (June 1998). "Cores and cavities in NGC 1333". In: 334, pp. 269–279.

Lefloch, B. et al. (June 1998). "Cores and cavities in NGC 1333". In: *Astronomy and Astrophysics* 334, pp. 269–279. ISSN: 0004-6361. URL: http://adsabs.harvard.edu/abs/1998A%26A...334..269L (visited on 03/15/2019).

Lefloch, Bertrand et al. (July 2017). "L1157-B1, a factory of complex organic molecules in a solar-type star-forming region". In: 469.1, pp. L73–L77. DOI: 10.1093/mnrasl/slx050. arXiv: 1704.04646 [astro-ph.GA].

Lefloch, Bertrand et al. (July 2017). "L1157-B1, a factory of complex organic molecules in a solar-type star-forming region". In: *Monthly Notices of the Royal Astronomical Society* 469, pp. L73–L77. ISSN: 0035-8711. DOI: 10.1093/mnrasl/slx050. URL: http://adsabs.harvard.edu/abs/2017MNRAS.469L..73L (visited on 04/21/2019).

Leger, A., M. Jura, and A. Omont (Mar. 1985). "Desorption from interstellar grains". In: 144.1, pp. 147–160.

Ligterink, N. F. W. et al. (Aug. 2017). "The ALMA-PILS survey: detection of CH_3NCO towards the low-mass protostar IRAS 16293-2422 and laboratory constraints on its formation". In: 469.2, pp. 2219–2229. DOI: 10.1093/mnras/stx890. arXiv: 1703.03252 [astro-ph.SR].

Lis, D. C. et al. (Nov. 2001). "Atomic Oxygen Abundance in Molecular Clouds: Absorption toward Sagittarius B2". In: 561.2, pp. 823–829. DOI: 10.1086/323518.

Liu, B and AD McLean (1973). "Accurate calculation of the attractive interaction of two ground state helium atoms". In: *J Chem Phys* 59.8, pp. 4557–4558.

Livingston, Frank E., Jamison A. Smith, and Steven M. George (July 2002). "General Trends for Bulk Diffusion in Ice and Surface Diffusion on Ice". In: *Journal of Physical Chemistry A* 106.26, pp. 6309–6318. DOI: 10.1021/jp014438c.

Loison, Jean-Christophe, Valentine Wakelam, and Kevin M. Hickson (2014). "The interstellar gas-phase chemistry of HCN and HNC". In: 443.1, pp. 398–410. DOI: 10.1093/mnras/stu1089. arXiv: 1406.1696 [astro-ph.GA].

Loison, Jean-Christophe, Valentine Wakelam, and Kevin M. Hickson (Sept. 2014). "The interstellar gas-phase chemistry of HCN and HNC". en. In: *Monthly Notices of the Royal Astronomical Society* 443.1, p. 398. DOI: 10.1093/mnras/stu1089. URL: https://ui.adsabs.harvard.edu/abs/2014MNRAS.443..398L/abstract (visited on 09/30/2019).

Loison, Jean-Christophe et al. (Mar. 2016). "The interstellar chemistry of H_2C_3O isomers". In: 456.4, pp. 4101–4110. DOI: 10.1093/mnras/stv2866. arXiv: 1512.01582 [astro-ph.GA].

Looney, Leslie W., Lee G. Mundy, and W. J. Welch (Jan. 2000). "Unveiling the Circumstellar Envelope and Disk: A Subarcsecond Survey of Circumstellar Structures". In: *The Astrophysical Journal* 529, pp. 477–498. ISSN: 0004-637X. DOI: 10.1086/308239. URL: http://adsabs.harvard.edu/abs/2000ApJ...529..477L (visited on 03/15/2019).

López-Sepulcre, A. et al. (May 2015). "Shedding light on the formation of the pre-biotic molecule formamide with ASAI". In: 449.3, pp. 2438–2458. DOI: 10.1093/mnras/stv377. arXiv: 1502.05762 [astro-ph.SR].

López-Sepulcre, A. et al. (Oct. 2017). "Complex organics in IRAS 4A revisited with ALMA and PdBI: Striking contrast between two neighbouring protostellar cores". In: 606, A121, A121. DOI: 10.1051/0004-6361/201630334. arXiv: 1707.03745 [astro-ph.GA].

Louvet, F. et al. (Nov. 2016). "Tracing extended low-velocity shocks through SiO emission. Case study of the W43-MM1 ridge". In: 595, A122, A122. DOI: 10.1051/0004-6361/201629077. arXiv: 1607.08668 [astro-ph.GA].

Lu, Yang, Qiang Chang, and Yuri Aikawa (Dec. 2018). "The Chemical Evolution from Prestellar to Protostellar Cores: A New Multiphase Model with Bulk Diffusion and Photon Penetration". In: 869.2, 165, p. 165. DOI: 10.3847/1538-4357/aaeed8. arXiv: 1809.02419 [astro-ph.SR].

López-Sepulcre, A. et al. (Oct. 2017). "Complex organics in IRAS 4A revisited with ALMA and PdBI: Striking contrast between two neighbouring protostellar cores". In: *Astronomy*

and Astrophysics 606, A121. ISSN: 0004-6361. DOI: 10.1051/0004-6361/201630334. (Visited on 03/15/2019).

Madzunkov, S. et al. (Feb. 2006). "Measurements of polyatomic molecule formation on an icy grain analog using fast atoms". In: 73.2, 020901, p. 020901. DOI: 10.1103/PhysRevA.73.020901.

Manicò, G. et al. (Feb. 2001). "Laboratory Measurements of Molecular Hydrogen Formation on Amorphous Water Ice". In: 548.2, pp. L253–L256. DOI: 10.1086/319116.

Manigand, S. et al. (Mar. 2020). "The ALMA-PILS survey: inventory of complex organic molecules towards IRAS 16293-2422 A". In: 635, A48, A48. DOI: 10.1051/0004-6361/201936299. arXiv: 2001.06400 [astro-ph.SR].

Marcelino, N. et al. (Nov. 2018). "ALMA observations of the young protostellar system Barnard 1b: Signatures of an incipient hot corino in B1b-S". en. In: *Astronomy and Astrophysics* 620, A80. DOI: 10.1051/0004-6361/201731955. (Visited on 07/17/2019).

Marcelino, Núria et al. (Jan. 2009). "Discovery of Fulminic Acid, HCNO, in Dark Clouds". In: 690.1, pp. L27–L30. DOI: 10.1088/0004-637X/690/1/L27. arXiv: 0811.2679 [astro-ph].

Marcowith, A. et al. (Apr. 2016). "The microphysics of collisionless shock waves". In: *Reports on Progress in Physics* 79.4, 046901, p. 046901. DOI: 10.1088/0034-4885/79/4/046901. arXiv: 1604.00318 [astro-ph.HE].

Maret, Sébastien and Edwin A. Bergin (Aug. 2007). "The Ionization Fraction of Barnard 68: Implications for Star and Planet Formation". In: 664.2, pp. 956–963. DOI: 10.1086/519152. arXiv: 0704.3188 [astro-ph].

Marois, Christian et al. (Nov. 2008). "Direct Imaging of Multiple Planets Orbiting the Star HR 8799". In: *Science* 322.5906, p. 1348. DOI: 10.1126/science.1166585. arXiv: 0811.2606 [astro-ph].

Martín, Juan C. Gómez, Mark A. Blitz, and John M. C. Plane (Jan. 2009). "Kinetic studies of atmospherically relevant silicon chemistry : Part I: Silicon atom reactions". In: *Physical Chemistry Chemical Physics (Incorporating Faraday Transactions)* 11.4, p. 671. DOI: 10.1039/B812946K.

Martín-Doménech, Rafael et al. (2014). "Thermal desorption of circumstellar and cometary ice analogs". In: *Astronomy & Astrophysics* 564, A8.

Matar, E. et al. (Dec. 2008). "Mobility of D atoms on porous amorphous water ice surfaces under interstellar conditions". In: 492.1, pp. L17–L20. DOI: 10.1051/0004-6361:200810434. arXiv: 0810.2242 [astro-ph].

Matar, E. et al. (2010). "Gas temperature dependent sticking of hydrogen on cold amorphous water ice surfaces of interstellar interest". In: *JOURNAL OF CHEMICAL PHYSICS* 133.10. ISSN: 0021-9606. DOI: {10.1063/1.3484867}.

Maté, Belén et al. (Nov. 2020). "Diffusion of CH_4 in amorphous solid water". In: 643, A163, A163. DOI: 10.1051/0004-6361/202038705. arXiv: 2102.13357 [astro-ph.IM].

Mathis, J. S., W. Rumpl, and K. H. Nordsieck (Oct. 1977). "The size distribution of interstellar grains." In: 217, pp. 425–433. DOI: 10.1086/155591.

Mathis, J. S., P. G. Mezger, and N. Panagia (Nov. 1983). "Interstellar radiation field and dust temperatures in the diffuse interstellar matter and in giant molecular clouds." In: 500, pp. 259–276.

Maury, A. J. et al. (Nov. 2011). "The formation of active protoclusters in the Aquila rift: a millimeter continuum view". In: 535, A77, A77. DOI: 10.1051/0004-6361/201117132. arXiv: 1108.0668 [astro-ph.GA].

Maury, A. J. et al. (Jan. 2019). "Characterizing young protostellar disks with the CALYPSO IRAM-PdBI survey: large Class 0 disks are rare". In: 621, A76, A76. DOI: 10.1051/0004-6361/201833537. arXiv: 1810.11221 [astro-ph.GA].

Maury, A. J. et al. (Jan. 2019). "Characterizing young protostellar disks with the CALYPSO IRAM-PdBI survey: large Class 0 disks are rare". en. In: *Astronomy and Astrophysics* 621,

A76. DOI: 10.1051/0004-6361/201833537. URL: https://ui.adsabs.harvard.edu/2019A&A...621A..76M/abstract (visited on 10/14/2019).

May, R. Alan, R. Scott Smith, and Bruce D. Kay (2013). "The release of trapped gases from amorphous solid water films. I. "Top-down" crystallization-induced crack propagation probed using the molecular volcano". In: *The Journal of Chemical Physics* 138.10, p. 104501. DOI: 10.1063/1.4793311. eprint: https://doi.org/10.1063/1.4793311. URL: https://doi.org/10.1063/1.4793311.

McElroy, D. et al. (Feb. 2013). "The UMIST database for astrochemistry 2012". In: 550, A36, A36. DOI: 10.1051/0004-6361/201220465. arXiv: 1212.6362 [astro-ph.SR].

McElroy, D et al. (2013). "The UMIST database for astrochemistry 2012". In: 550, A36.

McGuire, Brett A (2018). "2018 census of interstellar, circumstellar, extragalactic, protoplanetary disk, and exoplanetary molecules". In: 239.2, p. 17.

McGuire, Brett A. (Sept. 2021). "2021 Census of Interstellar, Circumstellar, Extragalactic, Protoplanetary Disk, and Exoplanetary Molecules". In: *arXiv e-prints*, arXiv:2109.13848, arXiv:2109.13848. arXiv: 2109.13848 [astro-ph.GA].

McGuire, Brett A. et al. (Jan. 2018). "Detection of the aromatic molecule benzonitrile (c-C_6H_5CN) in the interstellar medium". In: *Science* 359.6372, pp. 202–205. DOI: 10.1126/science.aao4890. arXiv: 1801.04228 [astro-ph.GA].

McGuire, Brett A. et al. (Sept. 2020). "Early Science from GOTHAM: Project Overview, Methods, and the Detection of Interstellar Propargyl Cyanide ($HCCCH_2CN$) in TMC-1". In: 900.1, L10, p. L10. DOI: 10.3847/2041-8213/aba632. arXiv: 2008.12349 [astro-ph.GA].

McKellar, A. (June 1940). "Evidence for the Molecular Origin of Some Hitherto Unidentified Interstellar Lines". In: 52.307, p. 187. DOI: 10.1086/125159.

McKellar, Andrew (1940). "Evidence for the molecular origin of some hitherto unidentified interstellar lines". In: *Publications of the Astronomical Society of the Pacific* 52.307, pp. 187–192.

Meisner, Jan, Thanja Lamberts, and Johannes Kästner (2017). "Atom Tunneling in the Water Formation Reaction H2 + OH H2O + H on an Ice Surface". In: *ACS Earth and Space Chemistry* 1.7, pp. 399–410. DOI: 10.1021/acsearthspacechem.7b00052. eprint: https://doi.org/10.1021/acsearthspacechem.7b00052. URL: https://doi.org/10.1021/acsearthspacechem.7b00052.

Mendoza, Edgar et al. (Nov. 2014). "Molecules with a peptide link in protostellar shocks: a comprehensive study of L1157". In: 445.1, pp. 151–161. DOI: 10.1093/mnras/stu1718. arXiv: 1408.4857 [astro-ph.SR].

Mendoza, Edgar et al. (Nov. 2014). "Molecules with a peptide link in protostellar shocks: a comprehensive study of L1157". en. In: *Monthly Notices of the Royal Astronomical Society* 445.1, p. 151. DOI: 10.1093/mnras/stu1718. URL: https://ui.adsabs.harvard.edu/abs/2014MNRAS.445..151M/abstract (visited on 10/21/2019).

Merrill, K. M., R. W. Russell, and B. T. Soifer (Aug. 1976). "Infrared observations of ices and silicates in molecular clouds." In: 207, pp. 763–769. DOI: 10.1086/154545.

Millar, T. J. et al. (Mar. 1991). "Gas phase reactions and rate coefficients for use in astrochemistry - The UMIST ratefile". In: 87.3, pp. 585–619.

Millar, T. J., Eric Herbst, and S. B. Charnley (Mar. 1991). "The formation of oxygen-containing organic molecules in the Orion compact ridge". In: *The Astrophysical Journal* 369, pp. 147–156. ISSN: 0004-637X. DOI: 10.1086/169745. URL: http://adsabs.harvard.edu/abs/1991ApJ...369..147M (visited on 04/08/2019).

Minissale, M. and F. Dulieu (July 2014). "Influence of surface coverage on the chemical desorption process". In: 141.1, 014304, p. 014304. DOI: 10.1063/1.4885847. arXiv: 1406.5594 [physics.chem-ph].

Minissale, M., E. Congiu, and F. Dulieu (Jan. 2016a). "Direct measurement of desorption and diffusion energies of O and N atoms physisorbed on amorphous surfaces". In: 585, A146, A146. DOI: 10.1051/0004-6361/201526702. arXiv: 1603.02897 [astro-ph.SR].

Minissale, M. et al. (Jan. 2016b). "Dust as interstellar catalyst. I. Quantifying the chemical desorption process". In: 585, A24, A24. DOI: 10.1051/0004-6361/201525981. arXiv: 1510.03218 [astro-ph.SR].

Minissale, M et al. (2016). "Dust as interstellar catalyst-I. Quantifying the chemical desorption process". In: *Astronomy & Astrophysics* 585, A24.

Mishra, Ajay and Aigen Li (Aug. 2015). "Probing the Role of Carbon in the Interstellar Ultraviolet Extinction". In: 809.2, 120, p. 120. DOI: 10.1088/0004-637X/809/2/120. arXiv: 1507.06599 [astro-ph.GA].

Mispelaer, F. et al. (July 2013). "Diffusion measurements of CO, HNCO, H_2CO, and NH_3 in amorphous water ice". In: 555, A13, A13. DOI: 10.1051/0004-6361/201220691.

Mitterdorfer, Christian et al. (2014). "Small-angle neutron scattering study of micropore collapse in amorphous solid water". In: *Phys. Chem. Chem. Phys.* 16 (30), pp. 16013–16020. DOI: 10.1039/C4CP00593G. URL: http://dx.doi.org/10.1039/C4CP00593G.

Miyauchi, N. et al. (Apr. 2008). "Formation of hydrogen peroxide and water from the reaction of cold hydrogen atoms with solid oxygen at 10 K". In: *Chemical Physics Letters* 456.1-3, pp. 27–30. DOI: 10.1016/j.cplett.2008.02.095. arXiv: 0805.0055 [astro-ph].

Mokrane, H. et al. (Nov. 2009). "Experimental Evidence for Water Formation Via Ozone Hydrogenation on Dust Grains at 10 K". In: 705.2, pp. L195–L198. DOI: 10.1088/0004-637X/705/2/L195. arXiv: 0907.5173 [astro-ph.GA].

Molpeceres, Germán and Johannes Kästner (Apr. 2020). "Adsorption of H2 on amorphous solid water studied with molecular dynamics simulations". In: *Physical Chemistry Chemical Physics (Incorporating Faraday Transactions)* 22.14, pp. 7552–7563. DOI: 10.1039/D0CP00250J. arXiv: 2003.08873 [physics.chem-ph].

Molpeceres, Germán et al. (Oct. 2021). "Carbon Atom Reactivity with Amorphous Solid Water: H_2O Catalyzed Formation of H_2CO". In: *arXiv e-prints*, arXiv:2110.15887, arXiv:2110.15887. arXiv: 2110.15887 [astro-ph.GA].

Muñoz Caro, G. M. et al. (Nov. 2010). "New results on thermal and photodesorption of CO ice using the novel InterStellar Astrochemistry Chamber (ISAC)". In: 522, A108, A108. DOI: 10.1051/0004-6361/200912462.

Myers, P. C. and P. J. Benson (Mar. 1983). "Dense cores in dark clouds. II. NH3 observations and star formation." In: 266, pp. 309–320. DOI: 10.1086/160780.

Myers, P. C. and E. F. Ladd (Aug. 1993). "Bolometric Temperatures of Young Stellar Objects". In: 413, p. L47. DOI: 10.1086/186956.

Müller, Holger S. P. et al. (May 2005). "The Cologne Database for Molecular Spectroscopy, CDMS: a useful tool for astronomers and spectroscopists". In: *Journal of Molecular Structure* 742, pp. 215–227. ISSN: 0022-2860. DOI: 10.1016/j.molstruc.2005.01.027. URL: http://adsabs.harvard.edu/abs/2005JMoSt.742..215M (visited on 02/13/2019).

Nanni, A. et al. (Sept. 2020). "The gas, metal, and dust evolution in low-metallicity local and high-redshift galaxies". In: 641, A168, A168. DOI: 10.1051/0004-6361/202037833. arXiv: 2006.15146 [astro-ph.GA].

Nesterenok, A. V. (July 2018). "Chemical evolution of the gas in C-type shocks in dark clouds". In: *Astrophysics and Space Science* 363, p. 151. ISSN: 0004-640X. DOI: 10.1007/s10509-018-3370-6. URL: http://adsabs.harvard.edu/abs/2018Ap%26SS.363..151N (visited on 05/04/2020).

Neufeld, D. A. et al. (2015). "Sulphur-bearing molecules in diffuse molecular clouds: new results from SOFIA/GREAT and the IRAM 30 m telescope". In: *Astronomy & Astrophysics* 577, A49. eprint: Arxiv:1502.05710v1. URL: http://arxiv.org/abs/1502.05710.

Neufeld, David A and Mark G Wolfire (2009). "The chemistry of interstellar molecules containing the halogen elements". In: 706.2, p. 1594.

Neufeld, David A. and Mark G. Wolfire (Aug. 2017). "The Cosmic-Ray Ionization Rate in the Galactic Disk, as Determined from Observations of Molecular Ions". In: 845.2, 163, p. 163. DOI: 10.3847/1538-4357/aa6d68. arXiv: 1704.03877 [astro-ph.GA].

Neustock, W et al. (1990). "The millimeter and submillimeter-wave spectrum of dimethylether". In: *Zeitschrift für Naturforschung A* 45.5, pp. 702–706.

Nguyen, T, J Stanton, and J Barker (May 2011). "Ab Initio Reaction Rate Constants Computed Using Semiclassical Transition-State Theory: HO+H_2 -> H_2O+H and Isotopologues". In: *Journal of Physical Chemistry A* 115.2, pp. L174–L178. DOI: 10.1021/jp2022743.

Noble, J. A. et al. (July 2011). "CO_2 Formation in Quiescent Clouds: An Experimental Study of the CO + OH Pathway". In: 735.2, 121, p. 121. DOI: 10.1088/0004-637X/735/2/121. arXiv: 1104.0031 [astro-ph.SR].

Noble, J. A. et al. (July 2012a). "The desorption of H_2CO from interstellar grains analogues". In: 543, A5, A5. DOI: 10.1051/0004-6361/201219437.

Noble, J. A. et al. (Mar. 2012b). "Thermal desorption characteristics of CO, O_2 and CO_2 on non-porous water, crystalline water and silicate surfaces at submonolayer and multilayer coverages". In: 421.1, pp. 768–779. DOI: 10.1111/j.1365-2966.2011.20351.x. arXiv: 1112.2162 [astro-ph.SR].

Noble, JA et al. (2012). "Thermal desorption characteristics of CO, O2 and CO2 on non-porous water, crystalline water and silicate surfaces at submonolayer and multilayer coverages". In: *MNRAS* 421.1, pp. 768–779.

Novoa, J and C Sosa (1995). "Evaluation of the Density Functional Approximation on the Computation of Hydrogen Bond Interactions". In: *The Journal of Physical Chemistry* 99, pp. 15837–15845.

Oba, Y et al. (2009). "Formation of compact amorphous H2O ice by codeposition of hydrogen atoms with oxygen molecules on grain surfaces". In: 701.1, p. 464.

Oba, Y et al. (2012). "Water formation through a quantum tunneling surface reaction, OH+ H2, at 10 K". In: 749.1, p. 67.

Oba, Y. et al. (Mar. 2018). "An infrared measurement of chemical desorption from interstellar ice analogues". In: *Nature Astronomy* 2, pp. 228–232. DOI: 10.1038/s41550-018-0380-9. arXiv: 1810.04669 [astro-ph.GA].

Oba, Yasuhiro et al. (Apr. 2010). "Experimental Study of CO_2 Formation by Surface Reactions of Non-energetic OH Radicals with CO Molecules". In: 712.2, pp. L174–L178. DOI: 10.1088/2041-8205/712/2/L174.

Öberg, K. I. et al. (Sept. 2009a). "Formation rates of complex organics in UV irradiated CH_3OH-rich ices. I. Experiments". In: 504.3, pp. 891–913. DOI: 10.1051/0004-6361/200912559. arXiv: 0908.1169 [astro-ph.GA].

— (2009b). "Formation rates of complex organics in UV irradiated CH_3OH-rich ices. I. Experiments". In: 504.3, pp. 891–913. DOI: 10.1051/0004-6361/200912559. arXiv: 0908.1169 [astro-ph.GA].

Öberg, K. I., E. F. van Dishoeck, and H. Linnartz (Mar. 2009c). "Photodesorption of ices I: CO, N_2, and CO_2". In: 496.1, pp. 281–293. DOI: 10.1051/0004-6361/200810207. arXiv: 0809.1333 [astro-ph].

— (Mar. 2009d). "Photodesorption of ices I: CO, N_2, and CO_2". In: 496.1, pp. 281–293. DOI: 10.1051/0004-6361/200810207. arXiv: 0809.1333 [astro-ph].

Öberg, K. I. et al. (Oct. 2009e). "Quantification of segregation dynamics in ice mixtures". In: 505.1, pp. 183–194. DOI: 10.1051/0004-6361/200912464. arXiv: 0907.3948 [astro-ph.GA].

Oberg, Karin I. (Sept. 2016). "Photochemistry and astrochemistry: photochemical pathways to interstellar complex organic molecules". In: *arXiv e-prints*, arXiv:1609.03112, arXiv:1609.03112. arXiv: 1609.03112 [astro-ph.GA].

Oberg, Karin I. and Edwin A. Bergin (Oct. 2020). "Astrochemistry and compositions of planetary systems". In: *arXiv e-prints*, arXiv:2010.03529, arXiv:2010.03529. arXiv: 2010.03529 [astro-ph.EP].

Öberg, Karin I. et al. (June 2007). "Photodesorption of CO Ice". In: 662.1, pp. L23–L26. DOI: 10.1086/519281.

Öberg, Karin I. et al. (Mar. 2009f). "Photodesorption of Ices. II. H_2O and D_2O". In: 693.2, pp. 1209–1218. DOI: 10.1088/0004-637X/693/2/1209. arXiv: 0812.1918 [astro-ph].

Öberg, Karin I. et al. (Aug. 2010). "The Effect of H_2O on Ice Photochemistry". In: 718.2, pp. 832–840. DOI: 10.1088/0004-637X/718/2/832. arXiv: 1006.2190 [astro-ph.GA].

Ohishi, M. and N. Kaifu (Jan. 1998). "Chemical and physical evolution of dark clouds. Molecular spectral line survey toward TMC-1". In: *Faraday Discussions* 109, p. 205. DOI: 10.1039/a801058g.

Olanrewaju, B O et al. (2011a). "missing". In: *The Journal of Physical Chemistry A* 115, p. 5936.

Olanrewaju, Babajide O et al. (2011b). "Probing the Interaction of Hydrogen Chloride with Low-Temperature Water Ice Surfaces Using Thermal and Electron-Stimulated Desorption". In: *The Journal of Physical Chemistry A* 115.23, pp. 5936–5942.

Onaka, Takashi and Alberto Salama (Dec. 2009). "AKARI: space infrared cooled telescope". In: *Experimental Astronomy* 27.1-2, pp. 9–17. DOI: 10.1007/s10686-009-9168-3.

Onishi, Toshikazu et al. (July 1998). "A $C^{18}O$ Survey of Dense Cloud Cores in Taurus: Star Formation". In: 502.1, pp. 296–314. DOI: 10.1086/305867.

Oort, J. H. (Sept. 1954). "Outline of a theory on the origin and acceleration of interstellar clouds and O associations". In: 12, p. 177.

Ortman, Bryan J. et al. (1990). "Reactions of small carbon clusters with water in cryogenic matrixes: the FTIR spectrum of hydroxyethynyl carbene". In: *The Journal of Physical Chemistry* 94.20, pp. 7973–7977. DOI: 10.1021/j100383a041. eprint: https://doi.org/10.1021/j100383a041. URL: https://doi.org/10.1021/j100383a041.

Ospina-Zamudio, J. et al. (Oct. 2018). "First hot corino detected around an isolated intermediate-mass protostar: Cep E-mm". en. In: *Astronomy and Astrophysics* 618, A145. DOI: 10.1051/0004-6361/201832857. URL: https://ui.adsabs.harvard.edu/2018A&A...618A.145O/abstract (visited on 10/01/2019).

Ospina-Zamudio, J et al. (Oct. 2019). "Molecules in the CepE-mm jet: evidence for shock-driven photochemistry?" In: *Monthly Notices of the Royal Astronomical Society* 490.2, pp. 2679–2691. ISSN: 0035-8711. DOI: 10.1093/mnras/stz2733. eprint: http://oup.prod.sis.lan/mnras/article-pdf/490/2/2679/30296789/stz2733.pdf. URL: https://doi.org/10.1093/mnras/stz2733.

Oya, Yoko et al. (June 2016). "Infalling-Rotating Motion and Associated Chemical Change in the Envelope of IRAS 16293-2422 Source A Studied with ALMA". In: 824.2, 88, p. 88. DOI: 10.3847/0004-637X/824/2/88. arXiv: 1605.00340 [astro-ph.SR].

Pack, James D and Hendrik J Monkhorst (1977). ""Special points for Brillouin-zone integrations"—a reply". In: *Phys Rev B* 16.4, p. 1748.

Padoan, Paolo and Åke Nordlund (Mar. 2011). "The Star Formation Rate of Supersonic Magnetohydrodynamic Turbulence". In: 730.1, 40, p. 40. DOI: 10.1088/0004-637X/730/1/40. arXiv: 0907.0248 [astro-ph.GA].

Padovani, M., D. Galli, and A. E. Glassgold (July 2009). "Cosmic-ray ionization of molecular clouds". In: 501.2, pp. 619–631. DOI: 10.1051/0004-6361/200911794. arXiv: 0904.4149 [astro-ph.SR].

Padovani, M. et al. (May 2016). "Protostars: Forges of cosmic rays?" en. In: *Astronomy and Astrophysics* 590, A8. DOI: 10.1051/0004-6361/201628221. URL: https://ui.adsabs.harvard.edu/abs/2016A%26A...590A...8P/abstract (visited on 10/16/2019).

Padovani, Marco and Daniele Galli (Jan. 2013). "Cosmic-Ray Propagation in Molecular Clouds". In: *Cosmic Rays in Star-Forming Environments*. Ed. by Diego F. Torres and Olaf Reimer. Vol. 34, p. 61. DOI: 10.1007/978-3-642-35410-6_6. arXiv: 1305.5393 [astro-ph.GA].

Padovani, Marco et al. (Mar. 2020). "Impact of Low-Energy Cosmic Rays on Star Formation". In: 216.2, 29, p. 29. DOI: 10.1007/s11214-020-00654-1. arXiv: 2002.10282 [astro-ph.GA].

Pagani, L., A. Bourgoin, and F. Lique (Dec. 2012). "A method to measure CO and N_2 depletion profiles inside prestellar cores". In: 548, L4, p. L4. DOI: 10.1051/0004-6361/201220137.

Pantaleone, Stefano et al. (2020). *Chemical desorption versus energy dissipation: insights from ab-initio molecular dynamics of HCO formation*. arXiv: 2004.11758 [astro-ph.GA].

Pantaleone, Stefano et al. (July 2020). "Chemical Desorption versus Energy Dissipation: Insights from Ab Initio Molecular Dynamics of HCO· Formation". In: 897.1, 56, p. 56. DOI: 10.3847/1538-4357/ab8a4b. arXiv: 2004.11758 [astro-ph.GA].

Pantaleone, Stefano et al. (May 2021). "H2 formation on interstellar grains and the fate of reaction energy". In: *arXiv e-prints*, arXiv:2105.06843, arXiv:2105.06843. arXiv: 2105.06843 [astro-ph.GA].

Papajak, Ewa et al. (2011). "Perspectives on basis sets beautiful: Seasonal plantings of diffuse basis functions". In: *JCTC* 7.10, pp. 3027–3034.

Parker, E. N. (Sept. 1966). "The Dynamical State of the Interstellar Gas and Field". In: 145, p. 811. DOI: 10.1086/148828.

Pascale, Fabien et al. (2004). "The calculation of the vibrational frequencies of crystalline compounds and its implementation in the CRYSTAL code". In: *J Comput Chem* 25.6, pp. 888–897.

Pauly, Tyler and Robin T. Garrod (Feb. 2016). "The Effects of Grain Size and Temperature Distributions on the Formation of Interstellar Ice Mantles". In: 817.2, 146, p. 146. DOI: 10.3847/0004-637X/817/2/146. arXiv: 1512.06714 [astro-ph.GA].

Peng, Ruisheng et al. (2010). "A comprehensive survey of hydrogen chloride in the Galaxy". In: 723.1, p. 218.

Penteado, E. M., C. Walsh, and H. M. Cuppen (July 2017). "Sensitivity Analysis of Grain Surface Chemistry to Binding Energies of Ice Species". In: 844.1, 71, p. 71. DOI: 10.3847/1538-4357/aa78f9. arXiv: 1708.01450 [astro-ph.GA].

Penteado, EM, C Walsh, and HM Cuppen (2017). "Sensitivity analysis of grain surface chemistry to binding energies of ice species". In: 844.1, p. 71.

Perets, Hagai B. et al. (July 2005). "Molecular Hydrogen Formation on Ice Under Interstellar Conditions". In: 627.2, pp. 850–860. DOI: 10.1086/430435. arXiv: astro-ph/0412202 [astro-ph].

Perrero, J. et al. (Feb. 2022). "Non-Energetic Formation of Ethanol via CCH Reaction with Interstellar H2O ". In: *ACS Earth and Space Chemistry* in press. arXiv: ,primaryClass={}, adsurl={},adsnote={}.

Persson, Magnus Vilhelm (Jan. 2014). *SEDs of the different protostellar evolutionary stages. figshare*. DOI: https://doi.org/10.6084/m9.figshare.1121574.v2.

Phan, V. H. M., G. Morlino, and S. Gabici (Nov. 2018). "What causes the ionization rates observed in diffuse molecular clouds? The role of cosmic ray protons and electrons". In: 480.4, pp. 5167–5174. DOI: 10.1093/mnras/sty2235. arXiv: 1804.10106 [astro-ph.HE].

Pickett, H. M. et al. (Nov. 1998). "Submillimeter, millimeter and microwave spectral line catalog." In: *Journal of Quantitative Spectroscopy and Radiative Transfer* 60, pp. 883–890. ISSN: 0022-4073. DOI: 10.1016/S0022-4073(98)00091-0. URL: http://adsabs.harvard.edu/abs/1998JQSRT..60..883P (visited on 02/13/2019).

Pierre, L, H Guignes, and C Lhuillier (1985). "ADSORPTION STATES OF LIGHT-ATOMS (H,D,HE) ON QUANTUM CRYSTALS (H2,D2,HE,NE)". In: *JOURNAL OF CHEMICAL PHYSICS* 82.1, 496–507. ISSN: 0021-9606. DOI: {10.1063/1.448772}.

Pineda, Jorge L. et al. (Sept. 2010). "The Relation Between Gas and Dust in the Taurus Molecular Cloud". In: 721.1, pp. 686–708. DOI: 10.1088/0004-637X/721/1/686. arXiv: 1007.5060 [astro-ph.GA].

Pizzarello, S., G. W. Cooper, and G. J. Flynn (2006). "The Nature and Distribution of the Organic Material in Carbonaceous Chondrites and Interplanetary Dust Particles". en. In: *Meteorites and the Early Solar System II*, p. 625. URL: https://ui.adsabs.harvard.edu/abs/2006mess.book..625P/abstract (visited on 09/29/2019).

Poch, Olivier et al. (Mar. 2020). "Ammonium salts are a reservoir of nitrogen on a cometary nucleus and possibly on some asteroids". In: *Science* 367.6483, aaw7462, aaw7462. DOI: 10.1126/science.aaw7462. arXiv: 2003.06034 [astro-ph.EP].

Podio, L. et al. (2014). "Molecular ions in the protostellar shock L1157-B1". In: 565, A64, A64. DOI: 10.1051/0004-6361/201322928. arXiv: 1402.2329 [astro-ph.GA].

Podio, L. et al. (Sept. 2016). "First image of the L1157 molecular jet by the CALYPSO IRAM-PdBI survey". In: *Astronomy and Astrophysics* 593, p. L4. ISSN: 0004-6361. DOI: 10.1051/0004-6361/201628876. (Visited on 04/30/2019).

Pontoppidan, K. M. (July 2006). "Spatial mapping of ices in the Ophiuchus-F core. A direct measurement of CO depletion and the formation of CO_2". In: 453.3, pp. L47–L50. DOI: 10.1051/0004-6361:20065569. arXiv: astro-ph/0605576 [astro-ph].

Pople, John A, Peter MW Gill, and Nicholas C Handy (1995). "Spin-unrestricted character of Kohn-Sham orbitals for open-shell systems". In: *Int J Quantum Chem* 56.4, pp. 303–305.

Poteet, Charles A., Douglas C. B. Whittet, and Bruce T. Draine (Mar. 2015). "The Composition of Interstellar Grains toward ζ Ophiuchi: Constraining the Elemental Budget near the Diffuse-dense Cloud Transition". In: 801.2, 110, p. 110. DOI: 10.1088/0004-637X/801/2/110. arXiv: 1501.02810 [astro-ph.GA].

Prasad, S. S. and Jr. Huntress W. T. (May 1980). "A model for gas phase chemistry in interstellar clouds: I. The basic model, library of chemical reactions, and chemistry among C, N, and O compounds." In: 43, pp. 1–35. DOI: 10.1086/190665.

Prasad, S. S. and S. P. Tarafdar (Apr. 1983). "UV radiation field inside dense clouds - Its possible existence and chemical implications". In: 267, pp. 603–609. DOI: 10.1086/160896.

Qasim, D. et al. (Apr. 2020). "An experimental study of the surface formation of methane in interstellar molecular clouds". In: *Nature Astronomy* 4, pp. 781–785. DOI: 10.1038/s41550-020-1054-y. arXiv: 2004.02506 [astro-ph.SR].

Qiu, Jianjie et al. (May 2018). "Deep millimeter spectroscopy observations toward NGC 1068". In: 613, A3, A3. DOI: 10.1051/0004-6361/201731035.

Quénard, David et al. (Feb. 2018). "Chemical modelling of complex organic molecules with peptide-like bonds in star-forming regions". In: 474.2, pp. 2796–2812. DOI: 10.1093/mnras/stx2960. arXiv: 1711.05184 [astro-ph.SR].

Raut, U. and R. A. Baragiola (2011). "SOLID-STATE CO OXIDATION BY ATOMIC O: A ROUTE TO SOLID CO 2 SYNTHESIS IN DENSE MOLECULAR CLOUDS". In: *The Astrophysical Journal* 737.1, p. L14. DOI: 10.1088/2041-8205/737/1/l14. URL: https://doi.org/10.1088/2041-8205/737/1/l14.

Raut, Ujjwal et al. (2007). "Characterization of porosity in vapor-deposited amorphous solid water from methane adsorption". In: *The Journal of chemical physics* 127.20, p. 204713.

Reboussin, L. et al. (June 2014). "Grain-surface reactions in molecular clouds: the effect of cosmic rays and quantum tunnelling". In: 440.4, pp. 3557–3567. DOI: 10.1093/mnras/stu462. arXiv: 1403.5189 [astro-ph.GA].

Redaelli, E. et al. (Sept. 2019). "High-sensitivity maps of molecular ions in L1544. I. Deuteration of N_2H^+ and HCO^+ and primary evidence of N_2D^+ depletion". In: 629, A15, A15. DOI: 10.1051/0004-6361/201935314. arXiv: 1907.08217 [astro-ph.SR].

Redhead, P A (1962). "Thermal desorption of gases". In: *Vacuum* 12, pp. 203–211.

Redman, M. P. et al. (Dec. 2002). "Molecular gas freeze-out in the pre-stellar core L1689B". In: 337.3, pp. L17–L21. DOI: 10.1046/j.1365-8711.2002.06106.x. arXiv: astro-ph/0210294 [astro-ph].

Redondo, Pilar, Carmen Barrientos, and Antonio Largo (Sept. 2014). "Peptide Bond Formation through Gas-phase Reactions in the Interstellar Medium: Formamide and Acetamide as Prototypes". In: 793.1, 32, p. 32. DOI: 10.1088/0004-637X/793/1/32.

Rimola, Albert, Bartolomeo Civalleri, and Piero Ugliengo (2008). "Neutral vs zwitterionic glycine forms at the water/silica interface: structure, energies, and vibrational features from B3LYP periodic simulations". In: *Langmuir* 24.24, pp. 14027–14034.

Rimola, Albert et al. (Dec. 2014). "Combined quantum chemical and modeling study of CO hydrogenation on water ice". In: 572, A70, A70. DOI: 10.1051/0004-6361/201424046.

Rimola, Albert et al. (2014). "Combined quantum chemical and modeling study of CO hydrogenation on water ice". In: 572, A70.

Rimola, Albert et al. (July 2018a). "Can Formamide Be Formed on Interstellar Ice? An Atomistic Perspective". In: *ACS Earth and Space Chemistry, vol. 2, issue 7, pp. 720-734* 2, pp. 720–734. DOI: 10.1021/acsearthspacechem.7b00156. URL: http://adsabs.harvard.edu/abs/2018ECS.....2..720R (visited on 04/05/2019).

— (2018b). "Can formamide be formed on interstellar ice? An atomistic perspective". In: *ACS Earth Space Chem* 2.7, pp. 720–734.

Roberts, J. F. et al. (Dec. 2007). "Desorption from interstellar ices". In: 382.2, pp. 733–742. DOI: 10.1111/j.1365-2966.2007.12402.x. arXiv: 0708.3374 [astro-ph].

Roser, Joe E. et al. (July 2001). "Formation of Carbon Dioxide by Surface Reactions on Ices in the Interstellar Medium". In: 555.1, pp. L61–L64. DOI: 10.1086/321732.

Rosi, Marzio et al. (2018). "Possible scenarios for SiS formation in the interstellar medium: Electronic structure calculations of the potential energy surfaces for the reactions of the SiH radical with atomic sulphur and S-2". In: *CHEMICAL PHYSICS LETTERS* 695, 87–93. ISSN: 0009-2614. DOI: {10.1016/j.cplett.2018.01.053}.

Rowe, B.R. and J.B. Marquette (1987). "CRESU studies of ion/molecule reactions". In: *International Journal of Mass Spectrometry and Ion Processes* 80, pp. 239–254. ISSN: 0168-1176. DOI: https://doi.org/10.1016/0168-1176(87)87033-7. URL: https://www.sciencedirect.com/science/article/pii/0168117687870337.

Ruaud, M. et al. (Mar. 2015). "Modelling complex organic molecules in dense regions: Eley-Rideal and complex induced reaction". In: 447.4, pp. 4004–4017. DOI: 10.1093/mnras/stu2709. arXiv: 1412.6256 [astro-ph.SR].

Ruaud, Maxime, Valentine Wakelam, and Franck Hersant (July 2016). "Gas and grain chemical composition in cold cores as predicted by the Nautilus three-phase model". In: 459.4, pp. 3756–3767. DOI: 10.1093/mnras/stw887. arXiv: 1604.05216 [astro-ph.GA].

Rubin, R. H. et al. (Oct. 1971). "Microwave Detection of Interstellar Formamide". In: 169, p. L39. DOI: 10.1086/180810.

Ruffle, Deborah P. and Eric Herbst (Dec. 2000). "New models of interstellar gas-grain chemistry - I. Surface diffusion rates". In: 319.3, pp. 837–850. DOI: 10.1046/j.1365-8711.2000.03911.x.

— (Apr. 2001). "New models of interstellar gas-grain chemistry - II. Surface photochemistry in quiescent cores". In: 322.4, pp. 770–778. DOI: 10.1046/j.1365-8711.2001.04178.x.

Russell, Henry Norris (July 1929). "On the Composition of the Sun's Atmosphere". In: 70, p. 11. DOI: 10.1086/143197.

— (Apr. 1934). "Molecules in the Sun and Stars". In: 79, p. 317. DOI: 10.1086/143539.

Sakai, Nami and Satoshi Yamamoto (Dec. 2013). "Warm Carbon-Chain Chemistry". In: *Chemical Reviews* 113.12, pp. 8981–9015. DOI: 10.1021/cr4001308.

Sakai, Nami et al. (Aug. 2014). "A Chemical View of Protostellar-disk Formation in L1527". In: 791.2, L38, p. L38. DOI: 10.1088/2041-8205/791/2/L38.

Sandford, Scott A. and Louis J. Allamandola (Sept. 1990). "The volume- and surface-binding energies of ice systems containing CO, CO $_2$ and H $_2$O". In: 87.1, pp. 188–192. DOI: 10.1016/0019-1035(90)90028-8.

— (Nov. 1993). "Condensation and Vaporization Studies of CH 3OH and NH 3 Ices: Major Implications for Astrochemistry". In: 417, p. 815. DOI: 10.1086/173362.

Santangelo, G. et al. (Dec. 2015). "Jet multiplicity in the proto-binary system NGC 1333-IRAS4A. The detailed CALYPSO IRAM-PdBI view". In: *Astronomy and Astrophysics* 584, A126. ISSN: 0004-6361. DOI: 10.1051/0004-6361/201526323. (Visited on 03/15/2019).

Saraceno, P. et al. (May 1996). "An evolutionary diagram for young stellar objects." In: 309, pp. 827–839.

Schäfer, Ansgar, Hans Horn, and Reinhart Ahlrichs (1992). "Fully optimized contracted Gaussian basis sets for atoms Li to Kr". In: *J Chem Phys* 97.4, pp. 2571–2577.

Schilke, P. et al. (May 1997). "SiO production in interstellar shocks." In: 321, pp. 293–304.

Schilke, Peter, TG Phillips, and Ning Wang (1995). "Hydrogen chloride in OMC-1". In: 441, pp. 334–342.

Schreiner, Peter R. and H. Peter Reisenauer (2006). "The "Non-Reaction" of Ground-State Triplet Carbon Atoms with Water Revisited". In: *ChemPhysChem* 7.4, pp. 880–885. DOI: https://doi.org/10.1002/cphc.200500555. eprint: https://chemistry-europe.onlinelibrary.wiley.com/doi/pdf/10.1002/cphc.200500555. URL: https://chemistry-europe.onlinelibrary.wiley.com/doi/abs/10.1002/cphc.200500555.

Scibelli, Samantha and Yancy Shirley (Mar. 2020). "Prevalence of Complex Organic Molecules in Starless and Prestellar Cores within the Taurus Molecular Cloud". In: 891.1, 73, p. 73. DOI: 10.3847/1538-4357/ab7375. arXiv: 2002.02469 [astro-ph.GA].

Seakins, Paul W. (2007). "Product branching ratios in simple gas phase reactions". In: *Annu. Rep. Prog. Chem., Sect. C: Phys. Chem.* 103 (0), pp. 173–222. DOI: 10.1039/B605650B. URL: http://dx.doi.org/10.1039/B605650B.

Semenov, D. et al. (Nov. 2010). "Chemistry in disks. IV. Benchmarking gas-grain chemical models with surface reactions". In: 522, A42, A42. DOI: 10.1051/0004-6361/201015149. arXiv: 1007.2302 [astro-ph.GA].

Senevirathne, Bethmini et al. (Mar. 2017). "Hydrogen atom mobility, kinetic isotope effects and tunneling on interstellar ices (I_h and ASW)". In: *Molecular Astrophysics* 6, pp. 59–69. DOI: 10.1016/j.molap.2017.01.005.

Senevirathne, Bethmini et al. (2017). "Hydrogen atom mobility, kinetic isotope effects and tunneling on interstellar ices (Ih and ASW)". In: *Mol Astrophys* 6, pp. 59–69.

Sewiło, Marta et al. (Feb. 2018). "The Detection of Hot Cores and Complex Organic Molecules in the Large Magellanic Cloud". In: 853.2, L19, p. L19. DOI: 10.3847/2041-8213/aaa079. arXiv: 1801.10275 [astro-ph.GA].

Shanno, David F (1970). "Conditioning of quasi-Newton methods for function minimization". In: *Math Comput* 24.111, pp. 647–656.

Shannon, R. L. et al. (Jan. 2013). "Accelerated chemistry in the reaction between the hydroxyl radical and methanol at interstellar temperatures facilitated by tunnelling." In: *Nature Chemistry* 5. DOI: https://doi.org/10.1038/nchem.1692.

Shen, C. J. et al. (Feb. 2004). "Cosmic ray induced explosive chemical desorption in dense clouds". In: 415, pp. 203–215. DOI: 10.1051/0004-6361:20031669.

Shimonishi, Takashi et al. (2018). "Adsorption Energies of Carbon, Nitrogen, and Oxygen Atoms on the Low-temperature Amorphous Water Ice: A Systematic Estimation from Quantum Chemistry Calculations". In: 855.1, 27, p. 27. DOI: 10.3847/1538-4357/aaaa6a. arXiv: 1801.08716 [astro-ph.GA].

Shimonishi, Takashi et al. (2018). "Adsorption Energies of Carbon, Nitrogen, and Oxygen Atoms on the Low-temperature Amorphous Water Ice: A Systematic Estimation from Quantum Chemistry Calculations". In: 855.1, p. 27.

Shingledecker, Christopher N. et al. (2018). "On Cosmic-Ray-driven Grain Chemistry in Cold Core Models". In: *The Astrophysical Journal* 861.1, p. 20. DOI: 10.3847/1538-4357/aac5ee.

Shu, F. H. (Sept. 1976). "Self-Similar Collapse of Isothermal Spheres and Star Formation." In: vol. 8, p. 547.

Shull, J. M. and M. E. van Steenberg (July 1985). "Galactic interstellar abundance surveys with IUE. I. Neutral hydrogen". In: 294, pp. 599–614. DOI: 10.1086/163327.

Siebert, Mark A. et al. (Jan. 2022). "CH_3-Terminated Carbon Chains in the GOTHAM Survey of TMC-1: Evidence of Interstellar CH_3C_7N". In: 924.1, 21, p. 21. DOI: 10.3847/1538-4357/ac3238. arXiv: 2110.13152 [astro-ph.GA].

Sims, I. R. et al. (1994). "Ultralow temperature kinetics of neutral–neutral reactions. The technique and results for the reactions CN+O2 down to 13 K and CN+NH3 down to 25 K". In: *The Journal of Chemical Physics* 100.6, pp. 4229–4241. DOI: 10.1063/1.467227. eprint: https://doi.org/10.1063/1.467227. URL: https://doi.org/10.1063/1.467227.

Sipilä, O., B. Zhao, and P. Caselli (Aug. 2020). "Effect of grain size distribution and size-dependent grain heating on molecular abundances in starless and pre-stellar cores". In: 640, A94, A94. DOI: 10.1051/0004-6361/202038353. arXiv: 2006.09741 [astro-ph.GA].

Sipilä, Olli, Kedron Silsbee, and Paola Caselli (Dec. 2021). "A Revised Description of the Cosmic Ray Induced Desorption of Interstellar Ices". In: 922.2, 126, p. 126. DOI: 10.3847/1538-4357/ac23ce. arXiv: 2106.04593 [astro-ph.GA].

Skouteris, D. et al. (June 2017). "New quantum chemical computations of formamide deuteration support gas-phase formation of this prebiotic molecule". In: 468.1, pp. L1–L5. DOI: 10.1093/mnrasl/slx012. arXiv: 1701.06138 [astro-ph.SR].

Skouteris, D. et al. (June 2017). "New quantum chemical computations of formamide deuteration support gas-phase formation of this prebiotic molecule". en. In: *Monthly Notices of the Royal Astronomical Society* 468.1, p. L1. DOI: 10.1093/mnrasl/slx012. URL: https://ui.adsabs.harvard.edu/abs/2017MNRAS.468L...1S/abstract (visited on 09/30/2019).

Skouteris, Dimitrios et al. (Dec. 2015). "Dimerization of methanimine and its charged species in the atmosphere of Titan and interstellar/cometary ice analogs". In: 584, A76, A76. DOI: 10.1051/0004-6361/201526978.

Skouteris, Dimitrios et al. (Feb. 2018). "The Genealogical Tree of Ethanol: Gas-phase Formation of Glycolaldehyde, Acetic Acid, and Formic Acid". In: 854.2, 135, p. 135. DOI: 10.3847/1538-4357/aaa41e. arXiv: 1712.08938 [astro-ph.SR].

Skouteris, Dimitrios et al. (Feb. 2018a). "The Genealogical Tree of Ethanol: Gas-phase Formation of Glycolaldehyde, Acetic Acid, and Formic Acid". In: *The Astrophysical Journal* 854, p. 135. ISSN: 0004-637X. DOI: 10.3847/1538-4357/aaa41e. URL: http://adsabs.harvard.edu/abs/2018ApJ...854..135S (visited on 03/31/2019).

— (2018b). "The genealogical tree of ethanol: Gas-phase formation of glycolaldehyde, acetic acid, and formic acid". In: 854.2, p. 135.

Skouteris, Dimitrios et al. (Jan. 2019). "Interstellar dimethyl ether gas-phase formation: a quantum chemistry and kinetics study". In: 482.3, pp. 3567–3575. DOI: 10.1093/mnras/sty2903. arXiv: 1810.10407 [astro-ph.GA].

Smith, Ian W. M. (Sept. 2011). "Laboratory Astrochemistry: Gas-Phase Processes". In: 49.1, pp. 29–66. DOI: 10.1146/annurev-astro-081710-102533.

Smith, K. W. et al. (Dec. 2000). "NGC 1333/IRAS 4: a multiple star formation laboratory". In: *Monthly Notices of the Royal Astronomical Society* 319, pp. 991–1000. ISSN: 0035-8711. DOI: 10.1046/j.1365-8711.2000.03564.x. URL: http://adsabs.harvard.edu/abs/2000MNRAS.319..991S (visited on 03/26/2019).

Smith, R. Scott et al. (1997). "The Molecular Volcano: Abrupt CCl_4 Desorption Driven by the Crystallization of Amorphous Solid Water". In: *Phys. Rev. Lett.* 79 (5), pp. 909–912. DOI: 10.1103/PhysRevLett.79.909. URL: https://link.aps.org/doi/10.1103/PhysRevLett.79.909.

Smith, R. Scott et al. (June 2011). "Crystallization Kinetics and Excess Free Energy of H2O and D2O Nanoscale Films of Amorphous Solid Water". In: *Journal of Physical Chemistry A* 115.23, pp. 5908–5917. DOI: 10.1021/jp110297q.

Smith, R Scott, R Alan May, and Bruce D Kay (2016). "Desorption kinetics of Ar, Kr, Xe, N2, O2, CO, methane, ethane, and propane from graphene and amorphous solid water surfaces". In: *The Journal of Physical Chemistry B* 120.8, pp. 1979–1987.

Smith, Robert G., K. Sellgren, and Alan T. Tokunaga (Sept. 1989). "Absorption Features in the 3 Micron Spectra of Protostars". In: 344, p. 413. DOI: 10.1086/167809.

Snell, R. L. et al. (Aug. 2000). "Water Abundance in Molecular Cloud Cores". In: 539.2, pp. L101–L105. DOI: 10.1086/312848. arXiv: astro-ph/0010393 [astro-ph].

Song, Lei and Johannes Kästner (Dec. 2017). "Tunneling Rate Constants for H_2CO+H on Amorphous Solid Water Surfaces". In: 850.2, 118, p. 118. DOI: 10.3847/1538-4357/aa943e. arXiv: 2009.05442 [astro-ph.GA].

Song, Lei and Johannes Kästner (2017). "Tunneling Rate Constants for H2COH on Amorphous Solid Water Surfaces". In: 850.2, p. 118. DOI: 10.3847/1538-4357/aa943e.

Sorrell, Wilfred H (2001). "Origin of amino acids and organic sugars in interstellar clouds". In: 555.2, p. L129.

Spaans, Marco and Joseph Silk (Dec. 2006). "Pregalactic Black Hole Formation with an Atomic Hydrogen Equation of State". In: 652.2, pp. 902–906. DOI: 10.1086/508444. arXiv: astro-ph/0601714 [astro-ph].

Spezzano, S. et al. (Jan. 2022). "Gas phase Elemental abundances in Molecular cloudS (GEMS) V. Methanol in Taurus". In: 657, A10, A10. DOI: 10.1051/0004-6361/202141971. arXiv: 2110.01675 [astro-ph.GA].

Strom, K. M., S. E. Strom, and F. J. Vrba (May 1976). "Infrared surveys of dark-cloud complexes. IV. The Lynds 1517 and Lynds 1551 clouds." In: 81, pp. 320–322. DOI: 10.1086/111891.

Strong, Andrew W., Igor V. Moskalenko, and Vladimir S. Ptuskin (Nov. 2007). "Cosmic-Ray Propagation and Interactions in the Galaxy". In: *Annual Review of Nuclear and Particle Science* 57.1, pp. 285–327. DOI: 10.1146/annurev.nucl.57.090506.123011. arXiv: astro-ph/0701517 [astro-ph].

Su, Timothy and Walter J. Chesnavich (1982). "Parametrization of the ion–polar molecule collision rate constant by trajectory calculations". In: *The Journal of Chemical Physics* 76.10, pp. 5183–5185. DOI: 10.1063/1.442828. eprint: https://doi.org/10.1063/1.442828. URL: https://doi.org/10.1063/1.442828.

Sure, Rebecca and Stefan Grimme (2013). "Corrected small basis set Hartree-Fock method for large systems". In: *J Comput Chem* 34.19, pp. 1672–1685.

Svanberg, M, J B C Pettersson, and Bolton K (2000). "missing". In: *The Journal of Physical Chemistry A* 104, p. 5787.

Swings, P. and L. Rosenfeld (Nov. 1937). "Considerations Regarding Interstellar Molecules". In: 86, pp. 483–486. DOI: 10.1086/143880.

Swings, Polydore and Léon Rosenfeld (1937). "Considerations regarding interstellar molecules". In: 86, pp. 483–486.

Tafalla, M. et al. (Sept. 1998). "L1544: A Starless Dense Core with Extended Inward Motions". In: 504.2, pp. 900–914. DOI: 10.1086/306115.

Tafalla, M. et al. (Mar. 2004a). "On the internal structure of starless cores. I. Physical conditions and the distribution of CO, CS, N_2H^+, and NH_3 in L1498 and L1517B". In: 416, pp. 191–212. DOI: 10.1051/0004-6361:20031704.

— (Aug. 2004b). "On The Internal Structure Of Starless Cores. Physical and Chemical Properties of L1498 and L1517B". In: 292.1, pp. 347–354. DOI: 10.1023/B:ASTR.0000045036.76044.bd. arXiv: astro-ph/0401148 [astro-ph].

Takahashi, Junko and David A. Williams (May 2000). "Chemically driven desorption of CO from icy grains in dark clouds". In: 314.2, pp. 273–278. DOI: 10.1046/j.1365-8711.2000.03291.x.

Talbi, D., G. S. Chandler, and A. L. Rohl (Jan. 2006). "The interstellar gas-phase formation of CO_2 - Assisted or not by water molecules?" In: *Chemical Physics* 320.2-3, pp. 214–228. DOI: 10.1016/j.chemphys.2005.07.033.

Taquet, V., C. Ceccarelli, and C. Kahane (Feb. 2012a). "20120201Multilayer modeling of porous grain surface chemistry. I. The GRAINOBLE model". en. In: *Astronomy and Astrophysics* 538, A42. DOI: 10.1051/0004-6361/201117802. URL: https://ui.adsabs.harvard.edu/abs/2012A%26A...538A..42T/abstract.

— (Mar. 2012b). "Formaldehyde and Methanol Deuteration in Protostars: Fossils from a Past Fast High-density Pre-collapse Phase". en. In: *The Astrophysical Journal* 748.1, p. L3. DOI: 10.1088/2041-8205/748/1/L3. URL: https://ui.adsabs.harvard.edu/abs/2012ApJ...748L...3T/abstract (visited on 07/24/2019).

Taquet, V., C. Ceccarelli, and C. Kahane (Feb. 2012). "Multilayer modeling of porous grain surface chemistry. I. The GRAINOBLE model". In: 538, A42, A42. DOI: 10.1051/0004-6361/201117802. arXiv: 1111.4165 [astro-ph.GA].

Taquet, V. et al. (Feb. 2013). "Water ice deuteration: a tracer of the chemical history of protostars". In: 550, A127, A127. DOI: 10.1051/0004-6361/201220084. arXiv: 1211.0514 [astro-ph.GA].

Taquet, V. et al. (Oct. 2019). "Seeds of Life in Space (SOLIS) VI. Chemical evolution of sulfuretted species along the outflows driven by the low-mass protostellar binary NGC1333-IRAS4A". In: *Astronomy & Astrophysics* submitted.

Taquet, Vianney, Steven B. Charnley, and Olli Sipilä (Aug. 2014). "Multilayer Formation and Evaporation of Deuterated Ices in Prestellar and Protostellar Cores". In: 791.1, 1, p. 1. DOI: 10.1088/0004-637X/791/1/1. arXiv: 1405.3268 [astro-ph.GA].

Taquet, Vianney et al. (May 2015). "Constraining the Abundances of Complex Organics in the Inner Regions of Solar-type Protostars". In: *The Astrophysical Journal* 804, p. 81. ISSN: 0004-637X. DOI: 10.1088/0004-637X/804/2/81. URL: http://adsabs.harvard.edu/abs/2015ApJ...804...81T (visited on 03/26/2019).

Taquet, Vianney, Eva S. Wirström, and Steven B. Charnley (Apr. 2016). "Formation and Recondensation of Complex Organic Molecules during Protostellar Luminosity Outbursts". In: 821.1, 46, p. 46. DOI: 10.3847/0004-637X/821/1/46. arXiv: 1602.05364 [astro-ph.GA].

Tasker, Elizabeth J. and Jonathan C. Tan (July 2009). "Star Formation in Disk Galaxies. I. Formation and Evolution of Giant Molecular Clouds via Gravitational Instability and Cloud Collisions". In: 700.1, pp. 358–375. DOI: 10.1088/0004-637X/700/1/358. arXiv: 0811.0207 [astro-ph].

Tasker, PW (1979). "The stability of ionic crystal surfaces". In: *Journal of Physics C: Solid State Physics* 12.22, p. 4977.

Tatewaki, Hiroshi and Sigeru Huzinaga (1980). "A systematic preparation of new contracted Gaussian-type orbital sets. III. Second-row atoms from Li through ne". In: *J Comput Chem* 1.3, pp. 205–228.

Tenorio-Tagle, Guillermo and Peter Bodenheimer (Jan. 1988). "Large-scale expanding superstructures in galaxies." In: 26, pp. 145–197. DOI: 10.1146/annurev.aa.26.090188.001045.

Tentscher, Peter R and J Samuel Arey (2013). "Binding in radical-solvent binary complexes: Benchmark energies and performance of approximate methods". In: *JCTC* 9.3, pp. 1568–1579.

Terada, Hiroshi and Alan T. Tokunaga (2012). "DISCOVERY OF CRYSTALLIZED WATER ICE IN A SILHOUETTE DISK IN THE M43 REGION". In: 753.1, p. 19. DOI: 10.1088/0004-637x/753/1/19.

The ISO Handbook Volume II: CAM - The ISO Camera (v 2.0) (Nov. 2003). Vol. 1262. ESA Special Publication.

Tielens, A. G. G. M. (2005). *The Physics and Chemistry of the Interstellar Medium*. Cambridge University Press. DOI: 10.1017/CBO9780511819056.

Tielens, A. G. G. M. (2010). *The Physics and Chemistry of the Interstellar Medium*.

Tielens, A. G. G. M. (2021). *Molecular Astrophysics*. Cambridge University Press. DOI: 10.1017/9781316718490.

Tielens, A. G. G. M. and L. J. Allamandola (1987). "Composition, Structure, and Chemistry of Interstellar Dust". In: *Interstellar Processes*. Ed. by David J. Hollenbach and Jr. Thronson Harley A. Vol. 134, p. 397. DOI: 10.1007/978-94-009-3861-8_16.

Tielens, A. G. G. M. and W. Hagen (Oct. 1982a). "Model calculations of the molecular composition of interstellar grain mantles". en. In: *Astronomy and Astrophysics* 114.2, p. 245. (Visited on 07/22/2019).

— (Oct. 1982b). "Model calculations of the molecular composition of interstellar grain mantles". en. In: *Astronomy and Astrophysics* 114.2, p. 245. URL: https://ui.adsabs.harvard.edu/abs/1982A%26A...114..245T/abstract (visited on 07/22/2019).

Tielens, A. G. G. M. and D. Hollenbach (Apr. 1985). "Photodissociation regions. II. A model for the Orion photodissociation region." In: 291, pp. 747–754. DOI: 10.1086/163112.

Tielens, A. G. G. M., W. Hagen, and J. M. Greenberg (Jan. 1983). "Interstellar ice." In: *Journal of Physical Chemistry* 87.21, pp. 4220–4229.

Tinacci, Lorenzo et al. (July 2021). "Structures and Properties of Known and Postulated Interstellar Cations". In: *arXiv e-prints*, arXiv:2107.11122, arXiv:2107.11122. arXiv: 2107.11122 [astro-ph.GA].

Tobin, J. and Vandam Orion Team (Jan. 2020). "The Distribution of Protostellar Disk Masses in the Orion Molecular Clouds". In: *American Astronomical Society Meeting Abstracts*. American Astronomical Society Meeting Abstracts, p. 328.04.

Tobin, John J. et al. (Feb. 2016). "The VLA Nascent Disk and Multiplicity Survey of Perseus Protostars (VANDAM). II. Multiplicity of Protostars in the Perseus Molecular Cloud". In: 818.1, 73, p. 73. DOI: 10.3847/0004-637X/818/1/73. arXiv: 1601.00692 [astro-ph.SR].

Tosoni, S et al. (2005). "Quantum mechanical calculation of the OH vibrational frequency in crystalline solids". In: *Mol Phys* 103.18, pp. 2549–2558.

Turner, B. E. (Oct. 1990). "Detection of Doubly Deuterated Interstellar Formaldehyde (D 2CO): an Indicator of Active Grain Surface Chemistry". en. In: *The Astrophysical Journal* 362, p. L29. ISSN: 0004-637X. DOI: 10.1086/185840. URL: https://ui.adsabs.harvard.edu/abs/1990ApJ...362L..29T/abstract (visited on 10/04/2019).

Ugliengo, Piero and A Damin (2002). "Are dispersive forces relevant for CO adsorption on the MgO (0 0 1) surface?" In: *Chem Phys Lett* 366.5-6, pp. 683–690.

Urso, R. G. et al. (Oct. 2016). "Combined infrared and Raman study of solid CO". In: 594, A80, A80. DOI: 10.1051/0004-6361/201629030.

Urso, R. G. et al. (Aug. 2019). "C_2O and C_3O in low-mass star-forming regions". In: 628, A72, A72. DOI: 10.1051/0004-6361/201834322.

van Dishoeck, E. F. et al. (Apr. 2021). "Water in star-forming regions: physics and chemistry from clouds to disks as probed by Herschel spectroscopy". In: 648, A24, A24. DOI: 10.1051/0004-6361/202039084. arXiv: 2102.02225 [astro-ph.GA].

van Dishoeck, Ewine F. and Geoffrey A. Blake (Jan. 1998). "Chemical Evolution of Star-Forming Regions". In: 36, pp. 317–368. DOI: 10.1146/annurev.astro.36.1.317.

van Dishoeck, Ewine F. et al. (July 1995). "Molecular Abundances and Low-Mass Star Formation. II. Organic and Deuterated Species toward IRAS 16293-2422". In: 447, p. 760. DOI: 10.1086/175915.

van Steenberg, Michael E. and J. Michael Shull (June 1988a). "Galactic Interstellar Abundance Surveys with IUE. II. The Equivalent Widths and Column Densities". In: 67, p. 225. DOI: 10.1086/191272.

— (July 1988b). "Galactic Interstellar Abundance Surveys with IUE. III. Silicon, Manganese, Iron, Sulfur, and Zinc". In: 330, p. 942. DOI: 10.1086/166525.

— (May 1989). "Galactic Interstellar Abundance Surveys with IUE. III. Silicon, Manganese, Iron, Sulfur, and Zinc: Erratum". In: 340, p. 624. DOI: 10.1086/167424.

Vandenbussche, B. et al. (June 1999). "Constraints on the abundance of solid O_2 in dense clouds from ISO-SWS and ground-based observations". In: 346, pp. L57–L60.

Vastel, C. et al. (May 2000). "Large [O]/[CO] ratios in cold molecular clouds towards W 49N". In: 357, pp. 994–1000.

Vastel, C. et al. (Dec. 2002). "Infrared Space Observatory Long Wavelength Spectrometer Observations of C^+ and O^0 Lines in Absorption toward Sagittarius B2". In: 581.1, pp. 315–324. DOI: 10.1086/344136. arXiv: astro-ph/0208193 [astro-ph].

Vastel, C. et al. (Nov. 2014). "The Origin of Complex Organic Molecules in Prestellar Cores". In: *The Astrophysical Journal Letters* 795, p. L2. ISSN: 0004-637X. DOI: 10.1088/2041-8205/795/1/L2. URL: http://adsabs.harvard.edu/abs/2014ApJ...795L...2V (visited on 04/21/2019).

Vasyunin, A. I. and Eric Herbst (Jan. 2013). "A Unified Monte Carlo Treatment of Gas-Grain Chemistry for Large Reaction Networks. II. A Multiphase Gas-surface-layered Bulk Model". In: 762.2, 86, p. 86. DOI: 10.1088/0004-637X/762/2/86. arXiv: 1211.3025 [astro-ph.GA].

Vasyunin, A. I. and Eric Herbst (May 2013). "REACTIVE DESORPTION AND RADIATIVE ASSOCIATION AS POSSIBLE DRIVERS OF COMPLEX MOLECULE FORMATION IN THE COLD INTERSLAR MEDIUM". en. In: *The Astrophysical Journal* 769.1, p. 34. ISSN: 0004-637X. DOI: 10.1088/0004-637X/769/1/34. (Visited on 07/22/2019).

Vasyunin, A. I. et al. (Feb. 2009). "A Unified Monte Carlo Treatment of Gas-Grain Chemistry for Large Reaction Networks. I. Testing Validity of Rate Equations in Molecular Clouds". In: 691.2, pp. 1459–1469. DOI: 10.1088/0004-637X/691/2/1459. arXiv: 0810.1591 [astro-ph].

Vasyunin, A. I. et al. (June 2017). "Formation of Complex Molecules in Prestellar Cores: A Multilayer Approach". In: 842.1, 33, p. 33. DOI: 10.3847/1538-4357/aa72ec. arXiv: 1705.04747 [astro-ph.GA].

Vasyunin, A. I. et al. (June 2017). "Formation of Complex Molecules in Prestellar Cores: A Multilayer Approach". en. In: *The Astrophysical Journal* 842.1, p. 33. DOI: 10.3847/1538-4357/aa72ec. URL: https://ui.adsabs.harvard.edu/abs/2017ApJ...842...33V/abstract (visited on 10/16/2019).

Vaupré, S. et al. (Aug. 2014). "Cosmic ray induced ionisation of a molecular cloud shocked by the W28 supernova remnant". In: 568, A50, A50. DOI: 10.1051/0004-6361/201424036. arXiv: 1407.0205 [astro-ph.GA].

Vazart, Fanny et al. (2016). "State-of-the-Art Thermochemical and Kinetic Computations for Astrochemical Complex Organic Molecules: Formamide Formation in Cold Interstellar Clouds as a Case Study". In: *JOURNAL OF CHEMICAL THEORY AND COMPUTATION* 12.11, 5385–5397. ISSN: 1549-9618. DOI: {10.1021/acs.jctc.6b00379}.

Vazart, Fanny et al. (Dec. 2020). "Gas-phase formation of acetaldehyde: review and new theoretical computations". In: 499.4, pp. 5547–5561. DOI: 10.1093/mnras/staa3060. arXiv: 2010.02718 [astro-ph.GA].

Vázquez-Semadeni, Enrique et al. (Dec. 2019). "Global hierarchical collapse in molecular clouds. Towards a comprehensive scenario". In: 490.3, pp. 3061–3097. DOI: 10.1093/mnras/stz2736. arXiv: 1903.11247 [astro-ph.GA].

Veeraghattam, Vijay K. et al. (July 2014). "The Sticking of Atomic Hydrogen on Amorphous Water Ice". In: 790.1, 4, p. 4. DOI: 10.1088/0004-637X/790/1/4.

Vidali, Gianfranco (Dec. 2013). "H2 Formation on Interstellar Grains". In: *Chemical Reviews* 113.12, pp. 8752–8782. DOI: 10.1021/cr400156b.

Vigren, E. et al. (2013). "Collision-induced dissociation of similar to 2-MeV O-3(+) and N-3(+) ions". In: *PHYSICAL REVIEW A* 87.5. ISSN: 1050-2947. DOI: {10.1103/PhysRevA.87.052707}.

Visser, R., E. F. van Dishoeck, and J. H. Black (Aug. 2009). "The photodissociation and chemistry of CO isotopologues: applications to interstellar clouds and circumstellar disks". In: 503.2, pp. 323–343. DOI: 10.1051/0004-6361/200912129. arXiv: 0906.3699 [astro-ph.GA].

Viti, S. et al. (May 2001a). "Chemical signatures of shocks in hot cores". In: 370, pp. 1017–1025. DOI: 10.1051/0004-6361:20010300.

Viti, S. et al. (May 2001b). "Interstellar oxygen chemistry". In: 370, pp. 557–569. DOI: 10.1051/0004-6361:20010246.

Viti, Serena and David A. Williams (May 1999). "Time-dependent evaporation of icy mantles in hot cores". In: 305.4, pp. 755–762. DOI: 10.1046/j.1365-8711.1999.02447.x.

Viti, Serena et al. (Nov. 2004). "Evaporation of ices near massive stars: models based on laboratory temperature programmed desorption data". In: 354.4, pp. 1141–1145. DOI: 10.1111/j.1365-2966.2004.08273.x. arXiv: astro-ph/0406054 [astro-ph].

Wakelam, V. et al. (Dec. 2006a). "Chemical sensitivity to the ratio of the cosmic-ray ionization rates of He and H_2 in dense clouds". In: 459.3, pp. 813–820. DOI: 10.1051/0004-6361:20065472. arXiv: astro-ph/0608551 [astro-ph].

Wakelam, V., E. Herbst, and F. Selsis (May 2006b). "The effect of uncertainties on chemical models of dark clouds". In: 451.2, pp. 551–562. DOI: 10.1051/0004-6361:20054682. arXiv: astro-ph/0601611 [astro-ph].

Wakelam, V. et al. (July 2010a). "Sensitivity analyses of dense cloud chemical models". In: 517, A21, A21. DOI: 10.1051/0004-6361/200913856. arXiv: 1004.1902 [astro-ph.GA].

— (July 2010b). "Sensitivity analyses of dense cloud chemical models". In: 517, A21, A21. DOI: 10.1051/0004-6361/200913856. arXiv: 1004.1902 [astro-ph.GA].

Wakelam, V. et al. (Mar. 2012). "A KInetic Database for Astrochemistry (KIDA)". In: 199.1, 21, p. 21. DOI: 10.1088/0067-0049/199/1/21. arXiv: 1201.5887 [astro-ph.GA].

Wakelam, V. et al. (Apr. 2015). "The 2014 KIDA Network for Interstellar Chemistry". In: 217.2, 20, p. 20. DOI: 10.1088/0067-0049/217/2/20. arXiv: 1503.01594 [astro-ph.GA].

Wakelam, V. et al. (Mar. 2017). "Binding energies: New values and impact on the efficiency of chemical desorption". In: *Molecular Astrophysics* 6, pp. 22–35. DOI: 10.1016/j.molap.2017.01.002. arXiv: 1701.06492 [astro-ph.GA].

Wakelam, V. et al. (Aug. 2021). "Efficiency of non-thermal desorptions in cold-core conditions. Testing the sputtering of grain mantles induced by cosmic rays". In: 652, A63, A63. DOI: 10.1051/0004-6361/202039855. arXiv: 2106.08621 [astro-ph.GA].

Wakelam, Valentine et al. (2015). "The 2014 KIDA network for interstellar chemistry". In: 217.2, p. 20.

Wakelam, Valentine et al. (2017). "Binding energies: new values and impact on the efficiency of chemical desorption". In: *Mol Astrophys* 6, pp. 22–35.

Wakelam, Valentine et al. (Dec. 2017). "H_2 formation on interstellar dust grains: The viewpoints of theory, experiments, models and observations". In: *Molecular Astrophysics* 9, pp. 1–36. DOI: 10.1016/j.molap.2017.11.001. arXiv: 1711.10568 [astro-ph.GA].

Walch, S. K. et al. (Nov. 2012). "Dispersal of molecular clouds by ionizing radiation". In: 427.1, pp. 625–636. DOI: 10.1111/j.1365-2966.2012.21767.x. arXiv: 1206.6492 [astro-ph.GA].

Walmsley, C. M., D. R. Flower, and G. Pineau des Forêts (May 2004). "Complete depletion in prestellar cores". In: 418, pp. 1035–1043. DOI: 10.1051/0004-6361:20035718. arXiv: astro-ph/0402493 [astro-ph].

Ward, Michael D, Isobel A Hogg, and Stephen D Price (2012). "Thermal reactions of oxygen atoms with CS2 at low temperatures on interstellar dust". In: *Monthly Notices of the Royal Astronomical Society* 425.2, pp. 1264–1269.

Ward-Thompson, D. et al. (May 1994). "A Submillimetre Continuum Survey of Pre Protostellar Cores". In: 268, p. 276. DOI: 10.1093/mnras/268.1.276.

Watanabe, Naoki and Akira Kouchi (June 2002). "Efficient Formation of Formaldehyde and Methanol by the Addition of Hydrogen Atoms to CO in H_2O-CO Ice at 10 K". In: 571.2, pp. L173–L176. DOI: 10.1086/341412.

Watanabe, Naoki and Akira Kouchi (2002a). "Efficient formation of formaldehyde and methanol by the addition of hydrogen atoms to CO in H2O-CO ice at 10 K". In: 571.2, p. L173.

— (June 2002b). "Efficient Formation of Formaldehyde and Methanol by the Addition of Hydrogen Atoms to CO in H₂O-CO Ice at 10 K". en. In: *The Astrophysical Journal* 571, p. L173. DOI: 10.1086/341412. URL: https://ui.adsabs.harvard.edu/2002ApJ...571L.173W/abstract (visited on 09/30/2019).

Watanabe, Naoki and Akira Kouchi (2008a). "Ice surface reactions: A key to chemical evolution in space". In: *Progress in Surface Science* 83.10, pp. 439–489. ISSN: 0079-6816. DOI: https://doi.org/10.1016/j.progsurf.2008.10.001. URL: https://www.sciencedirect.com/science/article/pii/S0079681608000476.

Watanabe, Naoki and Akira Kouchi (2008b). "Ice surface reactions: A key to chemical evolution in space". In: *Prog Surf Sci* 83.10-12, pp. 439–489.

Watanabe, Naoki et al. (May 2010). "Direct Measurements of Hydrogen Atom Diffusion and the Spin Temperature of Nascent H_2 Molecule on Amorphous Solid Water". In: 714.2, pp. L233–L237. DOI: 10.1088/2041-8205/714/2/L233.

Watson, W. D. and E. E. Salpeter (June 1972). "Molecule Formation on Interstellar Grains". In: 174, p. 321. DOI: 10.1086/151492.

Weingartner, J. C. and B. T. Draine (Dec. 2001a). "Electron-Ion Recombination on Grains and Polycyclic Aromatic Hydrocarbons". In: *American Astronomical Society Meeting Abstracts*. Vol. 199. American Astronomical Society Meeting Abstracts, p. 11.07.

Weingartner, Joseph C. and B. T. Draine (June 2001b). "Photoelectric Emission from Interstellar Dust: Grain Charging and Gas Heating". In: 134.2, pp. 263–281. DOI: 10.1086/320852. arXiv: astro-ph/9907251 [astro-ph].

Weinreb, S. et al. (Nov. 1963). "Radio Observations of OH in the Interstellar Medium". In: 200.4909, pp. 829–831. DOI: 10.1038/200829a0.

Werner, Michael (Nov. 2009). "Spitzer's Cold Look at Space". In: *American Scientist* 97.6, pp. 458–467.

— (Jan. 2012). "The Spitzer Space Telescope". In: *Optical Engineering* 51.1, 011008-011008-8, pp. 011008–011008–8. DOI: 10.1117/1.OE.51.1.011008.

Westley, M. S. et al. (Feb. 1995). "Photodesorption from low-temperature water ice in interstellar and circumsolar grains". In: 373.6513, pp. 405–407. DOI: 10.1038/373405a0.

Whittet, D. C. B. (Feb. 2010). "Oxygen Depletion in the Interstellar Medium: Implications for Grain Models and the Distribution of Elemental Oxygen". In: 710.2, pp. 1009–1016. DOI: 10.1088/0004-637X/710/2/1009. arXiv: 0912.3298 [astro-ph.GA].

Whittet, D. C. B. et al. (Feb. 2001). "Interstellar Extinction and Polarization in the Taurus Dark Clouds: The Optical Properties of Dust near the Diffuse/Dense Cloud Interface". In: 547.2, pp. 872–884. DOI: 10.1086/318421.

Whittet, D. C. B. et al. (Jan. 2007). "The Abundance of Carbon Dioxide Ice in the Quiescent Intracloud Medium". In: 655.1, pp. 332–341. DOI: 10.1086/509772.

Williams, David A. (Mar. 1968). "Physical Adsorption Processes on Interstellar Graphite Grains". In: 151, p. 935. DOI: 10.1086/149494.

Williams, Jonathan P. et al. (Aug. 1998). "The Ionization Fraction in Dense Molecular Gas. I. Low-Mass Cores". In: 503.2, pp. 689–699. DOI: 10.1086/306034.

Wilson, R. W., K. B. Jefferts, and A. A. Penzias (July 1970). "Carbon Monoxide in the Orion Nebula". In: 161, p. L43. DOI: 10.1086/180567.

Wirström, Eva S. et al. (Oct. 2016). "A Search for O_2 in CO-depleted Molecular Cloud Cores with Herschel". In: 830.2, 102, p. 102. DOI: 10.3847/0004-637X/830/2/102. arXiv: 1608.02714 [astro-ph.GA].

Wolfire, Mark G. et al. (Apr. 2003). "Neutral Atomic Phases of the Interstellar Medium in the Galaxy". In: 587.1, pp. 278–311. DOI: 10.1086/368016. arXiv: astro-ph/0207098 [astro-ph].

Woltjer, L. (Jan. 1972). "Supernova Remnants". In: 10, p. 129. DOI: 10.1146/annurev.aa.10.090172.001021.

Woon, David E. (Dec. 1999). "Ab Initio Quantum Chemical Studies of Reactions in Astrophysical Ices. 1. Aminolysis, Hydrolysis, and Polymerization in $H_2CO/NH_3/H_2O$ Ices". In: 142.2, pp. 550–556. DOI: 10.1006/icar.1999.6227.

— (Jan. 2001a). "Ab Initio Quantum Chemical Studies of Reactions in Astrophysical Ices. 2. Reactions in $H_2CO/HCN/HNC/H_2O$ Ices". In: 149.1, pp. 277–284. DOI: 10.1006/icar.2000.6524.

— (Oct. 2001b). "Ab Initio Quantum Chemical Studies of Reactions in Astrophysical Ices 3. Reactions of HOCH2NH2Formed in H2CO/NH3/H2O Ices". In: *Journal of Physical Chemistry A* 105.41, pp. 9478–9481. DOI: 10.1021/jp011830h.

Xu, Li-Hong et al. (2008). "Torsion–rotation global analysis of the first three torsional states (νt= 0, 1, 2) and terahertz database for methanol". In: *Journal of Molecular Spectroscopy* 251.1-2, pp. 305–313.

Yamamoto, Satoshi (2017). *Introduction to Astrochemistry*. DOI: 10.1007/978-4-431-54171-4.

Yu, HG, JT Muckerman, and TJ Sears (2001). "A theoretical study of the potential energy surface for the reaction OH+CO -> H+CO2". In: *CHEMICAL PHYSICS LETTERS* 349.5-6, 547–554. ISSN: 0009-2614. DOI: {10.1016/S0009-2614(01)01238-6}.

Zamirri, Lorenzo et al. (2017). "Forsterite surfaces as models of interstellar core dust grains: computational study of carbon monoxide adsorption". In: *ACS Earth Space Chem* 1.7, pp. 384–398.

Zamirri, Lorenzo et al. (2018). "IR spectral fingerprint of carbon monoxide in interstellar water–ice models". In: *MNRAS* 480.2, pp. 1427–1444.

Zamirri, Lorenzo, Stefano Pantaleone, and Piero Ugliengo (2019). "Carbon monoxide adsorption at forsterite surfaces as models of interstellar dust grains: An unexpected bathochromic (red) shift of the CO stretching frequency". In: *J Chem Phys* 150.6, p. 064702.

Zamirri, Lorenzo et al. (Aug. 2019). "Quantum Mechanical Investigations on the Formation of Complex Organic Molecules on Interstellar Ice Mantles. Review and Perspectives". In: *ACS Earth and Space Chemistry* 3.8, pp. 1499–1523. DOI: 10.1021/acsearthspacechem.9b00082.

Zamirri, Lorenzo et al. (2019). "Quantum Mechanical Investigations on the Formation of Complex Organic Molecules on Interstellar Ice Mantles. Review and Perspectives". In: *ACS Earth Space Chem* 3.8, pp. 1499–1523.

Zamora-Avilés, Manuel and Enrique Vázquez-Semadeni (Oct. 2014). "An Evolutionary Model for Collapsing Molecular Clouds and their Star Formation Activity. II. Mass Dependence of the Star Formation Rate". In: 793.2, 84, p. 84. DOI: 10.1088/0004-637X/793/2/84. arXiv: 1308.4918 [astro-ph.SR].

Zaverkin, Viktor, Germán Molpeceres, and Johannes Kästner (Dec. 2021). "Neural-Network Assisted Study of Nitrogen Atom Dynamics on Amorphous Solid Water – II. Diffusion". In: *arXiv e-prints*, arXiv:2112.05412, arXiv:2112.05412. arXiv: 2112.05412 [astro-ph.GA].

Zhao, Yan and Donald G Truhlar (2008a). "Exploring the limit of accuracy of the global hybrid meta density functional for main-group thermochemistry, kinetics, and noncovalent interactions". In: *Journal of Chemical Theory and Computation* 4.11, pp. 1849–1868.

— (2008b). "The M06 suite of density functionals for main group thermochemistry, thermochemical kinetics, noncovalent interactions, excited states, and transition elements: two new functionals and systematic testing of four M06-class functionals and 12 other functionals". In: *Theor Chem Acc* 120.1-3, pp. 215–241.

Zicovich-Wilson, CM et al. (2004). "Calculation of the vibration frequencies of α-quartz: The effect of Hamiltonian and basis set". In: *J Comput Chem* 25.15, pp. 1873–1881.

Zucker, Catherine et al. (Dec. 2018). "Mapping Distances across the Perseus Molecular Cloud Using CO Observations, Stellar Photometry, and Gaia DR2 Parallax Measurements". In: *The Astrophysical Journal* 869, p. 83. ISSN: 0004-637X. DOI: 10.3847/1538-4357/aae97c. URL: http://adsabs.harvard.edu/abs/2018ApJ...869...83Z (visited on 03/26/2019).

Öberg, Karin I. et al. (Oct. 2011). "Complex Molecules toward Low-mass Protostars: The Serpens Core". In: *The Astrophysical Journal* 740, p. 14. ISSN: 0004-637X. DOI: 10.1088/0004-637X/740/1/14. URL: http://adsabs.harvard.edu/abs/2011ApJ...740...14O (visited on 02/12/2020).

Appendix A

Benchmarking Grainoble+ with the previous version, Grainoble

In this section, I describe the benchmarking of the code with the results described in the Ceccarelli et al. (2018) study. They employed the previous version of Grainoble (Taquet et al., 2012; Taquet et al., 2014; Taquet et al., 2016) to model the chemical evolution of a molecular cloud in galaxies with different redshifts z, that is entirely shielded from external radiation. This section benchmarks their model at 10 K at redshift $z = 0$, namely a typical molecular cloud in the Milky Way.

The comparison shows that Grainoble+ can reproduce the results from Grainoble, which was used in Ceccarelli et al. (2018), with a very good agreement. I calculated the fractional difference

$$\delta_i = \frac{|n_i^{\rm g} - n_i^{\rm g+}|}{n_i^{\rm g}} \, , \tag{A.1}$$

where $n_i^{\rm g}$ and $n_i^{\rm g+}$ are the abundances in Grainoble and Grainoble+, as a function of time. The average fractional difference in percentage for the 10 most abundant species is within $\sim 2\%$, ~ 5 % for the 30, and $\sim 25\%$ for the 60 most abundant species in the two models.

A.1 The model description

The physical parameters used in the benchmarking are listed in Tab. A.1. The initial elemental abundances of the reference case is listed in Tab. A.2 and the binding energies are listed in Tab. A.5 (Ceccarelli et al., 2018; Taquet et al., 2012; Taquet et al., 2014). The rest of the assumptions in Ceccarelli et al. (2018) are as follows. The three-phase model (Hasegawa and Herbst,

TABLE A.1: Physical parameters used in Ceccarelli et al. (2018).

parameters	value
time [year]	1(7)
density $n_{\rm H}$ [cm^{-3}]	2(4)
extinction [mag]	20.0
$T_{\rm gas}$ [K]	10.
$T_{\rm dust}$ [K]	10.
$\zeta_{\rm H_2}$ [s^{-1}]	1(-17)
G_0 [-]	1

The H_2 CR ionization rate is denoted by $\zeta_{\rm H_2}$ and G_0 is the interstellar radiation field in Habing units (Habing, 1968).

TABLE A.2: Elemental abundances used in the reference case in Ceccarelli et al. (2018).

element	gas phase abundances $\left(\frac{n_X}{n_H}\right)$
H_2	0.50
He	8.50(-2)
C	1.30(-4)
N	6.80(-5)
O	2.50(-4)
F	2.00(-7)
Na	1.20(-8)
Mg	4.00(-7)
Si	3.20(-7)
P	2.60(-7)
S	1.30(-5)
Cl	1.50(-7)
Fe	3.50(-7)

1993b) is used to model the icy mantle on grain surfaces. Only the first two layers of the icy mantle are chemically active. The average radius of the refractory grain core is 0.1 μm, and it increases as the icy mantle grows. The dust to gas mass ratio is 1.0%, and the density of the refractory core is assumed to be 3 gr cm^{-3}. The sticking coefficient of neutral species to grains equals 1, except for atomic hydrogen that is calculated using Tielens (2005) formalism. The diffusion to binding energy ratio is 0.5 in the top two layers. The diffusion energy in the layers below the top layer is considered equal to their binding energy. The binding (and diffusion) energies of each species evolve as the composition of the active layers changes. The evolution is based mainly on the occupying fraction of H_2, H_2O, and the refractory part. Oxygen, carbon, nitrogen, and atomic and molecular hydrogen can diffuse through quantum tunneling and thermal hopping. Therefore their diffusion rate is calculated as a sum of the two. The rest of the species remain stuck at 10 K on the surface. The width of the rectangular potential through which these species can tunnel is 1 Å. Surface reactions follow the Langmuir-Hinshelwood mechanism (see, Tab. A.3). The reaction probability is equal to unity if there is no reaction energy barrier. In case the reaction has a energy barrier the Eckart model formalism is used if available (Tab. A.4); otherwise, a rectangular barrier with width=1 Å is assumed. Species can sublimate only from the surface layers; the bulk stays untouched. The desorption processes are thermal, cosmic-ray, photo- and chemical desorptions. The chemical desorption percentage of the product is 1.2%. The gas-phase reaction network is based on Wakelam et al. (2015) network with further updates from Balucani et al. (2015a), Loison et al. (2014), and Skouteris et al. (2017). They also take into account the self-shielding of H_2 and CO (see Sec. 4.4.1).

Grainoble+ benefits from many upgrades in parts thanks to the new quantum computational studies (see, Chap. 4). In this section, we revert back to the input parameters and files that were used for Ceccarelli et al. (2018). There are a few differences between Grainoble+ and Grainoble that was used for modelling in Ceccarelli et al. (2018). (1) Grain assisted charge exchange reactions in Grainoble+ is based on the study of Draine and Sutin (1987) (see, Sec. 4.4.2) whereas Grainoble treats them based on the study of Flower and Pineau des Forêts (2003) and Le Bourlot et al. (1995b). (2) Evolution of the binding energies based on the composition of the active layer is not considered in our model derived by Grainoble+ because

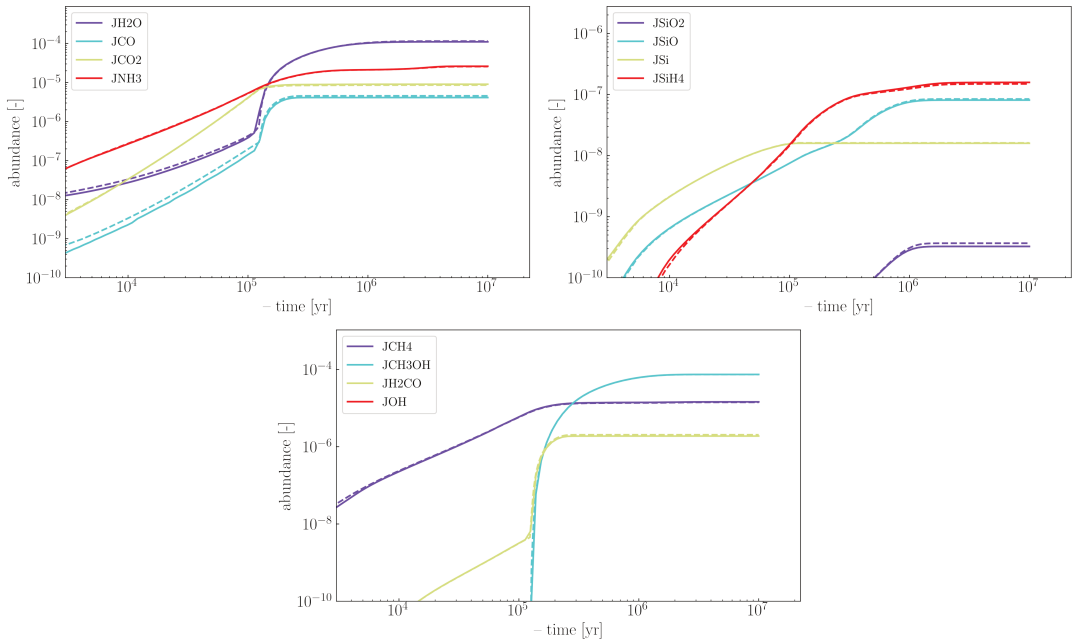

FIGURE A.1: Comparison of the predicted mantle abundances computed with Grainoble+ (solid lines) and Grainoble (dashed lines) for the molecular cloud modeled in Ceccarelli et al. (2018). "J" prefix denotes solid species.

the main constituent of the ice mantle is water ice.

A.2 Results

In Fig. A.1, we change two of the input parameters in Grainoble to make it similar to Grainoble+ input parameters. Namely, we set the number of active layers to one. Secondly, we turn off the binding energy evolution parameter so that it keeps them constant throughout the test. The results are almost exactly identical in this setting.

We plotted the fractional difference (Eq. A.1) in percentage between the two models as a function of time in Fig. A.2. The dark blue curve shows the average fractional difference in the 10 most abundant species. The difference for the abundant solid species (denoted with a prefix "J") are also plotted in colored curves. The small sharp peak before 2×10^5 years correspond to the difference in the onset of grain mantle formation in the two models.

TABLE A.3: List of surface reactions used in Ceccarelli et al. (2018).

reactions		branching ratio	activation energy [K]
H + H →	H_2		
CO + H →	HCO		2000
HCO + H →	H_2CO		
H_2CO + H →	CH_3O		2000
CH_3O + H →	CH_3OH		
O + O →	O_2		
O_2 + O →	O_3		
O + H →	OH		
OH + H →	H_2O		
O_2 + H →	HO_2		
HO_2 + H →	H_2O_2		
H_2O_2 + H →	H_2O + OH		2000
OH + OH →	H_2O_2	0.8	
OH + OH →	H_2O + O	0.2	
O_3 + H →	O_2 + OH		
OH + H_2 →	H_2O + H		2100
N + H →	NH		
NH + H →	NH_2		
NH_2 + H →	NH_3		
C + H →	CH		
CH + H →	CH_2		
CH_2 + H →	CH_3		
CH_3 + H →	CH_4		
Si + H →	SiH		
SiH + H →	SiH_2		
SiH_2 + H →	SiH_3		
SiH_3s + H →	SiH_4		
SiO + O →	SiO_2		1000
SiO + OH →	SiO_2 + H		80
HCO + O →	CO_2 + H		
CO + O →	CO_2		1000
CO + OH →	CO_2 + H	0.99	80
CO + OH →	tHOCO	0.01	80
CO + OH →	cHOCO	0.01	80
tHOCO + H →	CO_2 + H_2	0.33	
tHOCO + H →	H_2O + CO	0.33	
tHOCO + H →	HCOOH	0.33	
cHOCO + H →	CO_2 + H_2	0.33	
cHOCO + H →	H_2O + CO	0.33	
cHOCO + H →	HCOOH	0.33	
O + CO →	O...CO*		
O...CO + H →	CO_2 + H	0.49	
O...CO + H →	tHOCO	0.00495	
O...CO + H →	CO + OH	0.495	
O...CO + H →	tHOCO	0.01	1000
O...CO + H →	cHOCO	0.01	1000
O + CO →	O...CO		

(∗) This reaction follows the Eley-Rideal formalism and O...CO is a CO and O van der Waals complex (Goumans and Andersson, 2010).

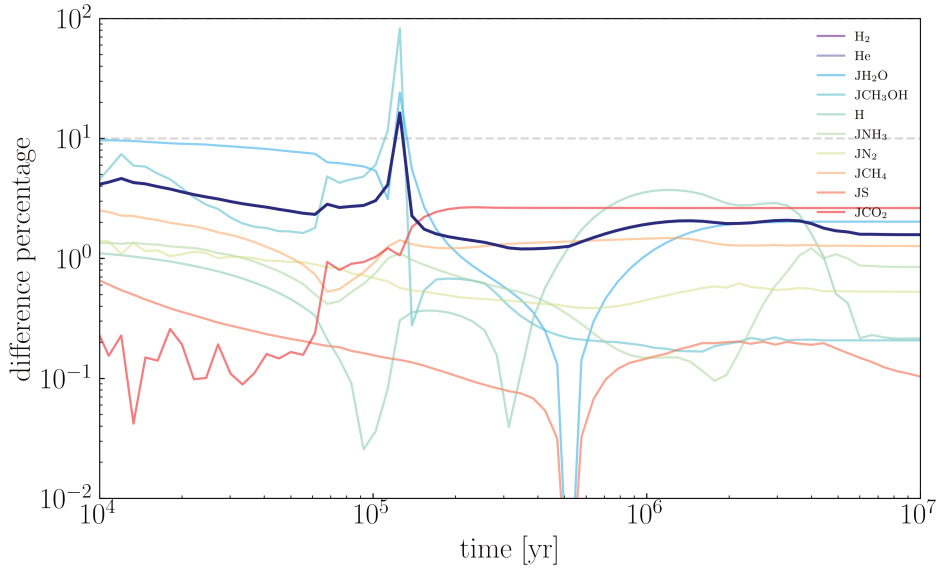

FIGURE A.2: The fractional difference between the Grainoble+ and Grainoble as a function of time (Eq. A.1). The colored curves show the differences for the abundant solid species (denoted with a "J" prefix) and the dark blue curve is the average over the differences as a function of time.

TABLE A.4: List of surface reactions with Eckart models used in Ceccarelli et al. (2018).

reactions		V_f [K]	V_b [K]	ω [cm^{-1}]
CO + H →	HCO	1979	8909	793.6
H_2CO + H →	CH_3O	2028	27290	1037
OH + H_2 →	H_2O + H	2935	10210	1293
H_2O_2 + H →	H_2O + OH	2508	36360	1054
CO + OH →	CO_2 + H	285.0	13050	261.0
CO + OH →	tHOCO	285.0	13050	261.0
CO + OH →	cHOCO	2128	14050	379.0
O...CO + H →	tHOCO	775.4	13050	261.0
O...CO + H →	cHOCO	2618	14050	379.0
tHOCO + →	CO + OH	13050	285.0	261.0
tHOCO + →	cHOCO	4114	3272	584.0
cHOCO + →	tHOCO	3272	4114	584.0
cHOCO + →	CO_2 + H	12440	12900	2053

V_f and V_b are the forward and back potentials in K and ω is the frequency of transition state in cm^{-1}. O...CO is a CO and O van der Waals complex (Goumans and Andersson, 2010).

TABLE A.5: List of binding energies used in Grainoble (Ceccarelli et al., 2018; Taquet et al., 2014).

Species	Eb_b	Eb_{ASW}	Eb_{H_2}	Eb_x
H	660	500	45	45
He	100	100		100
C	800	800		800
N	800	800		800
O	1390	1390		1390
Si	2700	2700		2700
S	1100	1100		1100
Fe	4200	4200		4200
Na	11800	11800		11800
Mg	5300	5300		5300
P	5300	5300		5300
F	5300	5300		5300
Cl	850	850		850
H_2	640	322	45	45
O_2	895	920		915
O_3	1700	1700		1700
H_2O	1870	5775		5775
OH	1300	2820		2820
O_2H	1700	2820		2820
H_2O_2	2500	5775		5775
CO	830	870		855
HCO	2050	2200		2300
H_2CO	3260	3260		3765
CH_2OH	5000	5000		4000
CH_3O	3800	3800		4000
CH_3OH	5530	5530		4230
tHOCO	2500	3000		3000
cHOCO	2500	3000		3000
OCO	1650	1950		1950
CO_2	2270	2690		2270
HCOOH	5570	5570		5000
CH	870	870		870
CH_2	945	945		945
CH_4	1090	1100		1090
CH_3	1017	1017		1017
NH	2380	2380		1560
NH_2	3960	3960		2320
NH_3	5535	5535		3080
SiH	3150	3150		3150
SiH_2	3600	3600		3600
SiH_4	4500	4500		4500
SiO	3500	3500		3500
SiH_3	4050	4050		4050
SiO_2	4300	4300		3500

The binding energy (BE) of selected species on different substrates in K (Ceccarelli et al., 2018; Taquet et al., 2014). Eb_b on a bare grain, Eb_{ASW} on an ASW surface, Eb_{H_2} denotes the BE on an H_2 substrate, and Eb_x on the same substrate.

Appendix B

Comparison between Grainoble+ with Aikawa 2020

In this section, we compare the results obtained with the Grainoble+ code with those described by Aikawa et al. (2020) (Ai20 hereafter) in the static phase. We focused on the most abundant species in ices: H_2O, CO, CO_2, CH_3OH, CH_4 and their counterparts in the gas phase. We were unable to retrieve all the parameters used by Ai20. Therefore, to find a solution that best compares with Ai20 published plots we ran several models and varied some of the model parameters to understand where the difference lies and which parameters has the most impact on the results.

As expected, the abundance of solid species strongly depends on the surface reaction parameters. Many of the parameters are poorly constrained, such as the activation energy barrier width, or they are inherently difficult to measure, such as the diffusion energy. Therefore, we focus our effort on understanding the impact of surface reaction parameters.

We ran two grids of models. The first grid of models contains the reference model, which has the model parameters that are as close as possible to Ai20 parameters. In the additional 10 models, we vary one parameter at a time with respect to the reference model. We compared our computed abundances with the abundances in Ai20 static phase at 1 Myrs. The reference model did not reproduce all the results from Ai20. The results from the parameter variation grid showed us that the width of the surface reaction energy barrier had the most impact on the computed abundances. In consequence, we ran an additional 9 models varyig the width of the energy barriers from 2 to 3 Å to find which model reproduces the Ai20 static phase results the best. The model with the energy barrier width of 2.2 Å produced a better agreement with Ai20 computed abundances (see, Sec. B.3 for more discussion).

The following sections describe the model parameters in the two model grids, the results and concludes with a brief discussion.

B.1 Description of the models

We follow the initial elemental abundances and physical profile of the static phase of Aikawa et al. (2020) listed in Tab. B.2, and Tab. B.1, respectively in all the models. The main model (Model id, 1) adopts the chemical parameters in Ai20 as closely as possible. We ran several additional models to investigate the impact of parameter variations on the computed abundances. The adopted parameters in the various models are listed in Tab. B.3 and are described in the following paragraphs. The second column lists the choice of parameters in the Model 1, the third column lists the parameter value that is changed with respect to the reference model, and the fourth column lists the id number of the models.

To make the comparison as best as possible, we employ the model parameters chosen by Ai20. However, there remain several differences that we list here. (1) Ai20 adopts a seven-phase model (gas, surface, and 5 bulk phases). The ice surface consists of 4 layers, and each

TABLE B.1: Physical profile as described in Ai20.

model physical parameter	Ai20
duration [year]	10^6
n_H [cm^{-3}]	2.28(4)
A_ν [mag]	4.5
ζ_{H_2} [s^{-1}]	1.3(−17)
G_0 [Habing unit]	1.
T_g [K]	10
T_d [K]	10

TABLE B.2: Initial elemental abundances in Ai20.

elements	Ai20
H_2	0.5
He	9.75(-2)
C^+	7.86(-5)
N	2.47(-5)
O	1.80(-4)
Mg^+	1.09(-8)
Si^+	9.74(-9)
S^+	9.14(-8)
Fe^+	2.74(-9)
Na^+	2.25(-9)
Cl^+	1.00(-9)
P^+	2.16(-10)

bulk phase consist of a few tens of layers at most. We adopt a three-phase model and the surface consists of only 1 layer. (2) Ai20 assumes that each of the 5 bulk phases is chemically active but do not chemically interact with one another. The diffusion to binding energy ratio in the bulk is 0.8. The bulk in our model is chemically inert. (3) Photolysis processes on ices are included in Ai20 but not in our model. (4) Their gas and grain surface networks and list of binding energies (BEs) are from Garrod (2013) with some additional updates are listed in Ai20 work. We use our gas phase and surface reaction networks, activation energies, and BEs (see, Sec. 4.4.1, 4.4.4, and 4.3.3).

The reference model (model 1) The choice of parameters adopted in the reference model (model 1) is listed in the second column in Tab. B.3. In summary, the reference model considers only thermal hopping as the mean of diffusion with the diffusion to binding energy ratio on the surface equal to 0.4. The atomic hydrogen BE in this model is 450 K from Garrod (2013) work. The rest of the BEs are chosen from Tab. 4.2. The surface reaction efficiency or probability follows the Garrod and Pauly (2011) (GP11 hereafter) formalism. The surface reaction activation barrier is modeled with a rectangular width of 1 Å. The activation energy barrier and the barrier with of (s-CO + s-H $\longrightarrow$ s-HCO) and (s-H_2CO + s-H $\longrightarrow$ s-CH_3O) reactions on the surface are 1455 and 2320 K (Garrod, 2013). The chemical desorption percentage is 1%.

The activation energy barrier (model 2) In model 2, we study the impact of the activation energy barrier in the methanol network reactions.

Quantum tunneling (model 3) Below a specific temperature known as crossover temperature T_c, diffusion through quantum tunneling becomes the dominant mean of diffusion on the surface (Hänggi et al., 1990). According to the study of Senevirathne et al. (2017), for atomic hydrogen, T_c ranges between 5 and 13 K. In our series of models, the dust temperature is 10 K which is within this range. Therefore, it is crucial to understand the effect of tunneling as a means for diffusion. Model 3 focuses on the effect of quantum tunneling as a means of diffusion for light atoms H, O, N, and C.

The Eckart model (model 4) The activation energy barrier is often approximated by a rectangular barrier with an assumed width between 1 and 2 Å (see, Garrod and Pauly, 2011;

TABLE B.3: List of parameter variation in the comparison with the Ai20 models

Parameter	Reference	Variation w.r.t Model 1	Model id
Activation energy, E_a[a] [K]	1455 and 2320	2000 for both	2
Surface diffusion	TH[b]	TUN[c] + TH	3
Surface reaction activation barrier	rectangular	Eckart	4
E_{diff}/BE ratio	0.4	0.3, 0.5	5, 6
BE of atomic H [K]	450[d]	490[e]	7
Surface reaction efficiency	GP11[f]	HH92[g], ER21[h]	8, 9
Surface reaction barrier width [Å]	1.0	2.0	10
chemical desorption (CD) (%)	1	10	11

[a] Activation energy for (s-CO + s-H $\longrightarrow$ s-HCO) and (s-H_2CO + s-H $\longrightarrow$ s-CH_3O) reactions (Garrod, 2013).
[b] Thermal hopping.
[c] Diffusion through quantum tunneling for H, C, O and N atoms.
[d] From Garrod (2013).
[e] Median value for the BE distribution of atomic H with zero point energy correction Senevirathne et al. (2017).
[f] Garrod and Pauly (2011) method.
[g] Hasegawa et al. (1992) method.
[h] Enrique-Romero et al. (2021) method.

TABLE B.4: The parameters used in the models comparing with Ai20 static phase results.

model parameter	value
dust to gas mass ratio	1%
grain density [grcm^{-3}]	3
cell size [Å]	3.5
grain radius [μm]	0.1
grain radius growth	no
number of active surface layers	1
n-phase	three-phase
BE evolution	no
self shielding	included
H sticking coefficient	Hollenbach and McKee (1979)
Gas phase reaction network	GreToBaPe-GAS
Surface reaction network	GreToBaPe-GRAIN network (see Tab. 4.7)
CR desorption	Hasegawa and Herbst (1993b) model

Hasegawa et al., 1992; Tielens and Hagen, 1982a). However, there are other models that better describe the barrier. More accurate modeling of the barrier allows us to deduce a more reliable transmission probability through the barrier. The Eckart model by Eckart (1930) describes a barrier with three parameters: Potential energies of the forward and backward reactions and the frequency of the transition state (see, also, Joohnston and Heicklen, 1962). In model 4, we employ this model for the main surface reaction network: methanol, water, and CO_2 (see Tab. 4.6 and the values reported in Taquet et al., 2012).

The diffusion to binding energy ratio (model 5 and 6) Measurements of the diffusion energy of different species on ice surfaces in experimental laboratories and theoretical works is a difficult task. The range of adopted E_{diff}/BE ratio in the literature is between 0.3 and 0.85 (Cooke et al., 2018; Cuppen et al., 2009; Hama et al., 2012; Karssemeijer and Cuppen, 2014; Katz et al., 1999; Lauck et al., 2015; Livingston et al., 2002; Maté et al., 2020; Mispelaer et al., 2013; Perets et al., 2005; Ruffle and Herbst, 2000; Tielens and Hagen, 1982a; Watanabe et al., 2010). Recent studies mostly agree on E_{diff}/BE ratios between 0.3 and 0.5. For example, the experimental work of He et al. (2018) on light species on amorphous solid water (ASW) find a range between 0.3 - 0.6 (see their Table 3). On the other hand, the theoretical work of Karssemeijer and Cuppen (2014) suggests a smaller range of 0.3 - 0.4. Senevirathne et al. (2017) estimated this ratio for atomic H to be 0.37. Given the uncertainties in the measurements, in our model, we compare the reference model with two other models (number 5 and 6), in which we assume 0.3 and 0.5.

The atomic hydrogen binding energy (model 7) The study of atomic H BE is critical. In low temperatures in the ISM, hydrogen is practically one of the few species that can diffuse and, as a consequence, react with other species on the surface. BE dictates the rate of diffusion and desorption of atomic hydrogen. Therefore, it highly affects the rate of hydrogenation of species on the surface, such as CO. Many theoretical, experimental, and computational works have focused on measuring the BE of atomic H on different substrates. Pierre et al. (1985) has measured the atomic H on a quantum crystal of H_2 equal to 45 K. The work of Buch and Zhang (1991) estimated the atomic H BE on ASW with molecular dynamics (MD) simulations within the range of 650$\pm$195 K. Al-Halabi and van Dishoeck (2007) has done BE measurement on ASW and crystalline surfaces. On ASW, the BE is 650$\pm$10 K, and on crystalline water, it is 400$\pm$5 K. Garrod (2013) lists 450 K for atomic H BE and Wakelam et al. (2017) lists 580 K based on experimental data for ASW. Senevirathne et al. (2017) estimates the hydrogen BE distributions by taking into account the zero-point energy correction within the range of 255-730 K (see their Table 2) (see, also, Amiaud et al., 2007; Hama et al., 2012; Kuwahata et al., 2015b; Matar et al., 2008; Perets et al., 2005; Watanabe et al., 2010). In model 7, we compare the reference model with our choice of parameter, 490 K, which is the median of the BE distribution in Senevirathne et al. (2017) that is one of the most recent studies on atomic hydrogen BE.

The surface reaction efficiency (model 8 and 9) In an earlier study of Hasegawa et al. (1992) (HH92 hereafter), the reaction efficiency of a reaction with an activation energy barrier is calculated as the quantum tunneling probability of a reaction to occur upon a single collision. It is expressed as the quantum tunneling probability. However, the occurrence of a reaction does not depend only on a single collision. The two reactants have the opportunity to collide multiple times or hop away to an adjacent binding site or evaporate before a reaction occurs. The latter two are processes competing with the reaction. It means the reaction efficiency depends not only on the quantum tunneling but also on the frequency of the collision of

the two reactants and the rate of hopping and desorption. Later studies such as Enrique-Romero et al. (2021) and Garrod and Pauly (2011) (GP11 and ER21 hereafter, respectively) consider these possibilities in estimating the reaction efficiency. For example, GP11 considers the hopping of the two reactants and estimates the collision frequency as the largest of the vibrational frequency of the two reactants. On the other hand, ER21 includes the possibility of thermal evaporation. In models 8 and 9, we compare the outcomes considering the different approaches of HH92 and ER21.

The activation energy barrier width (model 10) As mentioned earlier, the energy barrier width of the surface reaction is poorly constrained. It is approximated to about 1-2 Å (Garrod and Pauly, 2011; Hasegawa et al., 1992; Tielens and Hagen, 1982a). It affects the transmission rate through a rectangular energy barrier. Therefore, in model 10, we focus on the impact of this parameter choice.

The chemical desorption probability (model 11) If a reaction is exothermic, the excess energy can result in the evaporation of a fraction of the product. Experiments and models show the chemical desorption probability depends on the reactants, products, and surface composition. Therefore in model 11, we set the percentage to 10%. The main goal is to see which one of the species is affected most by this parameter.

B.2 Results and discussion

Fig. B.1 shows the chemical evolution of the selected solid species (with a "s-" prefix in the plots) and their gaseous counterpart in time for the different model assumptions described in Tab. B.3. The brown star indicates the Ai20 static phase abundances at the end of the static phase at 1 Myrs for each species. The vertical line area indicates a range of a factor of three around each point to account for the combined modeling uncertainties (Herbst and Dishoeck, 2009). Fig. B.2 shows the abundances of the selected species at 1 Myr and compares that to the Ai20 static phase results that are shown with a brown horizontal line. The colored area shows a factor of three enveloping Ai20. In other words, Fig. B.2 is Fig. B.1 at 1 Myrs.

The following sections compare the reference model to the Ai20 results. Following that, we describe the impact of each chemical parameter variation by comparing the abundances to those in the reference model.

B.2.1 The comparison between the reference model and the Ai20 abundances (model 1)

The comparison of our reference model (colored purple in Fig. B.1 and Fig. B.2 with Ai20 results at 1 Myrs (colored brown in the figured mention earlier) provides the following results:

- s-H_2O, s-CH_4 and CO are in within a factor of 2 w.r.t Ai20 static phase results.
- H_2O is overproduced by about a factor of 4 w.r.t the Ai20 value.
- CH_4 is within a factor of 4 of the Ai20 abundance.
- s-CO_2 is under-produced by a factor of 4.
- $CO_2$and CH_3OH are overproduced by a factor of 4.
- s-CO is under-produced by about 3 orders of magnitude.
- s-CH_3OH in our reference model is overproduced by 1.5 orders of magnitude.

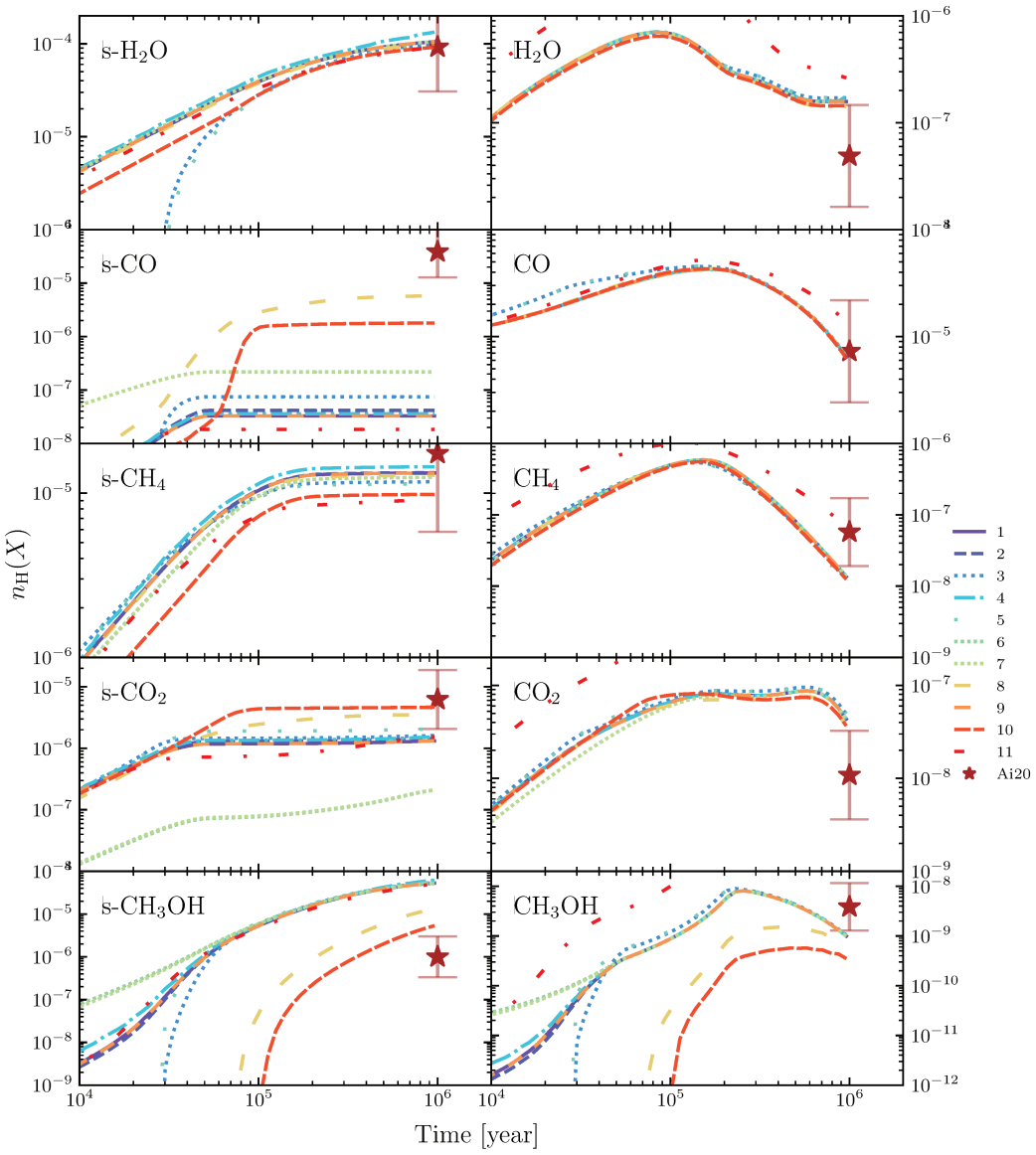

FIGURE B.1: Chemical evolution of selected solid (prefixed with "s-") and gaseous species based on models described in Tab. B.3. Model 1 (in purple) is the reference model. The brown star at 1 Myrs for each species shows the Ai20 static phase results and its vertical line shows a factor of three around the point.

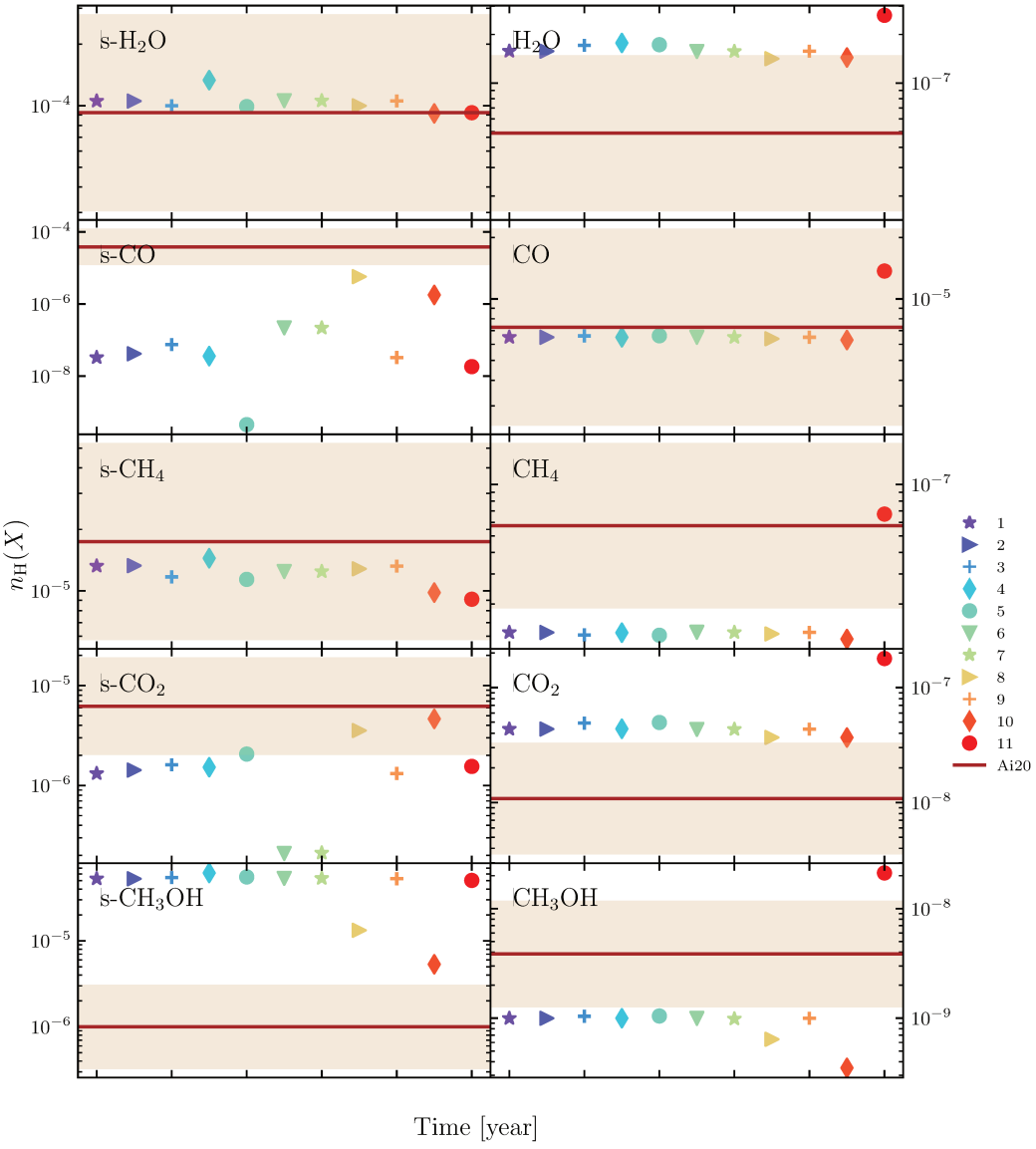

FIGURE B.2: Chemical abundance of selected solid (prefixed with "s-") and gaseous species at 1 Myrs based on models described in Tab. B.3. Model 1 (in purple) is the reference model. The horizontal brown line shows the results in Ai20 static phase at 1 Myrs and the colored area signifies the factor three around it.

The abundances of s-CO, s-CH_3OH, and s-CO_2 show the strongest difference with respect to the reference model to the Ai20 results.

In the following, we describe the effect of the chemical parameter variations (Tab. B.3) with respect to the reference model (see, Fig. B.1 and B.2).

The activation energy barrier (model 2) Variation of the activation energy barriers in the methanol network hardly affects the chemical evolution of the species. This is because the CO hydrogenation is due to the tunneling of hydrogen atom through the barrier.

Quantum tunneling (model 3) Diffusion through quantum tunneling increases the diffusion rate of atoms, especially hydrogen. The strongest effect of the inclusion of quantum tunneling is on the s-CO abundances by a factor of $\sim$ 2.5 increase. The rest of the species remain unaffected.

The Eckart model (model 4) The solid and gaseous abundances in this model are well within a factor of two of the reference model.

The diffusion to binding energy ratio (model 5 and 6) The hydrogen diffusion rate is higher with lower E_{diff}/BE ratio. Model 5 with E_{diff}/BE=0.3, shows 2 orders magnitude decrease in s-CO abundance and model 6 with E_{diff}/BE= 0.5 increases by about 1 order of magnitude with respect to model 1. The change in E_{diff}/BE ratio also affects CO_2. Model 5 shows an increase with less than a factor two in s-CO_2, and model 6 shows a decrease with less an one order of magnitude comparing with the reference model. Therefore, the atomic hydrogen diffusion energy is a major parameter affecting the results.

The Atomic hydrogen binding energy (model 7) An increase in BE of atomic hydrogen decreases the rate of thermal hopping of hydrogen and therefore reduces the rate of hydrogenation. s-CO abundance is about 1 order of magnitude larger with respect to model 1. s-CO_2 abundance are smaller by almost an order of magnitude. The abundance of methanol does not change significantly.

The surface reaction efficiency (model 8 and 9) The difference between model 8 and 9 and model 1 are the choice of the formalism in calculating the surface reaction efficiency. Model 1 follows the formalism by GP11, model 8 by HH92 and model 9 by ER21. HH92 calculates the reaction efficiency factor taking into account only one encounter. In contrast, GP11 and ER21 take into account multiple encounters. Therefore, the efficiency calculated based on HH92 formalism for reactions on the surface with reaction activation energy barrier is significantly lower. For example, the reaction rate coefficient of CO hydrogenation in model 1 which uses the GP11 formalism to calculate the efficiency is 1.8×10^7 cm^3s^{-1}. On the other hand, in model 8, which employs the HH92 formalism, it is equal to 7.8×10^4 cm^3s^{-1} which is about 250 times smaller in comparison to the one of model 1. The s-CO abundance increases by about a factor of 200 in model 8, in comparison to model 1. s-CO_2 abundance increases by a factor of 3 and methanol abundance in ices decreases by a factor of 0.2.

ER21 formalism includes thermal evaporation as a competing process as well. However, at temperatures of about 10 Kelvin, thermal evaporation is very small. Therefore, model 9 shows results similar to the model 1 results.

The activation energy barrier width (model 10) Increase of the reaction activation energy barrier width reduces the rate of hydrogenation of CO, OH and C on ice surfaces. Consequently, the abundance of s-CO and s-CO_2 increases, while the abundance of s-CH_3OH, s-H_2O, and s-CH_4 decreases. The barrier width variation shows the strongest impact on solid species. s-CO abundance increases with about 2 orders of magnitude and the s-CH_3OH abundance with one order of magnitude. The main source of methanol in the gas phase in low temperature is through desorption of s-CH_3OH. The decrease in s-CH_3OH abundance decreases the gaseous methanol abundance with a factor of 0.3.

The chemical desorption probability (model 11) Increase of the chemical desorption percentage increases the abundance of gaseous species and slightly decreases the abundances of icy species.This increase effects the methanol abundance in the gas phase the most, by about a factor of 20. Water shows the least impact with increase of less than a factor of 2. In ices, the s-CH_4 abundance shows the strongest impact with a decrease by a factor of 0.7.

Summary of the model comparisons

Overall, the variation of the parameters involved in the grain-surface chemistry strongly affects the abundance of solid species. The gaseous abundance remains relatively unaffected, except for the increase of the chemical desorption percentage, which increases the abundances of the gaseous species, especially the CH_3OH abundance. We summarize the key points in the following.

The s-H_2O and H_2O abundances are the least affected. The abundances remain within a factor of 2 compared with the reference model.

The abundance of s-CH_4 decreases with an increase in the chemical desorption percentages. After chemical desorption, the reaction barrier width is the most impactful parameter in the formation of s-CH_4 in ices.

The abundance of CO is hardly affected by the chemical parameter variation, except for the case of chemical desorption. On the other hand, the s-CO abundance varies strongly with chemical parameter variation. The decrease in the diffusion to binding energy ratio decreases the s-CO abundance with $\sim$2 orders of magnitude due to an increase in the hydrogenation rate of CO. On the other hand, an increase in the reaction barrier width increases the s-CO abundance by 2 orders of magnitude due to a decrease in the rate of CO hydrogenation.

s-CH_3OH formation through hydrogenation of s-CO remains efficient in most of the models. The choice of HH92 efficiency methodology and an increase in the reaction barrier width decreases the abundances up to an order of magnitude. On the other hand, CH_3OH is practically only affected by an increase in the chemical desorption process.

s-CO_2 abundance increases with an increase in the activation barrier with and has the lowest value using higher atomic hydrogen BE or E_{diff}/BE ratio. The gaseous CO_2 abundance remains unaffected.

B.2.2 Further investigation on the reaction activation barrier width

The change in the width of the reaction activation barrier is the most impactful parameter among the ones on our list. Therefore, we run 8 more models varying the width of the barrier from 2 to 3 Å, relative to the reference model whose width is equal to 1 Å. We show the results in Fig. B.3 and B.4. The labels of the two plots are the width of the reaction activation energy barrier in Å. The models with widths $\geq$2.2 Å have the closest agreement with Ai20 results. The only exception is methanol in the gas phase. Abundance of s-CH_3OH and as a consequence CH_3OH decrease rapidly with the increase of the barrier width, which is due to the rapid decrease in the rate of s-CO hydrogenation.

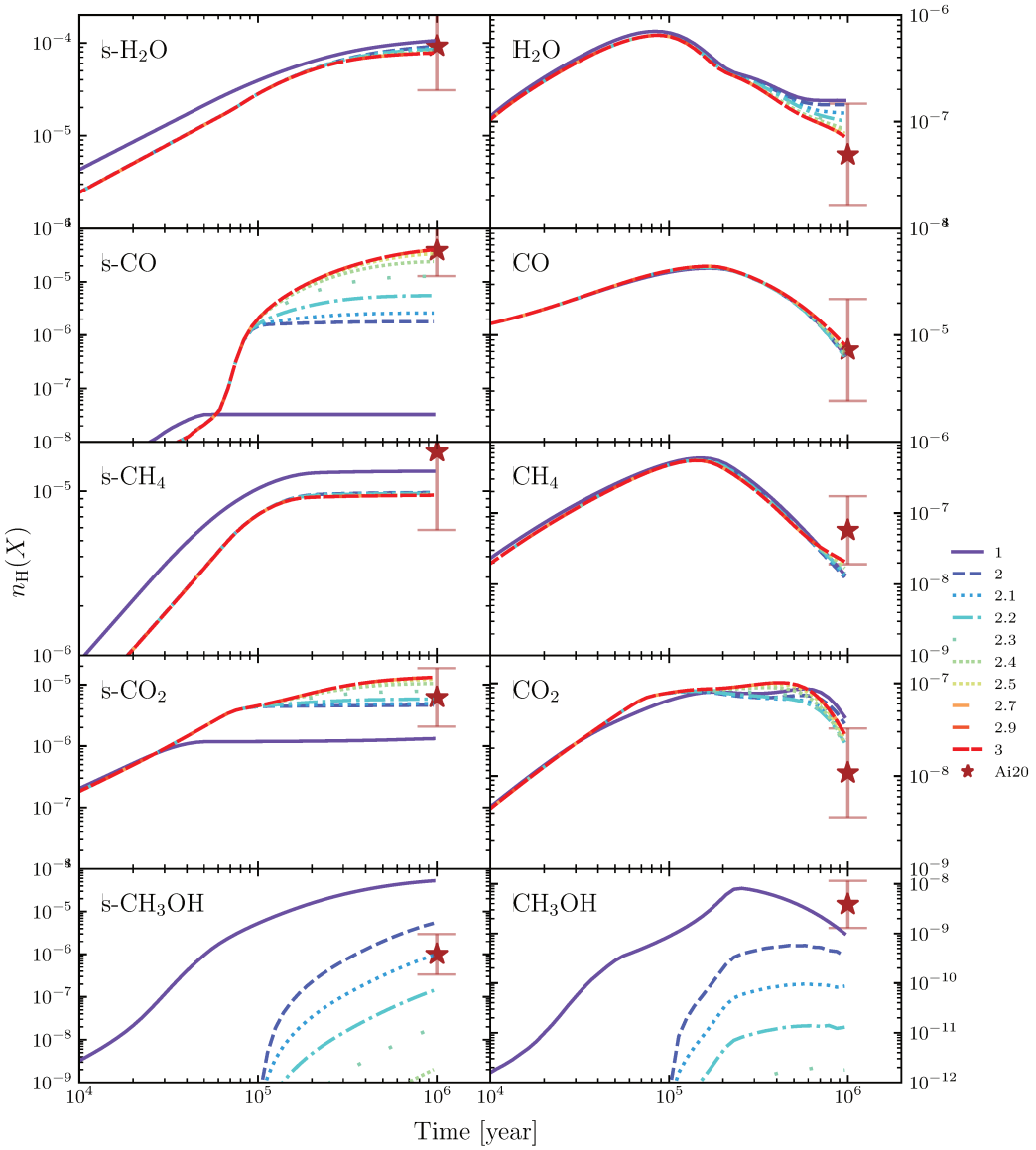

FIGURE B.3: Chemical evolution of the selected species in ices (prefixed with "s-") and in the gas phase based on various models. The first model in solid purple line, is the reference model described in Tab. B.3. The rest of the models are based on the reference 1 with only one variation: the surface reaction barrier width. The labels of the curves denote the width chosen for that model in Å. The brown star at 1 Myr for each species shows the Ai20 static phase results and its vertical line shows the a factor of three offset range around the point.

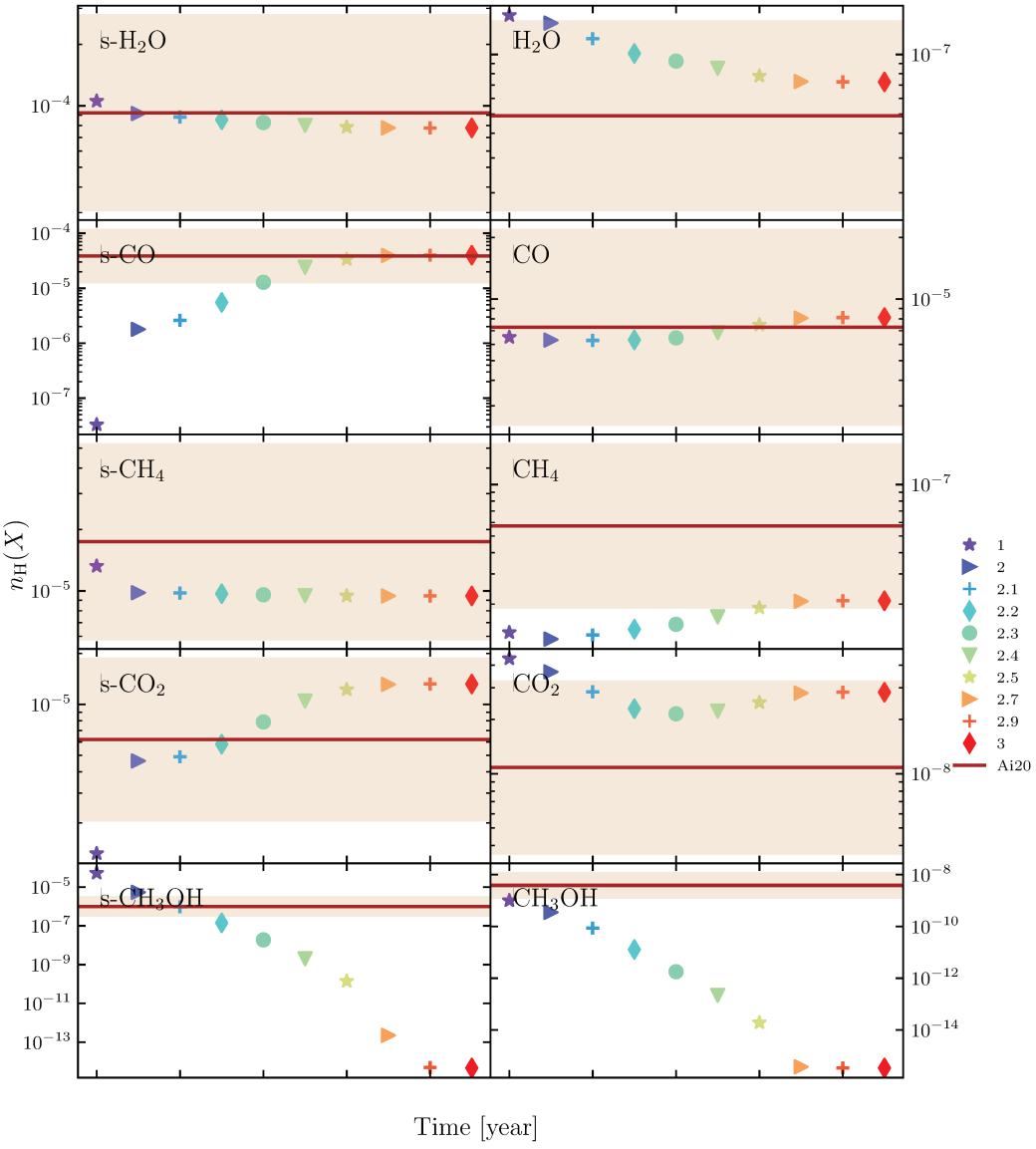

FIGURE B.4: Chemical abundance of the selected species in ices (prefixed with "s-") and in the gas phase at 1 Myr based on various models. The first model in purple star marker, is the reference model described in Tab. B.3. The rest of the models are based on the reference 1 with only one variation: the surface reaction barrier width. The labels of the curves denote the width chosen for that model in Å. The horizontal brown line shows the results in Ai20 static phase at 1 Myr and the colored area signifies the factor three offset around it.

B.3 Discussion and conclusion

In this section, we compared our results with the static model in Ai20 and examined the impact of various chemical parameters on the abundance of solid and gaseous species. Our reference model, which has the closest set of model parameters, reproduced the s-H_2O, CO, and s-CH_4 from Ai20 within a factor of 2. The rest of the abundances were within a factor 4 of Ai20 results, except for s-CO and s-CH_3OH which differs by more than a factor of 10.

We varied the chemical parameters to examine their impact on the solid and gaseous species. The variation in width of the rectangular energy barrier of a reaction was the most impactful chemical parameter (the width enters as an exponent in the transmission probability, Eq. 4.28). As the next step, we varied the width to examine its influence on the s-CO and s-CH_3OH abundances. The model with a width of 2.2 Å reproduces the Ai20 abundances best. As per our conversation with Prof. Aikawa, the energy barrier width they used in their paper is 1.35 Å.

Additionally, we have noticed that the CH_3OH/s-CH_3OH ratio in Ai20 is about 4×10^{-3}. This ratio in all of our models remains between 2×10^{-5} and 4.2×10^{-4}. In Ruaud et al. (2015, their model A) and Kalvāns (2015a) this ratio is also about 10^{-5}.

Appendix C

The Grainoble+ algorithm and code

Grainoble+ is an astrochemical model simulating the chemical evolution in the gas and ices in star-forming regions. Grainoble+ is a modular model with the flexibility to easily add, remove, or modify any physical or chemical processes.

The code consists of two main parts: The main code and a wrapper. The main code, implemented in object-oriented Fortran 2003, is the calculating core of the model that simulates the chemical evolution of the system. It solves a first-order stiff ordinary differential equation using DLSODES subroutine from the ODEPACK (Hindmarsh, 1983)[1]. The main code can be used self sufficiently without the Python wrapper. The wrapper, implemented in Python 3.8.8, is the user interface module of the model. The wrapper has a front-end and a back-end. It creates the input files and reads the outputs for a single model. It can also create a combined set of models, run them, and create combined plots. It is added to (1) facilitate formatting the input files into the core readable style and (2) read the results and plot for further analysis.

Grainoble+ upgraded upon Grainoble also on the technical sides:

a) Inclusion of a python wrapper has made dealing with files easier because Python is much more flexible in reading and converting information from files with various format.

b) An astrochemical model deals with many input parameters, which increases the possibility of small errors. If unseen, it can lead to wrong results. The new python functions have tried to automate checking for errors, typos or mistakes in the inputs to make it easier for the user.

c) Most astrochemical models require a user to list the species in a file separate from the reaction files. This method increases the chance of making mistakes or typos. It means that each time the reaction list is changed, the species file also needs to change. Grainoble+ does not require such a second file. The python wrapper creates a list of species with their elements directly from the reaction file. The only additional information the user needs is to provide the list of elemental abundances.

d) The inclusion of uni-molecular processes is more straightforward in Grainoble+. The user does not need to add lines to the reaction files for each process. For example, in a model with 500 gaseous species, 250 of which are neutral, and 5 processes: adsorption, thermal, chemical, CR, and photo- desorptions, the reaction file needs to add 1250 more lines in order to include these processes. This method of including processes is subject to many errors. It is now a matter of adding a single number (0=not used, 1=used on the surface, 2=used in bulk) in the input parameter file. The code will automatically generate the list of processes with the list of species it already has.

e) The Fortran and the Python codes have exit strategies at every iteration. If an error were to occur, such as reading an incorrect input or the conservation of elements does

[1] https://computing.llnl.gov/casc/odepack/

not hold, the code exits that iteration. It ends the program by writing the results files up to the time index it was stopped and informs the user in the log file about the errors. Otherwise, the results will not be correct, and it will take the user's time to check them by hand every time it happens.

The following sections present a brief description of how the code works (§ C.1), the input files (§ C.2), the Fortran code modules (§ C.4), and the Python classes (§ C.3 and C.6), the output files (§ C.5), and plots (§ C.6).

C.1 How does Grainoble+ work?

The first steps The first step after downloading the files is to compile the code by calling make gfort on the terminal in the Fortran source code directory. Then to run the code, one should call the test input file with the executable in the terminal: ./gplus [/absolute or relative directory/input file name]. If the test is successful, the user is notified on the terminal.

From input files to the end To create a model, the user has two options (1) use the Python interface or (2) create the input files directly for the Fortran core code. The user needs to choose the model parameters and collect the input and data files in a folder or list their path directories in the input file or the Python interface function for either of the two choices. If the Python path is chosen, the code recommends checking for redundancies or possible mistakes in the reaction files for the first time use by utilizing the appropriate keyword in the *create_inputfiles* class in the *gplus.py* file. The input files used by the Fortran core code are the input parameter file and the reaction and other data files. The input parameter file lists the path directories of all the relevant reaction and data files. After the input files are created, the user can run the model by calling the input parameter file with the *gplus* executable in the terminal. The model creates the results folder as it is indicated in the input file. If the last folder in the results path directory is *date*, the code creates a folder according to the current date and time. For example, if the date and time are March 20th, 2019, 22:58:27[2], the folder name will be *20190320_225827*. A log file is written as the model starts running. It collects the progress, warning, or error messages so that the user can follow the run as it goes. When the model is finished, the terminal indicates the success or failure of the run is a message. The results are written in the designated files in the output directory. If the run was unsuccessful, the results are written only up to the stopped time index. This way, the results are not lost, and the user may understand the problem with the help of the log file that collects the error messages.

The Fortran core code The Fortran core code starts by reading the terminal commands and the input parameter file. It creates the results folder and opens the log file. It distributes the input information through the various modules and sets up the integrators variables. After the initiation, the code calls the integrator, DLSODES, in a double iterative scheme. The outer time loop iterates over the time indices from the input file. Those are times at which all the parameters are saved in arrays. The DLSODES is inside the inner loop that iterates between the beginning and the end in the outer time loop. DLSODES numerically solves the rate equations and calculates the abundances as a function of time. The inner and outer loop's iteration steps are dynamic and depend on the integration and the ice layer formation statuses. For example, if the physical conditions change rapidly, the iteration becomes smaller, or if the system has reached a steady state, the iteration steps are usually wider. The main reason for

[2]It was the moment of the spring equinox in 2019 (CET local time). The spring equinox marks the new year in my country.

the double loop system is that, at times, the integrator breaks the integration cycle before it reaches the *timeout* following its criteria and algorithm. Therefore, to keep the iteration going, we adapted this method. Inside each cycle, the code checks the integrator's messages and adjusts the integration parameter, if necessary, updates the physical parameters, builds the ice mantle, and checks for the conservation of elements. The code saves the parameters and the calculated chemical abundances at the end of each outer loop iteration. Finally, after the integration is over, it writes the results in various files, closes the log file with the final messages, and deallocates all the allocated memories.

The code has exit strategies at every step. If an unavoidable error occurs, such as an incorrect input or if the conservation of the elements did not hold, the code exits the integration loop. It writes the results up to the stopped time index and informs the user about the error message in the log file. The following paragraphs briefly review the function of each Fortran file/module.

C.2 The input files

The list of input parameters and files with or without the Python wrapper is the same. The wrapper only sorts them and writes them into the correct, readable format for the Fortran main code.

The following paragraphs review the files used by the core Fortran code.

The input parameter file It is a single text file that lists the input parameters and input files. Fig. C.1 shows an example input file. The code meticulously avoids using hardcoded variables. Therefore, the input file keeps a record of the files or any other variable used by the Fortran core code. The Python wrapper can create the input file, or the user can write one separately. The file is divided into the following sections:

a) The directory path[3] of the results directory.

b) The directory path of the physical profiles file.

c) The dust parameters: the dust to gas mass ratio, the grain's density [grcm^{-3}], the lattices site's side [Å], the grain size distribution model parameters, and the options: the grain radius growth with mantle formation, the binding energy evolution with layer coverage, the ice model (gas-phase, bulk-phase, or gas-grain phase), and the number of layers in the surface (see §4.2).

d) The species file and the option of multi- or single binding energy.

e) The gas, surface, and photodissociation reactions files and the option to include them or not.

f) The self-shielding parameters and data file.

g) The pararmeters of the charge exchange with grain process,

h) The list of options for the following processes: to include or not the processes such as desorptions (thermal, CR, photo-, and H_2 formation induced), adsorption, and crystalization, the choice for the diffusion model for various species, the diffusion potential barrier width, the diffusion barrier in bulk, the reaction efficiency formula, the surface reaction rate options, and the list of corresponding files (see §4.4).

[3]Each directory path can be absolute or relative.

i) The option that was developed for the shock model grid (see, Chap. 5).

j) The option to write only a specific number of species files.

Profile and reaction files

Cloud and Dust physical profile: This file contains the physical parameters as a function of time. The first column is time [year], and the rests are the physical parameters used in the model as a function of time. These parameters are number density [cm^{-3}], visual extinction [mag], CR ionization rate [s^{-1}], radiation field scale [Habing unit], secondary UV photons flux [$cm^{-2}s^{-1}$], and gas and grain temperatures [K]. If multi-grain mode is used, the grain temperature should be listed for all the grain bins in the model. The profiles could be pseudo-time-dependent or time-dependent. The file header indicates the order of the columns. The results are saved at the listed times (§ 4.1 and 4.2).

Species file: This file contains the list of gas-phase species (see §4.3). The information listed for each species are charge, list of elements in the species, initial elemental abundance relative to H-nuclei, sticking coefficient, number of binding energies (BE) on the amorphous solid water surface (ASW), BE on the crystalline water surface, the list of BEs on ASW, fractional distribution of them (α), BE on refractory core, BE on a hydrogen substrate, BE on a substrate of its own, diffusion energy to BE ratio and any comment at the end of the line if necessary. Note that Grainoble+ does not require reading a list of solid species separately. It will generate them automatically, if necessary.

Gas and surface reaction files: Gas-phase and surface reactions are listed in three separate files for convenience. The structure of the files is the same and is adapted from the KIDA[4] reaction network file format. Each line lists up to 3 reactants and 5 products (if present) following three reaction rate constants (A, B, and C in the file). The last columns are the assigned type and formula, the temperature range of the reaction in K, and the width of the rectangular reaction energy barrier in Å. The gas-phase reactions follow the KIDA typing scheme. In Grainoble+, the type and formula of LH reactions are 21, 22 for ER reactions, and 23 for photodissociation reactions (see §4.4.1 and §4.4.4). The three parameters, A, B, and C, are the branching ratio, the chemical desorption fraction, and the reaction activation energy in LH reactions. The temperature range is relevant for gas-phase reactions, while the energy barrier width is relevant for the LH reactions.

Self shielding file: This file lists the self-shielding coefficients as a function of CO and H_2 column densities (§4.4.1).

The charge exchange file It lists the charge exchange reactions with space for 3 reactants and 5 products in each line. The reduced cross-section is calculated in the code and is not written in the file (see §4.4.2).

Diffusion rate constants It lists the diffusion rate constants of solid species. At the moment, it has the oxygen diffusion rate constants from Congiu et al. (2014).

Hydrogen diffusion rate coefficient The file contains the hydrogen diffusion rates as a function of temperature from Senevirathne et al. (2017).

CO and H thermal desorption and diffusion rates The thermal desorption and diffusion rates of hydrogen and CO as a function of temperature from the quantum computational calculations reported in Witzel et al. submitted. The diffusion to binding energy ratios for each species are 0.3, 0.4, and 0.5.

[4] kida's website

```
> !--- input parameters and files for GRAINOBLE+
> !--- Arezu Witzel-Dehghanfar, Cecilia Ceccarelli (2019)
> !------------------------------------ outdir
> /output_directory/
> !------------------------------------ cloud and dust
> /directory/cloud_dust.in
> 1.0e-02                     ! Dust-to-gas mass ratio
> 3.0e+00                     ! density of grain [grcm-3]
> 3.5e+00                     ! lattice site's side [A]
> 1.0e-01  1.0e-01  const  1  ! grain radii [um] (min, max, const/MRN, nbins)
> 0                           ! Grain radius evolve with mantle: 1=yes, 0=no
> 1                           ! Binding energy evolution (1=yes, 0=no)
> 5         1                 ! ices: gso=1,bulk=2, ML=3, sur=4, xch=5 /
Nactsurlay
> !------------------------------------ species  :: (1=average BE ,2=all BE)
> 1        /directory/species.in
> !------------------------------------ reactions (gas, sur, phdiss) ::
0=no,sur=1,ice=2
> 1        /directory/reactions_gas.in
> 1        /directory/reactions_sur.in
> 0        /directory/reactions_sur_phdis.in
> !------------------------------------ self shielding :: (yes/no, evolve/not
file)
> 1   1    /directory/self_shielding_data.dat
> !------------------------------------ charge exchange   (Draine+Sulin1982)
> 1     1                  ! 0=none, 1=file  / electric potential  1=yes/ 0=not
> 6.30e+07   4.10e+08      ! grain assisted charge exchange, electron extraction
> /directory/reactions_charge_exchange.in
> !------------------------------------ ice processes
> 1        2      1      0    ! desorption (thermal,CR,photo,H2Ediss)
(0=nope,1=surface,2=ice)
> 1        0                  ! adsorption , crystalization
> 6        8      7      1    ! diffusion:  H, O, CO, the rest (including C and N,
H2):: 1=thformula, 2=tunsqr, 3=tuneck, 4=thform+tunsqr, 5=thform+tunEck,
6=tunfile_rates, 7=thfile_rate, 8=rate_constants
> 1        1                  ! H and CO thermal desorption (1=from file,
0=default (formula))    ! these are from JER work for ER21 and Witzel21
> 2.0e+00         2.0e+00     ! diffusion barrier width AA (square)    /
Ediff_bulk/Ediff_sur ratio
> 2                           ! 1=HH92, 2=competition(JER2021)
3=competition(GP2011)
> 3        4      2           ! (CO + H), (H2CO + H), and the rest of the
reactions  ::   1=square    2=eckart     3=file_rate   4=file_rateconst
> /directory/diffusion_rate_constants.dat
> /directory/Hdiffusion_rate_coeff.dat
> /directory/reaction_CO_H_desthdiff_rates.dat
> /directory/reactions_eckart.in
> /directory/reaction_COhyd_coeff.dat
> /directory/reaction_rate_constants.dat
> !------------------------------------ observing_tests
> 0       00.0      None
> !------------------------------------ species to write
> 0       /directory/species_to_write.in
```

FIGURE C.1: This figure shows a Grainoble+ input file example.

Reactions with the Eckart model: It lists the reactions that have Eckart potential parameters. In each line of this file, similar to the gas and surface reaction files, 3 reactants and 5 products are listed. It is followed by the potential barrier parameters: the forward and backward potentials V_f and V_r in K, and the imaginary frequency of the transition state, ω in cm^{-1} (see Tab. 4.6).

CO hydrogenation file: It lists the CO hydrogenation rate as a function of temperature from the quantum computational calculations reported in Witzel et al. submitted.

Reaction rate constants: It lists the rate constant parameters for selected reactions. The file now contains the formaldehyde hydrogenation parameters from Song and Kästner (2017).

C.3 Python front-end

Python front end contains various classes. The main interface is the *create_inputfiles* class in the *gplus.py* file. This class takes input parameters and files and calls the *writeinp* functions to read them and write the appropriate files for the Fortran core code. The written files are in a format compatible with the Fortran subroutines. Also, it looks for anomalies that might compromise the results, such as redundancies, missing information, or conservation of elements in each reaction. It has other advantages as well. For example, the user does not need to supply a separate file listing the species. The Python code creates the file by reading the reaction files. This method minimizes the blunders and human errors while creating or modifying input files. The user can write only a single set of inputs for one test using the *create_inputfiles* class or design and write a grid of models using *creates_grid*, which is in the same file. They can be called from the terminal or in a Jupyter notebook environment.

C.4 Main code's modules

As said in the introduction, the first step is to compile the code by calling make gfort in the terminal in the Fortran source code directory (where the *MakeFile* is). Then to run the code, one should call the input file with the executable in the terminal: ./gplus [/absolute or relative path directory/input file name].

The main code reads the input files, checks for inconsistencies, runs the code as in calculates the chemical abundance in the gas and the grain phase and finally writes the results in different files. Additionally, while it is running, it writes a log file detailing the progress of the run and the error or warning messages, if any, and informs the user of the run's success status. The code has exit strategies at every step. If an unavoidable error occurs, such as an incorrect input or if the conservation of the elements did not hold, the code exits the integration loop. It writes the results up to the stopped time index and informs the user about the error message in the log file. The following paragraphs briefly review the function of each Fortran file/module.

main The main module is the start and end of the program. It calls the subroutines in the other modules in the following order: (1) it calls the subroutine in *readinMod* that reads the commands and the name of the input parameter file from the terminal, reads the input parameter file and distributes the information in the *cloudMod*, *dustMod*, *speciesMod*, and *processesMod*.; (2) it calls the subroutine that assigns the integrator's parameters; (3) it calls the integrator's loop that calculates the chemical abundances as a function of time; and (4) it calls the *writeMod* subroutines to write the results in the result's directory and deallocate the memories.

readinMod This module contains the subroutines that read the terminal commands and the main input file, create the results main folder and subfolders, and initiate the log file. It distributes the file directories and parameters to the other modules *cloudMod*, *dustMod*, *speciesMod*, and the *processMod*. This module can only communicate with one single subroutine in each module.

cloudMod This module keeps the information and subroutines related to the system's physical condition. This module reads the cloud profiles file and creates the *environment* object and a list of *cloud* objects inside the *environment* object. Each *cloud* object is populated with physical properties listed in the file. The length of the *cloud* objects array is equal to the size of the listed time in the physical profile file.

dustMod This module keeps the information and subroutines about the dust, the grains, and the ice mantle. It contains the classes *dust*, *grain*, and *layer*. The module populates these classes with the input parameters and creates a *dust* object that contains an array of *grain* objects, and each *grain* object contains an array of *layer* objects. The number of *grain* objects depends on the model choice in the input file. Each *grain* is treated independently in the model. If, for example, the MRN model is chosen with 10 bins, it calculates the grain abundance in each bin and creates 10 *grain* objects.

speciesMod This module keeps the information and subroutines about all the species in the model. It contains three classes: *species_list*, *species*, and *element*. Each element object stores the elemental abundances as a function of time during the program. The abundance is calculated as the sum of the elements in various molecules. It is a way to check for the conservation of the elements through the program. Each species in the model is an object of the *species* class. The *species_list* stores an array of all the *species* objects. The information stored in each object is, for example, its category, gaseous or solid, binding energy, and diffusion rate constants. As said in the previous section, the code does not require the user to list all the solid species. If a process involves solid species (e. g., accretion) in the input file, it automatically creates solid species. Each object stores the input information and the abundances and rates calculated in the program. If the species is solid, the species create a list of *grain* objects, the length of which is equal to the size of the grains array in the *dust* object and stores the abundances and rates relevant to each grain bin in that grain object. This module also contains other relevant functions that, for example, calculate the vibrational frequency or the thermal velocity of a species.

processesMod This module keeps the information and subroutines on all the processes and reactions. It contains *processes*, *reaction*, *development*, and *self-shielding* classes.

If self-shielding process is chosen in the input parameter file, this module creates an object from the *self-shielding* class that stores the input parameters for H_2 and CO self-shielding. Aside from the *self-shielding* class, the subroutines in this module can be divided into two groups. (1) Reading reaction files and creating arrays of *reaction* objects for each file and (2) reading the input parameter file and create arrays *development* objects for each process. The former reads the reactions and their rate constants and other properties from the input reaction files. If a reaction involves solid species, it creates an array of *grain* objects (with the length equal to the number of grain bins) for that reaction and stores the abundances and rates on each of the grains separately. For a uni-molecular process that does not have reaction rate constants, such as adsorption or desorption, the *developement* class is used. This module reads the options in the input parameter file and creates the process for every species. The advantage of this automation is minimizing human error and reducing the number of input

files. The *developement* class is similar to the *reaction* class. All the arrays above are stored in the *processes_list* object to facilitate the use.

odeMod This module serves two purposes: (1) It stores the parameters used by the integrator, DLSODES (Tab. C.1), and (2) checks the integrator's output ISTATUS. In summary, the DLSODES subroutine requires from the user the size of the array, neq, an array of the initial variables, Y(neq), The function, F(neq), the Jacobian matrix, PDJ(neq,neq), and the time steps at which the outputs are saved. The function that the user should provide calculates the left-hand side of the rate equation and the Jacobian matrix, in our case (see the DLSODES documentation for more information). The *check_ode_output* subroutine checks the integrator's output messages such as the ISTATUS and RWORK and takes action accordingly. For example, if necessary, it increases the absolute or relative tolerances or reset the integration to an earlier step and starts with a smaller time step.

kprMod This module contains the subroutine and functions that calculate the reaction and processes rate coefficients. It also updates the binding energies if the option was used (see, Chap. 4).

rateMod This module contains the subroutines that calculate the rates and the elements of the Jacobian matrix. The DLSODES subroutine calls this module's rate equation function, F(neq) at each iteration.

evolMod This module contains a diverse set of subroutines developed for different tasks.

The neq variable: The *assign_eqidx* subroutine calculates the neq variable for the DLSODES. neq is the size of the variables array in the integrator which is usually equal to the number of species plus three more that are the neutral and charged grains. But if the model is using the multi-grain mode, this number is increased. The general formula is

$$\text{neq} = n_{\text{gas sp.}} + n_e + n_{\text{grain bins}} \times \left(n_{\text{solid sp.}} + 3\right) \ . \tag{C.1}$$

If the bulk chemistry option is used, the number of solid species is multiplied by two to account for species in bulk. Each species or grain saves their index in this array in their respective objects for internal use.

Intermediate checks: At each iteration, the code checks the mantle formation rate in the *check_conditions* subroutine and calculates the length of the next step in the *set_reset_step* subroutine.

Mantle evolution: After the intermediate checks, the program calls the *build_mantle* subroutine to update variables related to the ice mantle: the surface and the bulk parameters.

Updating and saving parameters: The parameters that evolve in time and are ultimately saved in each object are stored in two fashions: in a non-array type and an array type variable. The non-array (floating) variable is updated inside the time loop and is stored in the array type variable at time indices listed from the input. The *init_floating_variables* and *update_floating_variables* subroutines initiate and update the non-array variables and *save_parameters* and *save_proc* subroutines save the variable in the array type ones.

Each time the *update_floating_variables* subroutine is called, it checks the conservation of elements. It calculates the fractional difference between the elements abundance and its initial value,

$$\delta_i = \frac{|n^i_{\text{elem}_\text{i}} - n^0_{\text{elem}_\text{i}}|}{n^0_{\text{elem}_\text{i}}}, \tag{C.2}$$

TABLE C.1: The odeMod module parameters.

parameters	description *
rateacc, kacc, Yacc	accuracy of the variables: rate (rateacc=10^{-40}), rate coefficient (kacc=10^{-40}) and abundances (Yacc=10^{-25})
thebase, thejump, thewalk	the timein, and timeout variables of DLSODES that are provided by user. Thewalk is used for smaller time steps in the integrator if needed.
neq	The number of rate equations, the size of the initial values array.
Y(neq)	Initial values for the integrator. DLSODES uses the same array for its output
F(neq)	$\mathrm{d}n/\mathrm{d}t$, the left hand side of the rate equation.
PDJ(neq,neq)	The Jacobian matrix $\left[\partial \frac{\mathrm{d}n_i}{\mathrm{d}t} / \partial n_j\right]_{neq,neq}$
MF	$= 121$, The method used to calculate the Jacobian. Here we chose to supply a full Jacobian.
ATOLini	$= 10^{-20}$, The initial value of the absolute error tolerance.
ITOL	$= 4$, The choice of the weighted error formula in DLSODES.
RTOL(neq)	$= 10^{-4}$, The relative error tolerance.
ATOL(neq)	$= 10^{-20}$, The absolute error tolerance.
ITASK	$= 1$, Normal computation of the output at timeout.
ISTATE	The state of success or failure of the integration.
IOPT	$= 1$, If the optional outputs in RWORK and IWORK are used
LRW	Length of RWORK array which has to be long enough for DLSODES internal use. Here, it is $10 \times (20 + 9NEQ + 2000NEQ)$.
RWORK(LRW)	It is a REAL variable array. the Memory allocated to DLSODES to use for integration and sending messages in and out. The user can use this array to tweak some parameters in DLSODES.
LIW	$= 30$ The length of IWORK array.
IWORK(LIW)	It is a INTEGER variable array. The memory allocated to DLSODES to use for integration and sending messages in and out. The user can use this array to tweak some parameters in DLSODES. For example, the number of attempted steps on each call $IWORK(6) = 1000$, or the number of messages written in the terminal: $IWORK(7) = 1$.
IA(neq), JA(neq,neq), nz	If band Jacobian is used, DLSODES uses these variables to send the location and the number of non-zero elements of the Jacobian matrix to the integrator.

(∗) See the documentation of DLSODE and DLSODES in the ODEPACK for an extended description of each parameter.

for each element. If δ_i becomes larger than 10^{-10}, the program exits the iteration and the run is rendered unsuccessful.

writeoutMod It contains the subroutines to write the results files. Additionally, it deallocates all the arrays and writes the concluding messages in the log file and on the terminal.

constantsMod This module contains a collection of physical constants and basic subroutines and functions, such as the reduced mass function or array sort subroutine. They are accessible to all the other modules.

C.5 Results' files

After each run is complete, a series of files are written in the results directory. The files contain physical parameters used in the model, such as the grain density or the initial elemental abundances, and the abundances and rates as a function of time calculated in the model. The following paragraphs briefly review the list.

General information Three files provide general information about the model: The *res_inpar.in* file is a copy of the input file used for this run. The *geninfo.out* file contains basic information about the input options. The *log.out* file contains the progress and error messages. The latter is continuously updated while the program is running. In the end, if the run is successful, the file is renamed to *log_successful.out*; otherwise, to *log_unsuccessful.out*.

The physical parameters The *cloud.out* file contains the time and the physical parameters, density [cm^{-3}], visual extinction [mag], the gas temperature [K], CR ionization rate [s^{-1}], external irradiation scaling factor [Habing unit], and the flux of secondary UV photons [$cm^{-2}s^{-1}$] at each time.

The dust parameters The parameters such as the gas to dust mass ratio and the lattice site side are written in the *dust.out* file. The information about each grain bin is written in two files in the *grains* subfolder of the results. The files are subscripted with the grain bin ID number that runs from 1 to the total number of grain bins indicated in the input parameter file. The *grain_*.out* file(s) contains, for example, the number of layers or the grain radius evolution as a function of time. On the other hand, the *grain_abund_*.out* file(s) contains the abundance, and the formation and destruction rates of neutral, positively charged, and negatively charged grains.

The species parameters The *species.out* file contains the species list in the model. Each line lists the species name, category, charge, mass, initial and final abundances, sticking coefficient, binding energy, diffusion to desorption ratios on the surface and in bulk, species assigned an ID number, and its list of elements. If multi-grain mode is used, the final abundance of a solid species is the total sum of the abundances in all the grain bins.

The rest of the information is written in various files in the *species* subfolder. For example, a file in the *species* subfolder that is named *X.out* lists the following species: X, X^-, X^+, and their solid counterparts. For each species, the species number, category, the grain bin number, the abundances, the formation and destruction rates, and the binding energy (if relevant) as a function of time are written. The grain bin number for gaseous species is 0 in this file.

The elements parameters The *elements.out* file list the elemental abundances in the gas phase and on ices as a function of time for each element. An element's abundance at a given time is the sum over the abundances of species containing that element. The file also lists the time evolution of the system's positive and negative charges, summed over all the positively or negatively charged species.

The processes Each category of processes is written in a different file in the *processes* subfolders, such as the gas-phase, grain surface, and photodissociation reaction files and adsorption, and thermal, chemical, CR-, and photo- desorptions files. Each file lists the reaction's rate and rate coefficient as a function of time. If the reaction was on grain, the grain bin number and the reaction efficiency as a function of time are also listed. If the bulk chemistry option was used, the surface reaction file also writes the rates, the rate coefficients, and the reaction rate efficiency in the bulk as a function of time.

C.6 Python back-end

The python backend is designed to read the output files and plot the interesting information. The backend usually uses a Jupyter notebook as its interface. It calls the *setitup* function in the *readres.py* file to create python objects of the information in the files using the *readres* class. The structure of the class is very similar to the class structure used in the Fortran core code. The reason for using this method is that it facilitates the plotting routine, especially when a grid of models is considered.

The list of available plotting functions for a single model or for a combined set of models are:

- Abundances of selected species as a function of time or other physical parameters (e. g., visual extinction), over plotted with the observed abundances if provided.
- The number of layers as a function of time or other parameters.
- The abundance of solid species as a function of time and layer numbers, in other words, the ice layers.
- Animation of ice formation or sublimation.
- The reaction rates and rate coefficients for selected species as a function of time.
- The elemental budget distribution as a function of time or other physical parameters.
- The numerical accuracy on the total elemental budget as a function of time.
- Benchmarking plots to compare with the previous version, Grainoble.

Appendix D

The Labice algorithm and code

Labice is an experimental chemistry model aiming at simulating and reproducing the TPD (Temperature Programmed Desorption) experiments. It models a layered ice structure and keeps track of each layer's composition during the simulation.

The structure and the disciplines in Labice are similar to Grainoble+ in almost every way. It is similarly modular and can easily be upgraded with new processes. It tries to minimize possible mistakes from the inputs or during the program. The model follows the rate equation approach to solve stiff first-order ordinary differential equations. The entire Labice code is implemented in Python 3.8.8. The code calls the odeint integrator from the scipy.integrate python package, which uses ISODA from the Fortan odepack (Hindmarsh, 1983).

The code is smaller than Grainoble+ and contains only one file with the main functions and an interface function that takes the input parameters and files. The input files are usually a binding energy file, a file listing the TPD experiments, and the TPD experiment results. It considers only two processes at the moment, thermal desorption and crystallization. The number of species often does not exceed 3. Therefore, adding more processes will not make the model much more complex. The model starts with an ice slab; either the layers are built from a specific instruction from the inputs or constructed randomly from a given bulk ratio. On the other hand, Grainoble+ starts with a bare grain, and ice is built through the adsorption of gaseous molecules.

The following sections present a brief description of how the code works (§ D.1), the interface and the keywords used to create a simulation (§ D.2), what the input and output files and plots are (§ D.3), and the role of each function (§ D.4).

D.1 How does Labice work?

The first steps to start Labice is to select the data and binding energy files, set up the structure and composition of the ice slab, the temperature range and the heating rate, and the list of processes involved. The user can set up a single simulation or create a grid of models, if desired.

The composition of the layers can be declared specifically for each layer or only a bulk ratio can be declared. In the latter case, the composition is randomly distributed over the layers by calling the *make_struc* function. The interface function takes the input parameters and files in the Jupyter notebook. It calls the main code, *labice*, and distributes the information and constructs objects from the subclasses, which are the *environment*, the *ice* and its *layer*(s), the *species*, and *process*(es). The processes are thermal desorption and crystalization. Thermal desorption only concerns the surface layers, while crystallization takes place on the entire ice slab.

The program then starts the TPD simulation by calling the *odeint* integrator in each iteration to calculate the abundance evolution as a function of time. Similar to Grainoble+, the iteration steps are calculated inside the code. It is such that the simulation can follow the

sublimation layer by layer. Each iteration saves the layer structure and the sublimated material. At the end, if the goal of that simulation was to compare with a specific experiment, the code also calculates the reduced χ^2. Finally, it keeps the results in a pickled[1] format in the specified path directory and plots the desorption rates and abundances using the prebuilt functions inside the program.

D.2 Python interface

The interface is a function that can be executed in a Jupyter notebook or on the terminal. It creates an object from the *Labice* class. In other words, each simulation is an object from the *Labice* class. The interface distributes the path directories and the input parameters in the *Labice* functions. Fig. D.1 shows a screenshot of an example interface function in a Jupyter environment. The keywords used to create a simulation are as follows:

a) *inpdir:* The directory path[2] of the input and data files.

b) *resdir:* The results path directory.

c) *Tbeg:* The starting temperature.

d) *Tend:* The final temperature.

e) *beta:* The heating rate, $\beta = \mathrm{d}T/\mathrm{d}t$.

f) *nlay:* The number of layers in the ice slab.

g) *A:* The size of a lattice site (binding site) to calculate the vibrational frequency, if necessary.

h) *cold_finger:* The constituent of the sample holder.

i) *take_sub:* The option to differentiate the binding energies relative to the substrate.

j) *struc:* The layer structure of the simulated ice.

k) *fill:* The option to fill the empty and unspecified layer fractions with a certain species.

l) *fill_where:* There option to *fill* all the unspecified fractions or to fill all but the top layer and leave it exactly as specified in *struc*.

m) *sur:* The multi-binding energy option.

n) *enfilename:* The binding energies file name.

o) *prlists:* The list of the processes in the simulation which are currently thermal desorption (*desth*) and crystallization (*cryst*).

[1] See the documentation here: https://docs.python.org/3/library/pickle.html .
[2] The directory paths can be absolute or relative.

```python
def setup(_struc=None,_nl=None,_suff='',_beta=None,_exp=None,resdir=None):
    """
    #information needs to be [Tbeg,beta,Tend] or [Tbeg,beta,yrend], or
    [Tbeg,Tend,Yrend]  #(and if you give all the four, i will take it as
    the priority listed above.)
    #mult,ave,1st # desth,codes_1/4,cryst,reaction,bulk, cal/exp
    #energies_2020_exp_v2,energies_2020_kida,energies_2020_exp_v3_Fran
    #int/ode
    """
    inpdir='/Directory/SIRC/insrc/'                          #inpute data
    if(resdir is None): resdir='/Directory/SIRC/Results/'    # results

    ld=labice(inpdir=inpdir,resdir=resdir,pom=False,suffidx=_suff)   #initiation

    ld.set_env(Tbeg=10.,Tend=200.,beta=0.1,yrend=None)   #the temprature setup
    #the keywords of the ice structure
    ld.set_ice(profile='cloud',\
               ngr=1,A=3.16, finger='H2O',graingrowth='no',Ebcovdep='no',\
               take_sub=False,\
               nlay={1:3},
               struc={1:{2:[['CO',.5]],3:[['CO',.5]]},{1:{2:[['D2O',.5]],\
                                        3:[['D2O',.5]]}},\
               fill=None,fill_where='body')
    # binding energies and processes
    ld.set_species_processes(enfilename='energies_2020_exp_v2.in',\
                             filetype='exp',sur='1st',\
                            prlist=['desth','cryst'])

    ld.run(method='ode') #the integration

    ld.post_analysis(exp=_exp) #calculating chi2s
    pickle.dump(ld,open(ld.pickle_filename,'wb')) #saving the run

    plot(which=['abund','rate','des']) #plotting

    return ld
```

FIGURE D.1: This figure shows a screenshot of an example Labice interface.

D.3 The input and output files and plots

The first file the code requires contains the binding energies of the listed species. Additionally, suppose a simulation was to compare with specific experiments. In that case, the code needs a file listing those experiments and files containing the experimental data: the temperature and the desorption rates.

The following paragraphs briefly review the structure of the input files, how the simulation outputs are stored, and the plotting routine.

The binding energies file This file contains the list of binding energies of various species from experiments. If the information is available, each species additionally list the prefactor, the substance of the substrate, and the diffusion energy and its prefactor. If multi-binding energies are listed, the fractional distribution of the binding energies should be listed as well.

The TPD experiments files The TPD experiments need to be listed in a "master" file. The required information for each experiment are: the constituents, the bulk ratio, the heating rate, and the path directory of the experiment's data. Each data file usually contains the desorption rate of the species in the experiment as a function of temperature.

Results' files Each test is an object of the *Labice* class and is stored in the listed path directory in a pickled format. Pickling is chosen over text file writing for convenience. A pickle is a binary file and occupies less memory than text files. Additionally, since the code from start to finish is implemented in python, if the results need to be reviewed or plotted again, python can quickly reopen the pickle files and use them.

Plotting The plotting functions can be called in tandem with a simulation or not. If they are called separately, they can read the pickled files. The second option is useful when running a grid of models. The list of available plotting functions for a single model or a combined set of models are:

- Abundance of selected species as a function of temperature or time.
- The ice layers composition.
- The desorption rates as a function of temperature or time, over plotted with the experimental results.
- The reaction rates and rate coefficients for selected species as a function of temperature or time.

D.4 The functions

The following paragraphs briefly review the functions in the order they are called.

make_structure This function creates a random layer structure. It reads the number of layers, the budget ratio between the species in the ice, and the stochasticity level. It then creates the ice layers by randomly distributing the budget of the constituents over the layers. The ratio between the species in the layers follows a uniform distribution, while the total budget is fixed. The layer structure is returned in a dictionary format readable by the *struc* keyword in the *set_ice* function. This function should be called before initiating the *Labice* class, if the user decides to construct an ice slab with a random species distribution over the layers.

__init__ This function initiates an object from the Labice class and creates the result path directories. The *Labice* class has a few subclasses initiated at the start of the program, *env*, *dust*, and *grain* with an array of *layer*(s), *species* that has an array of *layer*(s), *process*, and *ode*.

set_env This function sets up the systems starting and ending temperatures with a given heating rate, $\beta = \mathrm{d}T/\mathrm{d}t$. The information is saved in an *env* object.

set_ice This function sets up the ice and its layer structure by taking into account the input parameters and options. It also updates the layer composition at each iteration. This function initiates the dust, grain, and layer objects. The dust and the grain objects keep a general information about the cold finger and other internal variables. The grain object contains an array of layers (as objects) and constructs the layers using the *struc*, *fill*, and *fill_where* variables.

set_species_processes This function sets the information about the species and the processes. First, it reads the binding energies file and stores the information in a dictionary. The names, binding energies, substrates, total budget, layer structure, cold finger's substance, and list of processes are required to initiate a species object. The function also sets up the processes and initiates the integrator's internal parameters. Each species or process object also store the abundances and rates at each iteration.

run This function calculates the chemical evolution of the system using the numerical integrator *odeint*. At each iteration, it calculated the rates and the Jacobian, calls the integrator, updates the ice layer composition, and saves the abundances in the arrays.

post_analysis If the simulation is multi-component and one of them is water, it calculates the trapped fraction by calculating the co-desorbed fractions. Additionally, if an experiment's desorption data were listed in the inputs, this function calculates the reduced χ^2.

Appendix E

Résumé en français

abstrait

Jusqu'à présent, la Terre est la seule planète connue hébergeant la vie, basée sur la chimie organique. Les petits objets du système solaire (par exemple, les comètes et les astéroïdes) sont enrichis en composés organiques, ce qui soulève la question de savoir si les premières étapes de la chimie organique qui ont conduit à la vie terrestre ont commencé pendant la formation du système solaire. Les étoiles et les systèmes planétaires comme notre système solaire se forment en permanence dans la Voie lactée. Ainsi, en principe, nous pouvons étudier la chimie dans ces objets pour récupérer les premières étapes de la chimie organique du jeune système solaire. Dans cette thèse, j'ai travaillé sur deux objectifs principaux, la modélisation de l'évolution chimique dans les régions de formation d'étoiles avec Grainoble+ et la modélisation des glaces formées dans un montage expérimental avec Labice.

Le premier objectif de la thèse se concentre sur les processus chimiques qui forment et détruisent les molécules organiques complexes interstellaires (alias iCOM) en phase gazeuse et sur les surfaces des grains dans les régions de formation d'étoiles de type solaire. Pour cela, j'ai développé un code d'astrochimie, Grainoble+. Le modèle est basé sur une version antérieure, Grainoble (Taquet et al., 2012). Grainoble+ est un code astrochimique multigrain triphasé gaz-grain utilisant les dernières valeurs d'énergies de liaison et de vitesse de diffusion et de réaction issues de calculs de chimie quantique. J'ai suivi deux objectifs avec Grainoble+ : modéliser la formation d'iCOMs dans les régions choquées de NGC 1333 IRAS 4A (De Simone et al., 2020) et modéliser la composition de la glace dans les Taurus MCs (Witzel et al. 2022, soumis.).

Le deuxième objectif de la thèse est de simuler la structure en couches des glaces telle que réalisée dans des expériences de laboratoire et de simuler la désorption thermique des espèces en se basant sur les techniques de Désorption Programmée en Température (TPD). Dans ce but, j'ai développé Labice, un modèle qui simule les expériences TPD avec l'approche d'équation de taux. Labice est une version plus simple de Grainoble+ qui utilise l'approche triphasée pour modéliser la glace et la désorption thermique pour une configuration expérimentale donnée. Avec ce modèle, je peux montrer l'impact des différents paramètres, tels que l'énergie multi-liaison ou l'effet de piégeage de la glace d'eau ; paramètres qui seront utilisés dans les modèles astrochimiques. En particulier, j'ai modélisé l'impact de l'approche énergétique multi-liaison sur la sublimation des espèces (Ferrero et al., 2020) et modélisé et étalonné les glaces composites eau et CO en utilisant la fraction CO piégée (Witzel et al. 2022, en préparation).

Objectif de la thèse

Dans cette thèse, je me suis concentré sur la modélisation (1) de l'évolution chimique dans les régions de formation d'étoiles de type solaire et (2) de la glace cultivée en laboratoire, en

particulier dans les expériences de désorption programmée en température (TPD).

La première étape de l'évolution chimique commence par la chimie dans les nuages moléculaires (MC). Dans les températures froides des MC ($\sim 10 - 20$ K), les espèces finissent par geler sur les manteaux de glace des grains. Les espèces congelées peuvent être sublimées dans la phase gazeuse dans les derniers stades de la formation d'étoiles, enrichir la phase gazeuse avec des molécules et déclencher la formation de molécules plus complexes dans la phase gazeuse. Il est évident que comprendre **comment s'est formé le manteau de glace est la première question à se poser et la première étape à modéliser**. Le Chap. 6 tente de répondre à cette question en utilisant le modèle astrochimique Graionble+ (Chap. 4) que j'ai recodé et réimplémenté. Les régions choquées le long des écoulements sont peut-être le meilleur endroit pour examiner l'une des principales questions en astrochimie : *La chimie organique est-elle née de réactions de surface sur des manteaux de grains ou de réactions en phase gazeuse ?* Grâce aux observations les plus récentes, j'ai eu l'opportunité de modéliser la chimie dans la région choquée des écoulements NGC1333 IRAS 4A (Chap. 5).

La modélisation astrochimique est une recherche interdisciplinaire, la pièce maîtresse du puzzle entre la chimie théorique et expérimentale et les observations. L'astrochimie de laboratoire mène des expériences sur des analogues de glace interstellaire dans des conditions de type interstellaire (basses températures et faibles densités). La modélisation des glaces expérimentales a commencé comme un module de Grainoble+ jusqu'à ce qu'il devienne un package autonome nommé Labice. J'ai utilisé le même formalisme pour être auto-cohérent avec Grainoble+ pour dériver les paramètres physiques des résultats expérimentaux, comme les énergies de liaison, que les codes astrochimiques utiliseront ensuite (Chap. 7).

Des expériences et des observations ont montré que les glaces d'eau peuvent piéger des espèces volatiles même dans les régions chaudes ($30 < T < 100$ K). L'effet de piégeage de l'eau impacte fortement l'évolution chimique dans les régions protostellaires. J'ai réalisé différentes simulations pour modéliser la fraction piégée dans des mélanges de glace CO et H_2O dans le but de mieux comprendre les glaces en montage expérimental (Chap. 8).

La glace interstellaire dans les régions froides (100 K) a une nature amorphe avec une surface potentielle irrégulière qui crée de nombreux sites de liaison différents pour les espèces solides. La prise en compte de la distribution énergétique multi-liaison des espèces solides dans les modèles astrochimiques va fortement affecter l'évolution chimique, ce que je montre au Chap. 9 avec le modèle de Labice.

Structure de la thèse

Cette thèse débute par trois chapitres introductifs. Une courte description de la formation des étoiles se trouve au Chap. 1. Ce chapitre donne un bref aperçu de l'évolution chimique et physique dans les régions de formation d'étoiles de faible masse. Le chapitre 2 se concentre sur les modèles astrochimiques de la littérature qui ont été utilisés pour simuler les conditions chimiques dans les régions de formation d'étoiles. Le chapitre 3 décrit les dernières avancées en chimie computationnelle et expérimentale quantique qui ont été incluses dans Grainoble+. Ce chapitre détaille divers travaux portant sur les calculs de vitesse de réaction et d'énergie de liaison et les expériences TPD.

Le chap. 4 décrit le modèle que j'ai développé au cours de ma thèse, Grainoble+. Je passe en revue l'algorithme et l'analyse comparative du modèle dans Apx. C et Apx. A, respectivement. Les applications de Grainoble+ sont présentées aux Chap. 5 et Chap. 6. La première application du modèle est utilisée dans De Simone et al. (2020) pour modéliser le rapport méthanol gazeux sur acétaldéhyde observé dans les écoulements NGC 1333 IRAS 4A. La deuxième application (Witzel et al. 2022 soumis) utilise les derniers calculs de taux de réaction et d'énergie de liaison et les conditions physiques à partir d'observations pour simuler la formation de glaces dans le TMC1 à une extinction visuelle de 20 magnitudes.

Le chapitre 7 explique le package Labice que j'ai développé pour modéliser les résultats d'expériences de laboratoire d'astrochimie, en particulier les expériences TPD. Son algorithme et ses applications sont présentés dans Apx. D et Chap. 8 et 9. Sa première application (au chap. 8) est de comparer simulations et expériences en simulant la fraction de CO piégé dans les expériences TPD listées dans Kruczkiewicz et al 2022 (en prép). Sa deuxième application est utilisée dans Ferrero et al. (2020), où nous avons simulé un simple analogue de glace avec un mélange d'eau et de méthanol pour examiner l'impact des simulations d'énergie à liaisons multiples dans les modèles astrochimiques et comparé les résultats avec des simulations d'énergie à liaison unique.

Enfin, le Chap. 10 conclut les résultats de ce travail et discute des perspectives futures.

Applications de Garinoble+

Application I : Molécules organiques complexes interstellaires dans les NGC 1333 IRAS 4A outflows

Contexte Il existe deux voies de formation proposées pour les molécules organiques complexes interstellaires (iCOM): formation sur le manteau de glace et sublimation directe, ou formation par des réactions en phase gazeuse après que les espèces parentales se sont sublimées à partir des glaces. Les régions choquées le long des sorties de protoétoiles de faible masse fournissent un environnement unique pour étudier et examiner cette hypothèse car l'âge cinétique d'une région choquée peut fournir une contrainte supplémentaire, la dépendance temporelle, sur les prédictions du modèle. Ce type d'étude sur les iCOM observés dans les régions choquées n'a été réalisé que pour les sorties L1157-B1 (Codella et al., 2017). Pour comprendre si le cas de L1157-B1 est unique, nous avons imagé et étudié les écoulements IRAS 4A dans la région de formation d'étoiles NGC 1333.

La source IRAS 4A IRAS 4A fait partie des systèmes multiples IRAS 4 situés à 299 $\pm$ 15 pc de distance dans la région NGC 1333 du complexe de Persée (Tab. 2). C'est un système binaire avec deux corinos chauds de classe 0, 4A1 et 4A2, séparés par 1.″8. Trois lobes de sortie émanent du système binaire. L'écoulement sud-est (SE) est entraîné par l'IRAS 4A1, tandis que ceux du nord (N) et du sud-ouest (SW) proviennent de 4A2 (Fig. 1 et 2).

La méthodologie et les résultats des observations Pour imager les écoulements bipolaires à grande échelle entraînés par le système binaire IRAS 4A, nous avons utilisé l'interféromètre NOrthern Extended Millimeter Array (NOEMA) dans la bande de 3 mm (Tab. 1). Nous rapportons pour la première fois la détection de plusieurs iCOMs dans les écoulements de IRAS 4A1 et IRAS 4A2 : six lignes de méthanol (CH_3OH), huit d'acétaldéhyde (CH_3CHO), une de formamide (NH_2CHO) et quatre d'éther diméthylique (CH_3OCH_3). Leurs densités de colonnes calculées sont reportées dans le Tab. 4. Nous avons trouvé une différence chimique significative entre les écoulements. Le rapport méthanol/acétaldéhyde, CH_3OH/CH_3CHO, dans les lobes SE et N est relativement bas (8 -20), tandis que le lobe SW montre un rapport de $\sim$ 44.

Modélisation astrochimique Pour reproduire les observations et comprendre la différence dans le rapport CH_3OH/CH_3CHO observé, nous avons exécuté une série de modèles avec Grainoble+. Notre modèle suppose que le méthanol se forme dans les manteaux de glace et est sublimé directement à partir des grains dans les régions choquées. Nous avons discuté de deux voies de formation possibles pour l'acétaldéhyde, la formation sur les surfaces de glace par la réaction radicalaire CH_3 + HCO et la sublimation directe dans la phase gazeuse

et la formation par réaction en phase gazeuse CH_3CH_2 + O , où le radical éthyle, CH_3CH_2, est injecté à partir des glaces.

Pour simuler le passage d'un choc dans IRAS 4A, nous avons utilisé le mode phase gazeuse de GRAINOBLE+. Les simulations suivent deux étapes : (1) l'étape de pré-choc : une phase gazeuse moléculaire froide avec une densité de noyaux H de 2×10^4 cm^{-3} et à 10 K ; et (2) la phase de choc : une phase gazeuse post-choc où la densité et la température grimpent à 2×10^6 cm^{-3} et 70 K d'après les observations. Le taux d'ionisation CR de H_2 dans les deux étapes est $\zeta_{H_2} = 3 \times 10^{-16}$ s^{-1} en analogie avec la région choquée L1157-B1. La deuxième étape hérite de la composition chimique en phase gazeuse de l'étape précédente. Notre modèle suppose une pulvérisation de grains au début de la deuxième étape, qui infuse la phase gazeuse avec la composition du manteau de glace (Tab. 5). Tout d'abord, nous avons exécuté une grille de 169 modèles faisant varier les abondances infusées de méthanol et de CH_3CH_2 entre $4 \times 10^{-8} - 4 \times 10^{-6}$ et $4 \times 10^{-9} - 4 \times 10^{-7}$, respectivement (toutes les abondances dans nos modèles sont relatives aux noyaux d'hydrogène). La figure 5 montre le graphique de contour du rapport méthanol sur acétaldéhyde en fonction des abondances infusées de méthanol et de radical éthyle à 1000 ans après le passage du choc. Dans un second temps, nous avons étudié l'influence de la densité et du taux d'ionisation CR sur le rapport en fonction du temps. Nous avons choisi un modèle de l'étape de modélisation précédente qui reproduisait le rapport CH_3OH/CH_3CHO à 1000 ans dans les trois lobes, SW, N et SE. Dans ce modèle, les abondances de radicaux méthanol et éthyle sont respectivement de 3×10^{-6} et 3×10^{-7}. Nous avons exécuté deux modèles supplémentaires faisant varier la densité et ζ_{H_2} à 2×10^5 cm^{-3} et 3×10^{-17} s^{-1}, respectivement par rapport au modèle choisi dans cette étape. La figure 6 montre les abondances et les ratios des trois modèles en fonction du temps après le passage du choc. L'abondance de méthanol n'a pas été affectée par les changements de densité et de ζ_{H_2} et reste constante jusqu'à $\sim 2 \times 10^3$ ans. La formation d'acétaldéhyde après le passage du choc diminue en abaissant la densité due à l'augmentation des réactions avec les ions. ζ_{H_2} n'affecte pas l'acétaldéhyde dans les premières années. Enfin, nous avons exécuté un modèle en supposant que l'acétaldéhyde est synthétisé sur des glaces et éjecté directement dans la phase gazeuse par le passage du choc. L'abondance d'acétaldéhyde dans les premières années ne change pas, comme pour le méthanol, ce qui montre que la différence entre les hypothèses de synthèse de grain ou de gaz dans nos modèles n'est que dans les 200 premières années après le passage du choc.

Conclusions Après L1157-B1, l'écoulement IRAS 4A est maintenant le deuxième à montrer une complexité chimique évidente. Quatre iCOM ont été observés le long des sorties IRAS 4A dans cette étude. L'éther diméthylique et le formamide semblent concentrés dans une tache d'interface apparente entre les écoulements 4A1 et 4A2. En revanche, le méthanol est répandu, tandis que l'acétaldéhyde est le plus brillant dans les lobes sud. Le rapport méthanol sur acétaldéhyde dans SE (associé à l'écoulement 4A1) est $\sim$ 2 fois plus grand que SW et N (associé à 4A2).

Nous avons exécuté divers cas avec Grainoble+ et reproduit le rapport méthanol/acétaldéhyde observé en supposant que le méthanol est synthétisé sur des glaces et directement sublimé au passage du choc, et que l'acétaldéhyde est produit via la réaction en phase gazeuse CH_3CH_2 + O. De plus, la différenciation chimique entre les deux écoulements suggère que l'écoulement IRAS 4A1 est probablement plus jeune que l'IRAS 4A2. Une enquête plus approfondie est nécessaire pour limiter l'âge de l'écoulement. De plus, des observations de chocs encore plus récents sont nécessaires pour confirmer et étayer notre conclusion. Il serait également intéressant d'observer CH_3CH_2 pour contraindre le mécanisme de formation de l'acétaldéhyde, mais étant donné que ses fréquences sont inconnues, de futures études spectroscopiques sur cette espèce sont nécessaires. Le rapport observé des sorties L1157 B1 (130–250) est supérieur aux sorties IRAS 4A, ce qui pourrait être dû à la différence de composition chimique ou à

l'âge cinétique de la sortie. Une différence de rapport similaire peut être observée lors de la comparaison des sources de classe 0 et de classe I, ce qui pourrait indiquer une différence de composition chimique entre ces sources et les écoulements IRAS 4A (Fig. 7).

Application II : Formation du manteau de glace interstellaire dans les nuages moléculaires

Context Comment les nuages moléculaires (MC) se forment à partir des neutres plus diffus, et en particulier des milieux neutres froids (CNM), et combien de temps vivent les MC sont des questions qui ont été discutées pendant des décennies. Les observations des raies moléculaires et des modèles théoriques hydrodynamiques/magnéto-hydrodynamiques montrent que les MC peuvent se former de différentes manières aboutissant à des masses, des densités et des tailles différentes.

Observations vers TMC1 Nous utiliserons les observations vers la région du Taurus Molecular Cloud (TMC) appelée TMC1, un nuage sombre très bien étudié (e.g. Fuente et al., 2019) avec une extinction visuelle d'environ 20–25 mag.

Les modèles de composition chimique de TMC1 tendent à suggérer qu'il s'agit d'un MC relativement jeune, l'âge de TMC1-CP étant estimé à environ 10^5 ans (Agúndez and Wakelam, 2013; Howe et al., 1996; Ruaud et al., 2016).

Les espèces porteuses d'O et de C en phase solide les plus abondantes observées vers TMC sont H_2O, CO, CO_2 et CH_3OH (Boogert et al., 2015). Boogert et al., 2015 rapporte également une compilation des densités de colonne de solides H_2O, CO, CO_2 et CH_3OH en fonction de A_v vers TMC. Le seuil de solides H_2O et CO_2 est $A_v \sim 1,6$ mag, tandis que le CO solide apparaît à ~ 3 mag. Le seuil solide CH_3OH est le plus grand, avec $A_v = 9 \pm 3$ mag, reflétant probablement le gel tardif du CO (Boogert et al., 2015).

Processus à la surface des grains et paramètres cruciaux L'énergie de liaison (BE) et l'énergie de diffusion (DE) des espèces à la surface des grains sont des paramètres cruciaux dans tout modèle astrochimique. Ils régulent respectivement la congélation des espèces et leur vitesse de diffusion à la surface des grains. Nous utilisons les résultats de l'état de l'art dans nos modèles. Dans ce qui suit nous apportons quelques exemples de choix de paramètres (voir, 6).

L'énergie de liaison (BE) et l'énergie de diffusion (DE) des espèces à la surface des grains sont des paramètres cruciaux dans tout modèle astrochimique. Ils régulent respectivement la congélation des espèces et leur vitesse de diffusion à la surface des grains. Dans ce travail, nous adoptons notre valeur calculée, 350 K, et explorons l'effet de la changer en valeurs plus élevées utilisées dans d'autres modèles astrochimiques, 450 K (Garrod, 2013) et 580 K (Wakelam et al., 2017). L'énergie de diffusion (DE) est mal contrainte car il est intrinsèquement difficile de mesurer (voir, Cuppen et al., 2017; Hama and Watanabe, 2013, reviews). Bien que difficile, de nombreux groupes ont tenté de mesurer sa valeur pour les espèces astrochimiquement pertinentes. Compte tenu de l'incertitude de la valeur ƒ, dans le présent travail, nous adoptons 0,3 comme valeur de bonne foi, et nous explorons la variation des prédictions du modèle en prenant également 0,4 et 0,5.

Résumé des modèles d'exécution et de la stratégie Nous exécutons plusieurs grilles de modèles dans le but d'évaluer l'influence sur les prédictions du modèle des différents paramètres entrant dans la modélisation. Ces derniers peuvent être séparés en deux grandes classes : les paramètres macro-physiques, qui décrivent le nuage à modéliser, et les paramètres micro-physiques, qui entrent dans la physique des processus chimiques se produisant en phase

gazeuse et à la surface des grains. Nous avons adopté une stratégie en plusieurs étapes pour évaluer séparément les effets dus aux deux classes de paramètres. (1) Nous avons d'abord défini un modèle "de référence", qui contient les paramètres qui, a priori, décrivent le mieux à la fois le nuage TMC1 et les processus micro-physiques. (2) Nous avons exécuté une grille de modèles faisant varier la densité et la température du gaz, dans la plage des valeurs observées dans TMC1, pour deux valeurs probables des taux d'ionisation CR. (3) Nous avons exécuté la même grille de l'étape 1, mais avec les abondances élémentaires initiales EA-TMC1, EA2 et EA3. (4) Nous avons exécuté la même grille de l'étape 1, avec le CO BE le plus bas, à savoir 1100 K. (5) À partir des exécutions précédentes, nous avons sélectionné les paramètres des grilles de l'étape 1 à l'étape 3 dont les prédictions du modèle correspondent mieux aux observations. Ensuite, nous avons exécuté une grille de modèles où nous avons fait varier les processus et les paramètres micro-physiques qui sont incertains.

Discussion et conclusion Dans le présent travail, nous nous concentrons particulièrement sur les différents paramètres qui influencent la chimie grain-surface et l'impact qu'ils ont sur les abondances prédites dans un nuage sombre, en prenant comme référence le TMC1 bien étudié. Nous nous concentrons uniquement sur les réservoirs solides et gazeux majeurs d'O et de C, car s'ils ne sont pas reproduits correctement par le modèle, il n'y a aucune utilité à essayer de reproduire des espèces traces, dont l'abondance dépend fortement de la quantité de carbone ou d'oxygène qui leur reste libre. former.

Comme premier commentaire, les processus et paramètres micro-physiques mal connus discutés dans § 6.3 ont une énorme influence sur les prédictions du modèle résultant. Les espèces les plus touchées sont le CO solide et gazeux ainsi que le méthanol solide. Il existe un lien très direct entre ces trois espèces, car elles dépendent toutes les unes des autres.

Un deuxième commentaire concerne l'impact de l'âge du nuage sur la composition et l'observabilité du manteau du grain. En fait, le petit nombre de couches dans les jeunes nuages peut avoir un impact sur la détection des espèces à l'état solide. Par exemple, si le nuage est très jeune, comme cela semble être le cas de TMC1, un nombre relativement faible de couches sont présentes dans le manteau : 40 à 0,1 Myr contre 240 à 10 Myr. En pratique, un manteau nuageux très jeune a environ un facteur 6 de densité de colonne de matière solide en moins par rapport à un nuage plus ancien. De plus, la composition dépend de l'âge du nuage. Un jeune nuage de 0,1 Myr aurait une plus petite densité de colonne de CO solide par rapport à un plus ancien et même l'absence de méthanol. La dispersion observée dans les mesures des densités de colonnes solides de ces deux espèces pourrait donc (§6.2) être due à un statut évolutif différent des différentes régions du nuage.

Enfin, les résultats récents sur la chimisorption des atomes de C sur les surfaces de grains glacés conduisent à prédire qu'une fraction importante du carbone initial se trouve en réalité dans du C gelé, ce qui est totalement impossible à détecter. Dans le modèle de référence, nous avons constaté qu'environ la moitié du carbone élémentaire initial pouvait résider sous cette forme. Que ce soit le carbone manquant mentionné dans § 6.5.4 reste une possibilité intéressante à approfondir. Il est également intéressant d'étudier plus avant, bien que beaucoup plus spéculative, la possibilité que ce carbone soit responsable de la formation de nouvelles poussières dans les nuages sombres invoquée par certains auteurs pour expliquer les courbes d'extinction aux décalages vers le rouge élevés (eg Asano et al., 2013; Ginolfi et al., 2018) même si le problème semble avoir été atténué par les modèles les plus récents (eg De Looze et al., 2020; Nanni et al., 2020).

Applications de Labice

Application I : La fraction de CO piégé dans les glaces : simulations expérimentales versus Labice

Ce chapitre décrit la modélisation de la fraction de CO piégé dans les glaces mixtes eau et CO avec Labice. Nous nous concentrons sur la simulation de la fraction CO piégée des expériences TPD menées par Kruczkiewicz et ses collaborateurs (Kruczkiewicz et al. 2022, en prép., ci-après Kr2022) avec le modèle de Labice décrit au Chap. 7.

le modèle Labice est un modèle visant à simuler la structure en couches formée dans une configuration expérimentale et le manteau de glace interstellaire en utilisant une approche d'équation de vitesse pour rester cohérent avec les codes astrochimiques, tels que Grainoble+. Labice vise à extraire les paramètres majeurs qui caractérisent la glace, tels que l'énergie de liaison des espèces qui constituent la glace, la porosité et l'homogénéité de la glace, informations qui pourront finalement être utilisées par des modèles astrochimiques.

Pour simuler une glace cultivée en laboratoire avec notre modèle, nous devons d'abord comprendre quels paramètres contrôlent sa forme et sa morphologie.

glace cultivée dans des installations expérimentales De nombreux groupes de travail ont mené des expériences et des simulations pour quantifier la formation de la structure de la glace en fonction des paramètres de dépôt et quantifier la cinétique d'évolution de la morphologie de la glace et la transition de phase sous chauffage. Ici, nous résumons brièvement les principaux points de conclusion des expériences et des simulations sur la morphologie de la glace discutées dans les sections précédentes (Cazaux et al., 2015; Clements et al., 2018; Collings et al., 2004; He et al., 2019; Kimmel et al., 2001a,b).

La glace ASW cultivée dans n'importe quelle condition montre un certain degré de porosité. La porosité augmente avec une augmentation de l'angle d'incidence et de la température de surface et une diminution de la vitesse de dépôt. La structure de la porosité dans les glaces épaisses ($\gtrsim 10-25$ ML, selon l'étude) diminue légèrement avec une augmentation de l'épaisseur de la glace. En revanche, les glaces plus minces présentent une surface exceptionnellement élevée, ce qui indique que la structure de la glace est quelque peu irrégulière et que la structure poreuse observée dans les glaces plus épaisses n'est pas complètement développée. De plus, la glace ASW sous chauffage devient plus dense mais conserve sa porosité. La raison en est que le compactage est dû à la fusion de pores plus petits. Le changement de morphologie sous chauffage emprisonne physiquement les espèces volatiles dans les glaces mixtes, qui sont libérées pendant la phase de transition de l'eau (ASW à CI) en raison de la formation de fissures induites par la cristallisation et lorsque l'eau commence à s'évaporer. La fraction des espèces volatiles piégées augmente avec l'épaisseur de l'eau.

les expériences Ils ont utilisé un faisceau incident à angle nul pour co-déposer le H_2O et le CO sur un substrat d'or à 10 K. Le rapport de co-déposition de H_2O:CO dans 6 expériences est de 3:1 et de 2:1 dans le reste. Dans toutes les expériences, la glace est réchauffée avec une vitesse de chauffage de 0,2 K/s jusqu'à ce que la glace soit complètement évaporée. Leurs résultats TPD montrent qu'une fraction du CO reste piégée à l'intérieur de la glace jusqu'à ce qu'elle s'évapore lors de la cristallisation et de l'évaporation des molécules d'eau.

Nous avons exécuté deux ensembles de modèles avec des rapports 3:1 et 2:1 sans aucun paramètre de porosité. Pour chaque ensemble, nous avons fait varier le nombre total de ML de 1 à 100 ML et les niveaux de stochasticité de 1 à 25 %. Nous avons exécuté des modèles au total > 50000 pour montrer l'écart et augmenter nos statistiques. La distribution sur les couches de chaque glace a été créée en fonction du paramètre de stochasticité suivant le

modèle de distribution uniforme aléatoire décrit dans Sec. 7.2. Pour mieux comprendre ce comportement, nous trouvons le minimum χ^2 parmi les modèles avec la même épaisseur d'eau et le même rapport de composition et un pourcentage de stochasticité différent.

Discussion et conclusion Cela montre que nos modèles, sous l'hypothèse d'absence de porosité, ne peuvent pas reproduire de manière concluante la fraction piégée pour les glaces dont l'épaisseur d'eau est inférieure à $\sim$ 8 ML. Cela peut suggérer que ces glaces n'ont pas une structure poreuse régulière (comme on le voit dans les glaces plus épaisses) et montrent une surface élevée, similaire aux conclusions de He et al. (2019) and Kimmel et al. (2001a)

Nos simulations indiquent que les pourcentages de stochasticité diminuent avec l'épaisseur de l'eau au-dessus de $\sim$ 8 ML de $\sim$ 25% à $\sim$ 1%. Ce résultat peut indiquer que la stochasticité peut dépendre de l'épaisseur de l'eau. Cela pourrait signifier que le rapport entre l'eau et le CO dans chaque couche ne s'écarte pas largement du rapport de co-déposition et que cet écart diminue avec l'épaisseur de l'eau. Cela peut indiquer que l'homogénéité du mélange d'eau et de CO sur les couches augmente avec l'épaisseur de l'eau.

Nos résultats peuvent suggérer que les mélanges de glace d'eau (dans ce cas, avec du CO) au-dessus d'un seuil d'épaisseur d'eau de $\sim$ 8 MLs (correspondant à une épaisseur totale de $\sim 10-12$ MLs) peuvent également avoir une structure compacte et peu poreuse. structure dans laquelle le mélange d'eau et de CO est de plus en plus homogène sur les couches, similaire aux résultats de He et al. (2019), qui montre que la surface effective diminue avec l'augmentation du nombre de ML.

Les résultats montrent que la porosité et la diffusion des molécules et les fusions des pores peuvent être des facteurs très influents dans le modèle même dans les glaces compactes formées avec des faisceaux à angle nul et doivent être pris en compte dans les modèles. Il est également important non seulement de comparer les résultats avec des expériences, mais également avec des simulations de Monte Carlo pour créer un modèle plus fiable qui peut être utilisé pour extraire des paramètres statiques et cinétiques d'expériences, qui peuvent ensuite être utilisés dans des modèles astrochimiques. L'inclusion de la porosité est la prochaine étape dans nos modèles pour comprendre leur impact sur les résultats.

Application II : Énergies de liaison des molécules interstellaires sur des modèles cristallins et amorphes de glace d'eau par calculs ab initio

Le contexte Les observations dans le proche infrarouge de noyaux froids denses dans l'ISM montrent la présence de grains de poussière submicroniques enveloppés de manteaux glacés. La glace est composée principalement d'eau qui est mélangée à d'autres espèces volatiles en plus petites quantités. Une évaluation précise de l'énergie de liaison des espèces (BE) est cruciale pour que les modèles astrochimiques reproduisent les observations puisque les BE régissent les taux de sublimation et de diffusion des espèces sur les surfaces de glace. Les BE peuvent être déduits d'expériences ou de calculs théoriques.

Les calculs BE Nous calculons le BE de 21 espèces pertinentes sur le plan astrochimique (dont 4 radicaux) à l'aide de méthodes de calcul quantique (Fig. 4). Pour imiter la nature d'une surface de glace à grains interstellaires, nous considérons à la fois des modèles de surface cristalline (Fig. 1) et amorphe (Fig. 2 et 3) en utilisant une approche périodique. Nous considérons également pleinement la coopérativité des liaisons hydrogène dans les petits amas de glace. Nous avons utilisé les méthodes de la théorie fonctionnelle de la densité (DFT) pour prédire la structure et les BE du système (la surface et les espèces).

Nous avons simulé la structure et les caractéristiques énergétiques d'adsorption des 21 molécules. Les simulations montrent que les surfaces ASW présentent une grande variété de

sites de liaison d'adsorption, tandis que les surfaces cristallines présentent une plage limitée en comparaison (Fig. 9 et Tab. 1 et 2). L'étendue de la distribution dépend de la structure de la surface de la glace et de la position de l'absorbat, ce qui se traduit par une distribution des BE sur une surface ASW. Une surface cristalline est plus dense qu'une surface ASW ; par conséquent, le réseau d'interaction est plus étroit. Il en résulte un coût de relaxation géométrique plus faible lors de l'adsorption qu'un système ASW. En raison de ce comportement, les BE calculés sur une plaque cristalline sont généralement plus élevés que ceux sur une dalle ASW.

Comparaison avec les valeurs de la littérature Les BE obtenus sont majoritairement en accord avec les valeurs issues des expériences, sauf pour O_2 et dans une moindre mesure H_2 (Tab. 3 et Fig. 11). Notre BE de O_2 est inférieur aux valeurs expérimentales. Nous avons également comparé nos résultats avec les travaux de Wakelam et al. (2017) et Das et al. (2018) qui simulaient respectivement des surfaces avec 1 et 6 molécules d'eau. L'approche périodique dans notre modèle de glace nous permet de considérer la coopérativité des liaisons hydrogène. Il améliore la force d'interaction de l'adsorbat et des atomes dH terminaux exposés à la surface. Les deux travaux théoriques mentionnés ne tenaient pas compte de cet effet, ce qui pourrait expliquer l'écart dans les résultats. Par exemple, dans nos résultats, les CH_3CN et HCOOH BE sont plus grands, alors que les H_2 et O_2 BE sont comparativement plus faibles. Nous arrivons à des conclusions similaires en comparant nos résultats aux bases de données KIDA et UMIST, car les deux sont des collections de travaux théoriques expérimentaux et antérieurs.

Implications astrochimiques Nous avons développé un modèle jouet pour montrer l'impact potentiel de l'hypothèse de multi-BE dans les modèles astrochimiques. Le but des simulations n'est pas de comparer avec les expériences ou observations TPD mais de montrer l'impact des différents BE sur les espèces sublimées. Ce modèle de jouet simulait un composite de glace à 10 couches d'eau et de méthanol. Les cinq couches inférieures sont constituées uniquement d'eau, tandis que les cinq couches supérieures contiennent 20% de méthanol et 80% d'eau. La structure en couches de la glace signifie qu'à un moment donné, seules les espèces qui sont exposés et disponibles pour la sublimation. Les couches du dessous restent piégées jusqu'à ce que celle(s) du dessus se sublime. Nous effectuons deux simulations. La première suppose une distribution normale des BE calculés dans notre travail pour chaque espèce, CH_3OH et H_2O, et la seconde utilise un seul BE de la base de données KIDA pour chacune. Dans ces simulations, nous augmentons la température de 10 K à 400 K sur 10^5 ans pour imiter la vitesse de chauffage d'une protoétoile de type solaire qui s'effondre. La figure 12 montre le taux de désorption des deux simulations en lignes pleines et en pointillés (normalisé à 1 dans le sous-graphique inférieur). La simulation avec des BE simples montre un pic de désorption à $\sim$ 110 K pour l'eau et deux pour le méthanol à $\sim$ 95 K et $\sim$ 110 K. Les pics de méthanol correspondent à la sublimation des molécules non piégées et celles co-désorbé avec de la glace d'eau, respectivement. La simulation multi-BE montre plusieurs pics pour les deux espèces allant de $\sim$ 75 à $\sim$ 190 K, résultant de l'hypothèse multi-BE.

Comme mentionné précédemment, ce modèle vise à démontrer l'impact de l'hypothèse de multi-BE dans les modèles astrochimiques. Nous avons considéré une distribution normale des BE, mais en réalité, cette distribution dépend de la structure et de la composition de la surface. Par rapport aux simulations BE uniques, nous pouvons conclure que la distribution des BE peut être la raison pour laquelle des espèces peuvent être présentes dans la phase gazeuse à des températures inférieures à celles attendues des modèles astrochimiques supposant des BE uniques.

Discussion et conclusions Dans ce travail, nous avons calculé le BE de 21 molécules astrochimiquement pertinentes sur ASW et des dalles de glace cristalline en utilisant des méthodes DFT de calcul quantique. Les résultats montrent qu'en raison de la propagation des sites de liaison sur la glace ASW, les BE pour chaque espèce montrent une distribution. Les nouveaux BE de CO et N_2 pourraient expliquer pourquoi l'épuisement de N_2H^+ est plus tardif que le CO dans les noyaux préstellaires. Nos résultats montrent que HCl se dissocie à la surface de la glace d'eau. Cela pourrait expliquer les faibles abondances observées dans les sources protostellaires. Notre nouveau modèle ne nous permet pas d'estimer la fonction de distribution des BEs pour chaque espèce. Une étude statistique est nécessaire pour une telle estimation. La présente étude montre l'importance des calculs théoriques d'énergie de liaison sur des surfaces de glace simulées de la manière la plus réaliste possible car ils impactent significativement les prédictions des modèles astrochimiques. D'autres études de ce type doivent être menées pour inclure davantage de molécules utilisées dans les modèles astrochimiques afin de mieux comprendre l'évolution chimique de l'ISM.

Conclusion

Au cours de mon doctorat, je me suis concentré sur la modélisation des premières étapes de l'évolution chimique dans les régions de formation d'étoiles de faible masse. J'ai exploré deux objectifs, modéliser l'évolution chimique dans les régions de formation d'étoiles avec Grainoble+ et modéliser la glace expérimentale avec Labice.

Modélisation astrochimique avec Graionble+

Le premier objectif de la thèse était de comprendre les processus chimiques qui forment et détruisent les molécules organiques complexes interstellaires (alias iCOM) dans les régions de formation d'étoiles de type solaire. Pour cela, j'ai développé un code d'astrochimie, Grarinoble+. J'ai suivi deux objectifs avec Grainoble+, modéliser la formation d'iCOMs dans les régions choquées de NGC 1333 IRAS 4A et modéliser la composition de la glace dans les Taurus MCs.

Objectif I, formation d'iCOMs dans les régions choquées de NGC 1333 IRAS 4A : Les régions choquées le long des écoulements de protoétoiles de faible masse fournissent un environnement unique pour étudier et examiner les paradigmes de formation des iCOM (par la chimie en phase gazeuse ou sur des surfaces de grains) car l'âge cinétique d'une région choquée peut fournir une contrainte supplémentaire, la dépendance temporelle, sur les prédictions du modèle (voir, Codella et al., 2017, pour la modélisation sur les sorties L1157-B1). J'ai exécuté différents modèles faisant varier la composition chimique initiale et les conditions physiques avec le mode en phase gazeuse Grainoble+ pour prédire les abondances dans les régions choquées le long des sorties d'IRAS 4A1 et IRAS 4A2.

J'ai reproduit le rapport méthanol/acétaldéhyde observé dans les régions choquées de la source IRAS 4A en supposant que le méthanol est synthétisé sur des glaces et directement sublimé au passage du choc, et que l'acétaldéhyde est produit via la réaction en phase gazeuse CH_3CH_2 + O où CH_3CH_2 est sublimé à partir des manteaux de grains. De plus, le rapport méthanol/acétaldéhyde entre les régions choquées des deux sorties (CH_3OH/CH_3CHO $\sim$ 44 dans IRAS 4A1 et 8-20 dans les sorties IRAS 4A2) et les résultats de l'astrochimique les modèles que j'ai menés suggèrent que l'écoulement IRAS 4A1 est probablement plus jeune que celui d'IRAS 4A2. Les ratios sont beaucoup plus faibles que les ratios observés dans les écoulements L1157 B1 (130–250), ce qui suggère que la composition chimique et l'âge cinétique des écoulements dans ces deux sources sont différents.

Objectif II, composition du manteau de glace dans les Taurus MC : La complexité chimique commence dans les nuages moléculaires (MC). J'ai utilisé Grainoble + pour modéliser la transition CNM à MC, en particulier dans Taurus MC à une extinction visuelle de 20 mags, et prédire la composition chimique gazeuse et glacée dans les MC, qui se compose principalement d'eau, de CO, de CO_2 et de méthanol. Les prédictions dépendent de grandeurs macroscopiques qui décrivent l'état physique du nuage dans le modèle et de paramètres microscopiques qui décrivent la cinétique des processus chimiques en phase gazeuse et à la surface des grains. Ce dernier ensemble de paramètres est mal connu. Les modèles astrochimiques actuels adoptent des réactions qui utilisent des paramètres cinétiques estimés en phase gazeuse et à la surface des grains. Cependant, les derniers calculs de chimie quantique nous ont fourni les énergies de liaison et les taux de réaction et de diffusion à la surface des grains dans les MC, comme le réseau de formation d'eau et de méthanol (voir, par exemple, Enrique-Romero et al., 2021; Ferrero et al., 2020; He et al., 2018; Senevirathne et al., 2017; Vazart et al., 2020), que j'ai inclus dans notre modèle.

J'ai exécuté plusieurs modèles faisant varier les conditions physiques dans la plage observée dans le TMC1 pour trouver l'ensemble de paramètres physiques qui reproduit le mieux la composition observée du manteau de glace. Dans la deuxième étape, j'ai exécuté une grille de modèles faisant varier les paramètres chimiques et l'abondance élémentaire initiale dans le modèle.

Nos résultats montrent que le modèle avec $n_{H_2} = 8 \times 10^4$ cm^{-3}, T=10 K et $\zeta_{H_2} = 3 \times 10^{-18}$ reproduisent au mieux la composition de la glace dans le nuage TMC1. Les principaux résultats de la deuxième étape sont les suivants. Les résultats montrent que pour reproduire la composition chimique dans un MC spécifique, il est impératif d'utiliser les abondances élémentaires initiales dérivées des observations dans cette région. Des taux de désorption plus élevés diminuent le taux d'hydrogénation du s-CO et la formation de s-CH_3OH. L'utilisation du saut thermique estimé en fonction de l'énergie de liaison pour calculer le taux de diffusion peut surestimer les abondances de s-CH_3OH.

Simulation de glaces cultivées en montage expérimental avec Labice

J'ai développé le modèle Labice qui simule les expériences TPD, qui utilise l'approche d'équation de taux similaire à Grainoble+. J'ai poursuivi deux objectifs avec le modèle de Labice, modéliser les glaces composites eau et CO en utilisant la fraction CO piégée et modéliser l'impact de l'approche énergétique multi-liaison sur la sublimation des espèces.

Objectif I, Modélisation des glaces composites eau et CO à partir de la fraction CO piégée : Ici, j'ai cherché à simuler une expérience TPD et à comparer la fraction de CO piégé et le modèle de glace avec les résultats des expériences précédentes. J'ai modélisé diverses glaces compactes dans lesquelles la composition totale de la glace est fixe tandis que leur rapport dans chaque couche s'écarte du rapport de masse total tiré d'une distribution uniforme pour simuler la distribution stochastique des espèces sur les couches. J'ai fait varier le nombre total de couches et le paramètre de stochasticité de la glace pour reproduire la fraction de CO piégé en fonction de l'épaisseur de l'eau dans les glaces H_2O:CO avec des rapports 3:1 et 2:1.

Les simulations dans des glaces plus minces ($<$ 8 ML) ne peuvent pas reproduire de manière concluante la fraction piégée pour les glaces dont l'épaisseur d'eau est inférieure à $\sim$ 8 ML, en supposant qu'il n'y a pas de porosité. Cela suggère que ces glaces n'ont pas une structure poreuse régulière (comme on le voit dans les glaces plus épaisses) et montrent une surface élevée, similaire aux conclusions de He et al. (2019) and Kimmel et al. (2001a)

Nos simulations indiquent que les pourcentages de stochasticité diminuent avec l'épaisseur de l'eau au-dessus de $\sim$ 8 ML de $\sim$ 25% à $\sim$ 1%, ce qui peut indiquer que la stochasticité peut dépendre de l'épaisseur de l'eau. Cela signifie que l'homogénéité du mélange d'eau et

de CO sur les couches augmente éventuellement avec l'épaisseur de l'eau. Des expériences et des simulations antérieures sur des glaces d'eau pure ont montré que les glaces cultivées à un angle d'incidence nul sont plutôt compactes, et celles au-dessus de $\sim$ 10 ML d'épaisseur ont un petit pourcentage de surface qui diminue lentement avec l'épaisseur de l'eau (He et al., 2019). Nos résultats semblent suggérer que les mélanges de glace d'eau (dans ce cas, avec du CO) au-dessus d'un seuil d'épaisseur d'eau de $\sim$ 8 MLs (correspondant à une épaisseur totale de $\sim 10-12$ MLs) peuvent également avoir une structure compacte et faible. structure poreuse dans laquelle l'eau et le CO sont répartis de manière de plus en plus homogène sur les couches.

Objectif II, L'impact des multiples énergies de liaison dans la désorption des espèces volatiles : Le manteau glacé des grains interstellaires est composé principalement d'eau qui est mélangée à d'autres espèces volatiles en plus petites quantités. Une évaluation précise de l'énergie de liaison des espèces (BE) est cruciale pour que les modèles astrochimiques reproduisent les observations puisque les BE régissent les taux de sublimation et de diffusion des espèces sur les surfaces de glace. Les BE peuvent être déduits d'expériences ou de calculs théoriques. Ce travail a calculé le BE de 21 molécules astrochimiquement pertinentes sur ASW et des dalles de glace cristalline en utilisant des méthodes de calcul quantique. Les résultats montrent qu'en raison de la propagation des sites de liaison sur la glace ASW, le BE pour chaque espèce montre une distribution.

J'ai utilisé le modèle Labice pour montrer l'impact potentiel de l'hypothèse de multi-BE dans les modèles astrochimiques et les espèces sublimées dans ce travail. Labice a simulé un composite de glace à 10 couches d'eau et de méthanol où les 5 couches supérieures contiennent 20% de méthanol. J'ai simulé une augmentation de température de 10 K à 400 sur dix mille ans pour imiter la phase d'échauffement d'une protoétoile de type solaire qui s'effondre. J'ai fait deux simulations. La première suppose une distribution normale des BE calculés dans ce travail pour chaque espèce, et la seconde utilise un seul BE de la base de données KIDA pour chacune.

Alors que la simulation BE unique montre un pic de désorption à $\sim$ 110 K pour l'eau et deux pour le méthanol à $\sim$ 95 K et $\sim$ 110 K correspondant respectivement aux pics de désoption thermique et de co-désorption, la multi- La simulation BE montre plusieurs pics pour les deux espèces allant de $\sim$ 75 à $\sim$ 190 K, résultant de l'hypothèse multi-BE. Cela pourrait être la raison pour laquelle certaines espèces sont présentes dans la phase gazeuse à des températures plus basses que ne le prédisent les modèles énergétiques à liaison simple.

Perspective

Perspective Grainoble+

J'ai développé Grainoble+ de manière modulaire afin qu'il puisse être facilement modifié ou mis à jour. De plus, j'ai conçu une interface python afin que d'autres utilisateurs puissent facilement utiliser Grainoble+ pour leurs modélisations. Par conséquent, une grande variété de projets peuvent suivre mon travail de thèse. La liste suivante est les quelques exemples de projets qui peuvent être réalisés avec Grainoble+ avec peu ou pas de modifications supplémentaires dans le code par rapport à son état actuel.

Modélisation de l'effondrement du cœur Je peux modéliser un effondrement du cœur en utilisant des profils physiques dépendant du temps comme étape suivante. Le modèle comprendra deux étapes : statique et effondrement. Cette étape peut utiliser Witzel et al. 2022 (soumis) hypothèses physiques et chimiques et la composition du manteau de glace pour

calculer les abondances d'iCOMs qui peuvent se former pendant la phase d'effondrement. Je me suis concentré sur la modélisation du TMC1 dans notre article, et je peux poursuivre avec la modélisation du noyau préstellaire L1544 et des sources HL tau de classe I, qui sont toutes deux étudiées en profondeur (e. g., Scibelli and Shirley, 2020).

Modélisation multi-grains Grainoble+ a mis en place les bases de la modélisation multi-grains. Deux projets peuvent suivre (1) montrant l'impact de la modélisation multi-grains sur la composition du manteau de glace dans le nuage TMC1. Je peux utiliser les mêmes paramètres dans Witzel et al. soumis (2022) avec l'option multi-céréales. (2) Simuler un modèle d'effondrement de cœur à l'aide de multi-grains et examiner son impact sur la formation d'iCOMs.

Procédés de désorption CR Je suis également intéressé par la modélisation des processus induits par le CR proposés par Shingledecker et al. (2018) comme une variante des trois projets mentionnés ci-dessus et pour examiner son effet sur les abondances d'iCOMs.

Désorption induite par la formation de H_2 Roberts et al. (2007) ont montré que la formation de H_2 sur les glaces peut avoir un effet substantiel sur la désorption des espèces solides dans la modélisation des noyaux froids mais cela n'est peut-être pas suffisant pour reproduire les abondances gazeuses. Les travaux de Pantaleone et al. (2021) ont confirmé que, compte tenu du taux de formation de H_2 et d'accrétion de CO sur les surfaces de glace, il est possible que la désorption induite par la formation de H_2 puisse avoir un impact significatif sur le taux de désorption de CO dans les MC froids. J'ai implémenté la base de ce processus dans Grainoble+, en attendant la suite des travaux de Pantaleone et des collaborateurs sur Pantaleone et al. (2021). Après, je peux finaliser la modification dans Grainoble+ et commencer à modéliser la formation d'un MC et examiner cet impact.

Modélisation de l'évolution chimique dans les régions choquées le long des écoulements J'ai modélisé les régions choquées de NGC 1333 IRAS 4A (ci-après IRAS 4A) dans De Simone et al. (2020) pour reproduire le rapport méthanol sur acétaldéhyde et examiner la voie de formation de l'acétaldéhyde (s'il est d'origine en phase gazeuse ou s'il est synthétisé sur des manteaux de grains). IRAS 4A et L1157-B1 sont les deux régions choquées qui ont été observées et étudiées de manière approfondie jusqu'à présent. Les résultats préliminaires de Bouvier et de ses collaborateurs ont détecté du méthanol et de l'acétaldéhyde le long de l'écoulement prolongé de fir6c-a dans l'OMC-2/3. Cette sortie peut être la troisième région à modéliser et à examiner le paradigme de formation des iCOMs.

Modélisation énergétique multi-liaison Comme nous l'avons montré dans Ferrero et al. (2020), la modélisation avec l'hypothèse d'énergie multi-liaison peut avoir un effet substantiel sur l'abondance des espèces sublimées (voir, par exemple, Grassi et al., 2020). Il sera intéressant de voir son impact sur les taux de réaction de surface et l'abondance des espèces sublimées. Cet article peut être un article de suivi sur le Witzel et al.2022 (soumis) et le projet core-collapse.

Perspective Labice

Le modèle Labice est également implémenté de manière modulaire avec une interface facile à utiliser. Par conséquent, on peut inclure plus de processus si nécessaire, tels que la cristallisation et les réactions de surface.

Porosité Des expériences et des simulations ont montré que la glace d'eau formée dans toutes les conditions de dépôt a une structure poreuse. De plus, la porosité augmente la surface effective dans les glaces, ce qui affecte la désorption et le piégeage des espèces volatiles dans les glaces mixtes. Pour modéliser avec précision les glaces formées dans les montages expérimentaux, il est impératif de comparer les simulations avec les résultats expérimentaux. Comme prochaine étape de nos résultats actuels, Labice peut modéliser la porosité des mélanges de glace d'eau, simuler la désorption de la composition de la glace et comparer les résultats avec les expériences et simulations existantes, telles que les expériences menées par Kruczkiewicz et ses collaborateurs.

Énergie multi-binding Comme nous l'avons montré dans Ferrero et al. (2020), la modélisation énergétique multi-liaison a un impact significatif sur l'abondance des espèces sublimées. Dans Ferrero et al. (2020), j'ai supposé une distribution uniforme sur les BE en raison du manque d'informations statistiques sur la distribution des BE. À l'étape suivante, je peux considérer d'autres distributions, par exemple une distribution gaussienne ou des distributions issues de travaux théoriques (e. g., Bovolenta et al., 2020). L'idée est de discrétiser la distribution en un nombre fini de cases. Les questions sont : Combien de bacs sont suffisants pour voir l'impact sur les taux de désorption ?, Où est la limite où les résultats commencent à perdre de la sensibilité au nombre de bacs dans la distribution ?, Où est la limite au-delà de laquelle le modèle ne produire des résultats sensibles en raison peut-être des inexactitudes numériques qui peuvent augmenter ?

Labice peut simuler des hypothèses d'énergie multi-liaison et en déduire les paramètres limites avant son implémentation dans les codes astrochimiques, généralement plus complexes.

Cristallisation de l'eau L'eau amorphe est dans un état métastable. Cela signifie qu'avec le temps, que ce soit dans un état isotherme ou sous échauffement, il se transforme en glace cristalline. La cristallisation de la glace d'eau conduit à la libération d'espèces volatiles piégées à travers les fissures induites par la cristallisation (désorption volcanique). Labice peut modéliser la cristallisation en utilisant les taux issus d'expériences (Smith et al., 2011) pour simuler le pic de désorption volcanique des espèces volatiles.

Formation d'eau Le modèle de Labice utilise l'approche de l'équation de taux à trois phases. En principe, il peut inclure et modéliser des réactions de surface ou de volume. Le modèle peut être constitué de réseaux de réaction simples, tels que la formation de méthanol ou d'eau, et comparer les résultats avec les expériences existantes et les simulations de Monte Carlo (Cuppen et al., 2009, 2010).

Appendix F

Published Papers

A&A 640, A75 (2020)
https://doi.org/10.1051/0004-6361/201937004

Astronomy & Astrophysics

Seeds of Life in Space (SOLIS)

X. Interstellar complex organic molecules in the NGC 1333 IRAS 4A outflows*

M. De Simone[1], C. Codella[2,1], C. Ceccarelli[1], A. López-Sepulcre[3,1], A. Witzel[1], R. Neri[3], N. Balucani[4,1], P. Caselli[5], C. Favre[1], F. Fontani[2], B. Lefloch[1], J. Ospina-Zamudio[1], J. E. Pineda[5], and V. Taquet[2]

[1] Univ. Grenoble Alpes, CNRS, IPAG, 38000 Grenoble, France
e-mail: marta.desimone@univ-grenoble-alpes.fr
[2] INAF, Osservatorio Astrofisico di Arcetri, Largo E. Fermi 5, 50125 Firenze, Italy
[3] Institut de Radioastronomie Millimétrique (IRAM), 300 rue de la Piscine, 38400 Saint-Martin d'Hères, France
[4] Dipartimento di Chimica, Biologia e Biotecnologie, Università degli Studi di Perugia, Perugia 06123, Italy
[5] Max-Planck-Institut für extraterrestrische Physik (MPE), Giessenbachstrasse 1, 85748 Garching, Germany

Received 28 October 2019 / Accepted 12 June 2020

ABSTRACT

Context. The interstellar complex organic molecules (iCOMs) are C-bearing molecules containing at least six atoms; two main proposals for their formation are suggested: a direct formation in the icy mantle of the dust grains and formation through the reaction in gas phase of released grain mantle species. The shocked gas along outflows driven by low-mass protostars is a unique environment to study how the iCOMs can be formed as the composition of the dust mantles is sputtered into the gas phase.
Aims. The chemical richness in shocked material associated with low-mass protostellar outflows has been so far studied in the prototypical L1157 blue-shifted outflow to investigate the iCOM formation routes. To understand whether the case of L1157-B1 is unique, we imaged and studied the IRAS 4A outflows in the NGC 1333 star forming region.
Methods. We used the NOrthern Extended Millimeter Array interferometer as part of the IRAM Seeds Of Life in Space (SOLIS) Large Program to image the large-scale bipolar outflows driven by the IRAS 4A system in the 3 mm band, and we compared the observation with the GRAINOBLE+ astrochemical model.
Results. We report the first detection, in the IRAS 4A outflows, of several iCOMs: six lines of methanol (CH_3OH), eight of acetaldehyde (CH_3CHO), one of formamide (NH_2CHO), and four of dimethyl ether (CH_3OCH_3), all sampling upper excitation energy up to ~30 K. We found a significant chemical differentiation between the southeast outflow driven by the IRAS 4A1 protostar, showing a richer molecular content, and the north–southwest one driven by the IRAS 4A2 hot corino. The CH_3OH/CH_3CHO abundance ratio is lower by a factor of ~4 in the former; furthermore, the ratio in the IRAS 4A outflows is lower by a factor of ~10 with respect to the values found in different hot corinos.
Conclusions. After L1157-B1, the IRAS 4A outflow is now the second outflow to show an evident chemical complexity. Given that CH_3OH is a grain surface species, the astrochemical gas-phase model run with GRAINOBLE+ reproduced our observation assuming that acetaldehyde is formed mainly through the gas-phase reaction of the ethyl radical (CH_3CH_2) and atomic oxygen. Furthermore, the chemical differentiation between the two outflows suggests that the IRAS 4A1 outflow is likely younger than that of the IRAS 4A2. Further investigation is needed to constrain the age of the outflow. In addition, observation of even younger shocks are necessary. In order to provide strong constraints on the CH_3CHO formation mechanisms it would be interesting to observe CH_3CH_2, but given that its frequencies are not known, future spectroscopic studies on this species are needed.

Key words. astrochemistry – instrumentation: interferometers – stars: formation – ISM: jets and outflows – ISM: molecules – ISM: individual objects: NGC 1333 IRAS 4A

1. Introduction

Since the discovery of interstellar complex organic molecules (iCOMs[1], molecules containing carbon and at least six atoms: Herbst & van Dishoeck 2009; Ceccarelli et al. 2017) in solar-type protostars (Cazaux et al. 2003), the question whether they had a role in the appearance of life on Earth (and elsewhere in the Universe) has been raised. Although they are extremely small molecules compared to biotic molecules, iCOMs may have provided the bricks to build them. The presence of amino acids in meteorites and comets has certainly revived this possibility (e.g., Pizzarello et al. 2006; Elsila et al. 2009; Altwegg et al. 2016).

In addition to their possible role in the emergence of life, iCOMs represent a challenge for astrochemistry as their synthesis is all but obvious. Nowadays, two main paradigms are invoked (see, e.g., Herbst 2017) that argue that iCOMs are either synthesized on the grain surfaces (e.g., Garrod & Herbst 2006; Garrod 2008) or in the gas phase (e.g., Millar et al. 1991; Balucani et al. 2015; Skouteris et al. 2018). As a starting point, both pathways have the formation of simple hydrogenated molecules on dust grain mantles during the pre-stellar phase. Constraining which of the two ways to synthesize iCOMs is more efficient and where

* The reduced images are only available at the CDS via anonymous ftp to cdsarc.u-strasbg.fr (130.79.128.5) or via http://cdsarc.u-strasbg.fr/viz-bin/cat/J/A+A/640/A75

[1] We added "i" to the commonly used COMs acronym in order to be clear that these molecules are only complex in the interstellar context, contrary to what chemists consider complex in the terrestrial context.

the iCOMs form is not a simple task. Many methods have been used, from the comparison of the iCOM measured abundances in hot cores and hot corinos with model predictions to their measured deuterium fractionation (Turner 1990; Ceccarelli et al. 1998; Coutens et al. 2016; Skouteris et al. 2017; Jørgensen et al. 2018).

One method that turned out to be very efficient is to compare observations toward low-mass outflow shocks with model predictions (Codella et al. 2017). The advantage of this method is that the outflow shocks provide the time dependence as an additional constraint. Once the iCOM emission has been localized in a precise region (thanks to high spatial resolution observations), it is possible to identify in that region a shock event that corresponds naturally to a precise kinematical age (e.g., Gueth et al. 1996; Podio et al. 2016). After the passage of the shock, the chemistry in the shocked region evolves with time. Therefore, the comparison of observed iCOM abundances with model predictions provides strong constraints on the formation routes because it is possible to make the comparison at the precise kinematical shock age. This method was successfully applied in the L1157–B1 outflow shock to constrain the formation route of formamide. Thanks to interferometric high spatial resolution observations, Codella et al. (2017) found a difference in the spatial distribution between acetaldehyde and formamide emission, and consequently they were able to constrain the formamide formation as being due to gas-phase reactions. We note that these conclusions apply to L1157-B1 only. Given its power, it is important to apply the same method to other iCOMs and other protostellar shocks.

Unfortunately, there are very few observations of iCOMs in low-mass protostellar shocks. To our knowledge, iCOMs other than methanol have been detected only toward a handful of objects: several iCOMs toward L1157-B1 (Arce et al. 2008; Lefloch et al. 2017), formamide toward L1157-B2 (Mendoza et al. 2014), acetaldehyde toward IRAS 2A and IRAS 4A (Holdship et al. 2019), and acetaldehyde and dimethyl ether toward SMM4-W (Öberg et al. 2011). However, it is worth noting that all these works refer to single-dish observations at relatively low spatial angular resolution and are, by definition, unable to disentangle the different spatial distribution of iCOMs caused by the age of the shocks, so that the method described above cannot be used.

In this work, we present new high spatial observations toward the two outflows from IRAS 4A. This source is one of the targets of the Seeds Of Life In Space (SOLIS) Large Program (Ceccarelli et al. 2017) at the IRAM/NOrthern Extended Millimeter Array (NOEMA) interferometer, whose goal is to investigate iCOM chemistry during the earliest formation phases of solar-type stellar systems. The observations targeted three iCOMs in addition to methanol (CH_3OH): acetaldehyde (CH_3CHO), dimethyl ether (CH_3OCH_3), and formamide (NH_2CHO). All these iCOMs were detected in our data set. The detection of different iCOMs in the outflowing gas of IRAS 4A with high spatial resolution observations allows us to apply the method of model-observations comparison described above.

The article is organized as follows: we first give the IRAS 4A source background in Sect. 2, then present the observations in Sect. 3, and the results in Sect. 4; we derive the abundance ratios of the detected iCOMs in different positions of the IRAS 4A outflows in Sect. 5, and the model predictions to interpret them in Sect. 6; in Sect. 7 we discuss what our new observations imply, and finally in Sect. 8 we summarize our work.

2. IRAS 4A: source background

IRAS 4A is part of the multiple system IRAS 4, located at a distance of 299 ± 15 pc in the NGC 1333 region of the Perseus complex (Zucker et al. 2018). The system IRAS 4A is constituted of four objects: 4A, 4B, 4B′, and 4C (Lay et al. 1995; Looney et al. 2000; Smith et al. 2000; Di Francesco et al. 2001; Choi 2001). IRAS 4A is itself a binary system with two Class 0 objects, 4A1 and 4A2, separated by 1.″8 (~540 au; Looney et al. 2000; Santangelo et al. 2015; López-Sepulcre et al. 2017; Maury et al. 2019). At the millimeter wavelengths, 4A1 is three times brighter than 4A2. However, their respective luminosity is unknown since they are not resolved in the submillimeter to IR wavelengths where the luminosity peak lies. The bolometric luminosity of the whole IRAS 4A system is 9.1 $L_\odot$ (Kristensen et al. 2012; Karska et al. 2013).

IRAS 4A is the second hot corino ever discovered (Bottinelli et al. 2004), after IRAS 16293-2422 (Cazaux et al. 2003). Interferometric IRAM/PdBI (Plateau de Bure Interferometer, now evolved into NOEMA) observations later suggested that iCOM emission originates from 4A2 rather than 4A1 (Taquet et al. 2015; De Simone et al. 2017). More recently, López-Sepulcre et al. (2017) obtained high-resolution (~0.″5) ALMA images of IRAS 4A, and confirmed the huge contrast between 4A1 and 4A2: while 4A2 shows hot corino activity with enriched iCOM emission, no sign of iCOMs is detected in 4A1. López-Sepulcre et al. (2017) suggest that either 4A1 does not host a hot corino or, alternatively, the hot corino size is less than ~15 au (after scaling to 299 pc the distance adopted by López-Sepulcre et al. 2017), namely six times smaller than the 4A2 corino. However, thanks to recent observations at centimeter wavelengths performed with the *Jansky* Very Large Array (VLA), De Simone et al. (2020) have detected, for the first time, a clearly disentangled methanol emission toward both 4A1 and 4A2 revealing the 4A1 hot corino region that was obscured by the dust at millimeter wavelengths.

As for many Class 0 protostars, IRAS 4A is associated with a spectacular large-scale (a few arcminutes) bipolar outflow observed with several tracers, such as CO, SiO, SO, HCN (Blake et al. 1995; Lefloch et al. 1998; Choi 2005; Choi et al. 2011). Choi (2005) clearly traced the high-velocity component with SiO emission using VLA observations at 2″ spatial resolution. From their map it is possible to distinguish two different blue-shifted lobes toward the south and only one northern red-shifted lobe with a peculiar bending toward the northeast at 20″ from the protostars. Using IRAM/PdBI high spatial resolution observations (<1″), Santangelo et al. (2015) mapped the outflows at lower scale (~30″) with respect to the SiO map from Choi (2005). They traced different velocity components (from ~10 to ~60 km s $^{-1}$) using CO, SiO, and SO as tracers. With their study Santangelo et al. (2015) were able to clearly disentangle the two southern lobes, revealing a fast collimated jet associated with bright H_2 emission and driven by 4A1 (southeast lobe) and a slower and precessing jet driven by 4A2 (southwest lobe). Furthermore, the jets present different morphologies: the 4A2 jet shows a large spatial extent and an S-shaped pattern on small scales, probably due to jet precession; the 4A1 jet is faster, covers a smaller extent (~15″), and presents as C-shaped tilted toward the east of 4A1.

Thanks to a detailed study on sulfur species using interferometric observations, for the first time Taquet et al. (2020) were able to distinguish the outflow driven by 4A1 from the one driven by 4A2 also in the northern lobe.

The left panel of Fig. 1 summarizes the situation: it shows the distribution of the dust cores at large scale, traced by the

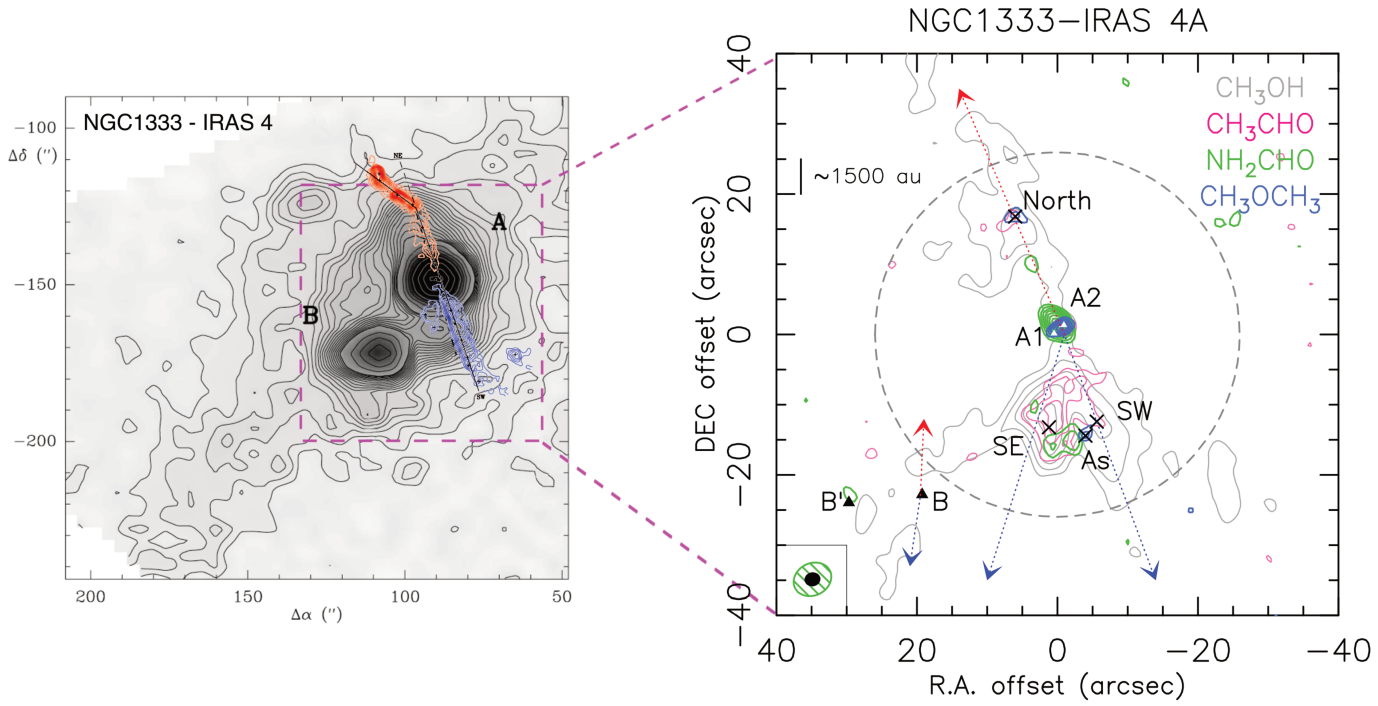

Fig. 1. *Left*: overlap of the contour map of the 1.25 mm continuum emission from NGC 1333 IRAS 4 region in Perseus, observed with the IRAM 30 m antenna (Lefloch et al. 1998), with the map of SiO line (VLA observations; Choi 2005). Axes offsets are in arcseconds from SVS 13 (α(2000) = 03^{h}29^{m}3^s.9 and δ(2000) = 31°16′8″). *Right*: zoomed-in image of the IRAS 4A system with NOEMA-SOLIS observations. Axes offsets are in arcseconds from IRAS 4A. A spatial separation of 5″ correspond to ~1500 au at a distance of 299 pc (Zucker et al. 2018). The white triangles give the position of the sources 4A1 and 4A2, while the black triangles give the position of the sources 4B and 4B′ (coordinates in Table 2). The black crosses give the analyzed positions in the outflows (SE, SW, North, and As; coordinates in Table 2). The dashed blue and red arrows indicate the direction of the blue- and red-shifted 4B outflow (from the HCN observations of Choi 2001) and of the 4A outflow. The contour map represents the iCOMs emission at 3 mm in the IRAS 4A outflows (this work). For all the iCOMs the contours start at 3σ with steps of 1σ, except for methanol whose contours have steps of 20σ. The emission distribution is the following: 1) methanol (CH_3OH in gray), integrated over the transitions $2_{0,2} - 1_{0,1}$ A, $2_{0,2} - 1_{0,1}$ E, and $2_{-1,2} - 1_{-1,1}$ E with σ = 75 mJy beam^{-1} km s^{-1}; 2) acetaldehyde (CH_3CHO, in magenta), here in the $5_{0,5} - 4_{0,4}$ A emission with σ = 11 mJy beam^{-1} km s^{-1}; 3) formamide (NH_2CHO, in green), $4_{1,4} - 3_{1,3}$ emission with σ = 10 mJy beam^{-1} km s^{-1}; dimethyl ether (CH_3OCH_3, in blue), $4_{1,4} - 3_{0,3}$ emission with σ = 9 mJy beam^{-1} km s^{-1}. The synthesized beams for the formamide line (green, ~4″) and for the other species (black, ~2″) are indicated in the lower left corner. The primary beam (~52″) is shown as a dashed gray circle.

Table 1. Characteristics of the SOLIS WideX backend setups.

Setup	Frequency range (GHZ) [GHz]	Spectral resolution [km s^{-1}]	[MHz]	Spatial resolution [″]	[au] [a]	Synthesized beam [″×″ (°)]	Primary beam [″]	[au] [a]
1	80.8–84.4	7	2	4	~1200	4.5 × 3.5 (27)	61.″4	~2 × 10^4
3	95.5–99.5	6	2	4	~1200	2.2 × 1.9 (96)	59.″2	~2 × 10^4

Notes. [a]Computed at the distance of the NGC 1333 region (~299 pc; Zucker et al. 2018).

continuum at 1.3 mm using the IRAM 30m (Lefloch et al. 1998), together with large-scale high-velocity outflow traced by the SiO (1-0) line using the VLA interferometer (Choi 2005).

3. Observations

IRAS 4A was observed with the IRAM/NOEMA interferometer during several tracks in June and September 2016. Two frequency setups were used, called 1 and 3 in Ceccarelli et al. (2017, Table 4), centered at ~82 and ~97 GHz, respectively. The array was used in configurations D and C with baselines from 15 m to 304 m for Setup 3 and from 16 to 240 m for Setup 1. Here, we present the data obtained using the WideX backend, whose characteristics are summarized in Table 1.

The phase center is on the IRAS 4A1 source, whose coordinates are listed in Table 2. The bandpass was calibrated on 3C454.3 and 3C84, while the flux was calibrated using MWC349 and LKHA101. The calibration of phase and amplitude was done observing 0333+321. The system temperatures typically ranged between 50 and 200 K. The calibration error associated with the absolute flux is ≤15%. The data were reduced using the packages CLIC and MAPPING of the GILDAS[2] software collection. The data were self-calibrated in phase only; the self-calibration solutions were applied to the data spectral cube, which was then cleaned. A continuum map (see Fig. 2) was obtained by averaging line-free channels from the self-calibrated data. The resulting synthesized beam is 2.″2 × 1.″9 (PA = 96°), for Setup 3, and

[2] http://www.iram.fr/IRAMFR/GILDAS

Table 2. Coordinates of the protostars (see also Choi 2001; Di Francesco et al. 2001; López-Sepulcre et al. 2017; Maury et al. 2019) and the analyzed emission peaks (chosen from methanol and dimethyl ether emission, see text) in the outflows.

Position	α(2000)	δ(2000)
4A1	$03^h29^m10\overset{s}{.}536$	$31°13'31\overset{''}{.}07$
4A2	$03^h29^m10\overset{s}{.}428$	$31°13'32\overset{''}{.}27$
4B	$03^h29^m12\overset{s}{.}000$	$31°13'08\overset{''}{.}10$
4B′	$03^h29^m12\overset{s}{.}813$	$31°13'06\overset{''}{.}97$
SE peak	$03^h29^m10\overset{s}{.}591$	$31°13'17\overset{''}{.}53$
SW peak	$03^h29^m10\overset{s}{.}061$	$31°13'18\overset{''}{.}61$
North peak	$03^h29^m10\overset{s}{.}966$	$31°13'47\overset{''}{.}87$
As region	$03^h29^m10\overset{s}{.}184$	$31°13'16\overset{''}{.}62$

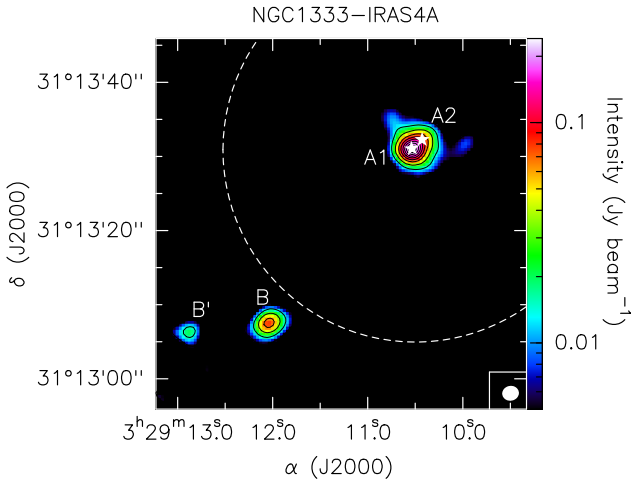

Fig. 2. Dust continuum emission maps of IRAS 4A at 95.85–99.45 GHz (Setup 3, see Table 1). Contours start at 3σ and increase by steps of 20σ, with σ = 1.5 mJy beam^{-1}. The synthesized beam (∼2″) is represented in white in the lower right corner of the panel, the primary beam (∼52″) is shown with a dashed white circle. The millimeter continuum sources in the field are labeled following the nomenclature used by Choi (2001) for 4A1 and 4A2 and Di Francesco et al. (2001) for B and B′.

4.″5 × 3.″5 (PA = 27°) for Setup 1. The half-power primary beam is 59.″2 and 61.″4 for Setup 3 and Setup 1, respectively.

4. Results

4.1. Dust continuum emission

Figure 2 shows the map of the dust continuum emission at 3 mm, whose emission peaks at the position of 4A1 and 4A2. As expected, the two sources are not disentangled as the angular resolution of ∼ 2″ is too close to their angular separation (∼1.″8; Sect. 3). In addition, the two protostars IRAS 4B and IRAS 4B′ were detected (e.g., Looney et al. 2000; Choi 2001; Di Francesco et al. 2001; Maury et al. 2019), even if they were located outside the primary beam of our observations (∼52″). The coordinates of all the four protostars are reported in Table 2.

The root mean square (RMS) noise level is 1.5 mJy beam^{-1} and the peak flux toward IRAS 4A1+4A2 is 240 ± 40 mJy beam^{-1}. Taking the error on the measured flux into account and considering the slightly different wavelength (2.7 mm) and angular resolution (∼1.″2) of the observations, this flux value is consistent with the value found by López-Sepulcre et al. (2017). The uncertainties in the flux measurements include the amplitude calibration error (∼15%) that dominates the RMS.

4.2. Line emission: maps

The present observations allow us to image both 4A1 and 4A2 and their molecular outflows. The study of the molecular content around the 4A1 and 4A2 protostars is beyond the scope of the present paper. Instead, we focus here on the molecular composition of the outflows.

Several lines from methanol (CH_3OH), acetaldehyde (CH_3CHO), dimethyl ether (CH_3OCH_3), and formamide (NH_2CHO) were detected along the outflows with a signal-to-noise ratio (S/N) higher than 3. Table 3 lists the detected lines with their spectroscopic properties. In Setup 3 we detected six lines of methanol that cover a range of upper level energy (E_{up}) from 7 to 28 K; eight lines of acetaldehyde with E_{up} between 13 and 23 K; and four lines of dimethyl ether, blended together and all with E_{up} = 10 K. In Setup 1 we detected one line of formamide with E_{up} of 28 K.

Figure 1 shows the distribution of the line emission of the four detected iCOMs. To obtain the methanol map we integrated from −36 to 36 km s^{-1} with respect to the systematic velocity of the source (∼6.5 km s^{-1}), for acetaldehyde between −15 to 15 km s^{-1}, while for formamide and dimethyl ether we integrated from −9 km to 9 km s^{-1}. First, the methanol emission is extended (∼ 1′) and covers the lobes of the two outflows from the two protostars: north (North) and southwest (SW) lobes of the outflow from 4A2, and the southeast (SE) lobe from 4A1. Second, acetaldehyde emission is less extended than the methanol one (∼15″) and it is bright toward the southern lobes, especially toward the SE one. The dimethyl ether emission is not resolved being less than the beam size (2″) in two positions, in the North lobe and in the region As (named by Ceccarelli et al. 2017) where the SE and SW lobes seem to cross. Finally, formamide emission is also compact (∼6″) and is located around the As position (see also Ceccarelli et al. 2017). The same iCOMs are also detected in the central protostars (4A1+4A2); we note that the methanol and acetaldehyde emission is not visible in Fig. 1 because it is hidden by the dimethyl ether and formamide contours. Figure 1 clearly shows a first important result: the evidence of a spatial segregation between the different iCOMs due to the fact that their emission covers different outflow regions.

4.3. Line emission: spectra and intensities

In order to do a quantitative analysis, we extracted the spectra from different positions of the three lobes where both methanol and acetaldehyde emit. The first two selected positions correspond to the emission peaks of methanol in the two southern lobes, SE and SW, while the last selected position corresponds to the emission peak of dimethyl ether in the northern lobe, North (Fig. 1). A fourth position is the one where formamide and dimethyl ether emit, called As. The spectra extracted at the pixels corresponding to the four positions are shown in Fig. 3. It is immediately evident that the SE position is richer and brighter in iCOMs when compared to the others (SW, North, and As).

We then derived the velocity-integrated line intensities of each detected transition using a Gaussian fit, obtained with the CLASS package of the GILDAS software. All the lines used for the analysis are not contaminated by other species and are well isolated. For instance, three of the six detected methanol lines, namely $2_{-1,2}$–$1_{-1,1}$ E (E_{up} = 13 K), $2_{0,2}$–$1_{0,1}$ A (E_{up} = 7 K), and

Table 3. Spectral parameters and fit results of the detected iCOM emission lines observed using the NOEMA WideX backend toward the IRAS 4A outflow peaks (see text and Table 2).

Transition	Spectral parameters			Outflow SE			Outflow SW			Outflow North			Region As [a]		
	Frequency [b] [GHz]	E_{up} [b] [K]	logA_{ij} [b]	Area [c] [K km s^{-1}]	T_{peak} [K]	RMS [d] [mK]	Area [c] [K km s^{-1}]	T_{peak} [K]	RMS [d] [mK]	Area [c] [K km s^{-1}]	T_{peak} [K]	RMS [d] [mK]	Area [c] [K km s^{-1}]	T_{peak} [K]	RMS [d] [mK]
CH_3OH															
$2_{1,2}$–$1_{1,1}$ A	95.91431	21.4	−5.6	17.1(0.9)	1.4	20	2.7(0.3)	0.4	20	5.1(0.5)	0.4	20	≤0.5	≤0.05	30
$2_{-1,2}$–$1_{-1,1}$ E [e]	96.73936	12.5	−4.6												
$2_{0,2}$–$1_{0,1}$ A [e]	96.74138	6.9	−5.6	199 (4)	12	20	69(4)	5	30	48(4)	3	20	37(1)	2.5	30
$2_{0,2}$–$1_{0,1}$ E [e]	96.74454	20.1	−5.5												
$2_{1,1}$–$1_{1,0}$ E	96.75550	28.0	−5.5	11.2(0.3)	0.9	20	2.0(0.2)	0.3	30	3.2(0.3)	0.2	20			
$2_{1,1}$–$1_{1,0}$ A	97.58280	21.6	−5.6	21.5(0.2)	1.9	20	2.5(0.3)	0.3	30	4.4(0.3)	0.4	30	≤0.5	≤0.05	30
CH_3CHO															
$5_{0,5}$–$4_{0,4}$ E	95.94744	13.9	−4.5	3.9(0.2)	0.4	20	≤0.6	≤0.06	20	0.8(0.4)	0.1	20	≤0.5	≤0.05	30
$5_{0,5}$–$4_{0,4}$ A	95.96346	13.8	−4.5	3.7(0.3)	0.4	20	1.7(0.4)	0.1	20	1.3(0.5)	0.1	20	≤0.5	≤0.05	30
$5_{2,4}$–$4_{2,3}$ A	96.27425	22.9	−4.6	1.1(0.4)	0.1	30	0.7(0.3)	0.07	20	1.0(0.2)	0.1	30	0.5(0.3)	0.1	20
$5_{2,4}$–$4_{2,3}$ E	96.42561	22.9	−4.6	1.1(0.2)	0.2	30	≤0.7	≤0.07	20	0.8(0.3)	0.06	30	≤0.3	≤0.03	20
$5_{2,3}$–$4_{2,2}$ E	96.47552	23.0	−4.6	0.8(0.2)	0.1	20	≤0.7	≤0.07	20	≤0.8	≤0.08	30	≤0.3	≤0.03	20
$5_{2,3}$–$4_{2,2}$ A	96.63266	23.0	−4.6	1.5(0.3)	0.1	20	≤0.7	≤0.07	20	≤0.8	≤0.08	30	≤0.3	≤0.03	20
$5_{1,4}$–$4_{1,3}$ E	98.86331	16.7	−4.5	2.3(0.4)	0.2	20	1.6(0.8)	0.1	20	2.1(0.5)	0.2	30	2.8(0.6)	0.1	20
$5_{1,4}$–$4_{1,3}$ A	98.90094	16.5	−4.5	2.5(0.5)	0.2	20	≤0.6	≤0.06	20	1.9(0.3)	0.2	30	2.0 (0.3)	0.1	20
CH_3OCH_3															
$4_{1,4}$–$3_{0,3}$ EA [e]	99.32443	10.2	−5.3	≤0.2	≤0.02	15	≤0.3	≤0.03	15	2.1(0.3)	0.12	15	1.8(0.5)	0.09	15
$4_{1,4}$–$3_{0,3}$ AE [e]	99.32443	10.2	−5.3												
$4_{1,4}$ - $3_{0,3}$ EE [e]	99.32521	10.2	−5.3												
$4_{1,4}$–$3_{0,3}$ AA [e]	99.32607	10.2	−5.3												
NH_2CHO [f]															
$4_{1,4}$–$3_{1,3}$	81.69354	12.8	−4.5	≤0.2	≤0.02	7	≤0.1	≤0.01	7	≤0.06	≤0.006	7	0.4(0.1)	0.04	10

Notes. [a]Region where formamide and dimethyl ether emits (Ceccarelli et al. 2017). [b]Frequencies and spectroscopic parameters are retrieved from the JPL (Jet Propulsion Laboratory; Pickett et al. 1998) molecular database and from the CDMS (Cologne Database for Molecular Spectroscopy; Müller et al. 2005): for CH_3OH by Xu et al. (2008), for CH_3CHO by Kleiner et al. (1996), for CH_3CHO_3 by Neustock et al. (1990), for NH_2CHO by Kirchhoff et al. (1973). Upper level energies refer to the ground state of each symmetry. [c]Mean velocity–integrated line flux over the whole velocity emission range from the spectra extracted at the CH_3CHO and CH_3OH transitions at each outflow peaks (see Table 2). In case of non–detection we report the 3σ limit. The lines are centered at ∼3 km s^{-1}, ∼1 km s^{-1}, ∼11 km s^{-1} for outflow SE, SW and North respectively, in agreement with the expected outflow velocity (Santangelo et al. 2015) given the WideX channel resolution (∼6 km s^{-1}). [d]The rms is computed over a 200 km s^{-1} band around each line. [e]These lines are blended together at the WideX resolution (∼2 MHz), therefore they are not used for the non-LTE analysis. [f]From Setup 1.

$2_{0,2}$–$1_{0,1}$ E (E_{up} = 21 K), are blended together at the WideX resolution (∼2 MHz); therefore, they were not used in the analysis described in the next section. Table 3 reports the fit results; in the case of non-detection, the 3σ limit is reported.

5. Derivation of the column densities and abundance ratios

5.1. Methanol and acetaldehyde

We used the detected lines of methanol and acetaldehyde to estimate their column densities in the four positions of Table 2. We used the standard rotational diagram method (Goldsmith & Langer 1999), which assumes local thermodynamic equilibrium (LTE) and optically thin line emission. We checked a posteriori that the latter assumption is valid. Also, because the map in Fig. 1 shows that the emission is more extended with respect to the observation beam, we did not apply a dilution factor. The used error bar of each data point includes the spectral RMS and the calibration error (∼15%).

Figure 4 shows the rotational diagrams of methanol and acetaldehyde in the SE, SW, and North positions (Table 2), and Table 4 lists the fitted values. In the As position, we could not build a rotational diagram for either of the two species as not enough lines were detected. In this case we obtained an estimate of their column density by assuming a rotational temperature ranging from 10 to 30 K, a range that includes the temperatures found in the other positions (SE, SW, and North). If no line was detected we used the 3σ limit.

To compute the methanol over acetaldehyde abundance ratios, quoted in Table 4, we adopted the assumptions that the lines emitted by the two species come from the same region, and therefore possess the same rotational temperature T_{rot}. Under these two assumptions the column density ratio R of the two species is obtained by taking the column density N_x of each species at the same rotational temperature T_{rot}, namely $R = N_1(T_{rot})/N_2(T_{rot})$. The error bar δR is then obtained by computing R at the smallest and largest T_{rot} of the two species. For example, in the Outflow SE the derived T_{rot} is equal to (11 ± 3) K and (9 ± 2) K in methanol and acetaldehyde, respectively;

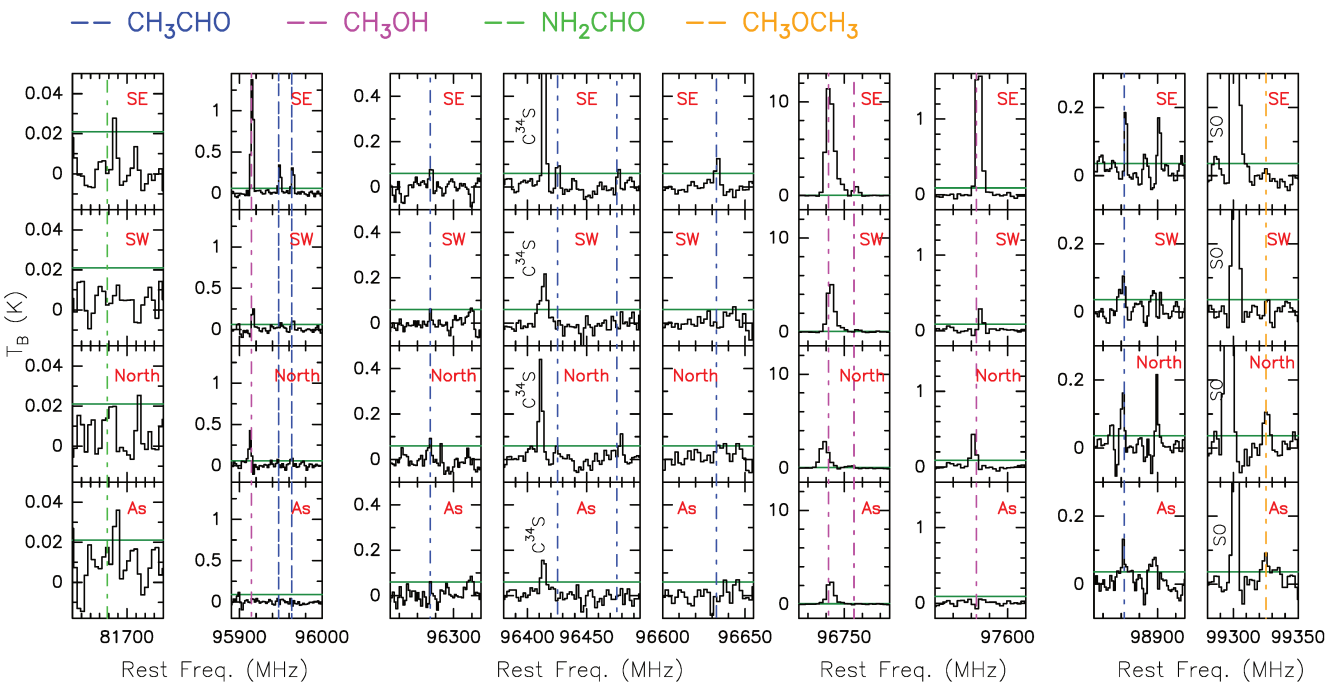

Fig. 3. Spectra toward the four positions along the outflows of IRAS 4A listed in Table 2. The horizontal green lines represent the 3σ levels (reported in Table 3); the vertical dashed lines in blue and magenta represent the rest frequency of acetaldehyde and methanol lines, respectively. The rest frequency corresponds to the protostar Local Standard of Rest (LSR) velocity (6.5 km s^{-1}).

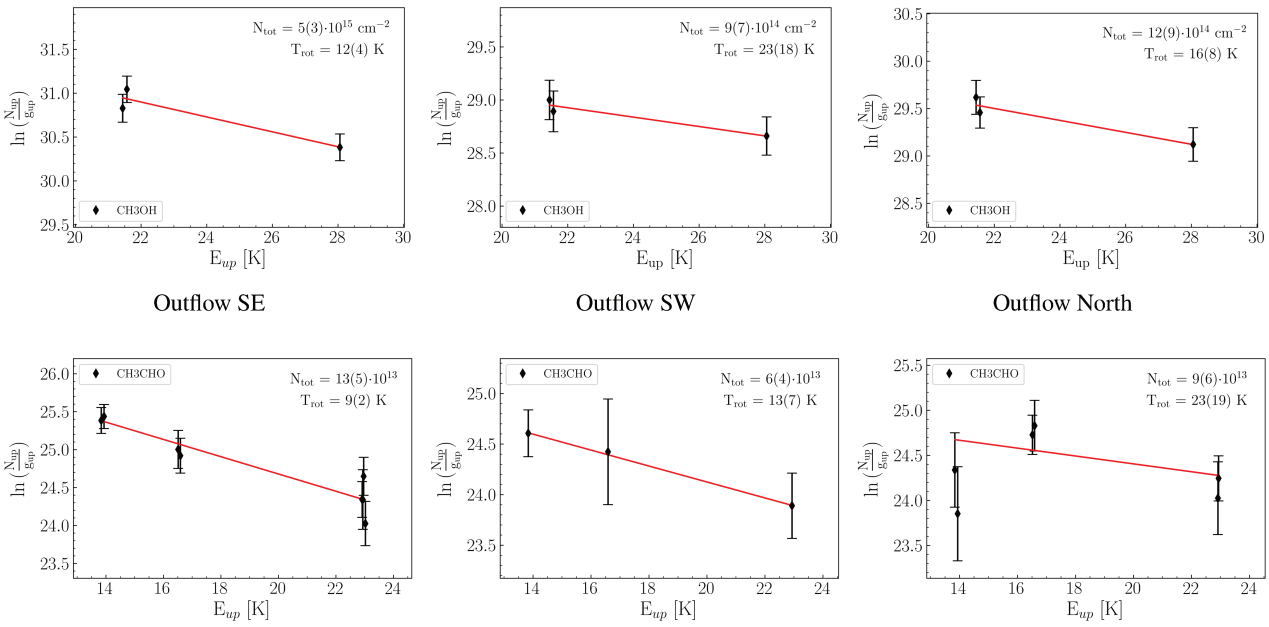

Fig. 4. *Upper panels*: rotational diagrams of methanol (CH_3OH) in outflow SE, SW, and North (*from left to right*). *Lower panels*: rotational diagrams of acetaldehyde (CH_3CHO) in outflow SE, SW, and North. The parameters N_{up}, g_{up}, and E_{up} are the column density, the degeneracy, and the energy of the upper level. The error bars on $\ln(N_{up}/g_{up})$ are computed by taking the calibration error on the integrated flux (15%) into account. The red lines represent the best fits.

therefore, to estimate the error δR we computed $R(T_{rot})$ at 7 and 14 K. We note that the method described above allows us to reduce the error bar in the abundance ratio because the calibration uncertainty, which enters in the column density estimate of each species, cancels out when considering the column density of two species derived with the same observation data set.

For methanol, we obtain a column density $N_{CH_3OH} \simeq 9 - 50 \times 10^{14}$ cm^{-2} and a rotational temperature T_{CH_3OH} between 11 and 23 K. For acetaldehyde, we obtain $N_{CH_3CHO} \simeq 0.6{-}1.3 \times 10^{14}$ cm^{-2} and T_{CH_3CHO} between 9 and 23 K. Their abundance ratios vary from 10–20 to ~44 in the three lobes; more precisely, the SE lobe is the one with the largest CH_3OH/CH_3CHO abundance ratio. In As we only derive a lower limit to the CH_3OH/CH_3CHO abundance ratio of ≥20. We note that our observations provide different values of the CH_3OH/CH_3CHO abundance ratio compared to those previously derived by

Table 4. Results of the LTE analysis with the rotational diagrams for each outflow peak, using the observation with the NOEMA WideX backend.

Molecule			Outflow SE	Outflow SW	Outflow North	Region As [(a)]	L1157-B1 [(b)]
CH_3OH	N_{tot}	[10^{14} cm^{-2}]	50(30)	9(7)	12(9)	5-15	130(30)
	T_{rot}	[K]	11(3)	23(18)	18(8)	10–30 [(c)]	10.0(1.1)
CH_3CHO	N_{tot}	[10^{14} cm^{-2}]	1.3(0.5)	0.6(0.4)	0.9(0.6)	≤(0.25–0.5)	0.7(0.3)
	T_{rot}	[K]	9(2)	13(7)	23(19)	10–30 [(c)]	8(1)
CH_3OCH_3	N_{tot}	[10^{14} cm^{-2}]	≤0.5	≤0.7	1.6(0.7)	1.0(0.4)	3
	T_{rot}	[K]	11	16	19	10–30 [(c)]	9
NH_2CHO	N_{tot}	[10^{14} cm^{-2}]	≤0.02	≤0.02	≤0.02	0.03(0.02)	–
	T_{rot}	[K]	11	16	19	10–30 [(c)]	–
$\frac{CH_3OH}{CH_3CHO}$ [(d)]			44(5)	11(3)	17(3)	≥20	190(60)

Notes. In the last row are shown the values of the abundance ratio of methanol to acetaldehyde for each outflow peak. [(a)]Region where formamide and dimethyl ether emit (Ceccarelli et al. 2017). [(b)]From Codella et al. (2020) based on interferometric observations. [(c)]Fixed rotational temperature used to derive a range of possible N_{tot}. [(d)]Abundance ratio computed dividing the best fit column densities derived assuming that the two species are tracing the same gas with the same properties (see text).

Holdship et al. (2019, ~300) toward the south and north lobes of the IRAS 4A outflows via single-dish observations. We attribute this difference to the fact that the single-dish observations of IRAS 4A by Holdship et al. (2019) include emission from a much larger region (including some from the central protostars) with respect to that probed by the present SOLIS observations. Moreover Holdship et al. (2019) do not explicitly derive the emitting size, even though they minimize with respect to this parameter; since the maximization is done independently for each species, their column density ratio has a relatively large intrinsic uncertainty. Therefore, the interferometric images allow us to minimize the risk of mixing different gas components (typical of shocked regions).

The abundance ratio analysis confirms what we can see from the emission maps (Fig. 1), namely that the methanol and acetaldehyde emission (and their relative abundance) is quite different in the SE lobe with respect to the SW and North lobes. We note that the difference cannot be attributed to excitation effects, having the methanol and acetaldehyde lines with similar upper level energies (E_{up} from 7 to 28 K), similar Einstein coefficients ($A_{ij} \sim 10^{-5}$ s^{-1}), and comparable derived temperatures, within the measurement errors.

To summarize, the SW and North lobes have a relatively low CH_3OH/CH_3CHO abundance ratio (8–20), whereas the SW lobe presents a ratio at least two times higher (~44). Since the SW and North lobes belong to the same outflow emanating from 4A2 and the SE lobe traces the outflow emanating from 4A1, it seems reasonable to attribute the observed difference to an intrinsic difference in the two outflows. We explore this hypothesis in the next section with the help of an astrochemical model.

5.2. Dimethyl ether and formamide

Regarding formamide and dimethyl ether, we detected only one line at most of the latter and four lines (blended at the WideX resolution, ~2 MHz) of the former in any position (see Table 3). For this reason, we did not carry out the rotational diagram analysis as we did for the other iCOMs. Furthermore, while formamide is marginally resolved at the As position, dimethyl ether is not resolved in any outflow peaks (see Fig. 1). If detected, we derived the column densities using the integrated area of the $4_{1,4}-3_{1,3}$ line for formamide and the blended ones for dimethyl ether, assuming fixed rotational temperatures. As for methanol and acetaldehyde, we used 11, 16, and 19 K for SE, SW, and North, respectively, and 10–30 for As. If not detected, an upper limit on the column density is derived considering the 3σ limit of the spectra and using the above rotational temperatures. The derived values are reported in Table 4.

6. Astrochemical modeling

We ran our model GRAINOBLE+ in order to reproduce the observations and understand what could be the cause of the observed difference in the CH_3OH/CH_3CHO abundance ratio in the different lobes of the IRAS 4A outflows.

There is solid evidence (observational, theoretical, and experimental) that methanol is synthesized on the grain surfaces via the hydrogenation of iced CO by the successive addition of H atoms (Boogert et al. 2015; Tielens & Hagen 1982; Watanabe & Kouchi 2002). On the contrary, the acetaldehyde formation route is less clear, and the two paths, formation in the gas phase or on the grain surfaces, are still debated. Specifically, grain surface models predict that CH_3CHO could be formed through the combination of the two radicals CH_3 and HCO (previously formed by photodissociation of methanol and formaldehyde, respectively) on the surface of the grains (Garrod & Herbst 2006). However, recent quantum chemistry computation by Enrique-Romero et al. (2016, 2019) show that alternative channels leading back to the two simple species CH_4 and CO are competitive. Conversely, the gas-phase models claims that acetaldehyde formation could occur by the oxidation of hydrocarbons (formed previously on the grain mantles via hydrogenation of carbon chains; Charnley et al. 1992; Charnley 2004). In particular, the injection from grain mantles of ethane (C_2H_6) is expected to drive CH_3CH_2 that will then react in the gas phase with atomic oxygen, giving CH_3CHO (Charnley 2004). The crucial reaction is therefore

$$CH_3CH_2 + O \rightarrow CH_3CHO + H. \quad (1)$$

Following these two possibilities, we ran a grid of astrochemical models in order to reproduce our observations and to understand the possible cause of the difference in the observed CH_3OH/CH_3CHO values in the two IRAS 4A outflows.

6.1. Model description

GRAINOBLE+ is a gas-grain model simulating the chemical evolution of gas and ices. It is the upgraded version of GRAINOBLE, initially developed by Taquet et al. (2012a); in particular, it is re-coded and improved in terms of computational efficiency and treatment of processes. The GRAINOBLE+ version[3] allows an easy incorporation of many complicated processes that occur in the gas and on the grain surfaces. The code can carry out an easy implementation of evolution of physical conditions of a cloud with a given time-dependent physical profile. Additionally, the new code allows a distribution of size for the grains, multi-layer formation of the grain ice mantle, growth and depletion of the ice, and desorption.

In this work we used a chemical network of 522 species and 7785 reactions based on the KIDA database[4], which has been updated from various recent works (e.g., Loison et al. 2014; Balucani et al. 2015; Skouteris et al. 2017, 2018).

In order to simulate the passage of a shock in IRAS 4A, we employed the gas-phase mode of GRAINOBLE+. The simulation follows two steps: (1) a cold molecular gas phase at 10 K and 2×10^4cm^{-3} H-nuclei density (n_H); (2) a post-shock gas phase where density and temperature suddenly jump to 2×10^6 cm^{-3} and 70 K. In other words, the second phase inherits the evolved chemical composition of the cloud from the cold phase[5]. Additionally, the gas is infused by species that were formerly synthesized in ice mantles due to the grain sputtering caused by the shock passage.

It is possible that before reaching the temperature of 70 K, the shocked gas passes through a short initial phase with high temperature. However, this phase unlikely affects the results reported in the next section because there are no known gas-phase reactions with activation barriers that form acetaldehyde. This is confirmed by models taking into account the temperature evolution in the shocked gas (e.g., Nesterenok 2018; Burkhardt et al. 2019).

We do not have precise estimates of the density and temperature in the positions where we derived the CH_3OH/CH_3CHO abundance ratio. However, the values derived at positions close to those selected here via a non-LTE analysis of observed SO_2 lines (Taquet et al. 2020) are similar to those adopted in our modeling. We assumed that the cosmic ray ionization rate is the same as toward L1157-B1 ($\zeta = 3 \times 10^{-16}$ s^{-1}; Podio et al. 2014) and that the abundance of the injected species are also similar to the values adopted for L1157–B1 (see Table B1 of Codella et al. 2017), listed in Table 5.

We ran series of models to compare the observed CH_3OH/CH_3CHO abundance ratio with the predicted ratio, and to understand what the ratio depends on. We start exploring the gas-phase formation route of acetaldehyde assuming that its formation is dominated by reaction (1) in the passage of shock. Oxygen is much more abundant than the injected ethyl radical in the post-shock phase; therefore, CH_3CH_2 is the bottleneck of the rate of the reaction (1).

First, we ran a grid of 169 models with different injected abundances at the beginning of the shocked phase for ethyl radical (CH_3CH_2) and methanol in the ranges $[4 \times 10^{-9}, 4 \times 10^{-7}]$ and $[4 \times 10^{-8}, 4 \times 10^{-6}]$, respectively. The methanol abundance range was chosen in order to include the observed values in the hot corinos and in the protostellar shocks (the L1157-B1 outflow in particular); the ethyl radical range was chosen in order to match our observed CH_3OH/CH_3CHO abundance ratio. The results are shown in Fig. 5 and described in the next section.

Second, we studied the influence of the density and cosmic ray ionization rate ζ on the chemical evolution, and how the CH_3OH and CH_3CHO abundances and their relative ratio depend on the time after the shock passage. We note that protostellar shocks could be local accelerators of cosmic ray protons (Padovani et al. 2016), and therefore in this work ζ is an unknown parameter. We then ran two additional models. In the first we decrease the chosen n_H density value to 2×10^5 cm^{-3}; in the second we decrease the chosen cosmic ray ionization rate value to $\zeta = 3 \times 10^{-17}$ s^{-1} for the post-shock phase. The injected abundances of methanol is 3×10^{-6} and for the ethyl radical it is 3×10^{-7} in both cases. These values are chosen such that the models reproduce the observed CH_3OH/CH_3CHO abundance ratios for the SW and North lobes (8-20) at 1000 yr (orange band in Fig. 5) and for the SE lobe as well. The results are shown in Fig. 6 and described in the next section.

Finally, we ran a model with the assumption that acetaldehyde is synthesized on the ice mantles and injected directly into the gas phase at the passage of the shock.

Table 5. Injected abundances (with respect to H-nuclei) into the gas phase at the second step of the model.

Molecules	Injected abundances (/H)
CO_2	3×10^{-5}
H_2O	2×10^{-4}
OCS	2×10^{-6}
H_2CO	1×10^{-6}
NH_3	2×10^{-5}

Notes. These values are based on previous observations toward L1157-B1 (Codella et al. 2017).

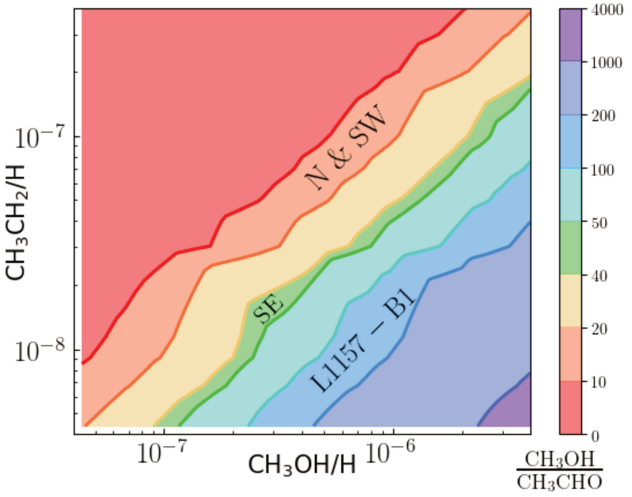

Fig. 5. Contour map of the CH_3OH/CH_3CHO abundance ratio at 1000 yr after the start of the shock passage. The x- and y-axis are the injected abundances of methanol $[4 \times 10^{-8}, 4 \times 10^{-6}]$ and the parent molecule of acetaldehyde, ethyl radical CH_3CH_2 $[4 \times 10^{-9}, 4 \times 10^{-7}]$, respectively. The measured methanol to acetaldehyde abundance ratio of the North and SW outflows (8–20) fall in the orange band, and that of SE (38–50) in the green band; the L1157-B1 value (130–250) is covered by the blue band (Codella et al. 2020).

[3] A detailed description of the GRAINOBLE+ model will be presented in a forthcoming dedicated article.

[4] http://kida.obs.u-bordeaux1.fr

[5] We do not compute the grain mantle composition as it is treated as a parameter in the following analysis.

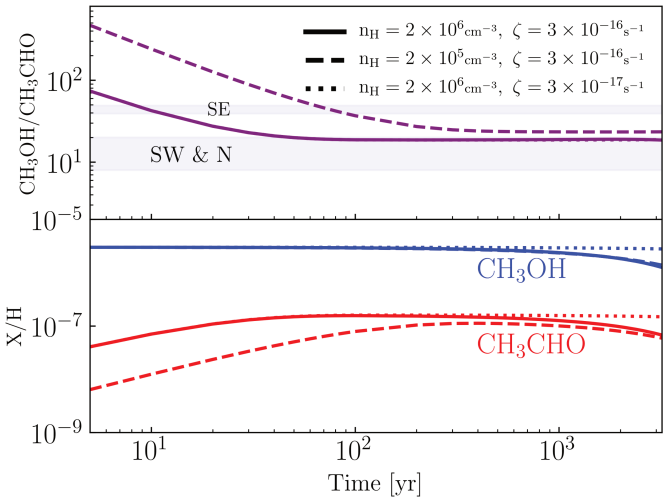

Fig. 6. Time evolution of abundances of methanol in blue and acetaldehyde in red (*bottom*) and their ratios in purple (*top*) for the same injected methanol abundance, 3×10^{-6}, and ethyl radical value, 3×10^{-7}. The different line styles correspond to models run with different conditions, as reported in the upper panel legend. The CH_3OH/CH_3CHO abundance ratio is constant if both species are directly injected from the grain mantles (see text).

6.2. Model results

Figure 5 shows the contour map of the CH_3OH/CH_3CHO abundance ratio at 1000 yr after the shock passage as a function of the injected methanol and ethyl radical, assuming that acetaldehyde is entirely synthesized in the gas phase. We note that the chosen age (1000 yr) is approximately the same magnitude as the kinematical age of L1157-B1 (Podio et al. 2016; Codella et al. 2017) and, likely, IRAS 4A outflows. First, the figure shows that there is a linear dependence of the CH_3OH/CH_3CHO abundance ratio on the injected methanol abundance and on the ethyl radical abundance in the range explored in our simulations. Second, reasonable values of methanol and ethyl radical abundance can reproduce the observed values in the four IRAS 4A outflow positions that we studied (Table 2).

In Fig. 6, we show the evolution of methanol and acetaldehyde abundance as a function of the time after the shock passage, for different densities n_H and cosmic ray ionization rates ζ. Given that methanol is a grain surface product, even by varying n_H or ζ, the injected abundance remains constant in the early stages of the shock up to $\sim 2 \times 10^3$ yr. The time evolution of acetaldehyde in the early stages is different from that of methanol; while the latter remains constant, acetaldehyde abundance increases soon after the shock passage. This is expected since we assumed that acetaldehyde is a gas phase product and its evolution is dominated by the formation through ethyl radical reaction (1). Furthermore, the time evolution of acetaldehyde in the post-shock phase is influenced by variation of n_H or ζ. Lower density slows down the formation rate of acetaldehyde in the early stages; this is due the fact that in lower density gas the ion abundance is higher. Therefore, the contribution of destruction rates is higher in the evolution. Similar to methanol, a lower cosmic ray ionization rate does not affect the early stages.

Finally, we ran a model in which acetaldehyde is synthesized on the icy dust surfaces and injected directly into the gas phase. Therefore, in the model the species injected into the gas phase right after the shock is no longer the ethyl radical but acetaldehyde, whose abundance is chosen to be equal to the observed one. Therefore, the gas-phase production of acetaldehyde is, in this case, negligible. As for methanol, the abundance of acetaldehyde, now injected from grains, remains constant up to $\sim 2 \times 10^3$ yr when the destruction by ions (H_3O^+ in this specific case) becomes dominant. Therefore, the difference in the abundance of acetaldehyde between the gas- and grain-synthesized models is only within the first 200 yr of the shocked phase, when acetaldehyde takes time to be formed by the reactions between ethyl radical with atomic oxygen.

7. Discussion

7.1. Two IRAS 4A outflows

Our new SOLIS observations show that the two outflows emanating from 4A1 and 4A2, previously identified by Choi (2005) and Santangelo et al. (2015) via simple molecules (SiO, CO, and SO), are enriched with methanol all across the three (visible) lobes. Conversely, acetaldehyde is spread only over the southern lobes and is concentrated in a compact spot in the northern one. Therefore, a first conclusion of this work is that in the protostellar post-shock regions there is the release in gas phase of methanol, previously formed on the grain surfaces, and the production of acetaldehyde. The statistics are very poor for the moment, with the two IRAS 4A outflows and the L1157–B1 outflow in which acetaldehyde is detected with interferometric observations (Codella et al. 2015, 2017, 2020).

For the IRAS 4A outflows, the SE lobe is richer in both methanol and acetaldehyde, specifically the outflow emanating from 4A1. We note that this is the opposite behavior with respect to the SiO emission, which is instead brighter along the 4A2 outflow (Choi 2005). This anti-correlation with SiO is also seen in other (simple) molecules, such as NH_3, H_2CO, and HCN by Choi et al. (2011). As Choi et al. (2011) suggested, it could be due to a different strength of the shock (the sputtering of Si could require different shock velocities with respect to the other molecules) or to SiO tracing different physical conditions with respect to the other molecules. For example, SiO could trace the jet, while the other molecules could have originated in the gas entrained by the jet (e.g., Bachiller et al. 1998; Ospina-Zamudio et al. 2018, 2019). Linked with this, the different spatial distribution between SiO and other species, could be due to time-evolution effects, namely different ages of the shocks, as previously observed in other outflows (e.g., Castets et al. 2001). We discuss this point further in the next section.

Finally, the origin of the iCOMs emission in the As position is not clear. It does not seem to be clearly associated with any of the two southern lobes, but rather with the point where they intersect. That would imply that additional shocks can occur at the interface of the swept-up cavities opened up by the jets. Higher spatial resolution observations are needed to confirm or reject this hypothesis.

7.2. CH_3OH/CH_3CHO abundance in IRAS 4A1 and 4A2 outflows

In Sect. 5 we measured the methanol to acetaldehyde abundance ratio toward the three positions of the two IRAS 4A outflows, in the North, SW, and SE lobes (Table 4). While the North and SW lobes have a similar values, between 8 and 20 (considering the error bars), the SE lobe has higher CH_3OH/CH_3CHO, 38–50. In other words, the methanol to acetaldehyde abundance ratio is about two times higher in the outflow emanating from 4A1 with respect to that from 4A2. In this section we try to understand the

origin of this difference, keeping in mind that while methanol is a past grain-surface product, acetaldehyde can either be itself a past grain-surface or a gas-phase product.

One easy possible explanation then of the CH_3OH/CH_3CHO difference is that the grain mantle composition is different in the two outflows. However, this seems unlikely because, on the one hand, no gradient in the ratio is seen between the North and SW lobes of the 4A2 outflow; moreover, the SW and SE lobes are very close in space, closer than the two 4A2 outflow positions where we estimated the CH_3OH/CH_3CHO abundance ratio. Therefore, although we cannot totally exclude it, it seems to us that the different grain composition is an improbable explanation.

If acetaldehyde is synthesized by the gas-phase reaction (1), there are more possibilities than a different grain mantle composition. As shown by the modeling in Sect. 6, a lower density or a younger age of the 4A1 outflow with respect to 4A2 would explain the observed CH_3OH/CH_3CHO difference. Specifically, if the two outflows are very young and 4A1 is younger than about 200 yr, then this would explain why its ratio is higher than the 4A2 value (see Fig. 6).

Unfortunately, our observations did not have enough methanol lines to allow a meaningful non-LTE analysis to derive the volume density, so we do not know if the density in the 4A1 outflow is lower than in the 4A2 outflow. With a non-LTE analysis on SO_2, Taquet et al. (2020) suggest that there is no significant difference in density between the outflow driven by 4A1 and that from 4A2. On the other hand, assuming a typical shock velocity of 100 km s^{-1}, we estimate a kinematical age of ~200 yr for the 4A1 outflow which has a very short extent; this seems to support the younger age of 4A1 hypothesis. Furthermore, Santangelo et al. (2015), using high spatial resolution observations of CO, SiO, and SO, showed that the 4A1 jet is faster than the 4A2 one; this, combined with the smaller spatial extension again supports the hypothesis that the 4A1 outflow is younger than that of 4A2. In favor of a different age for the two outflows there is also the observed chemical differentiation between the two driving sources: 4A1 is bright in the continuum but lacks iCOM line emission, exactly the opposite of 4A2 (e.g., López-Sepulcre et al. 2017). One of the possible explanations for this situation is the smaller hot corino size, which could also imply a younger age of 4A1, and this agrees with the younger age of its outflow as well.

In summary, the different CH_3OH/CH_3CHO abundance ratio measured in the 4A1 and 4A2 outflows is unlikely caused by a different grain mantle composition of the two outflows because the more extended 4A2 outflow shows no significant variation in this ratio on a scale of about 6000 au. On the contrary, the observed CH_3OH/CH_3CHO abundance ratio is consistent with the scenario in which (i) the 4A1 outflow is younger (and consequently faster) than the 4A2 outflow and (ii) in both outflows acetaldehyde is synthesized in the gas phase. The major reaction is between atomic oxygen and ethyl radical. The gas-phase synthesis hypothesis also agrees with theoretical quantum chemistry studies (Enrique-Romero et al. 2016, 2019). Thus, although terrestrial laboratory experiments show that acetaldehyde can be formed on the surfaces of dust grains (e.g., Bennett et al. 2005a,b; Öberg et al. 2009), our results provide evidence that the gas-phase formation route cannot be neglected, and actually appears to be the dominant process in the IRAS 4A outflows. We note that these conclusions are robust as they depend very little on the details of the modeling being based on known reactions in the gas phase.

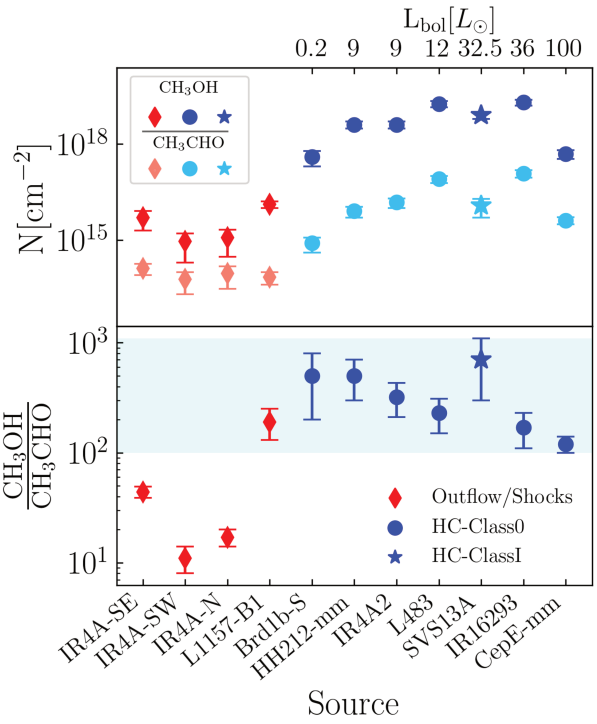

Fig. 7. Abundance ratios of CH_3OH to CH_3CHO (*bottom panel*) and the CH_3OH and CH_3CHO column density (*upper panel*) compared to different sources whose emitting size has been estimated via interferometric observations: the values in the outflows of IRAS 4A (this paper), in the outflow of L1157-B1 (Codella et al. 2020), the Class I source SVS 13A (Bianchi et al. 2019), and the Class 0 sources, in decreasing order of bolometric luminosity: Barnard1b-S (Marcelino et al. 2018), HH212-mm (Bianchi et al. 2017; Codella et al. 2020), IRAS 4A2 (Taquet et al. 2015; López-Sepulcre et al. 2017), L483 (Jacobsen et al. 2019), IRAS 16293-2422B (Jørgensen et al. 2016), CepE-mm (Ospina-Zamudio et al. 2018). The outflow values are shown in red (pink for CH_3CHO), the hot corinos in blue (cyan for CH_3CHO), using diamonds for the outflows, dots for Class 0 sources, and stars for the Class I sources. The cyan band represents the area in which the hot corino values fall.

7.3. Comparison with other solar-type objects

Figure 7 shows the methanol to acetaldehyde abundance ratio in the IRAS 4A outflows, compared with the values measured in other low and intermediate star forming regions for which the emitting size as been estimated via interferometric observations: the L1157-B1 molecular shock and seven hot corinos.

First, the IRAS 4A outflows have a much lower value for CH_3OH/CH_3CHO with respect to the L1157–B1 value (130–250), reliably measured by Codella et al. (2020). Following the discussion of the previous section, this could be due to a difference in the composition of the grain mantles, to a lower density, or to a younger age of the 4A outflows with respect to the L1157-B1 value. At present, we do not have enough information to support or rule out any of the three possibilities; a more accurate analysis of the IRAS 4A outflows is needed. Obviously, having more information of one key actor, the abundance of ethyl radical in these outflows, could shed more light on why the two outflow systems are different.

Finally, the same difference observed between the IRAS 4A and L1157 outflows, if not larger, is observed with respect to the values measured in Class 0 and I hot corinos (Marcelino et al. 2018; Bianchi et al. 2017, 2019; Taquet et al. 2015; López-Sepulcre et al. 2017; Jacobsen et al. 2019; Jørgensen et al. 2016; Codella et al. 2020; Ospina-Zamudio et al. 2018).

In Fig. 7, we ordered the hot corinos according to their increasing bolometric luminosity L_{bol}, keeping in mind that the measure of L_{bol} is relatively uncertain. It is possible to note an interesting trend: in the Class 0 hot corinos, the CH_3OH/CH_3CHO abundance ratio decreases with increasing L_{bol}. Our modeling (Sect. 6) is not directly applicable to the hot corino case for two main reasons: 1) the hot corino density ($n_H \sim 10^7 cm^{-3}$) is higher than those used in our model (Figs. 6 and 2) there is continuous injection of the infalling material toward the center. Having said that, it seems improbable that the behavior shown in Fig. 7 has something to do with a time effect. In the hot corino conditions (higher density and low cosmic ionization rate) the synthesis in the gas phase is fast during the first decades, while the destruction by molecular ions is slow in the later stages ($\geq 10^5$ yr), leading to a CH_3OH/CH_3CHO abundance ratio that is almost constant.

On the contrary, a possible interpretation is that higher luminosity corresponds to larger hot corino sizes (namely larger regions with a dust temperature $\geq$100 K; Ceccarelli et al. 2007) and, assuming a central peaked density distribution, regions with lower densities. Since methanol is produced during the pre-stellar phase by hydrogenation of frozen CO (Taquet et al. 2012b; Vasyunin et al. 2017), a higher density will bring a greater methanol abundance; acetaldehyde, on the other hand, could be either a past grain-surface or a present-day gas-phase product (see Sect. 6). Therefore, the decreasing CH_3OH/CH_3CHO abundance ratio could indicate that while methanol abundance decreases with density, acetaldehyde or its gas-phase precursors do not. We note that these conclusions have to be taken with caution as the errors on the hot corinos bolometric luminosity are relatively large, but they are worth a deeper study.

8. Conclusions

In this work we reported new observations using the IRAM/NOEMA interferometer in the context of the SOLIS Large Program, and the detection of several iCOMs in the two outflows emanating from IRAS 4A1 and 4A2: methanol, acetaldehyde, dimethyl ether, and formamide. This is the second ever outflow system, after the solar-type protostellar L1157 outflow, where multiple iCOMs have been detected using interferometers. Our main conclusions are the following:

- As in the case of L1157-B1 (Codella et al. 2017), iCOMs are not homogeneously distributed across the IRAS 4A outflows: methanol is more widespread over the two outflows, while acetaldehyde emission is only bright in the southern lobes, and dimethyl ether and formamide are concentrated in a spot at the (apparent) interface between the southern lobes of the 4A1 and 4A2 outflows. We therefore advise that derivation of iCOM abundance ratios from single-dish observations could be hazardous.
- The measured methanol to acetaldehyde abundance ratio is twice as large in the 4A1 outflow with respect to that in the 4A2 outflow; the comparison between these results with model predictions suggests that 1) the 4A1 outflow is younger than the 4A2 one and 2) acetaldehyde is synthesized in the gas phase by the reaction of atomic oxygen with ethyl radical. Alternatively, the grain mantle distribution might vary widely on small scales, which seems unlikely since the larger scale 4A2 outflow shows a similar CH_3OH/CH_3CHO value in two distant points of the southern and northern lobes.
- Considering the CH_3OH/CH_3CHO abundance ratio, the two IRAS 4A outflows show a sharp difference with respect to the L1157-B1 outflow. This may indicate that either the grain mantles or the gas volume densities are very different in the two regions. Additional observations are necessary to better constrain the reason of the observed difference.
- The methanol to acetaldehyde abundance ratio in the solar-type hot corinos is at least ten times higher than in the IRAS 4A outflows, again pointing to different grain mantle composition or densities. Interestingly, we note that CH_3OH/CH_3CHO tentatively decreases with increasing bolometric luminosity of the Class 0 hot corino; a possible reason could be the larger sizes of the hot corinos.

Acknowledgements. We are very grateful to all the IRAM staff, whose dedication allowed us to carry out the SOLIS project. This project has received funding from: (i) the European Research Council (ERC) under the European Union's Horizon 2020 research and innovation programme, for the Project "The Dawn of Organic Chemistry" (DOC), grant agreement No 741002. (ii) This work has been supported by the project PRIN-INAF 2016 The Cradle of Life - GENESIS-SKA (General Conditions in Early Planetary Systems for the rise of life with SKA). V.T. acknowledges the financial support from the European Union's Horizon 2020 research and innovation programme under the Marie Sklodowska-Curie grant agreement n. 664931. C.F. acknowledges support from the French National Research Agency in the framework of the Investissements d'Avenir program (ANR-15- IDEX-02), through the funding of the "Origin of Life" project of the Univ. Grenoble-Alpes

References

Altwegg, K., Balsiger, H., Bar-Nun, A., et al. 2016, Sci. Adv., 2, e1600285
Arce, H. G., Santiago-García, J., Jørgensen, J. K., Tafalla, M., & Bachiller, R. 2008, ApJ, 681, L21
Bachiller, R., Guilloteau, S., Gueth, F., et al. 1998, A&A, 339, L49
Balucani, N., Ceccarelli, C., & Taquet, V. 2015, MNRAS, 449, L16
Bennett, C. J., Jamieson, C. S., Osamura, Y., & Kaiser, R. I. 2005a, ApJ, 624, 1097
Bennett, C. J., Osamura, Y., Lebar, M. D., & Kaiser, R. I. 2005b, ApJ, 634, 698
Bianchi, E., Codella, C., Ceccarelli, C., et al. 2017, A&A, 606, L7
Bianchi, E., Codella, C., Ceccarelli, C., et al. 2019, MNRAS, 483, 1850
Blake, G. A., Sandell, G., van Dishoeck, E. F., et al. 1995, ApJ, 441, 689
Boogert, A. C. A., Gerakines, P. A., & Whittet, D. C. B. 2015, ARA&A, 53, 541
Bottinelli, S., Ceccarelli, C., Lefloch, B., et al. 2004, ApJ, 615, 354
Burkhardt, A. M., Shingledecker, C. N., Le Gal, R., et al. 2019, ApJ, 881, 32
Castets, A., Ceccarelli, C., Loinard, L., Caux, E., & Lefloch, B. 2001, A&A, 375, 40
Cazaux, S., Tielens, A. G. G. M., Ceccarelli, C., et al. 2003, ApJ, 593, L51
Ceccarelli, C., Castets, A., Loinard, L., Caux, E., & Tielens, A. G. G. M. 1998, A&A, 338, L43
Ceccarelli, C., Caselli, P., Herbst, E., Tielens, A. G. G. M., & Caux, E. 2007, Protostars and Planets V (Tucson, AZ: University of Arizona Press), 47
Ceccarelli, C., Caselli, P., Fontani, F., et al. 2017, ApJ, 850, 176
Charnley, S. B. 2004, Adv. Space Res., 33, 23
Charnley, S. B., Tielens, A. G. G. M., & Millar, T. J. 1992, ApJ, 399, L71
Choi, M. 2001, ApJ, 553, 219
Choi, M. 2005, ApJ, 630, 976
Choi, M., Kang, M., Tatematsu, K., Lee, J.-E., & Park, G. 2011, PASJ, 63, 1281
Codella, C., Fontani, F., Ceccarelli, C., et al. 2015, MNRAS, 449, L11
Codella, C., Ceccarelli, C., Caselli, P., et al. 2017, A&A, 605, L3
Codella, C., Ceccarelli, C., Bianchi, E., et al. 2020, A&A, 635, A17
Coutens, A., Jørgensen, J. K., van der Wiel, M. H. D., et al. 2016, A&A, 590, L6
De Simone, M., Codella, C., Testi, L., et al. 2017, A&A, 599, A121
De Simone, M., Ceccarelli, C., Codella, C., et al. 2020, ApJ, 896, L3
Di Francesco, J., Myers, P. C., Wilner, D. J., Ohashi, N., & Mardones, D. 2001, ApJ, 562, 770
Elsila, J. E., Glavin, D. P., & Dworkin, J. P. 2009, Meteorit. Planet. Sci., 44, 1323
Enrique-Romero, J., Rimola, A., Ceccarelli, C., & Balucani, N. 2016, MNRAS, 459, L6

Enrique-Romero, J., Rimola, A., Ceccarelli, C., et al. 2019, ACS Earth Space Chem., 3, 2158
Garrod, R. T. 2008, A&A, 491, 239
Garrod, R. T., & Herbst, E. 2006, A&A, 457, 927
Goldsmith, P. F., & Langer, W. D. 1999, ApJ, 517, 209
Gueth, F., Guilloteau, S., & Bachiller, R. 1996, A&A, 307, 891
Herbst, E. 2017, Int. Rev. Phys. Chem., 36, 287
Herbst, E., & van Dishoeck, E. F. 2009, ARA&A, 47, 427
Holdship, J., Viti, S., Codella, C., et al. 2019, ApJ, 880, 138
Jacobsen, S. K., Jørgensen, J. K., Di Francesco, J., et al. 2019, A&A, 629, A29
Jørgensen, J. K., van der Wiel, M. H. D., Coutens, A., et al. 2016, A&A, 595, A117
Jørgensen, J. K., Müller, H. S. P., Calcutt, H., et al. 2018, A&A, 620, A170
Karska, A., Herczeg, G. J., van Dishoeck, E. F., et al. 2013, A&A, 552, A141
Kirchhoff, W. H., Johnson, D. R., & Lovas, F. J. 1973, J. Phys. Chem. Ref. Data, 2, 1
Kleiner, I., Lovas, F. J., & Godefroid, M. 1996, J. Phys. Chem. Ref. Data, 25, 1113
Kristensen, L. E., van Dishoeck, E. F., Bergin, E. A., et al. 2012, A&A, 542, A8
Lay, O. P., Carlstrom, J. E., & Hills, R. E. 1995, ApJ, 452, L73
Lefloch, B., Castets, A., Cernicharo, J., Langer, W. D., & Zylka, R. 1998, A&A, 334, 269
Lefloch, B., Ceccarelli, C., Codella, C., et al. 2017, MNRAS, 469, L73
Loison, J.-C., Wakelam, V., & Hickson, K. M. 2014, MNRAS, 443, 398
Looney, L. W., Mundy, L. G., & Welch, W. J. 2000, ApJ, 529, 477
López-Sepulcre, A., Sakai, N., Neri, R., et al. 2017, A&A, 606, A121
Marcelino, N., Gerin, M., Cernicharo, J., et al. 2018, A&A, 620, A80
Maury, A. J., André, P., Testi, L., et al. 2019, A&A, 621, A76
Mendoza, E., Lefloch, B., López-Sepulcre, A., et al. 2014, MNRAS, 445, 151
Millar, T. J., Herbst, E., & Charnley, S. B. 1991, ApJ, 369, 147
Müller, H. S. P., Schlöder, F., Stutzki, J., & Winnewisser, G. 2005, J. Mol. Struct., 742, 215
Nesterenok, A. V. 2018, Astrophys. Space Sci., 363, 151
Neustock, W., Guarnieri, A., Demaison, J., & Wlodarczak, G. 1990, Z. Naturforsch. A, 45, 702
Öberg, K. I., Garrod, R. T., van Dishoeck, E. F., & Linnartz, H. 2009, A&A, 504, 891
Öberg, K. I., van der Marel, N., Kristensen, L. E., & van Dishoeck, E. F. 2011, ApJ, 740, 14
Ospina-Zamudio, J., Lefloch, B., Ceccarelli, C., et al. 2018, A&A, 618, A145
Ospina-Zamudio, J., Lefloch, B., Favre, C., et al. 2019, MNRAS, 490, 2679
Padovani, M., Marcowith, A., Hennebelle, P., & Ferrière, K. 2016, A&A, 590, A8
Pickett, H. M., Poynter, R. L., Cohen, E. A., et al. 1998, J. Quant. Spectr. Rad. Transf., 60, 883
Pizzarello, S., Cooper, G. W., & Flynn, G. J. 2006, Meteorites and the Early Solar System II (Tucson, AZ: University of Arizona Press), 625
Podio, L., Lefloch, B., Ceccarelli, C., Codella, C., & Bachiller, R. 2014, A&A, 565, A64
Podio, L., Codella, C., Gueth, F., et al. 2016, A&A, 593, L4
Santangelo, G., Codella, C., Cabrit, S., et al. 2015, A&A, 584, A126
Skouteris, D., Vazart, F., Ceccarelli, C., et al. 2017, MNRAS, 468, L1
Skouteris, D., Balucani, N., Ceccarelli, C., et al. 2018, ApJ, 854, 135
Smith, K. W., Bonnell, I. A., Emerson, J. P., & Jenness, T. 2000, MNRAS, 319, 991
Taquet, V., Ceccarelli, C., & Kahane, C. 2012a, A&A, 538, A42
Taquet, V., Ceccarelli, C., & Kahane, C. 2012b, ApJ, 748, L3
Taquet, V., López-Sepulcre, A., Ceccarelli, C., et al. 2015, ApJ, 804, 81
Taquet, V., Codella, C., De Simone, M., et al. 2020, A&A, 637, A63
Tielens, A. G. G. M., & Hagen, W. 1982, A&A, 114, 245
Turner, B. E. 1990, ApJ, 362, L29
Vasyunin, A. I., Caselli, P., Dulieu, F., & Jiménez-Serra, I. 2017, ApJ, 842, 33
Watanabe, N., & Kouchi, A. 2002, ApJ, 571, L173
Xu, L.-H., Fisher, J., Lees, R., et al. 2008, J. Mol. Spectr., 251, 305
Zucker, C., Schlafly, E. F., Speagle, J. S., et al. 2018, ApJ, 869, 83

The Astrophysical Journal, 904:11 (20pp), 2020 November 20 https://doi.org/10.3847/1538-4357/abb953

Binding Energies of Interstellar Molecules on Crystalline and Amorphous Models of Water Ice by Ab Initio Calculations

Stefano Ferrero[1,2], Lorenzo Zamirri[2,3], Cecilia Ceccarelli[4], Arezu Witzel[4], Albert Rimola[1], and Piero Ugliengo[2]
[1] Departament de Química, Universitat Autonoma de Barcelona, E-08193 Bellaterra, Catalonia, Spain
[2] Dipartimento di Chimica, Università degli Studi di Torino, via P. Giuria 7, I-10125, Torino, Italy; piero.ugliengo@unito.it
[3] Nanostructured Interfaces and Surfaces (NIS) Centre, Università degli Studi di Torino, via P. Giuria 7, I-10125, Torino, Italy
[4] Univ. Grenoble Alpes, CNRS, IPAG, F-38000 Grenoble, France; cecilia.ceccarelli@univ-grenoble-alpes.fr
Received 2020 April 28; revised 2020 August 25; accepted 2020 September 15; published 2020 November 17

Abstract

In the denser and colder ($\leqslant$20 K) regions of the interstellar medium (ISM), near-infrared observations have revealed the presence of submicron-sized dust grains covered by several layers of H_2O-dominated ices and "dirtied" by the presence of other volatile species. Whether a molecule is in the gas or solid-phase depends on its binding energy (BE) on ice surfaces. Thus, BEs are crucial parameters for the astrochemical models that aim to reproduce the observed evolution of the ISM chemistry. In general, BEs can be inferred either from experimental techniques or by theoretical computations. In this work, we present a reliable computational methodology to evaluate the BEs of a large set (21) of astrochemical relevant species. We considered different periodic surface models of both crystalline and amorphous nature to mimic the interstellar water ice mantles. Both models ensure that hydrogen bond cooperativity is fully taken into account at variance with the small ice cluster models. Density functional theory adopting both B3LYP-D3 and M06-2X functionals was used to predict the species/ice structure and their BEs. As expected from the complexity of the ice surfaces, we found that each molecule can experience multiple BE values, which depend on its structure and position at the ice surface. A comparison of our computed data with literature data shows agreement in some cases and (large) differences in others. We discuss some astrophysical implications that show the importance of calculating BEs using more realistic interstellar ice surfaces to have reliable values for inclusion in the astrochemical models.

Unified Astronomy Thesaurus concepts: Surface ices (2117); Interstellar dust (836); Interstellar molecules (849); Dense interstellar clouds (371); Interstellar medium (847); Solid matter physics (2090); Interstellar dust processes (838); Computational methods (1965)

Supporting material: figure set

1. Introduction

The presence of molecules in the extreme physical conditions of the interstellar medium (ISM) was considered impossible by astronomers, until the first diatomic species (CN, CH, and CH^+) were detected in the ISM from optical and ultraviolet transitions (Swings & Rosenfeld 1937; McKellar 1940; Douglas & Herzberg 1942). Nowadays more than 200 gaseous molecular species (including radicals and ions) have been identified in the diffuse and dense regions of the ISM, thanks to their rotational and vibrational lines in the radio to far-infrared (FIR) wavelengths (e.g., see the review by McGuire 2018). In the coldest ($\leqslant$20–90 K) and densest ($\geqslant 10^3$ cm^{-3}) ISM, some of these molecules are also detected in the solid state via near-infrared (NIR) observations (e.g., see the review by Boogert et al. 2015).

We now know that the solid-state molecules are frozen species that envelop the submicron dust grains that permeate the ISM and whose refractory core is made of silicates and carbonaceous materials (e.g., Jones 2013; Jones et al. 2017). The grain iced mantle composition is governed by the adsorption of species from the gas phase and by chemical reactions occurring on the grain surfaces. For example, the most abundant component of the grain mantles is H_2O, which is formed by the hydrogenation of O, O_2, and O_3 on the grain surfaces (e.g., Hiraoka et al. 1998; Dulieu et al. 2010; Oba et al. 2012).

The water-rich ice is recognized from two specific NIR bands at about 3 and 6 μm, which are associated with its O–H stretching and H–O–H bending modes, respectively (e.g., see the review by Boogert et al. 2015). In addition, species like CO, CO_2, NH_3, CH_4, CH_3OH, and H_2CO have also been identified as minor constituents of the ice mantles, which, for this reason, are sometimes referred to as "dirty ices" (Boogert et al. 2015). Furthermore, the comparison between the astronomical spectroscopic observations and the laboratory spectra of an analogous interstellar ice sample, principally based on the O–H stretching feature, has shown that the mantle ices very likely possess an amorphous-like structure resembling that of amorphous solid water (ASW; e.g., Watanabe & Kouchi 2008; Oba et al. 2009; Boogert et al. 2015).

Ice surfaces are known to have an important role in the interstellar chemistry because they can serve as catalysts for chemical reactions that cannot proceed in the gas phase, such as the formation of H_2, the most abundant molecule in the ISM (Hollenbach & Salpeter 1971). Ice surfaces can catalyze reactions by behaving as (i) a passive third body, this way absorbing part of the excess of energy released in the surface processes (adsorption and/or chemical reaction) (e.g., Pantaleone et al. 2020); (ii) a chemical catalyst, this way directly participating in the reaction reducing the activation energies (e.g., Rimola et al. 2018; Enrique-Romero et al. 2019, 2020); or (iii) a reactant concentrator, this way retaining the reactants and keeping them in close proximity for subsequent reaction (e.g., CO adsorption and retention for subsequent hydrogenation to form H_2CO and CH_3OH (e.g., Watanabe & Kouchi 2002; Rimola et al. 2014; Zamirri et al. 2019b). All three processes

depend on the binding energies (BEs) of the molecules either directly (e.g., the adsorption of the species) or indirectly (e.g., because the diffusion of a particle on the grain surfaces is a fraction of its BE) (see Cuppen et al. 2017). In addition, molecules formed on the grain surfaces can be later transferred to the gas phase by various desorption processes, most of which depend, again, on the BE of the species. In practice, BEs are crucial properties of the interstellar molecules and play a huge role in the resulting ISM chemical composition. This key role of BEs is very obvious in the astrochemical models that aim at reproducing the chemical evolution of interstellar objects, as clearly shown by two recent works by Wakelam et al. (2017) and Penteado et al. (2017), respectively.

Experimentally, the BEs of astrochemical species are measured by temperature programmed desorption (TPD) experiments. These experiments measure the energy required to desorb a particular species from the substrate, namely, a desorption enthalpy, which is equal to the BE only if there are no activated processes (He et al. 2016) and if thermal effects are neglected. A typical TPD experiment consists of two phases. In the first one, the substrate, maintained at a constant temperature, is exposed to the species that have to be adsorbed coming from the gas phase. In the second phase, the temperature is increased until desorption of the adsorbed species—collected and analyzed by a mass spectrometer—occurs. The BE is then usually extracted by applying the direct inversion method on the Polanyi–Wigner equation (e.g., Dohnalek et al. 2001; Noble et al. 2012). The BE values obtained in this way strongly depend on the chemical composition and morphology of the substrate and also on whether the experiment is conducted in the monolayer or multilayer regime (e.g., Noble et al. 2012; He et al. 2016; Chaabouni et al. 2018). Another issue related to the TPD technique is that it cannot provide accurate BBEs for radical species, as they are very reactive. In the literature, there are many works that have investigated the desorption processes by means of the TPD technique (e.g., Collings et al. 2004; Noble et al. 2012; Dulieu et al. 2013; Fayolle et al. 2016; He et al. 2016; Smith et al. 2016), but they have been conducted for just a handful of important astrochemical species, whereas a typical network of an astrochemical model can contain up to 500 species and very different substrates. In a recent work, Penteado et al. (2017) collected the results of these experimental works, trying to be as homogeneous as possible in terms of different substrates, estimating the missing BE values from the available data and performing a systematic analysis on the effect that the BE uncertainties can have on astrochemical model simulations.

BE values can also be obtained by means of computational approaches that, in some situations, can overcome the experimental limitations. Many computational works have so far focused on a few important astrochemical species like H, H_2, N, O, CO, and CO_2, in which BEs are calculated on periodic/cluster models of crystalline/amorphous structural states using different computational techniques (e.g., Al-Halabi & Van Dishoeck 2007; Karssemeijer et al. 2014; Karssemeijer & Cuppen 2014; Ásgeirsson et al. 2017; Senevirathne et al. 2017; Shimonishi et al. 2018; Zamirri et al. 2019a). In addition, other works have computed BEs in a larger number of species but with a very approximate model of the substrate. For example, in a recent work by Wakelam et al. (2017) BE values of more than 100 species are calculated by approximating the ASW surface with a single water molecule. The authors then fitted the most reliable BE measurements (16 cases) against the corresponding computed ones, obtaining a good correlation between the two data sets. In this way, all the errors in the computational methods and limitations due to the adoption of a single water molecule are compensated by the fitting with the experimental values, in the view of the authors. The resulting parameters are then used to scale all the remaining computed BEs to improve their accuracy. This clever procedure does, however, consider the proposed scaling universal, leaving aside the complexity of the real ice surface and the specific features of the various adsorbates. In a similar work, Das et al. (2018) have calculated the BEs of 100 species by increasing the size of a water cluster from one to six molecules, noticing that the calculated BE approaches the experimental value when the cluster size is increased. As we will show in the present work, these approaches, relying on an arbitrary and very limited number of water molecules, cannot, however, mimic a surface of icy grain. Furthermore, the strength of interaction between icy water molecules, as well as with respect to the adsorbates, depends on the hydrogen bond cooperativity, which is underestimated in small water clusters.

In this work, we followed a different approach, focusing on extended periodic ice models, either crystalline or amorphous, adopting a robust computational methodology based on a quantum mechanical approach. We simulate the adsorption of a set of 21 interstellar molecules, 4 of which are radical species, on several specific exposed sites of the water surfaces of both extended models. BE values have been calculated for more than one binding site (if present) to provide the spread of the BE values that the same molecule can have depending on the position in the ice. Different approaches, with different computational cost, have been tested and compared, and the final computed BEs have been compared with data from the computational approaches of Wakelam et al. (2017) and Das et al. (2018) and data from UMIST and KIDA databases, as well as available experimental data (e.g., McElroy et al. 2013; Wakelam et al. 2015). One added value of this work is the definition of both a reliable, computationally cost-effective ab initio procedure designed to arrive at accurate BE values and an ice grain atomistic model that can be applied to predict the BEs of any species of astrochemical interest.

2. Computational Details

2.1. Structure of the Ice: Periodic Simulations

Water ice surfaces have been modeled enforcing periodic boundary conditions to define icy slabs of finite thickness either entirely crystalline or of amorphous nature. Adsorption is then carried out from the void region above the defined slabs. Periodic calculations have been performed with the ab initio CRYSTAL17 code (Dovesi et al. 2018). This software implements both the Hartree–Fock (HF) and Kohn–Sham self-consistent field methods for the solution of the electronic Schrödinger equation, fully exploiting, if present, the crystalline or molecular symmetry of the system under investigation. CRYSTAL17 adopts localized Gaussian functions as basis sets, similar to the approach followed by molecular codes. This allows CRYSTAL17 to perform geometry optimizations and vibrational properties of both periodic (polymer, surfaces, and crystals) and nonperiodic (molecules) systems with the same level of accuracy. Furthermore, the definition of the surfaces through the slab model allows us to avoid the 3D fake replica of the slab as forced when adopting the plane wave basis set.

Computational parameters are set to values ensuring good accuracy in the results. The threshold parameters for the evaluation of the Coulomb and exchange bi-electronic integrals (TOLINTEG keyword in the CRYSTAL17 code; Dovesi et al. 2018) have been set equal to 7, 7, 7, 7, and 14. The needed density functional integration is carried out numerically over a grid of points, which is based on an atomic partition method developed by Becke (1988). The standard pruned grid (XLGRID keyword in the CRYSTAL17 code; Dovesi et al. 2018), composed of 75 radial points and a maximum of 974 angular points, was used. The sampling of the reciprocal space was conducted with a Pack–Monkhorst mesh (Pack & Monkhorst 1977), with a shrinking factor (SHRINK in the code CRYSTAL17; Dovesi et al. 2018) of 2, which generates $4k$ points in the first Brillouin zone. The choice of the numerical values we assigned to these three computational parameters is fully justified in Appendix A.

Geometry optimizations have been carried out using the Broyden–Fletcher–Goldfarb–Shanno (BFGS) algorithm (Broyden 1970; Fletcher 1970; Goldfarb 1970; Shanno 1970), relaxing both the atomic positions and the cell parameters. We adopted the default values for the parameters controlling the convergence, i.e., difference in energy between two subsequent steps, 1×10^{-7} Hartree; and maximum components and rms of the components of the gradients and atomic displacement vectors, 4.5×10^{-4} hartrees bohr^{-1} and 3×10^{-4} hartrees bohr^{-1}, and 1.8×10^{-3} bohr and 1.2×10^{-3} bohr, respectively. All periodic calculations were grounded on either the density functional theory (DFT) or the HF-3c method (Hohenberg & Kohn 1964; Sure & Grimme 2013). Within the DFT framework, different functionals were used to describe closed- and open-shell systems. For the former, we used the hybrid B3LYP method (Lee et al. 1988; Becke 1993), which has been shown to provide a good level of accuracy for the interaction energies of noncovalent bound dimers (Kraus & Frank 2018), added with the D3-BJ correction for the description of dispersive interactions (Grimme et al. 2010, 2011). For open-shell systems, treated with a spin-unrestricted formalism (Pople et al. 1995), we used the hybrid M06-2X functional (Zhao & Truhlar 2008), which has been proved to give accurate results in estimating the interaction energy of noncovalent binary complexes involving a radical species and a polar molecule (Tentscher & Arey 2013). The choice of these two different functionals is justified by two previous works describing the accuracy on the energetic properties of molecular adducts (Tentscher & Arey 2013; Kraus & Frank 2018). For all periodic DFT calculations we used the Ahlrichs triple-zeta quality VTZ basis set, supplemented with a double set of polarization functions (Schäfer et al. 1992). In the following, we will refer to this basis set as "A-VTZ*" (see Appendix D for details of the adopted basis set).

The HF-3c method is a new method combining the Hartree–Fock Hamiltonian with the minimal basis set MINI-1 (Tatewaki & Huzinaga 1980) and with three a posteriori corrections for (i) the basis set superposition error (BSSE), arising when localized Gaussian functions are used to expand the basis set (Jansen & Ros 1969; Liu & McLean 1973); (ii) the dispersive interactions; and (iii) short-ranged deficiencies due to the adopted minimal basis set (Sure & Grimme 2013).

Harmonic frequency calculations were carried out on the optimized geometries of both crystalline and amorphous ices to characterize the stationary points of each structure. Vibrational frequencies have been calculated at the Γ point by diagonalizing the mass-weighted Hessian matrix of second-order energy derivatives with respect to atomic displacements (Pascale et al. 2004; Zicovich-Wilson et al. 2004). The Hessian matrix elements have been evaluated numerically by a six-point formula (NUMDERIV = 2 in the CRYSTAL17 code; Dovesi et al. 2018), based on two displacements of ± 0.001 Å for each nuclear Cartesian coordinate from the minimum structure.

To avoid computational burden, only a portion of the systems has been considered in the construction of the Hessian matrix, including the adsorbed species and the spatially closest interacting water molecules of the ice surface. This "fragment" strategy for the frequency calculation has already been tested by some of us in previous works and is fully justified by the noncovalent nature of the interacting systems, where the coupling between the vibrational modes of bulk ice and adsorbate moieties is negligible (Tosoni et al. 2005; Rimola et al. 2008; Zamirri et al. 2017).

From the set of frequencies resulting from the "fragment" calculations we worked out the zero-point energy (ZPE) for the free crystalline ice surface, the free adsorbate, and the ice surface/adsorbate complex to arrive at the corresponding correction ΔZPE, as reported in Appendix A.1. From the ΔZPE we corrected the electronic BE for each adsorbate as BE(0) = BE − ΔZPE and found a good linear correlation BE(0) = 0.854 BE, as shown in Appendix A.1. While the "fragment frequency" strategy is fine for computing the ΔZPE of the crystalline ice model owing to the structural rigidity enforced by the system symmetry, the same does not hold for the amorphous ice. In that case, the large unit cell (60 water molecules) and their random organization render the ice structure rather sensitive to the adsorbate interaction, which causes large structural water molecule rearrangement. This, in turn, alters significantly the whole set of normal modes, and the numerical value of the ΔZPE becomes ill-defined. Nevertheless, considering that the kinds of interactions operative for the crystal ice are of the same nature as those for the amorphous one, we adopted the same scaling factor of 0.854 computed for the crystalline ice to correct the electronic BE for the amorphous one. In the following, we compared the experimental BE usually measured for amorphous ices with the BE(0) values. To discuss the internal comparison between adsorption features of different adsorbates on the crystalline ice, we still focused on the uncorrected BEs.

2.2. BE Calculation and Counterpoise Correction

When Gaussian basis sets are used, a spurious contribution arises in the calculation of the molecule/surface interactions, called the BSSE (e.g., Boys & Bernardi 1970). In this work, the BSSE for DFT calculations has been corrected making use of the a posteriori counterpoise (CP) correction by Boys and Bernardi (Davidson & Feller 1986). The CP-corrected interaction $\Delta E^{\rm CP}$ energy has been calculated as

$$\Delta E^{\rm CP} = \Delta E^{*} + \delta E + \Delta E_L - {\rm BSSE} \quad (1)$$

where ΔE^{*} is the deformation-free interaction energy, δE is the total contribution to the deformation energy, and ΔE_L is the lateral interaction (adsorbate−adsorbate interaction) energy contribution. Details on the calculation of each energetic term of Equation (1) can be found in Appendix A. By definition, BE

is the opposite of the CP-corrected interaction energy:

$$\Delta E^{\mathrm{CP}} = -\mathrm{BE}. \quad (2)$$

2.3. BE Refinement with the Embedded Cluster Method

With the aim of refining the periodic DFT BE values for the crystalline ice model, single-point energy calculations have been carried out on small clusters, cut out from the crystalline ice model, using a higher level of theory than the DFT methods with the Gaussian09 program (Frisch et al. 2009). The adopted cluster models were derived from the periodic systems and are described in Section 3.2.2. These refinements have been performed through the ONIOM2 approach (Dapprich et al. 1999), dividing the systems into two parts that are described by two different levels of theory. The Model system (i.e., a small moiety of the whole system, including the adsorbate and the closest water molecules) was described by the High level of theory represented by the single- and double-electronic excitation coupled-cluster method with an added perturbative description of triple excitations (CCSD(T)). The Real system (i.e., the whole system) was described by the DFT level of theory adopted in the periodic calculations with the two different functionals for open- and closed-shell species. In the ONIOM2 methodology, the BE can be written as

$$\mathrm{BE(ONIOM2)} = -\mathrm{BE(Low, Real)} + \Delta\mathrm{BE} \quad (3)$$

$$\Delta\mathrm{BE} = \mathrm{BE(High, Model)} - \mathrm{BE(Low, Model)}. \quad (4)$$

The final BE(ONIOM2) is also corrected by the BSSE following the same scheme described above. Our choices about the Model and Real systems will be extensively justified in Section 3.2.2.

3. Results

3.1. Ice Surface Models

3.1.1. Crystalline Ice Model

Despite the amorphous and perhaps porous nature of the interstellar ice, we adopted, as a paradigmatic case, a proton-ordered crystalline bulk ice model usually known as P-ice ($Pna2_1$ space group; Casassa et al. 1997). From P-ice bulk, we cut out a slab model, i.e., a 2D-periodic model representing a surface. Consequently, periodic boundary conditions are maintained only along the two directions defining the slab plane, while the third direction (z-axis) is nonperiodic and defines the slab thickness. The slab model adopted in this work represents the P-ice (010) surface, in accordance with previous work (Zamirri et al. 2018). This slab consists of 12 atomic layers, is stoichiometric, and has a null electric dipole moment across the z-axis. This ensures an electronic stability of the model with the increase of the slab thickness (Tasker 1979). The slab structure has been fully optimized (unit cell and atomic fractional coordinates) at both B3LYP-D3/A-VTZ* and M06-2X/A-VTZ* DFT levels. As can be seen from Figure 1 (panel (a)), the (010) P-ice unit cell is rather small, showing only one dangling hydrogen (dH) and oxygen (dO) as binding sites. For large molecules, to increase the number of adsorption sites and minimize the lateral interactions among replicas of the adsorbate, we also considered a 2×1 supercell. The electrostatic potential maps (EPMs; see Figure 1, panels (b) and (c)) clearly reveal positive (blue EPM regions) and negative (red EPM regions) potentials around the dH and dO sites, respectively.

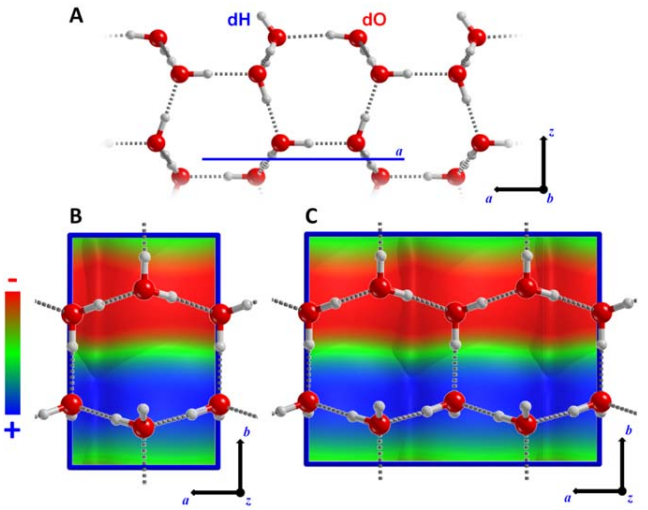

Figure 1. The (010) slab model of P-ice. (a) Side view along the $\boldsymbol{b}$ lattice vector. (b) Top view of the 1×1 unit cell ($|\boldsymbol{a}| = 4.500$ Å and $|\boldsymbol{b}| = 7.078$ Å) superimposed onto the EPM. (c) Top view of the 2×1 supercell ($|\boldsymbol{a}| = 8.980$ Å, $|\boldsymbol{b}| = 7.081$ Å) superimposed onto the EPM. The isosurface value for the electron density where the electrostatic potential is mapped is set equal to 10^{-6} au. Color code: +0.02 au (blue, positive), 0.00 au (green, neutral), and −0.02 au (red, negative).

3.1.2. Amorphous Solid Water (ASW)

As anticipated, the (010) P-ice surface might not be a physically sound model to represent actual interstellar ice surfaces, due to the evidence, from the spectroscopic feature of the interstellar ice, of its amorphous nature (Boogert et al. 2015). The building up of amorphous surface models is a nontrivial and not unique procedure, because of the lack of a consistent and universally accepted strategy. One common approach is to start from a crystalline model and heat it up to relatively high temperature by running molecular dynamics (MD) simulations for a few picoseconds. This step is followed by thermal annealing to freeze the ice in a glassy amorphous state. In this work, we adopted a different strategy. We refer to a recent work by Shimonishi et al. (2018) in which the BEs of a set of atomic species were computed on several water clusters, previously annealed with MD simulations. We reoptimized (at the B3LYP-D3/A-VTZ* level only) the whole set of ice clusters, and the three most stable clusters, composed of 20 water molecules each, were merged together to define a unit cell of an amorphous periodic ice. This procedure mimics somehow the collision of nanometric-scale icy grains occurring in the molecular clouds. The merger of the three clusters was carried out by matching the dH regions of one cluster with the dO ones of the other. As a result, we ended up with a large 3D-periodic unit cell (with lattice parameters $|\boldsymbol{a}| = 21.11$ Å, $|\boldsymbol{b}| = 11.8$ Å, and $|\boldsymbol{c}| = 11.6$ Å) envisaging 60 water molecules. This initial bulk model was optimized at HF-3c level in order to fully relax the structure from the internal tensions of the initial guess. After this step, we cut out a 2D-periodic slab from the bulk structure. The amorphous slab is composed of 60 water molecules in the unit cell and was further fully optimized (unit cell size and atomic coordinates) at the HF-3c, B3LYP-D3/A-VTZ*, and M06-2X/A-VTZ* levels of theory. The three final structures show little differences in the positions of specific

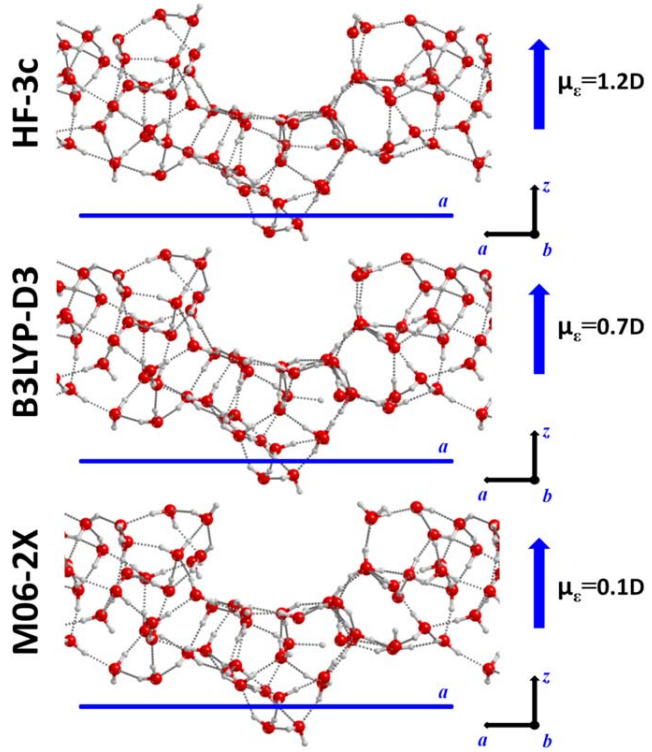

Figure 2. Side view of the amorphous slab models. The cell parameter ***a*** is highlighted as a blue line. Electric dipole moments μ_ϵ along the z-direction are shown on the right side.

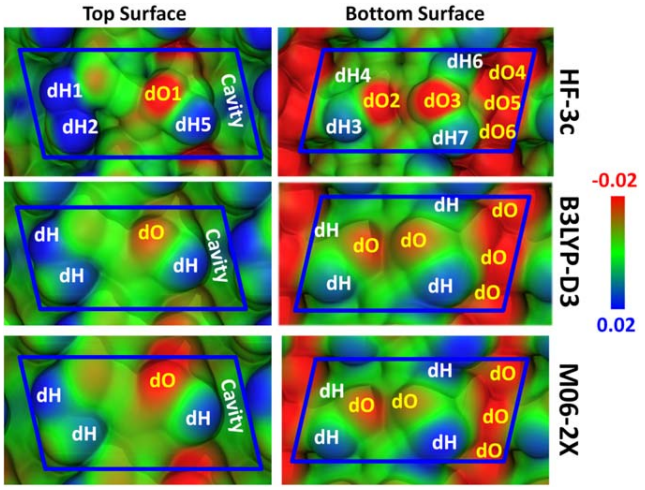

Figure 3. Color-coded EPMs mapped to the electron density for the "top" and "bottom" surfaces of the amorphous slab (HF-3c, B3LYP-D3, and M06-2X optimized geometries). The dO and dH sites are also labeled. The isosurface value for the electron density is set equal to 10^{-6} au, to which the electrostatic potential is mapped out. EPM color code: +0.02 au (blue, positive), 0.00 au (green, neutral), and −0.02 au (red, negative).

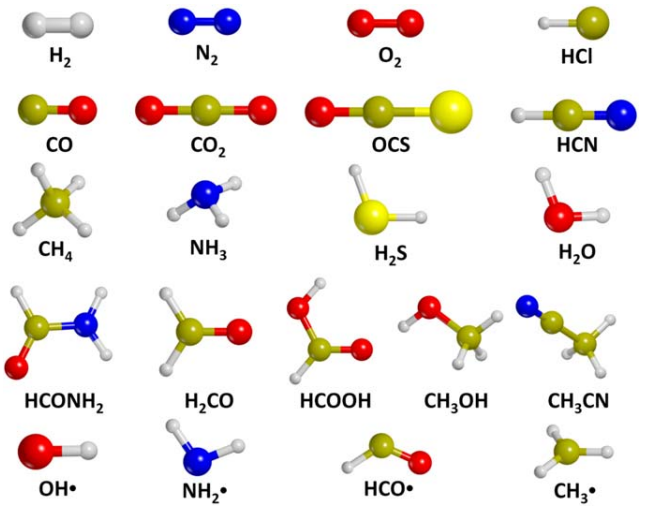

Figure 4. Set of molecular and radical species adopted within this work for the calculation of BE on different ice models. O_2 is an open-shell (spin-triplet) species (Borden et al. 2017).

water molecules, and, on the whole, the structures are very similar (Figure 2). The computed electric dipole moment across the nonperiodic direction (1.2, 0.7, and 0.1 D for the HF-3c, B3LYP-D3, and M06-2X structures, respectively) showed a very good agreement between different models, also considering the dependence of the dipole value on the adopted quantum mechanical method. These amorphous slab models show different structural features for the upper and lower surfaces, which imparts the residual dipole moment across the slab, and consequently exhibit a variety of different binding sites for adsorbates. To characterize the electrostatic features of these sites, which in turn dictate the adsorption process, we resorted to the EPMs for the top/bottom surfaces of each optimized slab (Figure 3). The general characteristics are very similar for the three models, with B3LYP-D3 and M06-2X giving the closest maps. HF-3c tends to enhance the differences between positive and negative regions owing to overpolarization of the electron density caused by the minimal basis set. "Top" surfaces show a hydrophobic cavity (the central greenish region, Figure 3, absent in the P-ice slab, surrounded by dH positive spots). "Bottom" surfaces show several prominent negative regions (from five dOs) mixed with less prominent positive potentials (due to four buried dHs).

3.2. BEs on Crystalline Ice

3.2.1. BE Computed with DFT//DFT Method

In this work, we simulated the adsorption of 17 closed-shell species and 4 radicals, shown in Figure 4. For each molecule/surface complex, geometry optimizations (unit cell plus all atomic coordinates without constraints) were performed. Initial structures were guessed by manually setting the maximum number of H-bonds between the two partners. The pure role of dispersion is estimated by extracting the D3 contribution from the total energy at the B3LYP-D3 level of theory. The energetics of the adsorption processes were then computed according to Equation (1).

As can be seen from the results of Table 1, a range of interactions of different strength is established between the adsorbed species and the crystalline P-ice surface. Some molecules do not possess a net electric dipole moment, while exhibiting relevant electric quadrupole moments (i.e., H_2, N_2, and O_2) or multipole moments of higher order (i.e., CH_4; see their EPMs in Appendix B). For these cases, only weak interactions are established so that BEs are lower than 1800 K (see BE disp values in Table 1). Interestingly, for the N_2, O_2, and CH_4 cases, interactions are almost repulsive if dispersive contributions are not accounted for in the total BE (compare

Table 1
Summary of the BE Values (in Kelvin) Obtained for the Crystalline P-ice (010) Slab with DFT//DFT and DFT//HF-3c Methods

Species	(010) P-ice Crystalline Slab DFT//DFT			(010) P-ice Crystalline Slab DFT//HF-3c		
	BE disp	BE no disp	-disp(%)	BE disp	BE no disp	-disp(%)
H_2	1191	565	625(53)	926	241	686(74)
O_2	1022	−373	1034(137)	794	−84	878(110)
N_2	1564	−72	1636(104)	1455	−180	1636(160)
CH_4	1684	−229	1912(113)	1912	−349	2261(118)
CO	2357	698	1660(71)	1948	60	1888 (97)
CO_2	3440	1540	1900(55)	3007	938	2069(69)
OCS	3476	120	3356(97)	3187	265	2923(92)
HCl	6507	4402	2093(32)	6314	3488	2237(39)
HCN	5124	3067	2057(29)	5725	3271	3043(48)
H_2O	8431	6844	1588(19)	8431	6808	1612(19)
H_2S	5677	3380	2297(40)	5232	3199	2105(40)
NH_3	7373	5533	1852(25)	7301	5484	1816(25)
CH_3CN	7553	4450	3103(41)	6916	3259	2598(44)
CH_3OH	8684	6014	2670(31)	8648	6026	2237(27)
H_2CO-SC1	5869	3885	1985(34)	5773	4053	2369(37)
H_2CO-SC2	6375	3692	2682(42)	6423	3716	2057(36)
$HCONH_2$-SC1	9610	6459	3151(33)	9321	6158	3163(34)
$HCONH_2$-SC2	10079	6483	3608(36)	9634	6074	3560(37)
HCOOH	9526	7325	2189(23)	9297	7168	2117(23)
HCOOH-SC	9442	7301	2021(21)	9405	7541	1864(20)
OH•	6543[a]			6795[a]		
HCO•	3476[a]			3548[a]		
CH_3•	2562[a]			2598[a]		
NH_2•	6038[a]			6050[a]		

Notes. Legend: "BE disp" = BE value including the D3 contribution; "BE no disp" = BE values not including D3 contribution; "-disp(%)" = absolute (percentage) contribution of dispersive forces to the total BE disp.
[a] For radical species (energy at M06-2X level) we cannot discern between disp and no disp data.

BE disp with BE no disp values of Table 1). Therefore, the adsorption is dictated by dispersive forces, which counterbalance the repulsive electrostatic interactions. For the H_2 case, electrostatic interactions are attractive mainly because of the synergic effect of both the surface dH and the dO on the negative and positive parts of the H_2 quadrupole, respectively (see Appendix B).

CO, OCS, and CO_2 also exhibit a quadrupole moment, but due to the presence of heteroatoms in the structure, they can also establish H-bonds with the dH site. Consequently, BEs are larger than the previous set of molecules (i.e., >2400 K; see Table 1). For these three cases, pure electrostatic interactions are attractive, but the dispersion contribution is the most dominant one over the total BE values (compare BE disp with BE no disp values of Table 1). CO, in addition to a net quadrupole, also possesses a weak electric dipole, with the negative end at the carbon atom (see its EPM in Figure 16; see also Zamirri et al. 2017). Thus, although the two negative poles (C and O atoms) of the quadrupole can both interact with the positive dH site, the interaction involving the C atom is energetically slightly favored over the O atom (Zamirri et al. 2017, 2019a). Accordingly, we only considered the C-down case, the computed BE being in good agreement with previous works (Zamirri et al. 2017, 2018). OCS also possesses a dipole and can interact with the surface through either its S- or O-ends, through dO or dH sites. However, due to the softer basic character of S compared to O, the interaction through oxygen is preferred and only considered here.

NH_3, H_2O, HCl, HCN, and H_2S are all amphiprotic molecules that can serve as both acceptors and donors of H-bonds from/to the dH and dO sites. The relative strong H-bonds with the surface result in total BE values that are almost twice as high as the values of the previous set of molecules (i.e., CO, OCS, and COS). Although also in these cases dispersive forces play an important contribution to the BE, the dominant role is dictated by the H-bonding contribution.

For the adsorption of CH_3OH, CH_3CN, and the three carbonyl-containing compounds, i.e., H_2CO, $HCONH_2$, and HCOOH, all characterized by large molecular sizes, we adopted the 2 × 1 supercell (shown in Figure 1) to minimize the lateral interactions between adsorbates. Consequently, two dHs and two dOs are available for adsorption. Therefore, for some of these species (i.e., the carbonyl-containing ones), we started from more than one initial geometry to improve a better sampling of the adsorption features on the (010) P-ice surface (the different cases on the supercell are labeled as SC1 and SC2 in Table 1, and the geometries are reported in Figure 16). The BE values of these species are among the highest ones, due to the formation of multiple H-bonds with the slab (and therefore increasing the electrostatic contribution to the interactions) and a large dispersion contribution due to the larger sizes of these molecules with respect to the other species.

The adsorption study has also been extended to four radicals (i.e., OH• NH_2• CH_3• HCO•), since they are of high interest owing to their role in the formation of interstellar compounds (Sorrell 2001; Bennett & Kaiser 2007). OH• and NH_2• form strong H-bonds with the dH and dO sites of the slab, at variance with CH_3• and HCO• cases, as shown by the higher BE values. Because of the nature of the M06-2X functional, we cannot separate the dispersion contributions to the total BEs.

Interestingly, in all cases we did not detect transfer of the electron spin density from the radicals to the ice surface, i.e., the unpaired electron remains localized on the radical species upon adsorption.

3.2.2. The ONIOM2 Correction and the Accuracy of the DFT//DFT BE Values

As described in Appendix A, the ONIOM2 methodology has been employed to check the accuracy of the B3LYP-D3/A-VTZ* and M06-2X/A-VTZ* theory levels, both representing the Low level of calculation. For this specific case, to reduce the computational burden, we only considered 15 species, leaving aside N_2, O_2, H_2O, CH_4, CH_3CN, and CH_3• radical. Here, the Real system is the periodic P-ice slab model without adsorbed species. Therefore, the BE(Low,Real) term in Equation (3) corresponds to the BEs at the DFT theory levels, hereafter referred to as BE(DFT, Ice). The Model system is carved from the optimized geometry of the periodic system: it is composed of the adsorbed molecule plus n ($n = 2$, 6; the latter only for the H_2 case) closest water molecules of the ice surface to the adsorbates. For the Model systems, two single-point energy calculations have been carried out: one at the High level of theory, i.e., CCSD(T), calculated with Gaussian09, and the other at the Low level of theory, employing the same DFT methods as in the periodic calculations, calculated with CRYSTAL17. For the sake of clarity, we renamed the two terms BE(High,Model) and BE(Low,Model) in Equation (3) for any molecular species μ as BE(CCSD(T), μ–$n$$H_2O$) and BE(DFT, μ–$n$$H_2O$), respectively.

As CCSD(T) is a wave-function-based method, the associated energy strongly depend on the quality of the adopted basis set (Cramer 2002). Consequently, accurate results are achieved only when complete basis set extrapolation is carried out (Cramer 2002); accordingly, we adopted correlation-consistent basis sets (Dunning 1989), here named as cc-pVNZ, where "cc" stands for correlation consistent and N stands for double (D), triple (T), quadruple (Q), etc. Therefore, we performed different calculations improving the quality of the basis set from Jun-cc-pVDZ to Jun-cc-pVQZ (and even Jun-cc-pV5Z when feasible) (Bartlett & Musiał, 2007; Papajak et al. 2011), extrapolating the BE(CCSD(T), μ–$n$$H_2O$) values for $N \rightarrow \infty$. Figure 5 shows, using NH_3 as an illustrative example, the plot of the BE(CCSD(T), μ–$n$$H_2O$) values as a function of $1/L^3$, where L is the cardinal number corresponding to the N value for each correlation-consistent basis set. For all other species, we observed similar trends. This procedure was used in the past to extrapolate the BE value of CO adsorbed at the Mg(001) surface (Ugliengo & Damin 2002).

The procedure gives for the extrapolated BE(CCSD(T), μ–$n$$H_2O$) a value of 4089 K, in excellent agreement with the value computed by the plain B3LYP-D3/A-VTZ* at periodic level of 4390 K (see Figure 5). Very similar agreement was computed for all considered species as shown in Figure 6, in which a very good linear correlation is seen between BE(ONIOM2) and BE(DFT). Therefore, we can confidently assume that the periodic B3LYP-D3/A-VTZ* (closed-shell molecules) or the M06-2X/A-VTZ* (radical species) plain BE values are reliable and accurate enough and are those actually used in this work.

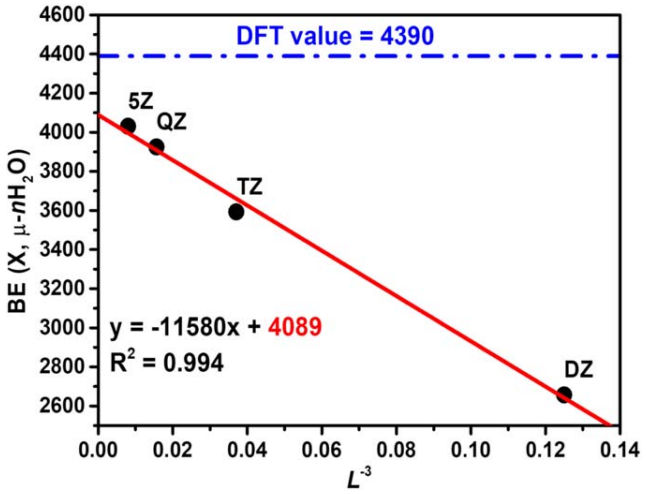

Figure 5. BE(X, μ–$n$$H_2O$) extrapolated value at infinite basis set for the case of NH_3. The dashed–dotted blue line represents the BE computed for the BE(DFT, μ–$n$$H_2O$) at the DFT//A-VTZ* level (4390 K). The solid red line represents the linear fit of the BE(CCSD(T), μ–$n$$H_2O$) values (red squares) calculated with DZ, TZ, QZ, and 5Z basis sets. The extrapolated BE(X, μ–$n$$H_2O$) at infinite basis set is highlighted in red in the fitting equation (4089 K).

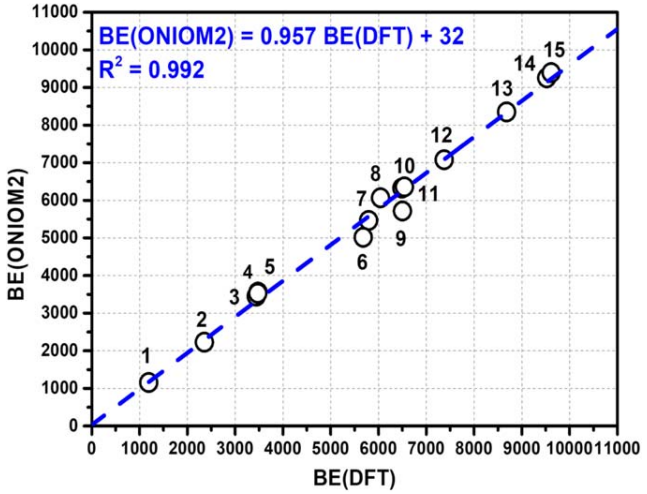

Figure 6. Linear fit between periodic DFT/A-VTZ* BE values (BE(DFT)) and the basis set extrapolated ONIOM2 BE values (BE(ONIOM2)). All values are in K. Fit parameters are also reported. Legend: 1—H_2; 2—CO; 3—CO_2; 4—HCO•; 5—OCS; 6—H_2S; 7—HCN; 8—NH_2•; 9—H_2CO; 10—HCl; 11—OH•; 12—NH_3; 13—CH_3OH; 14—HCOOH; 15—$HCONH_2$.

3.2.3. BE Computed with Composite DFT/HF-3c Method

In the previous section we proved the DFT/A-VTZ* as a reliable and accurate method to compute the BEs of molecules and radicals on the crystalline (010) P-ice ice slab. However, this approach can become very computationally costly when moving from the crystalline to amorphous model of the interstellar ice, as larger unit cells are needed to enforce the needed randomness in the water structure. Therefore, we tested the efficiency and accuracy of the cost-effective computational HF-3c method (see Section 2).

To this end, we adopted a composite procedure that has been recently assessed and extensively tested in the previous work by some of us on the structural and energetic features of molecular crystals, zeolites, and biomolecules (Cutini et al. 2016, 2017, 2019). We started from the DFT/A-VTZ* optimized structure just

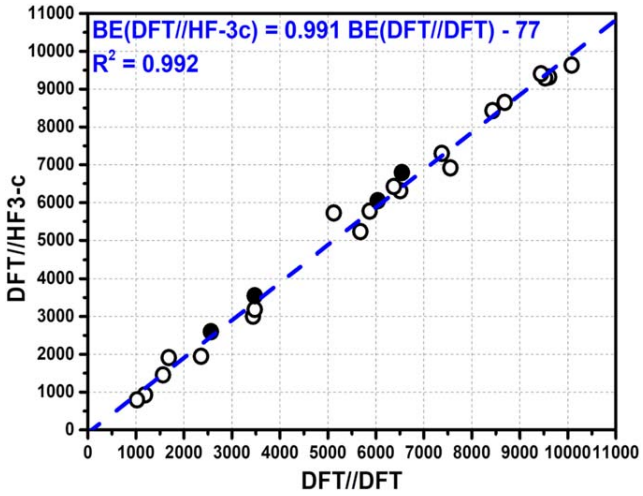

Figure 7. Linear fit between the BE values calculated with the full DFT computational scheme and the BE values calculated with the composite DFT//HF-3c computational scheme for the crystalline ice model (all values in K). Black filled and open circles stand for open-shell and closed-shell species, respectively.

discussed for the crystalline ice. We reoptimize each structure at the HF-3c level to check the changes in the structures resulting from the more approximated method. Then, we run a single-point energy calculation at the DFT/A-VTZ* (B3LYP-D3 and M06-2X) levels to evaluate the final BE values. The results obtained are summarized in Figure 7, showing a very good linear correlation between the BE values computed as described.

The largest percentage differences are found for the smallest BEs, that is, those dominated by dispersion interactions or very weak quadrupolar interactions (i.e., N_2, O_2, H_2, and CH_4) in which the deficiencies of the minimal basis set encoded in the HF-3c cannot be entirely recovered by the internal corrections. For higher BE values, the match significantly improves, in some cases being almost perfect. Even for radicals, the composite approach gives good results. It is worth mentioning that HF-3c optimized geometries are very similar to the DFT-optimized ones (only slight geometry alterations occurred), indicating that the adducts are well-defined minima in both potential energy surfaces. This successful procedure calibrated on crystalline ice is therefore adopted to model the adsorption of all 21 species on the proposed amorphous slab model, a task that would have been very expensive at the full DFT/A-VTZ* level.

3.3. BEs on Amorphous Solid Water

On the ASW model, due to the presence of different binding sites, a single BE value is not representative of the whole adsorption process as is the case for almost all adsorbates on the crystalline surface. Therefore, we computed the BE with the composite DFT//HF-3c procedure (see Section 3.2.3) by sampling different adsorption sites at both the "top" and "bottom" surfaces of the amorphous slab. The starting initial structures of each adsorbate were set up by hand, following the maximum electrostatic complementarity between the EPMs (see Figure 3) of the ice surface and that of a given adsorbate. For each molecule, at least four BE values have been computed on different surface sites. Figure 8 reports the examples of methanol and formamide: for each molecule, we show the geometry on the crystalline ice and in two different sites of

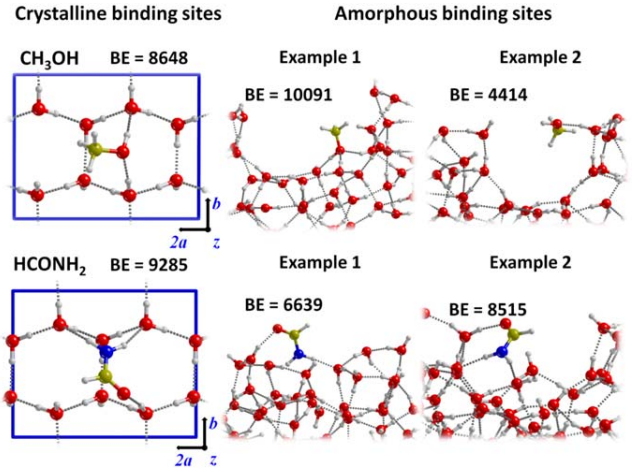

Figure 8. Comparison of the final optimized geometries for CH_3OH and $HCONH_2$ (as illustrative examples) on the crystalline ice (Section 3.1.1) and on the ASW (Section 3.1.2). The BE values (in kelvin) are reported in each plot.

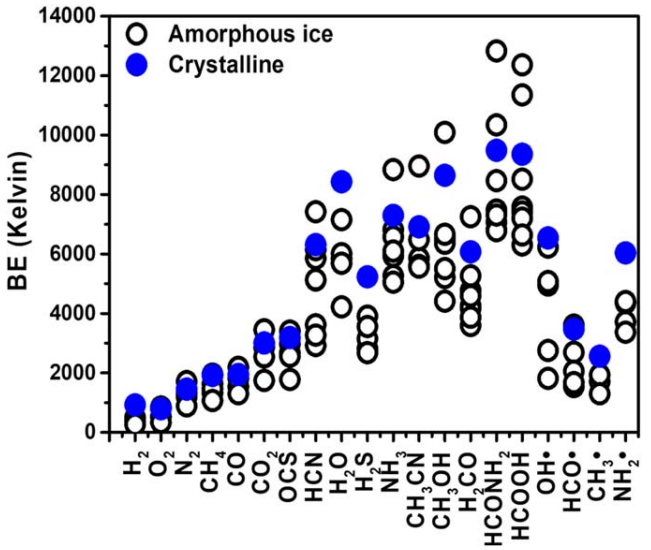

Figure 9. Comparison between the DFT//HF-3c BEs (in kelvin) computed on the crystalline ice (filled blue circles) and ASW (open circles), respectively, for 20 species studied here: HCl is missing as it dissociates on the ASW (see text).

ASW, as well as the BE associated with each geometry. For methanol, the BE is 8648 K in the crystalline ice, whereas it is 4414 and 10,091 K in the two shown ASW sites. Similarly, for formamide, BE is 9285 K on the crystalline ice and 6639 and 8515 K on the ASW. These two examples show that BEs on ASW can differ more than twice depending on the site and that the value on the crystalline ice can also be substantially different from that on the ASW.

Figure 9 shows the computed BEs, on crystalline ice and ASW, for the studied species. The list of all computed BE values on ASW is reported in Table 2, while Table 3 reports the computed minimum and maximum BE values on ASW and the BEs on the crystalline ice for all the studied species. As already mentioned when presenting the methanol and formamide examples, the amorphous nature of the ice can yield large differences in the calculated BEs with respect to the crystalline values. Figure 9 shows that while the BEs for crystalline versus amorphous ices are very close to each other for H_2, O_2, N_2,

Table 2
BE Values (K) Calculated with the DFT//HF-3c Method for Every Case on the Amorphous Slab Model, Where the ZPE Correction Has Not Been Added

	Amorphous Ice BE Values							
Species	Case 1	Case 2	Case 3	Case 4	Case 5	Case 6	Case 7	Case 8
H_2	469	505	277	361	265			
O_2	818	854	854	529	337			
N_2	1347	1708	1311	1191	890			
CH_4	1323	1960	1636	1467	1070			
CO	1816	2189	1540	1527	1299			
CO_2	2863	3452	2538	2550	1744			
OCS	3404	2971	2670	2562	1780			
HCN	2923	5124	3620	5136	3271	5857	6146	7421
H_2O	7156	5845	6014	5689	4222			
H_2S	2814	3909	3151	3560	2682			
NH_3	8840	5268	6820	5930	6579	6098	5052	
CH_3CN	8960	5857	5617	5557	6483			
CH_3OH	6531	4414	6519	6362	5208	6663	5509	10091
H_2CO	3596	4258	4174	4775	5268	4594	3873	7253
$HCONH_2$	12833	7481	10344	6820	8467	7072	6783	7313
HCOOH	7577	7409	8515	12364	6302	7204	6639	11354
OH•	6230	1816	4955	2754	5076			
HCO•	2694	2057	1540	3608	1672			
CH_3•	1708	1936	1299					
NH_2•	4354	3716	4402	3368				

Table 3
Summary of Our Computed BEs and Comparison with Data from the Literature

	BEs from This Work			BEs from Literature					
	Crystalline Ice	ASW		Computed		Databases		Experiments	
Species	BE(0) disp	Min	Max	Das[(a)]	Wakelam[(b)]	UMIST[(c)]	KIDA[(d)]	Penteado[(e)]	Others
H_2	790	226	431	545	800	430	440	480 ± 10	322–505[(f)]
O_2	677	287	729	1352	1000	1000	1200	914–1161	920–1520[(f)]
N_2	1242	760	1458	1161	1100	790	1100	1200	790–1320[(f1)]
									900–1800[(f1)]
CH_4	1633	914	1674	2321	800	1090	960	1370	960–1947[(f)–(h)]
CO	1663	1109	1869	1292	1300	1150	1300	863–1420	870–1600[(f)]
									980–1940[(f1)]
CO_2	2568	1489	2948	2352	3100	2990	2600	2236–2346	
OCS	2722	1520	2907	1808	2100	2888	2400	2325[a]	2430[(i)]
HCl	5557	(l)	(l)	4104	4800		5172		5172[(m)]
HCN	6392	2496	6337	2352	3500	2050	3700		
H_2O	7200	3605	6111	4166	4600	4800	5600	4815–5930	
H_2S	4468	2291	3338	3232	2500–2900	2743	2700	2296[a]	
NH_3	6235	4314	7549	5163	5600	5534	5500	2715[a]	
CH_3CN	5906	4745	7652	3786	4300	4680	4680	3790[a]	
CH_3OH	7385	3770	8618	4511	4500–5100	4930	5000	3820[a]	3700–5410[(n,o,p)]
H_2CO	5187	3071	6194	3242	5100	2050	4500	3260 ± 60	
$HCONH_2$	8104	5793	10960		6300	5556			7460–9380[(q)]
HCOOH	7991	5382	10559	3483		5000	5570	4532[a]	
OH•	5588	1551	5321	3183	3300–5300	2850	4600	1656–4760	
HCO•	2968	1315	3081	1857	2300–2700	1600	2400		
CH_3•	2188	1109	1654	1322	2500	1175	1600		
NH_2•	5156	2876	4459	3240	2800–4500	3956	3200		

Notes. Column (1) reports the species, Columns (2)–(4) the BEs computed in the present work and corrected for the ZPE, Columns (5) and (6) the values obtained via calculations from other authors, Columns (7) and (8) the values in the two astrochemical databases KIDA and UMIST (see text), and Columns (9) and (10) the values measured in different experiments. Units are in K, and the references are listed in the notes below. References: (a) Das et al. 2018; (b) Wakelam et al. (2017); (c) McElroy et al. (2013); (d) Wakelam et al. (2015); (e)Penteado et al. (2017); (f) He et al. (2016), note that (f1) refers to porous ice; (g) Raut et al. (2007); (h) Smith et al. (2016); (i) Ward et al. (2012); (l) HCl molecule dissociate; (m) Olanrewaju et al. (2011); (n) Minissale et al. (2016); (o) Martín-Doménech et al. (2014); (p) Bahr et al. (2008); (q) Chaabouni et al. (2018), note that the BE refers to the silicate substrate because it is larger than that of water ice.
[a] Results estimated from the work of Collings et al. (2004), reported in Table 2 of Penteado et al. (2017).

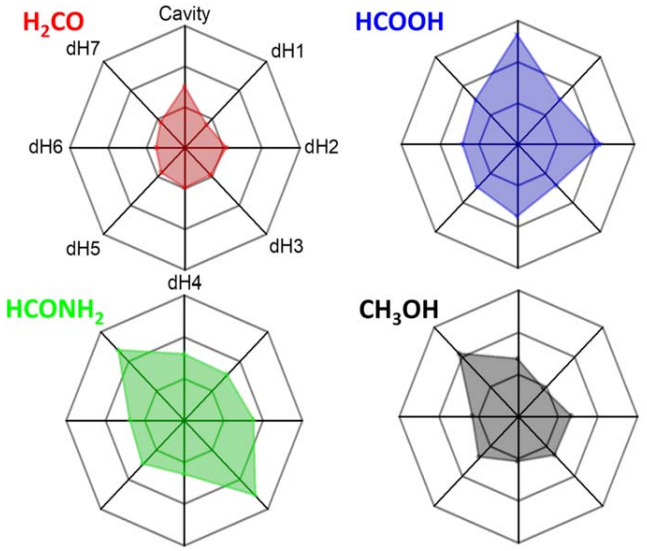

Figure 10. Spider graphs of the DFT//HF-3c BE values (in kelvin) calculated on the same eight adsorption sites of the ASW for the H_2CO (red), CH_3OH (black), $HCONH_2$ (green), and HCOOH (blue) molecules. The BE value scale goes from 0 K (center of the graph) to 14,433 K (vertices of the polygon) in steps of 4811 K. Labeling of dH and dO sites is referring to Figure 3.

CH_4, CO, CO_2, and OCS, the ones computed for the remaining molecules for the crystalline ice fall in the highest range of the distribution of the amorphous BE values. This behavior can be explained considering the smaller distortion energy cost upon adsorption for the crystalline ice compared to the amorphous one. The different local environment provided by crystalline versus amorphous ices is also the reason for HCl being molecularly adsorbed at the crystalline ice while becoming dissociated at the amorphous one. Further details about the case of HCl are reported in Appendix A.2. This probably will not occur for HF, not considered here, which is expected to be molecularly adsorbed on both ices owing to its higher bond strength compared to HCl. Nevertheless, as we did not explore exhaustively all possible configurations of the adsorbates at the amorphous surfaces, we cannot exclude that some even more/less energetic binding cases remain to be discovered.

Some adsorbates show similar trends in the BEs, despite their different chemical nature. This is shown in Figure 10, in which we plot the BE values on ASW for four molecules that have been adsorbed at the same adsorption sites: formaldehyde, formic acid, formamide, and methanol. The BE distributions for the H_2CO and HCOOH are very similar (in their relative values), and those for CH_3OH and $HCONH_2$ show some similarities, despite the large difference in the chemical functionality.

4. Discussion

A first rather expected result of our computations is that the BE of a species on the ASW is not a single value: depending on the species and the site where it lands, the BE can largely differ, even by more than a factor of two (Table 3). This has already been discussed in the literature, for instance, for H adsorption on both crystalline and amorphous ice models (Ásgeirsson et al. 2017). This has important consequences both when comparing the newly computed BE(0)s with those in the literature Section 4.1 and for the astrophysical implications in Section 4.2. We will discuss these two aspects separately in the next two sections.

4.1. Comparison BE Values in the Literature

Being such a critical parameter, BEs have been studied from an experimental and theoretical point of view. In this section, we will compare our newly computed values with those in the literature, separating the discussion for the experimental and theoretical values, respectively. We will then also comment on the values available in the databases that are used in many astrochemical models.

4.1.1. Comparison with Experimental Values

In the present computer simulation we have computed the BE released when a species is adsorbed on the surfaces of the ice models (either crystalline or amorphous) at very low adsorbate coverage θ ($\theta \longrightarrow 0$). The correct comparison with experiments would therefore be with microcalorimetric measurements at the zero-limit adsorbate coverage. In astrochemical laboratories, TPD is, instead, the method of choice and is related to the desorption activation energy (DAE). DAE derives indirectly from the TPD peaks through Readhead's method (Redhead 1962), or more sophisticated techniques. TPD usually starts from an ice surface hosting a whole monolayer of the adsorbate and therefore depends also on θ (He et al. 2016), rendering the comparison with the theoretical BE not straightforward (King 1975). Ice restructuring processes may also affect the final DAE. Sometimes, TPD experiments only provide desorption temperature peaks $T_{\rm des}$, without working out the DAE. This is the case of the fundamental work by Collings et al. (2004). Therefore, BEs reported in the review by Penteado et al. (2017) relative to the Collings et al. data (see Table 3) were computed through the approximate formula: $\mathrm{BE}(X) = [T_{\rm des}(X)/T_{\rm des}(H_2O)]\ \mathrm{BE}(H_2O)$, in which $T_{\rm des}(X)$ is the desorption temperature of the X species contrasted with that of water $T_{\rm des}(H_2O)$ to arrive at the corresponding BE(X) by assuming that of water to be 4800 K. For the above reasons, a one-by-one comparison between experiment and modeling is outside the scope of the present paper.

Following the above warnings, we can now analyze Table 3 reporting the recent compilation by Penteado et al. (2017) (*vide supra*) *plus* the values that appeared in the literature after that compilation. We start with the cases of two measurements carried out by He et al. (2016) on porous amorphous ice surfaces, for N_2 and CO. Table 3 shows two values reported by He et al. for the two extreme cases of when the ice is completely covered by the species (the smaller value) and when, on the contrary, it is less than a monolayer (the largest value), which is the one to compare with our computed values. Our BEs on amorphous ice models are in reasonable agreement with those measured by He et al. for CO (1109–1869 K vs. 1940 K) and on the lower side for N_2 (760–1455 K vs. 1800 K). It is worth noting that the comparison is much better when referring to the nonporous amorphous ice measurements by the same authors: for CO and N_2 the measured BE values are 1600 and 1320 K, indeed well bracketed by our BE(0). Data from Penteado et al. (2017) extracted from the TPD of Collings et al. (2004) for NH_3 adsorbed on the ice layer gave a BE of 2715 K. This value is, however, identical to that from the TPD of NH_3 adsorbed on the gold surface (no water ice), proving that that BE is relative to the NH_3/NH_3 lateral interaction within the

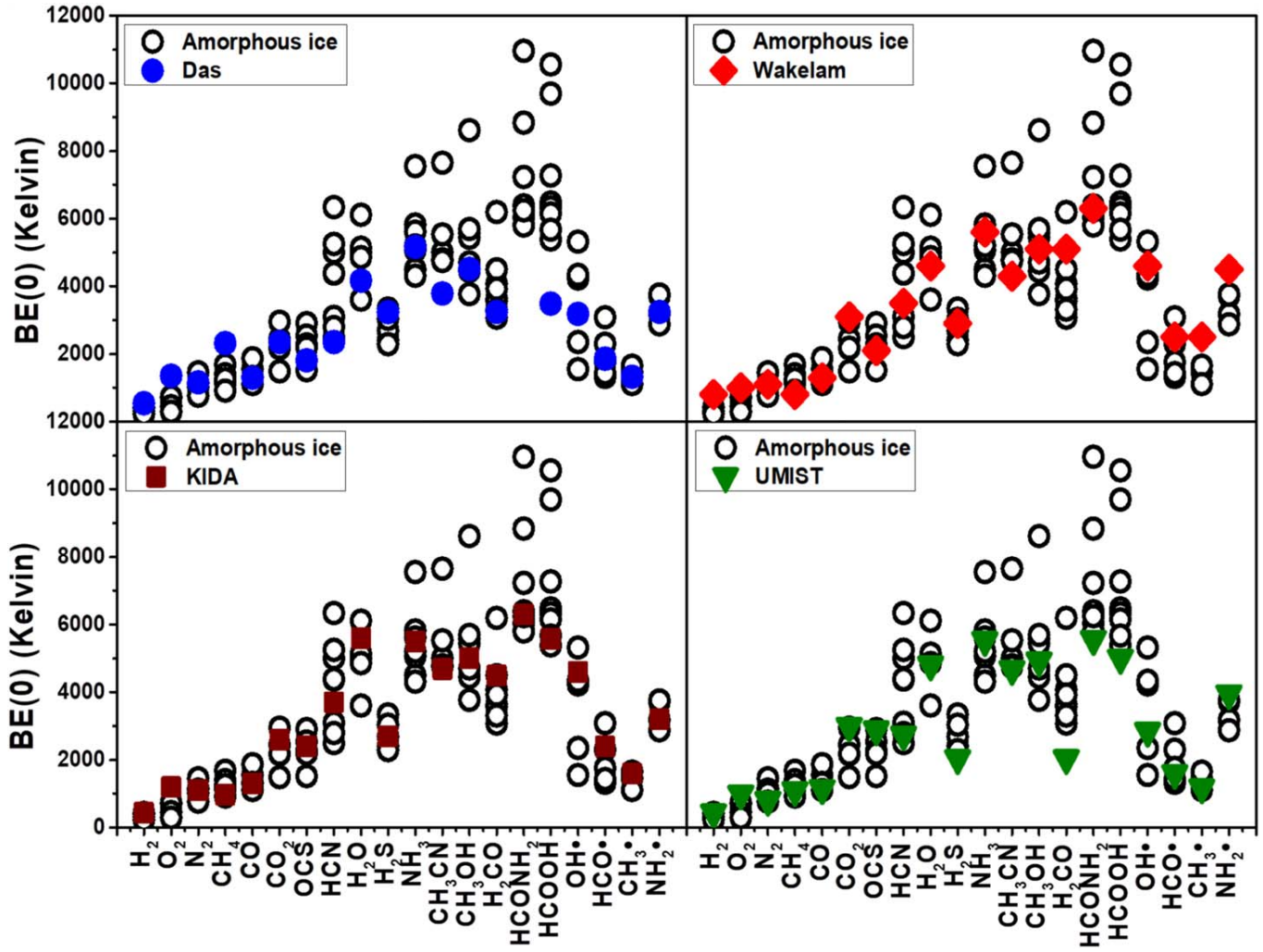

Figure 11. Comparison of the computed zero-point energy corrected BE(0)s for the amorphous ice model with respect to those by Das et al., by Wakelam et al., and reported in the KIDA and UMIST databases (McElroy et al. 2013; Wakelam et al. 2015, 2017; Das et al. 2018).

adsorbed NH_3 multilayer and not due to the interaction with the ice surface. For reasons explained in Collings et al. (2004), the BE of NH_3 on ice is assumed of the same order as that of water, i.e., around 4800 K, in better agreement with the UMIST value of 5500 K (McElroy et al. 2013). Indeed, our data (see Table 3, ZPE corrected) of 4300–7500 K bracket the experimental ones. The computed highest values emphasize the H-bond acceptor capability of NH_3 occurring on a few specific sites characterized by very high electrostatic potential, only important for very low NH_3 coverage, not easily accessible in the TPD experiments. For the H_2O case, the computed BE(0)s (Table 3) for the amorphous ice are in the 3605–6111 K range, reasonably bracketing the experimental one of 4815–5930 K.

In general, the comparison of our BE values computed on the ASW with those measured by the various experiments reported in Table 3 shows an excellent agreement, when considering the ranges in our values and the ranges in the values of the experiments. Only one species seems to have relatively different computed and measured BEs: O_2. For O_2, experiments tend to provide larger values with respect to what we computed (our largest value is 729 K, while the lowest measured value is 914 K). For many other species, except H_2, our computed lowest BE(0)s are within the range of the measured ones, but we predict sites where BE(0)s are larger, which may have important astrophysical implications (Section 4.2). Finally, for H_2 we predict sites where the BE(0) is (slightly) lower than the measured ones.

4.1.2. Comparison with Computed Values

In the literature, there are two works that reported computations of BEs for a large set of molecules, those by Wakelam et al. (2017) and those by Das et al. (2018). The former carried out computations considering only one water molecule, whereas the latter considered a cluster of up to six water molecules.

The first aspect to notice is, therefore, that neither of these two studies can, by definition, reproduce the strong adsorption sites that we have in our ASW model. Indeed, only the adoption of more realistic and periodically extended ice models allows us to fully consider the hydrogen bond cooperativity, which will enhance the strength of the interaction with adsorbates at the terminal dH atoms exposed at the surface. This important effect is entirely missed by the two above-mentioned works. It is not surprising, then, that our crystalline and ASW BEs differ, sometimes substantially, from the Wakelam et al. and Das et al. values (as, by the way, they differ between themselves as well). This is clearly shown in Figure 11, where we report the comparison of our computed values with those by Wakelam et al. and Das et al., respectively. In general,

both work values tend to lay in the low end of our computed BEs. As extreme examples, our ASW BEs are larger for CH_3CN and HCOOH. The inverse effect is observed for the smallest studied species: our BEs are smaller than those computed by Wakelam et al. and Das et al. for H_2 and O_2.

4.1.3. Comparison with Values in Astrochemical Databases

Two databases list the BEs of the species used by the astrochemical models: the Kinetic Database for Astrochemistry (KIDA, http://kida.astrophy.u-bordeaux.fr/; Wakelam et al. 2015) and UMIST (http://udfa.ajmarkwick.net/index.php; McElroy et al. 2013). The comparison between our newly computed values and those reported in the two databases is shown in Figure 11. The general remarks that we wrote for the comparison with the literature experimental and theoretical values (Sections 4.1.1 and 4.1.2) roughly apply here: the databases quote BE values in the low end of ours. This is not surprising, as the databases are compiled based on the experimental and theoretical values in the literature. We just want to emphasize here, once again, that the sites with large BEs are lacking, and this may have important consequences in the astrochemical model predictions.

4.2. Astrophysical Implications

BEs enter in two hugely important ways in the chemical composition of interstellar objects/clouds: (i) they determine at what dust temperature the frozen species sublimate, and (ii) they determine at what rate the species can diffuse in the ice, as the diffusion energy is a fraction of the BE species. Both processes are mathematically expressed by an exponential containing the BE. Therefore, even relatively small variations of the BE can cause huge differences in the species abundances in the gas phase and on the grain surfaces, where they can react with other species.

In this context, probably the most important astrophysical implication of the present study is that in our ASW model (which is likely the best description to represent the interstellar amorphous ice so far available in the context of the BE estimates) a species does not have a single value, but a range of values that depend on the species itself and the site where it is bound. The range can spread by more than a factor of two: this obviously can have a huge impact on the modeling and, consequently, our understanding of the interstellar chemical evolution.

4.2.1. Impact of Multiple BEs in Astrochemical Modeling

To give a practical example of the impact on the gaseous abundance, we built a toy model for the interstellar ice and simulated the desorption rate of the ice as a function of the temperature. Our scope here is not to compare the toy model predictions with astronomical observations or laboratory experiments: we only mean to show how multiple BEs (we used the electronic BEs) would lead, in principle, to a different behavior of the ice sublimation process. Therefore, we developed a toy model that does not contain diffusion or reaction processes on the ice surface or rearrangement of the ice during the ice heating, but only a layered structure with two species, specifically water and methanol, where molecules have the range of BEs calculated in Section 3. We then show how the multiple BEs affect the temperature at which peaks of desorption appear, considering that only species at the surface

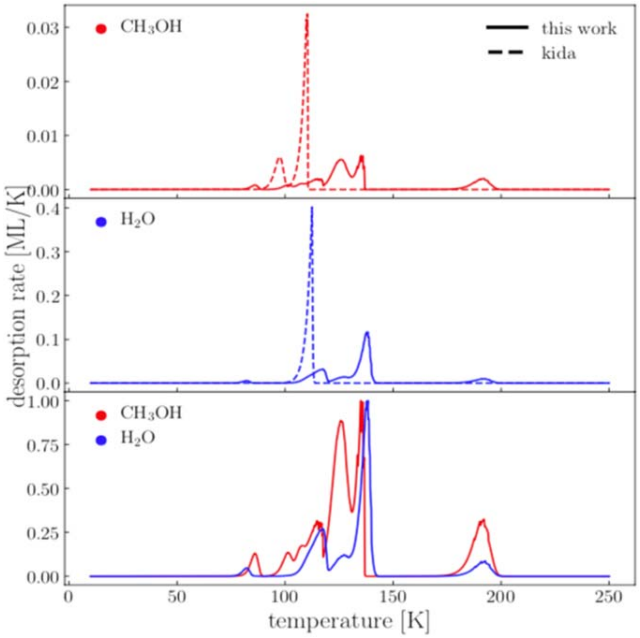

Figure 12. Desorption rate of methanol (red curves) and water (blue curves) as a function of the temperature. In these computations, the ice is assumed to be composed of 10 layers: the bottom five layers contain water, while the top five contain 80% water and 20% methanol. The ice is assumed to be at 10 K at the beginning of the simulation, and it reaches 400 K in 10^5 yr. The curves refer to the case when a single BE (from the KIDA database) is considered for water and methanol, respectively (dashed line), and when the multiple BEs of this work are considered (solid line). The bottom panel shows the methanol and water desorption rates normalized to 1.

of the ice, namely, exposed to the void, can sublimate (and not the entire bulk). In this toy model, we considered 10 layers for an icy grain mantle, where the bottom five are made entirely of water and each of the top five layers contains 80% water and 20% methanol. The methanol molecules with different BEs are distributed randomly on each layer, with the same proportion of BE sites. Looking at the BE values computed with the DFT//HF-3c method on the ASW model, methanol has eight BE values (4414, 5208, 5509, 6362, 6519, 6531, 6663, and 10,091 K), and at each layer there will be 12.5% methanol molecules with each of the eight BEs. The same applies for water molecules, for which we have computed five possible BEs (4222, 5689, 5845, 6014, and 7156 K), with 20% water molecules with each BE. In this model, only molecules of the layers in contact with the void can evaporate: for example, methanol molecules can be trapped if they have water molecules with larger BEs on top of them.

We start with an ice temperature of 10 K, and at the end it reaches 400 K in 10^5 yr, to simulate the heating of a collapsing solar-like protostar. The plot of the desorption rates is shown in Figure 12, where we also show them assuming the BE values from the KIDA database for methanol and water, respectively. First, when only the KIDA values for BE are assumed, water molecules desorb at about 110 K; methanol has two peaks of desorption rates, the first at about 95 K, corresponding to the desorption of the methanol molecules not trapped by the water molecules, and the second peak at about 110 K, when all water molecules desorb so that no methanol molecules are trapped. Note that the desorption of the water molecules of the bottom layers arrives at a slightly larger temperature.

Not surprisingly, the introduction of multiple BEs produces multiple peaks of desorption, for both water and methanol. Figure 12 shows that the water desorption rate has a small peak at ∼75 K, a larger one at ∼120 K, then another at ∼140 K, and, finally, a last peak at ∼190 K. Methanol starts to desorb at 80 K, the bulk is desorbed between 120 and 140 K, and a last peak is seen around 190 K. We emphasize again that this is a toy model meant to show the potential impact of the new BEs on the astrochemical modeling. The details will depend on the real structure of the water ice and how molecules are distributed on the icy mantles. They will determine how many sites have a certain BE value and how molecules are trapped in the ice. As a very general remark, we can conclude that species can be in the gas phase at lower and higher dust temperatures than if one only considers a single BE.

4.2.2. Looking Forward: Implementation of Multiple BEs in Astrochemical Models

Our toy model introduced in the previous subsection shows the importance of considering multiple BEs for each species in the astrochemical models to have more realistic predictions. In this work, we provide the possible BEs for 21 species (Table 3). Very likely, they cover most of the possibilities, as they span a large range of H-bonds within the water molecules of the ASW. However, from a computational standpoint, such an adsorption variability has to be fully explored, in which plotting the different calculated BEs in histograms is useful to provide insights on the shape of the BE distribution (Song & Kästner 2017). Moreover, in order to build a reliable astrochemical model, one would also need to know the relative probability for each BE, and our present study is unable to provide sensible numbers. For that, a statistical study on an ASW model that is much larger than the one used here is necessary. This is a step that we indeed plan to take in future studies. Meanwhile, we adopted a distribution in which we assign an equal fraction of molecules to each BE. If one looks carefully at the distribution of the BEs for each molecule, they are not uniformly distributed but peak around some values: for example, methanol has a peak around 6000 K and an extreme value of 10,091 K only, so that, very likely, this site will be less populated than the sites around 6000 K, as shown by Figure 10. Yet, considering even a smaller fraction of these extreme values may have important consequences, for example, in the so-called snow lines of protoplanetary disks, or even on the observed abundances toward hot cores and hot corinos, or, finally, toward prestellar cores.

4.2.3. Comments on N_2, CO, and HCl

Finally, we would like to comment on three species of the studied list, N_2, CO, and hydrogen chloride (HCl).

N_2 and CO: Our computations show that the BE of CO is definitively larger than that of N_2, against the values that are in the astrochemical databases (see Table 3): on average, our computed BEs differ by about 400 K, whereas in the databases the difference is 200 and 360 K in KIDA and UMIST, respectively. This difference very likely can explain why observations detect N_2H^+, which is formed in the gas phase from N_2, where CO is already frozen on the grain mantles (e.g., Bergin et al. 2002; Tafalla et al. 2004; Redaelli et al. 2019), a debate that has been going on for almost two decades (e.g., Öberg et al. 2009; Pagani et al. 2012). In order to quantify the effect, a specifically focused modeling will be necessary, which is beyond the scope of the present work. Here we want simply to alert that the new BEs might explain some long-standing mysteries. Another comment regards the difference in the BEs on crystalline surfaces and ASW. Again, the CO BE is about 500 K larger than that of N_2, and both are larger by about 300 K than those on the ASW, a difference that also has an impact on the snow lines of these two species in protoplanetary disks, where crystalline water ices have been detected (Terada & Tokunaga 2012).

HCl: Astrochemical models predict that HCl is the reservoir of Cl in molecular gas (e.g., Schilke et al. 1995; Neufeld & Wolfire 2009; Acharyya & Herbst 2017). However, all the observations carried out so far have found that only a tiny fraction of Cl is in the gaseous HCl, even in sources where all the grain mantles are supposed to be completely sublimated (Peng et al. 2010; Codella et al. 2011; Kama et al. 2015). One possible explanation is that HCl, once formed in the gas phase, is adsorbed on the grain icy mantles and dissociates, as shown by our calculations on the ASW model and also by previous calculations on the crystalline P-ice model (Casassa 2000) and for more sophisticated proton-disordered crystalline ice models (Svanberg et al. 2000). It is a matter to be studied whether the sublimation of the water, when the dust reaches about 100–120 K, would also provide a reactive channel transforming the Cl anion in the neutral atom, the latter obviously unobservable. This would help in solving the mystery of HCl not being observed in gas phase. Furthermore, if that were the case, the population of the chemically reactive atomic Cl would be increased, with an important role in the gas-phase chemistry (see, e.g., Balucani et al. 2015; Skouteris et al. 2018).

5. Conclusions

In this work, we present both a new computational approach and realistic models for crystalline and amorphous water ice to be used to address an important topic in astrochemistry: the BEs of molecules on interstellar ice surfaces. We simulated such surfaces by means of two (antipodal) models, in both cases adopting a periodic approach: a crystalline and an amorphous 2D slab model. We relied on DFT calculations, using the B3LYP-D3 and M06-2X widely used functionals. This approach was further validated by an ONIOM-like correction at the CCSD(T) level. Results from this combined procedure confirm the validity of the BEs computed with the adopted DFT functionals. The reliability of a cost-effective HF-3c method adopted to optimize the structures at the amorphous ice surface sites was proved by comparing the BEs computed at the crystalline ice surface at the DFT//DFT and DFT//HF-3c levels, which were found to be in very good agreement.

On both ice surface models, we simulated the structure and adsorption energetic features of 21 molecules, including 4 radicals, representative of the most abundant species of the dense ISM. A main conclusion is that the crystalline surfaces only show very limited variability in the adsorption sites, whereas the amorphous surfaces provide a wide variety of adsorption binding sites, resulting in a distribution of the computed BE. Furthermore, BE values at crystalline ice surface are in general higher than those computed at the amorphous ice surfaces. This is largely due to the smaller geometry relaxation cost upon adsorption compared to the amorphous cases, imposed by the tighter network of interactions of the denser crystalline ice over the amorphous ice.

Finally, the BEs obtained by the present computations were compared with literature data, from both experimental and computational works, as well as those on the public astrochemical databases KIDA and UMIST. In general, our BEs agree relatively well with those measured in the laboratory, with the exception of O_2 and, to a lesser extent, H_2. On the contrary, previous computations of BEs, which considered a very small number of ($\leqslant$6) water molecules, provide generally lower values with respect to our new computations and, with no surprise, miss the fact that BEs have a spread of values that depend on the position of the molecule on the ice. Since the two astrochemical databases mentioned above are based on the literature data, our BEs differ, sometimes substantially, from those quoted and do not report multiple BE values.

We discussed some astrophysical implications, showing that the multiple computed BEs give rise to a complex process of interstellar iced mantle desorption, with multiple peaks as a function of the temperature that depends (also) on the ice structure. Our new computations do not allow us to estimate how the BEs are distributed for each molecule, as only a statistical study is necessary for that. The new (multiple) BEs of N_2 and CO might explain why N_2H^+ depletes later than CO in prestellar cores, while the relatively low abundance of HCl, observed in protostellar sources, could be due to the fact that it dissociates into the water ice, as shown by our calculations.

Finally, the present study shows the importance of theoretical calculations of BEs on as realistic as possible ice surfaces. This first study of 21 molecules needs to be extended to the hundreds of molecules that are included in the astrochemical models to have a better understanding of the astrochemical evolution of the ISM.

A part of the computational results were from the SF Master thesis "Ab initio quantum mechanical study of the interaction of astrochemical relevant molecules with interstellar ice models," Dipartimento di Chimica, University of Torino, Torino, 2018. S.F., L.Z., and P.U. acknowledge financial support from the Italian MIUR (Ministero dell'Istruzione, dell'Università e della Ricerca) and from Scuola Normale Superiore (project PRIN 2015, STARS in the CAOS—Simulation Tools for Astrochemical Reactivity and Spectroscopy in the Cyberinfrastructure for Astrochemical Organic Species, cod. 2015F59J3R). The Italian CINECA consortium is also acknowledged for the provision of supercomputing time for part of this project. A.R. is indebted to the "Ramón y Cajal" program. MINECO (project CTQ2017-89132-P) and DIUE (project 2017SGR1323) are acknowledged. This project has received funding from the European Union's Horizon 2020 research and innovation program under the Marie Sklodowska-Curie grant agreement No. 811312 for the project "Astro-Chemical Origins" (ACO) and from the European Research Council (ERC) under the European Union's Horizon 2020 research and innovation program, for the Project "The Dawn of Organic Chemistry" (DOC), grant agreement No. 741002. Finally, we wish to acknowledge the extremely useful discussions with Prof. Gretobape.

Appendix A
Computational Details

In CRYSTAL17, the multielectron wave function is built as a Slater determinant of crystalline/molecular orbitals, which are linear combinations of localized functions on the different atoms of the structure that are called atomic orbitals (AOs). In a similar manner, the AOs are constructed by linear combinations of localized Gaussian functions that form a basis set. The basis set employed for this work is an Ahlrichts-TVZ (Schäfer et al. 1992), added with polarization functions.

A.1. BEs, Counterpoise, and Zero-point Energy Corrections

In a periodic treatment of surface adsorption phenomena one of the most relevant energy values, useful to describe the interacting system, is the BE, which is related to the interaction energy ΔE, so that

$$\mathrm{BE} = -\Delta E. \tag{A1}$$

The BE per unit cell per adsorbate molecule BE is a positive quantity (for a bounded adsorbate) defined as

$$\mathrm{BE} = [E_m(M//M) + E(S//S)] - E(SM//SM), \tag{A2}$$

where $E(SM//SM)$ is the energy of a fully relaxed unitary cell containing the surface slab S in interaction with the adsorbate molecules M, $E(S//S)$ is the energy of a fully relaxed unitary cell containing the slab alone, and $E_m(M//M)$ is the molecular energy of the free fully optimized adsorbate molecule (the symbol following the double slash identifies the geometry at which the energy, E, is calculated)

$$\mathrm{BE} = \mathrm{BE}^* - \delta E_S - \delta E_M \tag{A3}$$

$$\delta E_S = E(S//SM) - E(S//S) \tag{A4}$$

$$\delta E_M = E(M//SM) - E_m(M//M) \tag{A5}$$

$$\mathrm{BE}^* = [E(S//SM) + E(M//SM)] - E(SM//SM), \tag{A6}$$

in which δE_S is the deformation energy of the surface ($\delta E_S > 0$), whereas δE_M ($= \Delta E_M + \Delta E_L$) counts both the deformation energy of the molecule (ΔE_M) and the lateral intermolecular interactions (ΔE_L) between the infinite molecule images in the same spatial configuration occurring in the SM periodic system. The pure molecule's deformation energy can be computed as

$$\Delta E_M = E_m(M//SM) - E_m(M//M), \tag{A7}$$

in which $E_m(M//SM)$ is the molecular energy of the molecule frozen at the geometry occurring on the surface and $E_m(M//M)$ is the molecular energy of a fully optimized free molecule, so that $\Delta E_M > 0$. The lateral intermolecular interactions, ΔE_L, are defined as

$$\Delta E_L = E(M//SM) - E_m(M//SM) \tag{A8}$$

and can be either positive (repulsion) or negative (attraction). With those positions, the BE^* interaction energy is then deformation and lateral interaction free, being the result of energy differences between periodic calculations carried out at the geometry of the SM system. For instance, $E(M//SM)$ is the energy of the unit cell of a crystal containing only a molecule in

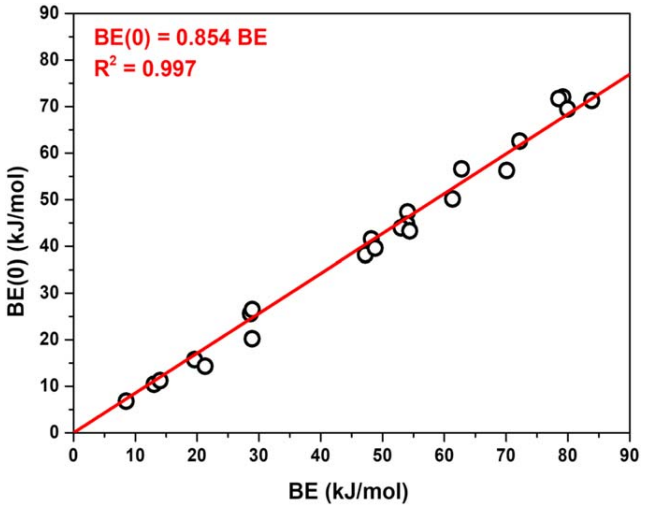

Figure 13. Linear regression between BE and BE(0) (zero-point-corrected) values computed for the considered adsorbates on the crystalline ice.

the same geometry assumed in the *SM* system. The above BE definition can be easily recast to include the BSSE correction, using the same counterpoise method adopted for intermolecular complexes (Boys & Bernardi 1970; Davidson & Feller 1986). The definition of the BSSE-corrected interaction energy BE^C is then

$$BE^C = BE^{*C} - \delta E_S - \Delta E_M - \Delta E_L^C \tag{A9}$$

$$BE^{*C} = [E(S[M]//SM) + E([S]M//SM)] - E(SM//SM) \tag{A10}$$

$$BSSE = BE - BE^C, \tag{A11}$$

in which $E(S[M]//SM)$ and $E([S]M//SM)$ are the energy of the slab plus the ghost functions of the molecules and the energy of the infinite replica of molecules with the ghost functions of the underneath slab, respectively. Because the variational theorem ensures that $BE^*C < BE^*$, it immediately results that $BSSE > 0$.

Each of the terms of Equation (A2) can be corrected by the zero-point vibrational contribution (in the harmonic approximation), ZPE, therefore arriving at the definition of the zero-point correct BE, BE(0), as

$$BE(0) = [E_m(M//M) + E(S//S)] - E(SM//SM) + [ZPE(M) + ZPE(S) - ZPE(SM)] \tag{A12}$$

$$BE(0) = BE - \Delta ZPE \tag{A13}$$

$$\Delta ZPE = ZPE(SM) - ZPE(M) - ZPE(S). \tag{A14}$$

In this work the ΔZPE has been evaluated for the crystalline ice cases only, and then the scaling factor found in the linear fit of Figure 13 was adopted to correct the BEs for the amorphous ice model for the reason described in Section 2.1.

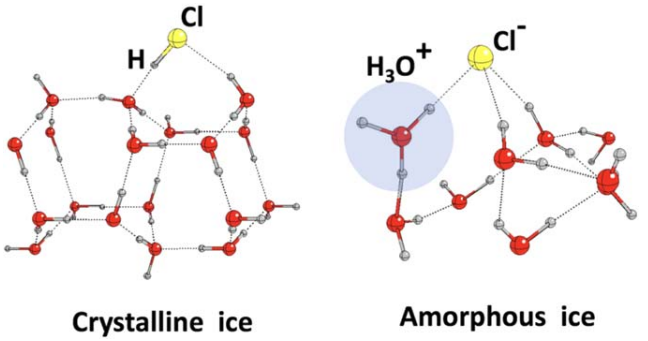

Figure 14. Enlarged views of HCl adsorbed on a crystalline and amorphous ice models.

A.2. Details on HCl Adsorbed on Crystalline and Amorphous Ices

Our calculations showed that HCl remains molecularly adsorbed at the crystalline ice surface. At the amorphous one it spontaneously deprotonates, making a locally stable ion pair (Cl^-/H_3O^+) (see the figure below). The reason is that for the surface selected to represent the crystalline ice, the ion pair cannot be stabilized by a large enough network of H-bonds owing to the rigidity of the structure. On the contrary, at amorphous surface, Cl^- is engaged in three H-bonds, while the hydronium ion remains embedded in the H-bonds provided by the ice surface. A good solvation of the ion pair is the key determining the final fate of HCl at the ice surfaces (molecular or ion pair) as already pointed out many years ago by Novoa and Sosa for a small water cluster hosting HCl (Novoa & Sosa 1995). While deprotonation of HCl cannot be excluded for specific crystalline ice surface sites as simulated by Svanberg et al. (2000) when enough dH can stabilize the anion, deprotonation would be much more common at amorphous ice surface or locally distorted crystalline ones, due to the presence of favorable local environment (see Figure 14). Dissociative adsorption was found early by Horn et al. (1992) through RAIRS spectroscopy of DCl adsorption on thin D_2O film, and by Olanrewaju et al. (2011) through thermal and electron-stimulated desorption experiments.

A.3. CRYSTAL17 Computational Parameters

In order to optimize the values of the shrinking factor, the tolerances on integrals of the integration grid (SHRINK, TOLINTEG, and GRID parameters in the code; Dovesi et al. 2018) as described in Section 2 of the article, NH_3 has been adopted as a test case. Geometry optimizations for the adsorption process on the crystalline slab model have been run with the previously described computational scheme, varying one by one the aforementioned parameters, with convergence on the pure ΔE as defined by Equation (A1) being the threshold. For this benchmark calculation, BSSE, distortion, and lateral interaction contributions have not been computed. Results are resumed in what follows.

From Table 4 it is clear that ΔE is practically unaffected by the SHRINK value; thus, SHRINK = (2 2) has been used for all calculations, allowing the saving of computational time.

Table 4
Optimization of the SHRINK Parameter

SHRINK	k Points in BZ	ΔE (K)
2 2	4	7873
3 3	5	7889
4 4	10	7889
5 5	13	7890
6 6	20	7890
7 7	25	7890
8 8	34	7890

Note. Tolerances of integrals (TOLINTEG) and integration grid (XLGRID) are fixed to default values.

Table 5
Optimization of the TOLINTEG Parameter (SHRINK = 2 2 and XLGRID)

TOLINTEG	ΔE (K)
6 6 6 6 12	7889
7 7 7 7 14	7906
8 8 8 8 16	8063
9 9 9 9 18	7981
10 10 10 10 20	7890

As for the SHRINK parameter, the variations of TOLINTEG values (see Table 5) do not practically affect the final ΔE value. Consequently, its values have been set equal to 7, 7, 7, 7, and 14.

Again, the ΔE is practically unaffected by changing the adopted grid (see Table 6); therefore, XLGRID was selected for all the remaining calculations. Resuming, every other calculation has been carried out with SHRINK = (2 2), TOLINTEG = (7 7 7 7 14), and XLGRID as computational parameters.

A.4. Description of Dispersive Forces

We optimized the geometry of two parallel benzene rings that interact with each other just because of dispersive forces given the apolar nature of the molecule. The results of Figure 15 clearly show that the B3LYP functional needs some a posteriori correction (like Grimme's D3) for dispersive forces in order to describe correctly the interaction (Grimme et al. 2010), whereas the M06-2X functional is able to describe it correctly without any a posteriori correction (Zhao & Truhlar 2008).

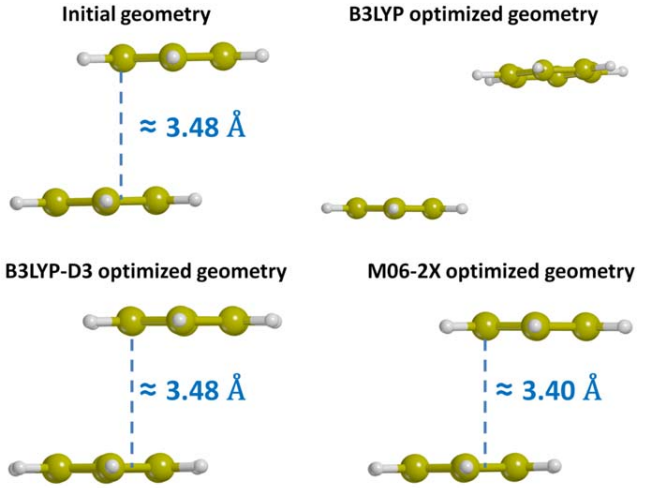

Figure 15. Initial and optimized geometry of two parallel benzene rings obtained with B3LYP (without dispersion corrections), B3LYP-D3 and M06-2X functionals. Distances between the planes of the two rings are reported in angstroms.

Table 6
Optimization of the Integration Grid Parameter (SHRINK = 2 2 and TOLINTEG = 7 7 7 7 14)

GRID	ΔE (K)
XLGRID	7951
XXLGRID	7951

Table 7
Summary of the Components Used for the Calculation of the ONIOM2 Correction to the BEs

Species	BE(CCSD(T), μ–nH_2O) Extrapolated	BE(DFT, μ–nH_2O)	BE(DFT, ice)	BE(ONIOM2)	| Diff |
H_2	843	796	1192	1240	47
CO	1127	1165	2356	2318	38
CO_2	1939	1817	3442	3564	121
OCS	1354	1138	3478	3695	216
H_2S	2443	2875	5679	5248	432
HCN	3300	3453	5795	5642	153
H_2CO	3199	3114	6490	6575	85
HCl	3993	4475	6501	6019	482
NH_3	4246	4389	7376	7233	143
CH_3OH	5196	5275	8681	8602	79
HCOOH	6263	6223	9522	9562	40
$HCONH_2$	5080	5056	9614	9638	24
OH•	4492	4502	6542	6532	10
NH_2•	3021	2788	6043	6276	233
HCO•	2339	2088	3474	3725	251

Note. The last column shows the absolute value of the difference between the BE(DFT, μ-$2H_2O$) value and the corrected BE(ONIOM2).

A.5. ONIOM2 Correction

In Table 7 we summarize the single components (namely, BE(CCSD(T), μ-$2H_2O$) extrapolated, BE(DFT, μ-$2H_2O$), BE(DFT, ice), and finally the corrected BE(ONIOM2)) of the ONIOM2 correction done with the extrapolation procedure already described in Section 2.

Appendix B
Crystalline Adsorption Geometries

The final optimized structures, together with BEs and structural properties for every molecule in our set, are presented in this appendix (see, e.g., Figure 16). For some notable cases, more than one initial structure has been modeled. All energetic quantities are in kelvin (K), while distances are in Å. For every molecule, the gas-phase optimized geometry and its ESP map are also presented. In the latter, the isovalue for the electron density is set equal to 1×10^{-6} au, while the values for the ESP (again in au) vary case by case and thus are reported close to the RGB scale legend.

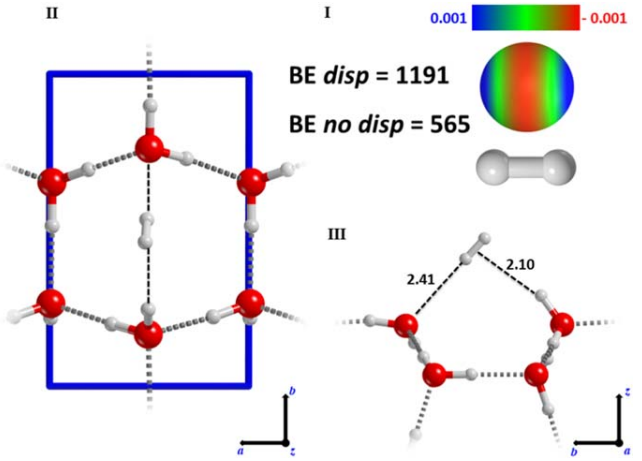

Figure 16. I) Representation of the hydrogen (H_2) molecule along with its ESP surface, BSSE-corrected binding energies (*BE*) with (*disp*) and without (*no disp*) dispersion. II) Top view of H_2-(010) P-ice surface interaction (unit cell highlighted in blue). III) Detail of the side view.

(The complete figure set (23 images) is available.)

Appendix C
Surface Distortion Energy on ASW

In Table 8 we present the distortion energy contributions calculated on the amorphous slab that will be compared with the same contributions calculated on the (010) P-ice model for some notable cases.

Table 8
Comparison of the Distortion Energy Contributions (in Kelvin) Calculated on the (010) P-ice Slab and the Mean Value of These Contributions Calculated on the Different Adsorption Cases on the Amorphous Ice Model

Species	δE_s Crystalline Ice	$\langle \delta E_s \rangle$ Amorphous Ice
CH_3OH	662	2790
H_2O	565	3211
HCN	589	1299
HCOOH	878	1660
NH_3	734	1082

Appendix D
Basis Set A-VTZ*

In Tables 9–14 we provide the basis sets in CRYSTAL17 format, used for H, C, N, O, S, and Cl atoms, respectively.

Table 9
Basis Set for the H Atom in CRYSTAL17 Format Used in This Work

H	0		
S	3	1	
		34.06134	6.03E-03
		5.123575	4.50E-02
		1.164663	0.201897
S	1		
		0.32723	1
S	1		
		0.103072	1
P	1		
		0.8	1

Table 10
Basis Set for the C Atom in CRYSTAL17 Format Used in This Work

C	0		
S	5	1	
		8506.038	5.34E−04
		1275.733	4.13E−03
		290.3119	2.12E−02
		82.0562	8.24E−02
		26.47964	0.240129
S	1		
		9.241459	1
S	1		
		3.364353	1

Table 10
(Continued)

C	0		
S	1		
		0.871742	1
S	1		
		0.363524	1
S	1		
		0.128731	1
P	4		
		34.7095	5.33E−03
		7.959088	3.59E−02
		2.378697	0.142003
		0.815401	0.342031
P	1		
		0.289538	1
P	1		
		0.100848	1
D	1		
		1.6	1
D	1		
		0.4	1

Table 11
Basis Set for the N Atom in CRYSTAL17 Format Used in This Work

N	0		
S	5	1	
		11913.42	−5.23E−04
		1786.721	−4.04E−03
		406.5901	−2.08E−02
		114.9253	−8.12E−02
		37.10588	−0.23871
S	1		
		12.97168	1
S	1		
		4.730229	1
S	1		
		1.252518	1
S	1		
		0.512601	1
S	1		
		0.179397	1
P	4		
		49.21876	5.55E−03
		11.34894	3.81E−02
		3.428509	0.149414
		1.179951	0.348982
P	1		
		0.417261	1
P	1		
		0.142951	1
D	1		
		2	1
D	1		
		0.5	1

Table 12
Basis Set for the O Atom in CRYSTAL17 Format Used in This Work

O	0		
S	5	1	
		15902.65	5.15E−04
		2384.954	3.98E−03
		542.7196	2.05E−02
		153.4041	8.03E−02
		49.54572	0.237668
S	1		
		17.33965	1
S	1		
		6.330336	1
S	1		
		1.699588	1
S	1		
		0.689545	1
S	1		
		0.23936	1
P	4		
		63.27052	6.07E−03
		14.62331	4.19E−02
		4.448952	0.161569
		1.528151	0.356828
P	1		
		0.529973	1
P	1		
		0.175094	1
D	1		
		2.4	1
D	1		
		0.6	1

Table 13
Basis Set for the S Atom in CRYSTAL17 Format Used in This Work

S	0		
S	5		
		103954	2.47E−04
		15583.79	1.92E−03
		3546.129	9.96E−03
		1002.681	4.04E−02
		324.9029	0.130675
S	1		
		115.5123	1
S	2		
		44.52821	0.504036
		18.39789	0.230681
S	1		
		5.510068	1
S	1		
		2.125987	1
S	1		
		0.436919	1
S	1		
		0.157309	1
P	5		
		606.6937	2.32E−03
		143.507	1.86E−02
		45.74616	8.60E−02
		16.87291	0.252484
		6.63992	0.446327
P	1		
		2.672714	1
P	1		
		1.000009	1
P	1		
		0.354389	1
P	1		
		0.116713	1
D	1		
		1.1	1
D	1		
		0.275	1

Table 14
Basis Set for the Cl Atom in CRYSTAL17 Format Used in This Work

Cl	0		
S	5		
		117805.8	2.42E−04
		17660.27	1.87E−03
		4018.597	9.74E−03
		1136.223	3.95E−02
		368.1206	0.127972
S	1		
		130.8615	1
S	2		
		50.47901	0.428741
		20.91681	0.196685
S	1		
		6.353139	1
S	1		
		2.494801	1
S	1		
		0.543359	1
S	1		
		0.194344	1
P	5		
		681.0688	2.37E−03
		161.1136	1.89E−02
		51.38664	8.78E−02
		18.95851	0.257074
		3.003516	0.371524
P	1		
		7.456529	1
P	1		
		1.060936	1
P	1		
		0.39452	1
P	1		
		0.133233	1
D	1		
		1.3	1
D	1		
		0.325	1

ORCID iDs

Stefano Ferrero https://orcid.org/0000-0001-7819-7657
Lorenzo Zamirri https://orcid.org/0000-0003-0219-6150
Cecilia Ceccarelli https://orcid.org/0000-0001-9664-6292
Arezu Witzel https://orcid.org/0000-0003-0518-944X
Albert Rimola https://orcid.org/0000-0002-9637-4554
Piero Ugliengo https://orcid.org/0000-0001-8886-9832

References

Acharyya, K., & Herbst, E. 2017, ApJ, 850, 105
Al-Halabi, A., & Van Dishoeck, E. 2007, MNRAS, 382, 1648
Ásgeirsson, V., Jónsson, H., & Wikfeldt, K. 2017, JPCC, 121, 1648
Bahr, S., Toubin, C., & Kempter, V. 2008, JChPh, 128, 134712
Balucani, N., Ceccarelli, C., & Taquet, V. 2015, MNRAS: Letters, 449, L16
Bartlett, R. J., & Musiał, M. 2007, RvMP, 79, 291
Becke, A. D. 1988, JChPh, 88, 2547
Becke, A. D. 1993, JChPh, 98, 1372
Bennett, C. J., & Kaiser, R. I. 2007, ApJ, 661, 899
Bergin, E. A., Alves, J., Huard, T., & Lada, C. J. 2002, ApJ, 570, L101
Boogert, A. A., Gerakines, P. A., & Whittet, D. C. 2015, ARA&A, 53, 541
Borden, W. T., Hoffmann, R., Stuyver, T., & Chen, B. 2017, JACS, 139, 9010
Boys, S. F., & Bernardi, F. 1970, MolPh, 19, 553
Broyden, C. G. 1970, JApMa, 6, 76
Casassa, S. 2000, ChPhL, 321, 1
Casassa, S., Ugliengo, P., & Pisani, C. 1997, JChPh, 106, 8030
Chaabouni, H., Diana, S., Nguyen, T., & Dulieu, F. 2018, A&A, 612, A47
Codella, C., Ceccarelli, C., Bottinelli, S., et al. 2011, ApJ, 744, 164

Collings, M. P., Anderson, M. A., Chen, R., et al. 2004, MNRAS, 354, 1133
Cramer, C. 2002, Essentials of Computational Chemistry (New York: Wiley)
Cuppen, H., Walsh, C., Lamberts, T., et al. 2017, SSRv, 212, 1
Cutini, M., Civalleri, B., Corno, M., et al. 2016, JCTC, 12, 3340
Cutini, M., Civalleri, B., & Ugliengo, P. 2019, ACS Omega, 4, 1838
Cutini, M., Corno, M., & Ugliengo, P. 2017, JCTC, 13, 370
Dapprich, S., Komáromi, I., Byun, K. S., Morokuma, K., & Frisch, M. J. 1999, JMoSt, 461, 1
Das, A., Sil, M., Gorai, P., Chakrabarti, S. K., & Loison, J.-C. 2018, ApJS, 237, 9
Davidson, E. R., & Feller, D. 1986, ChRv, 86, 681
Dohnalek, Z., Kimmel, G. A., Joyce, S. A., et al. 2001, JPhCB, 105, 3747
Douglas, A., & Herzberg, G. 1942, CJRes, 20, 71
Dovesi, R., Erba, A., Orlando, R., et al. 2018, Wiley Interdiscip Rev Comput Mol Sci, 8, e1360
Dulieu, F., Amiaud, L., Congiu, E., et al. 2010, A&A, 512, A30
Dulieu, F., Congiu, E., Noble, J., et al. 2013, NatSR, 3, 1338
Dunning, T. H., Jr 1989, JChPh, 90, 1007
Enrique-Romero, J., Álvarez-Barcia, S., Kolb, F., et al. 2020, MNRAS, 493, 2523
Enrique-Romero, J., Rimola, A., Ceccarelli, C., et al. 2019, ACS Earth Space Chem, 3, 2158
Fayolle, E. C., Balfe, J., Loomis, R., et al. 2016, ApJL, 816, L28
Fletcher, R. 1970, ComJ, 13, 317
Frisch, M., Trucks, G., Schlegel, H., et al. 2009, Gaussian 09 (Wallingford, CT: Gaussian, Inc.), 121, 150
Goldfarb, D. 1970, MaCom, 24, 23
Grimme, S., Antony, J., Ehrlich, S., & Krieg, H. 2010, JChPh, 132, 154104
Grimme, S., Ehrlich, S., & Goerigk, L. 2011, JCoCh, 32, 1456
He, J., Acharyya, K., & Vidali, G. 2016, ApJ, 825, 89
Hiraoka, K., Miyagoshi, T., Takayama, T., Yamamoto, K., & Kihara, Y. 1998, ApJ, 498, 710
Hohenberg, P., & Kohn, W. 1964, PhRv, 136, B864
Hollenbach, D., & Salpeter, E. 1971, ApJ, 163, 155
Horn, A. B., Chesters, M. A., S, M. M. R., & Sodeau, J. R. 1992, Journal of Chemical Society Faraday Transaction, 88, 1077
Jansen, H., & Ros, P. 1969, ChPhL, 3, 140
Jones, A. 2013, A&A, 555, A39
Jones, A., Köhler, M., Ysard, N., Bocchio, M., & Verstraete, L. 2017, A&A, 602, A46
Kama, M., Caux, E., López-Sepulcre, A., et al. 2015, A&A, 574, A107
Karssemeijer, L., & Cuppen, H. 2014, A&A, 569, A107
Karssemeijer, L., de Wijs, G., & Cuppen, H. 2014, PCCP, 16, 15630
King, D. A. 1975, SurSc, 47, 384
Kraus, P., & Frank, I. 2018, JPCA, 122, 4894
Lee, C., Yang, W., & Parr, R. G. 1988, PhRvB, 37, 785
Liu, B., & McLean, A. 1973, JChPh, 59, 4557
Martín-Doménech, R., Caro, G. M., Bueno, J., & Goesmann, F. 2014, A&A, 564, A8
McElroy, D., Walsh, C., Markwick, A., et al. 2013, A&A, 550, A36
McGuire, B. A. 2018, ApJS, 239, 17
McKellar, A. 1940, PASP, 52, 187
Minissale, M., Dulieu, F., Cazaux, S., & Hocuk, S. 2016, A&A, 585, A24
Neufeld, D. A., & Wolfire, M. G. 2009, ApJ, 706, 1594
Noble, J., Congiu, E., Dulieu, F., & Fraser, H. 2012, MNRAS, 421, 768
Novoa, J., & Sosa, C. 1995, JPCh, 99, 15837
Oba, Y., Miyauchi, N., Hidaka, H., et al. 2009, ApJ, 701, 464
Oba, Y., Watanabe, N., Hama, T., et al. 2012, ApJ, 749, 67
Öberg, K. I., van Dishoeck, E. F., & Linnartz, H. 2009, A&A, 496, 281
Olanrewaju, B. O., Herring-Captain, J., Grieves, G. A., Aleksandrov, A., & Orlando, T. M. 2011, JPCA, 115, 5936
Pack, J. D., & Monkhorst, H. J. 1977, PhRvB, 16, 1748
Pagani, L., Bourgoin, A., & Lique, F. 2012, A&A, 548, L4
Pantaleone, S., Enrique-Romero, J., Ceccarelli, C., et al. 2020, ApJ, 897, 56
Papajak, E., Zheng, J., Xu, X., Leverentz, H. R., & Truhlar, D. G. 2011, JCTC, 7, 3027
Pascale, F., Zicovich-Wilson, C. M., Lopez Gejo, F., et al. 2004, JCoCh, 25, 888
Peng, R., Yoshida, H., Chamberlin, R. A., et al. 2010, ApJ, 723, 218
Penteado, E., Walsh, C., & Cuppen, H. 2017, ApJ, 844, 71
Pople, J. A., Gill, P. M., & Handy, N. C. 1995, IJQC, 56, 303
Raut, U., Famá, M., Teolis, B., & Baragiola, R. 2007, JChPh, 127, 204713
Redaelli, E., Bizzocchi, L., Caselli, P., et al. 2019, A&A, 629, A15
Redhead, P. A. 1962, Vacuu, 12, 203
Rimola, A., Civalleri, B., & Ugliengo, P. 2008, Langm, 24, 14027
Rimola, A., Skouteris, D., Balucani, N., et al. 2018, ACS Earth Space Chem, 2, 720
Rimola, A., Taquet, V., Ugliengo, P., Balucani, N., & Ceccarelli, C. 2014, A&A, 572, A70
Schäfer, A., Horn, H., & Ahlrichs, R. 1992, JChPh, 97, 2571
Schilke, P., Phillips, T., & Wang, N. 1995, ApJ, 441, 334
Senevirathne, B., Andersson, S., Dulieu, F., & Nyman, G. 2017, MolAs, 6, 59
Shanno, D. F. 1970, MaCom, 24, 647
Shimonishi, T., Nakatani, N., Furuya, K., & Hama, T. 2018, ApJ, 855, 27
Skouteris, D., Balucani, N., Ceccarelli, C., et al. 2018, ApJ, 854, 135
Smith, R. S., May, R. A., & Kay, B. D. 2016, JPCB, 120, 1979
Song, L., & Kästner, J. 2017, ApJ, 850, 118
Sorrell, W. H. 2001, ApJL, 555, L129
Sure, R., & Grimme, S. 2013, JCoCh, 34, 1672
Svanberg, M., Pettersson, J. B. C., & K, B. 2000, JPCA, 104, 5787
Swings, P., & Rosenfeld, L. 1937, ApJ, 86, 483
Tafalla, M., Myers, P. C., Caselli, P., & Walmsley, C. M. 2004, A&A, 416, 191
Tasker, P. 1979, JPhC, 12, 4977
Tatewaki, H., & Huzinaga, S. 1980, JCoCh, 1, 205
Tentscher, P. R., & Arey, J. S. 2013, JCTC, 9, 1568
Terada, H., & Tokunaga, A. T. 2012, ApJ, 753, 19
Tosoni, S., Pascale, F., Ugliengo, P., et al. 2005, MolPh, 103, 2549
Ugliengo, P., & Damin, A. 2002, ChPhL, 366, 683
Wakelam, V., Loison, J.-C., Herbst, E., et al. 2015, ApJS, 217, 20
Wakelam, V., Loison, J.-C., Mereau, R., & Ruaud, M. 2017, MolAs, 6, 22
Ward, M. D., Hogg, I. A., & Price, S. D. 2012, MNRAS, 425, 1264
Watanabe, N., & Kouchi, A. 2002, ApJL, 571, L173
Watanabe, N., & Kouchi, A. 2008, PrSS, 83, 439
Zamirri, L., Casassa, S., Rimola, A., et al. 2018, MNRAS, 480, 1427
Zamirri, L., Corno, M., Rimola, A., & Ugliengo, P. 2017, ACS Earth Space Chem, 1, 384
Zamirri, L., Pantaleone, S., & Ugliengo, P. 2019a, JChPh, 150, 064702
Zamirri, L., Ugliengo, P., Ceccarelli, C., & Rimola, A. 2019b, ACS Earth Space Chem, 3, 1499
Zhao, Y., & Truhlar, D. G. 2008, Theor Chem Acc, 120, 215
Zicovich-Wilson, C., Pascale, F., Roetti, C., et al. 2004, JCoCh, 25, 1873